

Springer Proceedings in Materials

Zishan Husain Khan  
Mark Jackson  
Numan A. Salah *Editors*

# Recent Advances in Nanotechnology

Select Proceedings of ICNOC 2022

 Springer

# Springer Proceedings in Materials

Volume 28

## Series Editors

Arindam Ghosh, Department of Physics, Indian Institute of Science, Bangalore, India

Daniel Chua, Department of Materials Science and Engineering, National University of Singapore, Singapore, Singapore

Flavio Leandro de Souza, Universidade Federal do ABC, Sao Paulo, São Paulo, Brazil

Oral Cenk Aktas, Institute of Material Science, Christian-Albrechts-Universität zu Kiel, Kiel, Schleswig-Holstein, Germany

Yafang Han, Beijing Institute of Aeronautical Materials, Beijing, Beijing, China

Jianghong Gong, School of Materials Science and Engineering, Tsinghua University, Beijing, Beijing, China

Mohammad Jawaid , Laboratory of Biocomposite Technology, INTROP, Universiti Putra Malaysia, Serdang, Selangor, Malaysia

**Springer Proceedings in Materials** publishes the latest research in Materials Science and Engineering presented at high standard academic conferences and scientific meetings. It provides a platform for researchers, professionals and students to present their scientific findings and stay up-to-date with the development in Materials Science and Engineering. The scope is multidisciplinary and ranges from fundamental to applied research, including, but not limited to:

- Structural Materials
- Metallic Materials
- Magnetic, Optical and Electronic Materials
- Ceramics, Glass, Composites, Natural Materials
- Biomaterials
- Nanotechnology
- Characterization and Evaluation of Materials
- Energy Materials
- Materials Processing

To submit a proposal or request further information, please contact one of our Springer Publishing Editors according to your affiliation:

European countries: **Mayra Castro** ([mayra.castro@springer.com](mailto:mayra.castro@springer.com))

India, South Asia and Middle East: **Priya Vyas** ([priya.vyas@springer.com](mailto:priya.vyas@springer.com))

South Korea: **Smith Chae** ([smith.chae@springer.com](mailto:smith.chae@springer.com))

Southeast Asia, Australia and New Zealand: **Ramesh Nath Premnath** ([ramesh.premnath@springer.com](mailto:ramesh.premnath@springer.com))

The Americas: **Michael Luby** ([michael.luby@springer.com](mailto:michael.luby@springer.com))

China and all the other countries or regions: **Mengchu Huang** ([mengchu.huang@springer.com](mailto:mengchu.huang@springer.com))

This book series is indexed in **SCOPUS** database.

Zishan Husain Khan · Mark Jackson ·  
Numan A. Salah  
Editors

# Recent Advances in Nanotechnology

Select Proceedings of ICNOC 2022

 Springer



*Editors*

Zishan Husain Khan  
Department of Applied Sciences  
and Humanities  
Jamia Millia Islamia  
New Delhi, Delhi, India

Mark Jackson  
Department of Engineering Technology  
Kansas State Polytechnic  
Salina, KS, USA

Numan A. Salah  
Centre of Nanotechnology  
King Abdulaziz University  
Jeddah, Saudi Arabia

ISSN 2662-3161

ISSN 2662-317X (electronic)

Springer Proceedings in Materials

ISBN 978-981-99-4684-6

ISBN 978-981-99-4685-3 (eBook)

<https://doi.org/10.1007/978-981-99-4685-3>

© The Editor(s) (if applicable) and The Author(s), under exclusive license to Springer Nature Singapore Pte Ltd. 2023

This work is subject to copyright. All rights are solely and exclusively licensed by the Publisher, whether the whole or part of the material is concerned, specifically the rights of translation, reprinting, reuse of illustrations, recitation, broadcasting, reproduction on microfilms or in any other physical way, and transmission or information storage and retrieval, electronic adaptation, computer software, or by similar or dissimilar methodology now known or hereafter developed.

The use of general descriptive names, registered names, trademarks, service marks, etc. in this publication does not imply, even in the absence of a specific statement, that such names are exempt from the relevant protective laws and regulations and therefore free for general use.

The publisher, the authors, and the editors are safe to assume that the advice and information in this book are believed to be true and accurate at the date of publication. Neither the publisher nor the authors or the editors give a warranty, expressed or implied, with respect to the material contained herein or for any errors or omissions that may have been made. The publisher remains neutral with regard to jurisdictional claims in published maps and institutional affiliations.

This Springer imprint is published by the registered company Springer Nature Singapore Pte Ltd. The registered company address is: 152 Beach Road, #21-01/04 Gateway East, Singapore 189721, Singapore

# Preface

International Conference on Nanotechnology: Opportunities and Challenges (ICNOC-2022) was organized by the Department of Applied Sciences and Humanities, Jamia Millia Islamia, New Delhi during November 28–30, 2022 in virtual mode. The main aim of the conference was to provide platform to the scientists, researchers, academicians and students to discuss their ideas on the opportunities and challenges in the domain of Nanotechnology, and to share and disseminate their research with the delegates joining the conference from all over the world. The underlying motive behind organizing the conference was to share knowledge of the subject among researchers, who are looking for collaborative ventures, empirical learning and innovative technological breakthroughs. More than 45 internationally acclaimed experts from India as well as abroad delivered their talks and 600 participants presented their research outputs in the conference.

The conference was divided into three broad tracks, i.e., Nanoscience and Nanotechnology, Nanotechnology for Energy and Environment and Nanotechnology for Medical Sciences. The presentation under the track ‘Nanoscience and Nanotechnology’ were focused on the research works carried out to understand the science behind the novel nanoscale materials and systems. The understanding of the behavior of nature at the nanoscale is evolving day by day with the minute observations of the properties of the materials at this scale. The development of knowledge at nanoscale science has opened up new possibilities for the development of more efficient, precise, and effective technologies in various fields. Research outcomes on various topics especially Nanocomposites, Nanofabrication and Nano-engineering, Sensors and Actuators, Nano Electronics, Nano Photonics, Nano Chemistry, Nanoscale Modelling and Simulation and Societal Concerns and Ethical Issues were disseminated in the different technical sessions under this track.

Energy and environmental issues are closely linked as the production and use of energy often have significant impacts on the environment. Nanotechnology has the potential to revolutionize the field of energy and environment. Through the manipulation of materials at the nanoscale, new solutions for global challenges such as energy production, storage, and conservation can be created. In the area of energy production, nanomaterials can be used to improve the efficiency of solar cells and

fuel cells. Nanoscale thermoelectric materials can also be utilized for waste heat recovery. Energy storage can also benefit from nanotechnology, as nanomaterials can be used to develop more efficient and high-capacity batteries, supercapacitors, and hydrogen storage. Nanomaterials can also contribute to energy conservation, as they can be used to improve the efficiency of lighting, insulation, and windows. In the area of pollution control and remediation, nanomaterials can be used for air and water purification, as well as soil remediation. Keeping in mind the importance of this area of research, we dedicated one of the three tracks of ICNOC-2022 to the applications for Nanotechnology and Environment. Several topics in this domain were covered in the conference especially Renewable Energy, Hydrogen Production, Storage and Transportations, Energy Generation and Storage, Solar Cells, Fuel Cells, Batteries and Supercapacitor and Water treatment and filtration.

The Nanotechnology has significant potential in medical science and can contribute to transforming healthcare by creating innovative solutions for diagnosis, treatment, and prevention. By designing and manipulating materials at the nanoscale, researchers can develop new tools and devices that can interact with biological systems in novel ways. Nanotechnology can be utilized in many areas of medical science, including medical imaging, drug delivery, tissue engineering, and regenerative medicine. Nanoscale imaging agents can provide high-resolution images of internal organs and tissues for early detection and diagnosis of diseases. Nanoparticles can be used to deliver drugs precisely to targeted cells or tissues, which can improve the efficacy of treatments while reducing side effects. In tissue engineering and regenerative medicine, nanomaterials can be used to create scaffolds that mimic the structure and function of natural tissues, promoting the regeneration of damaged or diseased tissues. Nanoparticles can be utilized to deliver growth factors and other signaling molecules that stimulate tissue regeneration. Nanotechnology can also be used to develop advanced prosthetics and medical implants. Nanotechnology can also contribute to disease prevention through the development of vaccines and nanoscale sensors that can detect and respond to pathogens. In cancer treatment, nanotechnology-based therapies can deliver therapeutic agents directly to cancer cells while minimizing damage to healthy cells. In ICNOC-2022, a track on nanotechnology for medical science was created to bring together researchers, scientists, and professionals from various fields to discuss the latest advances, opportunities, and challenges in this field. The major topics included in this track were Nanomaterial for denture applications, Nanotechnology in medicine, Medicinal Nano-chemistry, Nano biosensors, Targeted cellular therapies, Nanomedicine-fusing therapy and diagnostics, Regenerative medicine and tissue engineering and Nanoscale formulation and targeted drug delivery systems.

The conference was organized with 1 inaugural session, 3 planetary sessions and 71 technical sessions (4 parallel sessions at a time). We received more than 1000 abstract altogether, out of which 600 were selected for the presentation in the conference after a peer review. Full papers were invited from participants who presented their work in the conference and out of 500 manuscripts, we accepted 181 papers for the publication in these proceedings after a strict peer review process based on the originality of work, novelty of research and scientific relevance of the research

outcomes. This proceeding is the balanced mix of the topics from all the three tracks of the conference and readers will be benefited from the research outcomes on the recent applications of Nanotechnology in different areas of these domains.

We hope this proceedings will serve as a source of inspiration and knowledge for all those who read it, and that it will encourage them to explore the fascinating domain of Nanotechnology further.

New Delhi, India  
Jeddah, Saudi Arabia  
Salina, USA

Prof. Zishan Husain Khan  
Prof. Numan A. Salah  
Prof. Mark Jackson

# Contents

<b>Design of Hetero-Dielectric Single-Metal Gate-All-Around MOSFET with Schottky Contact Source/Drain</b> .....	1
Ram Devi and Gurpurneet Kaur	
<b>The Optimization of Perovskite/CuSCN Solar Cell with SnO<sub>2</sub> Electron Transport Layer Using SCAPS-1D</b> .....	11
Shivani Chauhan and Rachna Singh	
<b>Metal/Polymeric Hierarchical Platform as Biosensor</b> .....	17
Shahzad Ahmed, Arshiya Ansari, Moin Ali Siddiqui, and Pranay Ranjan	
<b>Inexpensive Fabrication of Visible Dielectric Reflector for Improving the Performance of Visible Light Communication</b> .....	25
Yepuri Venkatesh, K. Balamurugan, and Bandaru Bhargav Santosh	
<b>Controllable Fast and Slow Light in a Quadratically Coupled Optomechanical System Assisted by Quantum Dot Molecules</b> .....	33
Sonam Mahajan, Neha Aggarwal, Madhav Kumar Singh, and Aranya B. Bhattacharjee	
<b>Performance Analysis of NiO/Ch<sub>3</sub>Nh<sub>3</sub>GeI<sub>3</sub>/SnO<sub>2</sub> Perovskite Solar Cell Using SCAPS 1D</b> .....	41
Chandni Tiwari and Varun Mishra	
<b>Enhanced Biodiesel Production from Waste Cooking Oil Using ZnO Nanocatalyst</b> .....	47
P. Gada, S. K. Dusi, and I. Abrar	
<b>Energy Conservation in the Vapour Compression Refrigeration System Using Nanorefrigerant</b> .....	55
S. S. Sanukrishna and S. Reshmi Krishnan	
<b>Facile Synthesis of Highly Fluorescent N-CQDs and Its Application for Dye Degradation and Sensing of Cr<sup>3+</sup></b> .....	61
Qurtulen and Anees Ahmad	

<b>TiO<sub>2</sub>/PEDOT: PSS Hybrid Matrix for Optoelectronic Devices</b> .....	67
Arshiya Ansari, Shahzad Ahmed, Moin Ali Siddiqui, Devendra Singh Negi, and Pranay Ranjan	
<b>Ag@CuO Nanohybrid-Based Electrochemical Biosensor for Trichlorfon Detection</b> .....	75
Saroj Paneru and Devendra Kumar	
<b>Novel Thermoelectric Material Ba<sub>2</sub>AlNbO<sub>6</sub> for Energy Harvesting Applications</b> .....	85
Mudasir Younis Sofi, Mohd. Shahid Khan, Javid Ali, and M. Ajmal Khan	
<b>Two-Dimensional Si<sub>2</sub>BNO<sub>4</sub>: A Potential Material for Optoelectronic Applications—An <i>Ab-Initio</i> Study</b> .....	93
Santy M. Thomas and P. Ravindran	
<b>Numerical Study of Perovskite Solar Cells Using DFT-Extracted Parameters of Lead-Free CsGeX<sub>3</sub> (X = I, Br) Light Absorbing Material</b> .....	101
Joy Sarkar and Suman Chatterjee	
<b>Affinity Optimization of Commercially Available Crystalline-Silicon Heterojunction Solar Cell by Using AFORS-HET Software</b> .....	111
Naima, Pawan K. Tyagi, and Vinod Singh	
<b>Theoretical Investigation by Density Functional Theory and Molecular Docking of a Naturally Occurring Anticancer Drug: 9-Hydroxyellipticine</b> .....	117
Abhinav Mishra, Dipendra Sharma, and Sugriva Nath Tiwari	
<b>Antimicrobial and Antibiofilm Activity of Silver Nanoparticles Derived from <i>Prolinoborus fasciculus</i> Against Multi-drug-resistant <i>K. pneumoniae</i> and <i>E. faecium</i>, Isolated from Effluent Samples</b> .....	125
Kunal Madhav and Archana Pandita	
<b>Design and Simulation of Pure CNTFET-OTA-Based Low-Pass Filters</b> .....	137
Maryam Raza, Imran Ahmed Khan, and M. Nizamuddin	
<b>Intrinsic Growth Challenges in Pulsed Laser-Deposited Al<sub>2</sub>O<sub>3</sub>/ TiO<sub>2</sub> Subnanometric Laminates as a Potential Dielectric Material for High-Density Storage Applications</b> .....	143
P. S. Padhi, S. K. Rai, R. S. Ajimsha, and P. Misra	
<b>Infrared Absorption in Silicon Nanostructure-Patterned Absorber</b> .....	149
Rangeeta Dhaka, Shankar Dutta, and A. K. Shukla	

<b>Exploring Eco-friendly Nanocellulose-Based Hydrogel Membranes as Flexible and Biocompatible Electrolyte in Supercapacitors</b> .....	155
Mohammed Saquib Khan, Shivani, Nikita Bhardwaj, Preeti Shakya, Deependra Jhankal, Malay Kumar Banerjee, and Kanupriya Sachdev	
<b>SCAPS-Based Analysis of ZrS<sub>2</sub>/CZTS/MoS<sub>2</sub>/Si Tandem Solar Cell Parameters</b> .....	163
Shubhra Gupta, Gayatri Shishodia, and P. K. Shishodia	
<b>Interaction of NO Gas Molecules with the Edges of Armchair ZnO Nanoribbons for Designing Nanosensors</b> .....	169
Kumar Ravindra, Rakesh Ajay Kumar, Govindan Anil, and Jaiswal Neeraj Kumar	
<b>Electrochemical UA Sensor Based on Spherical Shaped Co<sub>3</sub>O<sub>4</sub> Nanostructures</b> .....	175
Sakeena Masrat and Rafiq Ahmad	
<b>Synthesis of Silver Nanoparticles with Different Morphologies for SERS</b> .....	185
Tuiba Mearaj, Shobha Shukla, A. K. Hafiz, Manika Khanuja, R. A. Zargar, and Santosh Chackrabarti	
<b>Electrochemical Study of Reduced Graphene Oxide for Supercapacitor Application</b> .....	191
Deependra Jhankal, Mohammad Saquib Khan, Bhanu, Preeti Shakya, Nikita Bhardwaj, K. K. Jhankal, and K. Sachdev	
<b>Ultrathin and Flexible Gas Sensor Based on Monolayer Graphene for Environmental Monitoring</b> .....	197
Preeti Shakya, Mohammed Saquib Khan, Nikita Bhardwaj, Deependra Jhankal, Nisha Verma, and Kanupriya Sachdev	
<b>New Prime Number Counter: Design and Performance Analysis Using CMOS and Carbon Nanotubes</b> .....	205
Imran Ahmed Khan, Mudit Wadhwa, Prakhar Mishra, and Puneet Sharma	
<b>Simulation-Based Analysis of Plasma-Assisted Carbon Nanotube Field-Effect Transistor (CNTFET) for Improved Device Metrics and Applications</b> .....	213
Mansha Kansal, Suresh C. Sharma, and Manish K. Kansal	
<b>Raman Spectroscopy as a Potential Tool to Analyze Alzheimer's Disease Progression</b> .....	221
Umesh Chandra Garnaik and Shilpi Agarwal	
<b>Development of Passivation Layer Material for Quantum Dot-Sensitized Solar Cells</b> .....	227
Rahul Singh and Ragini Raj Singh	

<b>Thermal and Anti-Leakage Performance of PCM for Thermal Energy Storage Applications</b> .....	235
J. S. Aulakh and D. P. Joshi	
<b>Molecular Hydrogen Storage in Stone–Wales Defected Single-Walled Carbon Nanotubes Using Molecular Dynamics Simulation</b> .....	243
Saurabh Mishra and S. I. Kundalwal	
<b>0.9 V Graphene Transistor Based Triple Cascode Operational Transconductance Amplifier: A Comparative Analysis</b> .....	249
Faraz Hashmi, M. Nizamuddin, and Adil Zaidi	
<b>Enhanced Photocatalytic Activity of Hydrothermally Synthesized Nanostructured Monoclinic BiVO<sub>4</sub> Nanosheets</b> .....	255
Farheen Jahan, Waseem Ashraf, A. M. Siddiqui, and Manika Khanuja	
<b>Biomass Derived Fluorescent Nanocarbon Sensor for Effective Sensing of Toxic Cadmium Metal Ions</b> .....	265
Joseph Neethu, Mathew Aleena Ann, and Balachandran Manoj	
<b>Design, Simulation, and Comparative Study of CNTFET-Based Folded Cascode Op-Amp with Class AB Output Buffer and Gain Enhancement</b> .....	271
Zoya Ali, M. Nizamuddin, and Dinesh Prasad	
<b>Photoelectrochemical Response of Titania Photoanode Fabricated via Microwave Irradiation</b> .....	277
Asmat Hassan, Arshid Mir, Asif Majeed, Reyaz Ahmad, Malik Aalim, Aamir Sohail, Ab Mateen, and M. A. Shah	
<b>Study of Interaction Between Insulin and ZnO Micro-nano Particles Using Dielectric Characterization</b> .....	283
Urvashi Singh, Zeeshan Saifi, Mridul Kumar, and Soami Daya Krishnananda	
<b>Simulation of Highly Effective Eco-Friendly Inorganic Perovskite Solar Cell Using SCAPS-1D</b> .....	291
Vaibhava Srivastava, R. K. Chauhan, and Pooja Lohia	
<b>Photonic Crystal Fiber-Based Biosensor for Sensitive Detection of Breast Cancer Cells in THz Regime</b> .....	297
Sapana Yadav, Pooja Lohia, and D. K. Dwivedi	
<b>Performance Evaluation of Eco-Friendly (FA)<sub>2</sub>BiCuI<sub>6</sub> Double Perovskite Solar Cell for High Efficiency</b> .....	303
Shivangi Yadav, Anupam Sahu, and Pooja Lohia	



<b>Effect of NiO Hole Transport Layer Thickness on the Power Conversion Efficiency of Perovskite Solar Cell: A Numerical Simulation Study</b> .....	309
Saumya Vaish and Shiv Kumar Dixit	
<b>Visible-Light-Assisted Photocatalytic Degradation of Methyl Orange Using La–Ag<sub>3</sub>PO<sub>4</sub>/ZnO as Photocatalyst</b> .....	315
Neenamol John, P. S. Samjeev, Bony K. John, and Beena Mathew	
<b>CNTFET Folded Cascade Operational Transconductance Amplifier: Design and Comparative Analysis</b> .....	323
Mir Bintul Islam and M. Nizamuddin	
<b>Antibacterial Effect of Phosphorous-Doped Carbon Nanomaterial Derived from <i>Alstonia Venenata</i></b> .....	327
Meera Varghese, Kaviya Parambath Kootery, Suma Sarojini, and Manoj Balachandran	
<b>Comparative Study for Supercapacitive Performance of Polypyrrole Matrix Reinforced with Different Organic Fillers</b> .....	333
Sarfraz Ansari, Gobind Mandal, Debashish Nayak, Sanjeev Kumar, Jayanta Bauri, and Ram Bilash Choudhary	
<b>Sustainable Water Splitting Using Nanotechnology for Hydrogen Production: A Review</b> .....	341
Md. Merajul Islam, Neha Saxena, and Amina Nafees	
<b>Effect of Different Current Collectors on Electrochemical Performance of Activated Carbon-Based Supercapacitor</b> .....	347
Ritu Jangra, Manoj Karakoti, Poonam Mahendia, N. G. Sahoo, O. P. Sinha, and Suman Mahendia	
<b>Polymer-Based Nanomaterial as a Bacteriostatic Agent on Gram-Positive Bacteria</b> .....	353
Sooraj Anto Dennis, A. V. Sudhamshu, Aleena Ann Mathew, Joselyn Elizabeth Abraham, Elcey C. Daniel, and Balachandran Manoj	
<b>Nanotechnology for Water Treatment and Filtration</b> .....	359
Mehreen Shah	
<b>Evaluation of Treatment Performance and Development of Aerobic Granular Sludge in A/O/A Mode Sequencing Batch Reactor Fed with Sewage</b> .....	363
Mohd Rayaz, Mohammad Waqqas Mirza, Fehmeeda Khatoun, and Abid Ali Khan	
<b>First and Second Law Analyses of an Organic Rankine Cycle to Recover the Waste Heat from the Solar-Operated Combined Cycle Power Plants with Grid</b> .....	369
Wasim Akram, Mohd Parvez, Khwaja M. Rafi, and Osama Khan	

<b>Nanotechnological Advancements in Sports Rehabilitation to Elevate Athletic Performance Levels</b> .....	377
Adil Ali Ansari	
<b>An Electrochemical Ascorbic Acid Sensor Constructed by Ferrocene Palladium Nanoparticles Modified Graphite</b> .....	383
Kulveer Singh, Chitra Singh, and Manisha Malviya	
<b>Bimetallic Heterogeneous Catalysis for Oxygen Evaluation Reaction with Varying Concentrations of Silica</b> .....	389
Chitra Singh and Kulveer Singh	
<b>Rational Designing of Ni-Ag/C Bimetallic Nanoparticles</b> .....	395
Samika Anand and K. R. Sunaja Devi	
<b>Fabrication of Two-Dimensional MoS<sub>2</sub> Thin Film Using Chemical Vapor Deposition (CVD) for Gas Sensing Application</b> .....	403
Priyanka Berwal, Paul Singh, Suman Rani, Smriti Sihag, Sunil Kumar, Anushree Jatrana, Amit Kumar Gangwar, and Vinay Kumar	
<b>Performance Evaluation of CNT FET with High-K Dielectric</b> .....	409
Md Akram Ahmad and Jitendra Kumar	
<b>Employing Temperature-Dependent Photoluminescence of Tin Oxide (SnO<sub>2</sub>) Nanostructures for Designing of Efficient Light-Emitting Diodes</b> .....	415
Mohd Azharuddin and Rana Tabassum	
<b>Improvement of Thermal Resistivity of Brick/AAC Block Wall Using Air Encapsulated Clay Tile</b> .....	425
Sabista Siddiqui, Mohammad Danish, and Ibrar Ahmed	
<b>Structural and Electrochemical Characterizations of Sodium Doped Bimetallic Layered Nanocomposite for Sodium-Ion Capacitors</b> .....	431
Yamini Gupta, Poonam Siwatch, Shweta Rana, Reetika Karwasra, Kriti Sharma, and S. K. Tripathi	
<b>Dynamics of Double Nitrogen-Vacancy Centre in a Photonic Crystal Nanocavity: Optical Bistability and Four-Wave Mixing</b> .....	439
Tarun Kumar, Samantha Rath, and A. B. Bhattacharjee	
<b>Exploitation of <i>Carica papaya</i> Seeds for the Fabrication of Titanium Dioxide Nanoparticles and Determination of Their Antibacterial and Antidiabetic Potential</b> .....	451
Tabassum Siddiqui, Nida Asif, and Nida Jamil Khan	
<b>Development of a Nanocarrier for Plant-Derived Drug</b> .....	457
Tajunisa Munasuddin and Reshmi Nair	

<b>Recombination Analysis of <math>\text{CH}_3\text{NH}_3\text{PbI}_3</math> Perovskite Solar Cell for Optimized Device Structure</b> .....	465
Mohd Amir, Mukesh Pratap Singh, and Iram Masood	
<b>Comparative Analysis on Crystallographic Presentation of <math>\text{WS}_2</math> Polymorphs by VESTA Software</b> .....	471
Somveer, Davender Singh, and Dharamvir Singh Ahlawat	
<b>Titanium Dioxide Nanofillers Incorporated Glass Ionomer Cement with Carboxymethyl Chitosan for Superior Mechanical Properties</b> .....	477
Preety Kumari Kashyap, Jyoti Gupta, Bharath Govind, and Sunita Rattan	
<b>Synthesis of Curcumin Loaded Mesoporous Silica Nanoparticles for Anti-cancer Drug Delivery</b> .....	485
Harsha Gautam, Sameeksha Luthra, Aakanksha Chhokra, Saumya Anand, Prashant Kumar, Reshma Sinha, Sunil Kumar, Ravi Kumar, Manoj Kumar Khanna, and Daya Bhardwaj	
<b>Role of Grain Boundaries Governing the Giant Dielectric Constant in Bulk <math>\text{SnO}_2</math></b> .....	491
Shweta Dhiman, Nirmal Manyani, and S. K. Tripathi	
<b>Removal of Cationic and Anionic Dyes from Aqueous Phase by Biosynthesized Nickel Nanoparticles</b> .....	497
Harshvardhan Chauhan, Mohd Saquib Tanweer, and Masood Alam	
<b>Comparative Performance Analysis of Lead-Free Perovskite Solar Cell with Different Electron Transport Layer</b> .....	505
Jaiswal Vivek, Jha Kaushal, and Rawat Kusum	
<b>Printed Carbon Film-Based Self-Powered Triboelectric Nanogenerator as Flexible Tactile Sensor</b> .....	511
Pramila Viswanathan and Arunkumar Chandrasekhar	
<b>Heterogeneous Oxidation of Alcohols Catalyzed by Titania-Supported Palladium Nanoparticles in Aqueous Micellar Solution</b> .....	517
Ranjan Kumar Padhy and Sarita Sahu	
<b>Application of Salts, Alkalis, and Nanoparticles for Reducing Adsorption Loss of Anionic Surfactant for the Application in Enhanced Oil Recovery (EOR)</b> .....	529
Neha Saxena and Md. Merajul Islam	
<b>Cost Optimization of a Hybrid Stand-Alone Renewable Energy System for Remotely Located Areas</b> .....	535
Ameer Faisal and Naqui Anwer	

<b>Preparation and Energy Storage Assessment of <math>Ti_3C_2</math> 2d MXene and Its Possible Thinning Mechanism</b> .....	545
Diya Singh, Pinki Rani, Sayani Biswas, and Prashant S. Alegaonkar	
<b>Photocatalytic Approach of <i>Camellia sinensis</i> Extract-Mediated Green-Synthesized Magnesium Oxide Nanoparticles</b> .....	555
Pinky Yadav, Muskan Batra, Nancy Yadav, and Ayana Bhaduri	
<b>IV Characteristics and Subthreshold Slope Analysis of Si and SiGe-Based Dual-Gate MOSFET</b> .....	565
Ashutosh Pandey and Kousik Midya	
<b>Structural and Sensing Properties of <math>Sb_2O_3</math>-Doped Tin Oxide Thick Film Gas Sensor</b> .....	573
Poonam Yadav, Satish Kumar Yadav, Ankit Kumar Vishwakarma, Sesh Mani Yadav, and Lallan Yadava	
<b>Synthesis and Characterization of Highly Luminescent and Stable Cesium Lead Halide Perovskite Nanocrystals for Optoelectronic Applications</b> .....	583
Sultan Ahmad, Mohd. Bilal Khan, Mohammad Salman Khan, Hasan Abbas, Ankur Mishra, Reeba Marry Thomas, Asim Khan, and Zishan Husain Khan	
<b>Facile Synthesis of Lead-Free Mixed Halide Double Perovskite <math>Cs_2AgBiX_6</math> (<math>X = Br, I</math>) Nanocrystals (NCs) for Photovoltaics Applications</b> .....	591
Mohammad Salman Khan, Mohd. Bilal Khan, Sultan Ahmad, Hasan Abbas, Asim Khan, Ankur Mishra, Reeba Marry Thomas, and Zishan Husain Khan	
<b>Integrating Energy Devices for Wearable Electronics</b> .....	599
Sultan Ahmed, Ahsan Ahmed, M. Parvaz, Sultan Ahmad, M. A. Gondal, and Mukesh Pratap Singh	
<b>Enhanced Performance of Nanostructured <math>WSe_2</math> as an Electrode Material for Supercapacitor</b> .....	605
Asim Khan, Waseem Ashraf, Manika Khanuja, and Zishan Husain Khan	

## About the Editors



**Dr. Zishan Husain Khan** is currently a Professor and Head of the Department of Applied Sciences and Humanities, Faculty of Engineering and Technology, Jamia Millia Islamia, New Delhi, India. He obtained his Ph.D. degree from Jamia Millia Islamia, India. He has almost 25 years of research experience in semiconductor physics and nanotechnology. He has published more than 150 research papers in various international reputed journals and guided a number of Ph.D. students. He was a post-doctoral fellow at the Department of Materials Science and Engineering and Centre of Nanoscience and Nanotechnology National Tsing Hua University, Hsinchu, Taiwan from 2001 to 2005. During his postdoctoral research, his work on the fabrication of FET (field effect transistor) using individual (single) carbon nanotube was highly appreciated by the scientific community. His present research interests include hybrid solar cells, OLEDs, transition metals di-chalcogenides, carbonaceous nanomaterials, nano-sensors, and nano-bio sensors.



**Dr. Mark Jackson** is the McCune and Middlekauff Endowed Professor and University Faculty Fellow at Kansas State University, USA. He studied a degree in mechanical and manufacturing engineering at Liverpool Polytechnic. After graduating with the Master of Engineering (M.Eng.) degree with distinction, Dr. Jackson subsequently conducted research for his Ph.D. degree at Liverpool Polytechnic in the field of materials engineering focusing primarily on microstructure-property relationships in vitreous bonded abrasive materials. Dr. Jackson was a research fellow at the Cavendish Laboratory, University of Cambridge, working with Prof. John Field, O.B.E., F.R.S., and Prof. David Tabor, F.R.S., on condensed matter physics and tribology before becoming a lecturer in engineering at the University of Liverpool in 1998. At Liverpool, he attracted a number of research grants concerned with developing innovative manufacturing processes for which he was jointly awarded an Innovative Manufacturing Technology Centre from the Engineering and Physical Sciences Research Council in November 2001. Dr. Jackson was appointed a member of the United Nations Education, Scientific, and Cultural Organization's (UNESCO) International Commission for the Development of the 'Encyclopaedia of Life Support Systems' Theme on 'Nanoscience and Nanotechnologies', and still serves in this capacity. In March 2017, the degree of Doctor of Science (D.Sc.) in mechanical engineering was conferred upon Dr. Jackson in absentia by the congregation for sustained contributions made in the area of mechanical engineering and advanced manufacturing over a period of twenty years.



**Prof. Numan A. Salah** is currently working at the Center of Nanotechnology and Department of Nuclear Engineering, King Abdulaziz University, Saudi Arabia. He obtained his B.Sc. (Physics) from Baghdad University, Iraq, and M.Sc. (Physics) from Jawaharlal Nehru University (JNU), New Delhi, and his Ph.D. in Physics at the University of Delhi, India. He had also worked as a postdoctoral research fellow at the Inter-University Accelerator Center (IUAC), New Delhi. His major areas

of research interests include nanomaterials and their use in dosimetry, water, and energy applications. He has published/granted more than 10 US patents. He has published 153 research papers in respected international journals/conferences.

# Design of Hetero-Dielectric Single-Metal Gate-All-Around MOSFET with Schottky Contact Source/Drain



Ram Devi and Gurpurneet Kaur

**Abstract** One of the most promising device configurations for extending CMOS device scaling is the gate-all-around MOSFET since it provides excellent electrostatic control of the channel. In this work, hetero-dielectric single-metal gate-all-around MOSFETs with Schottky contact source/drain are designed and analyzed using COGENDA Visual TCAD. Through device simulations in a TCAD framework, the electrical properties of the devices, such as ON-current, leakage current, and subthreshold swing, have been examined. The proposed device features an unsymmetrical oxide geometry with Schottky source/drain regions and high-k ( $\text{Hf}_x\text{Ti}_{1-x}\text{O}_2$ ) on the source side (length dimension = 15 nm) and  $\text{SiO}_2$  on the drain side (length dimension = 5 nm), respectively. The design of the suggested device has taken into account physical theories including drift–diffusion, Lombardi mobility, band-to-band tunneling, and the Shockley–Read–Hall carrier recombination process. The proposed device offers reduced OFF-current and suppressed SCEs. Compared to conventional GAA MOSFET, leakage currents are dropped to a level between  $10^{-15}$  and  $10^{-9}$  A. With a subthreshold swing of  $62.7 \text{ mV dec}^{-1}$ , which almost achieves the ideal value, the device exhibits impressive subthreshold region performance. It has exceptionally low static power consumption due to decreased leakages, which makes it ideal for low-voltage and low-power digital execution. According to device modeling analysis, the hetero-dielectric single-metal gate-all-around MOSFET with Schottky contact source/drain is a strong design for convenience in low-power digital circuitry.

**Keywords** Hetero-Dielectric · Schottky contact · Gate all around (GAA)

---

R. Devi (✉) · G. Kaur

Department of Electronics and Communication Engineering, Guru Nanak Dev Engineering College, Ludhiana, Punjab, India

e-mail: [ramdevi14081@gmail.com](mailto:ramdevi14081@gmail.com)



## 1 Introduction

With current-generation technologies having gate widths smaller than 22 nm, silicon technology is still advancing quickly [1]. As one of the more encouraging device configurations for extending CMOS device scaling is the gate-all-around MOSFET since it provides excellent electrostatic control of the channel [2]. A microchip's transistor count doubles about it every two years, as said by Moore's law. A nanowire is a type of nanostructure that has a diameter of around one nanometer ( $10^{-9}$  m). Nanowires often have a changeable length and a thickness or diameter of tens of nanometers or less [3]. Except for the conducting channel being completely encircled by gates, GAA is somewhat comparable to FinFETs. As a result, the gate control-ability over the channel is improved. As we make the switch to nanoscale technology, the transistor density is increasing. As a result, a reduction in transistor size is required, although it reduces device performance. This deterioration is brought on by short-channel impacts which would include subthreshold current and drain-induced barrier lowering. A number of topologies, dual and triple-gate transistors, have been developed, in place of MOSFETs. Gate-all-around designs, as opposed to multi-gate FETs, have demonstrated the ability of reliable channel control via the gate. The best conductivity and electrical properties are offered [4]. These Schottky barrier MOSFETs having metallic source/drain areas have a favorable impact on the massive drop of transistor circuits to the submicron extent [5]. To determine the device's low leakage current and ON-state resistance, the Schottky barrier gap around both the source/drain metal and indeed the intrinsic silicon channel is a crucial measure [6].

When implementing the hetero-dielectric technique, two materials with clearly differing permittivity are put in the gate oxide. On both the source and the drain sides, respectively, low-permittivity and high-permittivity materials are frequently used. Charge carriers are prevented from tunneling from the channel to the gate area, where they were further exceeded by the greater work function of the gate metal, by the material with a greater permittivity on the drain side. Because it prevents charge carriers from tunneling, the additional electric flow at the channel drain contact gets lessened [7]. The creation of a modern technology platform using gate-all-around MOSFETs faces a variety of technical hurdles, which is noticeable. However, recent important experimental improvements demonstrate the great applicability of this technology for recent technology end devices [8].

## 2 Device Modeling

The hetero-dielectric single-metal gate-all-around MOSFET with Schottky contact source/drain that is the subject of the proposed design utilizes a single gate material with silicon of channel length 5 nm and high-k dielectric of the channel length of 15 nm, which is  $\text{Hf}_x\text{Ti}_{1-x}\text{O}_2$ . To assess performance parameters such as  $I_{\text{ON}}$ ,

$I_{OFF}$ ,  $I_{ON}/I_{OFF}$ , and SS, a simulation of the designed structure has been done. Four terminals make up a MOSFET: the source, drain, gate, and body. The MOSFET will not operate if there are not two connected to a favorable voltage, the gate, and the source. A channel can develop in the top portion of the material across oxide and p-type silicon thanks to the positive gate voltage. The p-type holes move farther apart, and the channel's cross-section increases when the gate voltage is raised. Thus, the increased quantity of current that may flow from source into drain likewise increases as gate voltage rises. The characteristics of a MOSFET vary as channel length decreases as a consequence of short-channel effects. MOSFETs experience threshold voltage shifts, increased leakage current, and increased output conductance for short gate lengths [9].

With a permittivity of 50, high-dielectric gate oxide  $Hf_xTi_{1-x}O_2$  embraces traditional gate oxide ( $SiO_2$ ) in a cylindrical shape. By boosting gate capacitance, high-k material lowers device leakages in the OFF state and residual power efficiency. High-k dielectrics built on Hf have gained support in the most contemporary works because of their increased thermodynamic stability, electrical properties, and interaction reliability [10].

The device has been held under specific boundary conditions to simulate these proposed structures. Drain voltages ( $V_d$ ) of 0.1, 0.6, and 1 V are specified, while the  $V_g$ , is scaled—0 to 1 V. The following designs have been made using COGENDA Visual TCAD to analyze performance traits like SS,  $I_{ON}$ ,  $I_{OFF}$ , and  $I_{ON}/I_{OFF}$  of different structures. Figure 1 depicts the 2D construction of a hetero-dielectric single-metal gate-all-aroundMOSFET with a Schottky contact source/drain. Figure 2 depicts the side views of the proposed devices, respectively, based on a model.

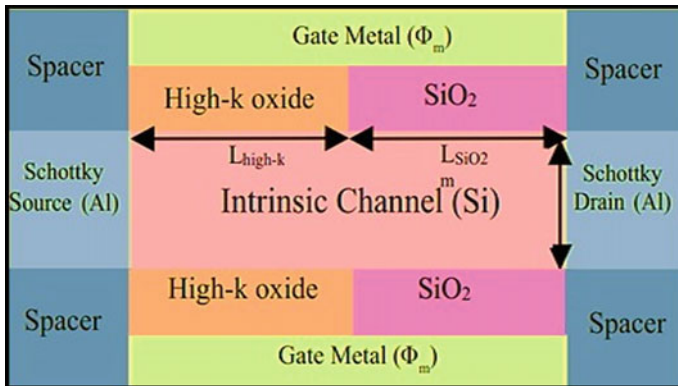


Fig. 1 Two-dimensional illustration of the proposed device model

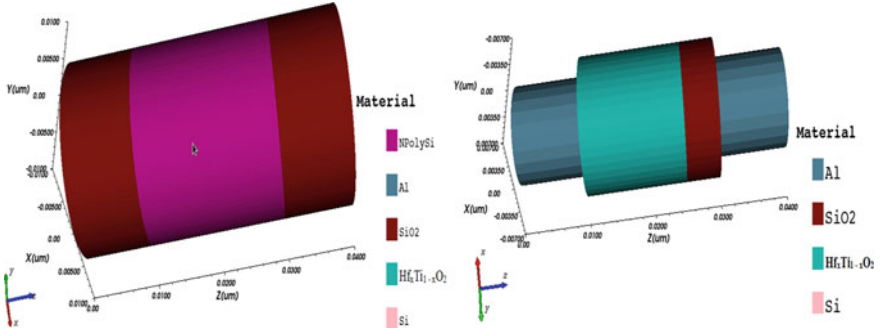


Fig. 2 Side views of the proposed device model

## 2.1 Influence on Electrical Characteristics

A hetero-dielectric single-metal gate-all-around (HD-SM-GAA) MOSFET with a Schottky contact source/drain is proposed in the study under consideration for low-power circuits. The proposed device makes use of Schottky source/drain regions with the drain side comprising  $\text{SiO}_2$  and the source side containing high-k ( $\text{Hf}_x\text{Ti}_{1-x}\text{O}_2$ ) with the oxide configuration [11]. Through the use of TCAD and the drift-diffusion transport mechanism, the effects of the overall consequences of a single-metal gate all around that is hetero-dielectric on the device's performance have been investigated. High-k dielectric is added to the proposed device to maximize storage capacity, decrease chip size, and improve scalability, making it appropriate for memory and application areas with high throughput. Research indicates that the proposed device provides greater SCEs immunity by lowering SS [12].

The performance of proposed structures has been tested via simulations in the TCAD environment for parameters including subthreshold swing (SS), OFF-state current ( $I_{\text{OFF}}$ ), and ON-state current ( $I_{\text{ON}}$ ) [13]. Then, 0.1, 0.6, and 1 V drain voltages ( $V_d$ ) are employed to calculate  $I_{\text{ON}}$  and  $I_{\text{OFF}}$  which are equivalent to a gate voltage ( $V_g$ ) of 0 V. Reduced subthreshold swing ( $62.7 \text{ mV dec}^{-1}$ ) at  $V_d = 0.1 \text{ V}$ , decreased OFF-current ( $1.39 \times 10^{-15} \text{ A}$ ), increased ON-current ( $4.24 \times 10^{-5}$ ) at  $V_d = 1 \text{ V}$ , and improved ON-current to OFF-current ( $I_{\text{ON}}/I_{\text{OFF}}$ ) ratio (in the order of  $10^{10}$ ) at  $V_d = 0.6 \text{ V}$  are the results of using the gate dielectric constant values of  $k = 3.9$  in  $\text{SiO}_2$  and  $k = 50$  in  $\text{Hf}_x\text{Ti}_{1-x}\text{O}_2$ .

## 2.2 Input/Output Characteristics

An output characteristic curve of the described design illustrates the correlation between the divergence in  $I_d-V_g$  when the drain voltage ( $V_d$ ) is 1 V. Figure 3 shows the output characteristics when  $V_d = 1 \text{ V}$ . The plot involving gate voltage ( $V_g$ ) and drain current ( $I_d$ ) is presented after the simulation of the stated device at varied drain

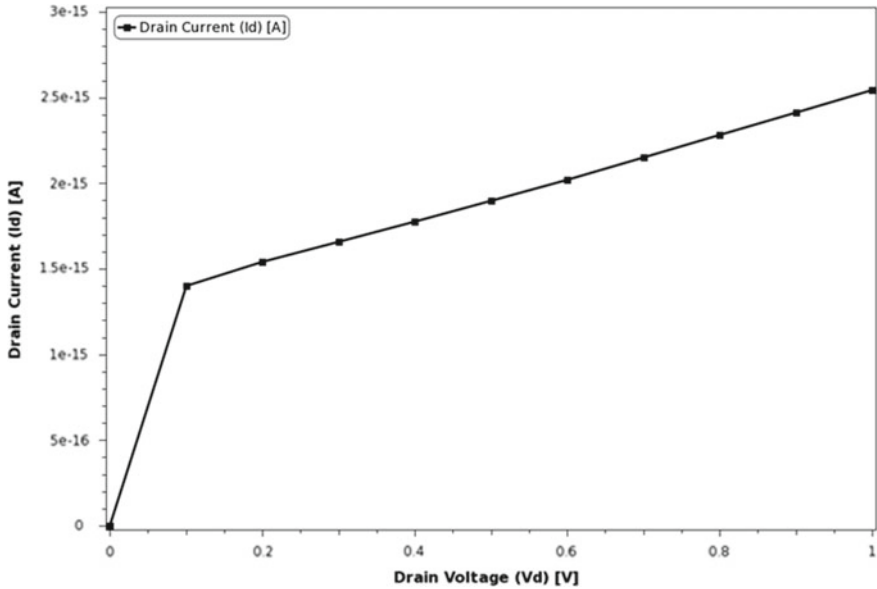


**Fig. 3** Output characteristics at  $V_d = 1$  V

voltages ( $V_d$ ) of 0.1 V, 0.6 V, and 1 V has successfully completed. The figure showed how the gate voltage ( $V_g$ ) influences drain current ( $I_d$ ). Figure 4 shows the drain current ( $I_d$ ) and gate voltage ( $V_g$ ) output characteristic for a device that has been adapted with  $V_g = 1$  V. The output characteristics indicate that as the drain voltage ( $V_d$ ) rises, the drain current does as well. The variability in gate voltage ( $V_g$ ) and drain current ( $I_d$ ) at varying drain voltage ( $V_d$ ) that is 0.1 V, 0.6 V, and 1 V is displayed by an optimized device's output characteristic curve. The  $I_d$ - $V_g$  input characteristics are shown in Fig. 5 for  $V_d = 0.1$  V,  $V_d = 0.6$  V, and  $V_d = 1$  V.

### 2.3 Device Physics

**Drift-Diffusion Model:** The drift-diffusion model's main purpose is to resolve the set of Poisson's equations. With the use of the drift-diffusion model, a series of Poisson equations is derived to represent the proposed devices. It is strong and functions rather quickly for actual work.

$$\nabla \cdot \varepsilon \nabla \varphi = q(p - n + N_D^+ - N_A^-) \quad (1)$$

$\varphi$  and  $q$  are symbols for the electron charge and the amount of vacuum's electric potential, respectively; also, the hole and electron collections are denoted by  $p$  and  $n$ , respectively; and the doping ionized concentration is denoted by  $N_D^+$  and  $N_A^-$ .

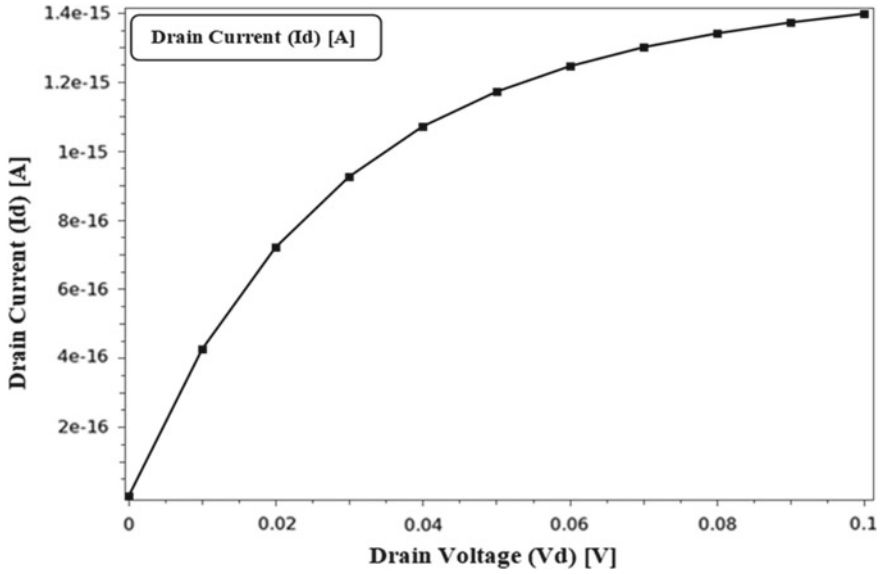


Fig. 4  $I_d$ - $V_g$  output characteristics at  $V_g = 1$  V

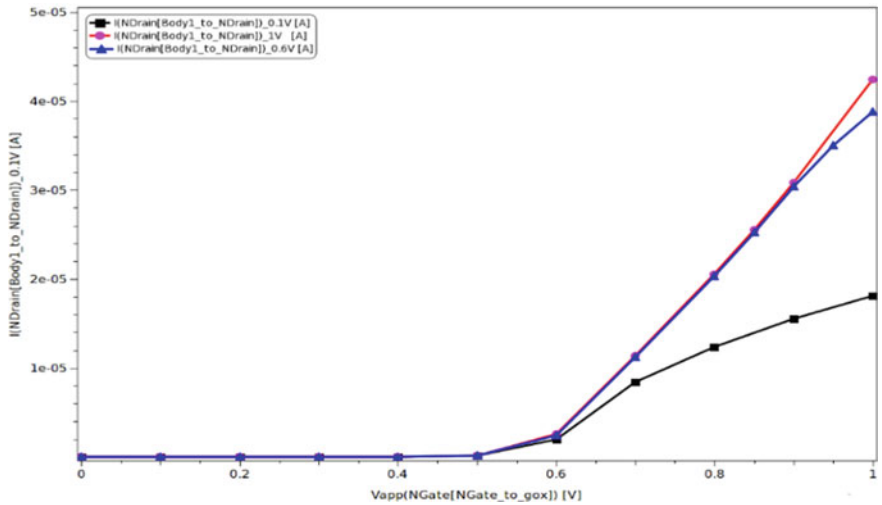


Fig. 5  $I_d$ - $V_g$  input characteristics for  $V_d = 0.1$  V,  $V_d = 0.6$  V,  $V_d = 1$  V

**The Mobility Lombardi Model:** To deal with charge transport in the inversion layer of the proposed device, the Lombardi mobility model was created. The equation for cumulative carrier mobility spanning doping in this model is

$$\mu_S^{-1} = \mu_B^{-1} + \mu_{AC}^{-1} + \mu_{SR}^{-1} \quad (2)$$

where the terms “bulk mobility,” “degradation/scattering mobility,” and “scattering mobility (as measured by surface roughness)” respectively refer with these three symbols  $\mu_B$ ,  $\mu_{AC}$ , and  $\mu_{SR}$ .

**Kane’s Model:** The following is Kane’s model for band-to-band tunneling (GBB)-based carrier generation:

$$G^{BB} = A.BBT \cdot \frac{E^2}{\sqrt{E_g}} \exp\left(-B.BBT \frac{E_G^{\frac{3}{2}}}{E}\right) \quad (3)$$

The electric field and bandgap energy are symbolized by the letters  $E$  and  $E_G$ , respectively, where A.BBT and B.BBT stand for the experimental fitting factors.

**Shockley–Read–Hall (SRH):** Using the Shockley–Read–Hall (SRH) carrier recombination process, the recombination rate is determined as follows:

$$U_{SRH} = \frac{pn - n_{ic}^2}{\tau_p \left[ n + n_i e^{\frac{E_T}{kT_L}} \right] + \tau_n \left[ p + n_i e^{\frac{-E_T}{kT_L}} \right]} \quad (4)$$

The intrinsic carrier concentration is represented by  $n_i$ , the lattice temperature is indicated by  $T_L$ , the carrier lifetime is represented by  $\tau_n$ , and the trap energy level is shown by  $E_T$  [14].

### 3 Results and Discussion

The Visual TCAD environment is used for all design and simulation work. The physical model’s band-to-band tunneling (BBT), drift–diffusion, Lombardi mobility, and Shockley–Read–Hall (SRH) carrier recombination mechanism are all part of the work. The performance of proposed structures has been assessed for parameters including ON-state current ( $I_{ON}$ ), OFF-state current ( $I_{OFF}$ ), and subthreshold swing (SS) through simulations in the TCAD environment.  $I_{OFF}$  is calculated with  $V_g$  of 0 V, and  $I_{ON}$  is calculated with  $V_d$  of 0.1 V, 0.6 V, and 1 V. SS is equivalent to subthreshold slope reciprocally (S).

The value of  $I_{OFF}$  ( $1.39 \times 10^{-15}$  A) was the lowest at  $V_d = 0.1$  V compared to the proposed device’s other voltages of 0.6 V and 1 V. OFF-current ( $I_{OFF}$ ) variation at various drain voltages ( $V_d$ ) is seen in Fig. 6. When compared to other voltages of the proposed device, such as 0.1 V and 1 V, the value of  $I_{ON}$  ( $4.24 \times 10^{-5}$  A) is the greatest at  $V_d = 1$  V. Figure 7 depicts the variation of the ON-current ( $I_{ON}$ ) at various drain voltages ( $V_d$ ). In comparison with other voltages of the proposed device, such as 0.1 V and 1 V, the value of  $I_{ON}/I_{OFF}$  ( $1.92 \times 10^{10}$ ) is the greatest at  $V_d = 0.6$  V.

**Fig. 6** OFF-current ( $I_{OFF}$ ) variation at different drain voltage ( $V_d$ )

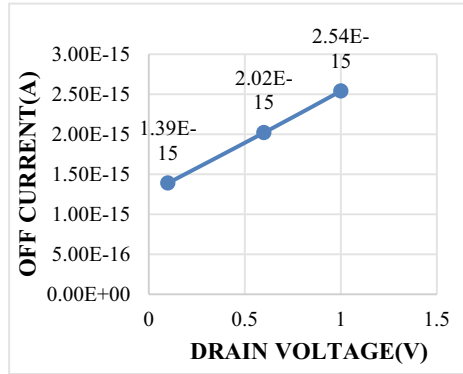


**Fig. 7** ON-current ( $I_{ON}$ ) variation at different drain voltage ( $V_d$ )

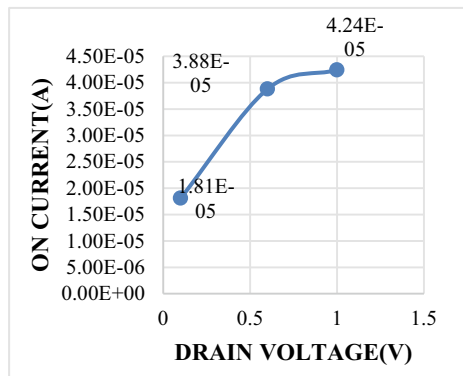
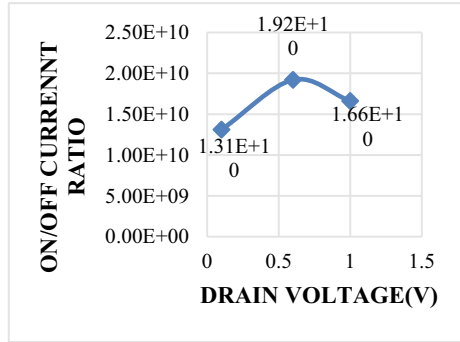


Figure 8 depicts the fluctuation of the  $I_{ON}/I_{OFF}$  ratio at various drain voltages ( $V_d$ ). In comparison with the other voltages of the proposed device, namely 0.6 V and 1 V, the value of the subthreshold swing (SS) ( $62.7 \text{ mV dec}^{-1}$ ) is the lowest at  $V_d = 0.1 \text{ V}$ . Subthreshold swing (SS) variance at various drain voltages ( $V_d$ ) is depicted in Fig. 9.

It has been found that the described device is suitable for low-powered digital systems. Table 1 provides a summary of how performance parameters affect the  $I_{ON}$ ,  $I_{OFF}$ ,  $I_{ON}/I_{OFF}$  ratio, and SS.

**Fig. 8**  $I_{ON}/I_{OFF}$  ratio variation at different drain voltage ( $V_d$ )



**Fig. 9** Subthreshold swing (SS) variation at different drain voltages ( $V_d$ )

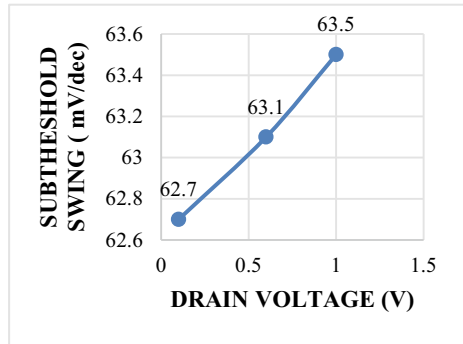


**Table 1** Summarized performance parameter effect on  $I_{ON}$ ,  $I_{OFF}$ ,  $I_{ON}/I_{OFF}$  ratio, and SS

Drain voltage ( $V_d$ ) (V)	Hf <sub>x</sub> Ti <sub>1-x</sub> O <sub>2</sub>	SiO <sub>2</sub>	$I_{ON}$ (A)	$I_{OFF}$ (A)	$I_{ON}/I_{OFF}$	SS (mV dec <sup>-1</sup> )
0.1	50	3.9	$1.81 \times 10^{-5}$	$1.39 \times 10^{-15}$	$1.31 \times 10^{10}$	62.7
0.6	50	3.9	$3.88 \times 10^{-5}$	$2.02 \times 10^{-15}$	$1.92 \times 10^{10}$	63.1
1.0	50	3.9	$4.24 \times 10^{-5}$	$2.54 \times 10^{-15}$	$1.66 \times 10^{10}$	63.5

## 4 Conclusion

The Visual TCAD simulation tool is used for all design and simulation activities. The physical model’s band-to-band tunneling (BBT), drift–diffusion, Lombardi mobility, and Shockley–Read–Hall (SRH) carrier recombination mechanism have all been included in the paper. High-k dielectric is used in the device to increase store volume, shrink chip size, and promote scalability, aiming to make it acceptable for high-speed operations and storage. The described device has been revealed to have superior SCEs tolerance. A strong design for reduced power digital circuitry is HD-SM-GAA MOSFETs with Schottky contact source/drain, according to the overall device modeling analysis. It displays a decreased OFF-state current of about  $1.39 \times$



$10^{-15}$  A. Having a subthreshold slope of  $62.7 \text{ mV dec}^{-1}$ , the device demonstrates outstanding subthreshold region performance. Because of its reduced leakages and exceptionally minimal static power usage, it is ideal for low-voltage and low-power digital applications. In a hetero-dielectric setup as opposed to a gate stack architecture, high-permittivity oxides are more effective at reducing leakage current. It is unnecessary to employ a mask that's because the device uses Schottky source/drain areas during the source/drain region production stage, making it less expensive and easier. When compared to a normal GAA MOSFET, the pattern of leakage currents is dropped to  $10^{-15}$  over  $10^{-9}$  A.

## References

1. Shailaja J, Priya YY (2017) A brief study on challenges of MOSFET and evolution of FINFETs. In: International conference on emerging trends in engineering, science and management, vol 05, no 03
2. Gautam R, Saxena M, Gupta RS, Gupta M (2013) Gate all around MOSFET with vacuum gate dielectric for improved hot carrier reliability and RF performance. *IEEE Trans Electron Devices* 60:1820–1827
3. Wikipedia, <https://en.wikipedia.org/wiki/Nanowire>, last accessed 2023/03/15
4. Signoffsemiconductors, <https://signoffsemiconductors.com/gate-all-around-fet/>, last accessed 2023/02/22
5. Kaur A, Mehra R, Saini A (2019) Hetero-dielectric oxide engineering on dopingless gate all around nanowire MOSFET with Schottky contact source/drain. *AEU Int J Electron Commun* 152888
6. Connelly D, Faulkner C, Clifton PA, Grupp DE (2006) Fermi-level depinning for low-barrier Schottky source/drain transistors. *Appl Phys Lett* 88:012105
7. Kumar A, Pattanaik M, Srivastava P, Jha KK (2020) Reduction of drain induced barrier lowering in DM-HD-NA GAAFET for RF applications. *IET Circ Dev Syst* 14:270–275
8. Barraud S, Lapras V, Previtali B, Samson MP, Lacord J, Martinie S, Jaud M-A, Athanasiou S, Triozon F, Rozeau O, Hartmann JM, Vizioz C, Comboroure C, Andrieu F, Barbe JC, Vinet M, Ernst T (2017) Performance and design considerations for gate-all-around stacked-nanowires FETs. In: 2017 IEEE international electron. devices meeting (IEDM)
9. Sinha SK, Kumar K, Chaudhury S (2015) Si/Ge/GaAs as channel material in nanowire-FET structures for future semiconductor devices. In: 2015 IEEE international conference on electron devices and solid-state circuits (EDSSC), pp 527–530
10. Robertson J (2004) High dielectric constant oxides. *Eur Phys J Appl Phys* 28:265–291
11. Rewari S, Nath V, Haldar S, Deswal SS, Gupta RS (2017) Gate-induced drain leakage reduction in cylindrical dual-metal hetero-dielectric gate all around MOSFET. *IEEE Trans Electron Dev* 1–8
12. Kaur G, Gill SS, Rattan M (2020) Impact of lanthanum doped zirconium oxide (LaZrO<sub>2</sub>) gate dielectric material on FinFET inverter. *Int J Smart Sens Intell Syst* 13:1–10
13. Kaur N, Rattan M, Gill SS (2019) Design and optimization of novel shaped FinFET. *Arab J Sci Eng* 44:3101–3116
14. Genius semiconductor device simulator reference manual

# The Optimization of Perovskite/CuSCN Solar Cell with SnO<sub>2</sub> Electron Transport Layer Using SCAPS-1D



Shivani Chauhan and Rachna Singh

**Abstract** The simulation study of lead-free wide-bandgap (1.8 eV) perovskite (PVSK) solar cells has been performed. An n-i-p cell structure with SnO<sub>2</sub>/PCBM/PVSK/CuSCN was proposed and analyzed theoretically using SCAPS-1D. The analysis of the absorber layer as a function of temperature, and the influence of bulk defect density on the thickness of the absorber layer, which significantly impacts the device performance is carried out. At the optimized thickness of 400 nm of the PVSK absorber layer, the overall power conversion efficiency of the device is 10.10%, with a high  $V_{oc}$  of 1.124 V.

**Keywords** Perovskite · CuSCN · SnO<sub>2</sub> · Lead-free solar cell

## 1 Introduction

One of the most dependable and cleanest renewable energy sources is solar energy. The third generation of solar cells refers to those made of perovskite (PVSK) material. By a Russian mineralogist named L. A. Perovski, the PVSK mineral CaTiO<sub>3</sub> (calcium titanate) was first described in 1839 [1]. In 2006, Miyasaka et al. published the first PVSK device, which had a PCE of 2.2% [2]. It is a novel material and may become far more efficient. The South Korean research team's cell's efficiency of 25.73% has been verified by the US National Renewable Energy Laboratory (NREL) [3]. In 2018, K. Z. Du et al. reported a lead-free PVSK (Cs<sub>2</sub>AgBi<sub>0.75</sub>Sb<sub>0.25</sub>Br<sub>6</sub>) with a bandgap of 1.8 eV [4] which is employed for calibration. CuSCN hole-transport material (HTM) is found to be more stable, has high hole mobility and has low manufacturing cost than the Spiro-OMeTAD [5]. In this work, the device is calibrated to reach the experimental results at the absorber thickness of 400 nm and determine the ideal

---

S. Chauhan (✉) · R. Singh  
Department of Electronics and Communication, Jaypee Institute of Information Technology,  
Noida, India  
e-mail: [20402002@mail.jiit.ac.in](mailto:20402002@mail.jiit.ac.in)

R. Singh  
e-mail: [Rachna.singh@mail.jiit.ac.in](mailto:Rachna.singh@mail.jiit.ac.in)

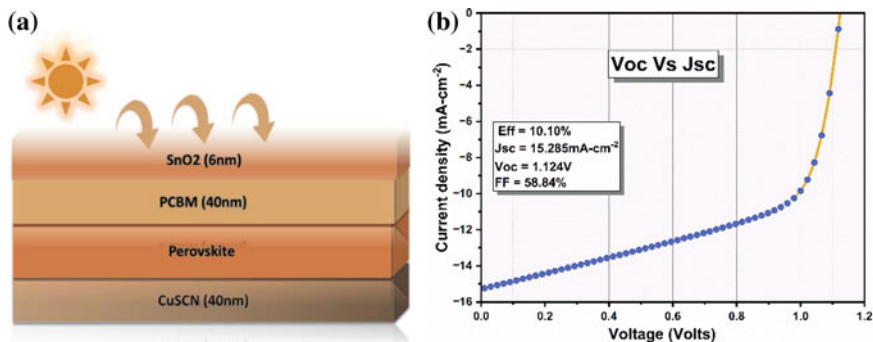


**Fig. 1** Illustration of PVSK solar cell. **a** J-V curve, **b** EQE curve

thickness of the absorber layer through simulation and analyzing photovoltaic (PV) characteristics, dependency of fill factor on series and shunt resistance and effect of temperature on device performance.

## 2 Material and Methods

The simulation study is carried out by the SCAPS-1D simulator for device structure shown in Fig. 1a. This simulator has the AC and DC electrical measurements that can be calculated in dark, light and at different temperature conditions. Simulator used the basic semiconductor equations under the steady-state condition [6]. The simulation parameters reported in Table 1 are carefully chosen from the results of prior theoretical studies and experimental data. In our cell HTL is CuSCN, and ETL is PCBM/SnO<sub>2</sub> and wide-bandgap perovskite absorber layer. Bulk defects in absorber layer and interface defects at ETL, HTL and absorber layer are taken into consideration. The thickness and bulk defect density ( $N_t$ ) of absorber layer are varied from 100 to 1200 nm and  $10^{13}$  to  $10^{17}$  cm<sup>-3</sup>. At 300 K temperature, electrons and holes have a thermal velocity of  $10^7$  cm/s.

## 3 Simulation Results and Discussion

The simulated J-V characteristics are shown in Fig. 1b, got an improved PCE of 10.10%,  $V_{oc}$  of 1.124 V,  $J_{sc}$  of 15.285 mA cm<sup>-2</sup> and FF of 58.84%. The aim is to improve the absorber layer performance.

The reported Fig. 2a shows the PCE as a function of defect density. As the defect density varied from  $10^{13}$  to  $10^{17}$  cm<sup>-3</sup> resulting in lower the PCE from ~ 10% to 2.3%. Corresponding to this with the increase in thickness from 100 to 1200 nm PCE

**Table 1** Simulated PV parameters of the solar cell

Parameters	SnO <sub>2</sub>	PCBM	PVSK	CuSCN
$t$ (nm)	6.0	40	Variable	40
$E_g$ (eV)	3.5	2.1	1.8	3.40
$\chi$ (eV)	4.0	3.90	3.58	1.90
$\epsilon_r$	9.0	4.0	6.50	10
$N_C$ (cm <sup>-3</sup> )	$2.2 \times 10^{18}$	$1 \times 10^{21}$	$2.2 \times 10^{18}$	$1.7 \times 10^{19}$
$N_V$ (cm <sup>-3</sup> )	$1.8 \times 10^{19}$	$1 \times 10^{20}$	$1.8 \times 10^{19}$	$2.5 \times 10^{21}$
$\mu_e$ (cm <sup>2</sup> /V s)	$1 \times 10^2$	$1 \times 10^{-2}$	2.0	$1 \times 10^{-4}$
$\mu_h$ (cm <sup>2</sup> (V s <sup>-1</sup> ))	$2.5 \times 10^1$	$1 \times 10^{-2}$	2.0	$1 \times 10^{-1}$
$N_D$ (cm <sup>-3</sup> )	$10^{16}$	$10^{15}$	$10^{13}$	–
$N_A$ (cm <sup>-3</sup> )	–	–	$10^{17}$	$10^{18}$

Obtained from published literatures [7, 8]

increases due to increase in  $J_{sc}$  values, and after 600 nm it saturates. The recombination is dependent on  $Nt$ . High  $Nt$  will increase the recombination as electrons and holes are likely to recombine on an increase in  $Nt$ , hence resulting in a decrease in PCE. Figure 2b shows the recombination current in the PVSK layer. At bulk defect density  $10^{13}$  cm<sup>-3</sup> is shown to achieve an efficiency of ~ 10%. At the optimized thickness of 500 nm and lower defect density of  $10^{13}$  cm<sup>-3</sup>, the recombination current is ~ 0.824 mA cm<sup>-2</sup>. Figure 3 shows the variation of the  $V_{oc}$  of the device by varying the temperature and dependency of FF on series and shunt resistance.  $V_{oc}$  reduces linearly with an increase in temperature due to the charge carriers' access to the density of states in the conduction and valence band, an increase in recombination current at bulk/interface. As carrier density-dependent SRH and Auger recombination are prominent at high temperatures, this slope becomes nonlinear for higher  $Nt$  ~  $10^{17}$  cm<sup>-3</sup>. Also, at high temperatures due to ion-migration, a variation of built-in voltage occurs.

$J_{sc}$  almost remains constant with temperature. Since resistance of the material also plays an important role in device performance, we examine the effect of series ( $R_s$ ) and shunt resistance ( $R_{sh}$ ) on FF shown in Fig. 2b. FF limits the absorber layer quality.  $Nt$  is one of the prime factors for lowering the device performance, will increase the  $R_s$  and lowering the  $R_{sh}$ . Increase in  $R_s$  will reduce FF and will ultimately reduce the PCE. We therefore tried to improve the alignment between simulation predictions and experimental results based on design considerations.

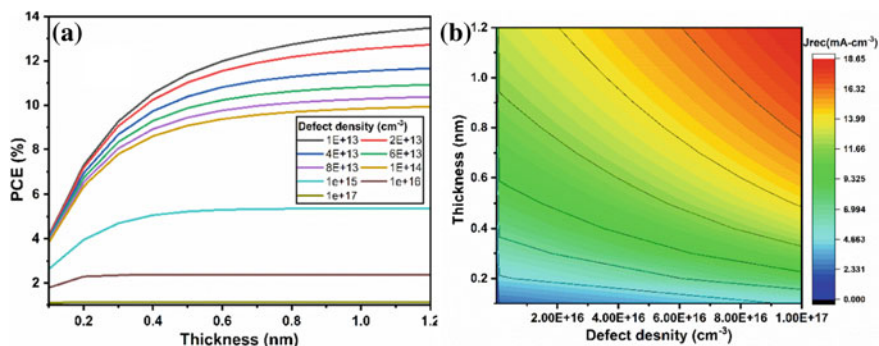


**Fig. 2** a PCE as a function of defect density at varied PVSK thickness, b total bulk recombination current in absorber layer as a function of defect density

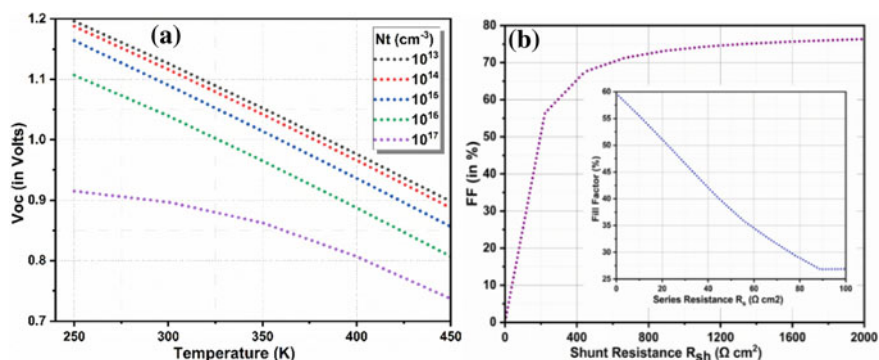


**Fig. 3** a  $V_{\text{oc}}$  at temperature variation for different defect density, b dependency of FF on series ( $R_{\text{s}}$ ) and shunt resistance ( $R_{\text{sh}}$ )

## 4 Conclusion

Using a SCAPS-1D simulator, we investigated a lead-free  $\text{Cs}_2\text{AgBi}_{0.75}\text{Sb}_{0.25}\text{Br}_6$  double PVSK absorber layer. In simulations, we conclude that at the optimized thickness of 500 nm with bulk defect density of PVSK layer  $10^{13} \text{ cm}^{-3}$  is optimal for lower recombination current, series and shunt resistance of device revealing an improved efficiency of 10.10% and a  $V_{\text{oc}}$  of 1.123 V.

**Acknowledgements** The authors would like to express their gratitude to Professor Marc Burgelman, who works in the Electronics and Information Systems (ELIS) department at the University of Gent in Belgium for providing SCAPS-1D to the writers.

**Declaration of Interest Statement** The authors declare that they have no competing interests.

## References

1. Il Seok S, Guo TF (2020) Halide perovskite materials and devices. *MRS Bull* 45(6):427–430. <http://doi.org/10.1557/mrs.2020.140>
2. Osman B, Abdolkader T, Ahmed I (2021) A review of perovskite solar cells. *Int J Mater Technol Innov*. <https://doi.org/10.21608/ijmti.2021.78369.1032>
3. Socol M, Preda N (2021) Hybrid nanocomposite thin films for photovoltaic applications: a review. *Nanomaterials* 11(5). <http://doi.org/10.3390/nano11051117>
4. Wu C et al (2018) The dawn of lead-free perovskite solar cell: highly stable double perovskite Cs<sub>2</sub>AgBiBr<sub>6</sub> film. *Adv Sci* 5(3):2–9. <https://doi.org/10.1002/advs.201700759>
5. Krishna BR, Veerappan G, Bhyrappa P, Sudakar C, Ramasamy E (2022) Dual-functional inorganic CuSCN for efficient hole extraction and moisture sealing of MAPbI<sub>3</sub> perovskite solar cells. *Mater Adv* 3(4):2000–2010. <https://doi.org/10.1039/d1ma00861g>
6. Mandadapu U (2017) Simulation and analysis of lead based perovskite solar cell using SCAPS-1D. *Indian J Sci Technol* 10(1):1–8. <https://doi.org/10.17485/ijst/2017/v11i10/110721>
7. Noman M, Shahzaib M, Jan ST, Shah SN, Khan AD (2023) 26.48% efficient and stable FAPbI<sub>3</sub> perovskite solar cells employing SrCu<sub>2</sub>O<sub>2</sub> as hole transport layer. *RSC Adv* 13(3):1892–1905. <https://doi.org/10.1039/d2ra06535e>
8. Madan J, Pandey R, Sharma R (2020) Device simulation of 17.3% efficient lead-free all-perovskite tandem solar cell. *Sol Energy* 197:212–221. <https://doi.org/10.1016/j.solener.2020.01.006>

# Metal/Polymeric Hierarchical Platform as Biosensor



Shahzad Ahmed, Arshiya Ansari, Moin Ali Siddiqui, and Pranay Ranjan

**Abstract** Histamine, a naturally developing substance in seafood, is identified to give rise to an undesirable erythrogenic reaction when ingested in excessive quantities. Consumption of histamine-rich meals can result in histamine poisoning, which causes symptoms including asthma, headaches, diarrhea, and nausea. As a result, accurate histamine detection and quantification in seafood is crucial. Here, a histamine electrochemical biosensor relying on a molecularly imprinted (MI) polymer was created utilizing a gold inverse opal (GIO) electrode, where the MI-polymer coating was assembled by electropolymerizing aniline (ANI) in the existence of histamine. By electropolymerizing 3,4-ethylenedioxythiophene (EOT), then the scaffold of GIO was altered before the MI-polymer formation, resulting in a substrate with better electrical properties. In order to increase selectivity and sensitivity, we present a synergistic method for the establishment of a hierarchical identifier substance that successfully combines three different approaches: inverse opal framework, molecular imprinting, and semicovalent. The established histamine electrochemical biosensor was selective against several analytes and manifested a linear output from 50 nM to 1  $\mu$ M with a 1.25 nM limit of detection.

**Keywords** Inverse opals · Histamine biosensor · 3-electrode system · Sensitivity · Selectivity · PANI (polyaniline)

## 1 Introduction

One of the significant biogenic amines, histamine, is formed when histidine is prone to decarboxylate. Due to bacterial fermentation occurring during food storage and fermentation, it may be spotted naturally in a wide range of foods and beverages,

---

S. Ahmed (✉) · A. Ansari · M. A. Siddiqui · P. Ranjan (✉)  
Department of Metallurgical and Materials Engineering, Indian Institute of Technology Jodhpur,  
Jodhpur, Rajasthan 342037, India  
e-mail: [shahzad.ahmed0610@gmail.com](mailto:shahzad.ahmed0610@gmail.com)

P. Ranjan  
e-mail: [pranay.ranjan@iitj.ac.in](mailto:pranay.ranjan@iitj.ac.in)

© The Author(s), under exclusive license to Springer Nature Singapore Pte Ltd. 2023  
Z. H. Khan et al. (eds.), *Recent Advances in Nanotechnology*, Springer Proceedings  
in Materials 28, [https://doi.org/10.1007/978-981-99-4685-3\\_3](https://doi.org/10.1007/978-981-99-4685-3_3)

although large amounts are present in protein-rich meals including cheese, beer, seafood, and processed meat. Histamine controls numerous inflammatory responses, hormone production, intestinal system, circulatory functioning, and neurotransmission. Histamine is a very hydrophilic substance that participates in a number of biological processes. The major signs of high histamine consumption include bronchoconstriction, headache, palpitations, extrasystole, hypertension, edema, and pruritus. Hence, it is critical to precisely estimate the amounts of histamine in meals due to its potentially dangerous impacts on individuals.

The electrochemical immunosensors have the advantages of great sensitivity, simple equipment, cost-effectiveness, and rapid response [1]. In principle, biosensors based on electrochemical systems offer excellent specificity and sensitivity, as well as convenience, accuracy, speed, and low equipment budgets [2].

As an analog to naturally generated biological recognition components, bioinspired substances such as MI-polymers may provide excellent selectivity, quick identification, and in-situ application practicality. MI-polymers are typically artificial substances processed by polymerization of the functional monomer and cross-linker in the vicinity of the intended template, then removing the template to produce binding affinity with equivalent shape, size, and functionalities [3]. Moreover, IO-based biosensors have been proven to be a potential biosensing framework to enhance the sensitivity of the device, owing to their porous platforms which lead to giving great surface-to-volume ratio [4–6].

In our study, we presented a metal/polymeric hierarchical platform for the recognition of the histamine molecule, the primary cause of scombroid poisoning and many other associated disorders, by combining IO and MI-polymer via an electrochemical technique. Due to its quick binding and simple template removal within a few minutes, a semicovalent intermediate bonding technique is being utilized. The goal of employing IO was to increase the biosensor's sensitivity, and MI-polymer was employed to do selective detection. Poly(3,4-ethylenedioxythiophene) (PEOT) is employed as an electrode modification film owing to its modest bandgap, superior transparency, electrochemically stable in the oxidized state, simplicity of production, flexibility, economical, and so on [7]. The quinoid ring architectures of PANI and PEOT significantly engage in a PEOT-PANI coating [7].

## 2 Materials and Methods

No further purification was performed before using any of the reagents.  $\text{NaHCO}_3$ ; styrene;  $\text{K}_2\text{S}_2\text{O}_8$ ;  $\text{NiSO}_4 \cdot 6\text{H}_2\text{O}$ ;  $\text{NiCl}_2 \cdot 6\text{H}_2\text{O}$ ; p-styrenesulfonate;  $\text{H}_3\text{BO}_3$ ;  $\text{HAuCl}_4$ ;  $\text{Na}_2\text{S}_2\text{O}_3$ ;  $\text{Na}_2\text{SO}_3$ ;  $\text{Na}_2\text{HPO}_4$ ;  $\text{LiClO}_4$ ;  $\text{K}_4[\text{Fe}(\text{CN})_6] \cdot 3\text{H}_2\text{O}$ ;  $\text{K}_3[\text{Fe}(\text{CN})_6]$ ;  $\text{H}_2\text{SO}_4$ ;  $\text{KCl}$ ; ANI; 3,4-ethylenedioxythiophene (EOT); DMF; deionized (DI) water; putrescine; histamine dihydrochloride; tryptamine; histidine; and cadaverine. All the chemicals were purchased from Central Drug House (CDH) and associated companies.



## 2.1 Construction of Colloidal Crystals

As shown in Fig. 1, there are various manufacturing procedures involved in the production of inverse opaline sensors. Firstly, 595 nm-diameter polystyrene (PS) microspheres were fabricated by the emulsion polymerization method without the use of emulsifiers. The 41 mL of styrene, 13 mM sodium bicarbonate, and 0.09 mM p-styrenesulfonate were added, and the polymerization process was started by the addition of 0.26 g potassium persulfate to the mixture. The bath temperature was kept at 75 °C for 16 h while being stirred frequently, and then it was lowered to 30 °C. The newly created PS microspheres were then dried, weighed, and dispersed at a concentration of 0.6 wt% in ethanol. The PS colloidal particles were produced using a vertically arranged electrophoresis method, with a  $7 \times 7 \text{ cm}^2$  stainless steel plate behaving as the counter electrode and a  $2.5 \times 2.5 \text{ cm}^2$  ITO working electrode (WE). The ITO substrate was first washed using an ultrasonic cleaner for about 20 min in a solution of deionized water and ethanol. ITO substrate is then incubated in 0.49 M sulfuric acid for 12 s and then washed with deionized water. The ITO is immersed in liquid ammonia for roughly 12 min as the last step in the cleaning procedure. An extremely ordered colloidal crystal having an FCC close-packed structure was created by forcing the PS microspheres to approach the WE for around 13 min using an electric field of magnitude  $6 \text{ V cm}^{-1}$ . After being isolated from the PS dispersion, the PS colloidal particles underwent a 48.5-h mild thermal treatment in air at 91 °C.

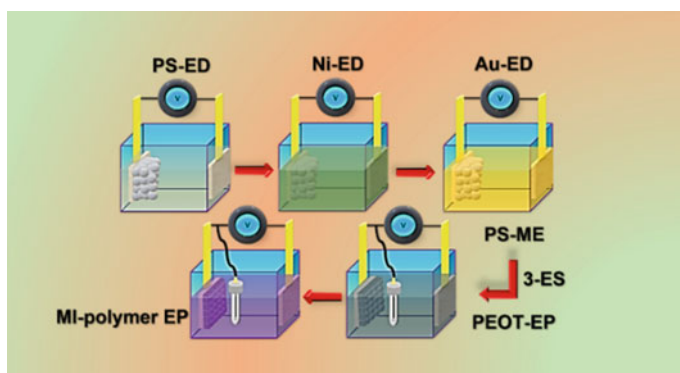


**Fig. 1** Schematic depicting the various stages in the manufacturing of polystyrene microspheres electrodeposition (PS-ED), as well as nickel electrodeposition (Ni-ED), gold electrodeposition (Au-ED), polystyrene microspheres elution (PS-ME), three-electrode system (3-ES), poly3,4-ethylenedioxythiophene electropolymerization (PEOT-EP), and molecularly imprinted polymer electropolymerization (MI-polymer EP)

## 2.2 Synthesis of GIO

We utilized Watt's electroplating method to backfill the PS colloidal particles with Ni (Fig. 1). PS colloidal particles as-deposited on ITO substrate measuring  $2.5 \times 2.5 \text{ cm}^2$  and a  $5 \times 5 \text{ cm}^2$  Ni plate served as the WE and counter electrode, respectively. The aqueous electrolyte comprised 0.130 M nickel (II) chloride, 0.49 M nickel sulfate hexahydrate, and 0.29 M boric acid. To deposit Ni on colloidal particles, a galvanostatic current of  $2.6 \text{ mA cm}^{-2}$  was applied for 11 min at  $26^\circ\text{C}$ . A cyanide-free gold aqueous electroplating recipe was then formed utilizing 0.049 M chloroauric acid, 0.43 M sodium thiosulfate, 0.43 M sodium sulfite, and 0.29 M disodium phosphate. A platinum foil ( $5 \times 5 \text{ cm}^2$ ) was employed as the counter electrode with a steady voltage of 0.9 V for 62 min, allowing the gold coating to be produced atop the sacrificial Ni coating. The goal of the Ni coating is to improve the adherence of the gold coating to the PS microspheres, as the direct gold coating on PS microspheres would be poor and uneven. The specimen was immersed in DMF at  $65^\circ\text{C}$  for 49 h after gold electrodeposition in order to completely eliminate the PS microspheres.

## 2.3 Synthesis of MI-Polymer/GIO

Deionized water was used to prepare every solution. A 0.009 M EOT in 0.039 M lithium perchlorate was generated. The construction of MI-polymer systems was done on a gold inverse opal platform. The MI-polymer coating was created using a 0.039 M lithium perchlorate solution containing 0.012 M histamine as a template substance and 0.024 M ANI as a monomer. Additionally, 0.039 M lithium perchlorate was employed to create histamine calibration reference solutions. The electrical variations at the surface of the film were observed using a solution of 11 mM  $[\text{Fe}(\text{CN})_6]^{3-/4-}$  (KFCN) produced in 0.09 M potassium chloride. PEOT, among the most stable conducting polymers presently known, was formed by electropolymerizing EOT [7]. It was utilized as a pretreatment procedure to enhance the biosensor's electrical responsiveness. This was performed by sweeping an EOT solution with CV. The surface of the WE of GIO was then coated with a small layer of the greatly conductive polymer PEOT. The PEOT coating worked as a modifying layer in this particular instance. Firstly, for the deposition of a highly stable and conducting modifying layer, CV was performed to do the electrochemical polymerization of EOT, as illustrated in Fig. 1. Following two cycles of CV sweeps with a sweep rate of  $20 \text{ mV s}^{-1}$  in the potential regime of 0–1.19 V on the GIOs, a conductive PEOT film was applied. The MI-polymer film was later developed by the same CV approach in a solution but comprising histamine, ANI, and lithium perchlorate for three CV sweeps at the same sweep rate of  $20 \text{ mV s}^{-1}$  and a potential regime of 0–1.19 V. Lastly, the template substance was then extracted from the deposited coating by submerging it in DI water for around 20 min.

### 3 Results and Discussion

#### 3.1 Morphological and Chemical Studies of the MEs

The modified electrodes (MEs) were characterized by SEM. The scanning electron microscopy (SEM) picture of PS colloidal particles showed an average particle diameter of 595 nm. The PS microspheres are organized in an fcc fashion within the tightly packed microstructure of the colloidal crystals. After Ni deposition onto the PS colloidal particles (Ni IOs), every hole in the Ni IOs was grouped in a hexagonal layout with six neighboring openings on the same plane, resulting in a flawless honeycomb microstructure. Additionally, the IOs' individual holes were connected by smaller hole pathways. Moreover, it demonstrated exceptional surface regularity and the inverse opaline granules' polycrystalline nature. In a similar fashion, GIOs were deposited onto the Ni IOs. The macropores show an approximate diameter of 554 nm. In addition, for each macropore, three interconnecting pathways that connected the three macropores beneath appeared. The average diameter of the interconnecting pore pathways was 150 nm. There were 12 interconnected pore pathways in each macropore. Interestingly, the GIOs' surfaces were uniform, indicating that the Ni interposer and GIOs had been electroplated appropriately. MI-polymer is laid over the scaffold of GIOs, which is coated with PEOT. The top-view SEM micrograph of molecularly imprinted polymer/poly(3,4-ethylenedioxythiophene)/GIO (MPGIO) is shown in Fig. 2a. The optimum incubation period of 21 min was chosen for the template extraction procedures, and the duration of 14 min was chosen for the rebinding testing.

#### 3.2 Electrochemical Characteristics of the MEs

The electrochemical properties of various modified electrodes were evaluated utilizing CV and EIS. The GIO, PEOT@GIO, and MPGIO are the modified electrodes. After construction, the GIO surface was altered to boost the background electrical output by applying a thin coating of the strongly conductive PEOT. To create the polymer coating, the 3-electrode configuration was submerged in the EOT solution while the CV sweep was carried out. According to Fig. 2b, the electrode surface was modified utilizing a PEOT layer and had an enhanced current density signal than before surface alteration. The real part of impedance ( $\text{Re } Z$ ), which represents the resistance, and its imaginary part ( $\text{Im } Z$ ) in EIS spectra (Fig. 2c) depict the mixed kinetic mechanism that happens at the electrode–electrolyte boundary. The associated EIS analysis reveals a fall in charge transfer resistance ( $cR_t$ ) in the Nyquist plot following modification when contrasted to the GIO surface. The CV analysis revealed an increase in current output, which was in accordance with previous findings, but the capacitive current also increased, as evidenced by the high peak recorded when

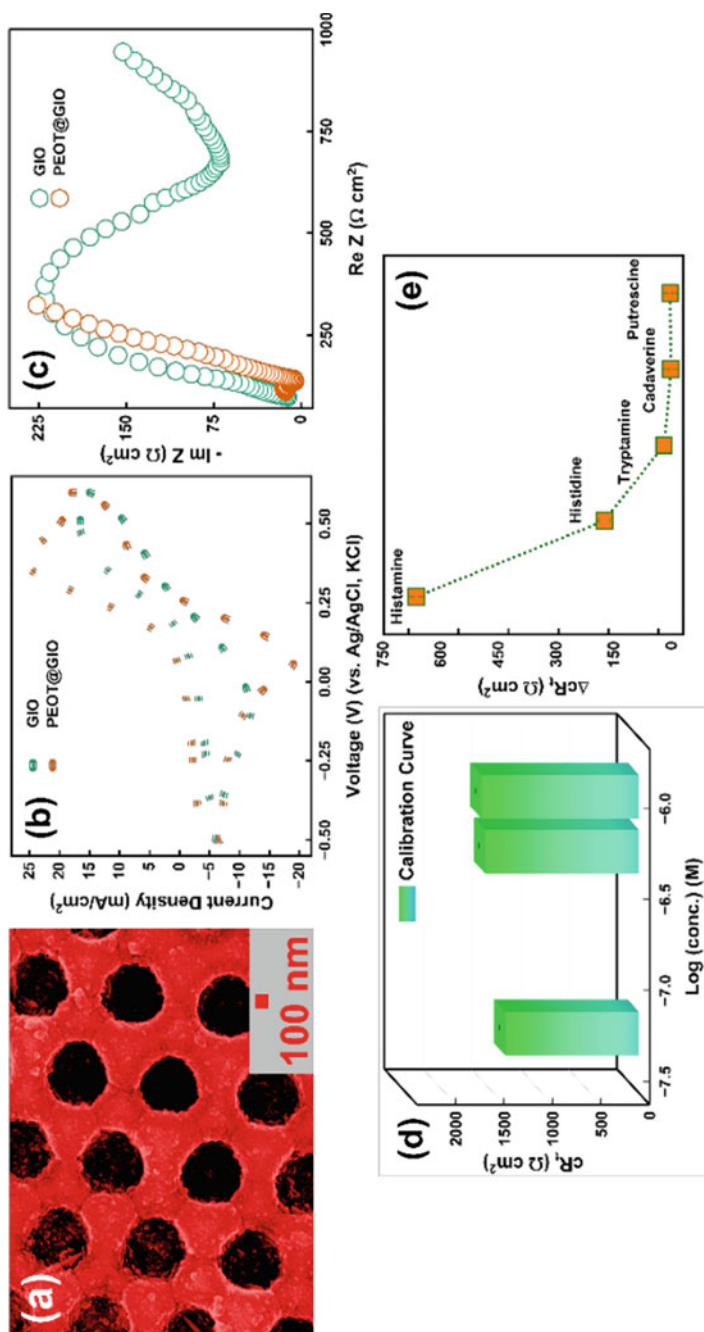


**Fig. 2** Typical SEM micrographs of PS spheres; **a** top view of MPGIOs; **b** CV; **c** EIS plots of electrodes (before and after modification) in a solution of 11 mM KFCN mixed in 0.09 M KCl of bare GIO and PEOT@GIO; **d** calibration curve, in 11 mM KFCN mixed in 0.09 M KCl, in standard solutions of histamine of rising concentrations, produced in lithium perchlorate; and **e** selectivity assessment of the fabricated MPGIO device for histamine ( $6 \times 10^{-4}$  M) against various interfering species. The same concentration of  $6 \times 10^{-4}$  M was used for all analytes during the analysis

PEOT was formed. Furthermore, to these features, the electrode electrical current signal was exceptionally stable, as earlier documented for this polymer.

### 3.3 Calibration and Selectivity Curve

Figure 2d depicts the calibration plot for  $cR_t$  with respect to the various histamine concentration on a logarithmic scale, which demonstrates the linear behavior. This graph also displays the error bars from five distinct sensing devices using 5 separate measurements (5 separate electrodes with the same standard solutions), highlighting the analytical system's exceptional reproducibility. Between 50 nM and 1  $\mu$ M, the linear fashion of the plot was observed in EIS calibrations (Fig. 2d). The minimal squared correlation coefficient ( $R^2$ ) for all calibration calculations was observed at 0.99766, and the average limit of detection (LOD) was measured to be 1.25 nM. The LOD of the method recommended in this investigation was determined using the equation shown below:  $LOD = 3(S.D)/s$ , wherein "S.D" and "s" stand for the analytical curve's standard deviation and slope, respectively. The efficacy of the device is then assessed by determining the change in  $cR_t$ , which is calculated as  $\Delta cR_t = (cR_{t, \text{analyte}} - cR_{t, \text{blank}})$ , where  $cR_{t, \text{analyte}}$  and  $cR_{t, \text{blank}}$  are the charge transfer resistance readings at the fixed concentration of the analyte and the blank, respectively. The test's findings are shown in Fig. 2e. The findings support the MI-polymer sensor's histamine specificity against various interfering species, i.e., histidine, tryptamine, cadaverine, and putrescine. The polymer matrices' molecular imprinting holes give the biosensor an exceptional selectivity for histamine identification.

## 4 Conclusion

In this work, a symbiotic electrochemical-based system for the identification and quantification of histamine was established by adequately combining three distinct techniques, encompassing semicovalent, MI-polymer, and IO architecture. The sensitivity of the biosensor and the establishing binding sites on the polymeric film were both enhanced by the distinctive 3D framework of GIO. In addition, PEOT was utilized as a modification layer to enhance the current output. Analytically, the biosensor was capable of detecting low levels of histamine across a whole broad linear range, from 50 nM to 1  $\mu$ M. The MPGIO device demonstrated outstanding analytical characteristics, notably excellent sensitivity over a broad range of linear outputs, excellent reproducibility, stability, and excellent specificity toward biogenic amines.

**Acknowledgements** The authors are grateful to the Indian Institute of Technology Jodhpur, Rajasthan, India, for providing research facilities. SA would like to thank MHRD for the financial support. PR, Devendra Singh Negi, and Amitava Banerjee would like to thank SERB for

SRG (Grant no. SRG/2022/000192, SRG/2022/000825, and SRG/2022/001377, respectively) for collaboration and SEED Grant No. I/SEED/PRJ/20220044.

**Declaration of Interest Statement** The authors declare that they have no conflict of interest.

## References

1. Imran M, Chaudhary AA, Ahmed S, Alam MM, Khan A, Zouli N et al (2022) Iron oxide nanoparticle-based ferro-nanofluids for advanced technological applications. *Molecules* 27(22):7931
2. Khan A, Ahmed S, Sun BY, Chen YC, Chuang WT, Chan YH et al (2022) Self-healable and anti-freezing ion conducting hydrogel-based artificial bioelectronic tongue sensing toward astringent and bitter tastes. *Biosens Bioelectron* 198:113811
3. Imran M, Ahmed S, Abdullah AZ, Hakami J, Chaudhary AA, Rudayni HA et al (2022) Nanostructured materials based optical and electrochemical detection of amoxicillin antibiotic. *Luminescence* 38(7):1064–1086
4. Madhaiyan G, Tung TW, Zan HW, Meng HF, Lu CJ, Ansari A et al (2020) UV-enhanced room-temperature ultrasensitive NO gas sensor with vertical channel nano-porous organic diodes. *Sens Actuators B Chem* 320:128392
5. Ahmed S, Khatun S, Sallam S, Ansari A, Ansari ZA, Kumar RR et al (2022) Photoresponse of porous silicon for potential optical sensing. *Europhys Lett* 139(3):36001
6. Ahmed S, Ansari A, Siddiqui MA, Khan A, Ranjan P (2023) A potential optical sensor based on nanostructured silicon. *J Mater Sci Mater Electron*. <https://doi.org/10.1007/s10854-023-10187-2>
7. Ahmed S, Ansari A, Haidyrah AS, Chaudhary AA, Imran M, Khan A (2022) Hierarchical molecularly imprinted inverse opal-based platforms for highly selective and sensitive determination of histamine. *ACS Appl Polym Mater* 4(4):2783–2793

# Inexpensive Fabrication of Visible Dielectric Reflector for Improving the Performance of Visible Light Communication



Yepuri Venkatesh, K. Balamurugan, and Bandaru Bhargav Santosh

**Abstract** White light as the source of visible light communication (VLC), that integrates wireless communication with it, offers numerous advantages. It transmits data at a gigabit per second rate and is free of electromagnetic interference (GBPS). Light emitting diodes (LEDs) are regarded as the most desirable choice for the VLCs due to their excellent illumination. However, its transmission performance is severely affected by the carrier life time and recombination factor and influence the transmission performance. This performance can be improved by incorporating the passive optical component dielectric reflector. In this letter, we report the experimental approach for the fabrication of titania and silica-based dielectric reflector with very few layers, i.e. five. Furthermore, field emission scanning electron microscopy research supported the formation of periodic titania and silica layers, while X-ray diffractogram (XRD) phase identification analysis revealed anatase phase of titania. A 100% reflectance in the visible spectrum with a centre wavelength of around 540 nm was supported by the reflectance study on the dielectric reflector.

**Keywords** Dielectric reflector · Titania and silica · Visible spectrum · Visible light communication · FESEM

## 1 Introduction

One-dimensional optical coatings captivated multitudinous domains of optical-engineering, photonic devices and modern office buildings these days. Anti-reflection and reflection coatings are very few among them, which are being adopted as the

---

Y. Venkatesh (✉) · B. B. Santosh

Department of Electrical and Electronics Engineering, Swarnandhra College of Engineering and Technology, Seetharampuram, Narsapur, Andhra Pradesh, India  
e-mail: [venkatesh.yepuri555@gmail.com](mailto:venkatesh.yepuri555@gmail.com)

K. Balamurugan

Department of Electronics and Communication Engineering, Swarnandhra College of Engineering and Technology, Seetharampuram, Narsapur, Andhra Pradesh, India

windshields in automotives and as energy saving windows in the building construction sites [1–3]. These coatings are very attractive due to the housing of fewer applications of multiple materials in a single structure [4]. The addition of dielectric interfaces with varying refractive index equivalent to the substrate can enhance the optical properties like reflection and can realize a passive device called as distributed Bragg reflector or dielectric reflector [5]. Dielectric reflectors can also serve as stop-band filters, the greater the refractive index contrast the wider will be the stop-band achieved. These stop-band filters can be equipped as wavelength filters and can be served as a multipurpose application, for instance ultraviolet reflector under this category not only filter the ultraviolet radiation but also aids the killing of air borne virus like SARS-CoV-2 (Novel corona virus) [6]. Visible light wavelength reflector equipped in the light emitting diodes can not only increasing the output efficiency, but also aids the high-speed transmission in VLC [7]. Infrared reflectors under this category can be installed to the office buildings and construction sites not only to reflect the warm radiation but also in heating the water at the on-sites [8].

Reflectors under this category can be fabricated by the various dielectric materials like  $\text{TiO}_2$ ,  $\text{SiO}_2$ ,  $\text{HfO}_2$ ,  $\text{ZrO}_2$ ,  $\text{ZnO}$  and  $\text{Al}_2\text{O}_3$ . Among the mentioned materials  $\text{TiO}_2$  (2.4) and  $\text{SiO}_2$  (1.4) are opted due to their high refractive index contrast. These reflectors can either be fabricated by profound technologies or by mere techniques available in nanotechnology. Chemical vapour deposition (CVD) [9, 10], physical vapour deposition [11] and glancing angle deposition (GLAD) [12] fiddle into profound technologies, whereas spin coating [13], dip-coating [14] and spray pyrolysis [15] fiddle into mere techniques. The profound technologies include high fabrication cost and processing time due to their necessity in high vacuum and elevated temperatures and also require skilled labour to operate, whereas the mere techniques are user-friendly and incurs low cost and fabrication time. Gel usage is a challenging task in the mere techniques; dip-coating and spray pyrolysis incur huge wastage, whereas spin coating reduces it. Hence, sol–gel spin coating technique was considered as the abrupt methodology in fabricating dielectric reflector with low cost and processing time.

Dielectric reflectors performance can be improved either by the number of multi-layers/stacks or by the thickness of the individual fabricating films [16]. Dubey et al. investigated multilayer structures of  $\text{TiO}_2/\text{SiO}_2$  using sol–gel spin coating technique. The studies were performed initially with three stacks and further increased to five and seven. It was clearly evident in the study that the increased number of stacks can increase the reflectance of the fabricated structure [17]. Furthermore, the fabricated reflector was suggested in the thin film solar cells as a back-end reflector. Lee et al. fabricated and investigated dielectric reflector with 1, 3, 5 and 7 stacks of silica with varied refractive index using ion-assisted deposition technique [18]. The investigations also endorsed increased reflectance with increased number of stacks and suggested the fabricated reflector for pressure sensing applications. Malliga et al. studied thin films of  $\text{TiO}_2$  with various number of coatings using sol–gel spin coating technique [19]. The structures were grown on the glass substrate with four, six, eight and ten coatings and observed increased reflectance with increased number of coatings which is attributed due to the decrease in number of crystallites. Zulkefle et al.



fabricated thin films of  $\text{TiO}_2$  with 1000, 2000, 3000 and 4000 RPM using sol–gel spin coating technique [20]. The increased spin rate of the fabricated decreased the thickness and also the roughness values of the fabricated films. Zhou et al. fabricated visible reflector using ion-beam sputtering technique with 14 stacks of  $\text{TiO}_2$  and  $\text{SiO}_2$  [21]. The fabricated reflector was equipped with GaN-based flip-chip light emitting diodes and observed 25.3% higher efficiency than that of FLED without reflector at 150 mA.

In this letter, we discuss the economical fabrication of a visible dielectric reflector using sol–gel spin coating with minimum number of layers, i.e. only five. The fabricated reflector can be utilized in Li-Fi technologies, solar cells, light emitting diodes and many opto-electronic applications for their improved performances.

## 2 Synthesis of Titania and Silica Gels

Titania sol is made by constantly agitating 1.2 ml of titanium isopropoxide (TTIP) (Sigma Aldrich) into a well-combined solution of the solvent 5 ml ethanol (Changshu Hongsheng Fine Chemicals) and the catalysts 1.2 ml acetic and 0.05 ml nitric acid (Sisco research laboratories). To allow the gel to form, the pH of the gel was adjusted to 3 and aggressively stirred for 15 s. The sol does not need to be aged further and may be used immediately for spin coating on glass substrates. Similarly, silica gel was made using the same molar quantities but a different precursor, tetraethyl orthosilicate (TEOS), instead of titanium isopropoxide (TTIP). All of the compounds listed here are of analytical quality and do not require additional purification.

### Deposition of multilayer titania/silica structure

In the first stage, the glass substrates were extensively soaked in soap solution and sonicated in ethanol for 30 min. Substrates were then washed in water and dried in a hot air oven to eliminate any remaining solvent residues. Layer by layer, titania and silica films were deposited on the cleaned substrates using spin coating at a spin rate of 3000 RPM for 30 s. Both the titania and silica films were dried in a hot air oven at 100 °C for 30 min to remove volatile solvents before being sintered at 500 °C and 300 °C for one hour to eliminate organic compounds and establish the crystalline structure. Five successive layers of titania and silica were used to grow the multilayer structure. The constructed structure was also investigated using XRD (XRD, Bruker, Germany) for phase identification, field emission scanning electron microscopy (FESEM, ZIESS, Germany) for thickness and structural investigation and ultraviolet visible spectroscopy (UV–Vis, UV 1800, Shimadzu, Japan) for reflectance study.

### 3 Results and Discussion

Figure 1 displays the XRD spectra of a dried and sintered sol-gel spin coated visible reflector made of titania and silica. The illustration clearly shows that the multilayer structure contained the well-defined anatase phase of titania and amorphous phase of silica. The planes (101), (004), (200) and (211) of anatase titania (JCPDS: 21-1272) may be indexed to the diffraction peaks of the visible reflector placed at  $2\theta = 25.27^\circ$ ,  $37.89^\circ$ ,  $49.21^\circ$  and  $56.12^\circ$ , and the breadth of the XRD spectrum indicated the amorphous nature of the silica films at a Bragg angle of  $25^\circ$ . This suggests that the titania in the multilayer structure is acceptable for XRD detection and is positioned appropriately with respect to the silica and is in good agreement with the published research [22, 23].

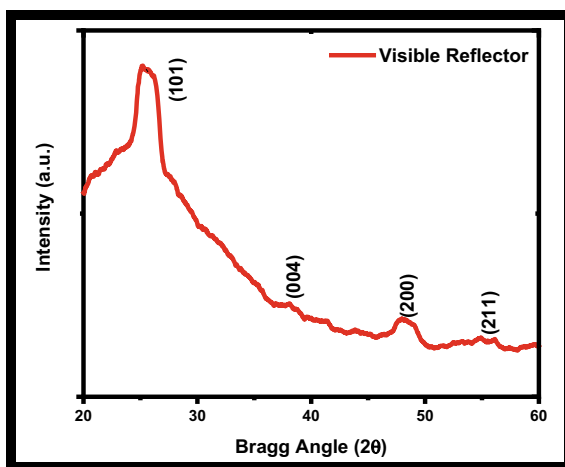
The cross-sectional FESEM analysis and energy dispersive spectrum analysis for the elemental analysis is presented in Fig. 2.

The morphological analysis reveals that the top surface of the visible dielectric reflector is uniform and free of pinholes, and the EDS analysis, as shown in the inset of Fig. 2a, demonstrates the presence of the elements Ti and Si with weight percentages of about 7 and 45, respectively, with the remainder composed of oxygen. Furthermore, the presence of titania and silica layers with bright and dark colours was confirmed by cross-sectional FESEM investigation on the visible dielectric reflector, with thicknesses estimated at 59/115/59/135/57 nm, respectively.

The reflectance spectra analysed using UV-Vis spectroscopy of a visible dielectric reflector made of a periodic multilayer structure of titania/silica/titania/silica/titania is shown in Fig. 3.

The results of the investigation confirmed that the periodic multilayer structure (titania/silica/titania/silica/titania) may experience constructive interference at the top of its surface and generate a dazzling reflection pattern in the visible spectral range with only five layers when compared with the seven-layer dielectric reflector

**Fig. 1** XRD spectra of the sol-gel spin coated visible dielectric reflector



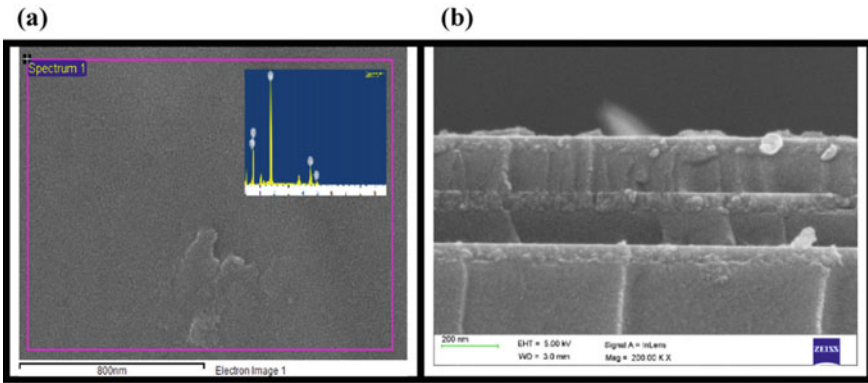


**Fig. 2** FESEM morphology with EDS (a) and cross-sectional image (b) of the sol-gel spin coated visible dielectric reflector

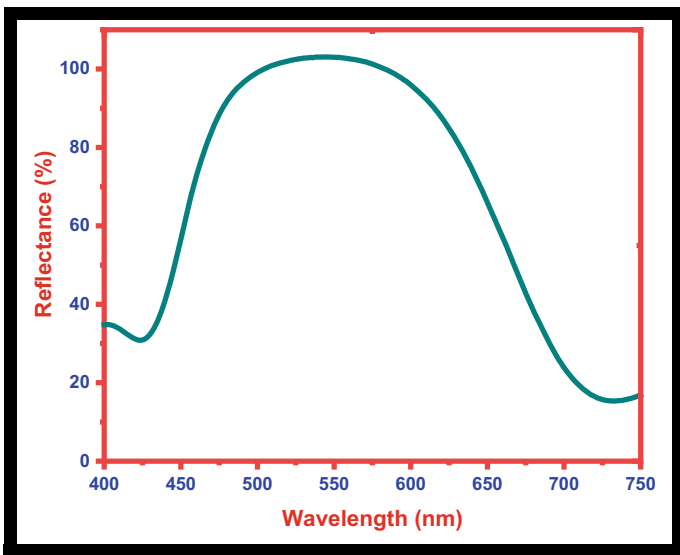


**Fig. 3** Reflectance spectra of the sol-gel spin coated visible dielectric reflector

published [24, 25]. The centre wavelength of the as-fabricated reflector was estimated about 550 nm with a 100% reflectance in the visible spectral region. The proposed optical components can be utilized in the visible light communication systems, opto-electronic and photonic devices for enhancing the photon accumulation.

## 4 Conclusions

Inexpensive fabrication of visible reflector with only five layers of titania and silica using sol–gel spin coating was demonstrated. XRD analysis of the fabricated visible reflector revealed an anatase phase of titania with the strongest peak at Bragg angle  $2\theta = 25.27^\circ$ . FESEM morphology and cross-sectional analysis revealed that the top surface of the dielectric reflector was uniform, and that titania and silica were alternately arranged with bright and dark colours. Finally, the reflectance analysis on the dielectric reflector endorsed the periodic multilayer structure with only five layers can reflect the visible spectrum 100% with a centre wavelength about 550 nm. The as-developed dielectric reflector is suggested in opto-electronic devices such as solar cells and LEDs for their improved photonic responses and VLCs for improving its band width.

**Competing Interests** The authors declare no competing interests.

## References

1. Stoessel CH (2018) Optical coatings for automotive and building applications. *Opt Thin Films Coat* 719–739
2. Li C, Lesuffleur A, Oudard JF, Ishikawa T (2018) Wide-viewing-angle anti-reflection and anti-glare surface treatment on the cover glass for auto-interior applications. In *SID symposium digest of technical papers*, vol 49, no 1, pp 1336–1338
3. Jeong SY, Tso CY, Ha J, Wong YM, Chao CYH, Huang B, Qiu H (2020) Field investigation of a photonic multi-layered TiO<sub>2</sub> passive radiative cooler in sub-tropical climate. *Renew Energy* 146:44–55
4. Bull SJ, Jones AM (1996) Multilayer coatings for improved performance. *Surf Coat Technol* 78(1–3):173–184
5. Fink Y (1998) A dielectric omnidirectional reflector. *Science* 282(5394):1679–1682
6. Buonanno M, Welch D, Shuryak I, Brenner DJ (2020) Far-UVC light (222 nm) efficiently and safely inactivates airborne human coronaviruses. *Sci Rep* 10(1)
7. Lin TC, Chen YT, Yin YF, You ZX, Kao HY, Huang CY, Huang JJ (2018) Large-signal modulation performance of light-emitting diodes with photonic crystals for visible light communication. *IEEE Trans Electron Devices* 1–6
8. Yepuri V, Dubey RS, Kumar B (2020) Rapid and economic fabrication approach of dielectric reflectors for energy harvesting applications. *Sci Rep* 10:15930
9. Guan B, Li P, Arafin S, Alaskar Y, Wang KL (2018) Investigation of single-mode vertical-cavity surface-emitting lasers with graphene-bubble dielectric DBR. *Photonics Nanostruct Fundam Appl* 28:56–60
10. Qiu P, Wu B, Fu P, Li M, Xie Y, Kan Q (2021) Fabrication and characterization of low-threshold single fundamental mode VCSELs with dielectric DBR mirror. *IEEE Photonics J* 13(4):1–6
11. Anjum F, Fryauf DM, Gold J, Ahmad R, Cormia RD, Kobayashi NP (2019) Study of optical and structural properties of sputtered aluminum nitride films with controlled oxygen content to fabricate distributed Bragg reflectors for ultraviolet A. *Opt Mater* 98:109405
12. Leem JW, Yu JS (2012) Broadband and wide-angle distributed Bragg reflectors based on amorphous germanium films by glancing angle deposition. *Opt Express* 20(18):20576–20581

13. Venkatesh Y, Dubey RS (2020) Fabrication and characterization of spectrally selective glazing dielectric multilayer structure. *Nanosyst Phys Chem Math* 11(4):488–492
14. Yuehui W, Xing Y (2018) High-reflection optical thin films based on  $\text{SiO}_2/\text{TiO}_2$  nanoparticles multilayers by dip coating. *Micro Nano Lett* 13(9):1349–1351
15. Venkatesh Y, Dubey RS, Kumar B (2019) Morphological and optical properties of dielectric multilayer structures prepared with distinct precursor concentrations. *Nanosyst Phys Chem Math* 10(3):355–360
16. Carniglia CK, Apfel JH (1980) Maximum reflectance of multilayer dielectric mirrors in the presence of slight absorption. *J Opt Soc Am* 70(5):523
17. Dubey RS, Ganesan V (2017) Fabrication and characterization of  $\text{TiO}_2/\text{SiO}_2$  based Bragg reflectors for light trapping applications. *Results Phys* 7:2271–2276
18. Lee G, Scripka DA, Wagner B, Thadhani NN, Kang Z, Summers CJ (2017) Design and fabrication of distributed Bragg reflector multilayers for dynamic pressure sensing. *Opt Express* 25(22):27067
19. Malliga P, Pandiarajan J, Prithivikumaran N, Neyvasagam K (2014) Influence of film thickness on structural and optical properties of sol–gel spin coated  $\text{TiO}_2$  thin film. *IOSR J Appl Phys (IOSR-JAP)* 6(1):22–28
20. Zulkefle MA, Abdul Rahman R, Yusof KA, Abdullah WFH, Rusop M, Herman SH (2016) Spin speed and duration dependence of  $\text{TiO}_2$  thin films pH sensing behavior. *J Sens* 1–8
21. Zhou S, Xu H, Liu M, Liu X, Zhao J, Li N, Liu S (2018) Effect of dielectric distributed Bragg reflector on electrical and optical properties of GaN-based flip-chip light-emitting diodes. *Micromachines* 9(12):650
22. Almeida RM, Rojas-Hernandez RE, Santos LF (2020) One-dimensional multilayer photonic crystals. *Sol-Gel Derived Opt Photonic Mater* 75–94
23. Saravanan S, Dubey R (2022) Optical investigation on dielectric multilayers prepared by sol-gel method. *Mater Today Proc* 49(7):2858–2861
24. Boxuan G, John Puthenparampil G, Jeroen B, Kristiaan N (2020) Design, fabrication and characterization of a distributed Bragg reflector for reducing the étendue of a wavelength converting system. *Opt Express* 28:12837–12846
25. Zhao W, Jia H, Qu J (2022) Sol-gel synthesis of  $\text{TiO}_2$ - $\text{SiO}_2$  hybrid films with tunable refractive index for broadband antireflective coatings covering the visible range. *J Sol-Gel Sci Technol*. <https://doi.org/10.1007/s10971-021-05719-3>

# Controllable Fast and Slow Light in a Quadratically Coupled Optomechanical System Assisted by Quantum Dot Molecules



Sonam Mahajan, Neha Aggarwal, Madhav Kumar Singh,  
and Aranya B. Bhattacharjee

**Abstract** The superluminal light and subluminal light behaviors of the output probe field are investigated theoretically in a hybrid quadratically coupled optomechanical system embedded with quantum dot molecules. A strong light field and a weak probe light field drive the optomechanical cavity. Various system parameters like tunneling strength, quadratic optomechanical coupling, the number of molecules of quantum dots and so on can coherently control the subluminal light and superluminal light of the output probe field. The influence of various system parameters on the output probe field is very helpful in optical devices and quantum units used in information processing.

**Keywords** Superluminal behavior · Subluminal behavior · Quantum dot molecules · The transmission spectrum

---

S. Mahajan (✉)

Department of Physics, DIT University, Dehradun, Uttarakhand 248009, India  
e-mail: [sonammahajan1987@gmail.com](mailto:sonammahajan1987@gmail.com)

N. Aggarwal

Department of Physics, Government College for Women, Faridabad, Haryana 121002, India

M. K. Singh

Department of Physics, Swami Sahjanand College, Jehanabad (Magadh University Bodhgaya), Jehanabad, Bihar 804408, India

A. B. Bhattacharjee

Department of Physics, Birla Institute of Technology and Science Pilani, Hyderabad Campus, Hyderabad, Telangana 500078, India

## 1 Introduction

In various quantum optomechanical devices, the subluminal and superluminal effects of the output probe field are often useful. In recent years, the most difficult task is to control fast light and slow light in the transmission of the output field. In Refs. [1, 2], various features of slow light and fast light are studied theoretically and experimentally. Subluminal (superluminal) behavior of light also known as slow (fast) light is the one in which the group velocity of output light is less (more) than the velocity of light in a vacuum. Till now, several methods are evolved to obtain fast and slow light in systems of solid materials [3, 4] and systems of atomic vapor [5, 6]. Further, slow and fast light has been observed in various optomechanical systems [7–9]. In one of these systems, a superluminal light of  $1.4 \mu\text{s}$  and an optical delay time of  $50 \text{ ns}$  were observed [7]. Another system observed slow light in an optomechanical system having Bose–Einstein condensates [8]. Moreover, fast light in transmission and slow light in reflection were seen in another optomechanical system [9].

Group delay can also be used to understand the tunable fast and slow light theoretically and experimentally [1]. Using group delay, it was shown that the subluminal effect can be changed to the superluminal effect by varying the atomic number and atom detuning frequency [10]. It was found that a tunable switch between slow and fast lights is possible using an optomechanical system with an optical parametric amplifier [11, 12]. Moreover, the increase in superluminal light was studied in a cavity field with the help of the polarization mode of coupling [13]. Also, the pulse propagation of fast light was obtained in a four-level atomic system [14]. The above-mentioned researches have important applications in quantum information [15, 16] and quantum precision measurements [17, 18]. Very recently, a hybrid linearly coupled optomechanical system having quantum dot molecules inside it observed the controllable fast light [19]. Contrary to this, controllable slow light was observed in another hybrid optomechanical system with quantum dot molecules inside it [20].

However, the previous proposals have linearly coupled optomechanical systems. In this paper, motivated by the previous research, the subluminal and superluminal light effect is studied in a quadratically coupled optomechanical system embedded with three-level quantum dot molecules using group delay.

## 2 Theoretical Model

The proposed theoretical model is shown in Fig. 1, which consists of an optomechanical cavity embedded with molecules of the quantum dots. The mode of the cavity field and resonator are coupled linearly via a linear coupling constant  $g_1$  and a quadratically coupling constant  $g_2$ . A pump laser with strong intensity and a probe laser with weak intensity having frequencies  $\omega_l$  and  $\omega_p$ , respectively, drive the cavity. The optical cavity interacts with the quantum dot molecules with coupling constant

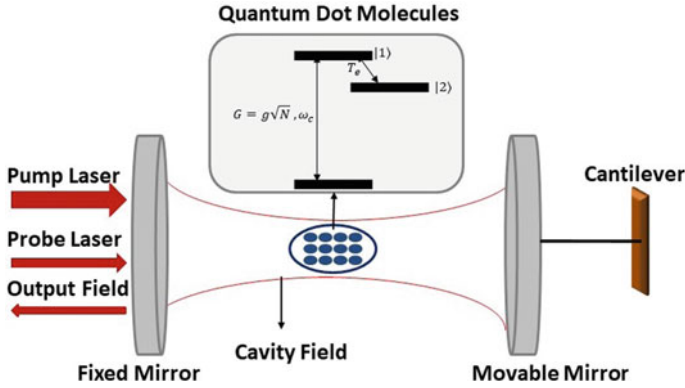


**Fig. 1** Schematic diagram of a quadratically coupled optomechanical system assisted by molecules of quantum dots within the optical cavity. The energy levels inserted are of quantum dot molecules

$G$ . An external electric pump field is used to tunnel the molecules from state  $|1\rangle$  to  $|2\rangle$  with tunneling strength  $T_e$ . No exciton state is state  $|0\rangle$  and many direct excitons' state is state  $|1\rangle$ . When an external electric field is applied, the molecules are present in the state  $|2\rangle$  for several indirect excitons [20]. The Hamiltonian that defines this novel system in rotating wave approximation is given by [19, 20].

$$\begin{aligned}
 H = & \hbar\Delta c^\dagger c + \frac{\hbar\omega_m}{2}(x^2 + p^2) + \hbar(\Delta_1 a^\dagger a + \Delta_2 b^\dagger b) \\
 & - \hbar(g_1 x + g_2 x^2)c^\dagger c + \hbar T_e(a^\dagger b + b^\dagger a) \\
 & + \hbar G(a^\dagger c + c^\dagger a) + i\hbar\varepsilon_l(c^\dagger - c) \\
 & + i\hbar\varepsilon_p(c^\dagger e^{-i\delta t} - c e^{i\delta t}).
 \end{aligned} \tag{1}$$

The first term in the Hamiltonian (Eq. 1) is for the free energy of the cavity field with  $\Delta = \omega_c - \omega_l$  being the detuning and  $c^\dagger(c)$  is the creation (annihilation) operator of the cavity optical field. The next term represents the mechanical energy of the resonator with  $\omega_m$  being the mechanical resonator and  $x(p)$  being its position and momentum operators. The third term represents the energy of  $N$  quantum dots due to the movement of the electrons from state  $|1\rangle$  to state  $|2\rangle$  in the presence of an electric pump field. Here,  $\Delta_1 = \omega_{10} - \omega_l$  is the quantum dot molecules detuning of the frequency when they move from state  $|0\rangle$  to state  $|1\rangle$  with pump laser frequency and  $a^\dagger a$  represents the movement of electrons from state  $|1\rangle$  to state  $|0\rangle$  and vice a versa in the  $i$ th quantum dot molecule. In the same way,  $\Delta_2 = \omega_{20} - \omega_l$  gives the quantum dot molecules detuning of the frequency when they move from state  $|0\rangle$  to  $|2\rangle$  with pump laser frequency and  $b^\dagger b$  represents the movement of electrons from  $|2\rangle$  to  $|0\rangle$  in  $i$ th quantum dot molecule. The next term represents the linear and quadratic optomechanical coupling between optical and mechanical modes. The fifth term arises due to quantum dots' tunneling effect in the presence of an external probe field. Here,  $T_e$  is the tunneling strength,  $a^\dagger b$  represents the movement of electrons



from state  $|2\rangle$  to  $|1\rangle$ , and  $b^\dagger a$  represents the transition of electrons from  $|1\rangle$  to  $|2\rangle$ . The next term is the coupling term between the optical cavity and quantum dot molecules. Here,  $G$  is the interaction constant collectively for all the molecules of quantum dots and the cavity. Here,  $N$  represents the number of molecules of quantum dots and  $g$  represents the interaction strength of the optical cavity field. The last two terms in the Hamiltonian give the interaction between the cavity with a laser of a pump that is strong and a laser of a probe that is weak, respectively. Here,  $\varepsilon_l$  is the strength of the strong pump,  $\varepsilon_p$  is the strength of the weak probe, and  $\delta = \omega_p - \omega_l$  represents the frequency of detuning of the pump laser field with the probe laser field.

Using  $G = g\sqrt{N}$  and Heisenberg–Langevin equations of motion, the mean values of equations of motion are found which are as follows:

$$\dot{x} = \omega_m p(t), \quad (2)$$

$$\dot{p} = -\omega_m x(t) + (g_1 + 2g_2 x(t))c^\dagger(t)c(t) - \gamma_m p(t) + \xi(t), \quad (3)$$

$$\begin{aligned} \dot{c} = & [i(g_1 + g_2 x(t))x(t) - i\Delta - \kappa]c(t) \\ & - iGa(t) + \varepsilon_l + \sqrt{\kappa}c_{\text{in}}(t) + \varepsilon_p e^{-i\delta t}, \end{aligned} \quad (4)$$

$$\dot{a} = -i\Delta_1 a(t) - iT_e b(t) - iGc(t) - \kappa_1 a(t), \quad (5)$$

$$\dot{b} = -i\Delta_2 b(t) - iT_e a(t) - \kappa_2 b(t). \quad (6)$$

Here,  $\gamma_m$ ,  $\kappa$ ,  $\kappa_1$ , and  $\kappa_2$  are the decay rates of mechanical mode, optical mode, transition mode of quantum dot molecules from state  $|0\rangle$  to state  $|1\rangle$ , and transition mode of quantum dot molecules from state  $|0\rangle$  to state  $|2\rangle$ , respectively. The steady-state solutions of all operators are evaluated using the above set of equations of motion which are not shown here. After this, the linearization of the above equations of motion around their steady-state values is done. The perturbation method is used to linearize the equations of motion (Eqs. 2–6). For this, the second-order and higher-order terms are neglected and thereby get the linearized quantum Langevin equations as

$$\left[ \frac{d^2}{dt^2} + \gamma_m \frac{d}{dt} + \omega_x^2 \right] \delta x = \omega_m g_x [c_0^* \delta c + c_0 \delta c^* + \delta c \delta c^*], \quad (7)$$

$$\delta \dot{c} = -iG\delta a + \varphi\delta c + ig_x c_0 \delta x + \varepsilon_p e^{-i\delta t}, \quad (8)$$

$$\delta \dot{a} = -\kappa_1 \delta a - iT_e \delta b - iG\delta c, \quad (9)$$

$$\delta \dot{b} = -\kappa_2 \delta b - iT_e \delta a. \quad (10)$$

Here,  $g_x = g_1 + 2g_2x_0$ ,  $\varphi = -i\Delta - \kappa + ix_0(g_1 + g_2x_0)$ , and  $\omega_x = \sqrt{\omega_m^2 - 2g_2|c_0|^2\omega_m}$ . Using ansatz  $\delta x = x_1^+ e^{-i\delta t} + x_1^- e^{i\delta t}$ ,  $\delta c = c_1^+ e^{-i\delta t} + c_1^- e^{i\delta t}$ ,  $\delta a = a_1^+ e^{-i\delta t} + a_1^- e^{i\delta t}$ , and  $\delta b = b_1^+ e^{-i\delta t} + b_1^- e^{i\delta t}$  in the above equations of motion,

$$x_1^+ [\delta^2 - i\gamma_m \delta + \omega_x^2] = g_x \omega_m (c_0^* c_1^+ + c_0 (c_1^-)^*), \quad (11)$$

$$x_1^- [-\delta^2 + i\gamma_m \delta + \omega_x^2] = g_x \omega_m (c_0^* c_1^- + c_0 (c_1^+)^*), \quad (12)$$

$$c_1^+ (\varphi + i\delta) = iGa_1^+ - ig_x c_0 x_1^+ - \varepsilon_p, \quad (13)$$

$$c_1^- (\varphi - i\delta) = iGa_1^- - ig_x c_0 x_1^-, \quad (14)$$

$$a_1^+ (\kappa_1 - i\delta) = -iT_e b_1^+ - iGc_1^+, \quad (15)$$

$$a_1^- (\kappa_1 + i\delta) = -iT_e b_1^- - iGc_1^-, \quad (16)$$

$$b_1^+ (\kappa_2 - i\delta) = -iT_e a_1^+, \quad (17)$$

$$b_1^- (\kappa_2 + i\delta) = -iT_e a_1^-. \quad (18)$$

Solving the above equations, the output field at probe frequency is found as  $c_1^+ = \frac{K_1 K_3 - i g_x |c_0|^2}{K_1 K_2 K_3 + i g_x |c_0|^2 K_3 - i g_x |c_0|^2 K_2} \varepsilon_p$ , where  $K_1 = \frac{-\delta^2 - i\gamma_m \delta + \omega_x^2}{g_x \omega_m}$ ,  $K_2 = \varphi + i\delta - \frac{G^2(\kappa_2 - i\delta)}{(\kappa_1 - i\delta)(\kappa_2 - i\delta) + T_e^2}$ , and  $K_3 = \left( \varphi - i\delta - \frac{G^2(\kappa_2 + i\delta)}{(\kappa_1 + i\delta)(\kappa_2 + i\delta) + T_e^2} \right)^*$ . Based on the input–output relation [9], one can easily obtain  $\varepsilon_T = \frac{2\kappa c_1^+}{\varepsilon_p}$ . Using this relation, the group delay is found as  $\tau_T = \text{Im} \left[ \frac{1}{\varepsilon_T} \frac{\partial \varepsilon_T}{\partial \omega_p} \right]$  [20]. The software MATHEMATICA 11.3 is used to find the group delays numerically and also used to plot the graphs using various system parameters which are discussed in the next section.

### 3 Results and Discussion

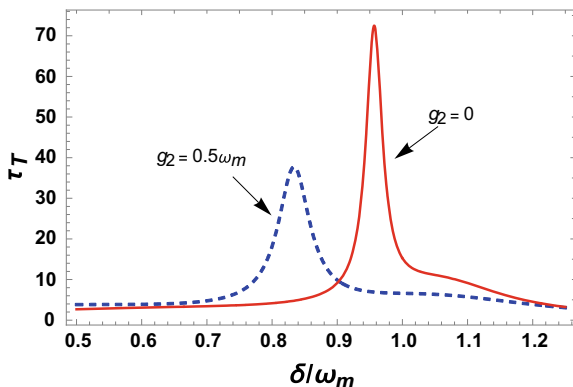
In this section, the effect of various system parameters on the velocity of light is understood. Moreover, how the absence and presence of quadratic optomechanical coupling affect the subluminal light behavior and superluminal light behavior of the output probe field is discussed in detail. Then, the same behavior is illustrated in the absence of strength of tunneling and by changing the number of molecules inside the

optical cavity. In the end, the same behavior is examined in the presence of strength of tunneling and the number of molecules is varying.

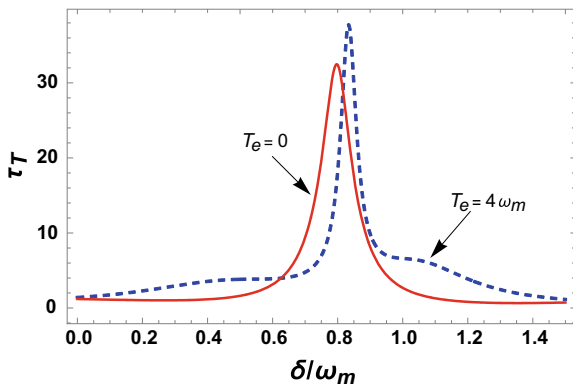
Figure 2 illustrates the group delay of the transmitted probe field in the absence and presence of quadratic optomechanical coupling. The positive values show the subluminal behavior of the output probe field. In the absence of a quadratic optomechanical coupling constant, the group delay of the output probe field shows more slow light. Compare to previous proposals [19, 20], the clear advantage of this work is that the quadratic coupling of the optomechanical cavity can be used as a new handle to control the slow light of the transmitted probe field.

Figure 3 illustrates the group delay of the output probe field when the strength of tunneling is absent and present. When this tunneling strength is zero, all the electrons in quantum dot molecules could not move to the state  $|1\rangle$  and state  $|2\rangle$ , so there will be an immediate dissipation of photons. This provides less slow light. Recently, the effect of tunneling strength on the subluminal behavior of transmitted light was reported in a very similar linearly coupled optomechanical system with quantum dot molecules inside it [19, 20].

**Fig. 2** Transmission group delay of probe field as a function of the probe-pumping detuning in the absence and presence of quadratic optomechanical coupling. The parameters used are  $g_1 = \omega_m$ ,  $g_2 = 0.5\omega_m$ ,  $\kappa_1 = \kappa_2 = \omega_m$ ,  $\kappa = 0.5\omega_m$ ,  $\Delta = \Delta_1 = \Delta_2 = \omega_m$ ,  $G = \omega_m$ ,  $\gamma_m = 10^{-5}\omega_m$ ,  $\varepsilon_1 = 0.5\omega_m$ , and  $T_e = 4\omega_m$



**Fig. 3** Transmission group delay of output field versus the probe-pumping detuning in the absence and presence of tunneling strength. The other parameters used are same as in Fig. 2



**Fig. 4** Group delay of output probe field versus the probe-pumping detuning with varying number of molecules of quantum dot. The other parameters used in this plot are same as in Fig. 2

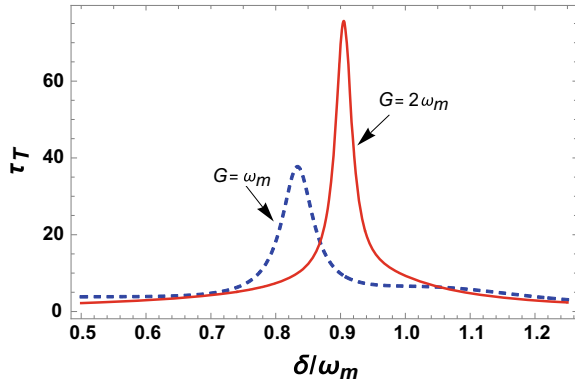


Figure 4 illustrates the group delay of the output probe field with varying the number of molecules of quantum dots. By increasing the number of molecules of quantum dots, the coupling strength  $G$  increases which leads to the weakening of the destructive interference of light in between the transition pathways. Also, the velocity of photons is decreased because of small dissipation that provides more slow light. The subluminal effect is increased if the number of molecules of quantum dots is increased. Hence, one can control subluminal and superluminal effects in our hybrid optomechanical system using various system parameters like tunneling strength, quadratic optomechanical coupling, and the number of quantum dot molecules. A similar kind of behavior is an increase in subluminal effect with an increase in the number of quantum dot molecules in a hybrid optomechanical system having quantum dot molecules assisted by linear optomechanical coupling observed [19].

## 4 Conclusion

In conclusion, the theoretical investigation of the slow light behavior of the transmitted output probe field is done in an optomechanical system with quantum dot molecules. The expression of group delay was found for the output probe field using nonlinear equations and the input–output theory. If the quadratic coupling constant is zero, the transmitted output probe field gives the slow light effect. This subluminal effect decreases in the presence of quadratic optomechanical coupling. Also, the slow light effect is more when the strength of the tunneling effect is zero. Further, it is observed that the subluminal light behavior of the output probe field increases by increasing the number of quantum dot molecules. Hence, by changing the strength of tunneling, quadratic optomechanical coupling, and the number of molecules of quantum dots, one can enhance or reduce the subluminal behavior of light in the present theoretical system. The presented model has a significant application in the technology of photons. It also gives a way toward optical devices and quantum information processing units.

**Declaration of Interest Statement** The authors of this research article declare that they have no conflict of interest.

## References

1. Boyd RW, Gauthier DJ (2009) Controlling the velocity of light pulses. *Science* 326:1074–1077
2. Kasapi A, Jain M, Yin GY, Harris SE (1995) Electromagnetically induced transparency: propagation dynamics. *Phys Rev Lett* 74:2447–2450
3. Turukhin AV, Sudarshanam VS, Shahriar MS, Musser JA, Ham BS, Hemmer PR (2001) Observation of ultraslow and stored light pulses in a solid. *Phys Rev Lett* 88(2):023602
4. Bigelow MS, Lepeshkin NN, Boyd RW (2003) Observation of ultraslow and stored light pulses in a solid. *Phys Rev Lett* 90:113903–113906
5. Kash MM et al (1999) Ultraslow group velocity and enhanced nonlinear optical effects in a coherently driven hot atomic gas. *Phys Rev Lett* 82:5229–5232
6. Budker D et al (1999) Nonlinear magneto-optics and reduced group velocity of light in atomic vapor with slow ground state relaxation. *Phys Rev Lett* 83:1767–1770
7. Safavi-Naeini AH et al (2011) Electromagnetically induced transparency and slow light with optomechanics. *Nature* 472:69–73
8. Chen B, Jiang C, Zhu KD (2011) Slow light in a cavity optomechanical system with a Bose-Einstein condensate. *Phys Rev A* 83:055803
9. Tarhan D, Huang S, Müstecaplıoğlu ÖE (2013) Superluminal and ultraslow light propagation in optomechanical systems. *Phys Rev A* 87:013824
10. Gu KH et al (2015) Tunable slow and fast light in an atom-assisted optomechanical system. *Opt Commun* 338:569
11. Li L, Nie W, Chen A (2016) Transparency and tunable slow and fast light in a nonlinear optomechanical cavity. *Sci Rep* 6(1):35090. <https://doi.org/10.1038/srep35090>
12. Biag M, Ghaffar A, Khan MA, Khan F, Niaz S (2021) Slow light effect in hybrid optomechanical system. *Int J Quantum Chem* 122:e26814
13. Smith DD, Chang H, Myneni K, Rosenberger A (2014) Fast-light enhancement of an optical cavity by polarization mode coupling. *Phys Rev A* 89:053804
14. Bacha BA, Ghafoor F, Ahmad I (2013) arXiv Preprint [arXiv:1311.6921](https://arxiv.org/abs/1311.6921)
15. Ma P-C, Yan L-L, Zhang J, Chen G-B, Li X-W, Zhan Y-B (2017) Tunable single-photon multi-channel quantum router based on an optomechanical system. *Laser Phys Lett* 15:015204
16. Ma P-C, Yan L-L, Chen G-B, Li X-W, Liu S-J, Zhan Y-B (2018) Multi-functional quantum router using hybrid opto-electromechanics. *Laser Phys Lett* 15:035201
17. Liu Z-X, Wang B, Kong C, Si L-G, Xiong H, Wu Y (2017) A proposed method to measure weak magnetic field based on a hybrid optomechanical system. *Sci Rep* 7:12521
18. Zhang J-Q, Li Y, Feng M, Xu Y (2012) Precision measurement of electrical charge with optomechanically induced transparency. *Phys Rev A* 86:053806
19. Ghaffar AA et al (2022) Controllable fast light in quantum dot molecules assisted hybrid optomechanical system. *Int J Quant Chem*. <https://doi.org/10.1002/qua.26955>
20. Yu C, Yang W, Sun L, Zhang H, Chen F (2020) Controllable transparency and slow light in a hybrid optomechanical system with quantum dot molecules. *Opt Quant Electron* 52:267

# Performance Analysis of NiO/ Ch<sub>3</sub>Nh<sub>3</sub>GeI<sub>3</sub>/SnO<sub>2</sub> Perovskite Solar Cell Using SCAPS 1D



Chandni Tiwari  and Varun Mishra

**Abstract** In this paper, we have used NiO as hole transport layer (HTL) along with Ch<sub>3</sub>Nh<sub>3</sub>GeI<sub>3</sub> perovskite layer and SnO<sub>2</sub> as ETL. Here, we have initially analyzed the performance of Ch<sub>3</sub>Nh<sub>3</sub>GeI<sub>3</sub>/SnO<sub>2</sub> solar cell without HTL layer using SCAPS 1D simulator. Further, we introduced HTL to the solar cell and the resulting efficiency increased to ~ 15.6%. Later, we have varied the thickness of perovskite, HTL and ETL, defects of absorber layer, and interface defects to see its impact on the efficiency of the NiO/Ch<sub>3</sub>Nh<sub>3</sub>GeI<sub>3</sub>/SnO<sub>2</sub> solar cell. We have also varied the electron affinity of SnO<sub>2</sub> and the temperature of solar cell to optimize the suitable working temperature. Hence, we have optimized various material's parameter which may result in to maximum efficiency.

**Keywords** Solar cell · Perovskite · SCAPS 1D · Simulation · Optimization

## 1 Introduction

The photovoltaic techniques have shown immense improvement in recent years in terms of materials [1]. The most popular material which is used in photovoltaics is crystalline silicon. Various materials both organic and inorganic have been studied in order to replace silicon. Out of those, perovskite material has given strong competition to silicon-based solar cells. These organometallic lead halides' based solar cell has shown efficiency up to 25.2% [2]. The major perovskite solar cells contain lead (Pb) as metal cation which imposes environmental restrictions on its use. Hence, various other cations such as Sn (tin) and Ge (germanium) have been studied to replace the lead in perovskite to provide a more sustainable and environmentally friendly alternative to silicon-based solar cells [3].

In Ch<sub>3</sub>Nh<sub>3</sub>GeI<sub>3</sub>, replacement of lead makes an efficient candidate to be used as environmentally friendly perovskite solar cell. There are several ETL materials such

---

C. Tiwari (✉) · V. Mishra

Department of Electronics and Communication Engineering, Graphic Era (Deemed to be University), Dehradun 248002, India  
e-mail: [chandnitiwari.ece@geu.ac.in](mailto:chandnitiwari.ece@geu.ac.in)

as  $\text{SnO}_2$ ,  $\text{ZnO}$ ,  $\text{CdS}$ ,  $\text{ZnSe}$  which have been explored with perovskite materials [2]. Out of these,  $\text{SnO}_2$  has shown excellent behavior [4]. Similarly, HTL materials such as  $\text{NiO}$ ,  $\text{Cu}_2\text{O}$ ,  $\text{CuO}$ , and  $\text{CuI}$  have been explored.  $\text{NiO}$  has shown favorable band alignment with perovskite and has shown excellent HTL properties [5]. However, optimizing the parameters of this solar cell using experimental techniques requires time and is non-economical. Hence, we have used simulation approach to optimize the parameters of this solar cell. The software which we are using is an open-source software known as SCAPS 1D. It is based on drift-diffusion physical model [6].

In this paper, we have simulated  $\text{NiO}/\text{CH}_3\text{NH}_3\text{GeI}_3/\text{SnO}_2$  solar cell using SCPAS 1D. Here, we have tried to see the influence of different material parameters' alteration on the efficiency of the device.

## 2 Materials and Methods

The materials which we have used here are  $\text{SnO}_2$ ,  $\text{CH}_3\text{NH}_3\text{GeI}_3$ , and  $\text{NiO}$ . We have used AM 1.5 G spectrum and  $1000 \text{ W/m}^2$  light intensity for this study. The various parametric values of materials are listed in Table 1.

**Table 1** Different parameters of materials required for simulation

Parameters	$\text{SnO}_2$	$\text{CH}_3\text{NH}_3\text{GeI}_3$	$\text{NiO}$
Thickness ( $\mu\text{m}$ )	0.1	2	0.2
Band gap (eV)	3.6	1.9	1.46
Affinity of electrons (eV)	4	3.98	3.8
Dielectric constant (relative)	9	10	10.7
Density of states of CB ( $\text{cm}^{-3}$ )	$4.36 \times 10^{18}$	$10^{16}$	$2.8 \times 10^{19}$
Density of states of VB ( $\text{cm}^{-3}$ )	$2.9 \times 10^{19}$	$10^{15}$	$1 \times 10^{19}$
Mobility of electron ( $\text{cm}^2/\text{V s}$ )	240	162	120
Mobility of hole ( $\text{cm}^2/\text{V s}$ )	25	10	2.8
Donor density $N_D$ ( $\text{cm}^{-3}$ )	$10^{17}$	$10^9$	0
Acceptor density $N_A$ ( $\text{cm}^{-3}$ )	0	$10^9$	$10^{18}$
Absorber defect ( $\text{cm}^{-3}$ )	$10^{11}$		
Interface defect ( $\text{cm}^{-3}$ )	$10^{11}$		
Defect type at bulk/interface	Donor/neutral		

### 3 Results

The device is initially simulated using the parameters listed in Table 1 and the schematic is shown in Fig. 1a. Initially, we have not considered HTL and have simulated the pn junction made between ETL and perovskite absorber material. We observed that the resulted efficiency is as low as ~ 8%. The solar cell resulted in enhanced efficiency ~ 15.6% when HTL is included. The comparative result of both the cells is included in Fig. 1b. The perovskite film thickness is varied from 0.5 to 5 μm to understand its effect on the performance working of the solar device. It can be perceived from Fig. 1c that the device’s efficiency is saturated after the thickness reached 2 μm. The increase in perovskite thickness leads to higher chances of recombination which decreases the efficiency. The contour plot of ETL and HTL thickness is plotted in Fig. 1d.

The thin ETL leads to low series resistance and electrons must travel less to reach to contact. Hence, chances of recombination are less which results in higher efficiency. Higher ETL leads to larger series resistance; however, suitable thickness overcomes the piercing effect obtained from back contact. Hence, a relatively larger thickness of HTL is resulting in higher efficiency.

The effective thickness of ETL is 0.05 μm and for HTL is 0.4 μm. Here, we have varied the defect concentration of the perovskite layer from 10<sup>10</sup> to 10<sup>15</sup> cm<sup>-3</sup>. The observed graph is shown in Fig. 1e. We can observe from the graph that the efficiency starts decreasing drastically after the defect concentration reaches 10<sup>14</sup> cm<sup>-3</sup>. Further, we can observe from the graph 1d that the best electron affinity suitable

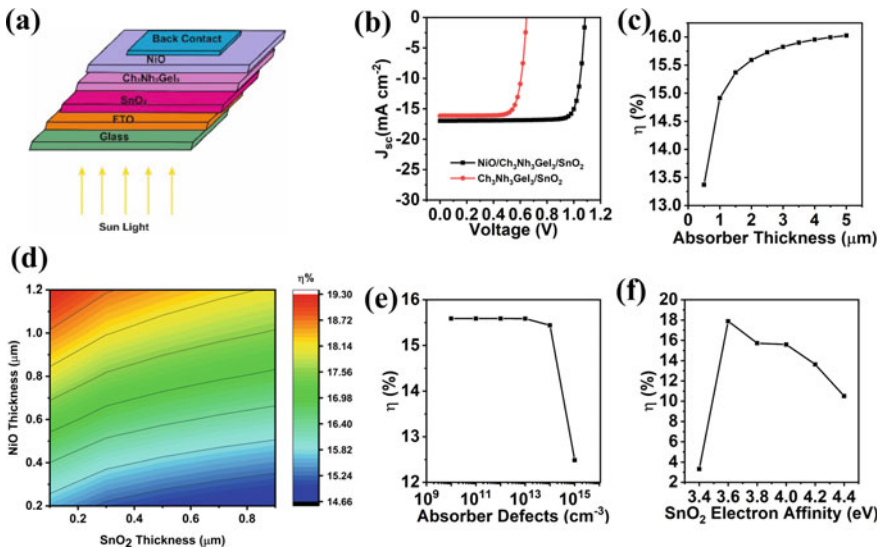


**Fig. 1** a Schematic, b I–V characteristic, c effect of absorber thickness, d contour plot of ETL and HTL thickness, e impact of absorber defect, and f impact on ETL electron affinity



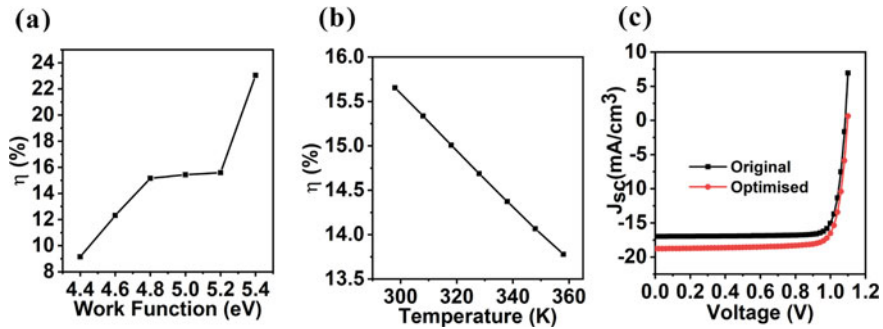


**Fig. 2** a Influence of metal contact work function, b temperature, and c I-V characteristics of the optimized device

for SnO<sub>2</sub> is 3.6 eV. The difference in electron affinity between ETL and perovskite increases energy barriers which hinders the flow of electrons and results in diminished efficiency. The work function of the back contact is altered from 4.4 to 5.4 eV, and the observed results are plotted in Fig. 2a. We can see that with increase in work function, the efficiency is increasing.

We have also adjusted the working temperature of the device from 25 to 60 °C. The graph is mentioned in Fig. 1b. The increased temperature results in higher carrier concentration. These increased charge carriers result in higher recombination rates which leads to diminished efficiency of the device. The curve clearly indicated that with increase in temperature, efficiency is decreasing. The optimized parameters are again used for simulation and the resulting efficiency reached to ~ 16.5%. The graph is shown in Fig. 2c.

## 4 Conclusion

We have simulated the NiO/CH<sub>3</sub>NH<sub>3</sub>GeI<sub>3</sub>/SnO<sub>2</sub> solar cell using SCAPS 1D simulator. The variation in absorber layer thickness indicated that the optimized thickness should be ~ 2 μm. The results indicated that the thickness of ETL should be lower and thickness of HTL should be higher. The variation in defect of absorber layer indicated that with increase in defects, the efficiency is decreasing. The elevated temperature resulted in diminished efficiency. The increase in work function of the back contact resulted in increased efficiency. The optimized efficiency of the device reached to ~ 16.5% after including all the parameters. Hence, this solar cell holds the potential to show significant efficiency and to be economical.

**Acknowledgements** The authors are extremely thankful to Dr. Marc Burgelman from University of Gent, Belgium, for SCAPS-1D simulator.

## References

1. Hussain S, Cao C, Usman Z, Chen Z, Nabi G, Khan WS, Ali Z, Butt FK, Mahmood T (2012) Fabrication and photovoltaic characteristics of Cu<sub>2</sub>O/TiO<sub>2</sub> thin film heterojunction solar cell. *Thin Solid Films* 522:430–434
2. Lakhdar N, Hima A (2020) Electron transport material effect on performance of perovskite solar cells based on CH<sub>3</sub>NH<sub>3</sub>GeI<sub>3</sub>. *Opt Mater (Amst)* 99:109517
3. Wang Q, Phung N, Di Girolamo D, Vivo P, Abate A (2019) Enhancement in lifespan of halide perovskite solar cells. *Energy Environ Sci* 12:865–886
4. Zhao P, Lin Z, Wang J, Yue M, Su J, Zhang J, Chang J, Hao Y (2019) Numerical simulation of planar heterojunction perovskite solar cells based on SnO<sub>2</sub> electron transport layer. *ACS Appl Energy Mater* 2:4504–4512
5. Yin X, Guo Y, Xie H, Que W, Kong LB (2019) Nickel oxide as efficient hole transport materials for perovskite solar cells. *Sol RRL* 3:1900001
6. Zhu Z, Bai Y, Liu X, Chueh C-C, Yang S, Jen AK-Y (2016) Enhanced efficiency and stability of inverted perovskite solar cells using highly crystalline SnO<sub>2</sub> nanocrystals as the robust electron-transporting layer. *Adv Mater* 28:6478–6484

# Enhanced Biodiesel Production from Waste Cooking Oil Using ZnO Nanocatalyst



P. Gada, S. K. Dusi, and I. Abrar

**Abstract** The demand for cleaner and renewable fuels has been on a rise in recent years due to the exhaustion of fossil fuels. In the current experimental investigation, waste cooking oil (WCO) was used for biodiesel production. Since WCO has a high free fatty acid (FFA) concentration, it results in poor biodiesel yield.  $H_2SO_4$  is used to reduce FFA content, which also helps to achieve a higher yield of biodiesel in a short span of time. WCO was collected from the college mess and was thoroughly cleaned to remove any food particles and inorganic residues suspended in the oil. Transesterification reaction was carried out at WCO-to-methanol ratio of 1:10 at 60 °C for two hours. Heterogeneous catalysts consisting of ZnO and  $H_2SO_4$  were used to improve the yield. The yield and properties of biodiesel were calculated after separation and purification. It was observed that with only  $H_2SO_4$  as catalyst, the yield of WCO-based biodiesel was 71.3%. The yield increased with addition of ZnO nanoparticles up to 81.94% at catalyst loading of 0.5% (w/w). Further increase in catalyst loading showed a decrease in the yield of biodiesel to 76.44% at catalyst loading of 1% (w/w). The calorific value of biodiesel was found to be 42.21 MJ/kg, and density was 0.89 g/ml. The acid value of biodiesel reduced to 0.62 as the addition of  $H_2SO_4$  acid lowered the FFA of the oil.

**Keywords** Waste cooking oil · Biodiesel · Nanoparticles · Heterogeneous catalysts · Renewable fuel

## 1 Introduction

The world is advancing day by day in terms of technology and innovation, and with the increasing advancements, the need for energy is also escalating. More than 80% of the energy requirements in the world are fulfilled by fossil fuels [1]. The substantial use of fossil fuels is damaging the environment in irreparable ways as they liberate

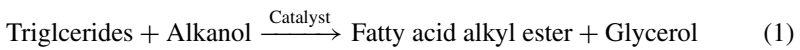
---

P. Gada · S. K. Dusi · I. Abrar (✉)

Department of Chemical Engineering, Birla Institute of Technology and Science, Pilani, Hyderabad Campus, Hyderabad, Telangana 500078, India  
e-mail: [iyman\\_abrar@yahoo.co.in](mailto:iyman_abrar@yahoo.co.in)

greenhouse gases like CO, CO<sub>2</sub>, and SO<sub>2</sub> when burnt [2]. These gases result in global warming which in turn leads to biodiversity loss and sea level rise. Also, they are non-renewable and require billions of years to be formed. So, it becomes crucial to look for substitute sources that can replace fossil fuels in the coming years. After thorough research in this field for decades, biofuels have been suggested as a better alternative. Not only does it produce fewer pollutants when compared to petroleum-based fuels, but also is found to be a durable fuel for automobiles.

Biofuels are majorly divided into first, second, and third generations. First-generation biofuels involve the use of edible oils as raw materials which leads to a food versus fuel debate, whereas the second-generation biofuels utilize non-edible oils and are often expensive compared to first-generation biofuels [3]. The third generation involves state-of-the-art machinery for biofuel synthesis. Vegetable oils have very high viscosities, approximately 10–20 times higher than petro-diesel. Transesterification is one of the most extensively used techniques to decrease the viscosity of the oils by transforming vegetable oils into biodiesel. The triglycerides of vegetable oils react with short-chain alcohol, usually methanol or ethanol, to yield fatty acid alkyl ester, known as biodiesel, as given in Eq. 1. Biodiesel is generally a straight-chain hydrocarbon, whereas diesel, on the other hand, involves ring structures. A high saturation level in fatty acids of biodiesel results in a greater value of cetane number, which is normally in the range of 44–69 [4]. Biodiesel usually contains up to 10% oxygen which results in improved combustion [5]. Though there are a variety of biofuels available, biodiesel is the most widely used and commercialized fuel. Since the properties of biodiesel are quite similar to those of petro-diesel, they are being used extensively as an alternative fuel [6].



The transesterification of vegetable oils can be achieved with or without the presence of catalyst. Catalysts are generally required to enhance the yield and reaction rate. Several types of catalysts can be used for this purpose and are mainly divided as homogeneous and heterogeneous catalysts. Homogeneous catalysts can be broadly classified as acid and base catalysts. Base catalysts, such as NaOH and KOH, are inexpensive and easily accessible, but require more energy. However, adding base catalysts increases the sensitivity towards the water and free fatty acids (FFA). On the other hand, acid catalysts, such as H<sub>2</sub>SO<sub>4</sub> and H<sub>3</sub>PO<sub>4</sub>, are not sensitive towards FFA [7]. However, they often form significant amounts of salt that leads to corrosion. Heterogeneous catalysts are considered to be more advantageous as they facilitate sustainable and economical biodiesel production [8]. With the development of nanotechnology, nanoparticles are being used as supplementary catalysts for biodiesel production mainly because they improve the yield of biodiesel, intensify the physicochemical properties of the fuel, and also boost its performance. Studies have shown that using nanoparticles as catalysts increases the rate of reaction due to their eccentric structure and properties such as small particle size and large specific surface area [9, 10]. Furthermore, unlike other catalysts, nanocatalysts do not get

deactivated very quickly and can be reused numerous times. The use of nanocatalyst also decreases the temperature of reaction, weight of catalyst required, and alcohol-to-oil ratio. Several kinds of heterogeneous catalysts can be used in the process such as transition metal oxide, ion exchange resins, and enzyme-based catalysts. For example, CaO was found to improve the yield of biodiesel obtained from transesterification of soybean oil [11]. A yield of 97.6% was obtained at 333 K when 3.7 wt% of catalyst was used. Combinations of catalysts have also been used to improve the yield of biodiesel. A combination of  $K_2CO_3/Al_2O_3$  at 333 K resulted in a yield of 94% which is quite high when compared to other cases which do not involve catalysts [12].

**Motivation:** The production of WCO is more than 190 MMT per year and is hazardous for the environment if left untreated [13]. However, a high percentage of FFA limits the yield of biodiesel production from WCO. Homogeneous catalysts like potassium hydroxide and sodium hydroxide generally used in transesterification reactions cause a few problems such as producing high amounts of waste, difficulty in reusing the catalyst, and soap formation. Hence, the current research work is dedicated to the use of heterogeneous catalysts to improve biodiesel yield with the help of combination of acid catalyst ( $H_2SO_4$ ) and nanocatalyst (ZnO). WCO can help in the development of low-cost sustainable fuels and fit into the new model of the circular economy.

## 2 Materials and Methods

### 2.1 Biodiesel Production

The major steps involved in biodiesel production from WCO include purification of WCO, transesterification, separation of glycerol from biodiesel, and purification of biodiesel. The WCO collected from the mess kitchens was first settled under gravity for 4–6 days at room temperature and later strained through sieves with pore size of 75 nm to remove any food particles and inorganic residues suspended in the oil. The WCO was then washed with water and again allowed to settle in order to remove the water-soluble impurities. It is followed by heating the oil at 110 °C for removal of any traces of water present in WCO. Transesterification was performed at oil-to-methanol ratio of 1:10. It was heated to 60 °C using a hot plate magnetic stirrer, and then methanol and sulphuric acid were added carefully. The speed was set to 350 rpm, and the reaction time was around two hours. After the reaction was complete, a mixture of biodiesel and glycerol was obtained. The end products were transferred to a separating funnel and left undisturbed for 15 min, where biodiesel and glycerol were separated out based on their dissimilar densities. The biodiesel obtained after separation was washed with deionised water. Biodiesel was again separated from water by allowing it to settle down in order to recover pure biodiesel, free from any impurities. The yield was calculated using Eq. 2.

$$\text{Yield (\%)} = \frac{\text{Weight of biodiesel obtained}}{\text{Weight of WCO used}} \times 100 \quad (2)$$

The effect of ZnO nanoparticles on yield of biodiesel was calculated by addition of 0.05, 0.1, and 0.2 wt% of ZnO, respectively, during transesterification reaction. In the experiments involving nanoparticles, a similar procedure was used, with the only difference being that the respective quantities of ZnO were first dispersed in methanol and then added to the WCO.

## 2.2 Measurement of Properties of Biodiesel

The density of produced biodiesel was established with the help of a specific gravity bottle of 25 ml capacity. Aniline point was found with the help of aniline point apparatus, using equal quantities of aniline and biodiesel. The temperature at which aniline and biodiesel were miscible was noted as the aniline point. The aniline point was used to calculate diesel index, as given in Eq. 3. The diesel index was further used to calculate cetane number empirically using Eq. 4 [14].

$$\text{Diesel index (DI)} = \frac{\text{Aniline point (}^{\circ}\text{F)} \times \text{API gravity}}{100} \quad (3)$$

$$\text{Cetane number} = (\text{DI} \times 0.72) + 10 \quad (4)$$

The calorific value of biodiesel was measured using bomb calorimeter apparatus, and the acid number was found by titrating WCO and WCO-based biodiesel against 1 M KOH solution.

## 3 Results and Discussion

### 3.1 Characterization of ZnO Nanoparticles

Energy dispersion X-ray fluorescence (ED-XRF) was used to identify and quantify the elements present in the nanoparticles. It was observed that the sample consisted of more than 95% Zn with traces of other elements like Si, S, and Ni. The X-ray diffraction (XRD) analysis was carried over a  $2\theta$  range from  $10^{\circ}$  to  $90^{\circ}$  with a scan width of  $0.01^{\circ}$  at a speed of  $2^{\circ}/\text{min}$ . The peaks obtained from XRD indicated crystalline phase with presence of hexagonal wurtzite structure, as shown in Fig. 1a, and were similar to those observed in literature [15]. Average crystallite size was found to be 8.73 nm. The thermal behaviour of ZnO nanoparticles was studied using TGA from 25 to  $900^{\circ}\text{C}$  at the rate of  $10^{\circ}\text{C}/\text{min}$ , as given in Fig. 1b. The weight loss

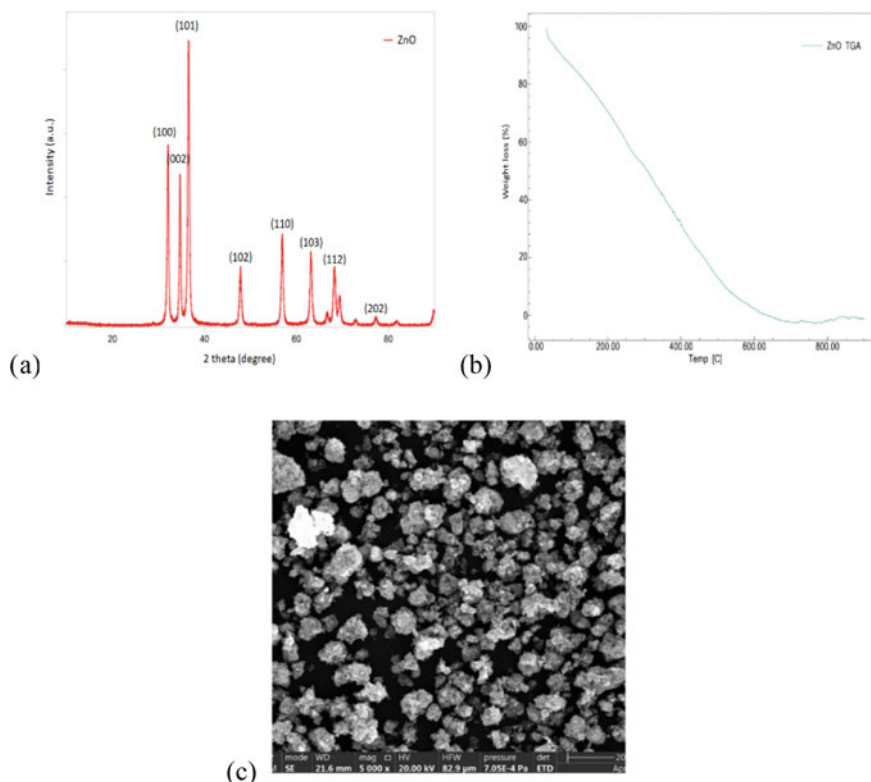


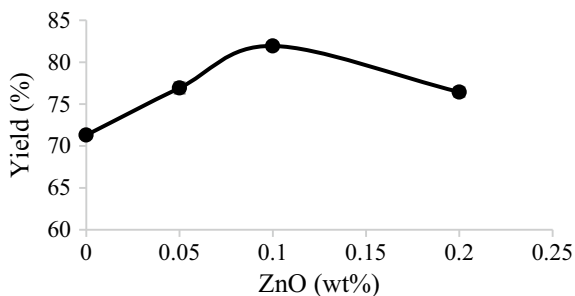
**Fig. 1** Characterization of ZnO nanoparticles. **a** XRD, **b** TGA analysis, **c** SEM at 5000X

started around 50 °C due to evaporation of water molecules adsorbed on nanoparticles. Around 50% of weight loss occurred at 300 °C, and 90% of weight loss occurred at 525 °C. No observable reactions occurred at temperatures above 600 °C. FE-SEM was used to obtain structural morphology of ZnO nanoparticles at magnifications of 5000X, as shown in Fig. 1c. It was observed that ZnO nanoparticles had average particle size of around 50 nm.

### 3.2 Effect of ZnO on Yield of WCO Biodiesel

In order to decrease the FFA percentage of WCO,  $H_2SO_4$  was used as an acid catalyst. A biodiesel yield of 71.3% is obtained with  $H_2SO_4$ . ZnO nanoparticles were added to the reaction mixture because the properties of nanoparticles help to improve the yield of biodiesel. The influence of ZnO nanoparticle loading on the yield of biodiesel is given in Fig. 2. With increase in the catalyst loading from 0.05 to 0.1 wt%, the biodiesel yield enhanced from 76.93 to 81.94%, respectively. Nonetheless, when the

**Fig. 2** Effect of ZnO nanoparticles on the yield of WCO biodiesel



catalyst loading was further increased to 0.2 wt%, the yield dropped to 76.44%. The main reason behind this is the diffusion limitation between WCO and methanol at increased solid interfaces in the reaction mixture at high nanoparticle concentrations.

### 3.3 Properties of WCO Biodiesel

The density of WCO was 0.92 g/ml, which reduced to 0.89 g/ml for WCO biodiesel. Even though the density of biodiesel is less than WCO, it still is greater compared to petro-diesel. The density of fatty acid alkyl ester produced depends on the degree of unsaturation, and its density increases when the unsaturation level increases. It is advisable to blend biodiesel with diesel in order to further decrease its density and use it as an alternative fuel for transportation [16]. The aniline point was found to be around 32 °C. A relatively lower value of aniline point indicates the presence of aromatic compounds in the biodiesel [17]. Consequently, the diesel index and cetane number were 24.6 and 27.7, respectively. The cetane number of petro-diesel is commonly around 44–60 for petroleum-based fuels. A lower cetane value was obtained due to the increasing blending ratio of methanol during transesterification, which can affect the combustion in the engine. The calorific value of WCO was 38.83 MJ/kg, which increased to 42.21 MJ/kg for biodiesel. The calorific value of WCO biodiesel was found to be close to that of petro-diesel. Similarly, the acid value of WCO was 3.12, which was reduced significantly to 0.62 for biodiesel. It is evident that the acid value of biodiesel is lesser than WCO as the addition of H<sub>2</sub>SO<sub>4</sub> acid lowered the FFA of the oil.

## 4 Conclusion

The main objective of the current work was to find an economical and sustainable alternative for petro-diesel, with similar performance. Waste cooking oil is generated worldwide from frying, which is one of the most common method for cooking.



Appropriate disposal of WCO remains to be a global issue and usually ends up contaminating the water and in the landfills. Hence, it was used as a raw material for biodiesel production.

Since WCO has a large FFA concentration, it cannot be directly used for biodiesel production. Therefore, sulphuric acid was used for transesterification of WCO which yielded 71.3% of biodiesel. In order to further improve the yield of biodiesel, ZnO nanoparticles were added during transesterification. The ZnO nanoparticles were characterized by XRD, TGA, ED-XRF, and SEM. It was noted that the average particle size of ZnO nanoparticles was around 50 nm, with crystallite size of 8.73 nm. The nanoparticles showed 90% of weight loss occurred at 525 °C and consisted mostly of Zn, with impurities of traces elements like Cl, P, S, and Ca. The nanoparticles helped to increase the yield of biodiesel. It was witnessed that initially the biodiesel yield improved with an increase in the percentage of catalyst, and after reaching the maxima of 81.94% yield for 0.1 wt% ZnO, the yield decreased with a further increase in catalyst loading. The biodiesel produced from WCO had lower density, lower acid value, and higher calorific value compared to WCO. However, the cetane number was also lower compared to the requirements of diesel fuel alternatives. Hence, more research needs to be performed in order to improve the cetane number of WCO biodiesel.

The application of WCO for biodiesel production would help in moving towards circular economy. Nanomaterials such as ZnO can be utilized to enhance the yield of biodiesel, but still, additional research has to be executed in order to comprehend the fate of these nanoparticles in the engine.

**Acknowledgements** Dr. Iyman Abrar would like to thank Birla Institute of Technology and Science, Pilani, Hyderabad Campus, India, for providing financial support by Research Initiation Grant (BITS/GAU/RIG/2021/H0774) and Additional Competitive Research Grant (BITS/GAU/ACRG/2021/H0774).

## References

1. Thompson H (2022) The geopolitics of fossil fuels and renewables reshape the world. *Nature* 603:364. <https://doi.org/10.1038/D41586-022-00713-3>
2. Abrar I, Bhaskarwar AN (2021) Performance and emission characteristics of constant speed diesel engine fueled by surfactant-free microemulsions. *Sustain Energy Technol Assessments* 47:101414
3. Abrar I, Bhaskarwar AN (2018) Performance of microemulsion fuels as an alternative for diesel engine. In: ASME 2018 internal combustion engine division fall technical conference ICEF2018, ASME, San Diego, CA, USA, pp 1–9. <http://doi.org/10.1115/ICEF2018-9566>
4. Hoekman SK, Broch A, Robbins C, Cenicerros E, Natarajan M (2012) Review of biodiesel composition, properties, and specifications. *Renew Sustain Energy Rev* 16:143–169
5. Abrar I, Bhaskarwar AN (2016) A microemulsion fuel composition and method of formulating. Indian Patent Application 201611039919
6. Abrar I, Bhaskarwar AN (2018) Formulation and extension of diesel-based microemulsion fuels for compression ignition engines. *INAE Lett* 3:33–39. <https://doi.org/10.1007/s41403-018-0037-0>

7. Ma F, Hanna MA (1999) Biodiesel production: a review. *Bioresour Technol* 70:1–15. [https://doi.org/10.1016/S0960-8524\(99\)00025-5](https://doi.org/10.1016/S0960-8524(99)00025-5)
8. Abrar I, Bhaskarwar AN (2019) An overview of current trends and future scope for vegetable oil-based sustainable alternative fuels for compression ignition engines. In: Basile A, Dalena F (eds) *Second and third generation of feedstocks*, 1st edn. Elsevier, pp 531–556. <http://doi.org/10.1016/B978-0-12-815162-4.00019-7>
9. Sekoai PT, Ouma CNM, du Preez SP, Modisha P, Engelbrecht N, Bessarabov DG, Ghimire A (2019) Application of nanoparticles in biofuels: an overview. *Fuel* 237:380–397
10. Abrar I, Bhaskarwar AN (2022) Mitigating exhaust emissions in CI engines using butanol–diesel–water microemulsions. *Environ Sci Pollut Res* 1–12. <http://doi.org/10.1007/s11356-022-24352-3>
11. Bharti P, Singh B, Dey RK (2019) Process optimization of biodiesel production catalyzed by CaO nanocatalyst using response surface methodology. *J Nanostruct Chem* 9:269–280
12. Di Serio M, Tesser R, Pengmei L, Santacesaria E (2008) Heterogeneous catalysts for biodiesel production. *Energy Fuels* 22:207–217
13. Mannu A, Garroni S, Porras JI, Mele A (2020) Available technologies and materials for waste cooking oil recycling. *Processes* 8:1–13. <https://doi.org/10.3390/PR8030366>
14. Haldar SK, Ghosh BB, Nag A (2009) Studies on the comparison of performance and emission characteristics of a diesel engine using three degummed non-edible vegetable oils. *Biomass Bioenerg* 33:1013–1018
15. López C, Rodríguez-Páez JE (2017) Synthesis and characterization of ZnO nanoparticles: effect of solvent and antifungal capacity of NPs obtained in ethylene glycol. *Appl Phys A Mater Sci Process* 123:1–16. <https://doi.org/10.1007/S00339-017-1339-X/FIGURES/10>
16. Abrar I, Bhaskarwar AN (2020) Effect of alcohol on the properties of water-in-diesel microemulsion fuels. *Environ Prog Sustain Energy* 39:13422. <https://doi.org/10.1002/ep.13422>
17. Uddin MR, Ferdous K, Uddin MR, Khan MR, Islam MA (2013) Synthesis of biodiesel from waste cooking oil. *Chem Eng Sci* 1:22–26. <http://doi.org/10.12691/CES-1-2-2>

# Energy Conservation in the Vapour Compression Refrigeration System Using Nanorefrigerant



S. S. Sanukrishna and S. Reshmi Krishnan

**Abstract** Every year, the world's energy consumption increases rapidly. One of the main causes of the rising pattern of energy consumption around the world is the increase in the number of refrigeration and air-conditioning systems in both the commercial and residential sectors. It is necessary to improve these systems' energy efficiency in light of environmental concerns and energy security. Investigating the R134a/TiO<sub>2</sub> nanorefrigerant's heat transfer properties is the main objective of the current effort. In a horizontal smooth tube, flow boiling heat transfer investigations have been carried out at varied mass fluxes, heat fluxes, particle concentrations, and vapour quality. The findings demonstrate that adding TiO<sub>2</sub> nanoparticles to the refrigerant significantly improves its heat transfer properties. It is discovered that the greatest increase enhancement factor is 101.3%. The performance of a vapour compression refrigeration system using nanorefrigerant was also investigated through experimental investigations, which produced the following findings. Using nanorefrigerants, the refrigeration system's performance coefficient is enhanced by 19.4%, and power consumption is decreased by 8.33%. The outcomes of the experiment point to the potential of using nanorefrigerants in the creation of energy-efficient refrigeration systems.

**Keywords** Nanolubricant · Nanorefrigerant · Heat transfer coefficient

## 1 Introduction

Nanofluids were first proposed as a revolutionary heat transfer medium by Choi et al. [1]. Nanofluids are created colloids of host fluids and nanoparticles. Researchers have recently considered using energy-efficient nanoparticles into lubricants and refrigerants. There are two categories of nanorefrigerants: direct refrigerants and lubricants-based refrigerants. Although in the latter, nanolubricants are combined with the

---

S. S. Sanukrishna (✉) · S. Reshmi Krishnan  
Sree Chitra Thirunal College of Engineering, Thiruvananthapuram, Kerala 695018, India  
e-mail: [sanukrishna@scetce.ac.in](mailto:sanukrishna@scetce.ac.in)

refrigerants, the former directly disperses the required amount of small nanoparticles in the host refrigerant [2]. The thermophysical and heat transport capacities notably increase when nanoparticles are introduced to refrigerants, which increases efficiency and reliability [3, 4]. The scientific community on nanofluids has published very few experimental studies about the behaviour of boiling in nanorefrigerants [5]. Most research, many of which are also inconsistent [6], have demonstrated both advantages and disadvantages of flow boiling heat transfer [7]. The current study [8] employs an experimental methodology to investigate the effects of incorporating  $\text{TiO}_2$  nanoparticles into R134a refrigerant, with a focus on flow boiling regime studies.

## 2 Experimental Methodology

### 2.1 *Flow Boiling Heat Transfer Studies on R134a/TiO<sub>2</sub> Nanorefrigerant*

To validate the experimental design, the estimated heat transfer coefficient for pure R134a from the literature is compared with the experimental value. Studies utilizing  $\text{TiO}_2$ -nano refrigerant were the next to investigate the impact of nanoparticles on the heat transfer coefficient. It was decided to use particle concentrations of 0.1, 0.4, and 0.8 vol%. The effects of particle concentration, heat flow, mass flux, and vapour quality are investigated concerning the heat transfer coefficient (HTC).

#### 2.1.1 Experimental Test Rig

ASTM D7863-17 standard is followed to conduct the convective heat transfer experiments [9]. Figure 1 shows the schematic diagram of the experimental set-up.

The test evaporator is a horizontal copper tube that is smooth, 10.2 mm in diameter, and 1 m long. The refrigerant is cycled through using a gear pump, which also makes up for pressure loss. To guarantee sub-cooled liquid at the pump's inlet, the temperature of the condensing medium is controlled concerning the saturation temperature of the refrigerant matching the pressure. It is anticipated that there will be no heat loss and that the heat input into the test portion will remain constant. T-type thermocouples are used at six different points along the test section to measure the outer tube wall temperature with an accuracy of  $0.50^\circ\text{C}$ . The heat transfer coefficients acquired from various sources are compared using the correlation for R134a given by Panek et al.

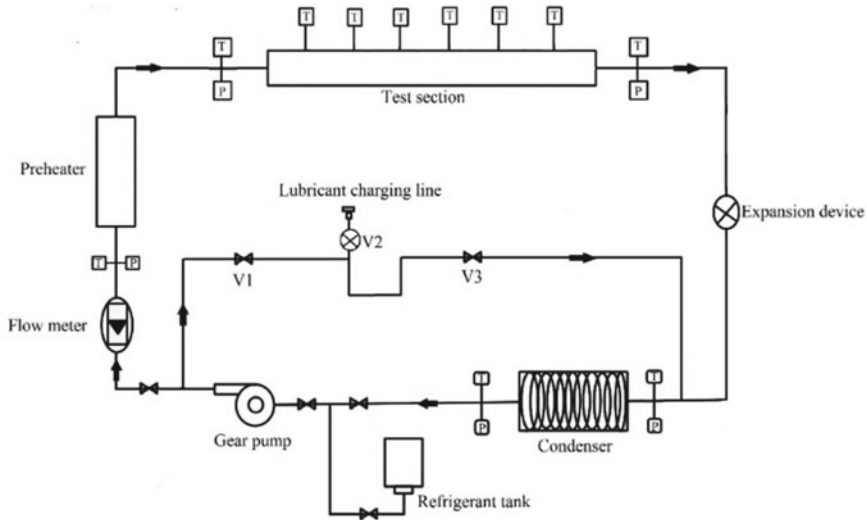


**Fig. 1** Schematic diagram of the experimental set-up

## 2.2 Performance Evaluation of Vapour Compression Refrigeration System (VCRS)

Experimental research has been done to explain how nanorefrigerant affects VCRS performance. For the performance tests, an in-house test rig is created. In the refrigerant compressor, tests are carried out using R134a+ pure PAG (poly alkylene glycol) lubricant and R134a+ TiO<sub>2</sub>-PAG nanolubricants. The experimental study's assumed particle concentration is 0.1 vol%. To establish repeatability, the experiments are repeated in identical environmental settings, and it is discovered that the results roughly match. For the purpose of calculating the performance characteristics, average values are used.

## 3 Results and Discussion

### 3.1 Flow Boiling Heat Transfer of R134a/PAG Oil and R134a/TiO<sub>2</sub>/PAG Oil

The heat transfer coefficients at various mass fluxes and volume fractions are compared in Fig. 2. It is evident that the flow boiling heat transfer properties are significantly influenced by the nanorefrigerant. The graph unequivocally demonstrates that, for all mass fluxes, the presence of nanoparticles in the refrigerant resulted in a higher heat transfer coefficient than the mixture of pure lubricant and refrigerant.

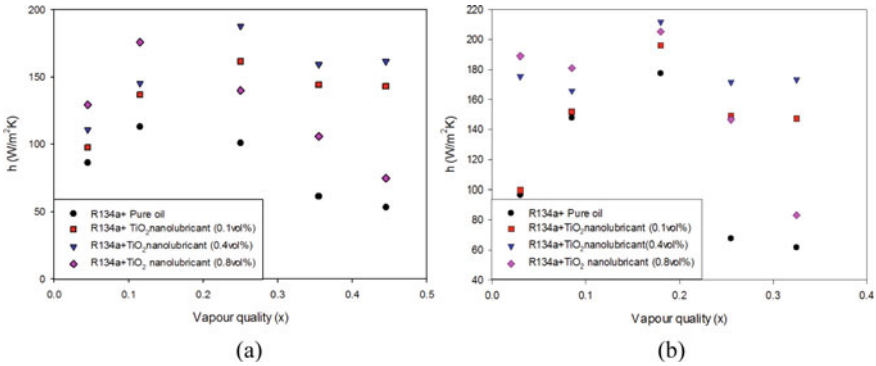


**Fig. 2** Comparison of heat transfer coefficient versus vapour quality at **a** mass flux of 34 kg/m<sup>2</sup> s, **b** mass flux of 47 kg/m<sup>2</sup> s

The outcomes also demonstrate that the mass flux is accompanied by an increase in the heat transfer coefficient. The reasons for the rise in HTC are a change in flow regimes and higher liquid velocities at higher mass fluxes. The maximum HTC for nanolubricants is 196.13, 211.28, and 205.28 W/m<sup>2</sup> K, respectively, for concentrations of 0.1, 0.4, and 0.8 vol%. With a volume fraction of 0.4%, nanolubricant exhibits the highest.

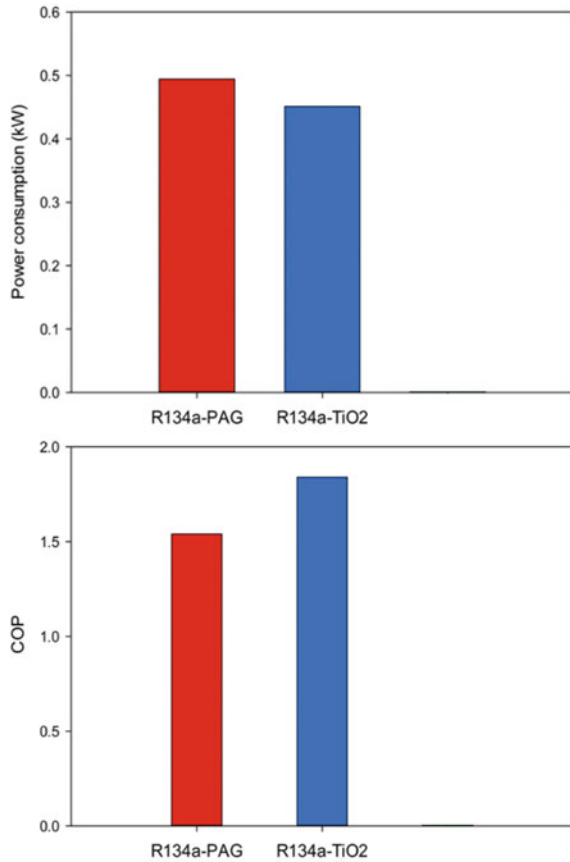
### 3.2 Power Consumption and COP of the VCRS

With pure lubricant and nanolubricant, the hermetic refrigerant compressor's power consumption is assessed. The comparison of the power used by the refrigerant compressor and COP in both scenarios is shown in Fig. 3. By substituting nanolubricants for pure lubricant, the power used by the refrigerant compressor is decreased. TiO<sub>2</sub> nanoparticles added to the lubricant have a notable impact on power usage. Compared with pure lubricant, there is an 8.33% decrease in power usage. The image makes it evident that adding nano-sized TiO<sub>2</sub> particles to the refrigerant greatly increases the COP of the VCRS. In comparison with pure lubricant-refrigerant mixture nanorefrigerant, R134a-TiO<sub>2</sub> exhibits a 19.4% increase in COP.

## 4 Conclusions

The current study examines the usage of nanorefrigerant in a VCRS from the perspective of energy conservation, as well as the experimental determination of the flow boiling heat transfer parameters of R134a/TiO<sub>2</sub>. The main conclusions are that (i) the flow boiling heat transfer properties of R134a-TiO<sub>2</sub> nanolubricant outperform

**Fig. 3** Comparison of power consumption and COP



those of pure refrigerant at all particle concentrations, and (ii) at a volume fraction of 0.4%, the greatest flow boiling heat transfer coefficient is observed. Also, the performance coefficient of the vapour compression refrigeration system is raised by 19.4%, while the power consumption of the hermetic reciprocating compressor is reduced by 8.33%. The use of a revolutionary nanolubricant could result in the creation of HVAC systems that use less energy.

## References

1. Eastman JA, Choi SUS, Li S, Thompson LJ, Lee S (1997) Enhanced thermal conductivity through the development of nanofluids. In: MRS proceedings, vol 457, pp 3–11
2. Nair V, Tailor PR, Parekh AD (2016) Nanorefrigerants: a comprehensive review on its past, present and future. *Int J Refrig* 67:290–307
3. Subramani N, Prakash MJ (2011) Experimental studies on a vapour compression system using nanorefrigerants. *Int J Eng Sci Technol* 3:95–102

4. Sharif MZ, Azmi WH, Redhwan AAM, Mamat R, Yusof TM (2017) Performance analysis of SiO<sub>2</sub>/PAG nanolubricant in automotive air conditioning system. *Int J Refrig* 75:204–216
5. Liu DW, Yang CY (2007) Effect of nano-particles on pool boiling heat transfer of refrigerant 141b. In: ICNMM, pp 789–793
6. Park KJ, Jung D (2007) Enhancement of nucleate boiling heat transfer using carbon nanotubes. *Int J Heat Mass Transf* 50:4499–4502
7. Peng H, Ding G, Jiang W, Hu H, Gao Y (2009) Heat transfer characteristics of refrigerant-based nanofluid flow boiling inside a horizontal smooth tube. *Int J Refrig* 32:1259–1270
8. Panek JS, Chato JC, Jabardo JMS, De Souza AL, Wattlelet JP (1992) Evaporation heat transfer and pressure drop in ozone-safe refrigerants and refrigerant-oil mixtures
9. ASTM D7863-17 (2017) ASTM International, West Conshohocken, PA. [www.astm.org](http://www.astm.org)



# Facile Synthesis of Highly Fluorescent N-CQDs and Its Application for Dye Degradation and Sensing of Cr<sup>3+</sup>



Qurtulen and Anees Ahmad

**Abstract** This work describes a low-impact method for generating nitrogen-doped carbon quantum dots. The N-CDs were produced by a hydrothermal procedure that used grass as a precursor. Surface morphology and functional groups were investigated using Fourier transform infrared spectroscopy (FTIR), transmission electron microscopy (TEM), and x-ray diffraction method (XRD). Moreover, UV–vis and fluorescence spectroscopy have been used to investigate N-CD optical performance. N-CDs provide both long-lasting fluorescence and excellent biocompatibility. Rhodamine B was chosen for this study to investigate the photocatalytic performance of the nanomaterial under UV–vis light irradiation. The carbon dots synthesized displayed excellent photocatalytic activity for Rh B dye at varied concentrations (10 and 20 ppm), with a degradation efficiency of up to 90%, suggesting the crucial role of N-CDs in increasing the separation migration efficiency of photoexcited e-h<sup>+</sup> couples. Surprisingly, as N-CDs are formed, they are highly sensitive to Cr<sup>3+</sup> ions and cause fluorescence quenching with a LOD of 0.16 μM.

**Keywords** Nitrogen-doped carbon quantum dots · Photocatalytic degradation · Sensing · Fluorescence quenching

## 1 Introduction

N-CDs are highly fluorescent zero-dimensional carbon-based nanomaterials having crystalline or amorphous structures [1]. Usually N-CDs have sp<sup>2</sup> hybridization, followed by sp<sup>3</sup> hybridization. Because of their biological properties, ease of synthesis, reduced toxicity, enhanced photostability, hydrophilicity, wavelength customizable emission, easy functionalization, and environmentally friendly nature [2], N-CDs are favoured over conventional heavy metal quantum dots. N-CDs were discovered in 2004 while purifying single-walled carbon nanotubes [3, 4]. Carbon quantum dots are primarily synthesized using two processes: top down and bottom up

---

Qurtulen (✉) · A. Ahmad  
Department of Chemistry, Aligarh Muslim University, Aligarh 202002, India  
e-mail: [qurtulen.123@gmail.com](mailto:qurtulen.123@gmail.com)

[5]. N-CDs are highly fluorescent nanomaterials with precise photoluminescent and optoelectronic properties due to their strong quantum confinement effect. Because of their chemical inertness and great biocompatibility, N-CDs are frequently used in analytical nanoscience, nanotechnology, and sensor creation [6]. It can also be used to identify biomolecules, detect heavy metals, and in photocatalysis [7]. In this paper, we describe the hydrothermal synthesis of N-CDs from grass. This synthesis uses a low-cost feedstock, has no toxicity, is environmentally benign, and uses water as a solvent. The N-CDs as synthesized have a high sensitivity to  $\text{Cr}^{3+}$  ions.

## 2 Materials and Instruments

Aluminium chloride ( $\text{AlCl}_3$ ), calcium chloride ( $\text{CaCl}_2$ ), cadmium chloride ( $\text{CdCl}_2$ ), chromium chloride ( $\text{CrCl}_3$ ), cobalt chloride ( $\text{CoCl}_2$ ), copper chloride ( $\text{CuCl}_2$ ), iron chloride ( $\text{FeCl}_3$ ), mercuric nitrate ( $\text{Hg}(\text{NO}_3)_2$ ), potassium chloride (KCl), magnesium chloride ( $\text{MgCl}_2$ ), manganese chloride ( $\text{MnCl}_2$ ), sodium chloride ( $\text{NaCl}$ ), nickel chloride ( $\text{NiCl}_2$ ), lead chloride ( $\text{PbCl}_2$ ), zinc chloride ( $\text{ZnCl}_2$ ), sodium hydrogen phosphate ( $\text{NaH}_2\text{PO}_4$ ) and ( $\text{Na}_2\text{HPO}_4$ ) were taken from CDH. Grass was harvested from the AMU campus as a forerunner. All of the solutions were made in double water. FTIR (Fourier transform infrared microscopy, Model Spectrum-BX, USA) was utilized to identify all functional groups of N-CDs, and x-ray diffraction (PW-1148/89 Netherlands with CuK $\alpha$  radiation) was employed for structural investigation. Transmission electron microscopy (TEM) 2100, JEOL, Japan was used to determine particle size at 200 kV. N-CDs UV–vis and fluorescence spectra were recorded using a UV–vis and fluorescence spectrometer (PerkinElmer) [8].

### 2.1 N-CDs Synthesis

5 g grass was washed by double distilled water and dried for the synthesis of N-CDs. The dried grass was then ground into powder and dissolved in 50 mL of distilled water. The entire mixture was placed in a Teflon-lined autoclave and put in a 250 °C oven for 3 h before being allowed to cool at room temperature. Finally, the solution was centrifuged for 20 min at 1000 rpm, and the resulting solution was filtered through a dialysis membrane (500–1000 MWCO) for 20 h. Then the suspension was stored at 4 °C [9].

## 2.2 Photocatalytic Activity and Fluorescence Quenching of N-CDs

To study the photocatalytic activity of the generated N-CDs, photocatalytic decomposition of aqueous solution of Congo red under UV light irradiation was used. A UV–visible spectrophotometer was employed to determine the degradation efficiency of the generated N-CDs at their distinct absorption maxima. The concentration of N-CDs was adjusted to 0.01 mg/mL and 300 ppm concentration of different 14 metal ions solutions ( $\text{Ca}^{2+}$ ,  $\text{Na}^+$ ,  $\text{Al}^{3+}$ ,  $\text{Cr}^{3+}$ ,  $\text{Co}^{2+}$ ,  $\text{Fe}^{3+}$ ,  $\text{Mn}^{2+}$ ,  $\text{Mg}^{2+}$ ,  $\text{Cu}^{2+}$ ,  $\text{Cd}^{2+}$ ,  $\text{Zn}^{2+}$ ,  $\text{Ni}^{2+}$ ) were prepared in distilled water. After 5 min all the samples were subjected to fluorescence measurement.

## 3 Results and Discussion

### 3.1 Morphological and Optical Studies of N-CDs

The functional groups present on the surface of the synthesized product were identified using FTIR spectra. As illustrated in Fig. 1a, the O–H/N–H bond's stretching vibrations were assigned a broad band at  $3400\text{ cm}^{-1}$ , while C–H bonds stretching vibrations were assigned a small peak at  $2900\text{ cm}^{-1}$ . The existence of –COO– was indicated by a peak at  $1650\text{ cm}^{-1}$ , stretching vibrations of C=C were indicated by a band at  $1440\text{ cm}^{-1}$ , and bending vibrations of the C–O group were indicated by a broad band at  $1055\text{ cm}^{-1}$ . The XRD pattern of the nanomaterial is shown in Fig. 1b depicts, where  $2\theta = 18^\circ, 22^\circ$ , indicating the amorphous nature of N-CDs. Figure 1c, d show TEM images of spherical and monodispersed N-CDs with an average diameter of 3 nm (as shown in Fig. 1d inset) computed using IMAGE-J software. As illustrated in Fig. 1e, the produced N-CDs exhibit absorption peaks at 275 nm and 330 nm, indicating the transition from  $\pi$ - $\pi^*$  and  $n$ - $\pi^*$ , respectively. As demonstrated in Fig. 1f, the emission spectra were shifted to longer wavelengths, with the intensity gradually decreasing as the emission wavelength increased [10].

### 3.2 Sensing of $\text{Cr}^{3+}$ and Photocatalytic Degradation of Rhodamine B Dye

The relationship between  $\text{Cr}^{3+}$  concentration and fluorescent quenching was explored in order to demonstrate the analytical performance of N-CDs-based fluorescence sensors. Figure 2a shows that raising the quantity of  $\text{Cr}^{3+}$  decreases the intensity of fluorescence at 360 nm, demonstrating that fluorescence quenching of N-CDs occurs when  $\text{Cr}^{3+}$  is added. Figure 2c displays the mechanism of fluorescence quenching as

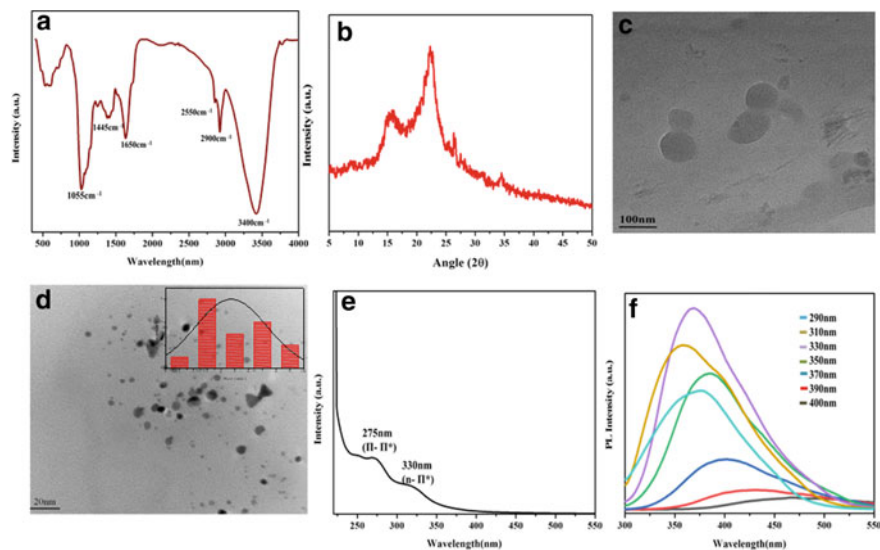


**Fig. 1** a FTIR spectra of N-CDs, b XRD pattern of the synthesized product, c, d TEM images of N-CDs, e UV spectrum of N-CDs, f Fluorescence spectrum of synthesized product

well as an excellent linear correlation across the range of 0.1 to 100 M with correlation coefficient squares ( $R^2 = 0.99$ ). The limit of detection (LOD) value is  $0.16 \mu\text{M}$  ( $S/N = 3$ ). The selectivity of  $\text{Cr}^{3+}$  over other metal ions is demonstrated in Fig. 2b, which shows that the fluorescence intensity of N-CDs is significantly reduced only in the presence of  $\text{Cr}^{3+}$  when compared with other metal ions. As a result,  $\text{Cr}^{3+}$  exhibits the maximum selectivity for the fluorescence quenching of N-CDs, demonstrating that N-CDs might be employed for the selective detection of  $\text{Cr}^{3+}$  in aqueous solutions [11].

The photocatalytic degradation of the resultant product was evaluated using the following RhB dye degradation. The obtained results demonstrated that the produced nanomaterial shows high degradation efficiency, and decomposition occurs in faster manner because of the production of reactive oxide species (ROS) in an aqueous solution RhB was completely degraded in 10 min at 5 ppm, with a degradation efficiency of 90%, as shown in Fig. 2d. With 10 ppm, degradation occurs within 30 min with a degradation efficiency of 87.7%, and degradation of 20 ppm dye occurs within 60 min with a degradation efficiency of 85% (as shown in Fig. 2e, f respectively). When exposed to UV light, free radicals formed, which cause decomposition. On the basis of these results, it is possible to deduce that degradation efficiency was significantly lowered as dye concentration increased. Furthermore, when increased the dye concentration, light photons are reacted by the molecules of dye before they strike the catalyst surface; as a result, radical hydroxyl formation is reduced, lowering the degradation efficiency [12].

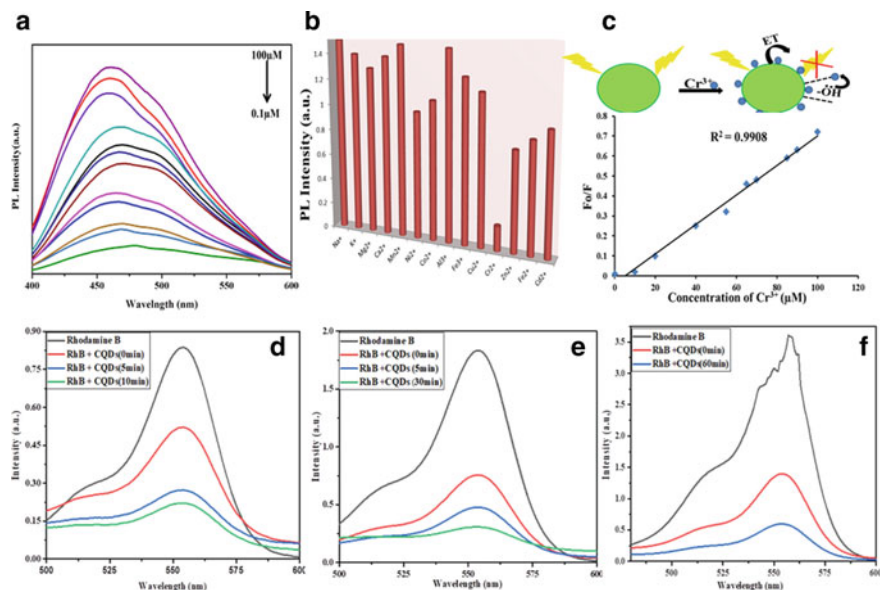


**Fig. 2** **a** Showing the intensity of N-CDs fluorescence at various  $\text{Cr}^{3+}$  concentrations (from 0.1 to 100  $\mu\text{M}$ ), **b** N-CDs (0.01 mg/mL) solution selectivity for  $\text{Cr}^{3+}$  over other ionic species. The red bars represent the addition of various metal ions to the N-CDs solution, **c** N-CDs-based fluorescence probe for  $\text{Cr}^{3+}$  sensing mechanism and Stern–Volmer plot of N-CDs at different concentrations of  $\text{Cr}^{3+}$  (0.01–100 M), where  $F_0/F$  is the fluorescence intensity of N-CDs in the presence and absence of  $\text{Cr}^{3+}$ . Degradation of RhB at **d** 5 ppm, **e** 10 ppm, **f** 20 ppm concentration

## 4 Conclusion

The synthesized N-CDs, employing a one-step hydrothermal procedure from grass, have negligible toxicity, outstanding photostability, and are economically feasible. XRD and FTIR confirmed that the CDs were amorphous and made up of carbon, oxygen, and nitrogen. The TEM images showed that the synthesized product has an average diameter of 3.4 nm. N-CDs demonstrated a high degradation efficiency of up to 90% for the degradation of Rh B dye, as well as a shorter degradation time. Additionally, the acquired product was used as a fluorescent sensor for the highly sensitive and specific detection of  $\text{Cr}^{3+}$ , which was developed advantageously because  $\text{Cr}^{3+}$  effectively quenches the fluorescence intensity of N-CDs.

**Declaration of Interest** There is no conflict of interest.

## References

1. Salimi Shahraki H, Ahmad A, Bushra R (2022) Green carbon dots with multifaceted applications—waste to wealth strategy. *FlatChem* 31
2. Salimi Shahraki H, Qurtulen, Ahmad A (2023) Synthesis, characterization of carbon dots from onion peel and their application as absorbent and anticancer activity. *Inorg Chem Commun* 150
3. Rajamanikandan S, Biruntha M, Ramalingam G (2022) Blue emissive carbon quantum dots (NCDs) from bio-waste peels and its antioxidant activity. *J Clust Sci* 33:1045–1053
4. Syed N, Huang J, Feng Y (2021) NCDs as emerging trends for future prospect in enhancement of photocatalytic activity. *Carbon Lett* 321(32):81–97
5. Shahraki HS, Bushra R, Shakeel N, Ahmad A, Qurtulen, Ahmad M, Ritzoulis C (2023) Papaya peel waste carbon dots/reduced graphene oxide nanocomposite: from photocatalytic decomposition of methylene blue to antimicrobial activity. *J Bioresour Bioprod* 8(2):162–175
6. Manikandan V, Lee NY (2022) Green synthesis of carbon quantum dots and their environmental applications. *Environ Res* 212:113283
7. Rani UA, Ng LY, Ng CY, Mahmoudi E (2020) A review of carbon quantum dots and their applications in wastewater treatment. *Adv Colloid Interface Sci* 278
8. Shen Y, Rong M, Qu X, Zhao B, Zou J, Liu Z, Bao Y, He Y, Li S, Wang X, Chen M, Chen K, Zhang Y, Niu L (2022) Graphene oxide-assisted synthesis of N, S Co-doped carbon quantum dots for fluorescence detection of multiple heavy metal ions. *Talanta* 241:123224
9. Sabet M, Mahdavi K (2019) Green synthesis of high photoluminescence nitrogen-doped carbon quantum dots from grass via a simple hydrothermal method for removing organic and inorganic water pollutions. *Appl Surf Sci* 463:283–291
10. Bozetine H, Meziane S, Aziri S, Berkane N, Allam D, Boudinar S, Hadjersi T (2021) Facile and green synthesis of a ZnO/NCDs/AgNPs ternary heterostructure photocatalyst: study of the methylene blue dye photodegradation. *Bull Mater Sci* 44:1–12
11. Bilge S, Karadurmus L, Snaž A, Ozkan SA (2021) Green synthesis and characterization of carbon-based materials for sensitive detection of heavy metal ions. *TrAC Trends Anal Chem* 145:116473
12. Qurtulen Q, Ahmad A, Shahraki HS, Shakeel N, Bushra R (2023) Cynodon dactylon derived fluorescent N-doped carbon dots: implications for photocatalytic and biological applications. *Surf Interfaces* 102812

# TiO<sub>2</sub>/PEDOT: PSS Hybrid Matrix for Optoelectronic Devices



Arshiya Ansari, Shahzad Ahmed, Moin Ali Siddiqui, Devendra Singh Negi, and Pranay Ranjan

**Abstract** Titanium dioxide (TiO<sub>2</sub>) nanoparticles are widely investigated for their crucial optoelectronic properties. However, when these TiO<sub>2</sub> nanoparticles were added to a hybrid framework made of the conductive polymer poly(3,4-ethylenedioxythiophene): poly(styrenesulfonate) (PEDOT: PSS), the sensitivity of the photoconductive material escalated by a factor of 1.3. The structural investigation through Raman spectroscopy, reveals the hybridization of the orbital of TiO<sub>2</sub> nanoparticles and PEDOT: PSS, wherein, the peaks shift (vibrational bond) has been observed. A facile route using the drop-casting technique has been utilized to engineer the hybrid TiO<sub>2</sub> nanoparticles and PEDOT: PSS onto the *p*-type silicon (*p*-Si) wafer. Morphological characterization through SEM and AFM reveals a layer thickness of around 1 μm and an average surface roughness of 0.191 nm, respectively. An ultraviolet (UV) light source of 365 nm wavelength and intensity of 200 mW cm<sup>-2</sup>, was exposed to record the change in photoconductivity in light and dark modes. The hybrid films showed a response of 21.5%, almost three times better than that for the pristine PEDOT: PSS having only 7.2%, which indicates an enhanced charge transport in the hybrid films under UV light radiation. Our design approach might be successfully used in the manufacturing of several sensors that could identify the dangerous UV radiation that causes sunburn, early aging, skin cancer, and numerous other UV-related skin illnesses. Additionally, our method may be useful in creating sensors for use in biomedical, space applications, and other areas, such as the detection of bioanalytes.

**Keywords** Ultraviolet sensor · Metal-oxide nanoparticles · Conducting polymer · Photoconductivity measurement

---

A. Ansari (✉) · S. Ahmed · M. A. Siddiqui · D. S. Negi (✉) · P. Ranjan (✉)  
Department of Metallurgical and Materials Engineering, Indian Institute of Technology Jodhpur,  
Jodhpur, Rajasthan 342030, India  
e-mail: [arshiya2106@gmail.com](mailto:arshiya2106@gmail.com)

D. S. Negi  
e-mail: [devendra@iitj.ac.in](mailto:devendra@iitj.ac.in)

P. Ranjan  
e-mail: [pranay.ranjan@iitj.ac.in](mailto:pranay.ranjan@iitj.ac.in)

## 1 Introduction

Ultraviolet (UV) photodetectors are often employed in a broad range of industrial and military applications, including safe space-to-space communication, environment monitoring, water disinfection, fire-sensing, and early missile plume detection [1]. The potential to combine the benefits of organic and inorganic substances has led to an increased interest in organic/inorganic hybrid substances in recent years. These materials are expected to produce new types of composite substances with coactive or complementary actions. These substances are also captivating for a number of new magnetic, optical, electronic, or catalytic domains since their attributes or performances could be boosted [2]. Investigations on the use of organic/inorganic hybrid sensing substances in various sensor domains, such as UV sensors, strain sensors, gas sensors [3], humidity sensors, as well as other sensors, have been reported.

Recently, in order to reduce costs and enable mass manufacturing, organic semiconductors or hybrids of these materials with certain inorganic semiconductors were being designed for UV detection. UV sensors relying on organic substances manifest to provide better flexibility in producing spectrum selective response since the absorption of such substances could be readily modified by changing the chemical arrangement. Wide-bandgap polymers and solution-prepared ZnO nanoparticles were employed in hybrid UV sensing devices with double-layer heterojunction structures [4], such as indium tin oxide (ITO)/PEDOT: PSS/polymer/ZnO/Al. In contrast to the long-wavelength cut-off, which was defined by the bandgap of the polymers, the optical output of the sensors solely occurred in the near-UV region (above 300 nm) due to the filtering action of the substrate. While poly(9-vinylcarbazole) (PVK) was utilized as the donor, the sensing device revealed a narrow-band output in the 300–360 nm domain. The output was extended to 400 nm, though, when PVK was substituted with a triarylamine-based polymer (TPD-BA) having narrower bandgap. However, the response area was diminished to 350 (375)–400 nm if the ITO substrate's rear side had an organic filter film pre-coated on it. As a consequence, wavelength-specific response to near-UV became feasible using hybrid electronics [5]. A variety of conducting polymers, including PEDOT and its complex structure PEDOT: PSS owing to its capacity to build vast area systems, optical transparency at the visible region, adjustable electrical photoconductivity, great flexibility, stretchability, and other properties, is a well-established conducting polymer that is widely utilized in research labs [6].

Due to its exceptional chemical, physical, and optical properties, TiO<sub>2</sub> (n-type semiconductor) is one of the most sought-after candidates in the wide-bandgap semiconductor family. TiO<sub>2</sub> nanostructure-based ultraviolet (UV) photodetectors have received much interest lately owing to their significant role in a variety of technical, commercial, and military domains of application [7–9]. In addition, TiO<sub>2</sub> has the benefit of being inexpensive, nontoxic, and extremely resilient in severe conditions [10].

In the present work, we have demonstrated a facile and cheap method to develop a UV photodetector based on TiO<sub>2</sub>/PEDOT: PSS hybrid matrix. Specifically, low-cost



starting ingredients and production procedures were coupled to create a conducting polymer and metal-oxide nanoparticle-based hybrid film. Proper dispersion of the TiO<sub>2</sub> nanoparticles in the PEDOT: PSS matrix is undoubtedly critical to ensure improved and homogenous characteristics for the produced hybrid. In order to realize this, both polymer and nanoparticles were ultrasonicated for a specific time period. Both pristine PEDOT: PSS (device-1) and TiO<sub>2</sub>/PEDOT: PSS hybrid (device-2) layers were exposed to UV-A 365 nm wavelength of radiation and the photoconductivity change was measured. Due to the UV absorption properties of the wide-bandgap TiO<sub>2</sub> nanoparticles, the responsivity of the sensor enhances from 7.27% for device-1 to 21.5% for device-2. Also, the rise and recovery time was reduced for device-2. Moreover, Raman spectroscopy was utilized to evaluate the chemical alterations caused by UV exposure, as well as the involvement of each film component in the overall output of the hybrid film.

## 2 Materials and Methods

### 2.1 Materials

PEDOT: PSS, titanium dioxide P25 (TiO<sub>2</sub>), Perdrogen 30% H<sub>2</sub>O<sub>2</sub> (w/w), H<sub>2</sub>SO<sub>4</sub>, DMSO, DI water, and ethanol (75% pure) were purchased from Chemical Drug House (CDH) and associated companies. *p*-type silicon (*p*-Si) wafer was purchased from a graphene supermarket.

### 2.2 Methods

The  $1 \times 1 \text{ cm}^2$  *p*-Si wafers were subjected to ultrasonication in soap solution for 15 min to remove organic impurities. This was followed by further sonication in ethanol and DI water each for another 15 min, respectively. After this, the films were treated with the Piranha solution to remove both organic and inorganic impurities and to make the silicon wafer hydrophilic in nature. 50  $\mu\text{l}$  of PEDOT: PSS was drop cast onto the silicon wafer and annealed at 60 °C for 15 min and cooled down to room temperature once the solvent is removed. After this, the device was taken to Keithley 4-point probe system in order to measure the photoconductivity of the film. The photoconductivity is measured in the dark condition and then under 365 nm wavelength and 200  $\text{mW cm}^{-2}$  intensity of UV source illumination. The change in photoconductivity with time is measured by the 4-point probe system as long as the photoconductivity keeps on changing. Once the photoconductivity becomes saturated, the UV source is turned off, and then again, the change in photoconductivity is measured till the saturation is reached. For device-2, TiO<sub>2</sub> and PEDOT: PSS were taken in the ratio of 2:5 (w/w), respectively. The solution was magnetically stirred

at 450 rpm for 30 min. After that, the solution was ultrasonicated for 15 min so that the dispersion becomes better and then 50  $\mu\text{l}$  of the solution was drop cast onto the silicon wafer and the same procedure was followed as above.

### 3 Results and Discussion

#### 3.1 Characterization of the Device

The morphology of commercially purchased  $\text{TiO}_2$  nanoparticles (P25) was investigated utilizing scanning electron microscopy (SEM). The morphology of  $\text{TiO}_2$  nanoparticles drop cast on the bare glass substrate and heated at 60  $^\circ\text{C}$  for 100 nm magnification is shown in Fig. 1a. The  $\text{TiO}_2$  nanoparticles have a spherical shape with a particle size of about 50 nm on average. The thickness of the composite device was measured through the cross-sectional view of the sample manifested in the inset of Fig. 1a and turned out to be 1  $\mu\text{m}$ . The AFM images, Fig. 1b, c show the root-mean-square surface roughness ( $R_q$ ) and the average surface roughness ( $R_a$ ) of device-1 and device-2, respectively. The root-mean-square surface roughness ( $R_q$ ) is 0.0611 nm and 0.191 nm for device-1 and device-2, respectively, while the average surface roughness ( $R_a$ ) is 0.0470 nm and 0.122 nm, respectively, for device-1 and device-2. The  $\text{TiO}_2$  nanoparticles of average size distribution  $\sim 50$  nm are embedded on top of the PEDOT: PSS polymer chains. The nanoparticles are smaller in size when compared with the polymer chain. So, due to this random distribution the surface roughness increases. The Raman spectra were obtained for the assessment of the UV sensor. In Fig. 2a, b, the peak at 1430  $\text{cm}^{-1}$  represents the extending of  $\text{C}_\alpha=\text{C}_\beta$  bonds which favors the benzoid or coil-like structure of the PEDOT chains, whereas the peak at 1425  $\text{cm}^{-1}$  correlates to the quinoid-type structure of the ring or more linear chains of PEDOT. When UV light is exposed to device-1, the band red-shifts, gets narrower, and the benzoid structure's intensity declines, all of which show that the PEDOT chains change from a coil confirmation to a linear or stretched coil shape. It is anticipated that the change in structure causes the change in electrical photoconductivity in response to UV light exposure because delocalization of the charge along the p-conjugated PEDOT backbones is facilitated by the linear interaction of the interchain, which lowers the energy blockade of the PEDOT chains. In the case of device-2, the shift in the peak is more apparent upon UV exposure, hence more change in the conformation of the polymer film. In Fig. 2c, the xray diffraction (XRD) pattern of device-1 (red) and device-2 (blue) is observed. For device-1, the characteristic peak of PEDOT is observed at 17.5 $^\circ$ , while for device-2, an additional peak is obtained at 26 $^\circ$  corresponding to  $\text{TiO}_2$  nanoparticles [11, 12]. The UV-vis spectroscopy was done to see the optical properties. In Fig. 2d, the UV-vis spectra of device-1 show an absorption peak at 265 nm, while for device-2, the peak shows a

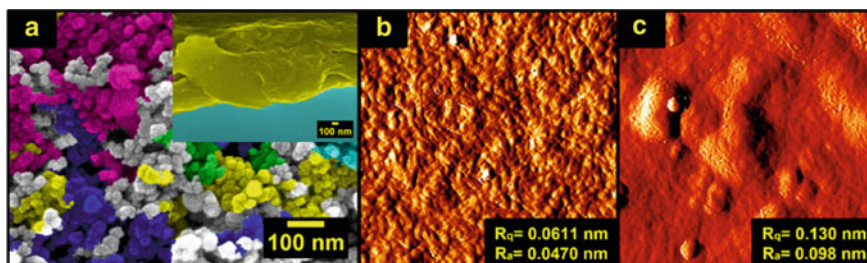


**Fig. 1** SEM images, **a** TiO<sub>2</sub> nanoparticles (inset shows the cross-sectional image of device-2). AFM images, **b** Device-1; **c** Device-2

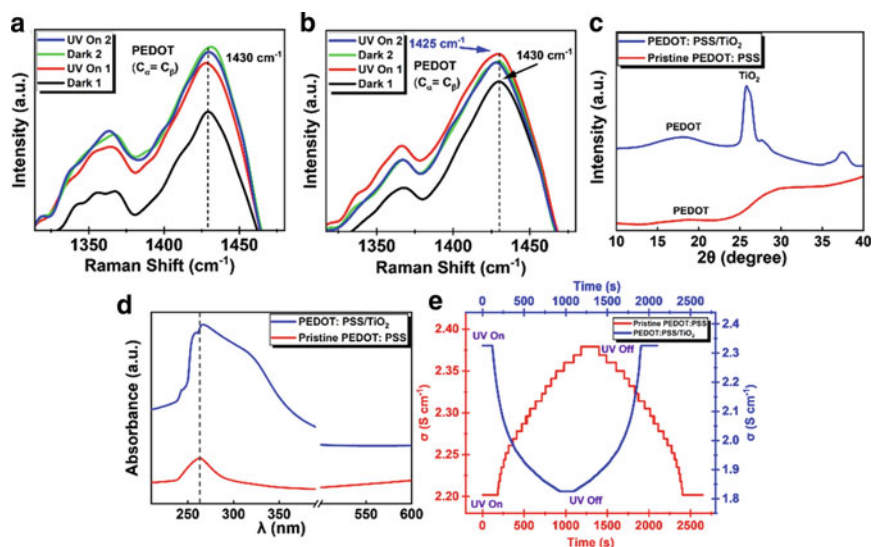


**Fig. 2** Raman spectra of **a** Device-1; **b** Device-2; **c** XRD spectra of device-1 (red) and device-2 (blue); **d** UV-vis spectra of device-1 (red) and device-2 (blue); **e** Real-time photoconductivity graph of device-1 (red) and device-2 (blue) after UV exposure

shift to the right side. The change in the PEDOT: PSS structure upon TiO<sub>2</sub> nanoparticles incorporation is confirmed by the band shift that was seen in the film's absorption spectra.

### 3.2 Photoconductivity Measurements

The photoconductivity of the device was investigated using, the key sight four-probe photoconductivity measurement system. From Fig. 2e, the initial photoconductivity

( $\sigma_i$ ) of device-1 was calculated to be  $2.2 \text{ S cm}^{-1}$ . After irradiating the film with UV illumination of wavelength 365 nm and intensity  $200 \text{ mW cm}^{-2}$ , the photoconductivity of the film starts to rise and reaches a saturation value of  $2.37 \text{ S cm}^{-1}$  ( $\sigma_f$ ) after  $\sim 1068 \text{ s}$ . When the UV light is switched off, the photoconductivity again falls and reaches its initial value after  $\sim 1018 \text{ s}$ . The responsivity of the device was found to be 7.27%. The response time which is the time needed for the UV sensing device to attain 90% of its final value was found to be  $\sim 783 \text{ s}$  and the recovery time which is the time red for the UV sensor to reach 10% of its initial value was  $\sim 970 \text{ s}$ . For device-2, the same procedure was carried out. The initial photoconductivity ( $\sigma_i$ ) was found to be  $2.32 \text{ S cm}^{-1}$ . After the continuous UV exposure for  $\sim 813 \text{ s}$ , it becomes  $1.82 \text{ S cm}^{-1}$  and then becomes saturated. Again, after turning off the UV light, the device reaches its initial photoconductivity value after  $\sim 813 \text{ s}$ . The responsivity of the device was found to be 21.5%. The response and recovery times of the sensing device were measured to be  $\sim 587$  and  $\sim 777 \text{ s}$ , respectively.

The initial rise in photoconductivity for device-1 was due to the electrons' excitation to the conduction band from the valence band upon UV exposure. However, when the radiation is removed, the excited electrons retain the ground state. Moreover, in the case of device-2, the photoconductivity drops upon UV exposure due to its nature as a *p*-type semiconductor. When exposed to UV light,  $\text{TiO}_2$  nanoparticles are excited, resulting in excited holes and electrons that trigger the redox processes. The phenomenon that occurred asserts that the electrons have been captured by the valence band of PEDOT: PSS, which lowers the charge carriers of PEDOT: PSS, that is, holes, and hence decreases the photoconductivity of hybrid films. In the absence of illumination, the injected electrons may be captured by electron acceptors like oxygen present in the air, increasing the charge carrier density of the PEDOT: PSS and thus enhancing the photoconductivity [13, 14].

## 4 Conclusion

The present work demonstrates a facile route to develop a potential UV sensor that works effectively under ambient atmospheric conditions. Under UV illumination, device-1 shows a low responsivity of 7.27%, while upon the incorporation of  $\text{TiO}_2$  nanoparticles, it enhances to 21.5%. The decrease in photoconductivity upon the UV light exposure corresponds to the fact that  $\text{TiO}_2$  nanoparticles are an n-type semiconductor, when forming a hybrid with p-type PEDOT: PSS, bending of the bands occurs and the electrons are trapped by the conduction band of the PEDOT: PSS, and hence the charge carriers, that is, holes, are reduced. Our designed method could effectively be used for the production of various sensors that may detect harmful UV radiation causing sunburn, premature aging, skin cancer, and many other UV-caused skin-related diseases. Moreover, our approach can also potentially benefit in designing the sensor related to space applications, biomedical, and bio-analyte detection, etc.

**Acknowledgements** The authors are grateful to the Indian Institute of Technology Jodhpur, Rajasthan, India, for providing research facilities. AA would like to thank MHRD for the financial support. PR, Devendra Singh Negi, and Amitava Banerjee would like to thank SERB for SRG (Grant no. SRG/2022/000192, SRG/2022/000825, and SRG/2022/001377 respectively) for collaboration and SEED Grant No. I/SEED/PRJ/20220044.

**Declaration of Interest Statement** The authors declare that they have no conflict of interest.

## References

1. Khan A, Islam SM, Ahmed S, Kumar RR, Habib MR, Huang K et al (2018) Direct CVD growth of graphene on technologically important dielectric and semiconducting substrates. *Adv Sci* 5(11):1800050
2. Imran M, Chaudhary AA, Ahmed S, Alam MM, Khan A, Zouli N et al (2022) Iron oxide nanoparticle-based ferro-nanofluids for advanced technological applications. *Molecules* 27(22):7931
3. Madhaiyan G, Tung TW, Zan HW, Meng HF, Lu CJ, Ansari A et al (2020) UV-enhanced room-temperature ultrasensitive NO gas sensor with vertical channel nano-porous organic diodes. *Sens Actuators B Chem* 320:128392
4. Khan A, Cong J, Kumar RR, Ahmed S, Yang D, Yu X (2022) Chemical vapor deposition of graphene on self-limited SiC interfacial layers formed on silicon substrates for heterojunction devices. *ACS Appl Nano Mater* 5(12):17544–17555
5. Imran M, Ahmed S, Abdullah AZ, Hakami J, Chaudhary AA, Rudayni HA et al (2022) Nanostructured materials based optical and electrochemical detection of amoxicillin antibiotic. *Luminescence* 38(7):1064–1086
6. Ahmed S, Ansari A, Haidiyrah AS, Chaudhary AA, Imran M, Khan A (2022) Hierarchical molecularly imprinted inverse opal-based platforms for highly selective and sensitive determination of histamine. *ACS Appl Polym Mater* 4(4):2783–2793
7. Siddiqui MA, Jaiswal P (2021) Photocatalytic behavior of ferroelectric materials: comparative study of BaTiO<sub>3</sub> and Ag-loaded BaTiO<sub>3</sub> for wastewater treatment. In: IOP conference series: materials science and engineering, vol 1166, no 1. IOP Publishing, p 012031
8. Ahmed S, Khatun S, Sallam S, Ansari A, Ansari ZA, Kumar RR et al (2022) Photoresponse of porous silicon for potential optical sensing. *Europhys Lett* 139(3):36001
9. Ahmed S, Ansari A, Siddiqui MA, Khan A, Ranjan P (2023) A potential optical sensor based on nanostructured silicon. *J Mater Sci Mater Electron*. <https://doi.org/10.1007/s10854-023-10187-2>
10. Khan A, Ahmed S, Sun BY, Chen YC, Chuang WT, Chan YH et al (2022) Self-healable and anti-freezing ion conducting hydrogel-based artificial bioelectronic tongue sensing toward astringent and bitter tastes. *Biosens Bioelectron* 198:113811
11. Yoo D, Kim J, Kim JH (2014) Direct synthesis of highly conductive poly (3, 4-ethylenedioxythiophene): poly (4-styrenesulfonate)(PEDOT: PSS)/graphene composites and their applications in energy harvesting systems. *Nano Res* 7:717–730
12. Al-Taweel SS, Saud HR (2016) New route for synthesis of pure anatase TiO<sub>2</sub> nanoparticles via ultrasound-assisted sol-gel method. *J Chem Pharm Res* 8(2):620–626
13. Sakai N, Prasad GK, Ebina Y, Takada K, Sasaki T (2006) Layer-by-layer assembled TiO<sub>2</sub> nanoparticle/PEDOT-PSS composite films for switching of electric conductivity in response to ultraviolet and visible light. *Chem Mater* 18(16):3596–3598
14. Dhar S, Chakraborty P, Majumder T, Mondal SP (2018) Acid-treated PEDOT: PSS polymer and TiO<sub>2</sub> nanorod Schottky junction ultraviolet photodetectors with ultrahigh external quantum efficiency, detectivity, and responsivity. *ACS Appl Mater Interfaces* 10(48):41618–41626

# Ag@CuO Nanohybrid-Based Electrochemical Biosensor for Trichlorfon Detection



Saroj Paneru and Devendra Kumar

**Abstract** The accumulation of organophosphate pesticide residues in the environment poses hazardous consequences for living beings. To address this issue, we propose the development of an acetylcholinesterase (AChE)-based electrochemical biosensor for trichlorfon detection. In the proposed work, Ag@CuO-based nanohybrid is prepared by the co-precipitation method and then characterized by X-ray diffraction (XRD), Fourier transform infrared spectroscopy (FTIR), scanning electron microscopy (SEM), and electrochemical techniques. For the fabrication of Ag@CuO/ITO-based biosensor, the prepared nanohybrid (Ag@CuO) is deposited onto the ITO-coated glass substrate, and then the AChE enzyme is immobilized onto the fabricated electrode surface by using cross-linker glutaraldehyde, which prevents the leaching of the enzyme from the electrode surface. The developed biosensor shows a good linear range, low detection limit, and good sensitivity of 5–35 nM, 1.59 nM, and  $3.195 \mu\text{A} (\text{nM})^{-1} (\text{cm})^{-2}$ , respectively.

**Keywords** Trichlorfon · Acetylcholinesterase · Copper oxide

## 1 Introduction

Due to the population growth, the requirement of crops production increases accordingly. To fulfill these requirements, organophosphate pesticides (Ops) are extensively used due to their properties like low cost and high eliminating power against pests and plant diseases [1, 2]. Despite their valuable characteristics, uncontrolled use causes various health problems worldwide. Ops residues enter in the living body and inhibit the activity of the acetyl cholinesterase enzyme (AChE). The inhibition of AChE causes neurotoxicity in animals and humans, which further causes numerous diseases [3]. To prevent these harmful effects of Ops, European Union has fixed the maximum limit of pesticide residue, which can be tolerated by animals

---

S. Paneru · D. Kumar (✉)  
Applied Chemistry, Delhi Technological University, New Delhi, India  
e-mail: [dkumar@dce.ac.in](mailto:dkumar@dce.ac.in)

and humans [4]. Therefore, it is urgently required to determine the accurate concentration of Ops in food, water, and soil. For this purpose, various chromatographic techniques such as gas chromatography [5], gas chromatography-tandem mass spectroscopy [6], and liquid chromatography associated with mass spectrometry [7] are available which are found accurate. However, their off-side procedure, requirements of large samples, overpriced instrumentations, and time-taking make them vulnerable in terms of implementation. Therefore, a new, simple, highly sensitive, and fast methodology is urgently required for determining the trace amount of pesticides from agricultural products.

Currently, AChE biosensors have acquired more popularity for the detection of pesticides owing to their high sensitivity, simple on-site procedure, fast response, and high selectivity. The sensitivity of enzyme-based biosensors depends on the effective immobilization of enzymes on the electrode surface. For this purpose, various methods like physical adsorption, covalent bonding, cross-linking, etc. have been developed [8]. Among all these methods, cross-linking is more popular. The cross-linking agent connects the enzyme and electrode surface which prevents the enzyme leaching. The choice of an effective transducer is also a key factor in enhancing the sensitivity of AChE-based biosensors, and therefore, various studies have been focused on the development of effective transducers [9–12].

In recent years, nanomaterials such as metal oxides [13–15], graphene [16], and carbon nanotubes [17] are used extensively for the fabrication of effective transducers. Among all these nanomaterials, metal oxides are preferred to use in various fields like supercapacitors [18], gas sensors [19], and photocatalysis [20] due to their highly stable nature, flexible structure, easy availability, and low cost. Among metal oxides, copper oxide (CuO) is harmless, highly conducting, and provides a high-density nanocomposite due to the presence of Cu and O orbitals. Its high affinity against thio compounds makes it more usable for AChE-based biosensors [21].

CuO nanoparticle's conductivity and catalytic power are further enhanced by doping with metal. In this regard, various studies have been conducted on different biosensors [22–28]. It reveals that Ag shows a high conducting nature and catalytic power out of all metals. It reduces the band gap of CuO nanoparticles which further makes it more conducting and enhances the electron transfer rate [29].

In this proposed work, an electrochemical biosensor is developed using Ag@CuO nanoparticles as a sensing platform for trichlorfon detection. The nanoparticles were synthesized by the co-precipitation method. The fabrication of the proposed biosensor is carried out by depositing the prepared nanoparticles onto the ITO-coated glass substrate. Subsequently, the AChE enzyme was immobilized onto the prepared electrode by cross-linking. The presence of cross-linking agent (glutaraldehyde) improves the enzyme's immobilization which further enhances the sensitivity of the proposed biosensor.

## 2 Experimental Section

### 2.1 Materials and Reagents

Acetyl cholinesterase (AChE) (C3389-2KU), acetyl thiocholine chloride (ATCl), trichlorfon,  $\text{CuSO}_4 \cdot 5\text{H}_2\text{O}$  (98.5%), sodium lauryl sulfate (85%), sodium hydroxide (NaOH) (97%), and silver nitrate ( $\text{AgNO}_3$ ) were purchased from Sigma-Aldrich. All the solvents including acetone, ethanol, and hydrochloric acid were also purchased from Sigma-Aldrich. Milli-Q water ( $18.2 \text{ M}\Omega \text{ cm}$ ) is used for the preparation of all solutions.

### 2.2 Preparation of CuO and Ag@CuO

The co-precipitation method was used for preparing the CuO and Ag@CuO nanoparticles. Firstly, CuO was prepared by dissolving 1.34 g of  $\text{CuCl}_2$  in 20 mL of DI water. Subsequently, 0.5 M NaOH was added until the pH reached 14, and the solution was stirred for 7 h at 80 °C. The obtained black-colored solution was centrifuged three to four times and then dried at 50 °C for 10 h. Finally, the black powder of CuO was calcined in a muffle furnace at 800 °C for 4 h. The Ag@CuO was synthesized by dissolving 1.34 g of  $\text{CuCl}_2$  and 0.60 g of  $\text{AgNO}_3$  into 20 ml of DI water and followed all the steps as discussed above for the synthesis of CuO.

### 2.3 Electrophoretic Deposition (EPD) and Biosensor Fabrication

Firstly, the colloidal solutions of CuO and Ag@CuO were prepared by adding 1 mg of both materials into the mixture of ethanol and water (5:1) through ultrasonication. Subsequently, 20 V DC was applied for 15 s for smooth electrophoretically deposition of CuO and Ag@CuO onto indium tin oxide (ITO)-coated glass substrate. The fabricated electrode was treated with 0.2% glutaraldehyde for 2 h. Subsequently, 20  $\mu\text{L}$  of AChE enzyme (0.1 mg/mL in PBS 7.4) was drop cast into the fabricated electrode. The developed biosensor (AChE/Ag@CuO/ITO) was further incubated for optimal immobilization at 4 °C for 12 h. The scheme for biosensor fabrication is discussed in Fig. 1.



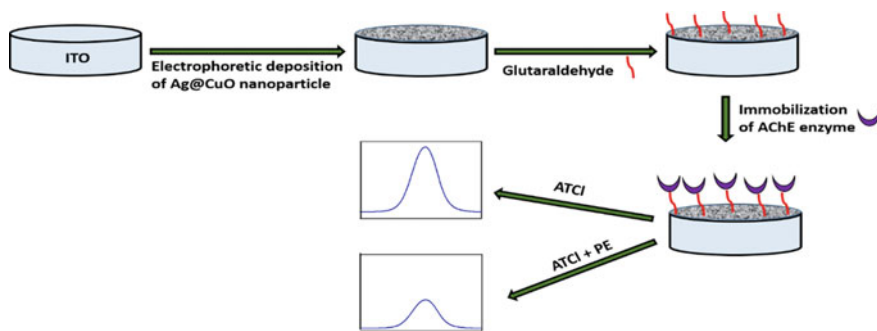


**Fig. 1** Schematic diagram for AChE/Ag@CuO/ITO-based biosensor for pesticide (PE) detection

### 3 Results and Discussion

#### 3.1 Structural Characterization of CuO and Ag@CuO

All the prepared materials were characterized by XRD and FTIR spectroscopy. In Fig. 2a, graph (a) represents the XRD pattern of CuO and the peaks at  $32.8^\circ$ ,  $35.5^\circ$ ,  $38.8^\circ$ ,  $48.9^\circ$ ,  $53.5^\circ$ ,  $58.5^\circ$ ,  $61.7^\circ$ ,  $66.3^\circ$ , and  $68.2^\circ$  which validate the successful synthesis of CuO. On the other hand, graph (b) represents all the characteristic peaks of CuO along with characteristic peaks of Ag ( $36.2^\circ$  and  $44.3^\circ$ ), which further validate that Ag was successfully incorporated onto CuO. The crystallite size of both the prepared materials was calculated by using Debye–Scherrer equation (Eq. 1). The crystallite size for Ag@CuO and CuO is found to be 78 and 60 nm, respectively.

$$D = K\lambda/\beta \cos \theta \quad (1)$$

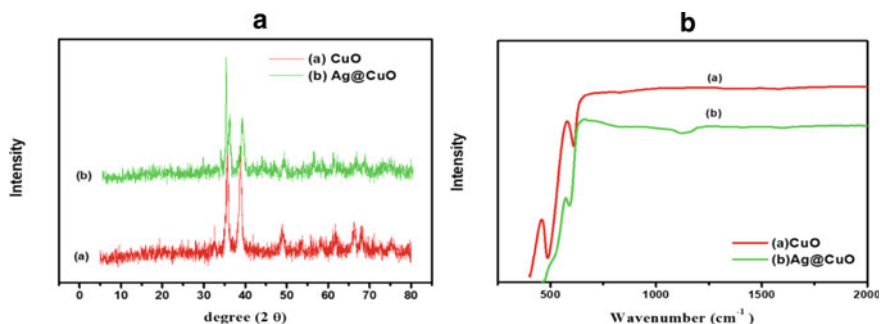


**Fig. 2** **a** XRD of (a) CuO and (b) Ag@CuO, **b** FTIR of (a) CuO and (b) Ag@CuO

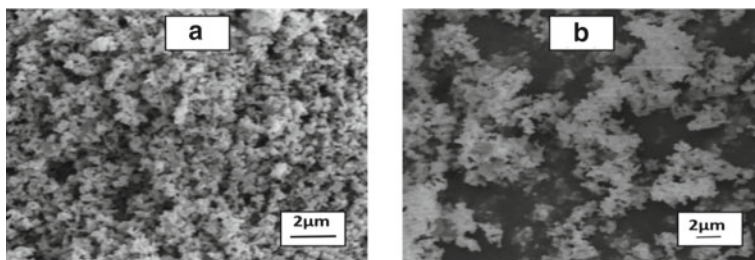


**Fig. 3** a SEM images of CuO and b Ag@CuO

Figure 2b represents the FTIR spectra of CuO (graph a) and Ag@CuO (graph b). In graph (a), all the bands positioned at less than  $1000\text{ cm}^{-1}$  appear due to metal–oxygen vibrations of the Cu–O bond. Simultaneously, the graph (b) represents that a band at  $1130\text{ cm}^{-1}$  is characteristic for Ag and a band at less than  $1000\text{ cm}^{-1}$  is due to the Cu–O bond [30].

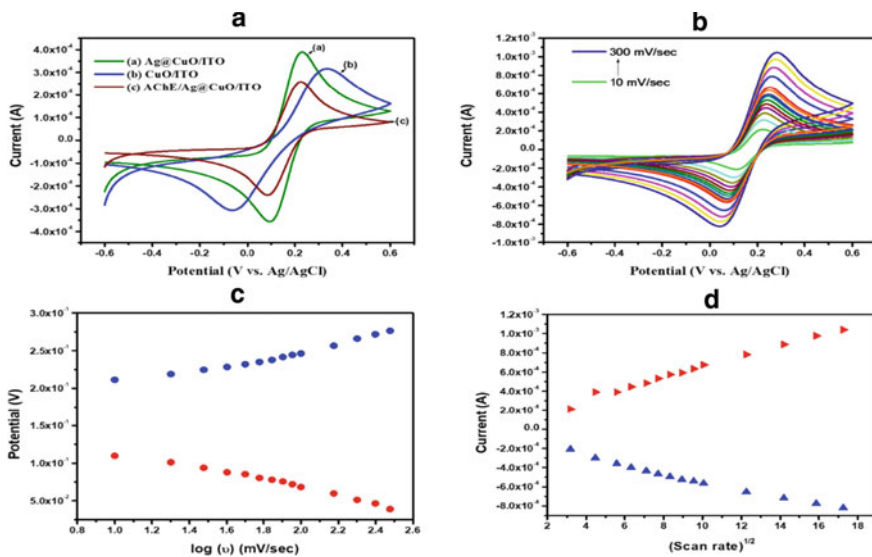
### 3.2 Morphological Characterization of Prepared Materials

Figure 3 represents the scanning electron microscopy (SEM) images of all the prepared materials. The tiny spherical particles in Fig. 3a, b represent the morphologies of CuO and Ag@CuO nanoparticles, respectively.

### 3.3 Electrochemical Characterization of Fabricated Electrodes

Cyclic voltammetry (CV) technique was used to characterize all the modified electrodes. This study was conducted in a 7.4 pH phosphate buffer saline (PBS) buffer containing 5 mM  $[\text{Fe}(\text{CN})_6]^{3-/4-}$  and 0.6% NaCl solutions. Figure 4a represents the CV curves of Ag@CuO/ITO (curve a), CuO/ITO (curve b), and AChE/Ag@CuO/ITO (curve c) at a scan rate of 30 mV/s. This figure confirms that the Ag@CuO/ITO electrode shows high conductivity and a high electron transfer rate in comparison with the CuO/ITO electrode. It is observed that the peak current decreases when the Ag@CuO/ITO electrode is immobilized with the AChE enzyme. This decrease in current is due to the non-conducting nature of the enzyme.

Figure 4b represents the CV of Ag@CuO/ITO electrode at scan rates varying from 10 to 300 mV/s. While Fig. 4c illustrates the linear relationship between the peak potentials ( $E_{\text{pa}}$  and  $E_{\text{pc}}$ ) of Ag@CuO/ITO and the logarithmic scale of scan rates, this linear relation complies the following equations:



**Fig. 4** **a** CV of Ag@CuO/ITO (a), CuO/ITO (b), and AChE/Ag@CuO/ITO (c) in 7.4 pH PBS containing 5 mM  $[\text{Fe}(\text{CN})_6]^{3/4-}$  and 0.8% NaCl at scan rate 50 mV/s. **b** CV of Ag@CuO/ITO electrode at scan rate varying from 10 to 300 mV/s. **c** Plot of potential versus log (scan rate) for Ag@CuO/ITO electrode. **d** Plot of current versus square root of scan rate for Ag@CuO/ITO electrode

$$E_{pa}[\text{Ag@CuO/ITO}] = 0.0457 \text{ V } \log(\nu) + 0.1574 \text{ V}; R^2 = 0.9592 \quad (2)$$

$$E_{pc}[\text{Ag@CuO/ITO}] = -0.0485 \text{ V } \log(\nu) + 0.1646 \text{ V}; R^2 = 0.9787 \quad (3)$$

Using the slope of these mentioned equations, the electron transfer coefficient ( $\alpha$ ) value is set to be 0.7368. In Fig. 4d, the linear curve between peak current and the square root of the scan rate of Ag@CuO modified ITO electrode confirms that the electron transfer through this electrode is a surface controlled process [31] and follows the below-mentioned equations:

$$I_{pa}[\text{Ag@CuO/ITO}] = 56.08 \mu\text{A/mV/s} \times \nu^{1/2} + 91.78 \mu\text{A}; R^2 = 0.9902 \quad (4)$$

$$I_{pc}[\text{Ag@CuO/ITO}] = -41.86 \mu\text{A/mV/s} \times \nu^{1/2} - 127.39 \mu\text{A}; R^2 = 0.9852 \quad (5)$$

Furthermore, the value of diffusion coefficient ( $D$ ) and effective surface area for Ag@CuO/ITO electrode is set to be  $1.34 \times 10^{-2} \text{ cm}^2 \text{ s}^{-1}$  and  $4.1 \times 10^{-1} \text{ cm}^2$ , respectively. These values are calculated by using the slope of the above-mentioned Eqs. (4) and (5) and the Randles–Sevcik equation (Eq. 5).

$$I_p/v^{1/2} = 2.69 \times 10^5 n^{3/2} AD^{1/2} C \quad (6)$$

In this equation,  $A$  is the area of the electrode,  $C$  is the concentration of  $[\text{Fe}(\text{CN})_6]^{3-/4-}$ ,  $v$  is the scan rate, and  $n$  is the transferred electrons during the redox reaction.

### 3.4 Electrochemical Detection of Trichlorfon

The developed biosensor (AChE/Ag@CuO/ITO) is further employed for detecting the trichlorfon using differential pulse voltammetry (DPV). This analysis was conducted in a 7.4 pH PBS buffer containing 5 mM  $[\text{Fe}(\text{CN})_6]^{3-/4-}$  and 2.5 mM of ATCl at 50 mV/s scan rate. Figure 5a illustrates the DPV response of the proposed biosensor by incubating different concentrations (5–35 nM) of trichlorfon. It is clearly shown in this figure that as the concentration of trichlorfon ( $C_{\text{trichlorfon}}$ ) increases, the associated current decreases sharply due to the inhibition of AChE enzyme. Figure 5b represents the calibration curve of current against the trichlorfon concentrations. The linear curve in the figure obeys Eq. (7).

$$I = 172.41 \mu\text{A} - 1.31 \mu\text{A}/\text{nM} \times C_{\text{trichlorfon}}; R^2 = 0.9904 \quad (7)$$

The limit of detection for trichlorfon and sensitivity of the proposed biosensor is found to be 1.59 nM and  $3.195 \mu\text{A} (\text{nM})^{-1} (\text{cm})^2$ , respectively. Table 1 data show clearly the supremacy of the proposed biosensor over other considered biosensors.

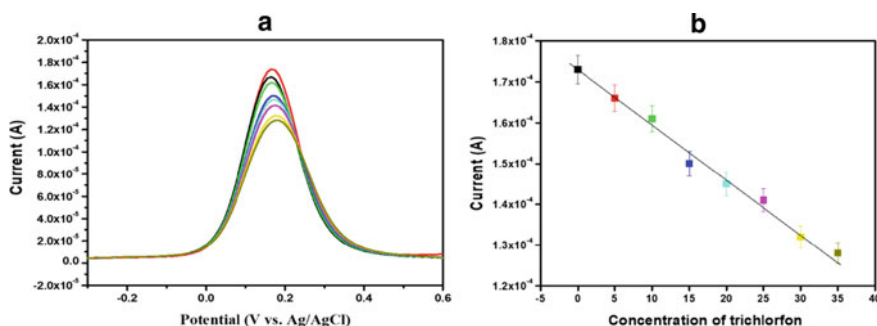


**Fig. 5** **a** DPV response of AChE/Ag@CuO/ITO electrode after incubation of different concentrations of trichlorfon (5–35 nM). **b** Calibration plot of log of trichlorfon and change in current

**Table 1** Comparative analysis of the developed biosensor with recently developed biosensors over trichlorfon detection

S. No.	Fabricated electrodes	Linear range	Detection limit	Sensor type	References
1.	Au NRs	27.8–11,111.1 $\mu\text{g}/\text{mL}$	0.132 $\mu\text{g}/\text{mL}$	Non-enzymatic	[32]
2.	Poly(FBThF)/Ag-rGO-NH <sub>2</sub> /AChE/GCE	0.0206–2.06 $\mu\text{g}/\text{mL}$	0.001 $\mu\text{g}/\text{mL}$	Enzymatic	[8]
3.	AChE/Ag@CuO/ITO	5–35 $\text{ng}/\text{mL}$	1.59 $\text{ng}/\text{mL}$	Enzymatic	Current work

## 4 Conclusion

In this work, we have developed an efficient electrochemical biosensor for trichlorfon detection by using Ag@CuO nanohybrid as a sensing platform. The sensitivity, limit of detection, and linear range of the proposed biosensor are compared with other recently developed biosensors for trichlorfon detection. This biosensor shows good results over other biosensors. The developed biosensor shows high sensitivity, good linear range, and low limit of detection.

**Acknowledgements** The first author acknowledges to the University Grants Commission (UGC), New Delhi, Government of India, for their financial support (Grant No. 351/CSIR-UGC NET DEC.2016).

**Declaration of Interest Statement** The authors declare that they have no conflict of interest.

## References

1. Pundir CS, Chauhan N (2012) Acetylcholinesterase inhibition-based biosensors for pesticide determination: a review. *Anal Biochem* 429(1):19–31
2. Rahmani T, Bagheri H, Behbahani M, Hajian A, Afkhami A (2018) Modified 3D graphene-Au as a novel sensing layer for direct and sensitive electrochemical determination of carbaryl pesticide in fruit, vegetable, and water samples. *Food Anal Methods* 11(11):3005–3014
3. Iqbal A, Ahmed M, Ahmad S, Sahoo CR, Iqbal MK, Haque SE (2020) Environmental neurotoxic pollutants. *Environ Sci Pollut Res* 27(33):41175–41198
4. Ionel B (2018) European regulation in the veterinary sanitary and food safety area, a component of the European policies on the safety of food products and the protection of consumer interests: a 2007 retrospective. Part two: regulations. *Universul Juridic, (Suplim)*, pp 16–19
5. Fernández-Cruz T, Martínez-Carballo E, Simal-Gándara J (2017) Optimization of selective pressurized liquid extraction of organic pollutants in placenta to evaluate prenatal exposure. *J Chromatogr A* 1495:1–11
6. Santos C, Oppolzer D, Gonçalves A, Barroso M, Gallardo E (2018) Determination of organophosphorous pesticides in blood using microextraction in packed sorbent and gas chromatography–tandem mass spectrometry. *J Anal Toxicol* 42(5):321–329

7. Shin Y, Lee J, Lee J, Lee J, Kim E, Liu KH et al (2018) Validation of a multiresidue analysis method for 379 pesticides in human serum using liquid chromatography–tandem mass spectrometry. *J Agric Food Chem* 66(13):3550–3560
8. Zhang P, Sun T, Rong S, Zeng D, Yu H, Zhang Z et al (2019) A sensitive amperometric AChE-biosensor for organophosphate pesticides detection based on conjugated polymer and Ag-rGO-NH<sub>2</sub> nanocomposite. *Bioelectrochemistry* 127:163–170
9. Turan J, Kesik M, Soylemez S, Goker S, Coskun S, Unalan HE, Toppare L (2016) An effective surface design based on a conjugated polymer and silver nanowires for the detection of paraoxon in tap water and milk. *Sens Actuators B Chem* 228:278–286
10. Kaur N, Thakur H, Prabhakar N (2016) Conducting polymer and multi-walled carbon nanotubes nanocomposites based amperometric biosensor for detection of organophosphate. *J Electroanal Chem* 775:121–128
11. Itsoponpan T, Thanachayanont C, Hasin P (2021) Sponge-like CuInS<sub>2</sub> microspheres on reduced graphene oxide as an electrocatalyst to construct an immobilized acetylcholinesterase electrochemical biosensor for chlorpyrifos detection in vegetables. *Sens Actuators B Chem* 337:129775
12. Xie X, Zhou B, Zhang Y, Zhao G, Zhao B (2021) A multi-residue electrochemical biosensor based on graphene/chitosan/parathion for sensitive organophosphorus pesticides detection. *Chem Phys Lett* 767:138355
13. Zhang Y, Liu Y, Su L, Zhang Z, Huo D, Hou C, Lei Y (2014) CuO nanowires based sensitive and selective non-enzymatic glucose detection. *Sens Actuators B Chem* 191:86–93
14. Cui HF, Wu WW, Li MM, Song X, Lv Y, Zhang TT (2018) A highly stable acetylcholinesterase biosensor based on chitosan-TiO<sub>2</sub>-graphene nanocomposites for detection of organophosphate pesticides. *Biosens Bioelectron* 99:223–229
15. Sohal N, Maity B, Shetti NP, Basu S (2021) Biosensors based on MnO<sub>2</sub> nanostructures: a review. *ACS Appl Nano Mater* 4(3):2285–2302
16. Li Y, Zhao R, Shi L, Han G, Xiao Y (2017) Acetylcholinesterase biosensor based on electrochemically inducing 3D graphene oxide network/multi-walled carbon nanotube composites for detection of pesticides. *RSC Adv* 7(84):53570–53577
17. Jacobs CB, Peairs MJ, Venton BJ (2010) Carbon nanotube based electrochemical sensors for biomolecules. *Anal Chim Acta* 662(2):105–127
18. Wang K, Dong X, Zhao C, Qian X, Xu Y (2015) Facile synthesis of Cu<sub>2</sub>O/CuO/RGO nanocomposite and its superior cyclability in supercapacitor. *Electrochim Acta* 152:433–442
19. He M, Xie L, Zhao X, Hu X, Li S, Zhu ZG (2019) Highly sensitive and selective H<sub>2</sub>S gas sensors based on flower-like WO<sub>3</sub>/CuO composites operating at low/room temperature. *J Alloys Compd* 788:36–43
20. Kannan K, Radhika D, Vijayalakshmi S, Sadasivuni KK, Ojiaku AA, Verma U (2022) Facile fabrication of CuO nanoparticles via microwave-assisted method: photocatalytic, antimicrobial and anticancer enhancing performance. *Int J Environ Anal Chem* 102(5):1095–1108
21. Bao J, Huang T, Wang Z, Yang H, Geng X, Xu G et al (2019) 3D graphene/copper oxide nano-flowers based acetylcholinesterase biosensor for sensitive detection of organophosphate pesticides. *Sens Actuators B Chem* 279:95–101
22. Tang Q, Hu XB, He M, Xie LL, Zhu ZG, Wu JQ (2018) Effect of platinum doping on the morphology and sensing performance for CuO-based gas sensor. *Appl Sci* 8(7):1091
23. Lupan O, Cretu V, Postica V, Polonskyi O, Ababii N, Schütt F et al (2016) Non-planar nanoscale p–p heterojunctions formation in Zn<sub>x</sub>Cu<sub>1-x</sub>O<sub>y</sub> nanocrystals by mixed phases for enhanced sensors. *Sens Actuators B Chem* 230:832–843
24. Cretu V, Postica V, Mishra AK, Hoppe M, Tiginyanu I, Mishra YK et al (2016) Synthesis, characterization and DFT studies of zinc-doped copper oxide nanocrystals for gas sensing applications. *J Mater Chem A* 4(17):6527–6539
25. Choi YH, Kim DH, Hong SH (2017) p-Type aliovalent Li (I) or Fe (III)-doped CuO hollow spheres self-organized by cationic complex ink printing: structural and gas sensing characteristics. *Sens Actuators B Chem* 243:262–270

26. Hu X, Zhu Z, Chen C, Wen T, Zhao X, Xie L (2017) Highly sensitive H<sub>2</sub>S gas sensors based on Pd-doped CuO nanoflowers with low operating temperature. *Sens Actuators B Chem* 253:809–817
27. Kim KM, Jeong HM, Kim HR, Choi KI, Kim HJ, Lee JH (2012) Selective detection of NO<sub>2</sub> using Cr-doped CuO nanorods. *Sensors* 12(6):8013–8025
28. Molavi R, Sheikhi MH (2020) Facile wet chemical synthesis of Al doped CuO nanoleaves for carbon monoxide gas sensor applications. *Mater Sci Semicond Process* 106:104767
29. Li YY, Kang P, Wang SQ, Liu ZG, Li YX, Guo Z (2021) Ag nanoparticles anchored onto porous CuO nanobelts for the ultrasensitive electrochemical detection of dopamine in human serum. *Sens Actuators B Chem* 327:128878
30. Iqbal S, Javed M, Bahadur A, Qamar MA, Ahmad M, Shoaib M et al (2020) Controlled synthesis of Ag-doped CuO nanoparticles as a core with poly (acrylic acid) microgel shell for efficient removal of methylene blue under visible light. *J Mater Sci Mater Electron* 31(11):8423–8435
31. Thakur D, Pandey CM, Kumar D (2022) Highly sensitive enzymatic biosensor based on polyaniline-wrapped titanium dioxide nano hybrid for fish freshness detection. *Appl Biochem Biotechnol* 1–14
32. Chen GY, Zhang CY, Yin SJ, Zhou HY, Tian T, Peng LJ et al (2022) Highly sensitive visual colorimetric sensor for trichlorfon detection based on the inhibition of metallization of gold nanorods. *Spectrochim Acta Part A Mol Biomol Spectrosc* 270:120850

# Novel Thermoelectric Material $\text{Ba}_2\text{AlNbO}_6$ for Energy Harvesting Applications



Mudasir Younis Sofi, Mohd. Shahid Khan, Javid Ali, and M. Ajmal Khan

**Abstract** For the first time, we performed calculations within the framework of density functional theory (DFT) to disclose the transport and other physical properties of a potential double perovskite,  $\text{Ba}_2\text{AlNbO}_6$ . The structural framework of this material corresponds to the  $Fm-3m$  symmetry with non-magnetic cubic phase stability. The generalized gradient approximation (GGA-PBE) and modified Becke–Johnson approach (GGA + mBJ) are employed to define the electronic structure, revealing the wide-bandgap semiconducting behavior in both approximations. The thermoelectric characteristics of the double perovskite  $\text{Ba}_2\text{AlNbO}_6$  have been methodically explored using semi-classical Boltzmann transport theory, with higher values of the Seebeck coefficient and figure of merit ( $zT$ ) being observed, offering potential utility in energy harvesting applications. Besides thermoelectric study, the optical response has been evaluated in terms of dielectric constant and refractive index, suggesting possible applications in optoelectronic devices in the visible and deep ultraviolet region.

**Keywords** Structural properties · Cohesive energy · Band structure · Seebeck coefficient · Figure of merit ( $zT$ ) · Dielectric constant

## 1 Introduction

Researchers are pushed to investigate innovative energy harvesting devices as alternatives to conventional energy sources in view of our planet's energy limitations and ecological challenges. The last decade has witnessed a surge of interest in thermoelectric (TE) materials due to their capability to transform the squandered heat into electrical energy. TE compounds are highly beneficial in addressing challenges in power generating and refrigeration systems [1, 2]. These materials are also effective for energy harvesting, smart sensors, and the emerging idea of thermo-power wave

---

M. Y. Sofi · Mohd. S. Khan · J. Ali · M. Ajmal Khan (✉)  
Department of Physics, Jamia Millia Islamia, New Delhi 110025, India  
e-mail: [majkhan@jmi.ac.in](mailto:majkhan@jmi.ac.in)



sources [3]. The suitability and applicability of a material for thermoelectric technology is decided by a dimensionless figure of merit,  $zT = \frac{S^2\sigma}{k}T$ , where  $S$ ,  $\sigma$ , and  $k$  address the Seebeck coefficient, electrical conductivity, and thermal conductivity, respectively [4]. Good thermoelectric materials ought to have eloquent values for the Seebeck and electrical conductivity along with low thermal conductivity value. In particular, the unprecedented values of the figure of merit ( $zT$ ) are highly desirable.

Perovskites featuring semiconducting properties, particularly double perovskites with  $A_2BB'O_6$  stoichiometric composition ( $A$ ,  $B$ ,  $B'$  are cations and  $O$  is an anion), have been extensively investigated for energy harvesting and optoelectronic applications. Ramesh et al. [5] recently examined the thermoelectric and optical characteristics of  $Sr_2AlMO_6$  ( $M = Nb$  and  $Ta$ ) double perovskites, concluding that these materials exhibit exceptional thermoelectric and optical performance. Herein, we have investigated the structural, electronic, thermoelectric, and optical properties of a potential semiconducting material,  $Ba_2AlNbO_6$ . The crystal structure and other properties of the given material have been explored via numerous experimental works [6]; however, no theoretical work has been conducted to examine its physical properties and possible applications. Hence, we performed DFT-based simulations to examine the structural, electronic, transport, and optical properties of  $Ba_2AlNbO_6$  double perovskite.

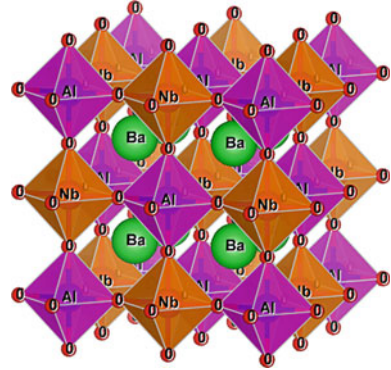
## 2 Computational Details

All the properties of the present material have been calculated using a full-potential Wien2k simulation code [7]. The exchange correlations effects are tackled via generalized gradient approximation (GGA) [8] and modified Becke–Johnson method (mBJ) [9]. Within the FP-LAPW approach, the unit cell is shared between the muffin spheres and interstitial regions. To assure charge and energy convergence for non-overlapping atomic spheres, the linearized augmented plane-wave basis with  $l_{\max} = 10$  and  $R_{MT}K_{\max} = 7$  ( $K_{\max}$  denotes the highest possible  $k$ -value, and  $R_{MT}$  is the radius of the smallest sphere) has been employed. The BoltzTraP code [10] has been used to investigate the thermoelectric response of the present material.

## 3 Results and Discussion

The predicted structural, electronic, thermoelectric, and optical properties of  $Ba_2AlNbO_6$  perovskite are discussed in the sections given below.

**Fig. 1** Crystal structure of Ba<sub>2</sub>AlNbO<sub>6</sub>



### 3.1 Structural Phase Stability and Cohesive Energy

The present material Ba<sub>2</sub>AlNbO<sub>6</sub> is experimentally reported to be stable in *Fm-3m* cubic configuration with a lattice parameter of 8.34 Å [6]. The crystal structure of Ba<sub>2</sub>AlNbO<sub>6</sub> double perovskite is illustrated in Fig. 1. The ground state magnetic phase stability has been obtained by minimizing the Birch Murnaghan's equation of state, as depicted in Fig. 2. The obtained structural parameters, such as the relaxed lattice constant, the bulk modulus, and the pressure derivative of the bulk modulus, are presented in Table 1. These parameters are found to be in pretty good agreement with previously studied comparable compounds [5], thereby validating our results. Cohesive energy has been further calculated to address the thermodynamic stability by using the relation;  $E_{\text{coh}}^{\text{Ba}_2\text{AlNbO}_6} = \frac{[2E_{\text{Ba}} + E_{\text{Al}} + \text{Nb} + 6E_{\text{O}}] - E_{\text{Optimized}}}{10}$ . Here,  $E_{\text{coh}}^{\text{Ba}_2\text{AlNbO}_6}$  represents the cohesive energy per atom of a material. The cohesive energy per atom of the present compound is 6.49 eV/atom, which is decently positive, subsequently presaging that the atoms are robustly held within the lattice structure of this compound.

### 3.2 Electronic and Thermoelectric Properties

The electronic properties of Ba<sub>2</sub>AlNbO<sub>6</sub> perovskite have been investigated in terms of electronic band structure (BS) and density of states (DOS) using GGA and GGA + mBJ potentials. The obtained electronic structure is shown in Fig. 2a–c, indicating that the given compound exhibits wide bandgap semiconducting character in both approximations. While analyzing Fig. 3a–c, it is clear that the valence band maxima (VBM) and conduction band minima (CBM) share a common symmetry point ( $\Gamma$ ), producing direct bandgap of values of 2.98 eV and 3.82 eV in the GGA and GGA + mBJ potentials, respectively. The bandgap in the mBJ potential expands due to the sweeping of energy bands at the Fermi level. Since mBJ potential replicates bandgap values that are close to the experimental value, we might remark that the

**Fig. 2** Optimized energy-volume plot of Ba<sub>2</sub>AlNbO<sub>6</sub> double perovskite

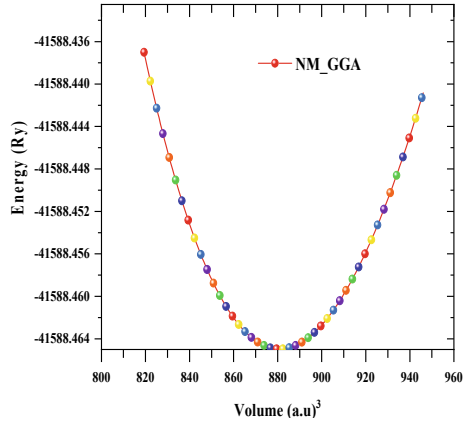


**Table 1** Calculated values of lattice constant ( $a_0$  in Å), bulk modulus ( $B_0$ ), pressure derivative of bulk modulus ( $B_0'$ ), ground state energy ( $E_0$  in Ry), and cohesive energy ( $E_{\text{coh}}$  in eV) of cubic Ba<sub>2</sub>AlNbO<sub>6</sub> compound

Compound	$a_0$	$B_0$ (GPa)	$B_0'$	$E_0$	$E_{\text{coh}}$
Ba <sub>2</sub> AlNbO <sub>6</sub> (our work)	8.052	167.29	4.46	- 41,588.464	64.94
Sr <sub>2</sub> AlNbO <sub>6</sub> [5]	7.78	172.05	5.78	-	-
Sr <sub>2</sub> AlTaO <sub>6</sub> [5]	7.78	170.4	5.80	-	-

given compound has a wide bandgap of 3.82 eV, which closely correlates with other comparable studied compounds [5].

The transport properties of the present material were explored using semi-classical Boltzmann theory implemented in the BoltzTraP code under constant relaxation time

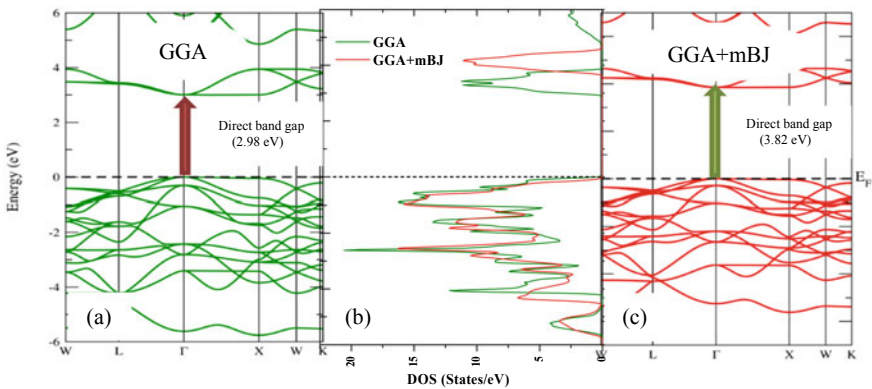


**Fig. 3** a–c Band structure and density of states of Ba<sub>2</sub>AlNbO<sub>6</sub> double perovskite determined via GGA and GGA + mBJ methods

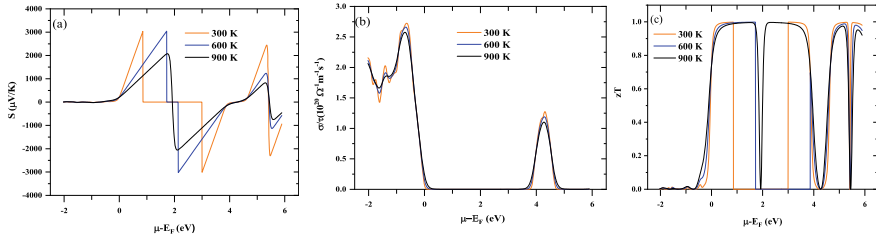


**Fig. 4** Thermoelectric coefficients of Ba<sub>2</sub>AlNbO<sub>6</sub> in response to the chemical potential; **a** Seebeck coefficient ( $S$ ), **b** electrical conductivity ( $\sigma/\tau$ ), and **c** figure of merit ( $zT$ ) at different temperatures (300, 600, 900 K)

approximation ( $\tau = 0.5 \times 10^{-15}$  s) [10]. In this study, we examined the impact of chemical potential in the energy range of  $(-2.5 \leq \mu \leq 6.5)$  on transport coefficients like Seebeck coefficient, electrical conductivity, and figure of merit at various temperatures (300, 600, 900 K), as shown in Fig. 4a–c.

Seebeck coefficient ( $S$ ) is defined as the ability of a material to generate induced emf when a temperature differential is applied and is given as;  $S = \frac{\Delta V}{\Delta T}$ , where  $\Delta T$  characterizes the temperature gradient. Figure 4a illustrates the chemical potential  $(-2.5 \leq \mu \leq 6.5)$  dependency of Seebeck coefficient for the given material at different Kelvin temperatures (300, 600, 900 K). It can be noticeably seen that the Seebeck coefficient exhibits prominent peaks and valleys in the entire range of chemical potential. The highest value of  $3000 \mu\text{V/K}^{-1}$  is obtained in the n-type region of the chemical potential. The higher Seebeck coefficient value for the present compound is due to wider bandgap and limited carrier mobility of the transport carriers. However, at higher temperatures,  $S$  is marginally reduced to  $2000 \mu\text{V/K}^{-1}$ . The decreasing tendency of Seebeck against rising temperature is due to the stimulation of bound electrons by thermal energy, producing electron–hole pairs (bipolar effect). The nonzero value of  $S$  even at higher temperatures makes this material a potential candidate for applications in thermoelectric generators, thermoelectric coolers, thermocouples, and temperature sensors.

Electrical conductivity ( $\sigma/\tau$ ) defines the ability of a substance to carry electric currents triggered by positive and negative charges. The fluctuations in electrical conductivity against chemical potential at varying temperatures are captured graphically in Fig. 4b. The  $\sigma$  of the given material has peaks in the energy range of  $-2$  to  $0$  and  $4$  to  $5$  eV region, while it has a negligible value in the range of  $0$ – $3.82$  eV. These results are consistent with the DOS plot, which depicts the presence and absence of electronic states in these specified regions, respectively. The peak value of  $2.75 \times 10^{20} (\Omega^{-1} \text{m}^{-1} \text{s}^{-1})$  is obtained in p-type doping region at 300 K.

The figure of merit reflects a material's true competency and applicability in thermoelectric technology ( $zT$ ). Thermoelectric devices are assumed to make effective use of materials with  $zT$  close to or greater than unity. These devices convert squandered heat into useful energy with the assistance of Seebeck effect. The graphical variation of electronic figure of merit ( $zT$ ) for Ba<sub>2</sub>AlNbO<sub>6</sub> is portrayed in Fig. 4c. One

can see the maximum value of  $zT$  at 300 K is 1.02, which is obviously greater than unity. The high  $zT$  of this material makes it potential candidate for energy harvesting applications.

### 3.3 Optical Properties

Optical properties are critical for investigating the response of any material under an externally applied electromagnetic field. The optical properties are characterized by complex dielectric function, which is mathematically expressed as;  $\epsilon(\omega) + i\epsilon_2(\omega)$  where  $\epsilon(\omega)$  corresponds to the real part of dielectric portraying polarization of light, while  $i\epsilon_2(\omega)$  symbolizes the imaginary part of the dielectric and is linked with the absorption of light. The graphical interpretations of real and imaginary dielectric against photon energy are illustrated in Fig. 5a, inferring that the initial critical point of  $\epsilon(\omega)$  happens at 3.82 eV. The threshold of direct optical transitions between VBM and CBM is specified by the splitting point,  $\Gamma_v-\Gamma_c$ , which is famously known as the basic adsorption edge. A crucial factor in defining the utilization of any material in optical devices is its refractive index. For the present material, refractive index against photon energy is plotted graphically and can be traced in Fig. 5b. It can be clearly seen that the refractive index increases linearly from 0 eV and exhibits different valleys and peaks. The peak value of refractive index is obtained at 4.5 eV. To conclude, the decent positive value of refractive index and low reflectivity of the studied material finds a route for this material in designing optoelectronic devices in the visible and deep UV region.

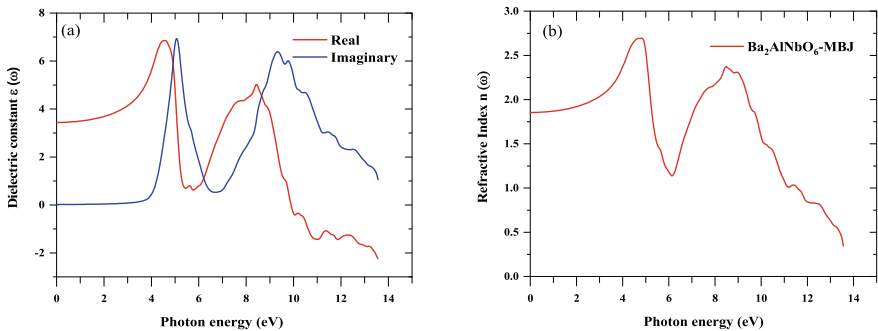


**Fig. 5** Optical properties of Ba<sub>2</sub>AlNbO<sub>6</sub> against photon energy; **a** dielectric constant, **b** refractive index

## 4 Conclusions

The structural, electronic, and thermoelectric aspects of double perovskite Ba<sub>2</sub>AlNbO<sub>6</sub> have been successfully predicted using DFT simulations incorporated into the Wien2k code. The total energy-volume calculations confirm the non-magnetic *Fm-3m* cubic stability. The GGA + mBJ potential is found to produce the wide bandgap of 3.82 eV. The thermoelectric analysis reveals a *zT* value of 1.02 for the given material at ambient temperature, making it a promising candidate to be employed in thermoelectric devices that convert squandered heat into electrical energy, i.e., energy harvesting applications. Apart from energy harvesting applications, the studied material offers potential optoelectronic device applications in the fields of transparent coatings in the visible and deep UV regions, as revealed by optical characteristics. The findings of our study will spur further research in theoretical and experimental domains to look deeper into the physical properties and possible energy harvesting applications of the studied material.

**Acknowledgements** Mudasir Younis Sofi (PMRF Fellow) would like to gratefully acknowledge the Prime Minister Research Fellowship (PMRF) program (PMRF ID; 3302522) for the financial support.

**Declaration of Interest Statement** The authors declare that they have no conflict of interests.

## References

1. Tritt TM (2011) Thermoelectric phenomena, materials, and applications. *Annu Rev Mater Res* 41:433–448
2. Zhang X, Zhao L-D (2015) Thermoelectric materials: energy conversion between heat and electricity. *J Materiomics* 1(2):92–105
3. Riffat SB, Ma XL (2003) Thermoelectrics: a review of present and potential applications. *Appl Therm Eng* 23:913–935
4. Lu Z, Zhang H, Lei W, Sinclair DC, Reaney IM (2016) High-figure-of-merit thermoelectric La-doped A-site-deficient SrTiO<sub>3</sub> ceramic. *Chem Mater* 28(3):925–935
5. Ramesh B, Mathrubutham R, Palanivel B (2015) Electronic structure, structural phase stability, optical and thermoelectric properties of Sr<sub>2</sub>AlM'O<sub>6</sub> (M' = Nb and Ta) from first principles calculations. *Comput Condens Matter* 58
6. de Lima MM, Domingues RO, Ferreir RAS, Yadav YP (2018) Production of Ba<sub>2</sub>AlNbO<sub>6</sub> ceramics and study of their stability in crude petroleum for the conservation of metallic sensing elements used in petroleum extraction. *Mater Res* 21(5):e20180139
7. Schwarz K, Blaha P, Madsen GKH (2002) Electronic structure calculations of solids using the WIEN2k package for material sciences. *Comput Phys Commun* 147(1–2):71–76
8. Perdew JP, Burke K, Ernzerhof M (1996) Generalized gradient approximation made simple. *Phys Rev Lett* 77(18):3865
9. Koller D, Tran F, Blaha P (2012) Improving the modified Becke–Johnson exchange potential. *Phys Rev B* 85(15):155109
10. Madsen GKH, Singh DJ (2006) BoltzTraP. A code for calculating band-structure dependent quantities. *Comput Phys Commun* 175(1):67–71

# Two-Dimensional Si<sub>2</sub>BNO<sub>4</sub>: A Potential Material for Optoelectronic Applications—An *Ab-Initio* Study



Santy M. Thomas and P. Ravindran

**Abstract** Herein, we propose Si<sub>2</sub>BNO<sub>4</sub> as a promising 2D material from our exploratory research on wide range of graphene oxide-based 2D materials with enhanced optoelectronic properties. We investigated the structural, electronic, and optical properties of Si<sub>2</sub>BNO<sub>4</sub> by hybrid density functional theory calculations. Our structural optimization predicts that Si<sub>2</sub>BNO<sub>4</sub> is energetically stable with low formation energy. Electronic structure studies show that this material has well-dispersed bands at the band edges resulting in low carrier effective mass and hence high electron/hole mobility. The band gap of this material falls within the visible part of the solar spectrum with an indirect bandgap value of 1.33 eV. Our optical property study shows that 2D phase of Si<sub>2</sub>BNO<sub>4</sub> possesses high optical absorption in the visible region than that of silicon making it a potential material for higher efficiency solar cell applications. We analyzed the photocatalytic water splitting capability of Si<sub>2</sub>BNO<sub>4</sub> for hydrogen production and found that it has good oxidation potential and hence this compound can be used more effectively in type II heterojunction/Z-scheme photocatalyst than a stand-alone photocatalyst. We have also investigated the plausibility of this material for higher efficiency solar cell applications by analyzing its performance parameters and found that it to be a promising candidate. Its constituents are earth-abundant and nontoxic elements and hence offer a cost-effective, environment-friendly, and pragmatic solution for renewable energy technologies.

**Keywords** 2D materials · Density functional theory · Photocatalytic water splitting · Solar cell

---

S. M. Thomas · P. Ravindran (✉)

Department of Physics, Central University of Tamil Nadu, Thiruvurur, Tamil Nadu, India  
e-mail: [raviphy@cutn.ac.in](mailto:raviphy@cutn.ac.in)

P. Ravindran

Simulation Centre for Atomic and Nanoscale MATerials (SCANMAT), Central University of Tamil Nadu, Thiruvurur, Tamil Nadu, India

## 1 Introduction

Rapid growth of mankind and fossil fuel-based energy use hampering the environmental sustainability and increased risk of climate change and as a result these have emerged as the greatest challenge currently. Development anchored in sustainable practices are quintessential and it has to be started with redirecting our energy dependence from non-renewable sources to environmentally friendly renewable methods. Photocatalytic water splitting for hydrogen gas production mimics the natural photosynthesis and leaves no harmful byproducts, making it a completely green technology for energy production and contribute to hydrogen economy. Similarly, solar cells harvest the abundant sunlight and produce electricity by generating electrons and holes as charge carriers. Both these technologies rely on sunlight, which is an inexhaustible source to ensure energy security. Identification of efficient materials for the production and usage of renewable energy as in the case of photocatalytic water splitting for hydrogen generation, solar cell, etc. has attracted the attention of the research community. The low-dimensional materials such as 2D materials with their promising features like high surface to volume ratio, low diffusion length, and possibility of band gap tuning offer enormous opportunities for various optoelectronic applications [1, 2]. Properties of 2D materials can be tailored using different methods like doping, application of strain or electric field, molecular adsorption, etc. [3–5]. In this work we are investigating 2D phase of  $\text{Si}_2\text{BNO}_4$  for optoelectronic applications, in particular, photocatalytic water splitting ability and solar cell prospects by means of Density Functional Theory (DFT).

## 2 Computational Methodology

From the search for higher efficiency optoelectronic materials by substituting graphene oxide with potential elements, we have identified a novel 2D material with composition  $\text{Si}_2\text{BNO}_4$ . The first principles total energy calculations are performed based on the DFT as implemented in VASP [6]. The generalized gradient approximation proposed by Perdew, Burke, and Ernzerhof (PBE) was adopted as the exchange–correlation functional to treat the electron–electron interaction. The long range van der Waals (vdW) interactions were accounted by using DFT-D2 vdW correction proposed by Grimme. The Heyd–Scuseria–Ernzerhof (HSE06) hybrid functional [7] was used to calculate the electronic structures because of the band gap underestimation of semiconductors by the PBE functional. Energy cut-off of 500 eV and a large vacuum of 15 Å were used. The geometric optimization was done with the energy convergence tolerance of  $10^{-6}$  eV per atom. The tolerance criteria of  $< 0.001$  eV/Å is set for the Hellman Feynman forces that acted on each atom upon ionic relaxation. The Brillouin zone was sampled using the Monkhorst–Pack scheme, with an employed k-mesh of  $12 \times 12 \times 1$  for the geometry optimization and the mesh of  $20 \times 20 \times 1$  for the optical and density of states calculations. The effective masses of the



charge carriers were estimated using the finite displacement method as implemented in VASPKIT [8].

### 3 Results and Discussion

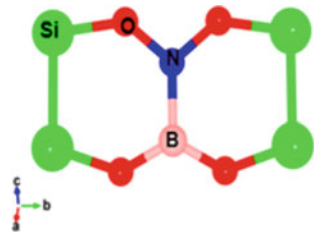
The optimized crystal structure of Si<sub>2</sub>BNO<sub>4</sub> monolayer after force and stress minimization is given in Fig. 1. Si<sub>2</sub>BNO<sub>4</sub> possess rectangular crystal structure with lattice constants 2.77 and 5.46 Å. We have calculated the formation energy,  $\Delta H_f$  to check the thermodynamic stability of this material and mathematically it can be represented as

$$\Delta H_f = E_{\text{products}} - E_{\text{reactants}} \quad (1)$$

If the  $\Delta H_f$  has a negative value, then the product is stable to form and can be synthesized experimentally. Si<sub>2</sub>BNO<sub>4</sub> the low formation energy value of  $-1.02$  eV/atom suggest that this material is stable and can be synthesized experimentally.

The calculated band structure obtained by using the PBE functional is depicted in Fig. 2, which shows that the Si<sub>2</sub>BNO<sub>4</sub> monolayer seems to be a direct bandgap semiconductor. But on a closer look, we found that it is an indirect bandgap semiconductor having a band gap value of 0.59 eV with valence band maximum (VBM) and conduction band minimum (CBM) located along  $X-\Gamma$  direction with a difference of  $\sim 30$  meV between direct and indirect band gaps. Even though the PBE calculation provided an indirect band feature with very small energy difference between direct and indirect band values, the HSE06 hybrid functional calculation resulted in a rearrangement of bands at the band edges and hence a well distinguished indirect band feature is appeared with a bandgap value of 1.33 eV along  $X-\Gamma$  direction. This indicates that, this material has the capability to harvest visible part of the solar spectrum and consequently enhance the photogeneration of charge carriers. It also has the advantage of preventing direct recombination of the electron-hole pairs and leads to a longer lifetime of photoexcited charge carriers. From the partial density of states analysis, it can be concluded that the CBM and VBM of Si<sub>2</sub>BNO<sub>4</sub> are dominated by Si-3*p* and N-2*p* states along with noticeable Si-3*s* states in CBM (Table 1).

**Fig. 1** Optimized structure of Si<sub>2</sub>BNO<sub>4</sub> monolayer



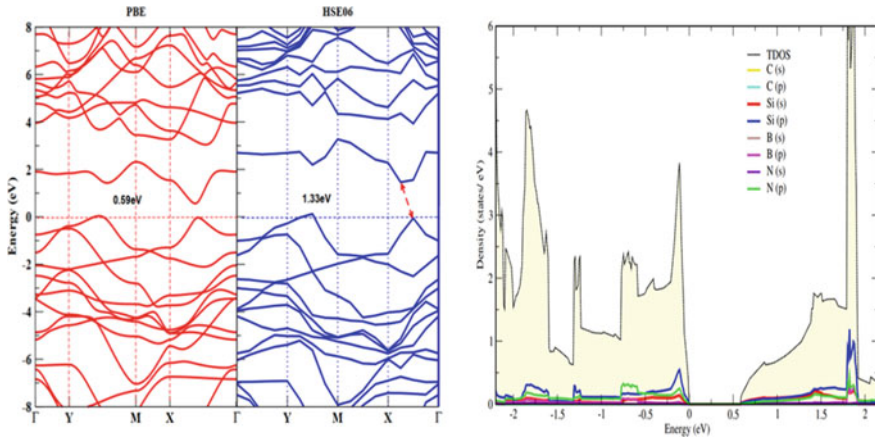


**Fig. 2** The calculated electronic band structure and partial and total density of states of  $\text{Si}_2\text{BNO}_4$  monolayer

**Table 1** The calculated band gap value (in eV) using PBE and HSE06 functionals, formation energy and effective mass of electron and hole (in  $m_0$ ) at the band edge for  $\text{Si}_2\text{BNO}_4$  monolayer

$\text{Si}_2\text{BNO}_4$	$E_g^{\text{PBE}}$	$E_g^{\text{HSE}}$	$\Delta H_f$ (eV/atom)	$\Delta H_f$ (kJ/mol)	$m_e$	$m_h$
	0.590	1.330	- 1.020	- 98.82	0.285	0.416

The electronic structure studies show that this material has well-dispersed bands at the band edges resulting in low electron and hole effective masses of 0.285 and 0.416  $m_0$ , respectively, at the band edge (where  $m_0$  is the free electron mass) and hence high electron as well as hole mobility. A material having an effective mass value of less than 0.5  $m_0$  in any of the crystallographic directions usually gives sufficient carrier mobility and hence such materials can be used in higher efficiency optoelectronic devices. It is interesting to note that, both electron and hole effective masses of  $\text{Si}_2\text{BNO}_4$  monolayer satisfy this criterion. Thus, it can boost the migration of photo-generated charge carriers to the surface and enhance the efficiency for optoelectronic application by lowering the recombination rate [9]. As shown in Fig. 3,  $\text{Si}_2\text{BNO}_4$  also possess high optical absorption in the visible part of the solar spectrum than that of silicon and hence this material can be used as a potential candidate for optoelectronic applications such as photocatalysis, higher efficiency solar cell. The absorption coefficient in the order of  $10^5 \text{ cm}^{-1}$  is potent enough to absorb optimum photon energy from solar spectrum. To use a material for the hydrogen production by means of photocatalytic water splitting, its band edges must straddle with the water redox potentials, i.e., the CBM and VBM should lie higher than the reduction potential and lower than the oxidation potential, respectively. The band alignment of the material to use for water reduction is also investigated and found that  $\text{Si}_2\text{BNO}_4$  monolayer has promising oxidation potential. However, the CBM is located at 0.38 eV lower than the  $\text{H}^+/\text{H}_2$  potential and hence it cannot act as a stand-alone photocatalyst. But our

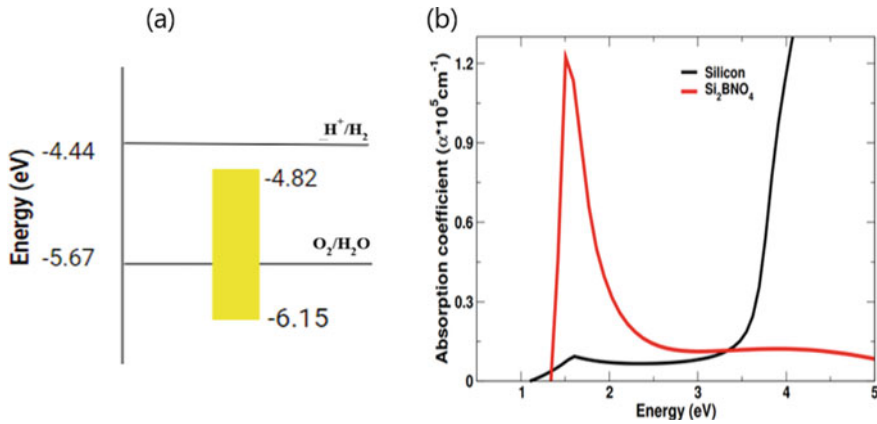


**Fig. 3** (a) Band alignment (yellow region) with respect to water redox potential at pH = 0 and (b) optical absorption coefficient of Si<sub>2</sub>BNO<sub>4</sub> monolayer

study suggest that this material can be used as an Z scheme or type 2 heterojunction photocatalyst for water reduction [10]. It may be noted that with suitable application of strain, electric field etc., the band gap as well as the band edges of this monolayer can be tuned to straddle with the water redox potential.

The photovoltaic properties of Si<sub>2</sub>BNO<sub>4</sub> were analyzed using performance parameters such as open circuit voltage ( $V_{oc}$ ), short circuit current density ( $J_{sc}$ ), fill factor (FF) and power conversion efficiency ( $\eta$ ) under AM 1.5G illumination and the results obtained are summarized in Table 2. Exciton binding energy ( $E_b$ ) is the energy required to dissociate the electron–hole pair and it can be estimated using the following relation

$$E_b = \frac{m_e m_h R_y}{m_0 (m_e + m_h) \epsilon_s^2} \quad (2)$$

where  $m_e$  and  $m_h$  corresponds to effective mass of electron and hole,  $R_y$  denotes the Rydberg constant and  $\epsilon_s$  is the static dielectric constant. The low exciton binding energy of Si<sub>2</sub>BNO<sub>4</sub> favors quick separation of electron and hole, consequently lowers recombination rate and improve efficiency. The calculated small value of exciton binding energy of 79.63 meV revealed that this material can be used as absorber layer in non-excitonic solar cell. To estimate  $J_{sc}$  we have adopted the Scharber model [11]; according to which,

**Table 2** The photovoltaic performance parameters for Si<sub>2</sub>BNO<sub>4</sub> monolayer

Si <sub>2</sub> BNO <sub>4</sub>	Dielectric constant	Exciton binding energy, $E_b$ (meV)	$V_{oc}$ (V)	$J_{sc}$ (mA/cm <sup>2</sup> )	FF	$\eta$ (%)
	4.82	79.63	1.03	17.17	86.96	15.38

$$J_{sc} = 0.65 J_{ph} \quad (3)$$

The high short circuit current density of  $\text{Si}_2\text{BNO}_4$  monolayer can be credited to its large optical absorption which in turn is improving the generation rate of charge carriers. The  $V_{oc}$ , is the maximum voltage available from a solar cell, whereas FF corresponds to the maximum power a solar cell can produce. As per the descriptor method proposed by Alharbi et al. [12] for a non-excitonic solar cell,  $V_{oc}$  and FF can be computed as follows:

$$V_{oc} = E_g - 0.2 - 0.114E_g^{1.8617} - 0.057E_g \quad (4)$$

where  $E_g$  corresponds to the band gap of the material. The FF is defined as

$$FF = \frac{V_{oc}}{V_{oc} + \alpha k_B T} \quad (5)$$

For non-excitonic solar cells,  $\alpha$  takes the value of 6,  $T$  denotes the room temperature and  $k_B$  is Boltzmann's constant. In order to evaluate the solar cell efficiency, we have calculated  $V_{oc}$  and FF and are having the values of 1.03 V and 86.93%, respectively. The power conversion efficiency of a solar cell can be calculated using the formula

$$\eta = (V_{oc} * J_{sc} * FF) / P_{in} \quad (6)$$

where  $P_{in}$  is the input solar radiation which takes the value of 100 mW/cm<sup>2</sup>, and it is considered to be standard for terrestrial photovoltaic devices. The monolayer of  $\text{Si}_2\text{BNO}_4$  is predicted to have a photoconversion efficiency of 15.38% and has comparable  $J_{sc}$  and higher  $V_{oc}$ , FF and efficiency than many of the lead free perovskite materials reported so far [13]. It may be noted that this material has higher photovoltaic performance parameters than graphene-based bulk heterojunction solar cells, dye-sensitized solar cells [14], etc. Generally, organic solar cells have the FF in the range of 50–70% [15]. Thus, the performance parameters analysis reveals that  $\text{Si}_2\text{BNO}_4$  monolayer can be used for developing higher efficiency solar cell.

## 4 Conclusion

We have studied the geometric, electronic, optical, photocatalytic, and photovoltaic properties of  $\text{Si}_2\text{BNO}_4$  monolayer and found that this material has the potential to use in optoelectronic applications. Our electronic structure and total energy calculations show that monolayer of  $\text{Si}_2\text{BNO}_4$  is stable with low formation energy, suitable band gap for visible light absorption and possess low carrier effective mass and thus high mobility. Even though it has promising oxidation potential, the conduction band edge is not straddling with the water reduction potential. Consequently, this material

can be used in Z scheme or Type 2 heterojunction photocatalyst for water splitting. The photovoltaic property analysis shows that monolayer of Si<sub>2</sub>BNO<sub>4</sub> has promising power conversion efficiency and it is suitable for solar cell applications.

**Declaration of Interest Statement** The authors declare that they have no conflict of interests.

## References

1. Jakhar M, Kumar A, Ahluwalia PK, Tankeshwar K, Pandey R (2022) Engineering 2D materials for photocatalytic water-splitting from a theoretical perspective. *Materials* 15(6):Art. no. 6. <https://doi.org/10.3390/ma15062221>
2. Zhao Y, Yu L, Sun M (2021) Recent progress in emerging 2D layered materials for organic solar cells. *Sol Energy* 218:621–638. <https://doi.org/10.1016/j.solener.2021.02.066>
3. Jiao Y, Ma F, Gao G, Bell J, Frauenheim T, Du A (2015) Versatile single-layer sodium phosphidostannate(II): strain-tunable electronic structure, excellent mechanical flexibility, and an ideal gap for photovoltaics. *J Phys Chem Lett* 6(14):2682–2687. <https://doi.org/10.1021/acs.jpcclett.5b01136>
4. Gu D, Tao X, Chen H, Ouyang Y, Zhu W, Du Y (2021) Two-dimensional polarized MoTe<sub>2</sub>/GeS heterojunction with an intrinsic electric field for photocatalytic water-splitting. *RSC Adv* 11(54):34048–34058. <https://doi.org/10.1039/D1RA05840A>
5. Ashwin Kishore MR, Sjästad AO, Ravindran P (2019) Influence of hydrogen and halogen adsorption on the photocatalytic water splitting activity of C<sub>2</sub>N monolayer: a first-principles study. *Carbon* 141:50–58. <https://doi.org/10.1016/j.carbon.2018.08.072>
6. Kresse G, Furthmüller J (1996) Efficient iterative schemes for ab initio total-energy calculations using a plane-wave basis set. *Phys Rev B* 54(16):11169–11186. <https://doi.org/10.1103/PhysRevB.54.11169>
7. Heyd J, Scuseria GE, Ernzerhof M (2003) Hybrid functionals based on a screened Coulomb potential. *J Chem Phys* 118(18):8207–8215. <https://doi.org/10.1063/1.1564060>
8. Wang V, Xu N, Liu J-C, Tang G, Geng W-T (2021) VASPKIT: a user-friendly interface facilitating high-throughput computing and analysis using VASP code. *Comput Phys Commun* 267:108033. <https://doi.org/10.1016/j.cpc.2021.108033>
9. Das T et al (2017) Investigation of the optical and excitonic properties of the visible light-driven photocatalytic BiVO<sub>4</sub> material. *Chem Mater* 29(8):3380–3386. <https://doi.org/10.1021/acs.chemmater.6b02261>
10. Xu Q, Zhang L, Yu J, Wageh S, Al-Ghamdi AA, Jaroniec M (2018) Direct Z-scheme photocatalysts: principles, synthesis, and applications. *Mater Today* 21(10):1042–1063. <https://doi.org/10.1016/j.mattod.2018.04.008>
11. Scharber MC et al (2006) Design rules for donors in bulk-heterojunction solar cells—towards 10 % energy-conversion efficiency. *Adv Mater* 18(6):789–794. <https://doi.org/10.1002/adma.200501717>
12. Alharbi FH, Rashkeev SN, El-Mellouhi F, Lüthi HP, Tabet N, Kais S (2015) An efficient descriptor model for designing materials for solar cells. *npj Comput Mater* 1(1):Art. no. 1. <https://doi.org/10.1038/npjcompumats.2015.3>
13. Wang M et al (2021) Lead-free perovskite materials for solar cells. *Nano-Micro Lett* 13(1):62. <https://doi.org/10.1007/s40820-020-00578-z>
14. Bellani S et al (2021) Solution-processed two-dimensional materials for next-generation photovoltaics. *Chem Soc Rev* 50(21):11870–11965. <https://doi.org/10.1039/D1CS00106J>
15. Qi B, Wang J (2013) Fill factor in organic solar cells. *Phys Chem Chem Phys* 15(23):8972–8982. <https://doi.org/10.1039/C3CP51383A>

# Numerical Study of Perovskite Solar Cells Using DFT-Extracted Parameters of Lead-Free CsGeX<sub>3</sub> (X = I, Br) Light Absorbing Material



Joy Sarkar and Suman Chatterjee

**Abstract** The power conversion efficiency for organic–inorganic lead halide Perovskite solar cells (PSC) has increased to 27.4% during the past decade. Despite this progress, lead poisoning continues to be a severe problem for commercialization. Cesium Germanium halide Perovskite (CsGeX<sub>3</sub>) has the potential to be a great alternative to lead-based perovskite because of its strong optical conductivity and optical absorbance. The electronic and optical properties of the Perovskite light absorber layer have the most decisive impact on PSC device performance. Density functional theory (DFT) uses a quantum–mechanical approach to accurately predict the properties of several charge transport layers, including the active perovskite layer. We use first-principles DFT calculations to determine the electronic and optical properties of lead-free inorganic CsGeI<sub>3</sub> and CsGeBr<sub>3</sub> perovskite materials. The SCAPS-1D device simulator is used to evaluate the performance of the modeled device in relation to the effect of the DFT-extracted band gap, the effective density of states, and the absorption spectrum of CsGeX<sub>3</sub> (X = I, Br). The energy band gap was calculated to be 1.169 eV for CsGeI<sub>3</sub> and 1.665 eV for CsGeBr<sub>3</sub>. The CsGeI<sub>3</sub>-based device achieved the highest power conversion efficiency (PCE) of 25.21%, which decreased to 20.32% after including calculated absorption data.

**Keywords** Lead-free perovskite · Density functional theory · All-inorganic perovskite · Absorption spectra · SCAPS-1D · Numerical simulation

---

J. Sarkar · S. Chatterjee (✉)

Department of Physics, University of North Bengal, Siliguri 734013, India

e-mail: [suman@nbu.ac.in](mailto:suman@nbu.ac.in)

J. Sarkar

e-mail: [joysarkar2019@nbu.ac.in](mailto:joysarkar2019@nbu.ac.in)

## 1 Introduction

Hybrid halide perovskites [1], where A, B, and X are inorganic cations, metal cations, and halogen anions, respectively, are promising for commercial usage due to their natural abundance and inexpensive cost. These types of perovskite solar cells have garnered the most interest in the scientific community due to their high power conversion efficiency (PCE), which has improved from 3.8 to 27.4% between 2009 and 2022 [2–4].  $\text{CH}_3\text{NH}_3\text{PbI}_3$  is one of the most common hybrid perovskites due to its optoelectronic features, including strong optical absorption, tunable band gaps, higher mobility, and long charge diffusion lengths. However, several factors like multiple phase transition, degradation upon moisture exposure, and lead toxicity prevent its large-scale application. On the other hand, lead-free  $\text{CsGeX}_3$  perovskite has the potential to replace conventional Pb-based PSCs because of its promising optoelectronic properties and stability at room temperature [5]. The performance of the PSC device is affected by several factors [6, 7], including the existence of interfacial defects, layer thickness, doping, carrier injection rate, and absorption spectrum. SCAPS-1D software is used to study the effects of these electronic parameters on the device's performance [8–10]. In this work, we use first-principles DFT calculations to derive the electronic and optical characteristics of lead-free  $\text{CsGeX}_3$  perovskite materials. At first, the calculated optical band gap and effective density of states values are utilized in the SCAPS-1D simulator to derive the device's performance. Then, the effect of the DFT-extracted absorption spectra on PCE is investigated.

## 2 Device Architecture

The architecture of the perovskite solar cell device has many stacked layers, including a transparent conductive oxide (FTO) layer,  $\text{TiO}_2$  as an electron transport layer (ETL), the perovskite absorber layer,  $\text{CuSCN}$  as a hole transport layer (HTL), and a back-metal contact layer as shown in Fig 1. The perovskite/ $\text{TiO}_2$  interface layer (IL1) and perovskite/ $\text{CuSCN}$  layer (IL2) have been considered in device simulations for interface recombination. At 300 K, the conventional AM 1.5G light spectrum ( $1 \text{ kW/m}^2$ ) is used to illuminate the solar cell at normal incidence. We have primarily focused on developing lead-free, all-inorganic perovskite solar cells that exhibit higher efficiency. In this work, we have exclusively investigated inorganic ETL and HTL materials to pursue this goal.

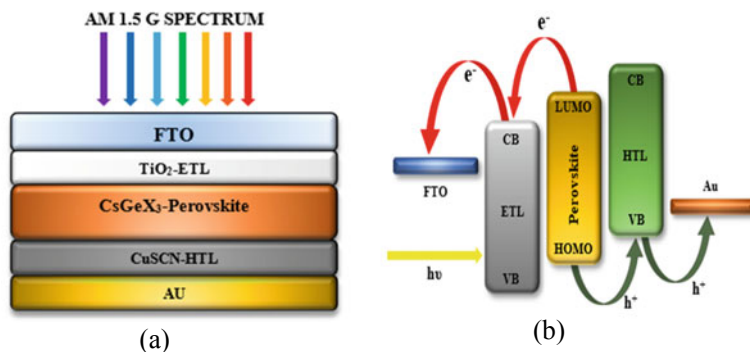


**Fig. 1** **a** Device architecture of PSC. **b** Energy band diagram of the device

### 3 DFT Calculations

To evaluate the structural, electronic, and optical properties of the material, we used the full potential linearized augmented plane wave (FP-LAPW) method based on the DFT of Blaha et al. [11] as implemented in the Wien2k code [12]. This study employs Perdew Burke Ernzerhof (PBE) exchange–correlation functional of the Generalized Gradient Approximation (GGA) since it is more efficient and precise [13]. In this method, ionic cores are formed when nuclei interact with the shell’s innermost electrons. This ionic core is then subject to the influence of the valence electrons. As a consequence, the electron–ion potential converges rapidly. The LAPW approach divides the unit cell into two halves. The first is non-overlapping muffin-tin (MT) spheres, where the wave functions fluctuate rapidly and are atomic-like. The second is the remaining interstitial region (IR), where the wave functions vary more slowly and are not atomic-like. Then, to provide an effective representation throughout space, each basis function is specified as a plane wave in the interstitial area coupled smoothly to a linear combination of atomic-like functions in the spheres. Extending the plane wave functions into the interstitial region up to a cutoff value of the wave vector  $K$  given by  $K_{\max} * R_{\text{MT}} = 7$ , the convergence of the energy eigenvalue is achieved.  $R_{\text{MT}}$  is defined as the minimum radius of a muffin-tin sphere. We consider the 4d, 5s, 5p, 6s orbital of Cs, the 3d, 4s, 4p orbital of Ge, the 3d, 4s, 4p orbital of Br, and the 4d, 5s, 5p orbital of I to be valence orbitals, whereas the lower states are considered as core states. The self-consistent potentials at 2000 k points for electronic and 3000 k points for optical properties have been calculated with convergence threshold energy to  $10^{-5}$  Ry.



## 4 Results and Discussion

### 4.1 Electronic Band Structure and Density of States

First, the built-in unit cell's geometries for our compounds with the space group cubic Pm3m (221) were optimized using the Murnaghan equation of state. The obtained lattice parameters are 6.35 Å for CsGeI<sub>3</sub> and 6.3 Å for CsGeBr<sub>3</sub>. The computation of electronic band structure provides the range of energy levels that electrons can have within it and the ranges of energy that they cannot have at a certain wavenumber ( $k$ ). The structure of the electronic band displays the energy range in which free electrons can exist (conduction band) and the region where no available free electrons are present (valence band). The fermi level (EF) is assumed to be 0 eV because all calculations were performed at 0 K without taking temperature into account. The empty area between the conduction band and the valence band shows the amount of energy that the electron must have to move from the valence band to the conduction band. The band gap has been obtained by subtracting the valence band maximum (VBM) from the conduction band minimum (CBM). The semiconductor material may feature a direct or indirect energy band gap depending on the band structure. The band gap is considered direct if the valence band's maxima coincide exactly with the minimum of the conduction band. Also, an indirect band gap is observed when the valence band maxima and the conduction band minima are not correctly aligned. For our investigated materials, the VBM and CBM are perfectly coincident and aligned at the exact high symmetry  $k$ -points value, as shown in Fig. 2a, b. The calculated values of the band gap for our materials are consistent with previously collected data [14, 15]. The straight band gaps of CsGeI<sub>3</sub> and CsGeBr<sub>3</sub> are 1.169 eV and 1.665 eV, respectively.

In Condensed matter physics, we described a system's density of states (DOS) as the number of states per unit interval of energy at each energy level available to be occupied. Figure 2c–f exhibit the Total DOS (TDOS) and Partial DOS (PDOS) of the investigated compounds. The principal peak of TDOS appears at  $-7.48$  and  $-0.25$  eV, respectively, for CsGeI<sub>3</sub> and CsGeBr<sub>3</sub>. This primary peak corresponds to the p-state of the Cs atom. In the energy range of  $-4$  to  $4$  eV, the valence and conduction band of the materials consists solely of the s and p states of Ge and halide atoms. This analysis validates that mostly Halide (I, Br) and Ge atomic states contribute to the formation of CB and VB. There is no high peak in the DOS plot at the fermi level, indicating that the materials are not pure conductors. However, the low energy band gap values of the materials imply that they are not insulators either. Consequently, these compounds will behave as semiconducting materials, an essential characteristic for use in optoelectronic devices.

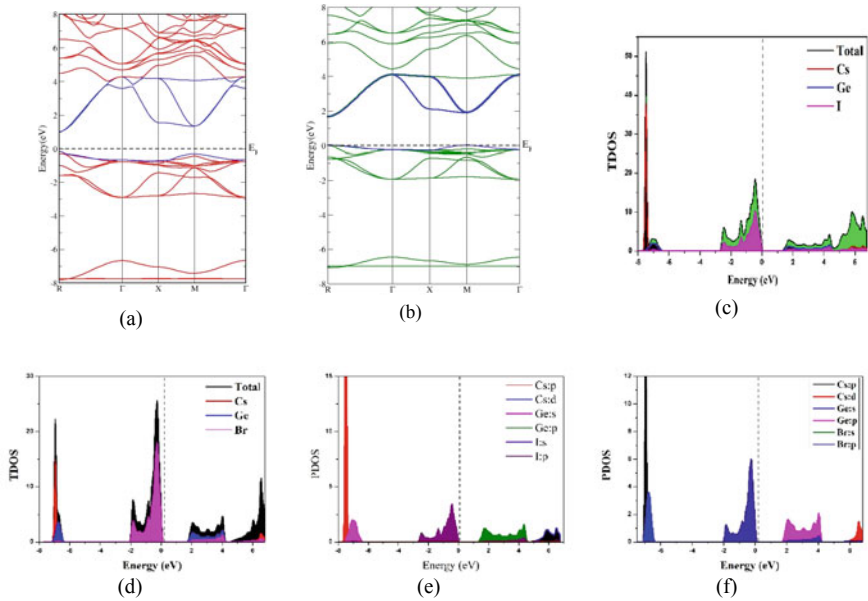


**Fig. 2** a–b The calculated band structures, c–d total DOS of CsGeI<sub>3</sub>, and CsGeBr<sub>3</sub>, e, f partial density of states of CsGeI<sub>3</sub> and CsGeBr<sub>3</sub> respectively

## 4.2 Optical Properties

To evaluate the optical properties of CsGeI<sub>3</sub> and CsGeBr<sub>3</sub>, several factors, including the coefficient of absorption, reflectivity, conductivity, and dielectric function, have been studied and analyzed using Eqs. (1)–(3). These properties result from wave-matter interaction, which is the interaction of the material with an electromagnetic wave (light). Figure 3 shows the observed optical characteristics of CsGeI<sub>3</sub> and CsGeBr<sub>3</sub>.

$$\varepsilon(\omega) = \varepsilon_1(\omega) + i\varepsilon_2(\omega) \quad (1)$$

$$I(\omega) = 2^{1/2}\omega \left[ \left\{ \varepsilon_1^2(\omega) + \varepsilon_2^2(\omega) \right\}^{1/2} - \varepsilon_1(\omega) \right]^{1/2} \quad (2)$$

$$R(\omega) = (n + ik - 1)/(n + ik + 1) \quad (3)$$

CsGeI<sub>3</sub> and CsGeBr<sub>3</sub> have primary reflectivity peaks at 2.489 and 2.735 eV, respectively. The coefficient of absorption spectra of a substance describes how much light of a certain wavelength or energy penetrates the medium before being absorbed [16]. CsGeI<sub>3</sub> and CsGeBr<sub>3</sub> have the highest absorption peaks at 8.91 and 10.71 eV, respectively. CsGeI<sub>3</sub> has a real conductivity peak at 6.136 eV. The real

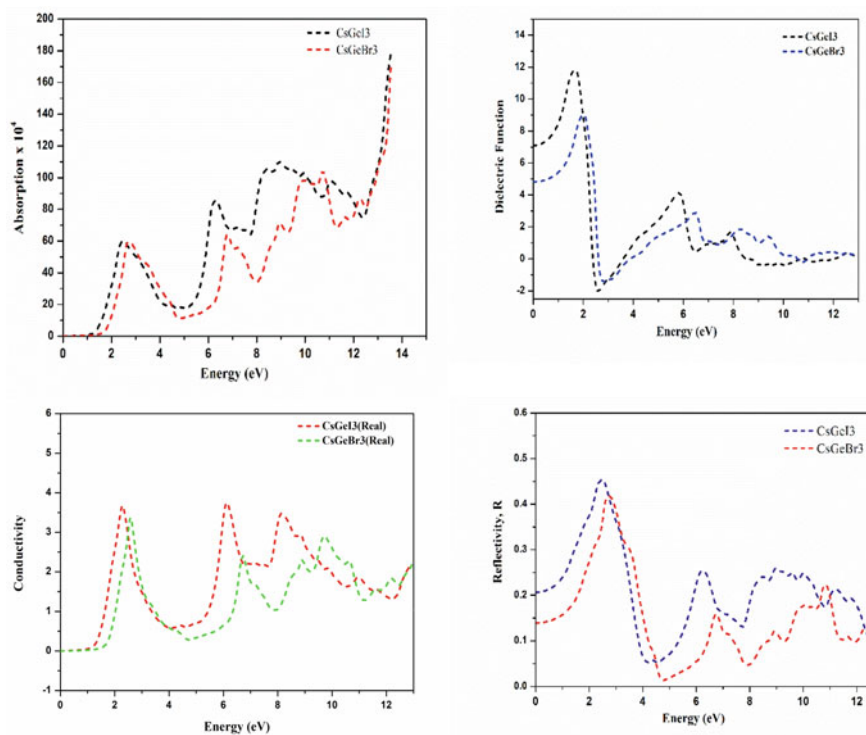


**Fig. 3** Relative investigation of optical properties of  $\text{CsGeI}_3$  and  $\text{CsGeBr}_3$

component of the dielectric constant characterizes a material's ability to interact with an electric field (store and release energy) without absorbing it. The value of the real dielectric function is 1.66 eV for  $\text{CsGeI}_3$ , while for  $\text{CsGeBr}_3$  is 2.02 eV.  $\text{CsGeI}_3$  has the maximum value of absorption coefficient and dielectric function compared to  $\text{CsGeBr}_3$ , as shown in Fig. 3. The optical and electronic properties of these compounds indicate that they are suitable for use in light-emitting diodes and solar cells; however,  $\text{CsGeI}_3$  has a lower band gap than  $\text{CsGeBr}_3$  perovskite material, making it a better candidate for these applications.

### 4.3 Solar Cell Characteristics

The simulation study reveals that the device configuration  $\text{FTO}/\text{TiO}_2/\text{CsGeX}_3/\text{CuSCN}/\text{Au}$  has an FF of 81.33% and 83.22% with PCE of 25.21%, 22.74% for  $X = \text{I}$  and  $\text{Br}$ , respectively. When a DFT-based absorption spectrum is used for the  $\text{CsGeX}_3$  ( $X = \text{I}, \text{Br}$ ) perovskite absorber layer, the PCE changes to 20.32% and 16.71%, respectively. Table 1 displays the optimum solar cell parameters required

**Table 1** Material parameters used in the simulation

Parameters	HTL (CuSCN)	Perovskite (CsGeX <sub>3</sub> ) (X = I, Br)	ETL (TiO <sub>2</sub> )
Thickness (nm)	170	800/600	50
Band gap (eV)	3.4	1.169/1.665	3.2
Electron affinity (eV)	1.9	3.76	3.9
CB effective density of states (1/cm <sup>3</sup> )	$1.7 \times 10^{19}$	$1.1 \times 10^{18}$	$2.2 \times 10^{18}$
VB effective density of states (1/cm <sup>3</sup> )	$2.5 \times 10^{21}$	$5.2 \times 10^{19}$	$1.8 \times 10^{19}$
Electron mobility (cm <sup>2</sup> /V.S.)	$2 \times 10^{-4}$	20	20
Hole mobility (cm <sup>2</sup> /V.S.)	$2 \times 10^{-1}$	20	10

for the simulation, including the DFT-extracted band gap and effective density of states value of the perovskite layer. After applying the DFT-based absorption spectrum to the perovskite absorber layer, we observed a decrease in efficiency. This is likely because the default absorption model of SCAPS-1D covers a wide range of the light spectrum, while our computed data only considers the visible spectrum. Despite the decrease in performance, we chose to limit our analysis to the visible spectrum to better align with experimental findings. Therefore, although the PCE value may decrease when using DFT-extracted data, this approach offers a more relevant representation of real-world experimental settings.

#### ***4.4 Effect of Thickness and Defect Density of the Perovskite Layer***

In the perovskite absorber layer, the absorption of light photons generates free charge carriers. Since photon absorption is dependent on the absorber layer's thickness, defect density, and other characteristics, the performance of the device is primarily determined by these factors. The thickness of the absorber layer and the diffusion length of the light carriers are associated. Hence, the rate of recombination and extraction of charge carriers highly depends on the absorber layer thickness. If the absorber layer is too thick, charge carriers may recombine in the charge transport layers before reaching the electrodes, resulting in a loss in device performance. Alternatively, if the absorber layer is too thin, photons may not be adequately absorbed, which lowers the number of photogenerated charge carriers and the device's overall photovoltaic performance. A thin layer of ETL is typically employed in perovskite solar cells to facilitate faster electron transition with reduced recombination. Through thickness optimization using SCAPS software, we have found that an ETL thickness of 50 nm is the optimum thickness for achieving the best performance. On the contrary, the HTL thickness in PSCs ranges from 150 to 200 nm, but in this specific device

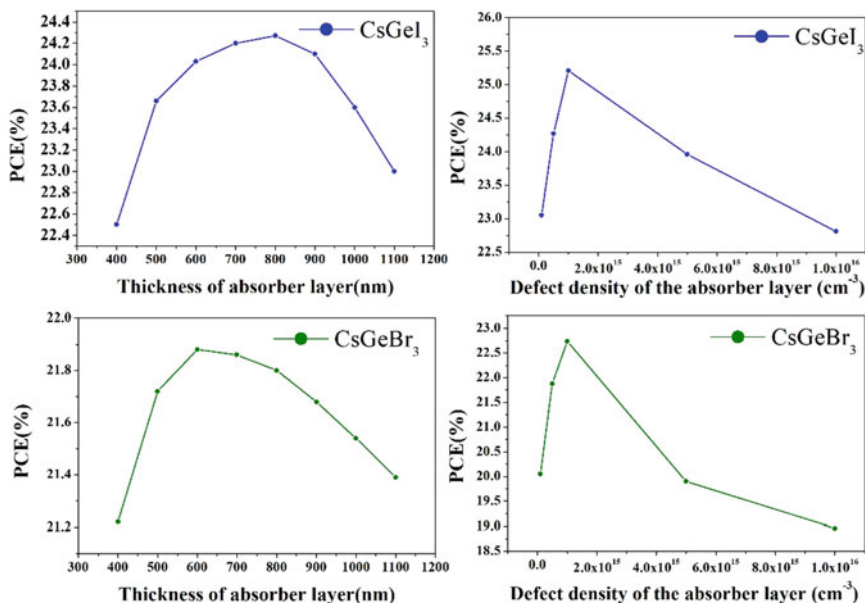


**Fig. 4** Variation of PCE of CsGeX<sub>3</sub> (X = I, Br)-based solar cell with the defect density and thickness of the perovskite absorber layer

configuration, the best performance has been observed with a thickness of 170 nm. In addition, the absorber layer thickness is changed from 400 to 1100 nm, while the HTL and ETL thicknesses are held constant at 170 nm and 50 nm, respectively. The optimal absorber layer thickness is 800 nm and 600 nm for CsGeI<sub>3</sub> and CsGeBr<sub>3</sub>, respectively.

Figure 4 illustrates the variation of PSC performance parameters with perovskite absorber layer thickness and defect density. The defect density of the perovskite layer is changed from  $1 \times 10^{14}$  to  $1 \times 10^{16}$  cm<sup>-3</sup>. After the simulation,  $1 \times 10^{15}$  cm<sup>-3</sup> is determined to be the optimal value for both the perovskite layers. For the device configurations, the capture cross section and thermal velocity of charge carriers are assumed to be  $10^{-15}$  cm<sup>2</sup> and  $10^7$  cm/s, respectively.

## 5 Conclusion

The first-principles simulations conducted in this study have calculated the structural and optoelectronic properties of all-inorganic metal halide cubic perovskites CsGeX<sub>3</sub> (X = I, Br). The outcomes of this study suggest that these materials exhibit a direct band gap, higher optical conductivity, and absorption spectra in the visible region, making them ideal for use in solar cell applications. Among the materials investigated,

CsGeI<sub>3</sub> is found to have the most favorable band gap for solar cell applications, and simulation results using SCAPS-1D suggest that a device based on CsGeI<sub>3</sub> performs best. In addition, it was noticeable that when the DFT-based absorption spectrum for the absorber layer is used, the PCE decreases significantly, which is expected because we considered only the visible region in the calculated absorption data. The findings of this study demonstrate the potential for combining DFT calculations and device simulations to extend beyond the investigation of all-inorganic metal halide cubic perovskites CsGeX<sub>3</sub>. The inclusion of additional layers, organic molecule additives, and metal dopants could provide further insight into the effectiveness of perovskite solar cells, paving the way for quantum-mechanical projections of PCE.

**Acknowledgements** The authors greatly acknowledge the Dept. of Physics, the University of North Bengal, for providing financial support and laboratory facilities for carrying out the research work. We would like to thank Mr. Marc Burgelman, the Electronics and Information Systems (ELIS), University of Gent, Belgium, for providing free access to SCAPS-1D simulation software. The author thanks the Department of Science and Technology (DST), Government of India, for providing the INSPIRE fellowship (INSPIRE Grant. No. IF180331).

**Data Availability** All data generated and calculated during this study are contained within this article.

**Declarations** No funding was received for this work. The authors declare that they have no known conflict of interest.

## References

1. Reshak AH, Abu-Jafar MS, Al-Douri Y (2016) Two symmetric n-type interfaces SrTiO<sub>3</sub>/LaAlO<sub>3</sub> in perovskite: electronic properties from density functional theory. *J Appl Phys* 119(24):245303
2. Fadila B, Ameri M, Bensaid D, Noureddine M, Ameri I, Mesbah S, Al-Douri Y (2018) Structural, magnetic, electronic and mechanical properties of full-Heusler alloys Co<sub>2</sub>YAl (Y = Fe, Ti): first principles calculations with different exchange-correlation potentials. *J Magn Magn Mater* 448:208–220
3. Ameri M, Amel S, Abidri B, Ameri I, Al-Douri Y, Bouhafis B, Varshney D, Aze-Eddine A, Nadia L (2014) Structural, elastic, electronic and thermodynamic properties of uranium filled skutterudites UFe<sub>4</sub>P<sub>12</sub>: first principle method. *Mater Sci Semicond Process* 27:368–379
4. Min H, Lee DY, Kim J, Kim G, Lee KS, Kim J, Paik MJ, Kim YK, Kim KS, Kim MG, Shin TJ (2021) Perovskite solar cells with atomically coherent interlayers on SnO<sub>2</sub> electrodes. *Nature* 598(7881):444–450
5. Young J, Rondinelli JM (2016) Octahedral rotation preferences in perovskite iodides and bromides. *J Phys Chem Lett* 7(5):918–922
6. Le Corre VM, Stolterfoht M, Perdígón Toro L, Feuerstein M, Wolff C, Gil-Escrig L, Bolink HJ, Neher D, Koster LJA (2019) Charge transport layers limiting the efficiency of perovskite solar cells: how to optimize conductivity, doping, and thickness. *ACS Appl Energy Mater* 2:6280–6287
7. Cho A-N, Park N-G (2017) Impact of interfacial layers in perovskite solar cells. *ChemSusChem* 10:3687–3704

8. Chakraborty K, Choudhury MG, Paul S (2019) Numerical study of  $\text{Cs}_2\text{TiX}_6$  ( $X = \text{Br}^-$ ,  $\text{I}^-$ ,  $\text{F}^-$  and  $\text{Cl}^-$ ) based perovskite solar cell using SCAPS-1D device simulation. *Sol Energy* 194:886–892
9. Laali J, Hamedani A, Alahyarizadeh G, Minucmehr A (2020) Performance analysis of the perovskite solar cells by a realistic, DFT-accurate optical absorption spectrum. *Superlattices Microstruct* 143:106551
10. Chouhan AS, Jasti NP, Avasthi S (2018) Effect of interface defect density on performance of perovskite solar cell: correlation of simulation and experiment. *Mater Lett* 221:150–153
11. Baktash A, Amiri O, Sasani A (2016) Improve efficiency of perovskite solar cells by using magnesium doped ZnO and  $\text{TiO}_2$  compact layers. *Superlattices Microstruct* 93:128–137
12. Kohn W, Sham LJ (1965) Self-consistent equations including exchange and correlation effects. *Phys Rev* 140(4A):A1133–A1138
13. Azri F, Meftah A, Sengouga N, Meftah A (2019) Electron and hole transport layers optimization by numerical simulation of a perovskite solar cell. *Sol Energy* 181:372–378
14. Raj A, Kumar M, Bherwani H, Gupta A, Anshul A (2021) Evidence of improved power conversion efficiency in lead-free  $\text{CsGeI}_3$  based perovskite solar cell heterostructure via scaps simulation. *J Vac Sci Technol B Nanotechnol Microelectron Mater Process Meas Phenom* 39(1):012401
15. Raj A, Kumar M, Singh PK, Singh RC, Bherwani H, Gupta A, Anshul A (2021) A computational approach to investigate the suitable ETL for lead-free  $\text{CsGeI}_3$  based perovskite solar cell. *Mater Today Proc* 47:1564–1569
16. Huang LY, Lambrecht WR (2013) Electronic band structure, phonons, and exciton binding energies of halide perovskites  $\text{CsSnCl}_3$ ,  $\text{CsSnBr}_3$ , and  $\text{CsSnI}_3$ . *Phys Rev B* 88(16):165203

# Affinity Optimization of Commercially Available Crystalline-Silicon Heterojunction Solar Cell by Using AFORS-HET Software



Naima, Pawan K. Tyagi, and Vinod Singh

**Abstract** In this report, we have investigated the crystalline-silicon heterojunction solar cell by using AFORS-HET software version 2.5, and the structure of the solar cell is designed as: ITO (TCO)/n-diamane/p-type c-Si/Ag (back contact). The simulation is carried out by optimizing the electron affinity of p-type c-Si wafer in the possible range of its values where the p-type c-Si layer also works as an absorbing layer or active layer which collect the photogenerated charge carriers that contribute in the generation of current flowing through the external circuit. The solar cell is illuminated by the monochromatic light under an Air Mass 1.5 Global, 10 nm spectral width and 100 mW/cm<sup>2</sup> of power supply. To do the entire simulation, practically available values of parameters of p-type c-Si have been taken. For the best optimized value of electron affinity, the value of open circuit voltage ( $V_{OC}$ ), current density ( $J_{SC}$ ), fill factor (FF) and efficiency ( $\eta$ ) is found to be 593 mV, 21.66 mA/cm<sup>2</sup>, 81.05% and 10.41%, respectively. This efficiency is the maximum efficiency achieved for the proposed structure when the commercially available values of the parameters of p-type c-Si layer were considered. This report investigated that the FF and  $\eta$  of the proposed solar cell first increase linearly with affinity of p-type c-Si layer and then start decreasing again linearly with the affinity. The simulated result shows that the best optimized value of efficiency is achieved probably somewhere at the middle value of affinity from its chosen range for carrying this simulation. The best optimized value of affinity is found to be 4 eV.

**Keywords** AFORS-HET software · Si heterojunction solar cell · Diamane

---

Naima (✉) · P. K. Tyagi · V. Singh  
Department of Applied Physics, Delhi Technological University, New Delhi 110042, India  
e-mail: [naima\\_2k20phdap01@dtu.ac.in](mailto:naima_2k20phdap01@dtu.ac.in)



## 1 Introduction

Solar energy as the best source of energy proved in today's world to fulfill the need of energy in day-to-day life with a device called solar cell. Solar cell basically converts the light coming from sun into electrical energy. This device works on photovoltaic effect in which the incident photons get converted into the current with the help of p–n junction, and therefore, it is also called as photovoltaic device. From a long time, many researchers are working on the solar cells in order to make it more convenient for society in terms of its cost and reliability. For to do so, some points are really required to work upon such as improvement in the efficiency and making it with thin absorbing layer (crystalline silicon). Various 2D materials have been used so far in making of solar cells such as graphene, phosphorene, molybdenum di-selenide ( $\text{MoS}_2$ ) and tungsten di-selenide ( $\text{WSe}_2$ ), where these materials are used as transparent conducting oxide (TCO) and emitter layer [1–4]. Recently, it has also been reported to use a newly synthesized 2D carbon material called diamane (Dn) as an emitter layer in the silicon heterojunction solar cell, in which the conversion efficiency was found to increase up to 16.8% for silicon heterojunction solar cell [5]. Various parameters of different layers used in making solar cell have also been optimized earlier with the help of software AFORS-HET version 2.5. This work motivated us to make a solar cell structure by using diamane as emitter layer and to check the validation of work carried out by optimizing the electron affinity of commercially available c-Si layer and then comparing it with the optimization of electron affinity of optimized silicon layer.

## 2 Designed Structure

The structure designed in order to do the required simulation is as follows: ITO (TCO)/n-Dn/p-type c-Si/Ag (back contact) as shown in Fig. 1 [5]. Here, indium tin oxide (ITO) is chosen as transparent conducting oxide (TCO) which basically transmits the light to the emitter layer. Diamane is taken as an emitter layer in the structure which extracts the electron/hole at the junction. A p–n junction is formed at the interface of emitter layer (n-type diamane) and the absorbing layer (p-type c-Si). The back contact is made up of silver (Ag) which basically reflects the carriers to the interface. A drift–diffusion interface is chosen at the n-Dn/p-type c-Si interface. M-S Schottky interface is chosen at the front as well as back interfaces. The optical parameters of ITO, Ag as well as silicon are taken from the software itself, whereas the optical parameters ( $n$ ,  $k$ ) for diamane layer are taken from the available literature [6]. Appropriate defects have also been set in the software during optimization, and the whole simulation is conducted out under Air Mass 1.5 Global, 10 nm spectral width and 100 mW/cm<sup>2</sup> power supply. Other simulation details are given in Table 1 [5].

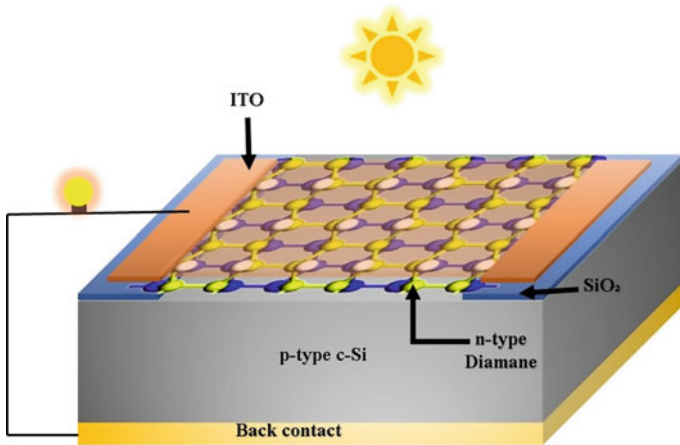


**Fig. 1** Schematic diagram of the structure of silicon heterojunction solar cell designed [5]

**Table 1** Details of the front and back contacts [5]

Variables	Front surface	Back surface
Material	ITO	Ag
Width (m)	$8 \times 10^{-8}$	$1 \times 10^{-4}$
File	Default	Default
Metal work function	Flat band	Flat band
Absorption loss	ITO. Abs	0
External reflection constant	0	0.05
Surface condition	Plane	Plane
Internal reflection constant	0	0

### 3 Results and Discussion

In this section, we have optimized the electron affinity of p-type c-Si layer in the range 3.6–4.5 eV, where the remaining values of parameters of p-type c-Si layer have been taken from the literature for practically available crystalline-silicon layer [1–5]. The results obtained while doing the simulation are shown in Fig. 2. From Fig. 2, it is observed that as the affinity increases from 3.6 to 4.5 eV,  $V_{OC}$  decreases from 593 to 591.4 mV. Similarly,  $J_{SC}$  also decrease from 21.87 to 21.51 mA/cm<sup>2</sup> linearly. On the other hand, fill factor and efficiency first increase with affinity from 3.6 eV to 4 eV and then start decreasing from 81.05% to 80.94% and 10.41% to 10.3%, respectively. This is because the affinity contrasted the work function of the layer, and therefore, as the affinity increases, the rate of carrier transport reduces consequently, the series resistance of the p-type c-Si layer as well as the cell increases. Therefore, after 4 eV the overall efficiency gets noticed to fall off from Fig. 2. The behavior observed in our

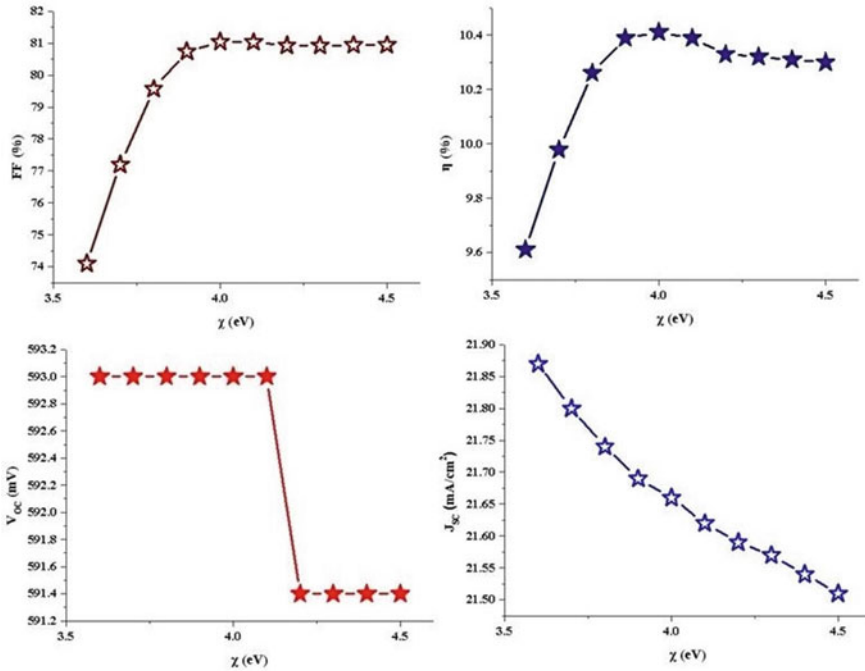


**Fig. 2** Optimization of electron affinity of commercially available crystalline-silicon layer where,  $\mu_n = 1500 \text{ cm}^2/\text{Vs}$ ,  $\mu_p = 500 \text{ cm}^2/\text{Vs}$ , @ p-type c-Si thickness =  $100 \mu\text{m}$

report is approximately same as observed while not using the practically available values [5]. This type of behavior shows that our results are in accordance with the commercially available solar cell.

### 4 Conclusion

In this report, we have simulated the silicon heterojunction solar cell designed as ITO/n-Dn/p-type c-Si/Ag with the help of AFORS-HET software v2.5. Here, ITO is considered as transparent conducting electrode (TCE) which works as an anti-reflector and also helps in generation as well as transportation of charge carriers. We found that the efficiency of the solar cell gets enhanced after optimizing the electron affinity of commercially available p-type c-Si layer which is also same for theoretical p-type c-Si layer. We have optimized the affinity of commercially available silicon layer, and an efficiency of 10.41% is found that is much toward the theoretical efficiency achieved, i.e., 16.84%. The whole work suggested that affinity of the absorbing layer independently plays an important role in c-Si solar cells.

**Acknowledgements** The authors are grateful to Delhi Technological University for the monetary sustenance and also the authors ascribed Helmholtz-Zentrum Berlin who endowed the AFORS-HET software.

## References

1. Patel K, Tyagi PK (2017) P-type multilayer graphene as a highly efficient transparent conducting electrode in silicon heterojunction solar cells. *Carbon* 116:744–752
2. Chaudhary R, Patel K, Sinha R, Kumar S, Tyagi PK (2016) Potential application of mono/bi-layer molybdenum disulfide ( $\text{MoS}_2$ ) sheet as an efficient transparent conducting electrode in silicon heterojunction solar cells. *J Appl Phys* 120:013104
3. Tiwari P, Patel K, Krishnia L, Kumari R, Tyagi PK (2017) Potential application of multi-layer n-type tungsten diselenide ( $\text{WSe}_2$ ) sheet as transparent conducting electrode in silicon heterojunction solar cell. *Comput Mater Sci* 136:102–108
4. Borah CK, Tyagi PK, Kuma S, Patel K (2018) Few-layer p-type phosphorene sheet: an efficient transparent conducting electrode in silicon heterojunction solar cell. *Comput Mater Sci* 151:65–72
5. Naima, Tyagi PK, Singh V (2022) N-type diamane: an effective emitter layer in crystalline silicon heterojunction solar cell. *Carbon Trends* 9:100209
6. Bouzidi S, Barhoumi M, Said M (2021) Optical properties of Janus and non-Janus diamane monolayers using ab-initio calculations. *Optik* 235:166642

# Theoretical Investigation by Density Functional Theory and Molecular Docking of a Naturally Occurring Anticancer Drug: 9-Hydroxyellipticine



Abhinav Mishra, Dipendra Sharma, and Sugriva Nath Tiwari

**Abstract** An organic heterotetracyclic compound 9-hydroxyellipticine is a natural product found in *Ochrosia elliptica* Labill. Its pharmacological properties are attributed to the intercalative binding into the successive base pairs of deoxyribonucleic acid helices. The present paper reports the physicochemical properties of the 9-hydroxyellipticine drug explored by DFT-B3LYP/6-311 G (d, p) process utilizing the Gaussian 16 package. HOMO–LUMO, MEP surface, and chemical reactivity descriptors have been examined. Further, molecular docking has been used to analyse inhibition activity along with binding sites of 9-hydroxyellipticine compound with three isomerase transcriptases (PDB ID: 1DID, 2YPI, and 1XIG).

**Keywords** Anticancer drug · DFT · Molecular docking

## 1 Introduction

Firstly obtained from leaves of several *Ochrosia* species in 1959, ellipticines are one of the most simple naturally occurring pyrido indole alkaloids having a plane geometry, which exhibits significant anti-HIV and antitumor activities [1–3]. Ellipticine and several of its derivatives yield promising results in treating kidney cancer, acute myeloblastic leukemia, osteolytic breast cancer metastases, and brain tumors [4]. The potent antitumor activity of ellipticines attracted many researchers toward their synthesis, pharmacological properties, and mechanism of drug action [5, 6]. Due to toxicity of ellipticine drug and related different type of side effects incited efforts devoted toward improving the pharmacological profile of the compound. Thus, in vivo hydroxylation of ellipticine led to a strong metabolite, 9-hydroxyellipticine. As compared to ellipticine, hydroxylated derivative is found to be more active but less toxic. Again, quaternization of its pyrido nitrogen provides the 9-hydroxy-2-methylellipticinium ion having better water solubility with no significant loss of

---

A. Mishra (✉) · D. Sharma · S. N. Tiwari  
Department of Physics, D.D.U. Gorakhpur University, Gorakhpur 273009, India  
e-mail: [abhinav.phy94@gmail.com](mailto:abhinav.phy94@gmail.com)

pharmacological activity. Ellipticine-caused DNA splitting seems to result due to rise of the cleavage formed rate in the ternary complex against inhibition of the relegation process [3].

The present paper embodies in silico analysis of the physicochemical along with electronic properties, MEP surface, HUMO, and LUMO energy of 9-hydroxyellipticine using ab initio DFT method. Further, molecular docking has been used for deciphering the pharmacological properties of the drug.

## 2 Computational Methods

Density functional theory (DFT) with functional Becke 3 Lee Yang Parr (B3LYP) and 6-311 G (d, p) basis set, as incorporated in Gaussian 16W package was used for optimizing 9-hydroxyellipticine drug [7]. Visualized on GaussView 6.0 software, optimized geometry of 9-hydroxyellipticine has been used to obtain its molecular geometrical parameters, frontier molecular orbitals, MEP surface, and global reactivity descriptors [8]. Further, molecular docking simulation of the drug with three isomerase transcriptases has been performed by SwissDock web server and visualized on UCSF Chimera software [9, 10].

## 3 Results and Discussion

### 3.1 Molecular Structure and Global Reactivity Descriptors Analysis

The DFT-optimized 9-hydroxyellipticine molecular structure is exhibited in Fig. 1. Evidently C–C, C–N, and C–H bond lengths of drug molecule range from 1.369 to 1.509 Å, 1.314 to 1.389 Å, and 1.081 to 1.096 Å, respectively. The calculated electronic properties and parameters describing global reactivity of 9-hydroxyellipticine drug are shown in Table 1. The MEP surface signifies the shape and size of 9-hydroxyellipticine drug. As depicted in MEP surface, the intense electronegative region is created by oxygen atom, and hence, it becomes more prone for electrophilic attack (Fig. 2). Electron donating and electron accepting ability are characterized by the HOMO and LUMO energy of a compound, while their chemical reactivity is estimated by the difference between them. For the 9-hydroxyellipticine, LUMO–HOMO energy gap comes out to be 3.633 eV, which makes it chemically more stable and suitable for electro-optic applications. Moderate value of LUMO–HOMO energy gap indicates the eventual occurrence of interactions due to transfer of charge within the 9-hydroxyellipticine drug. The HOMO–LUMO surfaces of the 9-hydroxyellipticine drug are depicted in Fig. 3. Here, chemical reactivity depends on the structural arrangement of the molecule. The formulae related to global reactivity descriptors

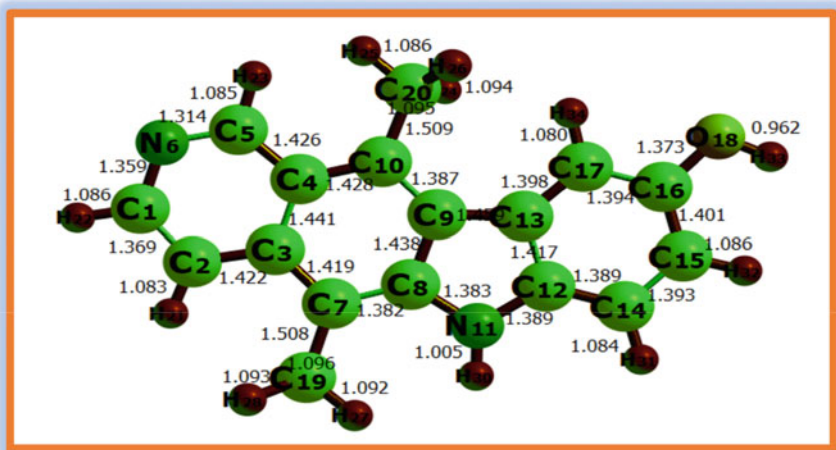


**Fig. 1** Molecular geometry of 9-hydroxyellipticine drug optimized by DFT-B3LYP/6-311 G (d, p) method

can be found in the literature [11–13]. Amount of energy essential to take out an electron of the molecule is defined as ionization potential (IP). Its high value signifies better stability and therefore leads to chemical inertness, whereas lower value of ionization energy implies that atoms or molecules inherit better reactivity. The ionization potential of 9-hydroxyellipticine is found to be 5.268 eV making it a good donor. When addition of an electron to a neutral molecule is done, the released energy is known as electron affinity. Table 1 evidences that the ellipticine drug is moderately reactive ( $EA = 1.635$  eV). Escaping tendency of an electron is estimated by its chemical potential, which comes out to be  $-4.269$  eV in this case. It is also associated with the electronegativity of the molecule. The extent of the stabilization of the system is obtained by electrophilicity index ( $\omega$ ), when electrons come from the environment to saturate the systems (atoms/molecules). A nucleophile, more reactive, good system is symbolized by a lower value of  $\omega$  and vice versa. For 9-hydroxyellipticine, electrophilicity index ( $\omega = 5.015$  eV) is selectively lower, and therefore, it is a good nucleophile [11].

## 4 Molecular Docking

Molecular docking is employed to investigate drug interaction with receptors and subsequently to determine the drug's effectiveness. Docking is therefore very important in the field of drug design [12, 13]. In this procedure, the energy associated with each conceivable configuration of the ligand is calculated. The full fitness (FF) score is then used to order the top binding modalities. The entire docking method carried out

**Table 1** Electronic and global reactivity descriptor parameters of 9-hydroxyellipticine drug

Total energy	– 22,889.846 eV
Dipole moment	5.561 Debye
HOMO energy	– 5.268 eV
LUMO energy	– 1.635 eV
Frontier orbital energy gap	3.633 eV
Chemical potential ( $\mu$ )	– 4.269 eV
Electronegativity ( $\chi$ )	4.269 eV
Electron affinity (EA)	1.635 eV
Ionization potential ( $I$ )	5.268 eV
Global hardness ( $\eta$ )	1.817 eV
Global softness ( $S$ )	0.275 eV <sup>-1</sup>
Global electrophilicity ( $\omega$ )	5.015 eV

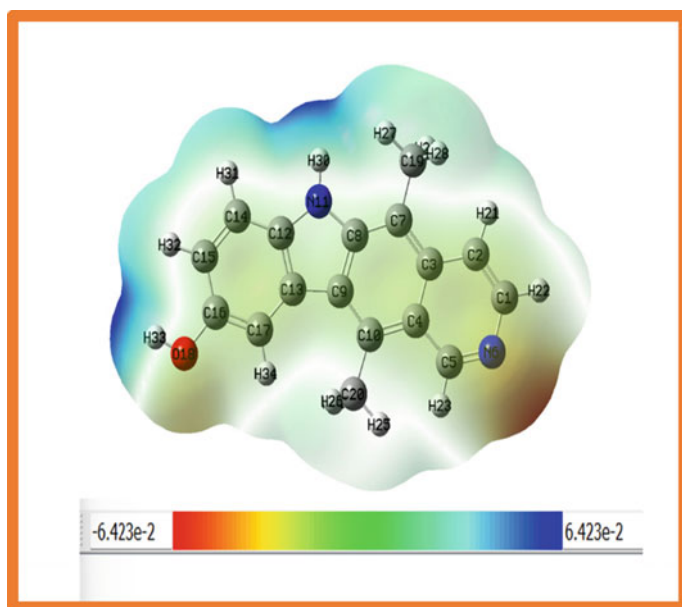


**Fig. 2** MEP surface of 9-hydroxyellipticine drug

by SwissDock is blind folded to prevent sampling bias by enveloping the complete receptor molecule and not assigning any particular area of the protein receptor as the binding pocket. Here, three protein receptors (PDB IDs: 1DID, 2YPI, and 1XIG) have been chosen to find suitable binding poses of protein–ligand complexes. The first protein receptor 1DID has many strong binding affinities with the drug. Depicted in Fig. 4a, the best pose of the protein–ligand complex corresponds to binding between protein residue ARG (67) and drug LIG (H10) with energy of – 4.91 kcal/mol



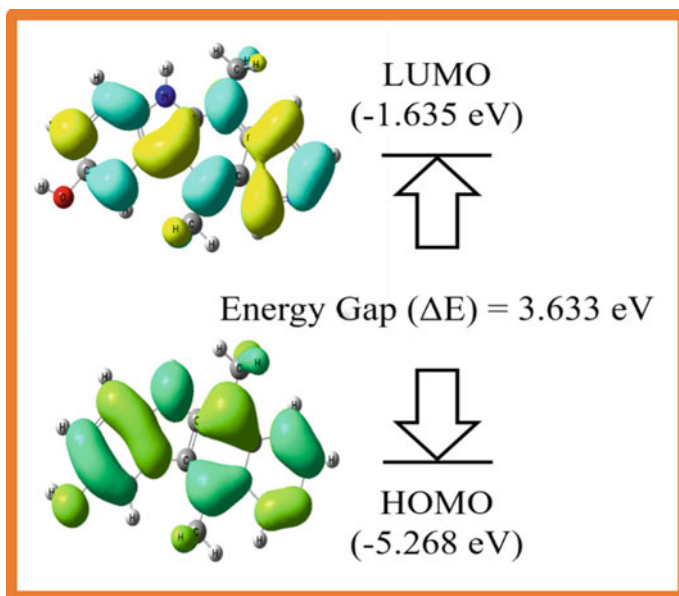


**Fig. 3** Frontier orbitals of 9-hydroxyellipticine drug

at the distance of  $2.214 \text{ \AA}$  having FF score of  $-1917.04 \text{ kcal/mol}$ . The second receptor 2YPI elicits its stable binding poses with the drug. The protein residue ARG (3) makes a stable binding complex with LIG (H13) having binding energy of  $-4.90 \text{ kcal/mol}$  (FF score =  $-2403.16 \text{ kcal/mol}$ ) at a distance of  $3.044 \text{ \AA}$ . The third protein receptor 1XIG forms a stable complex between the receptor GLY (197) and LIG (H11) with energy of  $-4.93 \text{ kcal/mol}$  at a separation of  $3.690 \text{ \AA}$  and FF score of  $-2168.29 \text{ kcal/mol}$ . These docking results suggest that 9-hydroxyellipticine drug elicits good binding affinity for 2YPI receptor as compared to 1DID and 1XIG protein receptors [14].

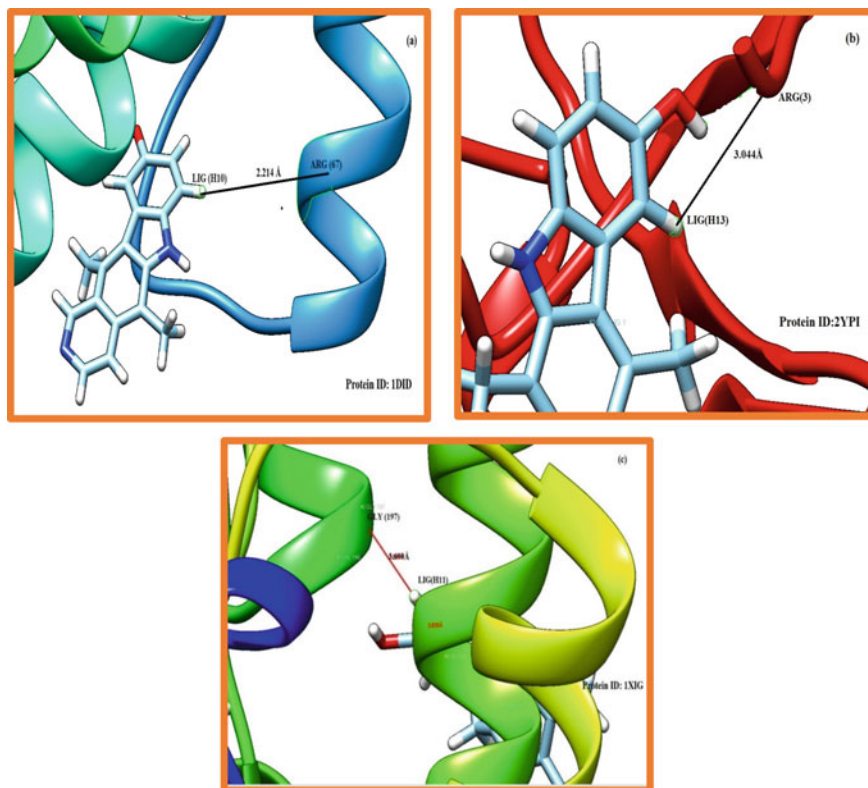


**Fig. 4** Molecular docking of ligand (9-hydroxyellipticine drug) with protein receptors

## 5 Conclusion

The optimized geometrical parameters nearly conform to the standard data. Frontier orbitals with molecular electrostatic potential surfaces suffice visualization of chemical reactivity as well as charge transfer in the drug molecule. Because of the higher electronegativity, 9-hydroxyellipticine is capable of attracting more shared electrons. Molecular docking vividly elucidates the most stable bindings of 9-hydroxyellipticine with the 2YPI receptor as compared to other two (1DID and 1XIG) protein receptors; hence, the drug activity of the 9-hydroxyellipticine may be attributed to this molecular docked complex.

**Acknowledgements** D. Sharma is thankful to UGC, New Delhi, India, for providing Start-Up grant [F.30-505/2020(BSR)].

## References

1. Goodwin S, Smith AF, Horning EC (1959) Alkaloids of *Ochrosia elliptica* Labill. J Am Chem Soc 81(8):1903–1908
2. Auclair C (1987) Multimodal action of antitumor agents on DNA: the ellipticine series. Arch Biochem Biophys 259(1):1–14
3. Pecq LBJ, Xuong ND, Gosse C, Paoletti C (1974) A new antitumoral agent: 9-hydroxyellipticine possibility of a rational design of anticancerous drugs in the series of DNA intercalating drugs. Proc Natl Acad Sci USA 71(12):5078–5082
4. Garbett NC, Graves DE (2004) Extending nature's leads: the anticancer agent ellipticine. Curr Med Chem Anticancer Agents 4(2):149–172
5. Miller CM, O'Sullivan EC, McCarthy FO (2019) Novel 11-substituted ellipticines as potent anticancer agents with divergent activity against cancer cells. Pharmaceuticals 12(2):90
6. Sanyal NK, Roychoudhury M, Tiwari SN (1985) Quantum mechanical studies on the activity of anticancerous drug—ellipticine. J Biosci 8:713–720
7. Frisch JM et al (2016) Gaussian 16, revision C.01. Gaussian Inc., Wallingford, CT
8. Dennington R, Keith TA, Millam JM (2016) GaussView version 6.1. Semichem Inc., Shawnee Mission, KS
9. Grosdidier A, Zoete V, Michielin O (2011) SwissDock a protein-small molecular docking web service based on EADock DSS. Nucleic Acids Res 39:270–277
10. Pettersen EF, Goddard TD, Huang CC, Couch GS (2004) UCSF Chimera—a visualization system for exploratory research and analysis. J Comput Chem 25(13):1605–1612
11. Tiwari G, Srivastava AK, Kumar R, Kumar A (2019) Quantum chemical and molecular docking studies on two potential hepatitis C virus inhibitors. Main Group Chem 18(2):107–121
12. Tiwari A, Palepu J, Choudhury A, Bhattacharya S, Kanungo S (2022) Theoretical analysis of the NH<sub>3</sub>, NO and NO<sub>2</sub> adsorption on boron-nitrogen and boron-phosphorous co-doped monolayer graphene—a comparative study. FlatChem 34(4)
13. Tiwari G, Chauhan MS, Sharma D (2022) Systematic in silico studies of corticosteroids and its binding affinities with glucocorticoid receptor for covid-19 treatment: ab-initio, molecular docking and MD simulation studies. Polycycl Aromat Compd 43(3):1–16
14. <https://www.rcsb.org/structure/1DID>; <https://www.rcsb.org/structure/2YPI>; <https://www.rcsb.org/structure/1XIG>. Accessed 2022/12/05

# Antimicrobial and Antibiofilm Activity of Silver Nanoparticles Derived from *Prolinoborus fasciculus* Against Multi-drug-resistant *K. pneumoniae* and *E. faecium*, Isolated from Effluent Samples



Kunal Madhav and Archana Pandita

**Abstract** In this investigation, different drug-resistant biofilm-producing bacteria were isolated from effluent samples for the assessment of the antimicrobial and antibiofilm activities of silver nanoparticles, BNP, produced from the cellular extract of a bacterial isolate obtained from soil, *Prolinoborus fasciculus*. 10 samples of effluent were taken in Greater Noida from diverse sources. For isolating effluent pathogens, the samples were serially diluted and plated on Nutrient Agar Media followed by incubation. Pathogens thus obtained were characterized by MALDI-TOF. The isolated pathogens were subsequently treated with the greenly produced *P. fasciculus* silver nanoparticles (BNPs), which were evaluated for their antibacterial efficacy and were characterized by UV–visible spectroscopic properties using XRD, FTIR, TEM, and Zeta Potential. BNPs, (concentration 50  $\mu\text{g/ml}$ ), were added in volumes ranging from 10 to 50  $\mu\text{l}$  to each well of the pathogen-containing plates to assess the antimicrobial activity. It was observed that *Enterococcus faecium* was more sensitive to the BNPs as compared to *Klebsiella pneumoniae*. Also, the antibiofilm activity of BNPs against *E. faecium* and *K. pneumoniae* biofilm, showed 59 and 60%, demonstrating their potent antibiofilm capabilities. According to the results of the current study, there are numerous drug-resistant infections that produce a biofilm that can be dealt with using green-produced BNPs as an alternative method.

**Keywords** Effluent waste · Antimicrobial activity · Green synthesis

---

K. Madhav · A. Pandita (✉)

Department of Biotechnology, Sharda University, Greater Noida 201310, India

e-mail: [archana.pandita@sharda.ac.in](mailto:archana.pandita@sharda.ac.in)

K. Madhav

Department of Microbiology, I.T.S. Dental College, Hospital and Research Centre, Greater Noida 201310, India

## 1 Introduction

One of the major international issues that must be addressed is the presence and prevalence of MDR microorganisms. Water is one of the most significant natural resources used by all living things on this world. Water pollution from effluent drainage has increased the number of pathogenic strains with MDR origin, which has resulted in several diseases in humans that are incurable [1–3]. Pathogenic bacteria like *Klebsiella pneumoniae* [4] and *Enterococcus faecium* [5, 6] make up the vast bulk of these pathogens. The creation of biofilms is one of several elements that contribute to the nature of the bacteria's drug resistance [7, 8]. Because of their MDR character, these organisms can produce infections that are difficult to treat, necessitating the urgent need for a different approach [9].

In the current work, bacteria that were isolated from a soil sample and cultured in broth culture were used to make silver nanoparticles. The multi-drug-resistant bacteria *K. pneumoniae* and *E. faecium* spp., which were isolated from effluent samples, were evaluated against the bacterial silver nanoparticles, which were made by reducing the 1 mM of AgNO<sub>3</sub> in the culture's supernatant.

### 1.1 Methodology

**Sample collection, processing, and isolation of effluent pathogens:** To isolate the pathogens, wastewater samples from industrial sites close to Gautam Buddha Nagar in Greater Noida were collected. Following collection, the effluent was diluted from 10<sup>-1</sup> to 10<sup>-5</sup>, and 100 μl from each dilution was then dispersed on Nutrient Agar Plates before being incubated at 37 °C. We selected the dilution plates with the fewest colonies for further processing and identification. The MALDI-TOF technique was then used to test the resultant isolates for identification.

**Identification of effluent pathogens by MALDI-TOF:** The standard solvent was mixed, and then the HCCA was dissolved before the concoction was vortexed at 25 °C until it was clear. The target MALDI plate with the HCCA solution on top, was covered with the isolated effluent sample bacteria. It was then dried at room temperature and placed into the AUTOFLEX speed for analysis after creating a separate well with 1 l of bacterial standard and matrix (Bruker Daltonik GmbH, Germany). The result that was thus obtained was examined using the MALDI Biotyper software 3.0.

**Assessment of the drug resistance amongst the effluent pathogens:** By using the Kirby Bauer Disc diffusion method, the pathogens that were isolated from the diluted effluent samples were exposed to a variety of antibiotics to determine their drug sensitivity and resistance patterns. Pathogens were classed as MDR and subsequently screened against silver nanoparticles if they were discovered to be resistant to three or more families of antibiotics.

**Isolation and identification of *Prolinoborus fasciculus* from soil sample:** 1 g of soil was serially diluted, out of which 100  $\mu$ l was spread on nutrient agar plates and incubated at 37 °C for 24 h. Those dilution plates that had the fewest colonies were chosen for additional processing and identification. The resulting isolates were identified using the 16S rRNA method for bacterial identification.

**Identification of *Prolinoborus* spp. by 16S rRNA technique:** The pure culture's genomic DNA was extracted using the ZR Fungal/Bacterial DNA MiniPrep kit (Make Zymo Research). Using the universal primers 27F (AGAGTTTGATCCTGGCTCAG) and 1492R, the 16S rRNA gene was amplified by PCR (TACGGYTACCTTGTTACGACTT). It was possible to see the PCR product on a 1% Agarose gel. The QIAquick Gel Extraction Kit was used to remove the PCR amplicon from the gel (Make Qiagen). The Sanger DNA sequencing method was used to sequence the purified PCR product. The Finch TV program version 1.4 was used to analyze and present the acquired sequences. The NCBI's BLAST tool and the EzBiocloud portal (<http://www.ezbiocloud.net/>) were used to compare the nucleotide sequences from the 16S rRNA gene assembly. The outcomes were subjected to an evolutionary maximum likelihood analysis using MEGA 11 software.

**Biosynthesis and characterization of silver nanoparticles:** Bacterium isolated from the soil sample was inoculated aseptically in 100 ml of nutrient broth and incubated at 37 °C for 72 h in shaking incubator set with 120 rpm. Post incubation, the bacterial sample was centrifuged at 12,000 rpm for 20 min. The supernatant thus obtained was used for the biosynthesis of silver nanoparticles (BNPs). 10 ml of the supernatant was mixed with 90 ml of 1 mM of AgNO<sub>3</sub> solution which was prepared by dissolving 0.0169 g of AgNO<sub>3</sub> in double autoclaved sterile distilled water. The prepared solution was then incubated under dark conditions at room temperature to prevent the photoactivity of the silver nanoparticles for 24 h. The prepared nanoparticles were labeled as BNPs and were further screened for their morphological and molecular characteristics by UV–Visible Spectroscopy, XRD, DLS, and TEM.

**Antibacterial and antibiofilm activity of silver nanoparticles against the effluent pathogens:** By using the well diffusion approach, effluent pathogens that were discovered to have MDR characteristics were tested against the BNPs. The pathogens were raised in sterile Brain Heart Infusion Broth before spending the night in the incubator at 37 °C. Following this, 100 l of the newly formed growth was swabbed onto sterile MHA or Muller Hinton Agar plates, and wells were drilled using a well borer. The well was then filled with 50 l of the BNPs and incubated for 24 h at 37 °C after that.

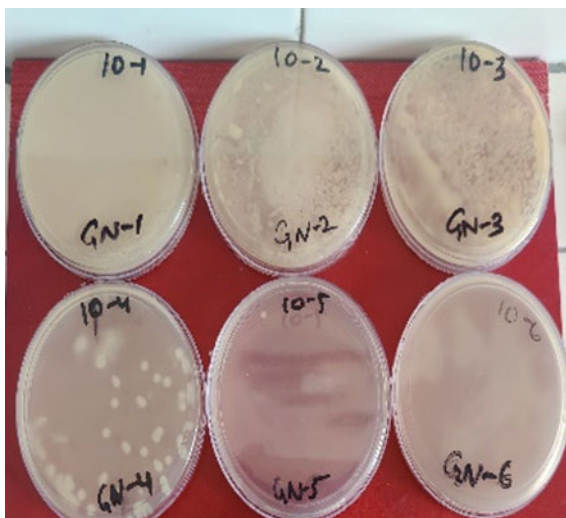
## 2 Result and Discussion

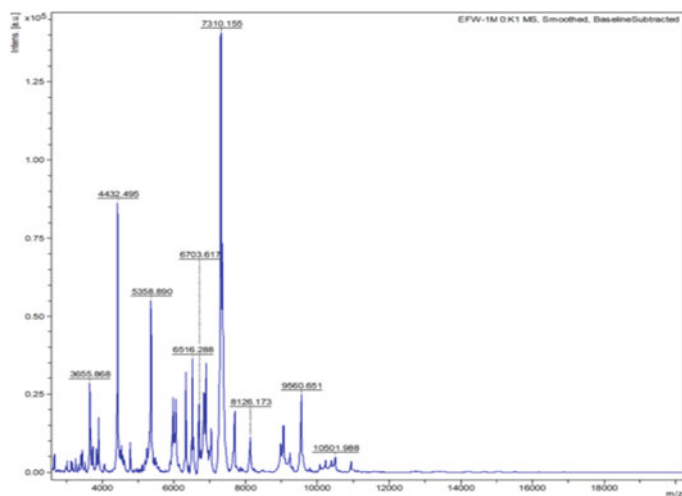
**Isolation and identification of effluent pathogens:** The pathogen isolated from plates 10-4 and 10-5 with the highest dilution was chosen for identification using MADLI-TOF, the results of which are shown in Fig. 1a. A strain's 1.7 log values with a strain in the database were used to interpret the results for the identification of the effluent pathogens, and value 2.0 were used to interpret the results as a member of the species. The effluent pathogens were identified as *E. faecium* and *K. pneumoniae* based on the score values, and their respective scores were 2.189 and 2.09, as shown in Fig. 2a, b, respectively.

**Analysis of the evolutionary pattern of *Prolinoborus fasciculus* through the maximum likelihood method:** The evolutionary history of *Prolinoborus fasciculus* was analyzed by Kimura 2-parameter model and the Maximum Likelihood technique. The analysis of the result is done by the determination of the tree, which describes the log probability ( $-1949.00$ ) and branches that displays taxa (Fig. 3). Automatic application of the Neighbor-Join and BioNJ algorithms to a matrix of pairwise distances calculated using the Maximum Composite Likelihood (MCL) approach, and then choosing the topology with the best log likelihood value, the initial tree(s) for the heuristic search were created. The branch lengths divided by the average number of substitutions per site determines the tree's scale. This investigation concentrated on six distinct nucleotide sequences, which included the first, second, third, and non-coding codon positions. The final datasets were analyzed on MEGA 11 software, where the total number of sites was found to be 1389.

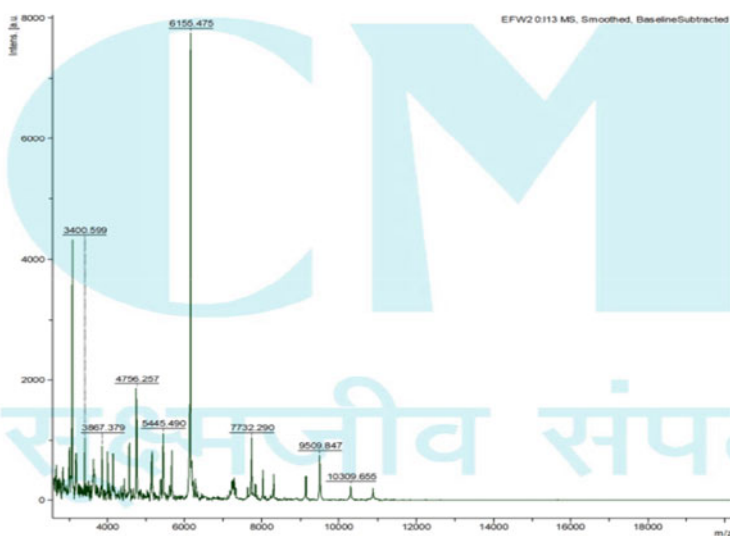
**Characterization of the biosynthesized nanoparticles:** The resulting nanoparticles underwent morphological and molecular characterization. With the XRD pattern at

**Fig. 1** Isolation of effluent pathogens on Nutrient Agar Media





(a)



(b)

**Fig. 2** **a** MALDI-TOF report of *E. faecium*. **b** MALDI-TOF report of *K. pneumoniae*

the 2 of  $38.0^\circ$  (1 1 1),  $44.2^\circ$  (2 0 0),  $64.4^\circ$  (2 2 0), and  $77.3^\circ$  (3 1 1) showing the crystalline nature of the BNPs, the surface plasmon resonance was identified at 422.5 nm (Fig. 4a, b). According to Fig. 4c, d, the BNPs' Zeta Potential and Zeta Size were discovered to be  $-19.7$  mV and 95.75 nm, respectively. The PDI value of 0.572 indicated the monodisperse nature of the BNPs. The presence of spherical silver nanoparticles was also shown by TEM investigation of the BNP, and the mean



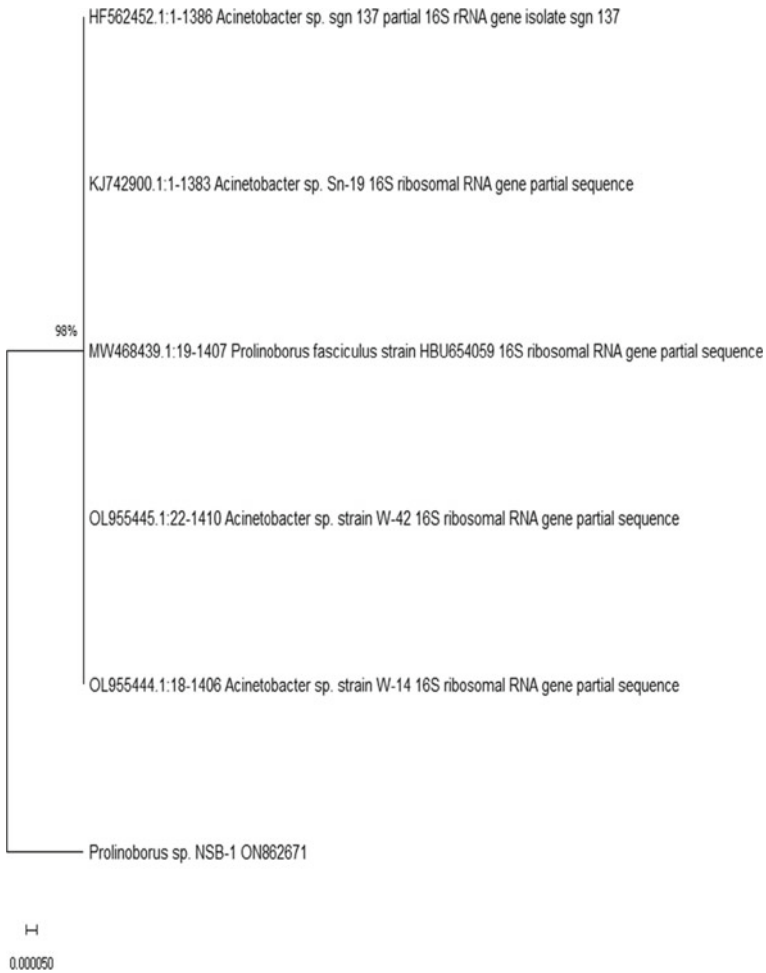


**Fig. 3** Evolutionary analysis of *Prolinoborus fasciculus*

diameter of the produced nanoparticles was shown to be approximately 19.02 nm, as shown in Fig. 4e.

**Antibacterial and antibiofilm activity of the silver nanoparticles:** By using the well diffusion method on the multi-drug-resistant effluent pathogens *E. faecium* and *K. pneumoniae*, BNP's antibacterial activity was evaluated. Measurements were made against each of the bacterial pathogens in the zones of each well containing 10–50  $\mu$ l of BNP at a concentration of 50  $\mu$ g/ml; more information is presented in Fig. 5a, b. *E. faecium* was found to be most susceptible to the BNP as compared to *K. pneumoniae*.

By evaluating biofilm development of *E. faecium* and *K. pneumoniae* with a crystal violet microtiter plate assay, antibiofilm activity of BNP was assessed. Blank

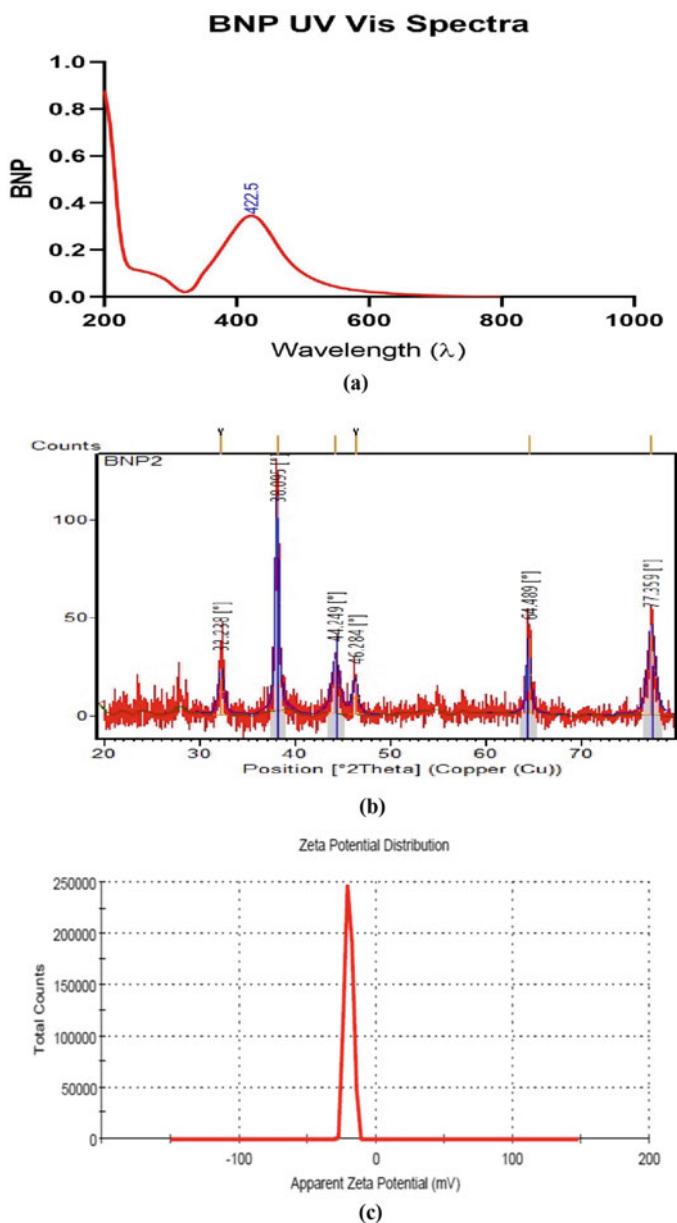
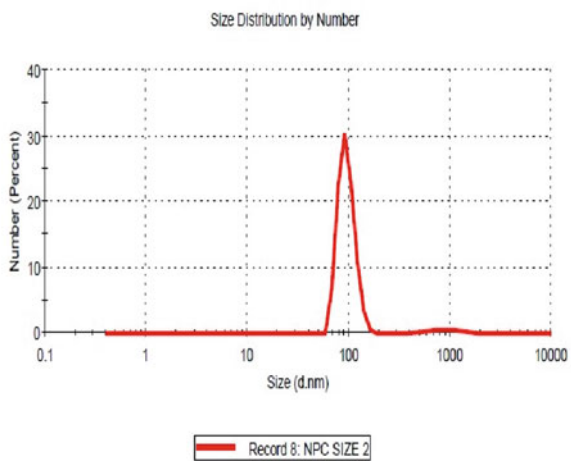
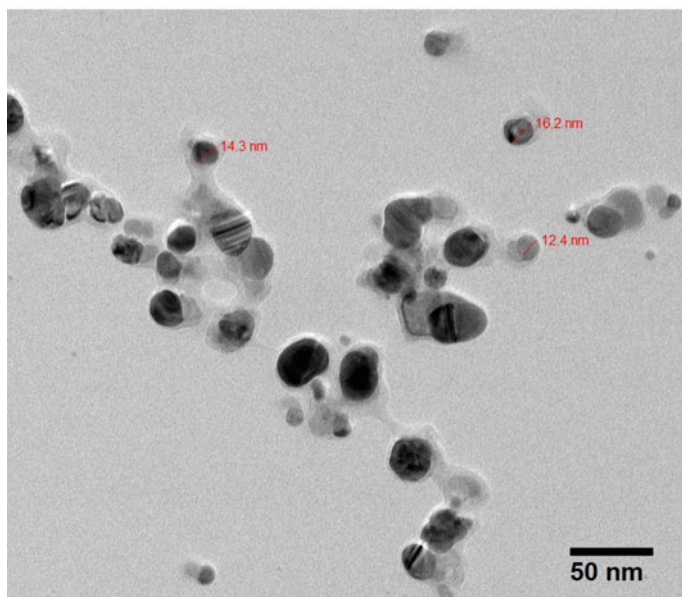


**Fig. 4** **a** BNP UV-Vis spectra. **b** XRD data of BNP. **c** Z potential = - 19.7 mV. **d** Zeta size = 95.75 nm. **e** TEM image of BNP



(d)



(e)

Fig. 4 (continued)



**Fig. 5 a, b** Antimicrobial activity of PSNP against effluent pathogens on MHA plate by well diffusion method. EF = *Enterococcus faecium* and KP = *Klebsiella pneumoniae*

consisting of nutrient broth along with bacteria served as the negative control while the test sample consisted of the same preparation with the addition of BNPs at the concentration of 50  $\mu\text{g/ml}$  by using the formula below was used to compute the percentage reduction in biofilm formation:

$$\text{Biofilm reduction \%} = \frac{(\text{Optical Density of Test})}{(\text{Optical Density of Blank})} \times 100$$

As per the data, shown in Fig. 6a, b, the BNP had a higher antibiofilm reduction capacity for *K. pneumoniae* (59.8%) and *E. faecium* (60.8%).

### 3 Summary and Conclusion

Water is an important natural source that is utilized by every living being on this planet, hence it is an essential commodity, care of which should be an utmost priority. In recent times due to the expulsion of various waste materials in water bodies, the prevalence of organic matter has increased several folds thereby increasing the number of pathogenic microorganisms. These pathogens become troublesome when they gain the property of resistance against various antibiotics, making the line of treatment difficult. Hence, to eliminate these pathogens, alternate methods are being looked for.

In the present study, we have attempted to analyze the antimicrobial and antibiofilm potential of the silver nanoparticles that were derived from a soil bacterium, *Prolinoborus fasciculus* (BNPs), against the multi-drug-resistant pathogens, *Enterococcus faecium* and *Klebsiella pneumoniae*, that were isolated from the water bodies contaminated with effluent waste. The experimental data revealed that the BNPs had a strong antimicrobial and antibiofilm activity on the

### Antibiofilm Activity of BNPs on MDR Effluent Pathogens

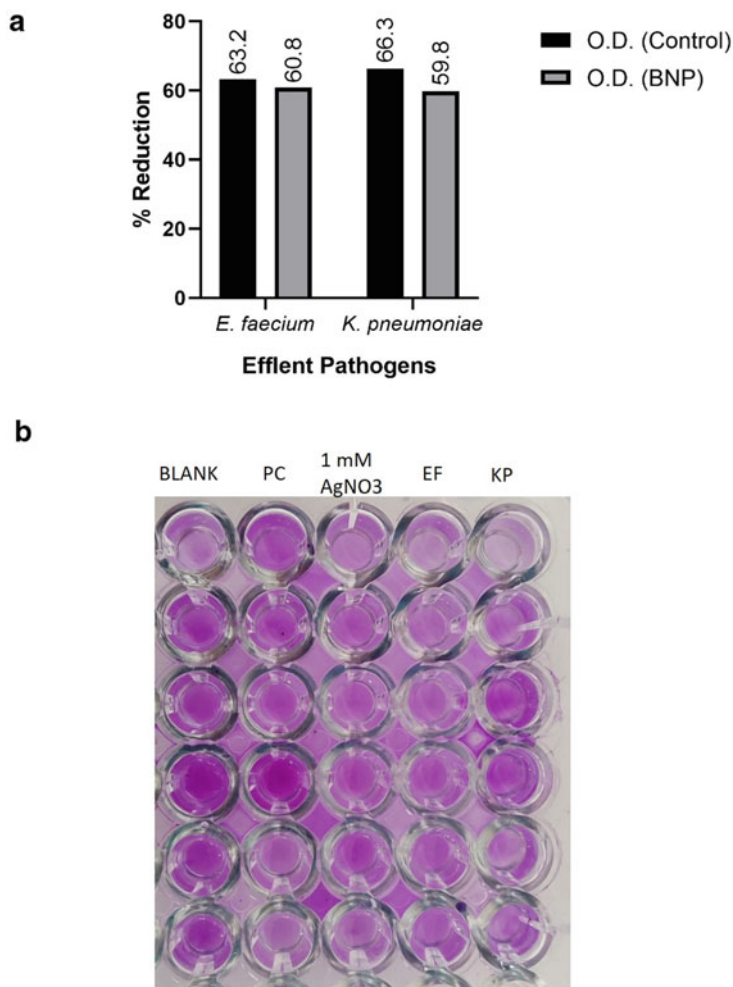


**Fig. 6** **a** Percentage reduction in biofilm formation of *Enterococcus faecium* and *Klebsiella pneumoniae* in presence of BNP. **b** Crystal violet assay for the detection of antibiofilm activity of BNPs

isolated pathogens and hence, can be used as an alternative to cure the ailments caused by these pathogens.

**Acknowledgements** The authors hereby acknowledge the significant contributions of research organizations AIIMS, Delhi IIT Delhi and NCMR, Pune for providing the facility of TEM, DLS, FTIR, XRD, and MALDI-TOF facilities. We are also grateful to Sharda University for providing the facility of UV-Vis spectrophotometer and to I.T.S. Dental College, Hospital and Research Center, Greater Noida, for permitting us to carry the microbiological experiments in their organization.

## References

1. Beheshti Maal K, Delfan AS, Salmanizadeh S (2015) Isolation and identification of two novel *Escherichia coli* bacteriophages and their application in wastewater treatment and coliform's phage therapy. *Jundishapur J Microbiol* 8(3)
2. Odjadjare EC, Olaniran AO (2015) Prevalence of antimicrobial-resistant and virulent *Salmonella* spp. in treated effluent and receiving aquatic milieu of wastewater treatment plants in Durban, South Africa. *Int J Environ Res Public Health* 12(8):9692–9713
3. Eze EC, El Zowalaty ME, Pillay M (2021) Antibiotic resistance and biofilm formation of *Acinetobacter baumannii* isolated from high-risk effluent water in tertiary hospitals in South Africa. *J Glob Antimicrob Resist* 27:82–90. <https://doi.org/10.1016/j.jgar.2021.08.004>
4. Siddiqui MK, Khatoon N, Roy PC (2016) Untreated liquid hospital waste: potential source of multidrug-resistant bacteria. *Bangladesh J Microbiol* 32(1):21–24
5. Pérez-Lazo G, Abarca-Salazar S, Lovón R, Rojas R, Ballena-López J, Morales-Moreno A et al (2021) Antibiotic consumption and its relationship with bacterial resistance profiles in ESKAPE pathogens in a Peruvian Hospital. *Antibiotics* 10(10)
6. Navidinia M (2016) The clinical importance of emerging ESKAPE pathogens in nosocomial infections. *J Paramed Sci* 7(3):43–57
7. Gurung J, Khyriem AB, Banik A, Lyngdoh WV, Choudhury B, Bhattacharyya P (2013) Association of biofilm production with multidrug resistance among clinical isolates of *Acinetobacter baumannii* and *Pseudomonas aeruginosa* from intensive care unit. *Indian J Crit Care Med* 17(4):214–218
8. Jiang Y, Geng M, Bai L (2020) Targeting biofilms therapy: current research strategies and development hurdles. *Microorganisms* 8(8):1–34
9. Song X, Liu P, Liu X, Wang Y, Wei H, Zhang J et al (2021) Dealing with MDR bacteria and biofilm in the post-antibiotic era: application of antimicrobial peptides-based nano-formulation. *Mater Sci Eng C* 128:112318. <https://doi.org/10.1016/j.msec.2021.112318>

# Design and Simulation of Pure CNTFET-OTA-Based Low-Pass Filters



Maryam Raza, Imran Ahmed Khan, and M. Nizamuddin

**Abstract** In this study, first-order, second-order, and third-order low-pass OTA-C filters are designed and simulated using operational transconductance amplifiers (OTAs) based on carbon nanotube field-effect transistors (CNTFETs). H-SPICE is used to simulate the suggested structures at 22 nm technology node using 0.9 V power supply. The suggested filters' fundamental characteristics, including frequency response, phase response, and average power dissipations, have all been studied. The designed structures have good low-pass filter performance at very low power dissipations and low voltage. The average power dissipation was found to be 0.1922 uW, 0.3840 uW, and 0.4152 uW for first order, second order, and third order, respectively.

**Keywords** Carbon nanotube field-effect transistor · Operational transconductance amplifier filter · Simulation · Power consumption · DC gain

## 1 Introduction

The operational transconductance amplifier is one of the most significant and popular analogue building blocks (OTA). The advantages and uses of this fresh group of OP-AMPs go beyond those of the traditional OP-AMP including some extra advantages and applications [1]. It has extra control terminals in addition to differential inputs, which expands the range of applications it can be used for. Large bandwidth, a broad dynamic range, the absence of surplus phase issues, adaptability and tunability, and the development of high-integration integrated circuits are further benefits of OTAs

---

M. Raza (✉) · I. A. Khan · M. Nizamuddin  
Department of Electronics and Communication Engineering, Faculty of Engineering and Technology, Jamia Millia Islamia, New Delhi, India  
e-mail: [maryam2008946@st.jmi.ac.in](mailto:maryam2008946@st.jmi.ac.in)

I. A. Khan  
e-mail: [iakhan2@jmi.ac.in](mailto:iakhan2@jmi.ac.in)

M. Nizamuddin  
e-mail: [mnizamuddin1@jmi.ac.in](mailto:mnizamuddin1@jmi.ac.in)

[1]. Low power and excellent performance have been made possible by CMOS-based OTA, but the era of CMOS is coming to an end. Short-channel effects and other reliability difficulties make future MOSFET scaling below 60 nm challenging [1]. Hence, there is an immediate need for devices and materials better than silicon to continue the order of scaling down the chip area for high-performance applications. Thus, the widespread use of silicon is expected to be replaced with CNT, which is seen as a promising material. Filters consistently reject undesirable noise and interference while maintaining the desired signal. Unless appropriately filtered, real-world signals, in particular biological signals, are frequently affected by unwanted noise, interference, and artefacts. These signals frequently overlap the frequency spectra of the desired signal. This makes the process of biomedical filtration challenging [2]. We can use analogue or digital filters to accomplish this purpose. The fundamental component of analogue active filters (OTA) is an operational amplifier (OPamp) or operational transconductance amplifier (OTA) [2]. OTA-C filters provide a wide frequency range for the proper filter cutoff frequencies among the many active filter types. Numerous biomedical signal processing applications use the OTA-C filters. Electrocardiograms (ECG) [3], bionic ears [4], neural recording interfaces [5], and electroencephalograms (EEG) [5] are a few examples. Researchers have developed many CNTFET-based circuits [6, 7]. We suggest OTA-C filter designs based on CNTFET-OTA in this paper.

## 2 CNTFET

CNTFET is a prospective technology that could be used to improve Moore's law's reliability and stand in contrast to the currently used silicon technology [8, 9]. A CNTFET can be easily devised by swapping the channel of a traditional bulk MOSFET with a parallel sequence of single-walled carbon nanotubes (SWCNTs) as shown in Fig. 1. A SWCNT can be conducting or semiconducting depending upon a vector known as the chirality vector. The following equation can be used to predict the gate's width [8], where  $N$  is the number of the nanotubes under the gate and  $W_{\min}$  is the minimum width of the gate. The number of CNTs ( $N$ ), inter-CNT pitch ( $S$ ), diameter of CNT ( $D_{\text{CNT}}$ ), and bandgap of CNTs ( $E_g$ ) have a powerful impression on the behaviour of CNTFET. These specifications can be altered to improve the capabilities of a CNTFET. These parameters are related by the following equations [10, 11]:

$$W = (N - 1) * S + D_{\text{CNT}}, \quad (1)$$

$$E_g = 0.84 \text{ eV} / D_{\text{CNT}}, \quad (2)$$

$$W_{\text{gate}} \approx \text{Min}(W_{\min}, N \text{ Pitch}) [9]. \quad (3)$$



**Fig. 1** Carbon nanotube field-effect transistor [10]

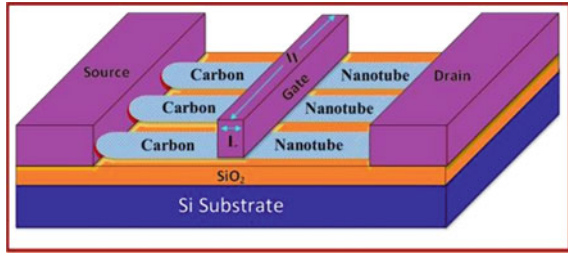
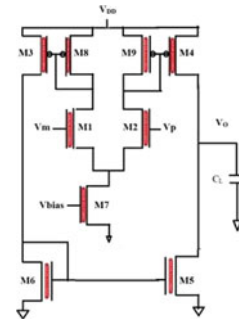


**Fig. 2** Pure CNTFET-OTA [6]



### 3 Operational Transconductance Amplifier (OTA)

The transconductor (OTA) is depicted in Fig. 2 and is implemented using N-type CNTFETs and P-type CNTFETs for the OTA-C filters. In order to model the actual OTA-C filters, we use the Synopsis H-SPIICE circuit simulation programme. Stanford University’s small spice model is used in CNFET devices. The transconductor’s output current expression is provided by:

$$I_{out} = g_m(V_p - V_m), \tag{4}$$

where  $g_m$  stands for the transconductance of the OTA (Fig. 2).

### 4 Active Filters

The fundamental component of OTA-C filters is OTAs. With a straightforward method, OTA-C filters can be tuned for a certain frequency by changing the OTA transconductance or by choosing the appropriate capacitor values and are more suited for on-chip integration [6]. When developing active filters, the OTA-C filter, which uses the fewest OTAs and capacitors possible, is an effective technique that offers greater flexibility in terms of gain and pass band width than modern active filters [10].

### 5 Results and Discussion

The carbon nanotube field-effect transistor (CNTFET) is used to create the OTA circuit, which is then simulated using H-Spice. The CNTFET-based OTA circuit is used to create the proposed first-order, second-order, and third-order low-pass filter circuits, which are then simulated using H-Spice (Figs. 3, 4, and 5).

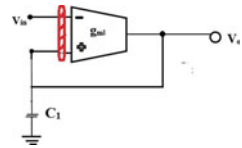
$$V_o/V_{in} = g_m/(SC + g_m), \tag{5}$$

$$V_o/V_{in} = g_{m1}g_{m2}/(S^2C_1C_2 + SC_1g_{m2} + g_{m1}g_{m2}), \tag{6}$$

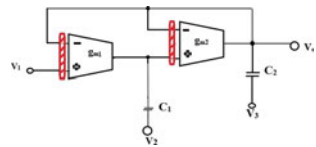
$$V_o/V_{in} = g_{m1}g_{m2}g_{m3}/S^3C_1C_2C_3. \tag{7}$$

This section presents and discusses the simulated outcomes. Figure 6 depicts the intended frequency response of first-order, second-order, and third-order CNTFET-OTA-based low-pass filters. The frequency response of the CNTFET-OTAs allows for low-pass filters to have optimum passband flatness and a quick transition from passband to stopband. Figure 7 shows the power graph of the first-order, second-order, and third-order low-pass filters (Table 1).

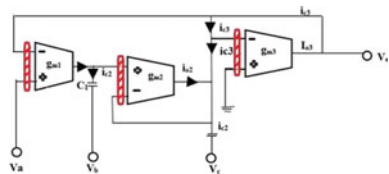
**Fig. 3** Proposed first-order LPF using CNTFET



**Fig. 4** Proposed second-order LPF using CNTFET



**Fig. 5** Proposed third-order LPF using CNTFET



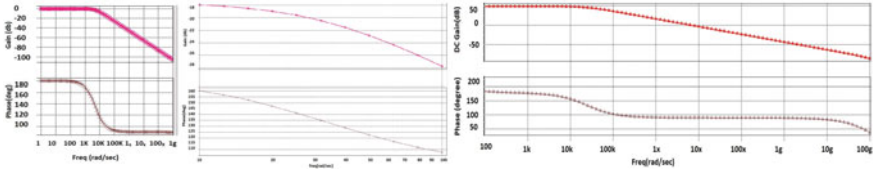


**Fig. 6** Frequency response of first-order, second-order, and third-order LPF using CNTFET, respectively

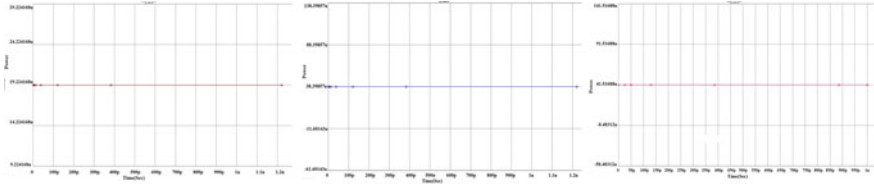


**Fig. 7** Power dissipation of first-, second-, and third-order LPF using CNTFET, respectively

**Table 1** Average power dissipation

S. No.	First-order LPF	Second-order LPF	Third-order LPF
Power consumption (µW)	0.1922	0.3840	0.4152

## 6 Conclusion

In this study, CNTFETs based first, second, and third orders of low-pass OTA-C filters are built and simulated using the H-SPICE simulation software. The suggested structures operate exceptionally well as low-pass filters with extremely reduced power dissipation and voltage. The analysis result shows that the average power dissipation can be reduced by using CNTFET.

## References

1. Loan SA et al (2014) Design of a novel high gain carbon nanotube based operational transconductance amplifier. In: Proceedings of the international multiconference of engineers and computer scientists, vol 2
2. Rahane SB, Kureshi AK, Kharate GK (2018) OTA-C filters for biomedical signal processing applications using hybrid CMOS-CNFET technology. In: 2018 international conference on intelligent and innovative computing applications (ICONIC). IEEE
3. Duan J et al (2015) An OTA-C filter for ECG acquisition systems with highly linear range and less passband attenuation. *J Semicond* 36(5):055006

4. Peng S-Y et al (2017) A power-efficient reconfigurable OTA-C filter for low-frequency biomedical applications. *IEEE Trans Circuits Syst I Regul Pap* 65(2):543–555
5. Jang J et al (2016) 16 channel ultralow power analog front-end for an implantable neural recording microsystem. *DEC J Integr Circuits Syst* 2(1):46–52
6. Loan SA et al (2015) Design and comparative analysis of high performance carbon nanotube-based operational transconductance amplifiers. *Nano* 10(03):1550039
7. Khan IA, Mahmood MR (2022) Design and analysis of power-efficient carbon nanotube-based parity checker circuits for high-data transmission rate. In: *Innovations in electronics and communication engineering*. Springer, Singapore, pp 597–603
8. Khan IA et al (2022) Design of low-power CNTFET parity generators for high-speed data transmission. In: *Innovations in electronics and communication engineering*. Springer, Singapore, pp 605–611
9. Khan IA (2022) Design and implementation of carbon nanotube based full adder at 32 nm technology for high speed and power efficient arithmetic applications. *J Phys* 2161(1):012050
10. Nizamuddin M et al (2015) Design, simulation and the comparative analysis of CNT based cascode operational transconductance amplifiers. *Nanotechnology* 26:395201
11. Nizamuddin M et al (2016) Design and simulation of high performance carbon nanotube based three stage operational amplifiers. *Mater Today Proc* 3(2):449–453

# Intrinsic Growth Challenges in Pulsed Laser-Deposited Al<sub>2</sub>O<sub>3</sub>/TiO<sub>2</sub> Subnanometric Laminates as a Potential Dielectric Material for High-Density Storage Applications



P. S. Padhi, S. K. Rai, R. S. Ajimsha, and P. Misra

**Abstract** Considering the potential applications of Al<sub>2</sub>O<sub>3</sub>/TiO<sub>2</sub> nanolaminates as an alternate high-*k* dielectric material, a pulsed laser deposition system was optimized toward growth of device-grade nanolaminates, where the role of sublayer thickness on dielectric properties was systematically investigated. Keeping the laser fluence close to ablation threshold, a set of NLs with sublayer thickness varying between 2 and 0.5 nm were fabricated. Structural characterization of these nanolaminates revealed a physically and chemically distinct interfaces. Reducing sublayer thicknesses from ~ 2 to 0.8 nm, a monotonic increment in dielectric constant from ~ 60 to 670 and a subsequent decrement in loss values from ~ 0.9 to 0.16, respectively, were found owing to enhanced Maxwell–Wagner interfacial polarization effect, whereas further reduction in sublayer thicknesses leads to enhanced interface intermixing and deterioration of the dielectric performances. These PLD-grown ATA NLs demonstrate their potential application as high-*k* material for next-generation storage devices.

**Keywords** Maxwell–Wagner interfacial polarization · High-*k* and low loss materials · Al<sub>2</sub>O<sub>3</sub>/TiO<sub>2</sub> nanolaminates

---

P. S. Padhi (✉) · R. S. Ajimsha · P. Misra  
Oxide Nano Electronics Lab., Laser Material Processing Division, Raja Ramanna Centre for Advanced Technology, Indore 452013, India  
e-mail: [partha.rrcat@gmail.com](mailto:partha.rrcat@gmail.com)

P. S. Padhi · S. K. Rai · P. Misra  
Homi Bhabha National Institute, Training School Complex, Anushakti Nagar, Mumbai 400094, India

S. K. Rai  
Accelerator Physics and Synchrotrons Utilization Division, Raja Ramanna Centre for Advanced Technology, Indore 452013, India

## 1 Introduction

Energy-storage capacitors being vital components in modern micro/nanoelectronics are subjected to stringent requirements such as high dielectric constant ( $k \geq 100$ ), high capacitance density ( $> 12 \text{ fF}/\mu\text{m}^2$ ), and low loss [1]. In search of a potential dielectric for such capacitors, several high- $k$  oxides such as  $\text{HfO}_2$ ,  $\text{ZrO}_2$ , and  $\text{TiO}_2$  have been investigated; however, scaling down of thickness has limited their application owing to increase in dielectric loss and leakage current [2]. Recently,  $\text{TiO}_2$  and  $\text{Al}_2\text{O}_3$  multi-layered nanolaminates (ATA NLs) have emerged as a promising candidate, owing to Maxwell–Wagner (M-W) interfacial polarization assisted high- $k$ , low loss, and low leakage values [3]. Although atomic layer deposition (ALD) technique is typically used to develop these multilayer heterostructures, pulsed laser deposition (PLD) is a viable growth method for these ATA NLs due to the scope of sequential ablation capability and adjustable laser parameters [4]. However, owing to the risk of interface interdiffusion from high energy-ablated species, it becomes challenging to grow subnanometric layers and distinct interfaces, as a result of which reports on PLD-grown ATA NLs are scanty in literature [5]. In relation to this scientific goal, we have optimized a pulsed layer deposition (PLD) system to fabricate high-quality device-grade ATA NLs, whose dielectric properties are systematically investigated toward high-density storage applications.

## 2 Experimental Section

Amorphous ATA NLs with various sublayer thicknesses ( $t_s$ ) ranging between 2 and 0.5 nm and total stack thickness of  $\sim 60$  nm were deposited on 50 nm TiN-coated Si and bare Si substrates at substrate temperature of 300 °C, oxygen partial pressure of 0.01 mbar, laser fluence of  $\sim 0.5 \text{ J}/\text{cm}^2$ , substrate-target separation of  $\sim 4.5$  cm, and pulse repetition rate of 5 Hz using a  $\sim 248$  nm KrF excimer laser-based PLD technique. The layered structure and the interface quality in these NLs were revealed by lab source (Cu-K $\alpha$ )-based X-ray reflectivity (XRR) measurements and cross-sectional transmission electron microscopy (TEM) measurements carried out at 200 keV using Philips CM 200 TEM system. The top and bottom layers of NLs are always kept  $\text{Al}_2\text{O}_3$  throughout the growth to avoid the contact effect with RF-sputtered TiN electrodes. The dielectric properties of NLs were measured in a TiN/ATA NL/TiN-based Metal–Insulator–Metal (MIM) capacitor structures using an impedance analyzer (Solartron make: SI-1206) in a frequency range of 1– $10^6$  Hz and a temperature range of 303–393 K. The top–bottom conducting TiN films as top electrodes ( $\sim 300 \mu\Omega \text{ cm}$ ) with  $\sim 50$  nm thickness and 220  $\mu\text{m}$  diameter were fabricated by RF-magnetron sputtering using shadow mask. The ATA NL with intended alternate  $t_s = 1$  nm (say) each is denoted as 1A-1T NL and the same nomenclature applies to all other NLs described in this manuscript.

### 3 Results and Discussion

Considering the energy of ablated species to be a critical growth parameter for subnanometric layers, a set of NLs are fabricated by varying laser fluence between 0.35 and 1 J/cm<sup>2</sup>, while keeping sublayer thickness fixed at ~ 1 nm. The interface quality of these as grown NLs can be depicted through measured XRR curves (as shown in Fig. 1a), where the improvement in overall reflectivity and hence the interface quality with decrease in fluence from 1 to 0.5 J/cm<sup>2</sup> is clearly visible and is plausibly owing to decrease in interface interdiffusion. With further decrease in fluence down to 0.35 J/cm<sup>2</sup>, the overall reflectivity is deteriorated plausibly owing to reduction in material density and growth rate. Hence, at an optimized fluence of ~ 0.5 J/cm<sup>2</sup>, a set of NLs consisting of 30 bilayers and bilayer thicknesses varying between 2 and 1.4 nm are fabricated and the appearance of Bragg peaks even in subnanometric regime of their measured XRR curves, as shown in Fig. 1b, confirms the periodic growth and distinct interfaces in these NLs, whereas the decrease in intensity and increase in broadening of Bragg peaks with decreasing *t<sub>s</sub>* indicate significant interface intermixing and aperiodic growth, respectively. Long-range sublayer thickness uniformity, flat interfaces, and a mild interface interdiffusion in 0.8A-0.8T NL are further confirmed from the cross-sectional TEM measurements (inset of Fig. 1b), which closely match with the XRR results. Further, the TEM diffraction pattern as shown in inset of Fig. 1b revealed the amorphous nature of both the sublayers in these ATA NLs.

The frequency dispersion dielectric constant ( $\epsilon_r$ ) and dielectric loss ( $\tan \delta$ ) spectra of ~ 60 nm thick ATA NLs, in a frequency range 10<sup>2</sup>–10<sup>6</sup> Hz, are depicted in Fig. 2a. A step like increase in dielectric constant and forming a plateau region toward lower frequency side is clearly observed when the *t<sub>s</sub>* ≤ 1.0 nm. A monotonic increment in  $\epsilon_r$  values from 60 to 670 and a decrement in  $\tan \delta$  values from ~ 0.9 to 0.16 can be observed with a reduction in *t<sub>s</sub>* from ~ 2 to 0.8 nm. However, the trend reversed for *t<sub>s</sub>* < 0.8 nm plausibly due to enhanced interface intermixing as revealed by XRR studies. The appearance of two distinct sets of thermally activated relaxation

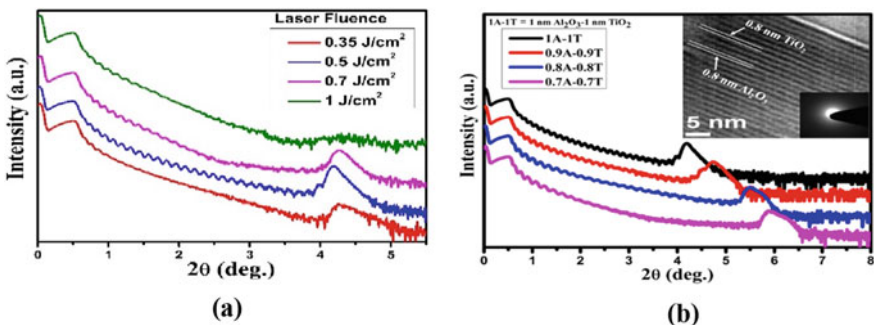


**Fig. 1** XRR plot for ATA NLs at different **a** fluences ranging between 1 and 0.35 J/cm<sup>2</sup>, **b** sublayer thickness ranging between 1 and 0.7 nm (inset) HRTEM image of NL with 0.8 nm sublayer thickness

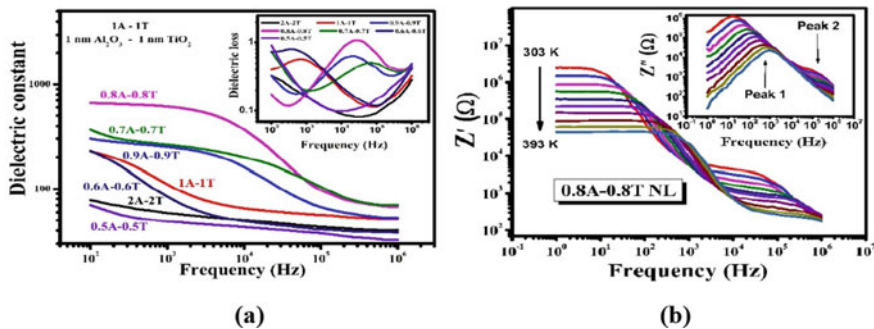


**Fig. 2** Frequency dispersion **a**  $\epsilon_r$  and (inset)  $\tan \delta$  spectra of NLs with sublayer thickness reducing from 2 to 0.5 nm, **b**  $Z'$  and (inset)  $Z''$  for 0.8A-0.8T NL at different temperatures

processes, owing to electrical inhomogeneity in these NLs, can be identified from the temperature-dependent dispersion in imaginary impedance ( $Z''$ ) of 0.8A-0.8T NL, as depicted in inset of Fig. 2b, which supports M-W interfacial polarization in these NLs [3]. The  $\epsilon_r$  values of  $\sim 670$  obtained for 0.8A-0.8T NL correspond to an equivalent oxide thickness (EOT) of 0.28 nm and a capacitance density of about  $\sim 97 \text{ fF}/\mu\text{m}^2$ , which are well above the required EOT of  $< 2 \text{ nm}$  for a sub- $0.1 \mu\text{m}$  complementary metal-oxide semiconductors (CMOS) and  $> 12 \text{ fF}/\mu\text{m}^2$  for MIM capacitor applications as set by International Technology Roadmap of Semiconductors (ITRS)-2022 [1].

### 4 Conclusions

In summary, an optimized PLD technique with laser fluence close to ablation threshold ( $\sim 0.5 \text{ J}/\text{cm}^2$ ) has been employed to fabricate device-grade  $\text{Al}_2\text{O}_3/\text{TiO}_2/\text{Al}_2\text{O}_3$  nanolaminates for high- $k$  dielectric applications. Formation of artificial periodic structures with physically distinct interfaces even in subnanometric regime was confirmed. A monotonous increment in dielectric constant from  $\sim 60$  to 670 and decrease in loss values from  $\sim 0.9$  to 0.16 were observed while reducing sublayer thickness down to 0.8 nm. The observed trend reversal in dielectric properties below 0.8 nm is plausibly owing to enhanced interface intermixing of sublayers as confirmed from XRR and TEM measurements. The observed enhancement in Maxwell–Wagner interfacial polarization assisted dielectric constant ( $\sim 670$ ) value for ATA NL with 0.8 nm sublayer thicknesses corresponds to a high capacitance density  $\sim 97 \text{ fF}/\mu\text{m}^2$  and a low equivalent oxide thickness of  $\sim 0.28 \text{ nm}$ , which makes it suitable for high-density storage applications.

**Acknowledgements** One of the authors (PSP) acknowledges Homi Bhabha National Institute (HBNI), Mumbai, India, for financial support. Authors would like to acknowledge Himanshu Srivastava and Arvind Srivastava of APSUD, RRCAT, for help in TEM measurements. Authors thank Mr.



Rakesh Kaul, Head, Laser Materials Processing Division and Associate Director, Materials Science and Advanced Technology Group of RRCAT, Indore, for constant encouragement and support.

## References

1. ITRS homepage. <http://www.itrs2.net/2022-its.html>. Accessed 26 Dec 2022
2. Padhi PS, Ajimsha RS, Chetia SK, Das AK, Sahu VK, Misra P (2020) Reduced leakage current in Al<sub>2</sub>O<sub>3</sub>/TiO<sub>2</sub>/Al<sub>2</sub>O<sub>3</sub> dielectric stacks grown by pulsed laser deposition. AIP Conf Proc 2265:030190-1–030190-4
3. Kahouli A, Lebedev O, Ben Elbahri M, Mercey B, Prellier W, Riedel S et al (2015) Structural and dielectric properties of subnanometric laminates of binary oxides. ACS Appl Mater Interfaces 7(46):25679–25684
4. Liu L, Mei Z, Tang A, Azarov A, Kuznetsov A, Xue Q-K, Du X (2016) Oxygen vacancies: the origin of n-type conductivity in ZnO. Phys Rev B 93(23):235305-1–235305-5
5. Ben Elbahri M, Kahouli A, Mercey B, Lebedev O, Donner W, Lüders U (2018) Study on the dielectric properties of Al<sub>2</sub>O<sub>3</sub>/TiO<sub>2</sub> sub-nanometric laminates: effect of the bottom electrode and the total thickness. J Phys D Appl Phys 51(6):065101 (9 pp)

# Infrared Absorption in Silicon Nanostructure-Patterned Absorber



Rangeeta Dhaka, Shankar Dutta, and A. K. Shukla

**Abstract** Nanostructures or microstructure-patterned based metamaterials are fabricated on semiconductors' surface to reduce the reflection and enhance the absorption of light. There is a particular interest to develop the infrared (IR) absorbers' materials that will improve the absorption in IR detector. This paper discusses about the mechanism of broadband absorption of infrared radiation in nanopatterned arrays of nanowires on silicon. In this work, the absorption and scattering cross-section of silicon nanowires in infrared region are simulated using COMSOL Multiphysics-based Wave Optics Module. Infrared response is analyzed in wavelength range 2.5–20  $\mu\text{m}$  for transverse electric polarizations at the normal and oblique incidence up to 60°. Simulation results reveal that the scattering of light is dominant over absorbance that enhances the extinction of the IR radiation.

**Keywords** Silicon nanowire · Infrared absorption · Finite element method

## 1 Introduction

Nowadays, ultrathin films or nanostructured pattern on semiconductors has abundant attention due to their tunable properties. These tunable properties are used to extract for designing nanopatterned-based novel electronic, photonic devices, sensors, etc. The nanopatterned structures show notable results with interaction of light due to the higher surface-to-volume ratio and exhibit localized surface plasmon resonance (LSPR) behavior invisible to infrared range which is responsible for light trapping and higher absorption [1, 2]. In semiconductor nano/microstructures, particularly silicon nano/micro wires/rods have their own broad area of applications in photovoltaics, sensing, electronics, etc. The optical absorption of silicon nanowires in 1–11 eV

---

R. Dhaka (✉) · A. K. Shukla

Laser-Assisted Materials Processing and Raman Spectroscopy Laboratory, Department of Physics, Indian Institute of Technology Delhi, New Delhi 110016, India  
e-mail: [rangeeta@physics.iitd.ac.in](mailto:rangeeta@physics.iitd.ac.in)

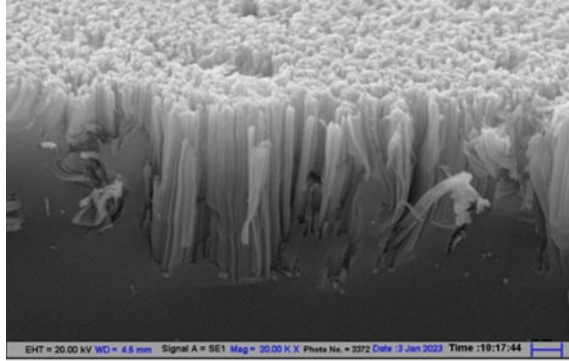
S. Dutta

Solid State Physics Laboratory, DRDO, Lucknow Road, Timarpur, Delhi 110054, India

© The Author(s), under exclusive license to Springer Nature Singapore Pte Ltd. 2023  
Z. H. Khan et al. (eds.), *Recent Advances in Nanotechnology*, Springer Proceedings in Materials 28, [https://doi.org/10.1007/978-981-99-4685-3\\_20](https://doi.org/10.1007/978-981-99-4685-3_20)

149

**Fig. 1** Silicon nanowires fabricated by metal-assisted chemical etching process



energy range is explored by many researchers [3–5]. Majority of previous theoretical and experimental studied in UV and visible range didn't focus on infrared range.

Still very few reports are existing on the optical response of silicon nanowires in shortwave IR (SWIR), mid-wave IR (MWIR), and long-wave IR (LWIR) range. In our recent communication [6], we observed broadband infrared absorption in the FTIR study ( $500\text{--}4000\text{ cm}^{-1}$ ) of fabricated silicon nanowires by process metal-assisted chemical etching (MACE), as shown in Fig. 1. The silicon nanowires have exhibited broadband infrared absorption in the FTIR study ( $500\text{--}4000\text{ cm}^{-1}$ ). The physical origin of these broadband IR absorption lies in the respective absorption and scattering cross-sections of the silicon nanowire. The current manuscript presents the simulations results of the absorption and scattering cross-sections on variation in diameter of the silicon nanowires to understand the origin of broadband IR. It was also observed that ratio of scattering to absorption cross-sections values changes within infrared range.

## 2 Modeling and Simulation

Fundamentally, the interaction of silicon nanowires with the incident radiation can be understood in terms of scattering and absorption cross-sections. The scattering cross-section over the nanowires volume can be presented as:

$$\sigma_{\text{sca}} = \frac{1}{I_0} \iint (\mathbf{k} \cdot \mathbf{S}_{\text{sca}}) dS, \quad (1)$$

where  $I_0$  is incident radiation intensity. The  $\mathbf{k}$  is a unit vector pointing outward from the nanowire surface and  $\mathbf{S}_{\text{sca}}$  is the Poynting vector for the scattered radiations. Absorption cross-section can be written as

$$\sigma_{\text{abs}} = \frac{1}{I_0} \iiint P dV, \quad (2)$$

where  $P$  is the radiation power loss density (in the particle).

Variations of diameter of the silicon nanowires on the scattering and absorption cross-sections are studied using finite element method (FEM)-based software—COMSOL Multiphysics. The simulation model is solved by ‘Wave Optics, Frequency Domain’ interfaces with ‘Wavelength Domain’ studies to calculate the scattering and absorption cross-section. In the nanowire arrays, optical responses arise due to the introduction of the refractive index of air between the nanowires, so the ‘electric displacement field model’ is chosen based on the ‘refractive index’.

To avoid the complexity of the simulation, the geometric parameters of the model are such that the diameters of silicon nanowires from 30 to 150 nm with length 1  $\mu\text{m}$ . Therefore, simulations are done to emulate the real condition for different polar angles ( $\theta$ ) and azimuthal angles ( $\phi$ ), as depicted in Fig. 2a. The optical constants in IR range ( $500\text{--}4000\text{ cm}^{-1}$ ) for silicon are taken from Shkondin et al. [7].

Perfectly Matched Layers (PMLs) are placed with the thickness (150 nm) over the unit cell to simulate the interaction of light with nanowires in a real scene and periodic boundary conditions are applied with the ‘Floquet period’ type to obtain the arrays of nanowires as shown in Fig. 2b. Each model has the same mesh pattern to maintain consistency in simulation results. Mesh is defined as free tetrahedral for air domain and substrate domain with maximum element size 5  $\mu\text{m}$  and minimum element size 20 nm and maximum element size  $5/n_{\text{Si}}\ \mu\text{m}$  (where  $n_{\text{Si}}$  is the value of refractive of silicon), respectively. Nanowire is also meshed by free tetrahedral with maximum element size equal to the diameter of nanowire. To avoid the interpolation errors over the ‘periodic boundaries’, boundaries have meshed with free triangular and PMLs are meshed with the swept with ten elements across. Meshed model is shown in Fig. 2c.

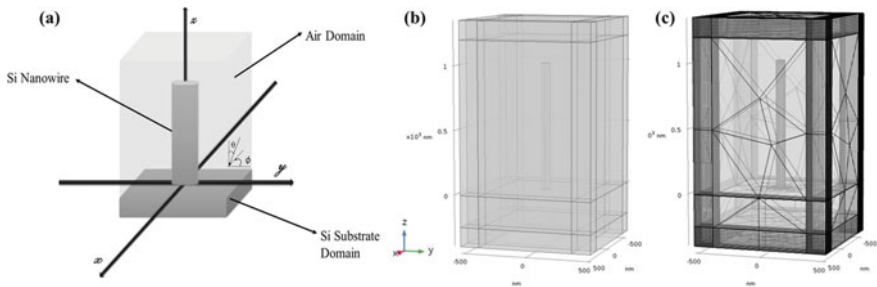


**Fig. 2** a Visualization of the unit cell of nanowires’ arrays for the simulation environment, b geometry of unit cell with periodic boundary and PMLs, c mesh of unit cell model

### 3 Results and Discussions

Figure 3a–h illustrate the variation in the  $\sigma_{\text{abs}}$  and  $\sigma_{\text{sca}}$  with different diameters (30–150 nm) of silicon nanowires having  $1 \mu\text{m}$  length for the incident IR radiation ( $500\text{--}4000 \text{ cm}^{-1}$ ) at  $0\text{--}60^\circ$  polar angle (theta). The value of  $\sigma_{\text{sca}}$  increasing with higher wavenumber (decreasing IR wavelength), whereas the value  $\sigma_{\text{abs}}$  exhibits a broad plasmonic peak around  $1000 \text{ cm}^{-1}$  ( $10 \mu\text{m}$  wavelength) [8], but pattern does not show any change with the variation in the polar angles ( $0\text{--}60^\circ$ ). Due to plasmonic effect absorption cross-section exhibits higher value till  $1500 \text{ cm}^{-1}$ , but it starts gradually to decrease with higher wavenumber. The simulated silicon nanowires exhibit  $\sigma_{\text{sca}}/\sigma_{\text{abs}}$  ratio of  $10^4\text{--}10^5$ ,  $10^3\text{--}10^4$ , and  $1\text{--}10$  in the part of SWIR ( $3400\text{--}4000 \text{ cm}^{-1}$ ), whole MWIR ( $2000\text{--}3300 \text{ cm}^{-1}$ ), and LWIR ( $600\text{--}1200 \text{ cm}^{-1}$ ) ranges, respectively.

In our recent reported results [6], MACE-synthesized silicon nanowires show prominent absorption in infrared range ( $500\text{--}4000 \text{ cm}^{-1}$ ) and also show enhancement in Raman scattering. The present results provide the physical reason behind the higher extinction in nanowires. Here, simulation results reveal that scattering phenomena are predominantly deciding the absorbance of IR radiation in the silicon nanowires. The reasons behind the higher scattering are the geometrical light trapping that leads to low reflectance due to Effective Medium Approximation (EMA) (Bruggeman's Model) [9]. The efficiency of infrared sensing devices is highly influenced by stronger infrared absorption so that silicon nanowires are promising material as broadband infrared absorbers and for infrared sensing devices.

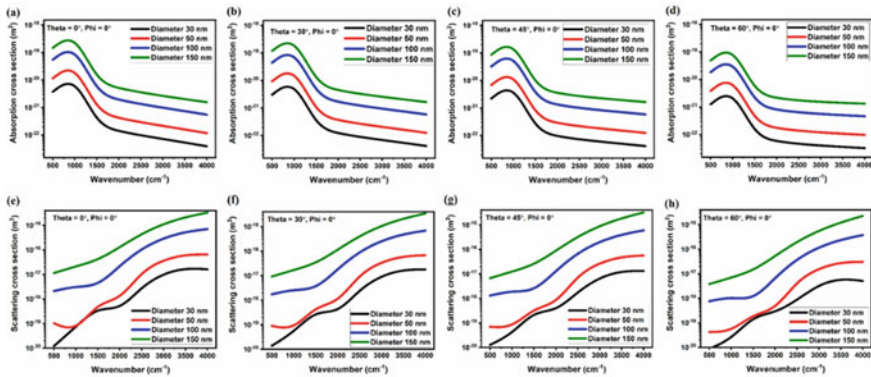


**Fig. 3** Absorption cross-section in **a–d** and scattering cross-section in **e–h** of silicon nanowires having variable diameter for length of  $1 \mu\text{m}$

## 4 Conclusion

The simulation results reveal that the values of  $\sigma_{\text{abs}}$  and  $\sigma_{\text{sca}}$  are increased with the diameter of nanowire from 30 to 150 nm of silicon nanowires having 1  $\mu\text{m}$  length for the incident IR radiation (500–4000  $\text{cm}^{-1}$ ). FEM simulation  $\sigma_{\text{abs}}$  and  $\sigma_{\text{sca}}$  of the silicon nanowires shows that the  $\sigma_{\text{sca}}/\sigma_{\text{abs}}$  ratio of  $10^4$ – $10^5$ ,  $10^3$ – $10^4$ , and 1–10 in the part of SWIR (3400–4000  $\text{cm}^{-1}$ ), whole MWIR (2000–3300  $\text{cm}^{-1}$ ), and LWIR (600–1200  $\text{cm}^{-1}$ ) ranges, respectively. The scattering phenomena are predominantly deciding the absorbance of IR radiation in the silicon nanowires.

**Acknowledgements** Rangeeta Dhaka acknowledges University Grants Commission, New Delhi, India, for financial assistance.

## References

1. Mortazavifar SL, Salehi MR, Shahraki M, Abiri E (2022) Optimization of light absorption in ultrathin elliptical silicon nanowire arrays for solar cell applications. *J Mod Opt* 69(7):368–380. <https://doi.org/10.1080/09500340.2022.2041123>
2. Bartschmid T, Wendisch FJ, Farhadi A, Bourret GR (2022) Recent advances in structuring and patterning silicon nanowire arrays for engineering light absorption in three dimensions. *ACS Appl Energy Mater* 5(5):5307–5317. <https://doi.org/10.1021/acsam.1c02683>
3. Lagos N, Sigalas MM, Niarchos D (2011) The optical absorption of nanowire arrays. *Photon Nanostruct* 9:163–167. <https://doi.org/10.1016/j.photonics.2010.09.005>
4. Tsakalacos L et al (2007) Strong broadband optical absorption in silicon NW films. *J Nanophoton* 1. <https://doi.org/10.1117/1.2768999>
5. Borgh G et al (2023) Plasmon resonances in silicon nanowires: geometry effects on the trade-off between dielectric and metallic behaviour. *Opt Mater Express* 13. <https://doi.org/10.1364/OME.475988>
6. Dhaka R, Rani S, Pandey A, Dutta S, Shukla AK (2023) Investigation of structural and infrared characteristics of silicon nanowires for bolometric application. *Silicon*. <https://doi.org/10.1007/s12633-023-02313-w>
7. Shkondin E et al (2017) Large-scale high aspect ratio Al-doped ZnO nanopillars arrays as anisotropic metamaterials. *Opt Mater Express* 7(5):1606–1627. <https://doi.org/10.1364/OME.7.001606>
8. Chou L-W, Shin N, Sivaram SV, Filler MA (2012) Tunable mid-infrared localized surface plasmon resonances in silicon nanowires. *J Am Chem Soc* 134(39):16155–16158. <https://doi.org/10.1021/ja3075902>
9. Niklasson GA, Granqvist CG, Hunderi O (1981) Effective medium models for the optical properties of inhomogeneous materials. *Appl Opt* 20(1):26–30. <https://doi.org/10.1364/AO.20.000026>

# Exploring Eco-friendly Nanocellulose-Based Hydrogel Membranes as Flexible and Biocompatible Electrolyte in Supercapacitors



Mohammed Saquib Khan , Shivani, Nikita Bhardwaj, Preeti Shakya, Deependra Jhankal, Malay Kumar Banerjee, and Kanupriya Sachdev 

**Abstract** Hydrogels are among the most potential electrolytes for flexible quasi-solid-state supercapacitors due to their splendid features such as ultra-stretchability, flexibility, and resistance to extreme temperatures. Usually, the evaporation of water from the hydrogel electrolyte results into stiffness in the gel, obstructed ionic motion leading retarded electrochemical performance of the energy storage device. Nanocellulose is well-known for its water retention properties owing to its hygroscopic properties and is considered as a sustainable material due to its recyclability and biodegradability. In this study, we propose that a hydrogel electrolyte made of nanocellulose-based polyvinyl alcohol (NC-PVA-NaClO<sub>4</sub>) can effectively address the problem of electrolyte drying in aqueous hydrogel electrolytes. To optimize the concentration of nanocellulose, four different NC-PVA-NaClO<sub>4</sub> hydrogel compositions are synthesized (NC: PVA in w/w ratios of 0:1; 0.5:1; 1:1; 2:1). The cyclic stability reveals that the NC-PVA-NaClO<sub>4</sub> hydrogel resulted into an enhanced capacitance conservation after 10,000 charge–discharge cycles in comparison to the neat PVA-NaClO<sub>4</sub> hydrogel electrolyte.

**Keywords** Nanocellulose · Biodegradable · Gel polymer electrolyte · Supercapacitors · Wearable electronics

---

M. S. Khan · Shivani · P. Shakya · K. Sachdev (✉)  
Materials Research Centre, Malaviya National Institute of Technology Jaipur, Jaipur, India  
e-mail: [ksachdev.phy@mnit.ac.in](mailto:ksachdev.phy@mnit.ac.in)

N. Bhardwaj · D. Jhankal · K. Sachdev  
Department of Physics, Malaviya National Institute of Technology Jaipur, Jaipur, India

M. K. Banerjee  
SGVU, Jaipur, India

## 1 Introduction

As wearable electronics and medical implants become more prevalent, gel polymer electrolytes (GPEs) have significant attention of researchers. A perfect GPE should be able to tolerate different degrees of deformation, such as bending, stretching or compressing, while maintaining its electrochemical stability and durability [1]. Polyvinyl Alcohol (PVA) is accepted and widely used as a host polymer [2] owing to its cost effectiveness, excellent membrane formation, high elasticity, thermal stability. Additionally, it has very good flexibility and a higher proportion of polar hydroxyl groups, both of which facilitate salt solvation [3]. However, PVA-based GPEs are far from perfect due to limited mechanical durability due to inadequate crosslinking, inappropriate interface between the electrodes and the electrolyte under mechanical force, possible degradation of electrochemical performance when bent or stretched, and evaporation of solvent from hydrogel electrolyte resulting in diminishing the electrochemical performance of electrochemical energy storage (EES) devices [4, 5]. Mixing two or more distinct polymers to create GPEs instead of utilizing a single polymer can enhance thermal stability, the existence of ion-hopping sites and mechanical characteristics. Nevertheless, mixing PVA with another polymers that have comparable properties might enhance the performance of the blended material as a result of strong hydrogen bond formation as compared to weak van der Waals interactions [6]. Nanocellulose (NC) has a backbone made of a hydrophobic polysaccharide and a number of hydrophilic carboxyl groups. The unshared set of electrons located on the oxygen atoms of NC readily react with the salt cation, resulting in the creation of polymer electrolytes that are based on NC. The glass transition temperature of NC which is an amorphous polymer, is also quite high. It performs exceptionally well at decreasing the crystallinity level of the PVA employed in the blending procedure. Since NC and PVA are both soluble in water and miscible with one another, developing a composite polymer blend is feasible.

## 2 Materials and Methods

### 2.1 Materials

Sodium perchlorate and polyvinyl alcohol and were procured from Loba Chemie Pvt Ltd.



## 2.2 Methods

### 2.2.1 $\text{NaClO}_4$ -PVA and NC- $\text{NaClO}_4$ -PVA Hydrogel Membrane Synthesis

5 g PVA added into 100 ml of DI water under continuous stirring at  $80^\circ\text{C}$ .  $\text{NaClO}_4$  1 M was added into the PVA solution. The resulting viscous liquid was cast into Petri plates made of borosilicate, and it was dried to yield neat  $\text{NaClO}_4$ -PVA hydrogel membrane. To synthesize NC-PVA- $\text{NaClO}_4$  hydrogel, nanocellulose powder 0.5 g, 1 g, and 2 g was added in the PVA- $\text{NaClO}_4$  mixture, resulting three solutions labelled as 0.5 g NC-PVA- $\text{NaClO}_4$ , 1 g NC-PVA- $\text{NaClO}_4$ , and 2 g NC-PVA- $\text{NaClO}_4$ , respectively.

## 3 Results and Discussion

Field emission scanning electron microscopy (FESEM) image of the nanocellulose fibre as shown in Fig. 1a has a nano-network of NC fibrils. These fibrils provide sufficient channels for the swift motion of the electrolytic ions through the gel polymer electrolyte. The FESEM image of reduced graphene oxide (rGO), shown in Fig. 1b, exhibits highly microporous and crumpled sheets/flakes. The high-temperature thermal annealing leads to wrinkles in the morphology of rGO. Wrinkled graphene sheets have various benefits, notably enhancing the charge storage capacity, surface to volume ratio, and exposing a large amount of electrochemical surface area to the electrolyte. The electrode slurry in Fig. 1c demonstrates rGO flakes are interwoven with the porous matrix of nanocellulose fibres.

In the Raman spectra, G band, appears at  $\approx 1560\text{--}1590\text{ cm}^{-1}$  and results from the  $E_{2g}$  oscillations of the hexagonal 2D lattice and the D band, which appears at  $\approx 1330\text{--}1360\text{ cm}^{-1}$  results from the irregularities and imperfections in the graphene lattice structure are represented by the  $A_{1g}$  vibrations in the  $sp^2$  carbon ring. The second-order two phonon process produces the 2D band at a wavelength range of  $2680\text{--}2710\text{ cm}^{-1}$  [7, 8]. These bands' intensity ratios give important details regarding the structural defect density and the graphene sample's number of layers [9]. Figure 2a

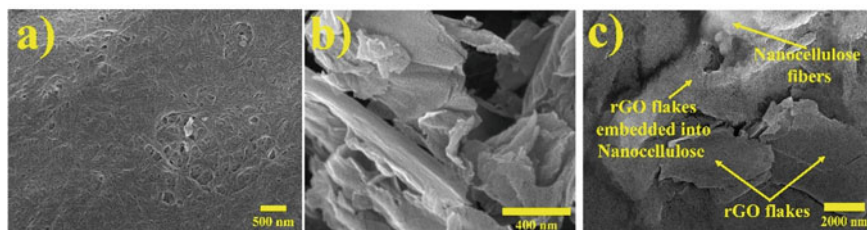


**Fig. 1** FESEM images of samples **a** nanocellulose fibres, **b** rGO flakes, **c** electrode slurry displaying graphene flakes partly embedded in nanocellulose fibres

shows the characteristic G and D bands for sample of graphene oxide (GO) at  $1588\text{ cm}^{-1}$  and  $1354\text{ cm}^{-1}$ , respectively, with a ratio of  $I_D$  to  $I_G \approx 0.79$ . The G band and D band appearing at  $1580\text{ cm}^{-1}$  and  $1344\text{ cm}^{-1}$ , respectively, in the rGO sample with an  $I_D$  to  $I_G$  ratio of  $\approx 1.1$ . The shifting of D band and G band was observed towards the lower wavenumber in the rGO sample can be attributed to the oxygen moieties removal from the graphene oxide structure during the reduction process. Moreover, the enhancement in the  $I_D$  to  $I_G$  ratio indicates the formation of more defect site due to the hydrothermal process and thermal annealing at high temperatures, leading to a constructive impact on electrochemical performance.

Figure 2b shows that the photoluminescence (PL) spectrum of the neat PVA have peaks (around 860 nm) due to the  $n \rightarrow \pi^*$  transitions of the hydroxyl group [3]. A successive reduction in the peak is observed on the increasing amount of nanocellulose (from neat PVA to 0.5 g NC-PVA- $\text{NaClO}_4$ ) and it vanishes in the higher loadings of NC. The PVA matrix encourages contacts between polymer chains and nanocellulose, which presumably helps explain why there are more free  $-\text{OH}$  groups undergoing recombination. Nevertheless, the PL bands in the range  $\sim 650$ – $750\text{ nm}$  is often caused by the presence of various organic chromospheres, such as

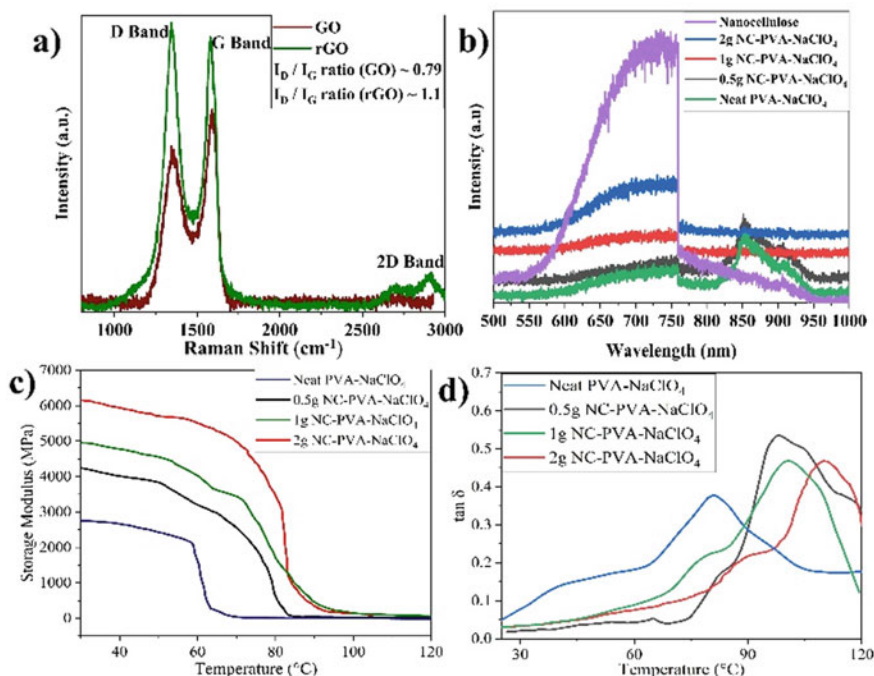


**Fig. 2** **a** Raman spectroscopy plots of graphene oxide (GO) and reduced graphene oxide (rGO) samples, **b** photoluminescence spectra of nanocellulose, 2 g NC-PVA- $\text{NaClO}_4$ , 1 g NC-PVA- $\text{NaClO}_4$ , 0.5 g NC-PVA- $\text{NaClO}_4$ , and neat PVA- $\text{NaClO}_4$  membranes, **c** dynamic mechanical analysis (DMA) storage modulus curve, **d** DMA tan  $\delta$  curve

carbonyl groups and other low-molecular derivatives of cellulose degradation, in the host matrix of cellulose [10]. These PL band also exhibit a decrease in the intensity on reducing the nanocellulose proportion in the electrolyte implying that the NC backbones are undergoing structural changes due to the merging with the polymeric chains of PVA.

To examine the reinforcement effect brought about by the inclusion of NC in the PVA matrix at various temperatures, the DMA analysis is carried out. Figure 2c shows the temperature-dependent storage modulus and  $\tan \delta$  for all synthesized nanocomposite membranes. The DMA curves (Fig. 2c, d) displays the rise in storage modulus and glass transition temperature ( $T_g$ ) with the increase in nanocellulose concentration indicating improved mechanical strength. It may be attributed to the constraints put in place by the PVA macromolecular chains on the mobility of surface-adsorbed nanocellulose chains, which led to an excellent elastic response in the material. The high storage modulus of the membranes is very significant since they are often used in high moisture and hot temperature environments.

The electrochemical performance was assessed in two electrode configuration using reduced graphene oxide as electrode material and separator-less GPE with 0 g, 0.5 g, 1 g, and 2 g concentration of nanocellulose in the PVA- $\text{NaClO}_4$  GPE labelled as Neat PVA- $\text{NaClO}_4$ , 0.5 g NC-PVA- $\text{NaClO}_4$ , 1 g NC-PVA- $\text{NaClO}_4$ , and 2 g NC-PVA- $\text{NaClO}_4$ , respectively. The fabricated devices were tested for 10,000 GCD cycles (Fig. 3c) at a current density of  $0.5 \text{ A g}^{-1}$  showing that the capacitance retention in the devices was in the order of  $1 \text{ g NC-PVA-NaClO}_4 > 2 \text{ g NC-PVA-NaClO}_4 > 0.5 \text{ g NC-PVA-NaClO}_4 > \text{Neat PVA-NaClO}_4$ . Cyclic voltammetry in the potential window of 0–1 V at a  $10 \text{ mV s}^{-1}$  scan rate was executed on all the as prepared devices and after completing their 10,000 galvanostatic charge discharge (GCD) cycles (Fig. 3a, b, respectively), it is established that the neat PVA- $\text{NaClO}_4$  PGE device shows a highest capacitive area under the curve before GCD cycling indicating superior capacitive performance. Interestingly, after 10,000 GCD cycles the neat PVA- $\text{NaClO}_4$  PGE device has a substantially smaller CV area (Fig. 3b) as a direct consequence of the evaporation of water from the hydrogel electrolyte. The addition of NC to PVA- $\text{NaClO}_4$  polymer gel diminishes the gel stiffness problem of the GPE owing to the water retention capabilities of nanocellulose fibre (NCF). The 1 g NC-PVA- $\text{NaClO}_4$  PGE device has the highest specific capacitance after GCD cycles, as shown by Fig. 3b, it is evident that the performance of neat PVA- $\text{NaClO}_4$  has degraded even lower to that of 0.5 g NC-PVA- $\text{NaClO}_4$  PGE which exhibits minimum capacitance.

Figure 3d, e illustrate the electrochemical impedance spectroscopy (EIS)-based Nyquist plots of the as constructed supercapacitor devices and after 10,000 GCD cycles, respectively, evaluated in the frequency range of  $0.01\text{--}4 \times 10^6 \text{ Hz}$ . It can be observed that the device containing neat GPE has the lowest equivalent resistance before GCD cycling, which maximize after 10,000 GCD cycling indicating poor long cycling performance of the neat GPE. The reduced ion transport between the electrode and electrolyte surfaces due to evaporation of water from the hydrogel electrolyte resulted in the increase in equivalent resistance. It is evident from Fig. 3e that the 1 g NC-PVA- $\text{NaClO}_4$  GPE device has the lowest resistance after 10,000 GCD

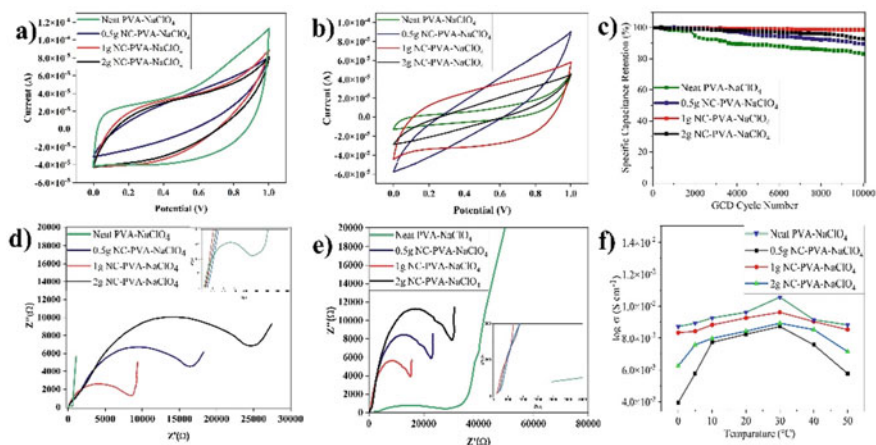


**Fig. 3** **a** Cyclic voltammery profiles of as fabricated supercapacitor devices, **b** cyclic voltammery profiles of the supercapacitor devices after six months, **c** cyclic stability plots for 10,000 cycles, **d** Nyquist plots of as fabricated supercapacitor devices, and **e** Nyquist plots of the supercapacitor devices after 10,000 GCD cycles, **f** ionic conductivity plots

cycles due to the polymerization of PVA monomers on the nanocellulose fibre, which created a porous nanostructure of NC-PVA complexes within the hydrogel electrolyte and facilitated electron transport. The ionic conductivities were also calculated using EIS technique at 0–50 °C (Fig. 3f) implying that the 1 g NC-PVA-NaClO<sub>4</sub> GPE has the highest ionic conductivity in comparison to the other NC-PVA composite hydrogels.

## 4 Conclusion

In conclusion, electrolytes in polymer blends based on polyvinyl alcohol (PVA) and combined with various ratios of nanocellulose were made using the casting approach. Nanocellulose (NC) has many hydrophilic functional groups and a hydrophobic polysaccharide framework. In order to create polymer electrolytes based on NC, the lone pair of electrons on the oxygen atoms of the NC interacts efficiently with the cation of the electrolyte salt. In the polymeric chains blending process, it is observed that NC, an amorphous polymer with a relatively high glass transition temperature, reduces the degree of crystallinity of the PVA, improving its characteristics. Shifting peaks and changes in the intensity of PL bands show that PVA and NC interact at the molecular level. It is evident from the cyclic stability data that the 1 g NC-PVA-NaClO<sub>4</sub> supercapacitor device exhibit remarkable cyclic stability after 10,000 charge–discharge cycles. The EIS technique has exhibited a lowest charge transfer resistance for the 1 g NC-PVA-NaClO<sub>4</sub> device after a 10,000 GCD cycles indicating its robustness and long life.

## References

1. Wang Y, Wu X, Han Y, Li T (2021) Flexible supercapacitor: overview and outlooks. *J Energy Storage*. Elsevier Ltd, 1 Oct, <https://doi.org/10.1016/j.est.2021.103053>
2. Saquib Khan M, Santhi Bhushan B, Chandra Bhamu K, Gu Kang S, Singh Kushwaha H, Sharma A et al (2023) Polymer hydrogel based quasi-solid-state sodium-ion supercapacitor with 2.5 V wide operating potential window and high energy density. *Appl Surf Sci* 607. <https://doi.org/10.1016/j.apsusc.2022.154990>
3. Brza MA, Aziz SB, Anuar H, Alshehri SM, Ali F, Ahamad T et al (2021) Membranes characteristics of a plasticized PVA-based polymer electrolyte membrane and H<sup>+</sup> conductor for an electrical double-layer capacitor: structural, morphological, and ion transport properties. <https://doi.org/10.3390/membranes11040296>
4. Janakiraman S, Surendran A, Biswal R, Ghosh S, Anandhan S, Venimadhav A (2019) Electrochemical characterization of a polar  $\beta$ -phase poly (vinylidene fluoride) gel electrolyte in sodium ion cell. *J Electroanal Chem* 833:411–417. <https://doi.org/10.1016/j.jelechem.2018.12.011>
5. Janakiraman S, Padmaraj O, Ghosh S, Venimadhav A (2018) A porous poly (vinylidene fluoride-co-hexafluoropropylene) based separator-cum-gel polymer electrolyte for sodium-ion battery. *J Electroanal Chem* 826:142–149. <https://doi.org/10.1016/j.jelechem.2018.08.032>
6. Abdullah AM, Aziz SB, Saeed SR (2021) Structural and electrical properties of polyvinyl alcohol (PVA): Methyl cellulose (MC) based solid polymer blend electrolytes inserted with sodium iodide (NaI) salt. *Arab J Chem* 14(11). <https://doi.org/10.1016/j.arabjch.2021.103388>
7. Wu JB, Lin ML, Cong X, Liu HN, Tan PH (2018) Raman spectroscopy of graphene-based materials and its applications in related devices. *Chem Soc Rev* 47(5):1822–1873. <https://doi.org/10.1039/c6cs00915h>
8. Khan MS, Shakya P, Bhardwaj N, Jhankal D, Sharma AK, Banerjee MK, Sachdev K (2022) Chemical vapor deposited graphene-based quasi-solid-state ultrathin and flexible sodium-ion supercapacitor. *J Electrochem Sci Eng* 12(4):799–813. <https://doi.org/10.5599/jese.1411>
9. No YS, Choi HK, Kim JS, Kim H, Yu YJ, Choi CG, Choi JS (2018) Layer number identification of CVD-grown multilayer graphene using Si peak analysis. *Sci Rep* 8(1):1–9. <https://doi.org/10.1038/s41598-017-19084-1>
10. Santos MV, Maturi FE, Pecoraro É, Barud HS, Lima LR, Ferreira RAS et al (2021) Cellulose based photonic materials displaying direction modulated photoluminescence. *Front Bioeng Biotechnol* 9. <https://doi.org/10.3389/fbioe.2021.617328>

# SCAPS-Based Analysis of ZrS<sub>2</sub>/CZTS/ MoS<sub>2</sub>/Si Tandem Solar Cell Parameters



Shubhra Gupta, Gayatri Shishodia, and P. K. Shishodia

**Abstract** The SCAPS-based simulation of monolithic two terminal transition metal chalcogenide (TMC) has been performed for tandem solar cell. The tandem device has been designed by using top ZrS<sub>2</sub> cell with bandgap of 1.7 eV and bottom MoS<sub>2</sub> cell with bandgap of 1.2 eV. Simulations have been carried out in two steps. Firstly, the top ZrS<sub>2</sub>/CZTS cell have been analysed and calibrated to fit a state of the art conversion efficiency of 7.43% and then the bottom MoS<sub>2</sub>/Si cell have been calibrated to 8.44% conversion efficiency by optimizing the thickness of top and bottom absorber layers. The optimized subcells were then investigated for tandem design to yield the maximum conversion efficiency of 12.54% and enhanced open circuit voltage ( $V_{oc}$ ) of 0.9966 V under the current density ( $J_{sc}$ ) matching conditions. A significant improvement has been observed in power conversion efficiency (PCE) of TMC subcells stacked serially in multi-junction tandem cell in comparison to standalone configuration. The performance parameters obtained for tandem cell are 18.12 mA cm<sup>-2</sup> ( $J_{sc}$ ) and 69.43% (FF).

**Keywords** SCAPS · Tandem solar cell · Simulations · Efficiency

## 1 Introduction

Enhancement of solar cell power by stacking materials of different bandgap has been an effective approach against single p–n junction photovoltaic device. As per Shockley-Queisser limit maximum reported theoretical efficiency of single junction

---

S. Gupta

Department of Electronics, Sri Venkateswara College, University of Delhi, New Delhi 110021, India

G. Shishodia

Department of Physics, Zakir Husain Delhi College, University of Delhi, New Delhi 110002, India

S. Gupta · P. K. Shishodia (✉)

Department of Electronics, Zakir Husain Delhi College, University of Delhi, New Delhi 110002, India

e-mail: [pkshishodia@zh.du.ac.in](mailto:pkshishodia@zh.du.ac.in)

solar cell is nearly 33% [1]. Thermal losses due to high energy photons and energy loss due to photons transparent to the bandgap limits the number of useful photons absorbed. Theoretical efficiency as high as 86% have been reported for multi-junction cells for concentrated light under one sun irradiance [1]. Present study reports the simulations of ZrS<sub>2</sub>/CZTS/MoS<sub>2</sub>/Si tandem solar cell using Solar Cell Capacitance Simulator (SCAPS) [2] developed at the Department of Electronics and Information Systems (ELIS) of University of Gent, Belgium. Detailed study on tandem device based on transition metal dichalcogenides (TMDC) have been targeted under standalone and tandem configurations. Amongst TMDCs, the main emphasis is laid on Zirconium disulphide (ZrS<sub>2</sub>), an important semiconductor material with high absorption coefficient ( $>10^4 \text{ cm}^{-1}$ ), mobility of  $1200 \text{ cm}^2\text{V}^{-1} \text{ s}^{-1}$  [3] and optical bandgap of 1.7 eV [4]. SCAPS does not support simulation of multi-junction solar cell so the top and bottom cells were simulated separately and thereafter current matching condition was obtained to analyse the performance of tandem device. Under ideal current matching conditions, top ZrS<sub>2</sub>/CZTS and bottom MoS<sub>2</sub>/Si cells in tandem have been optimized to give an efficiency of 12.54%.

## 2 Device Structure and Numerical Simulations

Functionality of SCAPS-1D is based on solving Poisson's and continuity equations for charge carriers under steady state conditions [2]. Optical model of SCAPS for the generation of mobile charge carriers is governed by the following fundamental equations. Generation of eh pairs ( $G(x)$ ) from incident photon flux,  $N_{\text{phot}}(\lambda)$  is calculated as

$$G(\lambda, x) = \alpha(\lambda, x) \cdot N_{\text{phot}}(\lambda, x) \quad (1)$$

where  $\alpha(\lambda, x)$  position dependant absorption and  $N_{\text{phot}}(\lambda, x)$  is defines as

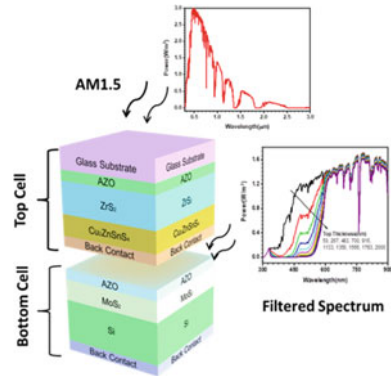
$$N_{\text{phot}}(\lambda, x) = N_{\text{phot0}}(\lambda) \cdot T_{\text{front}}(\lambda) \cdot \exp(-x\alpha(\lambda)) \cdot \frac{1 + R_{\text{back}}(\lambda) \cdot \exp(-2(d-x)\alpha(\lambda))}{1 - R_{\text{back}}(\lambda) \cdot R_{\text{int}} \cdot \exp(-2d\alpha(\lambda))} \quad (2)$$

where  $N_{\text{phot0}}(\lambda, x)$  is the light incident from the left contact,  $T_{\text{front}}(\lambda)$  is the wavelength dependant transmission at the front contact,  $R_{\text{back}}(\lambda)$  is the wavelength dependant reflection at the back contact and  $R_{\text{int}}$  is the internal reflection at the front contact.  $d$  is defined as the single layer thickness and  $\alpha(\lambda)$  as uniform absorption coefficient. Equation (1) is integrated over the entire wavelength range

$$G(x) = \int_{\lambda_{\text{min}}}^{\lambda_{\text{max}}} G(\lambda, x) d\lambda = \int_{\lambda_{\text{min}}}^{\lambda_{\text{max}}} \alpha(\lambda, x) \cdot N_{\text{phot}} d\lambda \quad (3)$$



**Fig. 1** Device structure used in simulations



In this work we propose the SCAPS-based simulation of tandem solar cell that consists of large bandgap (1.7 eV) AZO/ZrS<sub>2</sub>/CZTS top cell and relatively smaller bandgap (1.2 eV) [5] AZO/MoS<sub>2</sub>/Si bottom cell. Structures of top and bottom subcells are presented in Fig. 1.

Table 1 shows the layer parameters used in the simulations and have been defined as per the data available in literature or to the best approximations. Initial optimization has been done under standalone conditions where both the subcells were simulated with AM1.5 spectrum. The efficiency of 9.72 and 10.05% of optimized top and bottom cells have been obtained, respectively. To study the performance of tandem device top cell has been illuminated with AM1.5 spectrum and bottom cell have been illuminated with the filtered spectrum obtained from top cell. Transmitted spectrum,  $S(\lambda)$  from the top cell is wavelength dependant and can be obtained as [2]:

$$S(\lambda) = S_0(\lambda) \cdot \exp\left(\sum_{i=1}^n -(\alpha_{\text{material}_i}(\lambda) \cdot d_{\text{material}_i})\right) \tag{4}$$

Here,  $S_0(\lambda)$  represents the incident AM1.5 spectrum and  $n$  is the number of material layers. Owing to the limitation to analyse two terminal monolithic tandem configuration, SCAPS simulation tool utilizes this approach for current matching under ideal conditions which has been widely accepted.

### 3 Results and Discussion

Figure 2a, b shows the calibrated J-V and EQE curves of standalone configurations.  $J_{sc}$  for top and bottom cell is 25.16 mAcm<sup>-2</sup> and 32.99 mAcm<sup>-2</sup> and  $V_{oc}$  is 0.6051 and 0.4303 V, respectively. EQE is above 60% for both the cells for lower wavelengths. However, high bandgap ZrS<sub>2</sub>/CZTS top cell results in dropping of EQE above 700 nm. Impact of top layer thickness on J-V characteristic of top and



**Table 1** Material parameters used in simulations

Layer properties	Al-ZnO [6]	ZrS <sub>2</sub> [6]	CZTS [6]	MoS <sub>2</sub> [7]	Si [7]
Thickness (μm)	0.1	0.05	0.1	0.2	15
Bandgap (eV)	3.3	1.7	1.4–1.5	1.2	1.124
Electron affinity	4.5	4.95	4.5	4.22	4.05
Relative permittivity	9	1.5–10.5	10	18	11.9
N <sub>c</sub> (cm <sup>-3</sup> )	2.20E+18	5.16E+19	2.24E+18	1.00E+20	1.00E+18
N <sub>v</sub> (cm <sup>-3</sup> )	1.80E+19	1.50E+19	8.85E+18	1.00E+20	1.00E+18
Thermal velocity of electron (cm/s)	1.00E+07	1.00E+07	1.00E+07	1.00E+07	1.00E+07
Thermal velocity of hole (cm/s)	1.00E+07	1.00E+07	1.00E+07	1.00E+07	1.00E+07
Electron mobility (cm <sup>2</sup> /Vs)	200	1250	100	517	1450
Hole mobility (cm <sup>2</sup> /Vs)	5 to 50	695.8	25	270	450
Electron effective mass	0.24m <sub>0</sub>	1.62/0.31m <sub>0</sub>	0.2m <sub>0</sub>		
Hole effective mass	0.59m <sub>0</sub>	0.71m <sub>0</sub>	0.2–0.5m <sub>0</sub>		
N <sub>d</sub>	1.00E+19	8.50E+17	1.00E+10	1.00E+17	1.00E+00
N <sub>a</sub>	1.00E+15	1.00E+10	1.00E+15	1.00E+10	1.00E+12
Ln	NA	NA	0.11–0.17 μm	NA	NA

bottom subcells is presented in Fig. 2c, d. For standalone configurations ZrS<sub>2</sub> and MoS<sub>2</sub> thickness has been varied from 0.05–2.0 nm and 0.1–1.0 nm, respectively. It is observed that as the absorber layer thickness increases the short circuit current density also increases in both the devices. This may be attributed to enhancement of electron pair generations in active layer due to improved optical absorption. The rate of increase in  $J_{sc}$  is more at lower thickness, which then starts to saturate at higher thicknesses.

Optimized solar cells discussed above may now be considered for comprehensive study of tandem design. Initially, the top cell is simulated for PV characteristics with ZrS<sub>2</sub> thickness variation from 0.05–2 μm while keeping other layer thickness constant as reported in Table 1. Filtered spectrum from top cell for various top cell

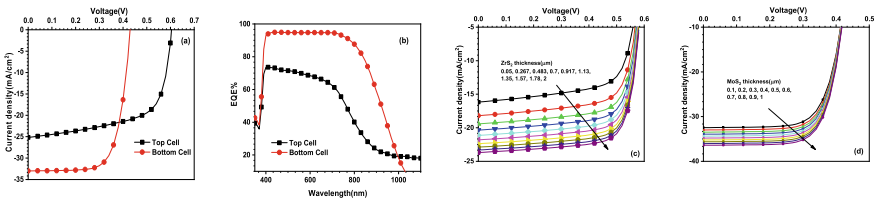


**Fig. 2** a Illuminated J-V curve b EQE curve c J-V characteristics with ZrS<sub>2</sub> thickness and d MoS<sub>2</sub> thickness variation of standalone top and bottom cells

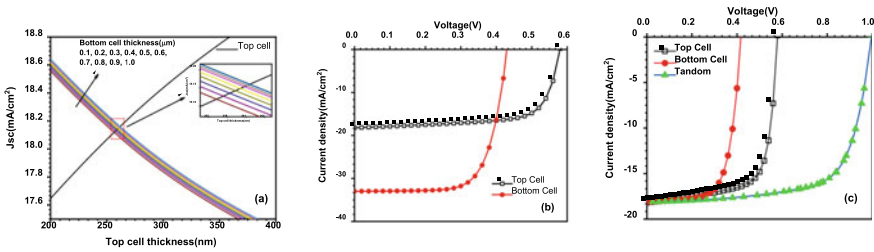


**Fig. 3** a Short circuit current density for top and bottom cells at different thickness of ZrS<sub>2</sub> and MoS<sub>2</sub>, b J-V curve of standalone and c under current matching conditions

thickness was then used to illuminate the bottom subcell (Fig. 1). Two terminal monolithic tandem solar cell configurations can be considered as two diodes connected in series. For overall tandem design the short circuit current in both the diodes should be same and open circuit voltage drop should be the sum of open circuit voltages in both the diodes. Therefore, the cell with lower  $J_{sc}$  is the limiting cell for overall tandem design [8]. In order to ensure flow of maximum  $J_{sc}$  through tandem design, a current matching condition has been used. Figure 3a shows the  $J_{sc}$  for top and bottom cells at different thickness of ZrS<sub>2</sub> and MoS<sub>2</sub> for current matching. Top cell has been illuminated under AM1.5 spectrum for ZrS<sub>2</sub> thickness varying in the range 0.05–2 μm in ten equal steps. At each thickness filtered spectrum is calculated which is used to illuminate the bottom cell. For every top cell thickness, bottom cell thickness (MoS<sub>2</sub>) has been varied from 0.1 to 1 μm in 10 equal steps. The current for the top and the bottom cell has been matched best at ZrS<sub>2</sub> thickness of 0.267 μm and MoS<sub>2</sub> thickness of 0.2 μm. At this thickness short circuit current density of 18.20 mAcm<sup>-2</sup> and 18.12 mAcm<sup>-2</sup> for top and bottom subcells has been obtained, respectively. Figure 3b shows the J-V curve of top and bottom cells illuminated under AM1.5 spectrum at optimized thickness and Fig. 3c shows the J-V curves under current matching conditions. The tandem solar cell characteristics have been plotted by adding the calibrated J-V curves obtain for top and bottom subcells. The open circuit voltage obtained is the sum of open circuit voltages from top and bottom cells, 0.9966 V and the short circuit current density is same. Efficiency of modelled tandem cell is 12.54% which is higher than top (7.43%) and bottom cells (8.44%) under current matching conditions.

## 4 Conclusion

Numerical simulations based on SCAPS simulating tool have been performed to design ZrS<sub>2</sub>/CZTS/MoS<sub>2</sub>/Si tandem solar cell. Initially, top ZrS<sub>2</sub>/CZTS solar cell has been calibrated to achieve efficiency of 9.72% and bottom MoS<sub>2</sub>/Si solar cell has been calibrated to achieve efficiency of 10.05% under standalone conditions. Both the solar cells were optimized by varying ZrS<sub>2</sub> and MoS<sub>2</sub> thickness in the range

0.05–2  $\mu\text{m}$  and 0.1–1  $\mu\text{m}$ , respectively, to obtain best current matching thickness. The short circuit current has been matched at 0.267 and 0.2  $\mu\text{m}$  thickness of  $\text{ZrS}_2$  and  $\text{MoS}_2$ , respectively. At equal currents the open circuit voltages of top and bottom subcells has been summed to obtain the open circuit voltage of overall tandem design. PV parameters for tandem solar cell are 18.12  $\text{mAcm}^{-2}$  ( $J_{sc}$ ), 0.9966 V ( $V_{oc}$ ), 69.43% (FF) and 12.54% ( $\eta$ ).

**Acknowledgements** Ms Shubhra Gupta is grateful to The Principal, Sri Venkateswara College, University of Delhi for encouraging to pursue the research work. The authors wish to thank Dr. M. Burgelman's group of Electronics and Information Systems (ELIS) University of Gent for the SCAPS-1D program tool.

## References

1. De Vos A (1980) Detailed balance limit of the efficiency of tandem solar cells. *J Phys D Appl Phys* 13(5):839–846
2. Burgelman M, Decock K, Niemegeers A, Verschraegen J, Degraeve S (2018) SCAPS manual. University of Ghent, Ghent, Belgium
3. Hamada M, Matsuura K, Sakamoto T, Muneta I, Hoshii T, Kakushima K, Tsutsui K, Wakabayashi H (2019) High hall-effect mobility of large-area atomic-layered polycrystalline  $\text{ZrS}_2$  film using UHV RF magnetron sputtering and sulfurization. *IEEE J Electron Devices Soc* 7:1258–1263
4. Moustafa M, Zandt T, Janowitz C, Manzke R (2009) Growth and band gap determination of the  $\text{ZrS}_x\text{Se}_{2-x}$  single crystal series. *Phys Rev B Condens Matter Mater Phys* 80(3):035206–035212
5. Cui Y, Zhou Z, Li T, Wang K, Li J, Wei Z (2019) Versatile crystal structures and (opto)electronic applications of the 2d metal mono-, di-, and tri-chalcogenide nanosheets. *Adv Funct Mater* 29(24):1900040–1900073
6. Gupta S, Shishodia G, Shishodia PK (2022) Computational analysis to study the effect of selenization on  $\text{ZrS}_2/\text{CZTS}$  heterostructure performance. *Eng Res Express* 4(3):035026–035038
7. Chaudhary R, Patel K, Sinha RK, Kumar S, Tyagi PK (2016) Potential application of mono/bi-layer molybdenum disulfide ( $\text{MoS}_2$ ) sheet as an efficient transparent conducting electrode in silicon heterojunction solar cells. *J Appl Phys* 120(1):013104–013114
8. Burdick J, Glatfelter T (1986) Spectral response and I–V measurements of tandem amorphous-silicon alloy solar cells. *Solar Cells* 18(3):301–314

# Interaction of NO Gas Molecules with the Edges of Armchair ZnO Nanoribbons for Designing Nanosensors



Kumar Ravindra, Rakesh Ajay Kumar, Govindan Anil,  
and Jaiswal Neeraj Kumar

**Abstract** The search of novel materials for designing upcoming sensors needs special attention to continue our journey of advanced sensor developments. With this quest, in current work, we discussed the adsorption and interaction of toxic gas (NO) molecules with the extremity of armchair ZnO nanoribbons (AZnONR) in various possible scenarios. Observations indicated that NO-molecule prefers to be attached at the nanoribbon edges via N-side. A stable chemical bond was formed to mediate the bonding between the host ribbon and the guest molecule. The calculated electronic band gap of H-passivated AZnONR are reciprocal to the ribbon size and varies from 3.32 to 2.27 eV corresponding to different widths. All the nanoribbons maintain their perfect planar geometry after NO-adsorption. Interestingly, the adsorption of NO-molecules has profound effect on the electronic properties of AZnONR. A direct to indirect band gap conversion as well as realization of semi-metallic and pure metallic character has been obtained depending upon the adsorption configuration of NO-molecules. Our findings indicate that AZnONR could be a potential material to adsorb and identify the existence of NO gas molecules via change in the electronic properties.

**Keywords** ZnO · Nanoribbon · Adsorption · Electronic structure · Sensing

## 1 Introduction

The nano-materials have been the centre of attraction for the evolution of efficient and efficient sensing devices [1, 2]. III–V nitride-based semiconductor nanoribbons have been investigated for the sensing of various air pollutant gases [3]. Srivastava et al. [4] have demonstrated that antimonene nanoribbons could be used for the

---

K. Ravindra (✉) · R. A. Kumar · G. Anil  
Department of Physics, M.M.H. College, Ghaziabad, Uttar Pradesh 201001, India  
e-mail: [rvndrgzb85@gmail.com](mailto:rvndrgzb85@gmail.com)

J. N. Kumar  
2-D Materials Research Laboratory, Discipline of Physics, PDPM Indian Institute of Information Technology, Design and Manufacturing, Jabalpur, Madhya Pradesh 482005, India

© The Author(s), under exclusive license to Springer Nature Singapore Pte Ltd. 2023  
Z. H. Khan et al. (eds.), *Recent Advances in Nanotechnology*, Springer Proceedings in Materials 28, [https://doi.org/10.1007/978-981-99-4685-3\\_23](https://doi.org/10.1007/978-981-99-4685-3_23)

169

detection of CO and NO-molecules. In another report, carbon doped BN nanosheets were found to have promising candidature towards detecting NO as well as NO<sub>2</sub> molecules [5]. ZnO is another promising material which exhibits graphene like planar and hexagonal structure. A monolayer of ZnO consists of Zn and O atoms in 50:50 ratios. Topsakal et al. [6] investigated ZnO material thoroughly considering its bulk, hexagonal planar as well as one-dimensional nanoribbons. Inspired by its perfect planar structure which gives it a higher surface to volume ratio, few efforts were also made to study its nanosheets and nanoribbons towards nanosensor applications [7]. However, mainly zigzag edged ZnONR were explored in this direction [8]. It inspired us to investigate the effects of armchair edges of ZnO nanoribbons towards the sensing of targeted hazardous gas molecules. Thus, in the present work, AZnONR have been studied to absorb and detect the presence of oxide-based (CO and NO) toxic gases.

## 2 Computational Details

The supercell-based approach under the flagship of density functional theory (DFT) was adopted to perform the following calculations. The exchange–correlation effects in the calculations are derived by using the generalized gradient approximation (GGA). The energy mesh cut off equal to 70 Ry has been selected with the k-point sampling of  $1 \times 1 \times 50$ . During the total energy minimization, all the atoms were relaxed and the process was completed while obtaining the force criteria of 0.05 eV/Å. The effect of ribbon width, i.e. dimensionality was taken care by choosing the nanoribbons of width  $N_a = 5, 7, 9$ . However, to be concise, the nanoribbons of largest width (i.e.  $N_a = 9$ ) has been taken as the representative case for displaying the findings. The considered geometries of NO-adsorbed AZnONR are depicted in Fig. 1.

## 3 Results and Discussion

Findings revealed that stable chemical bonds were established between the adsorbed NO-molecules in all the configurations except NO-AZnONR-NO and AZnONR-NO where the weak van der Waals bonding is involved. The bond strength between the host AZnONR and the guest NO-molecule has been assessed in terms of the adsorption energy ( $E_{ad}$ ) [9]

$$E_{ad} = [E_{Total} - E_{Bare} - E_H - E_{NO}] \quad (1)$$

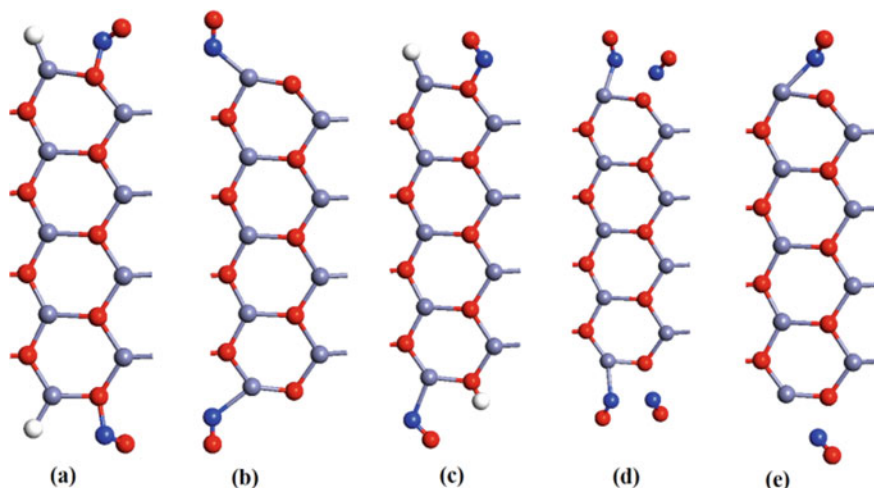


**Fig. 1** The optimized geometries of NO-molecule adsorption on AZnONR in a H-AZnONR-NO, b NO-AZnONR, c NO-AZnONR-H, d NO-AZnONR-NO, and e AZnONR-NO configurations. The grey, red, blue, and white spheres represent Zn, O, N, and H atoms, respectively

Here  $E_{\text{Total}}$ ,  $E_{\text{Bare}}$ ,  $E_{\text{H}}$ , and ( $E_{\text{NO}}$ ), respectively, represents total energies of the functionalized nanoribbons, bare ribbon, isolated H atom, and the NO-molecule. The obtained magnitudes of the  $E_{\text{ad}}$  values for considered configurations of NO-molecule(s) adsorption are shown in the Table 1.

It is revealed that adsorption results in large negative values of  $E_{\text{ad}}$  which signifies the exothermic nature as well as the energetic feasibility of NO-molecule adsorption. Furthermore, it is noticed here that single edge NO-molecule adsorption (while opposite edge of the ribbon is bare) is less favoured (energetically) as compared to other structures. On the other hand, NO-adsorption at either of the (Zn or O) edge while the opposite edge is H-passivated results in the maximum energetic stability. Furthermore, a small buckling is developed in the structures causing some of the constituent atoms to displace out of the ribbon's plane.

The largest negative  $E_{\text{F}}$  is reported for both edges NO-molecules adsorption, i.e. NO-AZnONR-NO among all other structures. It indicates that effect of increasing the concentration of adsorbed NO-molecules is to shift the  $E_{\text{F}}$  downward which is comparable to inducing p-type character as compared to bare AZnONR. It is well known that AZnONR exhibit a moderate electronic band gap ( $E_{\text{g}}$ ) [6] which is reciprocal to the nanoribbon width. The semiconducting behavior is a common feature in the band structures of bare as well as pristine (H-passivated) AZnONR. Our calculated values of  $E_{\text{g}}$  varies from 0.77 to 1.89 eV (2.07 to 3.32 eV) for bare (H-passivated) ribbons.

The obtained band structures have been presented in Fig. 2 for  $N_{\text{a}} = 9$ . It is noticed that among all the structures, H-AZnONR-NO exhibits highest value of  $E_{\text{g}}$ . Furthermore, all ribbons in NO-AZnONR and AZnONR-NO configurations exhibit

**Table 1** The calculated  $E_{\text{ad}}$ , electronic band gap ( $E_{\text{g}}$ ) and the Fermi energy ( $E_{\text{F}}$ ) as a function of ribbon width for the adsorption of NO-molecule on AZnONR. M indicates the metallic nature

Widths	H-AZnONR-NO			NO-AZnONR			NO-AZnONR-H			NO-AZnONR-NO			AZnONR-NO		
	$E_{\text{ad}}$	$E_{\text{g}}$	$E_{\text{F}}$	$E_{\text{ad}}$	$E_{\text{g}}$	$E_{\text{F}}$	$E_{\text{ad}}$	$E_{\text{g}}$	$E_{\text{F}}$	$E_{\text{ad}}$	$E_{\text{g}}$	$E_{\text{F}}$	$E_{\text{ad}}$	$E_{\text{g}}$	$E_{\text{F}}$
5	-10.79	2.10	-3.25	-2.04	M	-3.62	-11.38	M	-3.48	-5.73	0.52	-3.84	-2.35	M	-3.12
7	-11.62	2.01	-3.24	-2.45	M	-3.94	-12.65	0.10	-3.61	-7.30	0.20	-3.86	-2.80	M	-3.16
9	-11.54	2.00	-3.14	-2.78	M	-3.97	-12.22	0.23	-3.26	-6.99	0.13	-3.89	-2.51	M	-3.28

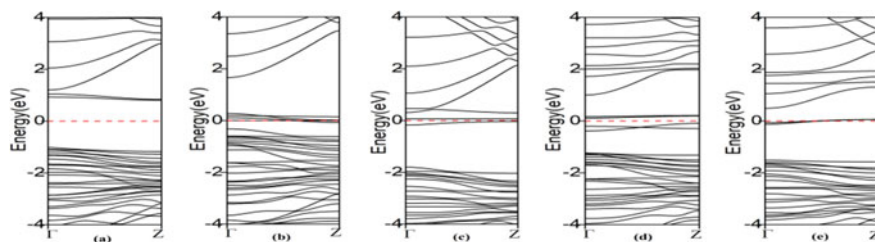


**Fig. 2** The obtained band structures for NO-molecule adsorption on AZnONR in **a** H-AZnONR-NO, **b** NO-AZnONR, **c** NO-AZnONR-H, **d** NO-AZnONR-NO, and **e** AZnONR-NO configurations. The dashed line at 0 eV represent the Fermi level

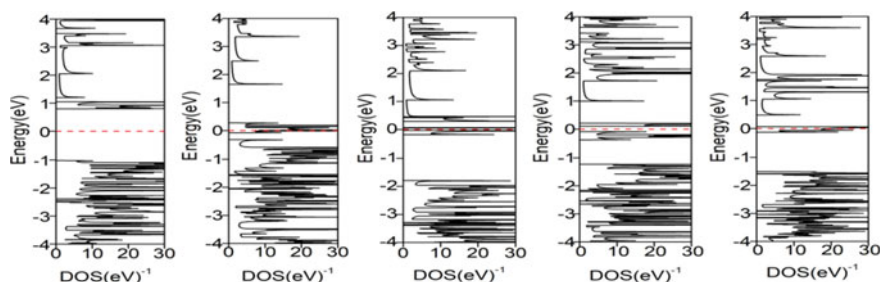


**Fig. 3** The obtained DOS profiles for the NO-molecule adsorption on AZnONR in **a** H-AZnONR-NO, **b** NO-AZnONR, **c** NO-AZnONR-H, **d** NO-AZnONR-NO, and **e** AZnONR-NO configurations. The dashed lines at 0 eV represent the Fermi level

metallic characteristic for all the ribbon widths. In contrast to this, a small magnitude of  $E_g$  has been observed in rest of the two (NO-AZnONR-H and NO-AZnONR-NO) structures. The similar electronic behavior is also confirmed by the corresponding DOS profiles as shown in the Fig. 3. The absence of electronic states across the  $E_F$  corresponds to the magnitude of  $E_g$  of the same configuration.

## 4 Conclusion

The effect of armchair edges of ZnONR has been studied within DFT-based calculations for the detection of NO gas molecules. It was found that the molecules prefer to bond with the nanoribbons via N sides at both the edges of AZnONR. The adsorption on AZnONR takes place via chemical bonding. However, for adsorption on NO-AZnONR-NO and AZnONR-NO configurations, the geometry stabilizes only after detachment of NO-molecule from O-side of the nanoribbon edge. A drastic change in the magnitude of  $E_g$  has been noticed as a result of NO-molecule adsorption. As the calculated  $E_g$  is found sensitive to the presence of NO-molecules, AZnONR could be useful for the advancement of upcoming advanced nano-sensing devices.



## 5 Declaration of Interest Statement

The authors declare that they have no conflict of interests.

**Data Availability** The article includes all of the data required to comprehend and support the study's findings.

## References

1. Srivastava P, Abhishek, Sharma V, Jaiswal NK (2020) First-principles investigation of anti-monene nanoribbons for sensing toxic NO<sub>2</sub> gas. *Phys Status Solidi (b)* 257(9):2000034
2. Zhang R, Fu D, Ni J, Sun C, Song S (2019) Adsorption for SO<sub>2</sub> gas molecules on B, N, and Al doped MoS<sub>2</sub>: the DFT study. *Chem Phys Lett* 715:273–277
3. Yogi R, Jaiswal NK (2021) First-principle investigations of zigzag III-V nitride nanoribbons as CS<sub>2</sub> scavengers. *Appl Surf Sci* 545:148969
4. Srivastava P, Sharma V, Jaiswal NK (2020) First-principle insights of CO and NO detection via antimonene nanoribbons. *Appl Phys A* 126:1–19
5. Esrafil MD, Rad FA (2019) Carbon-doped boron nitride nanosheets as highly sensitive materials for detection of toxic NO and NO<sub>2</sub> gases: a DFT study. *Vacuum* 166:127–134
6. Topsakal M, Cahangirov S, Bekaroglu E, Ciraci S (2009) First-principles study of zinc oxide honeycomb structures. *Phys Rev B* 80(23):235119
7. Kumar R, Rakesh AK, Yogi R, Govindan A, Jaiswal NK (2022) First-principles study of CO adsorption on zigzag ZnO nanoribbons towards nanosensor application. *J Mol Graph Model* 116:108232
8. Kumar R, Rakesh AK, Govindan A, Jaiswal NK (2022) Spin dependent electronic properties of NO-adsorbed zigzag ZnO nanoribbons: a DFT study. *Materials science and engineering*. In: IOP conference series, vol 1248, p 012030
9. Yogi R, Jaiswal NK, Srivastava P (2020) First-principles study of sensing SO<sub>2</sub> adsorption on III–V nitride nanoribbons. *Mater Chem Phys* 242:122437

# Electrochemical UA Sensor Based on Spherical Shaped $\text{Co}_3\text{O}_4$ Nanostructures



Sakeena Masrat and Rafiq Ahmad

**Abstract** Herein, we report synthesis of spherical shaped cobalt oxide using low temperature solution method. The as-synthesized nanostructures were examined by FE-SEM and XRD. The yield of as-synthesized nanostructure was in abundant quantity and bears sphere like shape as observed from FE-SEM. The crystalline nature of the as-synthesized material was examined from the XRD spectra. The electrochemical properties of spherical shaped cobalt oxide were studied using cyclic voltammetry. To investigate the application of spherical shaped nanostructures, the pristine material was utilized to develop an enzymeless electrochemical sensor by using screen-printed carbon electrode. The fabricated electrochemical sensor showed better response toward uric acid (UA) detection. Under optimized conditions it shows high sensitivity and good linear range. The fabricated sensitive non-enzymatic UA sensor is expected to be beneficial for the detection of UA in real samples.

**Keywords** Spherical · Cobalt oxide · Non-enzymatic · Sensitive · Uric acid

## 1 Introduction

Uric acid (UA) is a normal by-product present in human fluids such as urine and serum. It is generated when the chemicals called as purine nucleotides (naturally occurring substances in the body) are disintegrated by the body. If the concentration of UA in the blood gets increased from the normal range it will cause different diseases like gout and other associated diseases like tumor-lysis syndrome, UA stone-formation, and diabetes, etc. [1–4]. However, if the concentration decreases from the normal level it will lead to hypo-uricemia, which in turn gives rise to chronic-kidney failure, multiple sclerosis, etc. [5–9]. Thus, the unusual presence of uric acid concentration in the body is dangerous. So early disease diagnosis and its treatment is highly demanded. For the sensing of UA various standard techniques are available

---

S. Masrat · R. Ahmad (✉)

Sensors Lab, Centre for Nanoscience and Nanotechnology, Jamia Millia Islamia, New Delhi 110025, India

e-mail: [rahmad5@jmi.ac.in](mailto:rahmad5@jmi.ac.in)

such as mass-spectrometry/chromatography [10], phosphotungstic acid reduction [11], and enzymatic technique [12]. The mass-spectrometry/chromatography is a good choice due to its large sensitivity and better reliability, but its major disadvantage is high cost of the instrument. The reduction of phosphotungstic acid is better as compared to other methods because its operation is simple and easy. But its use is limited due to its interference effects. The enzyme-based processes are highly specific but not appropriate choice because of their difficult enzyme immobilization methods, large cost of enzymes, low repeatability, and severe operating conditions [13]. As a result, the research focus has switched to enzyme free sensors, which include devices that employ novel properties of metal nanoparticles and their oxides.

For the estimation of quantitative parameters (like sensitivity, limit of detection, selectivity, and good response, etc.) electrochemical sensing methods are suitable over other techniques in analytical-chemistry. Size, minimum cost, high sensitivity, reliability, and eco friendliness are important factors which comes into play while one works with electrochemical sensors. Furthermore, these enzyme less sensors when modified with suitable nanostructures show unique capability and enhanced sensing performance for measuring particular analytes such as ascorbic acid, L-cysteine, dopamine, hydrazine, glucose, and uric acid [14–21]. Presently, these nanomaterial-based electrochemical sensors are becoming eye catching for researchers due to their reliability, stability, and minimum cost. This could be attributed due to their enhanced electro active sites and surface area [22, 23]. For this reason, metal and their oxides are in high demand due to their unique and novel properties.

In the past metal and their oxides were studied extensively for electrochemical applications. For example, zinc oxide, nickel oxide, manganese oxide, bismuth oxide, iron oxide, and cobalt oxide, etc. were used for the development of electrochemical sensors [24–30]. Among them cobalt oxide is a standard nanomaterial used for the construction of non-enzymatic electrochemical sensors because of its outstanding chemical durability, non-toxic in nature, minimum cost, simple and facile experimental process [31]. For example, recently, Ahmad et al. reported nanoberry like cobalt oxide ( $\text{Co}_3\text{O}_4$ ) nanostructures-based non-enzymatic uric acid sensor. The sensitivity calculated was  $206 \mu\text{A}\text{mM}^{-1} \text{cm}^{-2}$  with a range of linearity  $0.005\text{--}3 \mu\text{M}$  and a low limit of detection  $\sim 2.4 \text{ mM}$  [32]. Kogularasu et al. utilized polyhedron shaped  $\text{Co}_3\text{O}_4$  nanostructures for the construction of hydrogen peroxide sensor, which showed  $15 \text{ nM}$  limit of detection with a wide range and high sensitivity [33]. Zhang and Liu described the effect of  $\text{Co}_3\text{O}_4$  nanosheets for the enzyme less detection of glucose [34]. The measured limit of detection (LOD) and linear range for the glucose sensor was  $0.15 \mu\text{M}$  and  $1\text{--}50 \mu\text{M}$ , respectively. Kang et al. studied the effect of nano-wire shape like  $\text{Co}_3\text{O}_4$  nanostructures for the glucose sensor [35]. The sensor constructed showed excellent sensitivity of  $300.8 \mu\text{A}\text{mM}^{-1} \text{cm}^{-2}$ , a LOD of  $5 \mu\text{M}$  with a dynamic linear-range of  $5.0\text{--}570 \mu\text{M}$ . Mondal et al. fabricated an enzymeless glucose sensor by using several nanostructures of cobalt oxide (like nano-flowers, porous nano-rods, and spherical nanoparticle) [36]. Chang et al. utilized several structures of cobalt oxide for example, nano-wire, lump, and flower like structures for the detection of lactic acid [37]. The sensing performance of their sensor showed good linear range of  $0.1 \text{ mM}$  to  $5.5 \text{ mM}$  using amperometry technique.

The work presented here reports the synthesis of spherical shaped-like Co<sub>3</sub>O<sub>4</sub> nanostructures via a low-cost-based hydrothermal method. Various material characterization (for example, FE-SEM and XRD) analysis is done in order to examine the structure and surface morphology of as-prepared sample. The as-synthesized nanostructure was fixed onto the working electrode (SPE) to develop an enzyme free electrochemical sensor for the detection of UA. The non-enzymatic electrochemical activity of as-prepared nanostructure is investigated using CV technique.

## 2 Materials and Methods

### 2.1 Materials

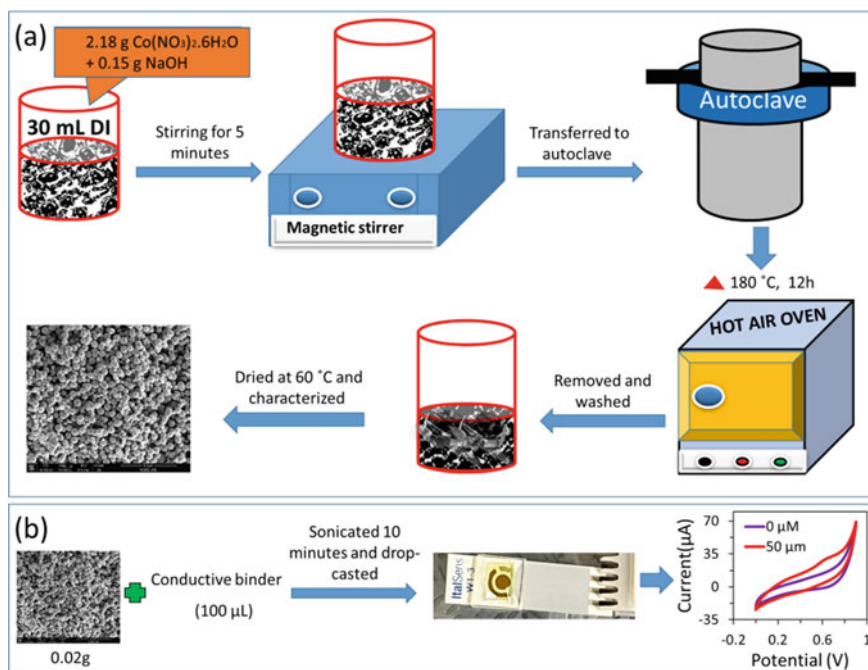
Cobalt nitrate hexahydrate (98%), sodium hydroxide pellets (97%), uric acid (99%), potassium hexacyanoferrate (III) (K<sub>3</sub>Fe(CN)<sub>6</sub>)<sup>3-/4-</sup> (≥99.0%), KCl (99.0–100.5%) were brought from Sigma-Aldrich. All chemicals used were of analytical grade. Phosphate buffer saline with pH = 7.4, an electrolyte were prepared by combining sodium hydrogen, sodium chloride, and potassium dihydrogen phosphate. All the solutions were prepared by making use of DI water.

### 2.2 Growth of Spherical Shaped-Like Co<sub>3</sub>O<sub>4</sub> Nanostructures

A low-temperature solution-based process has been employed for the synthesis of Co<sub>3</sub>O<sub>4</sub> nanostructures. Precisely, 2.18 g of Co(NO<sub>3</sub>)<sub>2</sub> · 6H<sub>2</sub>O and 0.15 g of NaOH pellets were dissolved in 30 mL of ultra-pure water. In order to get a homogenous solution, the 30 mL prepared solution was magnetic stirred for 5 min at 400 rpm. The final homogeneous solution was then transferred into a Teflon box maintained at a temperature of 180 °C for 12 h and then allowed to cool naturally at room temperature. In order to remove the impurities from the resulted black precipitate, the collected sample was washed with ultra-pure water and ethanol multiple times, respectively. The obtained sample was vacuum dried at 60 °C overnight. The detailed synthesis process is represented in Scheme 1a.

### 2.3 Uric Acid Sensor Fabrication and Electrochemical Analysis

To prepare suspension of cobalt oxide nanostructures, first 0.02 g of cobalt oxide nanostructure is mixed with 100 μL of conductive binder. Secondly, the resulted suspension is ultrasonicated for 5 min in order to get a uniform slurry. Finally, an



**Scheme 1** Detailed schematic representation of the spherical shaped  $\text{Co}_3\text{O}_4$  nanostructure synthesis (a) and enzyme free UA sensor fabrication (b)

optimized value of six  $\mu\text{L}$  of slurry is drop-casted onto the SP electrode and kept for drying in oven for six hours. The as-prepared modified electrode was denoted as spherical shaped like- $\text{Co}_3\text{O}_4$  nanostructures/binder/SPE as shown in Scheme 1b.

## 2.4 Characterizations

The surface morphology of the spherical shaped  $\text{Co}_3\text{O}_4$  nanostructures was analyzed using FE-SEM. An X-ray diffractometer (Rigaku) was utilized to characterize the structure of the as-synthesized  $\text{Co}_3\text{O}_4$  nanostructures, where  $\text{Cu}_\alpha\text{K}_\alpha$  X-ray radiation with wavelength of 1.5418 Å were used. All the electrochemical analysis were done at room temperature using a portable and compact “PalmSens4” Potentiostat. The  $\text{Co}_3\text{O}_4$  spherical shaped/SPE sensor construction was optimized using the cyclic voltammetry (CV) technique. The cyclic voltammetry analysis was done in the electrochemical probe [5 mM potassium ferricyanide ( $[\text{K}_3\text{Fe}(\text{CN})_6]^{3-/4-}$  and 100 mM potassium chloride)] solution. The sensing of UA was evaluated in phosphate buffer saline (PBS) solution with pH of 7.4 using cyclic voltammetry in a fixed range of potential.

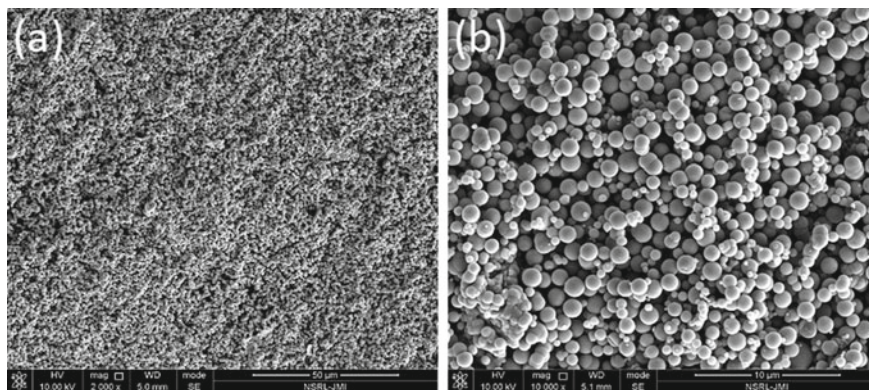


**Fig. 1** FE-SEM micrographs: low magnifications (a) and high magnifications (b) of spherical shaped cobalt oxide nanostructures

### 3 Results and Discussion

#### 3.1 Characterizations of $\text{Co}_3\text{O}_4$ Nanostructures

The surface morphology of as-synthesized spherical shaped  $\text{Co}_3\text{O}_4$  nanostructures is shown in Fig. 1. The high-resolution SEM images reveal the successful formation of spherical shaped  $\text{Co}_3\text{O}_4$  nanostructures (Fig. 2). The low magnification SEM images confirms that the prepared product is obtained in bulk with uniform shape as shown in Fig. 1a. The high-resolution SEM images shows that the obtained structure bears sphere like shape as can be seen in Fig. 1b. The structural analysis of sphere shaped like nanostructures of cobalt oxide is shown in the XRD pattern (Fig. 3). From the diffraction peaks the nanostructures synthesized are crystalline in nature without any additional peak present which confirms the purity of the as-synthesized material. The highest indexed peak [311] is observed at  $\theta = 36.5^\circ$ . All the observed peaks are indexed properly and matches well with the JCPDS card no. 42-1467 [38].

#### 3.2 Electrochemical Studies of $\text{Co}_3\text{O}_4$ Nanostructures/SPE Electrode

The electrochemical behavior of as-synthesized nanostructures is done by cyclic voltammetry (CV). The CV plots were obtained at various amounts of nanomaterial modifications of screen-printed electrode with spherical shaped cobalt oxide nanostructures in 0.05 mM  $[\text{K}_3\text{Fe}(\text{CN})_6]^{3-/4-}$  with 100 mM potassium chloride. The cyclic voltammetry response curve of modified electrode ( $\text{Co}_3\text{O}_4/\text{SPE}$ ) with 2, 4, and 6  $\mu\text{L}$  of obtained slurry is shown in Fig. 3a. The better electrical conductivity

**Fig. 2** XRD spectra of spherical shaped  $\text{Co}_3\text{O}_4$  nanostructures

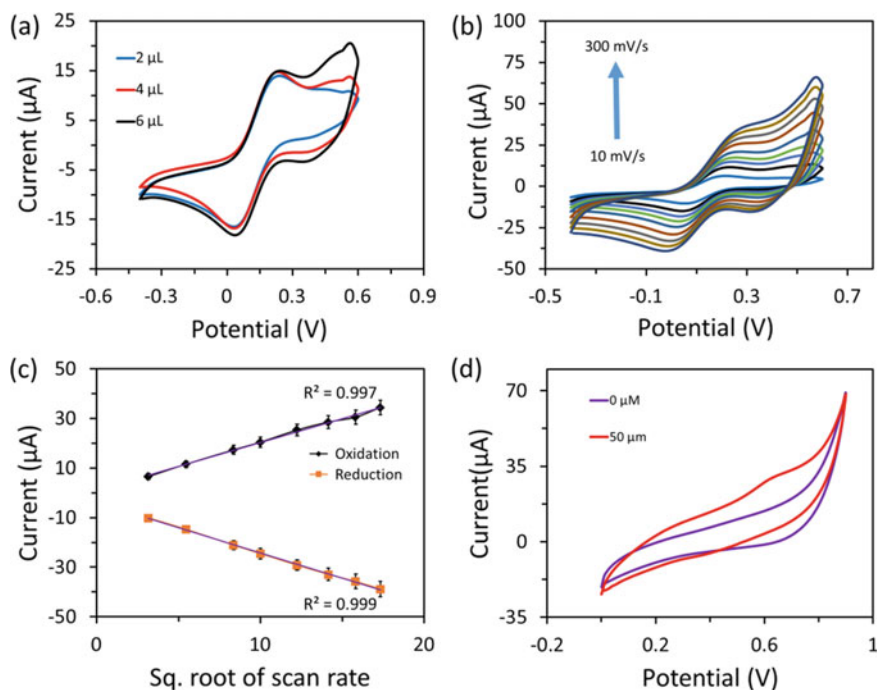
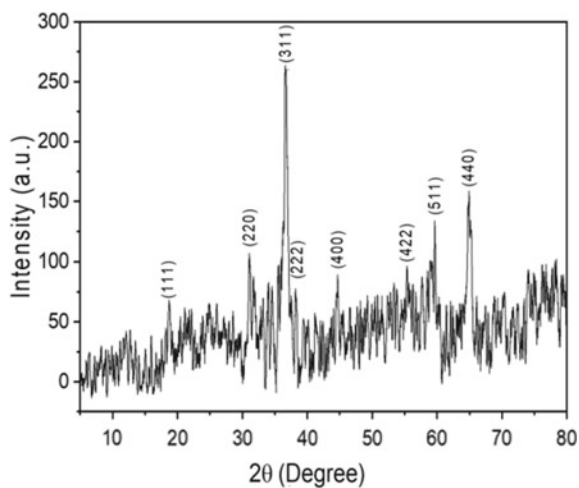


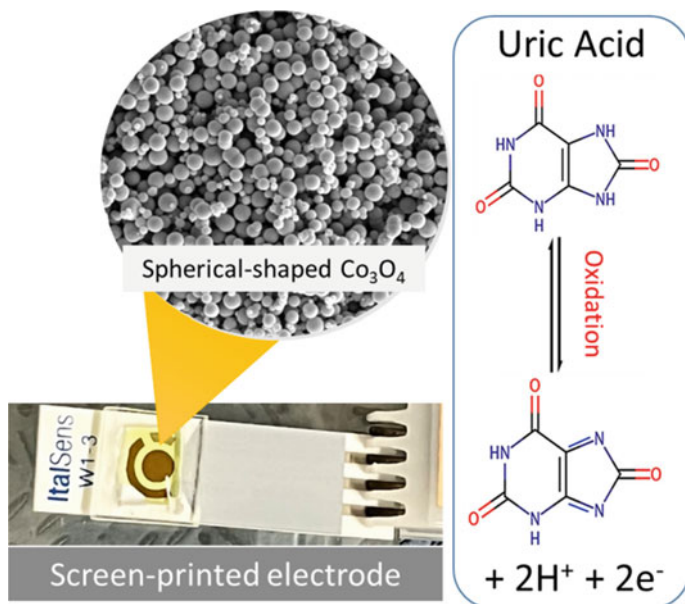
**Fig. 3** **a** CVs of 2–6  $\mu\text{L}$  slurry modified screen-printed electrode sensors, **b** CVs at scan rate of 6  $\mu\text{L}$  slurry modified screen-printed electrode sensors, **c** graph showing the  $I_p$  versus sq. root of scan rate, and **d** CVs with 0  $\mu\text{M}$  and with 50  $\mu\text{M}$  uric acid



was measured by using 6  $\mu\text{L}$  fixed onto the SPE. Then, the 6  $\mu\text{L}$  fixed onto the SPE was utilized for further analysis. Further the electrocatalytic phenomenon at the 6  $\mu\text{L}$  Co<sub>3</sub>O<sub>4</sub> nanospheres/SPE was evaluated at different scan rate of CV measurements. With the increase in scan rate there was a corresponding increase in the current response as shown in Fig. 3b. Figure 3c represents the peak value of current versus square root of scan rate which is obtained from CV response. This plot represents that the electron transfer phenomenon occurs via surface diffusion process [39, 40].

### 3.3 Detection of UA Using Cyclic Voltammetry

To evaluate the sensing performance of the modified Co<sub>3</sub>O<sub>4</sub> nanospheres/SPE uric acid sensor, the electro catalytic performance was examined in PBS solution. Figure 3d shows the comparison of cyclic voltammetric response in the presence of 0 and 50  $\mu\text{M}$  uric acid in PBS solution with scan rate of 50 mV/s. A clear oxidation peak at 0.69 V is shown in the graph which corresponds to the uric acid [41]. A possible uric acid detection is shown in Scheme 2.



**Scheme 2** Electrochemical oxidation of UA on the modified electrode



## 4 Conclusion

In conclusion, we successfully synthesized the spherical shaped cobalt oxide nanostructures in abundant quantity using hydrothermal method. The morphology and crystallinity were tested using FE-SEM and XRD analysis tools. The obtained spherical shaped cobalt oxide nanostructures were fixed onto the modified electrode of SPE to construct non-enzymatic UA sensor. The fabricated electrochemical sensor showed good response toward uric acid (UA) detection. The fabricated sensitive enzyme free UA sensor is expected to be beneficial for the sensing of uric acid in buffer and real samples.

**Acknowledgements** R. Ahmad gratefully acknowledges the Ramalingaswami Fellowship Award and research funding grant (BT/RLF/Re-entry/28/2018) from the Department of Biotechnology (DBT), Government of India. S.M. would like to thank Prime Minister's Research Fellows (PMRF) award from the Ministry of Education, Government of India.

### **Declaration of Interest Statement**

The authors declare that they have no conflict of interests.

## References

1. Rock KL, Kataoka H, Lai JJ (2013) Uric acid as a danger signal in gout and its comorbidities. *Nat Rev Rheumatol* 9:13–23
2. Evan AP, Worcester EM, Coe FL, Williams J, Lingeman JE (2015) Mechanisms of human kidney stone formation. *Urolithiasis* 43:19–32
3. Andrea V, Krc Mova LK, Melichar B, Svec F (2021) Non-invasive determination of uric acid in human saliva in the diagnosis of serious disorders. *Clin Chem Lab Med* 59:797–812
4. Soltani Z, Rasheed K, Kapusta DR, Reisin E (2013) Potential role of uric acid in metabolic syndrome, hypertension, kidney injury, and cardiovascular diseases: is it time for reappraisal. *Curr Hypertens Rep* 15:175–181
5. Alderman M, Aiyer KJV (2004) Uric acid: role in cardiovascular disease and effects of losartan. *Curr Med Res Opin* 20(3):369–379
6. Mallat SG, Kattar SA, Tanius BY, Jurjus A (2016) Hyperuricemia, hypertension, and chronic kidney disease: an emerging association. *Hypertens Rep* 18:74
7. King C, Lanaspa MA, Jensen T, Tolan DR, Sanchez-Lozada LG, Johnson RJ (2018) Uric acid in chronic kidney disease. *Contrib Nephrol* 192:88–102
8. El Ridi R, Tallima H (2017) Physiological functions and pathogenic potential of uric acid: a review. *J Adv Res* 8:487–493
9. Dobson R, Giovannoni G (2018) Multiple sclerosis—a review. *Eur J Neurol* 26:27–40
10. Perelló J, Sanchis JP, Grases F (2005) Determination of uric acid in urine, saliva and calcium oxalate renal calculi by high-performance liquid chromatography/mass spectrometry. *J Chromatogr B* 824:175–180
11. Alex S, Raja V (2022) Phosphotungstic acid capped gold nanoparticles for spectrophotometric determination of uric acid in diagnostics of gout. *J Anal Chem* 77:1267–1273
12. Block WD, Geib NC (1947) An enzymatic method for the determination of uric acid in whole blood. *J Biol Chem* 168:747–756
13. Pandey I, Bairagi PK, Verma N (2018) Electrochemically grown polymethylene blue nanofilm on copper-carbon nanofiber nanocomposite: an electrochemical sensor for creatinine. *Sensors Actuators B Chem* 277:562–570

14. Masrat S, Nagal V, Khan M, Moid I, Alam S, Bhat KS, Khosla A, Ahmad R (2022) Electrochemical ultrasensitive sensing of uric acid on non-enzymatic porous cobalt oxide nanosheets-based sensor. *Biosensors* 12(12):1140
15. Khan M, Nagal V, Masrat S, Tuba T, Tripathy N, Parvez MK, Al-Dosari MS, Khosla A, Furukawa H, Hafiz AK, Ahmad R (2022) Wide-linear range cholesterol detection using Fe<sub>2</sub>O<sub>3</sub> nanoparticles decorated ZnO nanorods based electrolyte-gated transistor. *J Electrochem Soc* 169:027512
16. Khan M, Nagal V, Nakate UT, Khan MR, Khosla A, Ahmad R (2021) Engineered CuO nanofibers with boosted non-enzymatic glucose sensing performance. *J Electrochem Soc* 168:067507
17. Ahmad R, Khan M, Mishra P, Jahan N, Ahsan MA, Ahmad I, Khan MR, Watanabe Y, Ali SM, Furukawa H, Khosla A (2021) Engineered hierarchical CuO nanoleaves based electrochemical nonenzymatic biosensor for glucose detection. *J Electrochem Soc* 168:017501
18. Ahmad R, Khan M, Tripathy N, Khan MIR, Khosla A (2020) Hydrothermally synthesized nickel oxide nanosheets for non-enzymatic electrochemical glucose detection. *J Electrochem Soc* 167:107504
19. Ahmad R, Bedük T, Majhi SM, Salama KN (2019) One-step synthesis and gold nanoparticle decoration of nickel oxide nanosheets for hydrazine sensing application. *Sens Actuators B Chem* 286:139–147
20. Ahmad R, Mahmoudi T, Ahn M-S, Yoo J-Y, Hahn Y-B (2018) Fabrication of sensitive non-enzymatic nitrite sensor using silver-reduced graphene oxide nanocomposite. *J Colloid Interface Sci* 516:67–75
21. Jung D-U-J, Ahmad R, Hahn Y-B (2018) Nonenzymatic flexible field-effect transistor based glucose sensor fabricated using NiO quantum dots modified ZnO nanorods. *J Colloid Interface Sci* 512:18–21
22. Hassan MH, Vyas C, Grieve B, Bartolo P (2021) Recent advances in enzymatic and non-enzymatic electrochemical glucose sensing. *Sensors* 21:4672
23. Majdinasab M, Daneshi M, Marty JL (2021) Recent developments in non-enzymatic (bio) sensors for detection of pesticide residues: focusing on antibody, aptamer and molecularly imprinted polymer. *Talanta* 232:122397
24. Hernández-Ramírez D, Mendoza-Huizar LH, Galán-Vidal CA, Aguilar-Lira GY, Álvarez-Romero GA (2021) Review-Trends on the development of non-enzymatic electrochemical sensors modified with metal-oxide nanostructures for the quantification of uric acid. *J Electrochem Soc* 168(5):057522
25. Ahmad R, Ahn MS, Hahn YB (2017) Fabrication of a non-enzymatic glucose sensor field-effect transistor based on vertically-oriented ZnO nanorods modified with Fe<sub>2</sub>O<sub>3</sub>. *Electrochem Commun* 77:107–111
26. Ahmad R, Tripathy N, Khan MY, Bhat KS, Ahn MS, Hahn YB (2016) Ammonium ion detection in solution using vertically grown ZnO nanorod based field-effect transistor. *RSC Adv* 6:54836–54840
27. Ahmad R, Mahmoudi T, Ahn M-S, Yoo J-Y, Hahn Y-B (2018) Recent advances in nanowires-based field-effect transistors for biological sensor applications. *Biosens Bioelectron* 100:312–325
28. Shrestha BK, Ahmad R, Mousa HM, Kim IG, Kim JI, Neupane MP, Park CH, Kim CS (2016) High-performance glucose biosensor based on chitosan-glucose oxidase immobilized polypyrrole/Nafion/functionalized multi-walled carbon nanotubes bio-nanohybrid film. *J Colloid Interface Sci* 482:39–47
29. Khan R, Ahmad R, Rai P, Jang LW, Yun JH, Yu YT, Hahn YB, Lee IH (2014) Glucose-assisted synthesis of Cu<sub>2</sub>O shuriken-like nanostructures and their application as nonenzymatic glucose biosensors. *Sens Actuators B Chem* 203:471–476
30. Masrat S, Poolla R, Dipak P, Zaman MB (2021) Rapid hydrothermal synthesis of highly crystalline transition metal (Mn & Fe) doped CuSe nanostructures: applications in wastewater treatment and room temperature gas sensing. *Surfaces and Interfaces* 23:100973

31. Dubey S, Kumar J, Kumar A, Sharma YC (2018) Facile and green synthesis of highly dispersed cobalt oxide ( $\text{Co}_3\text{O}_4$ ) nano powder: characterization and screening of its eco-toxicity. *Adv Powder Technol* 29:2583–2590
32. Nagal V, Tuba T, Kumar V, Alam S, Ahmad A, Alshammari MB, Hafiz AK, Ahmad R (2022) A non-enzymatic electrochemical sensor composed of nano-berry shaped cobalt oxide nanostructures on a glassy carbon electrode for uric acid detection. *New J Chem* 46:12333
33. Kogularasu S, Govindasamy M, Chen S-M, Akilarasan M, Mani V (2017) 3D graphene oxide-cobalt oxide polyhedrons for highly sensitive non-enzymatic electrochemical determination of hydrogen peroxide. *Sens Actuators B* 253:773–783
34. Zhang H, Liu S (2017) A combined self-assembly and calcination method for preparation of nanoparticles-assembled cobalt oxide nanosheets using graphene oxide as template and their application for non-enzymatic glucose biosensing. *J Colloid Interface Sci* 485:159–166
35. Kang L, He D, Bie L, Jiang P (2015) Nanoporous cobalt oxide nanowires for non-enzymatic electrochemical glucose detection. *Sens Actuators B* 220:888–894
36. Mondal S, Madhuri R, Sharma PK (2017) Probing the shape specific electrochemical properties of cobalt oxide nanostructures for their application as selective and sensitive nonenzymatic glucose sensors. *J Mater Chem C* 5:6497–6505
37. Chang AS, Memon NN, Amin S, Chang F, Aftab U, Abro MI, Chandio A, Shah AA, Ibupoto MH, Ansari MA, Ibupoto ZH (2019) Facile non-enzymatic lactic acid sensor based on cobalt oxide nanostructures. *Electroanalysis* 31:1296–1303
38. Yan Q, Zhi N, Yang L, Guangri X, Feng Q, Zhang Q, Sun S (2020) A highly sensitive uric acid electrochemical biosensor based on a nano-cube cuprous oxide/ferrocene/uricase modified glassy carbon electrode. *Sci Rep* 10:10607
39. Verma S, Singh A, Shukla A, Kaswan J, Arora K, Ramirez-Vick J, Singh P, Singh SP (2017) Anti-IL8/AuNPs/rGO/ITO as an immunosensing platform for noninvasive electrochemical detection of oral cancer. *ACS Appl Mater Interfaces* 9:27462–27474
40. Ibrahim AA, Ahmad R, Umar A, Al-Assiri MS, Al-Salami AE, Kumar R, Ansari SG, Baskoutas S (2017) Two-dimensional ytterbium oxide nanodisks based biosensor for selective detection of urea. *Biosens Bioelectron* 98:254–260
41. Pan A, Wang Y, Xu W, Nie Z, Liang S, Nie Z, Wang C, Cao G, Zhang J-G (2014) High-performance anode based on porous  $\text{Co}_3\text{O}_4$  nanodiscs. *J Power Sources* 255:125–129

# Synthesis of Silver Nanoparticles with Different Morphologies for SERS



Tuiba Mearaj, Shobha Shukla, A. K. Hafiz, Manika Khanuja, R. A. Zargar, and Santosh Chackrabarti

**Abstract** In this paper, we reported various silver nanoparticle (Nps) morphologies (spherical, triangular, and rod forms) that were created using a conventional chemical approach for surface enhanced Raman spectroscopy (SERS).  $\text{AgNO}_3$  was used as a precursor in the fabrication of the various morphologies, and then various chemicals and capping agents were added to produce the desired morphologies. Transmission electron microscopy analysis of the internal morphology verified the creation of various morphologies of silver Nps. Triangular-shaped particles generated the best results when the samples were tested using Surface Enhanced Raman Spectroscopy (SERS). UV–Vis Spectroscopy was used to record the absorption spectra of prepared samples for further detailed studies. Numerous optical, biological, antibacterial, and energy-storage applications are possible with these Nps.

**Keywords** SERS · UV–Vis · Silver · Nps

## 1 Introduction

Nanotechnology is attracting a lot of attention in current research because of its excellent practical applications for mankind. All materials with size between 1 and 100 nm are considered nanomaterials and due to their large surface area and Plasmon excitation phenomenon they exhibit unique features as compared to their macro scale [1–3]. In particular noble-metal nanoparticles have made significant contributions to a variety of sectors, including catalysis, sensing, photochemistry, optoelectronics energy conversion, and medicine [4–11]. Silver (Ag) among noble metals is of

---

T. Mearaj (✉) · A. K. Hafiz · M. Khanuja · S. Chackrabarti  
Centre for Nanoscience and Nanotechnology (CNN), Jamia Millia Islamia, New Delhi, India  
e-mail: [tuiba2008700@st.jmi.ac.in](mailto:tuiba2008700@st.jmi.ac.in)

S. Shukla  
Department of Metallurgical Engineering and Materials Science, IIT-Bombay, Mumbai, India

R. A. Zargar  
Department of Physics, Baba Ghulam Shah Badshah University, Rajouri, India

great interest for its potential applications in areas such as detection, sterilization, electronics, and optics [12–17].

Aside from semiconductors and certain novel intermetallic compounds [18, 19], the silver nanoparticle (Ag-np) has sparked a lot of attention during the last two decades. Ag-np offers an advantage over other metal nanoparticles in photochemical applications. In general, there are two strategies for creating nanoparticles: top-down method and bottom-up method. The top-down approach refers to the physical and mechanical processes used to synthesis materials from bulk materials. The bottom-up technique, on the other hand, refers to the process of synthesizing tiny molecule precursors utilizing chemical reactions [20]. Because of its simplicity, the bottom-up technique has dominated the synthesis of nanomaterials.

## 2 Materials and Methods

### 2.1 Chemicals Used

Silver nitrate ( $\text{AgNO}_3$ ), Polyvinylpyrrolidone (PVP), Sodium borohydride or sodium tetrahydridoborate ( $\text{NaBH}_4$ ), Trisodium citrate (TSC), Sodium hydroxide (NaOH), Polyvinyl alcohol (PVA), Ascorbic acid, Cetrimonium bromide (CTAB), and Distilled water(DI).

### 2.2 Method

In this paper we synthesized different morphologies of silver nanoparticles like spherical, triangular, and rod. Spherical silver nanoparticles were synthesized by reducing  $\text{AgNO}_3$  (silver precursor) and  $\text{NaBH}_4$  as reducing agent followed by addition of chemicals like PVP and TSC. 50 mL DI water was placed in a beaker, and 30 mM trisodium citrate was added to the solution under vigorous stirring for 5 min before adding 5 mM  $\text{AgNO}_3$ . After 30 s, 50 mM  $\text{NaBH}_4$  was added to the mixture followed by addition of 0.5 ml PVP. The color of the solution turned to yellow, indicating the creation of spherical silver nanoparticle.

Unlike spherical silver nanoparticles, triangular silver nanoparticles were also synthesized using  $\text{AgNO}_3$  as silver precursor and  $\text{NaBH}_4$  as reducing agent followed by  $\text{H}_2\text{O}_2$  and TSC. 0.05 mM  $\text{AgNO}_3$  was added to 24.14 ml DI water held on a magnetic stirrer. After adding of 50 mM of TSC to the beaker, 100  $\mu\text{l}$  of  $\text{H}_2\text{O}_2$  was added to the mixture followed by 100 mM  $\text{NaBH}_4$ . The color of the solution changed from yellow to blue after few minutes, confirming the creation of silver nanotriangles.

For silver nanorods, 23.7 mL DI water and 0.5 mL of TSC were taken in a beaker and mixed thoroughly on a magnetic stirrer followed by addition of 5 mM of  $\text{AgNO}_3$ . The beaker was filled with 400  $\mu\text{l}$  of PVP and 250  $\mu\text{l}$  of  $\text{H}_2\text{O}_2$ . Finally, 250  $\mu\text{l}$  of

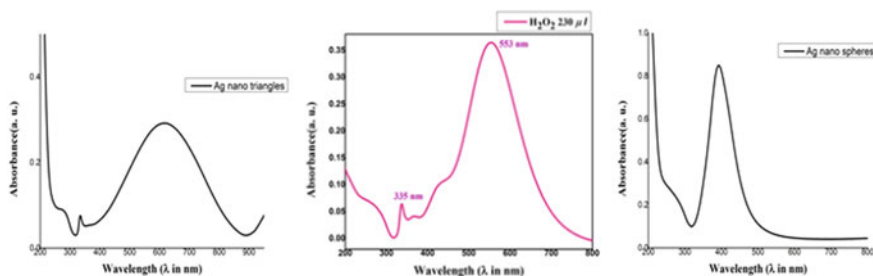


**Fig. 1** UV-Vis analysis of different morphologies of silver Nps

NaBH<sub>4</sub> were added to the beaker, resulting in a murky solution that indicated the creation of silver nanorods.

## 3 Results and Discussion

### 3.1 UV-Vis Spectroscopy

UV-Vis spectroscopic analysis was used to investigate the optical properties of silver colloid. This demonstrates a surface plasmon resonance that is well isolated from the interband transition.

Through UV-Vis analysis, typical silver sol absorption spectra are depicted. A broad plasmon absorption band with a central wavelength of 395 nm may be seen. Depending on the average size of the colloidal particle, this peak appears in the range 395–420 nm. Silver nanotriangles are formed at 698 and 333 nm [21, 22], while silver nanorods are formed at 335 and 553 nm [23, 24] (Fig. 1).

### 3.2 Transmission Electron Microscopy

Shape and size distribution of the synthesized Ag nanoparticles were characterized by transmission electron microscopic (TEM) study. Few drops of Ag nanoparticle solution were dropped onto a TEM grid, and the residue was removed by a filter paper beneath the TEM grid.

The average size distribution of the silver nanoparticles generated can be seen clearly in the TEM pictures, ranging from 20 to 50 nm as the morphology changes from spherical to triangular to rod (Fig. 2).

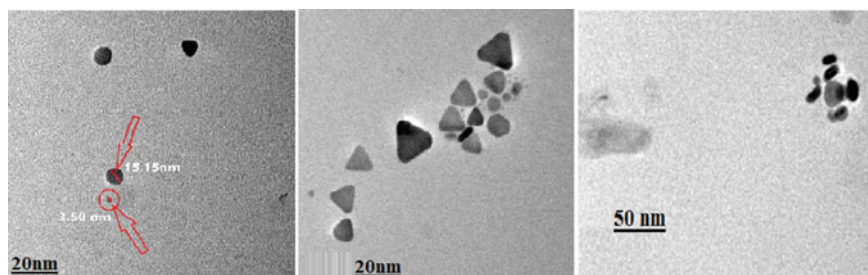


**Fig. 2** TEM images of different morphologies of silver Nps

### 3.3 Surface Enhanced Raman Spectroscopy (Sers)

Raman spectroscopy is usually applied to identify the vibrational modes of material [25]. In this work we have utilized methylene blue as a traditional SERS analyte because of its strong Raman signals, excellent spectrum, and water soluble nature. Out of all the synthesized Nps, nanotriangled samples demonstrated the best SERS (Fig. 3).

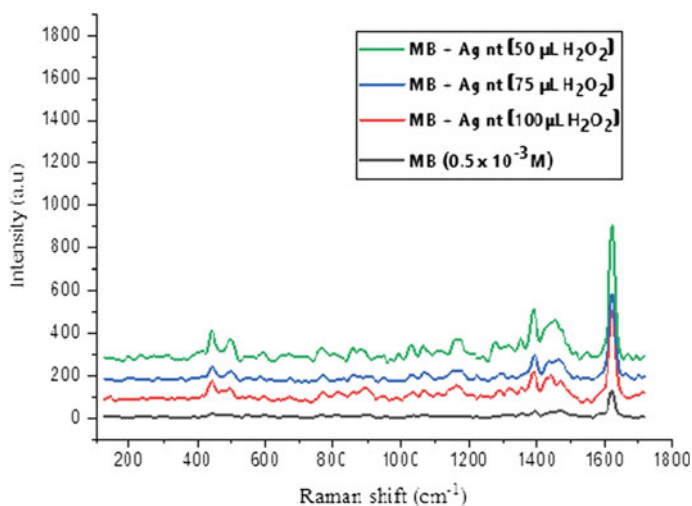


**Fig. 3** Raman spectra of different morphologies of silver Nps

## 4 Conclusion

In this paper we successfully synthesized the different morphologies of silver nanoparticles and it was concluded that out of all the morphologies silver nano-triangles demonstrated the best SERS.

**Acknowledgements** The author would like to thank the technical team at CNN, JMI for their continuous support throughout this tenure.

### Declaration of Interest Statement

The authors declare that they have no conflict of interests.

## References

1. Williams D (2008) The relationship between biomaterials and nanotechnology. *Biomaterials* 29(12):1737–1738
2. Sharma VK, Yngard RA, Lin Y (2009) Silver nanoparticles: Green synthesis and their antimicrobial activities. *Adv Coll Interface Sci* 145(1–2):83–96
3. El-Mahalawy AM, Wassel AR (2020) Enhancement of organic/inorganic hybrid photodetector based on pentacene/n-Si by surface plasmonic effect of gold and silver nanoparticles: a comparative study. *Opt Laser Technol* 131:106395
4. Anker JN, Hall WP, Lyandres O, Shah NC, Zhao J, Van Duyne RP (2010) Biosensing with plasmonic nanosensors. *Nanosci Technol: Collect Rev Nat JS*, pp 308–319
5. Jin R, Charles Cao Y, Hao E, Métraux GS, Schatz GC, Mirkin CA (2003) Controlling anisotropic nanoparticle growth through plasmon excitation. *Nature* 425(6957):487–490
6. Liu B, Gutha RR, Kattel B, Alamri M, Gong M, Sadeghi SM, Chan WL, Wu JZ (2019) Using silver nanoparticles-embedded silica metafilms as substrates to enhance the performance of perovskite photodetectors. *ACS Appl Mater Interfaces* 11(35):32301–32309
7. Kolya H, Kuila T, Kim NH, Lee JH (2019) Bioinspired silver nanoparticles/reduced graphene oxide nanocomposites for catalytic reduction of 4-nitrophenol, organic dyes and act as energy storage electrode material. *Compos B Eng* 173:106924
8. Abbar JC, Swetha GA, Meti MD, Byadagi KS (2022) Environmental applications of green engineered silver nanoparticles. In: *Phytonanotechnology*. Springer Nature Singapore, Singapore, pp 199–225
9. Hamouda HI, Abdel-Ghafar HM, Mahmoud MHH (2021) Multi-walled carbon nanotubes decorated with silver nanoparticles for antimicrobial applications. *J Environ Chem Eng* 9(2):105034
10. Kelzenberg MD, Boettcher SW, Petykiewicz JA, Turner-Evans DB, Putnam MC, Warren EL, Spurgeon JM, Briggs RM, Lewis NS, Atwater HA (2010) Enhanced absorption and carrier collection in Si wire arrays for photovoltaic applications. *Nat Mater* 9(3):239–244
11. Handoko CT, Huda A, Gulo F (2019) Synthesis pathway and powerful antimicrobial properties of silver nanoparticle: a critical review. *Asian J Sci Res* 12(1):1–17
12. Jiang ZJ, Liu CY, Sun LW (2005) Catalytic properties of silver nanoparticles supported on silica spheres. *J Phys Chem B* 109(5):1730–1735
13. Alivisatos P (2004) The use of nanocrystals in biological detection. *Nat Biotechnol* 22(1):47–52
14. Shen Z, Oh K, Kwon S, Toivakka M, Lee HL (2021) Use of cellulose nanofibril (CNF)/silver nanoparticles (AgNPs) composite in salt hydrate phase change material for efficient thermal energy storage. *Int J Biol Macromol* 174:402–412
15. Lee KJ, Jun BH, Kim TH, Joung J (2006) Direct synthesis and inkjetting of silver nanocrystals toward printed electronics. *Nanotechnology* 17(9):2424



16. Jain AS, Pawar PS, Sarkar A, Junnuthula V, Dyawanapelly S (2021) Bionanofactories for green synthesis of silver nanoparticles: toward antimicrobial applications. *Int J Mol Sci* 22(21):11993
17. Mikhailova EO (2020) Silver nanoparticles: mechanism of action and probable bio-application. *J Funct Biomater* 11(4):84
18. Huda A, Handoko CT, Bustan MD, Yudono B, Gulo F (2018) New route in the synthesis of Tin (II) oxide micro-sheets and its thermal transformation. *Mater Lett* 211:293–295
19. Arvizo RR, Bhattacharyya S, Kudgus RA, Giri K, Bhattacharya R, Mukherjee P (2012) Intrinsic therapeutic applications of noble metal nanoparticles: Past, present and future. *Chem Soc Rev* 41(7):2943–2970
20. Link S, Wang ZL, El-Sayed MA (1999) Alloy formation of gold—silver nanoparticles and the dependence of the plasmon absorption on their composition. *J Phys Chem B* 103(18):3529–3533
21. Amirjani A, Koochak NN, Haghshenas DF (2018) Synthesis of silver nanotriangles with tunable edge length: a promising candidate for light harvesting purposes within visible and near-infrared ranges. *Mater Res Express* 6(3):036204
22. Amirjani A, Koochak NN, Haghshenas DF (2019) Investigating the shape and size-dependent optical properties of silver nanostructures using UV–Vis spectroscopy. *J Chem Educ* 96(11):2584–2589
23. Lu Y, Wang Y, Chen W (2011) Silver nanorods for oxygen reduction: Strong effects of protecting ligand on the electrocatalytic activity. *J Power Sources* 196(6):3033–3038
24. Liu FK, Huang PW, Chang YC, Ko CJ, Ko FH, Chu TC (2005) Formation of silver nanorods by microwave heating in the presence of gold seeds. *J Cryst Growth* 273(3–4):439–445
25. Zargar RA (2022) Fabrication and improved response of ZnO–CdO composite films under different laser irradiation dose. *Sci Rep* 12(1):1–10

# Electrochemical Study of Reduced Graphene Oxide for Supercapacitor Application



Deependra Jhankal , Mohammad Saquib Khan, Bhanu, Preeti Shakya, Nikita Bhardwaj, K. K. Jhankal, and K. Sachdev 

**Abstract** Recently, graphene-based materials have received great attention towards the high-performance futuristic energy devices. In this study, we report a cost-effective environmental friendly hydrothermal synthesis strategy for the synthesis of reduced graphene oxide (rGO) and its electrochemical study for supercapacitor (SC) application. The morphological and structural analysis shows that high purity sheets of rGO are formed with good stoichiometry. The electrochemical study of rGO-electrode in three-electrode configuration reveals that the electrode has highest specific capacitance of  $140.8 \text{ F g}^{-1}$  and areal capacitance of  $281 \text{ mF cm}^{-2}$  at  $0.5 \text{ A g}^{-1}$  in  $1 \text{ M Na}_2\text{SO}_4$  electrolyte. The present study highlights the facile, eco-friendly and efficient synthesis process of rGO sheets for SC applications.

**Keywords** Energy devices · Charge–discharge · Hydrothermal

## 1 Introduction

The energy requirement is exponentially growing owing to the drastic increase in population and a simultaneous exhaustion of fossil fuels, which has led to researchers developing and implementing sustainable and advanced energy devices. Batteries and supercapacitors (SCs) are widely used as the superior potential energy storage systems since they not only store energy but can also transform it when needed. In contrast to batteries, which only have high energy density, SCs have high energy and power densities, making them suitable for use in high-power applications [1, 2]. Electrical double-layer capacitance (EDLC) nature is the primary mechanism used

---

D. Jhankal · Bhanu · N. Bhardwaj · K. Sachdev (✉)  
Department of Physics, Malaviya National Institute of Technology, Jaipur 302017, India  
e-mail: [ksachdev.phy@mnit.ac.in](mailto:ksachdev.phy@mnit.ac.in)

M. S. Khan · P. Shakya · K. Sachdev  
Materials Research Centre, Malaviya National Institute of Technology, Jaipur 302017, India

K. K. Jhankal  
Department of Chemistry, University of Rajasthan, Jaipur 302004, India

for charge storage in capacitive type of electrodes and carbon materials are primarily employed as the electrode material because of their good surface area, appropriate mechanical strength, and high conductivity [3]. Recently, the graphene derivatives such as graphene oxide (GO), reduced graphene oxide (rGO) and its composites have been widely reported as the negative electrode material for the supercapacitors [4].

Herein, we synthesized reduced graphene oxide (rGO) using hydrothermal method, and KOH and NaOH were utilized as the green reducing agent. The capacitive performance of rGO-electrode was employed in a three-electrode setup through various electrochemical techniques.

## 2 Methodology

### 2.1 Reagents

Chemicals were procured from Alfa Aesar: sulphuric acid (97%), sodium hydroxide (NaOH), graphite powder mesh. Fisher Scientific provided the glycerol anhydrous and ethylene glycol.  $\text{KMnO}_4$ -99% and potassium hydroxide (KOH) were purchased from LOBA Chemie.

### 2.2 Synthesis Process of GO and rGO

In the beginning, graphite powder (2 g) was combined with 50 ml of sulphuric acid ( $\text{H}_2\text{SO}_4$ ) and stirred for 4 h in a conical flask. The flask was then submerged in an ice bath to preserve the low temperature (10–15 °C) conditions, whilst  $\text{KMnO}_4$  (6 g) was progressively added to the mixture. The mixture was left to stir constantly for the following 8 h. The addition of 250 ml of DI water was then done whilst the mixture was constantly agitated. The solution turned yellowish-brown when  $\text{H}_2\text{O}_2$  (10 ml) was added to it. Two times with a 2 M HCl solution were employed to clean the resulting GO suspension (to remove the metallic ion impurities). After three to four cycles of DI water rinsing, the solution was separated using centrifugation (pH of the GO suspension reached seven) and dried at 50 °C [5].

The hydrothermal approach was then used to obtain the rGO. In a 60 ml mixture of 4 M KOH and 2 M NaOH, 1 g of GO flakes were added. After mixing and being constantly sonicated for an hour, the solution was put to a Teflon autoclave (100 mL), where it was warmed at 160 °C. The final precipitate was collected and properly rinsed with ethanol and DI water.

### 3 Results and Discussion

#### 3.1 FE-SEM, Raman and XRD Analysis

The surface morphology of material was illustrated using FE-SEM analysis (Nova Nano FE-SEM-450 scanning electron microscopy). Figures 1a, b represent the FE-SEM pictures of rGO, which shows the highly wrinkled and exfoliated flakes/sheets structure of rGO. It is well recognized that the highly wrinkled structure of rGO not only improves the surface-to-volume ratio but also enhances the charge-carrying capability resulting superior capacitive performance [6].

In the Raman spectra (using STR 500 Confocal Micro Spectrometer, = 532 nm), two major peaks of rGO are observed at about  $\sim 1351$  (*D* band) and  $\sim 1579$   $\text{cm}^{-1}$  (*G* band) and are depicted in Fig. 1c. The *D* band arises owing to the disorder present in graphitic sample, whereas the *G* band is ascribed to the  $\text{sp}^2$  vibration of  $\text{C}=\text{C}/\text{C}-\text{C}$  bonds. Further, the  $I_D/I_G$  was employed to investigate the degree of disorder present in graphene-based samples [7]. There are more defects in the rGO sample, as seen by the greater value of  $I_D/I_G$  (1.02 versus 0.96 for GO), and higher  $I_D/I_G$  may have the good influence on the performance of material.

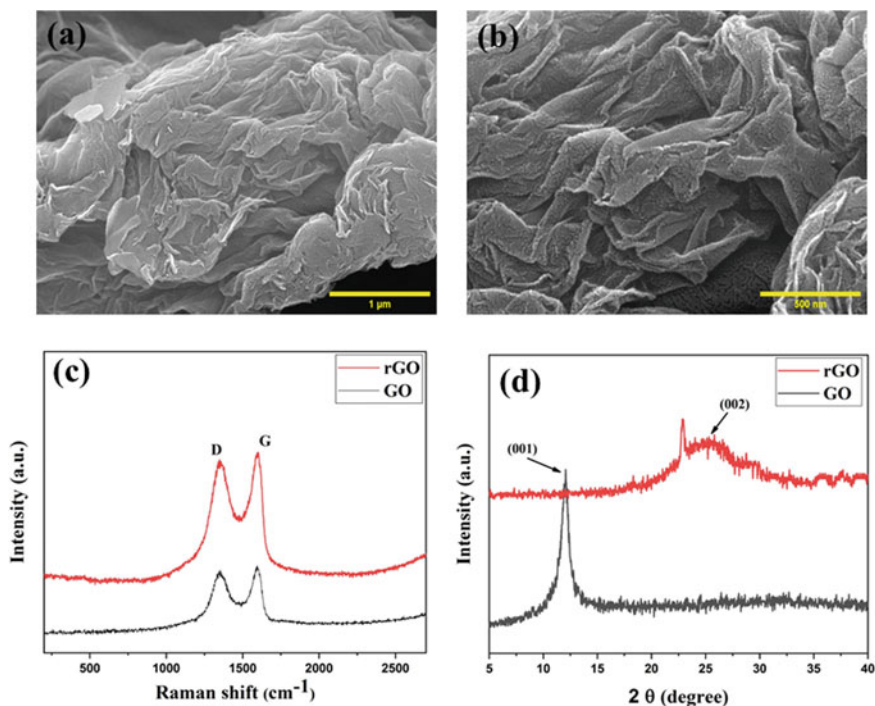


Fig. 1 FE-SEM picture of rGO (a, b), Raman (c) and XRD (d) analysis of GO and rGO

The powder XRD was performed to evaluate the phase and purity of GO and rGO. Figure 1d shows major peak of GO at  $2\theta = \sim 10.53^\circ$  related to (001) plane and a wide diffraction peak of rGO at  $2\theta = \sim 24.4^\circ$  associated with (002) plane, which indicates the amorphous nature of rGO [5].

### 3.2 Electrochemical Evaluations of GO and rGO

The capacitive performance of negative electrode (rGO-electrode) was carried out in 1 M  $\text{Na}_2\text{SO}_4$  electrolyte (using Mehozm AUTO LAB, PGSTAT30 work station). The CV study of rGO-electrode (Fig. 2a) displays the nearly square shape of CV plots at all sweep rates, indicating the ideal capacitive characteristic of the rGO-electrode [8]. Figure 2b and inset of Fig. 2b depict the calculated value of gravimetric ( $C_{sp}$ ) and areal ( $C_a$ ) specific capacitance from CV study, respectively. The EIS Nyquist diagram of the rGO-electrode is depicted in Fig. 2c, which includes a semicircle and Warburg zone in high- and low-frequency zone, respectively. The semicircle's intercept on the real axis and diameter are used to estimate the series resistance ( $R_s$ ) and charge transfer resistance ( $R_{ct}$ ) [9]. The small value of  $R_s$  (1.8  $\Omega$ ) and  $R_{ct}$  (4.20  $\Omega$ ) illustrates the good conductivity of electrode material and fast electron/ion transportation during electrochemical processes.

Figure 2d depicts the GCD study of rGO-electrode at several current densities (0.5–2 A  $\text{g}^{-1}$ ), which shows almost linear shape during both charging and discharging

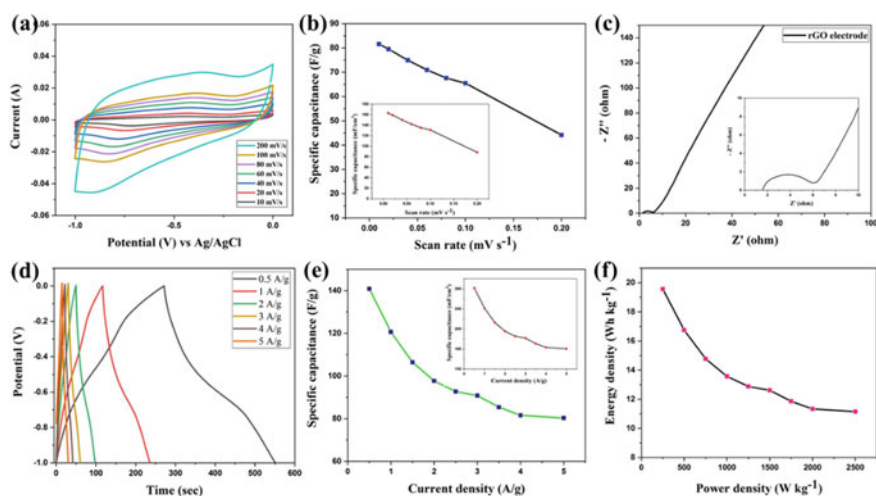


**Fig. 2** **a** CV study of rGO-electrode at several sweep rates **b** measured  $C_{sp}$  ( $\text{F g}^{-1}$ ) as the function of sweep rates [inset shows  $C_a$  ( $\text{F cm}^{-2}$ ) as the function of sweep rates] **c** EIS of rGO-electrode **d** GCD plots of rGO-electrode **e** variation of  $C_{sp}$  ( $\text{F g}^{-1}$ ) and [inset shows  $C_a$  ( $\text{F cm}^{-2}$ )] as a result of current density **f** Ragone curve for rGO-electrode

suggesting the non-faradic capacitive charge storage mechanism of rGO-electrode. The calculated values of  $C_{sp}$  ( $F g^{-1}$ ) (Fig. 2e) and  $C_a$  ( $F cm^{-2}$ ) (inset of Fig. 2e) from GCD curves are 140.8 ( $281 mF cm^{-2}$ ), 120.6 ( $241 mF cm^{-2}$ ), 97 ( $195 mF cm^{-2}$ ), 90 ( $181 mF cm^{-2}$ ), 82 ( $163 mF cm^{-2}$ ), and  $78 F g^{-1}$  ( $160 mF cm^{-2}$ ) at current density of 0.5, 1, 2, 3, 4, and 5  $A g^{-1}$ , respectively. It can be noted that the rGO-electrode retains the high value of  $C_{sp}$  even at high value of current density demonstrating the better strength of the electrode. The Ragone plot of rGO-electrode (Fig. 2f) shows the highest energy and power density of 19 and  $250 W kg^{-1}$ , respectively, indicating the superior rate performance of rGO-electrode towards the negative electrode for particle device applications.

## 4 Conclusion

An economical and environmental effective synthesis approach was adopted for synthesis of rGO for supercapacitor. The Raman study indicates that the rGO has high defects as compared to GO, which can be beneficial for good capacitive performance of rGO-electrode. The rGO-electrode contains maximum specific capacitance of  $140.8 F g^{-1}$  at  $0.5 A g^{-1}$ . This work shows the potential rGO as an improved material for advanced supercapacitors.

## References

1. Conway BE (1991) Transition from “supercapacitor” to “battery” behavior in electrochemical energy storage. Proc Int Power Sour Symp. 138:319–327. <https://doi.org/10.1149/1.2085829>
2. Phrompet C, Maneesai K, Tuichai W, Karaphun A, Sriwong C, Ruttanapun C (2020) Electrochemical properties of tricalcium aluminate hexahydrate: reduced graphene oxide nanocomposites for supercapacitor device. J Energy Storage 30:101474. <https://doi.org/10.1016/j.est.2020.101474>
3. Chen X, Paul R, Dai L (2017) Carbon-based supercapacitors for efficient energy storage. Natl Sci Rev 4:453–489. <https://doi.org/10.1093/nsr/nwx009>
4. Ke Q, Wang J (2016) Graphene-based materials for supercapacitor electrodes: a review. J Mater 2:37–54. <https://doi.org/10.1016/j.jmat.2016.01.001>
5. Sharma V, Jain Y, Kumari M, Gupta R, Sharma SK, Sachdev K (2017) Synthesis and characterization of graphene oxide (GO) and reduced graphene oxide (rGO) for gas sensing application. Macromol Symp 376:1–5. <https://doi.org/10.1002/masy.201700006>
6. Saquib Khan M, SanthiBhushan B, Chandra Bhamu K, Gu Kang S, Singh Kushwaha H, Sharma A, Dhiman R, Gupta R, Kumar Banerjee M, Sachdev K (2023) Polymer hydrogel based quasi-solid-state sodium-ion supercapacitor with 2.5 V wide operating potential window and high energy density. Appl Surf Sci 607:154990. <https://doi.org/10.1016/j.apsusc.2022.154990>
7. Jhankal D, Saquib M, Jhankal KK, Sachdev K (2023) Charge storage kinetics of MoS<sub>2</sub> flower decorated reduced graphene oxide for quasi solid-state symmetric supercapacitor. J Phys Chem Solids 173:111117. <https://doi.org/10.1016/j.jpics.2022.111117>

8. Tuichai W, Karaphun A, Ruttanapun C (2020) Ag nanomaterials deposited reduced graphene oxide nanocomposite as an advanced hybrid electrode material for asymmetric supercapacitor device. *J Alloys Compd* 849:156516. <https://doi.org/10.1016/j.jallcom.2020.156516>
9. Ye J, Hu B, Jin Y, Wang Z, Xi Y, Fang L, Pan Q (2020) Interface engineering integrates fractal-tree structured nitrogen-doped graphene/carbon nanotubes for supercapacitors. *Electrochim Acta* 349:136372. <https://doi.org/10.1016/j.electacta.2020.136372>

# Ultrathin and Flexible Gas Sensor Based on Monolayer Graphene for Environmental Monitoring



Preeti Shakya , Mohammed Saquib Khan, Nikita Bhardwaj, Deependra Jhankal, Nisha Verma, and Kanupriya Sachdev 

**Abstract** In this study, the toxic gas detection ability of chemical vapor-deposited (CVD) monolayer graphene (MLG) is examined. The electron beam deposition technique is utilized in order to deposit silver (Ag) onto a pliable polyethylene terephthalate (PET) substrate for the production of the interdigitated electrode (IDE) composed of the aforementioned material. The grown CVD graphene is transferred through PMMA-free approach using PVA on the IDE-deposited PET substrates. Raman spectroscopy mapping revealed an appropriate quality of MLG with uniformity. The use of both FE-SEM and HR-TEM allows for a comprehensive analysis of the growth of monolayer graphene. FE-SEM provides information about the surface morphology, while HR-TEM gives details about the structure and atomic arrangement of the material. The gas sensing characteristics of the fabricated sensing device are tested for environmental pollutants ( $\text{NO}_2$ ,  $\text{NH}_3$ ) at room temperature. The sensing mechanisms in the presence of oxidizing and reducing gases are further discussed. The response/recovery time and sensitivity are also evaluated, and the MLG gas sensor showed good stability and repeatability.

**Keywords** Interdigital electrodes · Single-layer graphene · Chemical vapor deposition · Flexible gas sensor · Chemiresistive gas sensor

---

P. Shakya · M. S. Khan · N. Verma · K. Sachdev (✉)  
Materials Research Centre, Malaviya National Institute of Technology Jaipur, JLN Marg,  
Jaipur 302017, India  
e-mail: [ksachdev.phy@mnit.ac.in](mailto:ksachdev.phy@mnit.ac.in)

N. Bhardwaj · D. Jhankal · K. Sachdev  
Department of Physics, Malaviya National Institute of Technology Jaipur, JLN Marg,  
Jaipur 302017, India



## 1 Introduction

Toxic gas detection and sensing are essential in number of applications, including industrial applications, environmental and safety monitoring, and relevant applications. Compact size, low power consumption, great sensitivity, and excellent selectivity toward diverse gases are fundamental criteria for contemporary gas sensors [1]. The sensing process is based on the alteration of sensing material's electrical conductivity in the presence of certain gas molecules. Some of the materials that have been used to develop small, energy-efficient, highly sensitive, and dependable sensing devices include metal oxides, inorganic semiconductors, conducting polymers, dyes, and allotropes of carbon [2–5]. Among these materials, graphene has attracted the most interest because of its thin two-dimensional structure, superior response characteristics, and low electrical noise [6]. Owing to its huge surface area, negligible power utilization, and feasibility for substantial scale production, graphene is very suitable for chemical gas detection [7]. Experimental evidence has shown that multilayer epitaxial graphene exhibits a significantly reduced response to NO<sub>2</sub> compared to single-layer epitaxial graphene, which exhibits extreme sensitivity to NO<sub>2</sub> [8]. CVD graphene is most promising for gas sensing application because of the high-quality, economical industrial scale production of graphene [9].

Based on the formerly stated literature, the selected sensing material is a single-layer graphene film in this study for environmental monitoring. The interdigitated electrode (IDE) was fabricated using the metal mask deposition technique, and the MLG was transferred to the flexible PET substrate (IDE patterned). A PMMA-free new transfer method was used for transferring the monolayer graphene from the substrate. The response of the MLG gas sensor for environmental pollutants was observed in ambient condition.

## 2 Materials and Methods

### 2.1 Materials

Copper foil of 0.1 mm thickness (99.7%) was purchased from Loba Chemie Pvt. Ltd.

### 2.2 CVD Growth of Monolayer Graphene

The copper substrate was heated for 120 min at 950 °C in argon gas and hydrogen gas at flow rates of 100 and 50 standard cubic centimeters per minute (sccm) (Fig. 2a), respectively. The synthesis of graphene material was carried out within a chamber under high-temperature conditions of 1000 °C and pressure of 6 kPa for a duration

of 15 min. The CVD furnace was rapidly cooled to ambient temperature after the growth phase was over.

### ***2.3 Transfer Process of Monolayer Graphene and Device Fabrication***

The first step in the procedure is the spin coating of 10% solution of polyvinyl alcohol (PVA) in deionized water on graphene copper samples having pre-existing graphene layer. The PVA was laminated onto the graphene using hot lamination at 120 °C for 5 min. The copper substrate is separated from the PVA (Fig. 2d), and the PVA with graphene is then placed on the PET substrates with silver-deposited IDE patterns. Finally, the PVA coating is removed by dissolving it in the DI water at 50 °C, leaving only MLG on the IDE-patterned PET substrate.

## **3 Results and Discussion**

### ***3.1 Characterization of MLG***

In Raman spectra (Fig. 1a), two main peaks G band (graphitic band) and 2D band (second-order defective carbon band), appearing at 1580 and 2690  $\text{cm}^{-1}$ , are observed, which are comparable with the other reports [10]. In graphene, the G band relates to the  $\text{sp}^2$ -hybridized carbon bonds, and the 2D band, the second order of the D band, is associated with zone boundary defects. Since the intensity of the 2D band was found to be about two times greater than that of the G band, it is clear that the graphene that was grown is of high quality. As per previous studies, it is widely acknowledged that the quantification of graphene layer count in the specimen can be achieved by normalizing the intensity ratio of the 2D band to the G band ( $I_{2D}/I_G$ ). In this regard, the  $I_{2D}/I_G$  ratio was determined to be  $\sim 2$ , thereby unambiguously confirming the fabrication of MLG on the substrate [11].

Raman mapping was also performed to evaluate the quality and to ensure uniform transfer of the monolayer graphene on the Ag-IDEs. The Raman mapping was performed using diode laser 532 nm, with 15 mW power, 5 s exposure time at 50 $\times$  magnification, mapping area was selected of (300  $\times$  300  $\mu\text{m}$ ) including the four-contact pads of IDE pattern, and MLG was found to be on the Ag-IDE edge to edge. In Fig. 1b, the Raman mapping of the G band of the MLG is shown on the IDE pattern. These results further confirm that graphene is uniformly coated on the IDE patterns, whereas the intensity of MLG on the contact pads is less in comparison to the intensity of MLG between the interspacings. In Fig. 1c, the mapping of the 2D band of the MLG is shown and it can be seen that the MLG is uniformly transferred on the contact pads of the Ag-IDEs. Figure 1e depicts the Raman mapping of silver

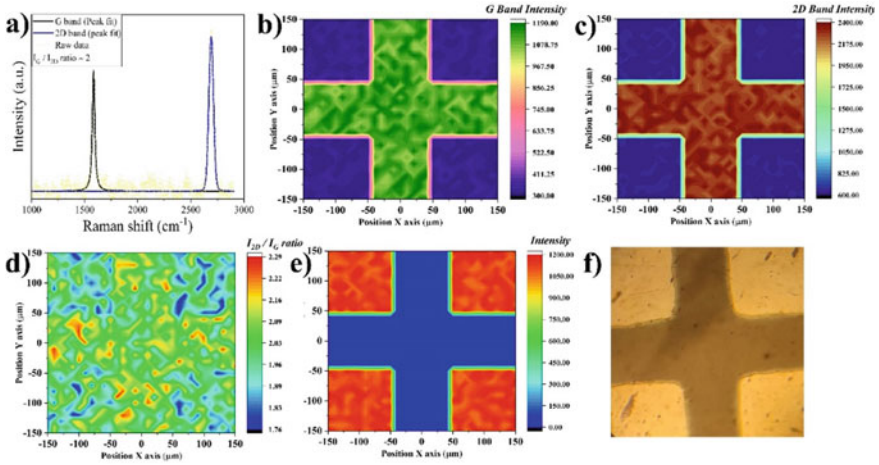


**Fig. 1** a Raman spectra of monolayer graphene, Raman mapping of monolayer graphene on IDE pattern showing, **b** mapping of G band in green color, **c** mapping of 2D band in brown color, **d** mapping of  $I_{2D}/I_G$  ratio, **e** mapping of silver IDE pattern in red color, **f** optical microscope image of the IDE pattern

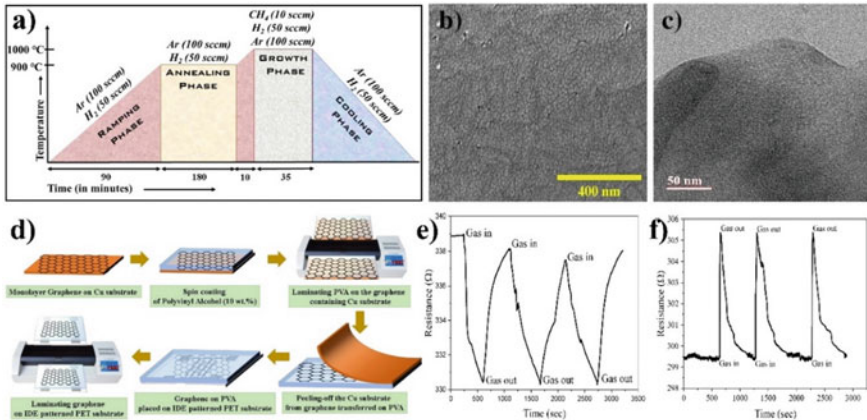


**Fig. 2** a Process parameters of CVD for monolayer graphene growth, **b** scanning electron microscopy image of monolayer graphene, **c** transmission electron microscopy of monolayer graphene, **d** transfer process of monolayer graphene using polyvinyl alcohol on IDE-patterned PET substrate, sensing curves of the monolayer graphene, **e** in the presence of nitrogen dioxide ( $\text{NO}_2$ ) at 10 ppm concentration, and **f** in the presence of nitrogen dioxide ( $\text{NH}_3$ ) at 10 ppm concentration

on IDE pattern, and it can be visually seen that the contact pads are intact after the graphene transfer. It is evident from the Raman mapping that the transfer of the MLG on the Ag-IDE was of high quality and the MLG was uniformly present on all of the IDE contact pads.

The SEM image (Fig. 2b) of the monolayer graphene reveals the uniform distribution of micro-island growth on the substrate which indicates the high quality and uniform growth of the monolayer graphene. To further investigate topological characteristics of monolayer graphene, the MLG was transferred onto a copper grid employing fishing technique. Typically, in this procedure, the MLG transferred on the PVA using hot lamination is placed onto the copper grid and dipped in DI water at 60 °C for 2 h which was changed three times. The TEM image (Fig. 2c) reveals transparent monolayer of graphene with folded graphene regions. The folding in graphene may have occurred due to the imperfect transfer to the copper substrate. However, the highly transparent monolayer regions are the evidence of the formation of monolayer graphene [12].

The source measuring unit was employed to measure the output I–V characteristics of monolayer graphene transferred on the IDE, and a linear behavior was observed in the both positive and negative biases. The mean resistance of the fabricated device calculated is 338.2  $\Omega$ .

### 3.2 Testing of the Fabricated Device

Gas sensing capabilities of MLG were investigated by detecting the resistance's change as gases were passed in various environments. Sensor response (S) was determined using Eq. 1 [13].

$$S(\%) = \frac{\Delta R}{R_a} \times 100 \quad (1)$$

In this context, the symbol  $\Delta R$  represents the alteration in resistance of the material when exposed to the analyte gas, while  $R_a$  refers to the resistance of the sensing material in the absence of the test gas.

**Sensing mechanism:** In general, reducing reaction and direct charge transfer processes can be used to explain detection of NO<sub>2</sub> using graphene at low temperatures. When it comes to the reducing reaction process, at low or room temperature, chemisorbed oxygen species (O<sub>2</sub><sup>-</sup>) could form on graphene surface. Owing to a lack of activation energy, this reaction is not expected to take place at low temperatures (< 100 °C). Therefore, it appears that dominant process for the graphene gas sensing of NO<sub>2</sub> gas at room temperature is direct charge transfer. When test gas molecules are chemisorbed on the graphene surface, direct charge transfer takes place between graphene surface and gas molecules [14]. When gas molecules interact with graphene, electrons are released from graphene which results in reduction of resistance due to increase in the number of dominant charge carriers which is holes in this case, due to p-type character of graphene [15]. Due to reducing nature of ammonia gas, it is expected that the graphene surface would accept the electrons from the NH<sub>3</sub> molecules. Following that recombination will occur between hole and electrons,

resulting the increase in resistance due to reduction in the dominant charge carriers. Finally, it is represented by increase in sensor resistance [16]. After the  $\text{NH}_3$  supply is halted, there is a decrease in  $\text{NH}_3$  molecules within the gas sensing chamber. This leads to the detachment of  $\text{NH}_3$  from the MLG surface. After  $\text{NH}_3$  desorption, the graphene surface will not experience electron transfer, and the resistance will slowly return to its original value [17]. Figure 2e demonstrates the change in resistance of fabricated MLG gas sensor after exposure to  $\text{NO}_2$  gas at a 10 ppm concentration at room temperature. The MLG gas sensor exhibits a *p*-type sensing characteristic to an oxidizing gas by rapidly decreasing resistance when exposed to  $\text{NO}_2$ , then recovering in the continuous flow of nitrogen. The response of the fabricated sensing device was measured for three consecutive cycles, and the average sensor response, response time, and recovery time were calculated to be 7%, 5.4 min, and 7 min, respectively. Figure 2f shows the sensing curve of monolayer graphene for the  $\text{NH}_3$  gas with 10 ppm concentration at room temperature. It is noted that the device's resistance increased after the analyte was injected into the chamber and the MLG gas sensing device responded rapidly and recovered slowly. The sensor response and response/recovery time of the MLG gas sensor was calculated after the three consecutive cycles of the testing, and the average sensor response and response and recovery time were evaluated to be 5.4% and 21.9/8.26 min, respectively. The MLG gas sensor was tested for oxidizing and reducing gas and the sensing response for both analytes is different, which can be further processed as sensing signal for environmental monitoring.

## 4 Conclusion

In this study, the gas sensing device was successfully developed using the simple transfer of monolayer CVD graphene sheets to the IDE-patterned flexible PET substrate and systematically characterized for  $\text{NO}_2$  and  $\text{NH}_3$  sensing. Raman spectral analysis showed that monolayer graphene is of high quality and SEM confirmed the uniformity of the monolayer graphene. The direct charge transfer method was used to essentially explain the  $\text{NO}_2$  sensing mechanism of graphene, that was most effective for monolayer graphene device fabricated by transferring CVD graphene onto interdigitated Ag electrodes. The MLG sensor has shown significant sensitivity toward both the environment pollutants and has the potential to be developed as a flexible environmental monitoring sensor. It is proposed to check the feasibility of graphene sensor for other environmental pollutant such as  $\text{CO}$ ,  $\text{CO}_2$ ,  $\text{CH}_4$ , and  $\text{SO}_2$ , and surfaces of single-layer graphene layers might be functionalized for enhancing sensitivity.

## References

1. Wang C, Wang Y, Yang Z, Hu N (2021) Review of recent progress on graphene-based composite gas sensors. *Ceram Int* 47(12):16367–16384
2. Mahajan S, Jagtap S (2021) Nanomaterials-based resistive sensors for detection of environmentally hazardous H<sub>2</sub>S gas. *J Electr Mater* 50(2):2531–2533
3. Wong YC, Ang BC, Haseeb ASMA, Baharuddin AA, Wong YH (2020) Review: conducting polymers as chemiresistive gas sensing materials: a review. *J Electrochem Soc* 167:037503
4. Sun YF, Liu SB, Meng FL, Liu JY, Jin Z, Kong LT, Liu JH (2012) Metal oxide nanostructures and their gas sensing properties: a review. *Sensors* 12(3):2610–2631
5. Yang S, Jiang C, Wei S (2017) huai: Gas sensing in 2D materials. *Appl Phys Rev* 4(2):1579
6. Mbayachi VB, Ndayiragije E, Sammani T, Taj S, Mbuta ER, Khan A (2021) Graphene synthesis, characterization and its applications: a review. *Results Chem* 3:100163
7. Khan MS, Shakya P, Bhardwaj N, Jhankal D, Sharma AK, Banerjee MK, Sachdev K (2022) Chemical vapor deposited graphene-based quasi-solid-state ultrathin and flexible sodium-ion supercapacitor. *J Electrochem Sci Eng* 12:799–813
8. Pearce R, Iakimov T, Andersson M, Hultman L, Spetz AL, Yakimova R (2011) Epitaxially grown graphene based gas sensors for ultra sensitive NO<sub>2</sub> detection. *Sens Actuat B Chem* 155:451–455
9. Ibrahim WL, Sar H, Ay F, Kosku Perkgöz N (2022) Enhanced performance of supercapacitors based on rotationally stacked CVD graphene. *J Appl Phys* 131:16
10. Choi W, Shehzad MA, Park S, Seo Y (2017) Influence of removing PMMA residues on surface of CVD graphene using a contact-mode atomic force microscope. *RSC Adv* 7:6943–6949
11. Shteplyuk I, Ivanov IG, Pliatsikas N, Iakimov T, Jamnig A, Sarakinos K, Yakimova R (2020) Probing the uniformity of silver-doped epitaxial graphene by micro-Raman mapping. *Phys B Condens Matter* 580:411751
12. Saravanan A, Huang BR, Kathiravan D (2022) Surface and interface properties of monolayer graphene on hydrophobic and hydrophilic ultrananocrystalline diamond structures for hydrogen sensing applications. *Int J Hydrogen Energy* 47:4959–4969
13. Ge L, Mu X, Tian G, Huang Q, Ahmed J, Hu Z (2019) Current applications of gas sensor based on 2-D nanomaterial: a mini review. *Front Chem* 7:839
14. Chen Z, Wang J, Umar A, Wang Y, Li H, Zhou G (2017) Three-dimensional crumpled graphene-based nanosheets with ultrahigh NO<sub>2</sub> gas sensibility. *ACS Appl Mater Interf* 9:11819–11827
15. Yang L, Zheng G, Cao Y, Meng C, Li Y, Ji H, Chen X, Niu G, Yan J, Xue Y, Cheng H (2022) Moisture-resistant, stretchable NO<sub>x</sub> gas sensors based on laser-induced graphene for environmental monitoring and breath analysis. *Microsyst Nanoeng* 8:78
16. Cadore AR, Mania E, Alencar AB, Rezende NP, de Oliveira S, Watanabe K, Taniguchi T, Chacham H, Campos LC, Lacerda RG (2018) Enhancing the response of NH<sub>3</sub> graphene-sensors by using devices with different graphene-substrate distances. *Sens Actuat B Chem* 266:438–446
17. Liang T, Liu R, Lei C, Wang K, Li Z, Li Y (2020) Preparation and test of NH<sub>3</sub> gas sensor based on single-layer graphene film. *Micromachines* 11:965

# New Prime Number Counter: Design and Performance Analysis Using CMOS and Carbon Nanotubes



Imran Ahmed Khan, Mudit Wadhwa, Prakhar Mishra, and Puneet Sharma

**Abstract** In this work, a new JK Flip-flop and Prime Counter have been proposed. This work is focused on comparison for JK Flip-flop and Prime Counter constructed from CMOS and CNTFET. The analysis is done by varying temperature and supply voltage from 25 to 100 °C and 0.7 to 1.3 V, respectively. For all conditions, the proposed CNTFET Flip-flop and CNTFET Prime Counter have low operating power, high speed, and very low PDP. SPICE is used for simulation. In spite of difficult fabrication process of CNTFET, the results obtained in this paper proved the benefits of the proposed Flip-flop and Prime Counter for higher speed and low power systems.

**Keywords** Flip-flop · Counter · Temperature · Synchronous circuits · Propagation delay · Power consumption

## 1 Introduction

In synchronous counter, all the Flip-flops receive the clock signal at their inputs simultaneously. The Flip-flop changes state in a prescribed sequence [1]. It is difficult to design MOSFET channel lengths beyond a certain limit. This leads to problems in fabrication [2–4]. Size of MOSFET in nanometers' range generates lesser transconductance, gate oxide leakage, lesser ON-current, mobility degradation [5]. Hence, carbon nanotubes (CNTs) need to be used to mitigate the problems experienced due to CMOS technology. There is remarkable excitement in researchers for CNTs because of their potential and properties [6]. Using CNTFET, we can make the circuit and systems of needed threshold voltage ( $V_t$ ) [7]. CNTs may be single-wall

---

I. A. Khan (✉) · M. Wadhwa · P. Mishra · P. Sharma  
Department of Electronics and Communication Engineering, Jamia Millia Islamia, New Delhi,  
India  
e-mail: [iakhan2@jmi.ac.in](mailto:iakhan2@jmi.ac.in)

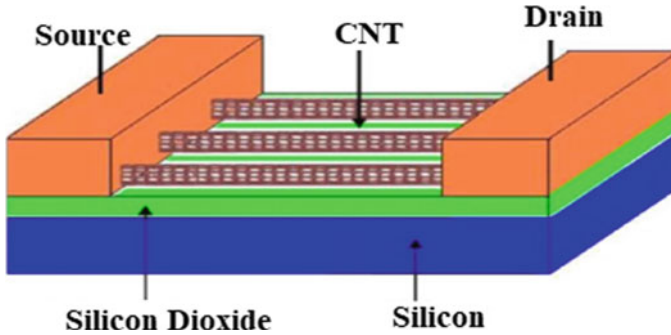


**Fig. 1** CNTFET structure [12]

carbon nanotubes (S.W.C.N.T. having diameters in nanometer) or multi-wall carbon nanotubes (M.W.C.N.T.) having nested single-wall carbon nanotubes weakly bound together by van der Waals interactions in a tree ring-like structure [8, 9].

CNTFET is emerging nanoscaled devices to design power-efficient circuits and systems [10]. CNTs are placed in the channel, i.e., in the middle of source and drain regions as shown in Fig. 1. Carbon nanotubes' FET has several advantages as compared to MOSFET. The main advantages are reduced gate capacitance and ballistic transport of carriers that result in high-performance circuits [11].

## 2 Prime Number Counter

In this research paper, we have designed a 3-bit Prime Counter. In order to design a synchronous counter, we take a counter with clock whose amplitude is 0.9 V as our default chosen value and perform transient analysis. The states of the Prime Counter may be: 2, 3, 5, 7, 11, 13, 17, 19, 23, 29, etc. For the proposed 3-bit Prime Number Counter, the states are: 2, 3, 5, 7. They can be represented in binary format as: 010 => 011 => 101 => 111 => 010. Using  $K$  map, this was simplified as follows (Fig. 2).

To implement this circuit, three JK Flip-flops are required. In this paper, a JK Flip-flop (JKFF) is proposed. The proposed Flip-flop is the modification of the Flip-flop proposed by Imran in [13]. Figure 3 illustrates presented JK Flip-flop (Fig. 4).



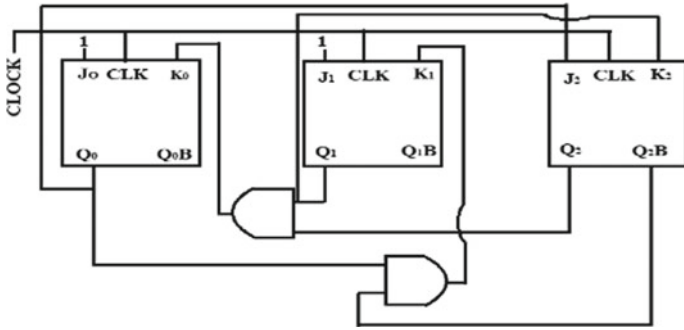


**Fig. 2** Three-bit Prime Number Counter.  $J_0 = 1, K_0 = Q_1 \cdot Q_2, J_1 = 1, K_1 = Q_0 \cdot Q_2', J_2 = Q_0, K_2 = Q_1$

$$J_0=1, K_0=Q_1 \cdot Q_2, J_1=1, K_1=Q_0 \cdot Q_2', J_2=Q_0, K_2=Q_1$$

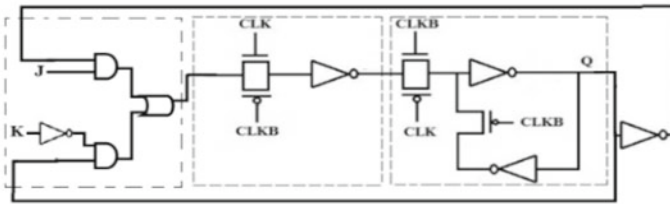


**Fig. 3** Proposed JK Flip-flop using CMOS

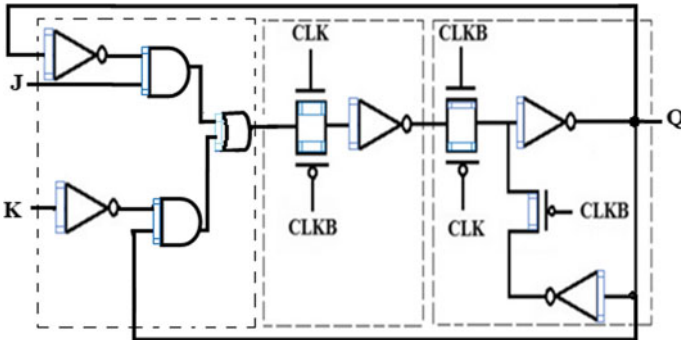


**Fig. 4** Proposed CNTFET JK Flip-flop

### 3 Simulation Results and Analysis

Table 1 shows temperature analysis of proposed JK Flip-flop and Prime Counter. It is clear from the table that propagation delay increases with temperature. Also, the propagation delay of CNTFET-based JKFF is always lesser than its CMOS counterpart. Table 1 also shows that the delay of CNTFET-based Prime Number Counter remains constant with temperature and has a much lower magnitude of propagation delay, average power, and PDP than its CMOS counterpart. The CMOS-based Prime Number Counter has increasing values of delay and power with temperature.

The carbon nanotube FETs, due to unique properties, are used in modifying the performance of the circuits [14]. Table 2 shows voltage analysis of JK Flip-flop and voltage analysis of Prime Counters. For all supply voltages, CNT JKFF has lesser delay, average power, and PDP as compared to CMOS counterpart. Table 2 also shows that both CNTFET and CMOS-based Prime Number Counter have decreasing propagation delay and increasing average power with increasing supply voltage. Also, CNTFET always gives smaller values of propagation delay, average power, and PDP than its CMOS counterpart.

### 4 Conclusion

In this work, a new JK Flip-flop and Prime Counter have been proposed and the performance comparison of CMOS and CNTFET-based JK Flip-flop and Prime Counter is completed to find the capabilities of CNTFET technology for nanoelectronic circuits. It can be concluded that the proposed CNTFET-based Flip-flop and Prime Counter are more efficient than its proposed CMOS counterpart by simple comparison from the corresponding tables. Hence, CNTFET-based Prime Number Counter and Flip-flop are viable for high-performance applications and can significantly help in power efficiency as well as being temperature resistant.

**Table 1** Propagation delay, average power, and PDP for Prime Counter and JK Flip-flop with varied temperature

JK Flip-flop temp. analysis		Temp. analysis of Prime Counters																		
		Temp. (°C)		Delay (ps)		Power (µW)		PDP (10 <sup>-17</sup> J)		Temp. (°C)		Delay (ps)		Power (µW)		PDP (10 <sup>-17</sup> J)				
Temp. (°C)		MOS JKFF	CNT JKFF	MOS JKFF	CNT JKFF	MOS JKFF	CNT JKFF	MOS JKFF	CNT JKFF	Temp. (°C)	PC MOS	PC CNT	PC MOS	PC CNT	Power (µW)	PC MOS	PC CNT	PDP (10 <sup>-17</sup> J)	PC MOS	PC CNT
25		21.1	8.87	1.14	0.206	2.41	0.18	24.51	9.17	25	2.99	0.6	7.34	0.55	2.99	0.6	7.34	0.55		
50		23.8	8.46	1.18	4.14	2.82	3.5	27.7	9.17	50	3.15	0.6	8.71	0.55	3.15	0.6	8.71	0.55		
75		26.6	6.76	1.25	0.287	3.31	0.19	31.05	9.17	75	3.35	0.6	10.4	0.55	3.35	0.6	10.4	0.55		
100		29.4	6.49	1.33	2.65	3.91	1.72	34.53	9.17	100	3.62	0.6	12.49	0.55	3.62	0.6	12.49	0.55		

**Table 2** Propagation delay, average power, and PDP of JK Flip-flop and prime number counter with variation of supply voltage  
JK Flip-flop voltage analysis

Vol. (V)	Delay (ps)						Power ( $\mu$ W)						PDP ( $10^{-17}$ J)						Voltage analysis of Prime Counters																																				
	MOS JK		CNT JK		JK		MOS JK		CNT JK		JK		MOS JK		CNT JK		JK		MOS JK		CNT JK		JK		MOS JK		CNT JK																												
	MOS JK	CNT JK	MOS JK	CNT JK	MOS JK	CNT JK	MOS JK	CNT JK	MOS JK	CNT JK	MOS JK	CNT JK	MOS JK	CNT JK	MOS JK	CNT JK	MOS JK	CNT JK	MOS JK	CNT JK	MOS JK	CNT JK	MOS JK	CNT JK	MOS JK	CNT JK	MOS JK	CNT JK																											
0.7	37.6	11.3	0.643	0.0957	2.42	0.11	0.7	42.13	12.1	1.67	0.39	7.02	0.47	0.9	21.1	8.87	1.14	0.206	2.41	0.18	0.9	24.51	9.17	2.99	0.6	7.34	0.55	1.1	13.1	6.74	2.28	0.498	2.97	0.34	1.1	16.05	5.85	6.11	1.23	9.81	0.72	1.3	8.11	3	8.11	1.87	6.58	0.56	1.3	10.73	6.47	35.42	2.18	38	1.41

## References

1. Pokhrel H, Kumar D, Sharma A (2017) Design and analysis of 4-bit binary synchronous counter by leakage reduction techniques. *Int J Comput Trends Technol* 50(2):101–106
2. Khan IA, Beg MT (2014) Clock gated single edge triggered flip-flop design with improved power for low data activity applications. *Int J Electr Eng Inform* 6(3):562–576
3. Zhang R, Walus K, Wang W, Jullien GA (2004) A method of majority logic reduction for quantum cellular automata. *IEEE Trans Nanotechnol* 3(4):443–450
4. Khan IA, Beg MT (2019) Power efficient design of semi-dynamic master slave single edge triggered flip-flop. *Int J Electr Eng Inform* 11(2):252–262
5. Saravanan V, Kannan V (2011) Semiconducting: carbon nanotube field effect transistor based logic gates. *I-Manager's J Electr Eng* 1(4):56–60
6. Sahoo R, Mishra RR (2010) Carbon nanotube field effect transistor: a promising alternative to nanoscale Mosfet. *IUP J Phys* 3(4):50–65
7. Zahoor F et al (2021) Carbon nanotube field effect transistor (CNTFET) and resistive random access memory (RRAM) based ternary combinational logic circuits. *Electronics* 10(1):79
8. Chowdhury AR, Roy K (2007) Carbon nanotube electronics: design of high-performance and low power digital circuits. *IEEE Trans Circ Syst I Regul Papers* 54(11):2391–2401
9. Díez-Pascual AM (2021) Chemical functionalization of carbon nanotubes with polymers: a brief overview. *Macromol* 1(2):64–83
10. Mehta P, Pandey S (2019) Low power and low PDP ternary adder design based on CNTFET technology. *Int J LNCT* 3(15):1–5
11. Pable SD, Imran A, Hassan M (2010) Performance optimization of CNFET based subthreshold circuits. In: *Proceedings of the 2010 annual IEEE India conference (INDICON)*, pp 1–4
12. Jaiswal M, Singh AR (2015) Design and analysis of CNTFET-based SRAM. *Int Res J Eng Technol* 2:11–15
13. Khan IA, Beg MT (2013) Design and analysis of low power master slave flip-flops. *InformacijeMidem J Microelectr Electr Compon Mater* 43(1):41–49
14. O'Connor I et al (2007) CNTFET modeling and reconfigurable logic-circuit design. *IEEE Trans Circ Syst I* 54(11):2365–2379

# Simulation-Based Analysis of Plasma-Assisted Carbon Nanotube Field-Effect Transistor (CNTFET) for Improved Device Metrics and Applications



Mansha Kansal, Suresh C. Sharma, and Manish K. Kansal

**Abstract** In the current research, a numerical simulation is carried out so as to evaluate the device performance and real-life applications of Carbon Nanotube Field-Effect Transistor (CNTFET). Carbon Nanotube (CNT) is a next-generation superior material which is the core of a CNTFET that has garnered the interest of researchers ever since its discovery. By definition, a Carbon Nanotube is a rolled-up sheet of graphene. It benefits from superior mobility, thermal and electrical conductivity, better efficiency, and impeccable scaling capabilities. The advantage it holds over silicon and other conventional materials has only increased manifolds as researchers have unlocked more potential with time. The rising popularity of CNTs has given the entire field of nanotechnology a huge boost. This analysis is done in order to investigate a cylindrical CNTFET featuring a Plasma-Enhanced Chemical Vapor Deposition (PECVD)-grown Carbon Nanotube as the channel for real-life applicability in health monitoring, as biosensors, gas sensors, etc. PECVD offers superior control over the geometry of the yielded vertically aligned CNT, thus making it a favorable synthesis mechanism. The investigation is done by evaluating the device's performance metrics for a variety of alterations. Further, the device is assessed for sensing applications using dielectric modulation in a nanogap. The results open the window for the simulated device to be used in the future for commercial sensing applications.

**Keywords** PECVD · CNT · CNTFET · Sensing applications

---

M. Kansal (✉) · S. C. Sharma  
Department of Applied Physics, Delhi Technological University, Bawana Road, Delhi 110085,  
India  
e-mail: [kansal.mansha@gmail.com](mailto:kansal.mansha@gmail.com)

M. K. Kansal  
Department of Physics, Hindu College, University of Delhi, Delhi, India

## 1 Introduction

With the global power surge, researchers are faced with a two prong problem statements—increase performance while simultaneously reduce physical dimensions of the device. Keeping the problem statement in mind, Carbon Nanotubes have started to gain a lot of importance. They are a new age material and the primary candidate to replace conventional materials while ensuring the relevancy of CMOS technology owing to their fascinating properties [1–8]. While researchers have spent enormous resources in squeezing every ounce of performance from conventional materials, the next phase of performance surge will only come from incorporation of new age material such as CNT. CNTFETs can be effectively used as advanced sensors owing to their ability to swiftly react to external changes. The research here tackles the simulation of a CNTFET device to be used for sensing applications. The novelty of the research is maintained since the research tackles PECVD-grown CNT for research and analysis. Among the other models widely being used for the synthesis of CNT, PECVD method has grown importance owing to two big reasons—lower operating temperatures and greater control over the device’s dimensions. Plasma parameters at play during PECVD have a direct impact on the radius and length of the resultant CNT. Since they can be manually controlled, researchers can yield CNTs with the dimensions of their preference. Performance gains of CNT are abundantly known and documented. Hence, this research does not divulge into the same. Instead, it focuses on real-life applications of devices using CNT as channel material and sees what performance one can expect. Using a cavity created in the oxide region of the CNTFET, the device is tested for its performance as a sensor using dielectric modulation. The cavity is filled with a dummy material with controllable dielectric constant. The results following dielectric modulation confirm the device’s capabilities as a sensor. The device is able to maintain its stability under all possible scenarios simulated using dielectric modulation. Better performance is tilted toward higher  $k$  dielectric.

## 2 Materials and Methods

The device in contention is a Carbon Nanotube Field-Effect Transistor (CNTFET) implemented and simulated using Silvaco TCAD simulator. As the name suggests, the device uses a CNT as a channel material having dimensions of 1.5  $\mu\text{m}$  length and 5 nm radius. The FET uses a dual-gate system with one gate having work function 4.4 and another 4.7 at drain and source ends, respectively. Accompanying the dual-gate setup is a 2 nm thick gate oxide made of  $\text{SiO}_2$ , which offers robustness owing to superior bonding with CNT channel material. To conduct dielectric modulation, a nanogap is etched into the oxide layer, which is then filled by a dummy material with varying dielectric constants that the research focuses on. To implement the simulations, Silvaco provides many models that are used in this research as well.

**Fig. 1** Three-dimensional structure of cylindrical CNTFET

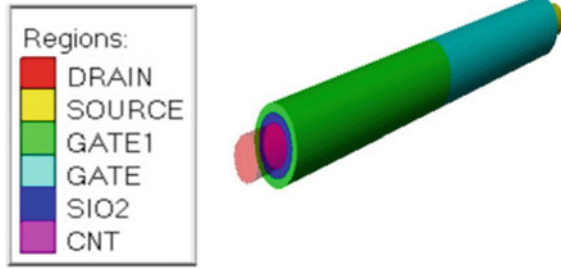
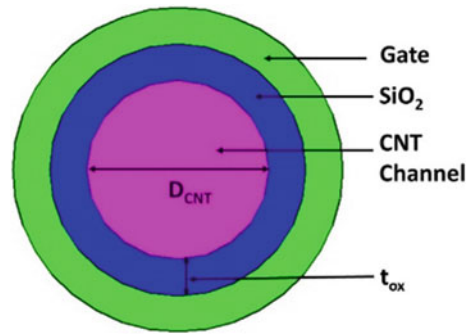


**Fig. 2** Cross-sectional view of cylindrical CNTFET



SRH model is used to implement leakage currents. Minority carrier recombinations are taken into account using the Auger recombination model [9]. Carrier statistics are looped in using the Boltzmann model. To help with numerical solutions, Gummel and Newton techniques are used.

Figures 1 and 2 show the 3D and the cross-sectional views of the SiO<sub>2</sub>-based Plasma-Assisted Carbon Nanotube Field-Effect Transistor (CNTFET).

### 3 Results and Discussion

Sharma and Tiwari have proposed a physical model that draws a connection between the plasma parameters and device geometry. This allows for superior control over the resultant CNT geometry. Their work, and therefore this research as well, involves the use of two sets of plasma parameters—electron density  $n_e$  and electron temperature  $T_e$ , ion density  $n_i$  and ion temperature  $T_i$ . PECVD parameters also known as plasma parameters have a direct influence or impact on device characteristics because of their influence on device geometry (such as radius and length) [10–14].

Creating a Gate-All-Around Carbon Nanotube Field-Effect Transistor (GAA-CNTFET) using PECVD-grown CNTs involves several steps. First, CNTs are grown on a silicon wafer substrate using PECVD. PECVD process for growing CNTs



involves depositing a catalyst on a substrate, introducing a carbon-containing gas into a vacuum chamber, creating a plasma, and allowing the carbon to self-assemble into CNTs on the surface of the catalyst. The next step is to pattern the CNTs into the desired configuration, such as a nanowire or nanotube array. A gate electrode is then deposited on the substrate, covering the CNTs. A gate dielectric layer is then deposited over the gate electrode and CNTs to insulate the gate electrode from the CNTs and provide a high capacitance. Source and drain electrodes are deposited on the substrate, connecting to the CNTs. The device is then annealed at a high temperature to improve the electrical properties and the adhesion between the CNTs and the substrate. Finally, the device is characterized and tested to ensure that it meets the required electrical and sensing properties for the intended application.

Control and more idea of these plasma parameters are quite important for deciphering device performance. This research aims in taking the broader problem of unknowns of PECVD parameters and breaks down their control over the device. Silvaco 3D ATLAS TCAD simulator aids in the designing and simulation of the proposed device and its subsequent analysis for performance metrics. The improvement in performance with increasing dielectric constant can be seen in Figs. 3a, b. With increasing  $k$ -value, the capacitive strength increases, thus increasing the electric field lines. This increases the drain current and effectively the transconductance  $g_m$ . Both these metrics showcase improving results with higher  $k$ -values. Figure 4 displays the variation of  $I_{ON}/I_{OFF}$  ratio for the chosen values of dielectric constant. This ratio represents the switching speed of the device for numerous digital applications [15–17]. Therefore, a high value is recommended to infer the real-life application of the device. The sensitivity analysis is an important way to assess the performance of the device for its sensing abilities. It is a metric of how quick or how equipped the device is to detect changes to external conditions, and hence, a higher value is preferred. Based on Fig. 5a, the drain current sensitivity of a specific molecule compared to air improves with higher dielectric constant ( $k$ )-values, leading to an enhanced drain current with an increase in dielectric constant in the cavity. Figure 5b demonstrates the variation of the  $I_{ON}/I_{OFF}$  sensitivity ratio, which reflects the relative improvement in the  $I_{ON}/I_{OFF}$  ratio of a specific molecule compared to air. Figure 6 shows the comparison in terms of  $I_{ON}/I_{OFF}$  Sensitivity Ratio for both devices Silicon Nanowire Field-Effect Transistor (SiNW FET) and CNTFET. It can be clearly observed that how the proposed device shows significant improvement in performance compared to already existing conventional Si-based device. The research conducted solidifies the case of CNTFET to be used as a sensor device. CNT owing to its superior material properties brings in superior detection speed along with significantly better scalability strength. The novel device presented in this research has been subjected to a dielectric modulation analysis for the first. CNT-based sensors can be widely deployed in various environmental, medical like health monitoring systems, and many more important industries.

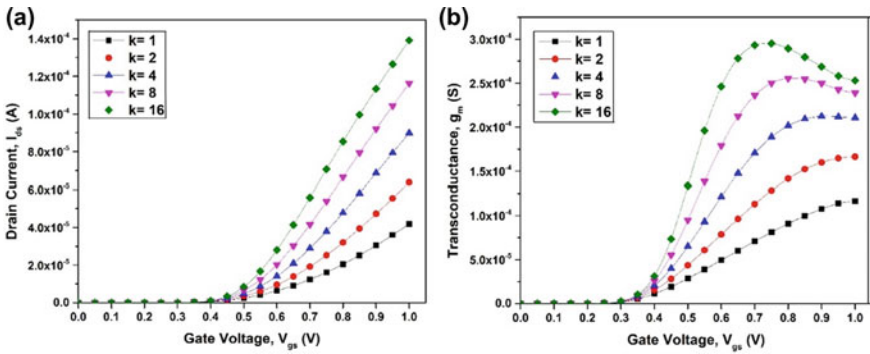


**Fig. 3** Variation of dielectric constant on **a** transfer characteristics **b** transconductance,  $g_m$  at  $V_{ds} = 1.0$  V

**Fig. 4** Variation of dielectric constant on  $I_{ON}/I_{OFF}$  Ratio at  $V_{ds} = 1.0$  V

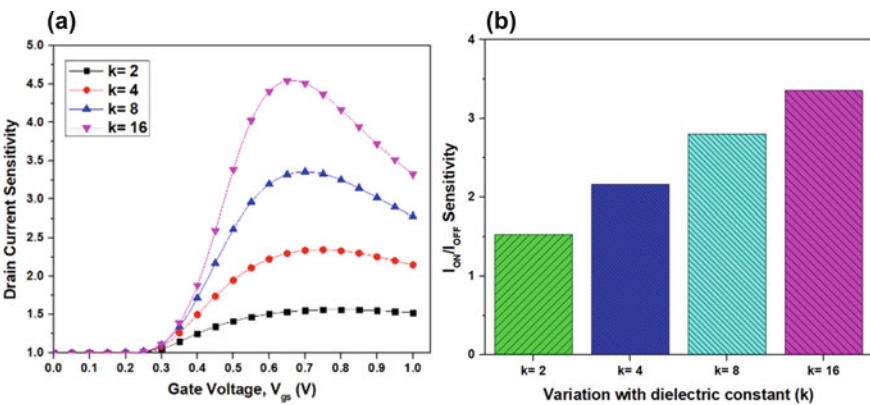
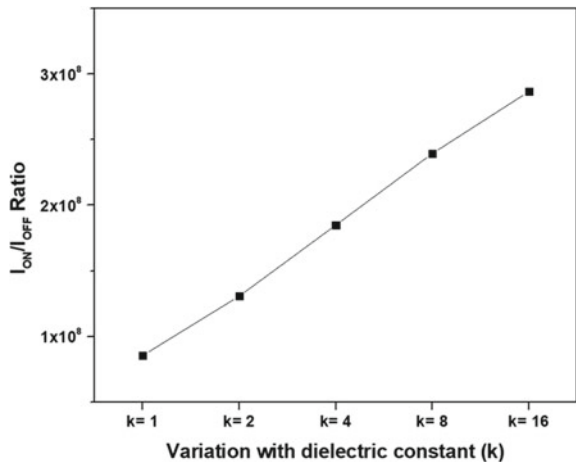


**Fig. 5** Variation of dielectric constant on **a** drain current sensitivity, **b**  $I_{ON}/I_{OFF}$  sensitivity at  $V_{ds} = 1.0$  V

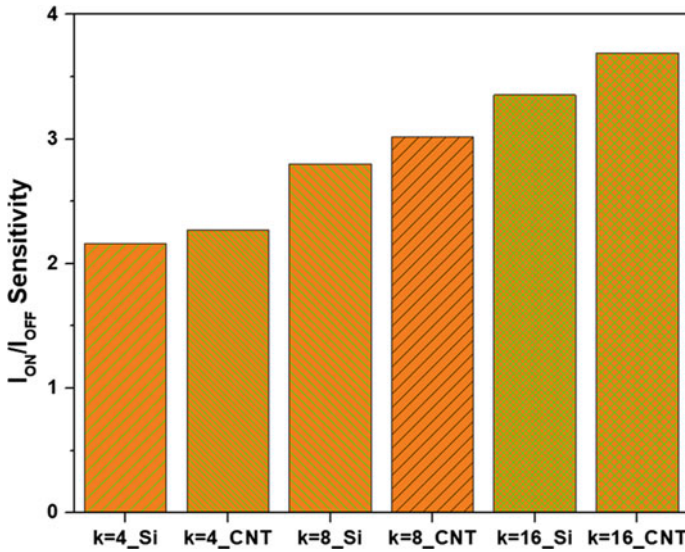


**Fig. 6** Comparison of  $I_{ON}/I_{OFF}$  sensitivity ratio for SiNW FET and CNTFET at  $V_{ds} = 1.0$  V

## 4 Conclusion

With the advancements in nanotechnology, materials like carbon nanotubes (CNTs) have gained significant attention. The primary objective of this manuscript is to comprehend the relevance of CNT-based devices in our daily lives. Due to its superior material properties, CNTs have emerged as strong contenders to be used as channel materials for MOSFETs. The aim of this research is to expand the range of applications for CNT-based devices by utilizing them for sensing purposes. We have adopted the technique of dielectric modulation by creating a nanogap in the oxide layer and varying the dielectric constant, which has resulted in significant changes in the device characteristics. Such devices can be employed in health monitoring systems and other areas to improve efficiency.

**Conflict of Interest** The authors declare that they have no conflict of interests.

## References

1. Ono Y, Kishimoto S, Ohno Y, Mizutani T (2010) Thin film transistors using PECVD-grown carbon nanotubes. *Nanotechnology* 21(20):205202
2. Dang T, Anghel L, Leveugle R (2006) CNTFET basics and simulation. In: International conference on design and test of integrated systems in nanoscale technology, DTIS 2006, pp 28–33. <https://doi.org/10.1109/DTIS.2006.1708731>

3. Martel R, Schmidt T, Shea HR, Hertel T, Avouris P (1998) Single- and multi-wall carbon nanotube field-effect transistors. *Appl Phys Lett* 73:2447
4. Guo J, Hasan S, Javey A, Bosman G, Lundstrom M (2005) Assessment of high-frequency performance potential of carbon nanotube transistors. *IEEE Trans Nanotechnol* 4(6):715–721. <https://doi.org/10.1109/TNANO.2005.858601>
5. Nougaret L, Happy H, Dambrine G, Derycke V, Bourgoin J-P, Green AA, Hersam MC (2009) 80 GHz field-effect transistors produced using high purity semiconducting single-walled carbon nanotubes. *Appl Phys Lett* 94:243505
6. Choi YC, Bae DJ, Lee YH, Lee BS, Park G-S, Choi WB, Kim JM (2000) Growth of carbon nanotubes by microwave plasma-enhanced chemical vapor deposition at low temperature. *J Vacuum Sci Technol A Vacuum Surf Films* 18(4):1864–1868
7. Sharma SC, Gupta N (2015) Theoretical modeling of the plasma-assisted catalytic growth and field emission properties of graphene sheet. *Phys Plasmas* 22(12):123517
8. Tewari A, Sharma SC (2015) Theoretical modeling of temperature dependent catalyst-assisted growth of conical carbon nanotube tip by plasma enhanced chemical vapor deposition process. *Phys Plasmas* 22(2):023505
9. ATLAS User's Guide (2018) SILVACO Int. Santa Clara, CA, USA, Version 5.26.1.R
10. Mizutani T, Ohnaka H, Okigawa Y, Kishimoto S, Ohno Y (2009) A study of preferential growth of carbon nanotubes with semiconducting behavior grown by plasma-enhanced chemical vapor deposition. *J Appl Phys* 106(7):073705. <https://doi.org/10.1063/1.3234389>
11. Gupta R, Sharma SC, Sharma R (2017) Mechanisms of plasma-assisted catalyzed growth of carbon nanofibres: a theoretical modelling. *Plasma Sour Sci Technol* 26(2):024006
12. Kato T, Hatakeyama R (2010) Growth of single-walled carbon nanotubes by plasma CVD. *J Nanotechnol*
13. Li Y, Mann D, Rolandi M, Kim W, Ural A, Hung S, Javey A, Cao J, Wang D, Yenilmez E, Wang Q, Gibbons JF, Nishi Y, Dai H (2004) Preferential growth of semiconducting single-walled carbon nanotubes by a plasma enhanced CVD method. *Nano Lett* 4(2):317–321
14. Srivastava SK, Shukla AK, Vankar VD, Kumar V (2005) Growth, structure and field emission characteristics of petal like carbon nano-structured thin films. *Thin Solid Films* 492(1–2):124–130. <https://doi.org/10.1016/j.tsf.2005.07.283>
15. Rewari S, Nath V, Haldar S, Deswal SS, Gupta RS (2017) Hafnium oxide based cylindrical junctionless double surrounding gate (CJLDSG) MOSFET for high speed, high frequency digital and analogy applications. *Microsyst Technol* 25(5):1527–1536. <https://doi.org/10.1007/s00542-017-3436-3>
16. Kansal M, Sharma SC (2022) Performance evaluation and linearity distortion analysis for plasma-assisted dual-material carbon nanotube field effect transistor with a SiO<sub>2</sub>-HfO<sub>2</sub> stacked gate-oxide structure (DM-SGCNFET). Silicon
17. Kansal M, Sharma SC (2022) Plasma-based nanoarchitectonics for vertically aligned dual-metal carbon nanotube field-effect transistor (VA-DMCNFET) device: effect of plasma parameters on transistor properties. *Appl Phys A* 128(1):1–11

# Raman Spectroscopy as a Potential Tool to Analyze Alzheimer's Disease Progression



Umesh Chandra Garnaik and Shilpi Agarwal

**Abstract** Alzheimer's disease (AD) is a neurodegenerative disorder that affects cognition, function, and behaviour of a person's daily activity which is gradual and irreversible. Today, determining an Alzheimer's disease diagnosis requires several clinical tests and is a complicated process. Various studies had shown that amyloid beta ( $A\beta$ ) peptides abnormally aggregate to induce AD. Hence, detecting abnormal oligomeric  $A\beta$  peptides and visualization of amyloid beta plaques are regarded as potential diagnostic approaches for AD. In this work, we propose a Raman nanoprobe using amine-functionalized spherical gold nanoparticles (AuNPs) in conjugation with Rose Bengal (RB) dye which possesses strong Raman signatures and a high affinity for amyloid beta peptides. We find that this peptide-probe interaction shows a Raman shift at a particular spectral region. Raman spectroscopy offers the whole biochemical content of the body fluid, allowing for the detection of minor but characteristic physiological alterations associated with pathology. Our method features a clearer concept for a more precise and alternative tool for diagnosing Alzheimer's disease.

**Keywords** Raman spectroscopy · Alzheimer's disease (AD) · Gold nanoparticles (AuNPs)

## 1 Introduction

The most common kind of neurodegenerative disorder, Alzheimer's disease affects many old aged people worldwide. The loss of memory and cognitive function that results from AD is irreversible [1]. The amyloid hypothesis claims that plaque formation following amyloid beta ( $A\beta$ ) aggregation is the main cause of all physiological problems affecting the brain that change synaptic function [2], activate microglia [3]

---

U. C. Garnaik · S. Agarwal (✉)

Optics and Photonics Laboratory, School of Physical Sciences, Jawaharlal Nehru University, New Delhi 110067, India

e-mail: [shilpiagarwal@mail.jnu.ac.in](mailto:shilpiagarwal@mail.jnu.ac.in)

and astrocytes, and induce oxidative harm. A $\beta$  peptides are formed during the proteolytic breakdown of a bigger glycoprotein known as an amyloid precursor protein, (APP) [4]. The length of peptides varies depending on the point of cleavage, although those with 40 (A $\beta$ 40) or 42 (A $\beta$ 42) amino acids make up the majority of A $\beta$  peptides. As A $\beta$ 40 peptides are more prevalent, A $\beta$ 42 peptides are thought to be the main pathogenic factor because of their higher toxicity and quicker fibrillation rate. Early and accurate identification of A $\beta$ 42 for the diagnosis of AD will give excellent opportunities for preventative treatment of AD symptoms. The aetiology of AD has been explained by a variety of processes during the past few decades, and numerous clinical trials have been examined using a variety of methodologies [5–7]. Raman spectroscopy is found suitable for early diagnosis of Alzheimer's disease, as this is noninvasive and nondestructive to the human brain and bodily parts. Conjugation with biomolecular targeting ligands such as peptides, antibodies, or molecules, nanoparticles can be used to target cells and molecules with high affinity and specificity [8–11]. As per our understanding conjugation of organic synthetic dye and surface enhance-based nanoparticles plays an important role in the in-vivo detection of amyloid beta peptides [12]. Various negatively charged dyes were tested for adsorption on the surface of gold and silver nanoparticles. It has been proven to sufficiently enhance Rose Bengal dye with gold nanoparticles [13]. This paper uses Raman nanoprobe (RB-AuNPs) for the A $\beta$ 42 detection by surface-enhanced Raman spectroscopy (SERS).

## 2 Methods

In this study, we used surface-enhanced Raman spectroscopy to monitor the A $\beta$ 42 and make an early diagnosis of Alzheimer's disease. The RB molecules were covalently linked with amine-functionalized spherical gold nanoparticles (AuNPs) for the creation of the Raman nanoprobe via carboxylic group crosslinking with the amine-functional group of AuNPs.

Raman spectra of A $\beta$  42 with Raman nanoprobe were recorded using a confocal Raman in Via WITec alpha300 RA Raman spectrometer (Oxford Instruments, Ulm, Germany) that includes a CCD camera which is electrically cooled. The excitation laser wavelength was 532 nm and the laser power was 5 mW in all cases for the sample.

## 3 Results and Discussions

The Raman spectra of the A $\beta$ 42 power sample under dry condition was measured using confocal Raman illustrated in Fig. 1a. We observed aromatic amino acids-phenylalanine at  $1001.3\text{ cm}^{-1}$  [14]. This peak may explain the interaction of peptide and probe. The Amide III band present at  $1234.8\text{ cm}^{-1}$  shows a  $\beta$ -sheet structure, it

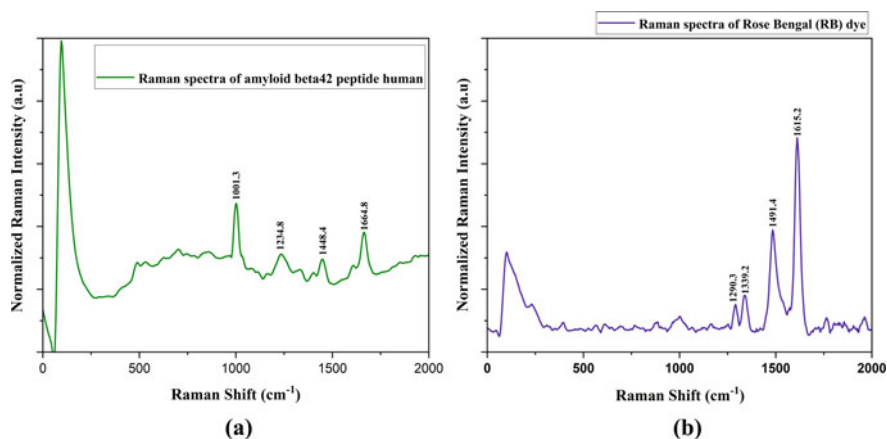


**Fig. 1** Raman spectra of **a** Amyloid beta 42 human, **b** Rose Bengal (RB) dye

can also correlate to the amide I band present at  $1664.8\text{ cm}^{-1}$  which explains the  $\beta$ -turn structure [15, 16] As a result, we discovered that the locations and widths of the amide I and amide III bands between  $1650\text{--}1700$  and  $1200\text{--}1300\text{ cm}^{-1}$ , respectively, are depending on backbone-peptide conformations. From Fig. 1b we observe the Raman spectra of RB dye which has a good affinity with A $\beta$  peptide.

We obtained the Raman spectra of nanoprobe (RB-AuNPs) and nanoprobe with  $2\text{ }\mu\text{M}$  of A $\beta$ 42 which is shown in Fig. 2a, b respectively. The spectral alteration occurred in the two primary peaks in  $1491.4$  and  $1615.5\text{ cm}^{-1}$ . AuNP has no such significant enhancement but after conjugation with RB molecules, it shows a great enhancement for detecting the required bands of A $\beta$ 42 peptides. From Fig. 2b modifications are caused by the mechanical squinching of the aromatic rings in RB wedged between the A $\beta$ 42 peptides and AuNPs. The bands observed in the Raman spectra of nanoprobe with A $\beta$ 42 peptides are of  $\Delta\text{CH}_2$  and amide I present at  $1491.4$  and  $1615.5\text{ cm}^{-1}$ . Amide I represent the antiparallel  $\beta$ -sheet structure [17]. The peak at  $1068\text{ cm}^{-1}$  represents phenylalanine which binds the peptide with RB molecules. When compared with the signal  $1491.4\text{ cm}^{-1}$ , the signal strength of  $1615.5\text{ cm}^{-1}$  decreased much more. The ratio between the primary two peaks (intensity at  $1491.4\text{ cm}^{-1}$ /intensity at  $1615.5\text{ cm}^{-1}$ ) changed. In the free state, the rotations and vibrations of RB dye molecules release more excitation energy [13]. Interaction with A $\beta$ 42 peptides restricts molecule rotations and vibrations, requiring more energy to be liberated by photon emission, resulting in an increased spectrum [18].

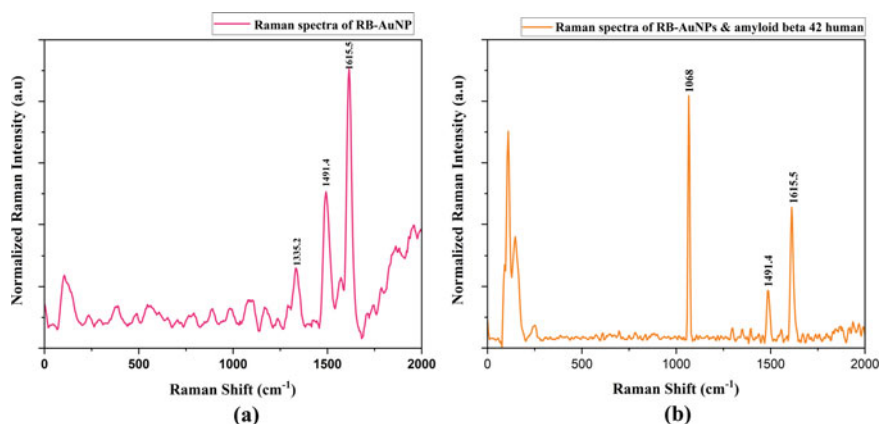


**Fig. 2** Raman spectra of **a** Conjugated nanoprobe RB-AuNPs, **b** RB-AuNP with 2  $\mu\text{M}$  amyloid beta ( $\text{A}\beta$ ) 42 peptides

## 4 Conclusion

Confocal Raman based detection of  $\text{A}\beta$ 42 peptides is done using RB linked spherical gold nanoparticles as a Raman nanoprobe. From this experiment, we observed that when RB dye molecules are coupled to AuNPs, their Raman scattering is greatly amplified, and the Raman spectrum exhibits discernible alterations in the presence of  $\text{A}\beta$ 42 peptides. This peptide-probe interaction illustrates before the peptides bind, the vibrations and rotations of RB dye molecules can release energy from excitation photons. Once the peptides attach, the rotations and vibrations are constrained, resulting in an enhancement that can be shown with Raman spectroscopy.

**Acknowledgements** The authors acknowledge the financial support from DST-Device Development Programme (DDP), (file no-DST/TDT/DDP-47/2021). We are also thankful to AIRF JNU for providing characterization facility.

## References

1. Knopman DS et al (2021) Alzheimer's disease. *Nat Rev Dis Prim* 7(1):33
2. Cai W et al (2022) Physiological roles of  $\beta$ -amyloid in regulating synaptic function: implications for AD pathophysiology. *Neurosci Bull* 14:1–20
3. Zhang C et al (2023) Exploring the associations between Alzheimer's disease and GBM mediated by microglia based on network analysis. *J Prevent Alzheimer's Dis* 10(2):1–4
4. Chen GF et al (2017) Amyloid beta: structure, biology, and structure-based therapeutic development. *Acta Pharmacol Sin* 38(9):1205–1235
5. Panza F et al (2019) A critical appraisal of amyloid- $\beta$ -targeting therapies for Alzheimer's disease. *Nat Rev Neurol* 15:73–88



6. Musiek ES et al (2021) Aducanumab for Alzheimer's disease: the amyloid hypothesis moves from bench to bedside. *J Clin Invest* 131(20):e154889
7. Porsteinsson AP et al (2021) Diagnosis of early Alzheimer's disease: clinical practice in 2021. *J Prevent Alzheimer's Dis* 8(3):371–386
8. Kinney JW et al (2018) Inflammation as a central mechanism in Alzheimer's disease. *Alzheimer's Dement Transl Res Clin Intervent* 4:575–590
9. Korte N, Nortley R, Attwell D (2020) Cerebral blood flow decrease as an early pathological mechanism in Alzheimer's disease. *Acta Neuropathol* 140(6):793–810
10. Smith AM et al (2014) Mapping the spatial distribution of charge carriers in quantum-confined heterostructures. *Nat Commun* 5:4506
11. Stockman MI (2015) Nanoplasmonics: fundamentals and applications. In: Di Bartolo B, Collins J, Silvestri L (eds) *Nano-structures for optics and photonics* (2015) NAPS. Springer, New York, pp 3–102
12. Jeong WJ et al (2018) Peptide-nanoparticle conjugates: a next generation of diagnostic and therapeutic platforms? *Nano Converg* 5(1):38
13. Xia Y et al (2019) Bifunctional fluorescent/Raman nanoprobe for the early detection of amyloid. *Sci Rep* 9:8497
14. Aliaga AE et al (2011) Surface-enhanced raman scattering and theoretical studies of the C-terminal peptide of the  $\beta$ -subunit human chorionic gonadotropin without linked carbohydrates. *Biopolymers* 95(2):135–143
15. Bandekar J et al (1992) Amide modes and protein conformation. *Biochim Biophys Acta* 1120(2):123–143
16. Stenner RS (2021) The combined use of amide I band in polarized Raman, IR, and vibrational dichroism spectra for the structure analysis of peptide fibrils and disordered peptides and proteins. *J Raman Spectrosc* 52(12):2479–2499
17. Nurettin D et al (2004) Two-dimensional infrared spectroscopy of antiparallel  $\beta$ -sheet secondary structure. *J Am Chem Soc* 126(25):7981–7990
18. Accardo A et al (2014) Amyloid  $\beta$  peptide conformational changes in the presence of a lipid membrane system. *Langmuir* 30(11):3191–3198

# Development of Passivation Layer Material for Quantum Dot-Sensitized Solar Cells



Rahul Singh  and Ragini Raj Singh 

**Abstract** The chemistry involved in synthesizing zinc sulphide (ZnS) at different parameters, mainly pH value and precursor, always shows its essence for application in sensitized solar cells (DSSC and QDSSC) as a passivation layer. We have recently tried synthesizing ZnS at 11.5 pH using zinc acetate as a precursor because of its organic nature compared to other inorganic ones. As a result, novel zinc sulfo-oxide (ZnSO) was formed, showing similar optical properties to the ZnS. Therefore, in this study, different pH values 9.5, 10.5, and 11.5 were considered for the synthesis of ZnS. Initial studies were completed for optical and structural properties. Photoluminescence (PL) shows a drastic change in the emission peaks from 338 to 391 nm for the material synthesized at 11.5 and 9.5 pH values, respectively. In contrast, structural studies show the formation of mixed phase ZnO and polytype-10H ZnS, which leads to synthesis novelty for polytype-10H ZnS. Synthesized materials can be employed as a passivation layer and UV range sensitizer in QDSSC.

**Keywords** QDSSC · Polytype ZnS-10H · Zinc acetate · Passivation layer

## 1 Introduction

Quantum dot-sensitized solar cells (QDSSC) have reached a maximum efficiency of 18.1% on the laboratory scale when compared to the theoretical calculated value of ~ 44% [1, 2]. The main reasons behind this low efficiency are surface traps and defects, lattice mismatch, and charge recombination rates [3]. Surface passivation of the sensitizers using wide band gap semiconductors can be helpful to reduce the above-stated issues in low-efficient QDSSCs [4]. ZnS is best suitable for sensitized solar cells as a surface passivation layer because of direct-large band gap value of 3.68 eV, exciton Bohr radius ( $a_B$ ) of 2.5 nm, and 39 meV value for excitonic binding energy. ZnS is also non-toxic, economical, and mainly chemically stable [4]. The

---

R. Singh · R. R. Singh (✉)

Nanotechnology Laboratory, Department of Physics and Materials Science, Jaypee University of Information Technology, Wanknaghat, Solan, Himachal Pradesh 173234, India  
e-mail: [raginirajsingh@gmail.com](mailto:raginirajsingh@gmail.com)

chemical stability of the material is also crucial in aqueous-based methods since the preparation of the material depends on several factors including choice of precursors, reducing agents, temperature and mainly the pH value of the prepared solution. The pH value of the solution describes the presence of  $\text{OH}^-/\text{H}^+$  ions, which is responsible for controlling the rate of reaction and growth of particle size. Therefore, ongoing chemical reactions in the solution depending on the solution's pH value and the opted synthesis method, thus synthesizing the final product. Our group has recently tried to synthesize ZnS at a higher pH value, i.e. 11.5, where ZnSO was formed instead of ZnS, showing similar optical properties [5]. Also, the XRD studies observed the peak of polytype ZnS, i.e. ZnS-10H [5]. Therefore, in this work, pH has been monitored for the formation of passivation layer material. Comparative optical and structural studies have been done at initial stages for pH values at 10.5 and 9.5 with respect to 11.5. Also, possible chemical reactions are discussed, which explains role of pH with the help of XRD and PL results.

## 2 Materials and Methods

All the materials used in the aqueous-based method were of analytic grade. 50 ml double distilled water was used as solvent where zinc acetate dihydrate (zinc ion source) and hydrazine hydrate (complexing agent) were mixed in a beaker with continuous stirring. Ammonia solution (25%) was added to the ongoing reaction to maintain the pH value of the solution at 10.5 and 9.5. The solution temperature was kept at 70 °C to optimize the material characteristics for their application in QDSSC. Thiourea was added as a sulphur source, and the solution was kept under stirring for 4 h. The prepared nanoparticles solution was then washed, centrifuged, and dried in an oven at 40 °C. Collected samples were then characterized for PL and PLE, and XRD using Perkin Elmer LS-55 spectrophotometer, and XRD-6000 diffractometer, respectively.

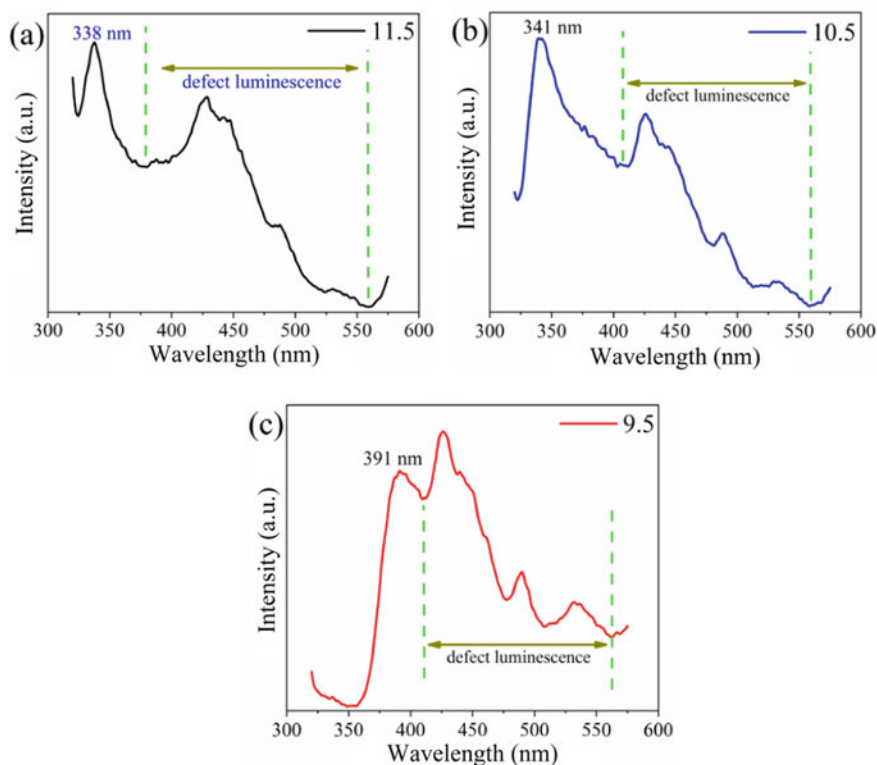
## 3 Results and Discussion

### 3.1 Optical Study (PL and PLE)

Figure 1a–c shows the PL spectra of samples prepared at 11.5, 10.5, and 9.5, respectively. Peaks at 338, 341, and 391 nm correspond to band edge emission (BEE) in Fig. 1a–c for the samples prepared at pH values 11.5, 10.5, and 9.5. A slight red-shift (~ 3 nm) was observed when the pH value was changed from 11.5 to 10.5, which shows negligible effect on the optical property of the as-prepared sample. However, a significant red-shift (~ 50 nm) was observed in the BEE peak when the pH value was changed from 10.5 to 9.5. Since, in our previous work, ZnSO formed at 11.5

pH shows two phases, i.e. ZnS and ZnO [5]. Therefore, possible reason behind this significant shift can be explained on the basis of dominating phase in as-synthesized sample, if formed at 9.5 pH also. Since BEE peaks for ZnS can be observed after 335 nm (3.68 eV), peaks at 338 and 341 nm can be due to dominating phase of formed ZnS, but for the sample synthesized at pH value 9.5, the peak was observed at 391 nm. This emission peak may be due to the ZnO phase if formed since the emission peak for the ZnO can be observed after 367 nm (3.37 eV).

Besides BEE, the PL spectrum of all samples (Fig. 1a–c) also shows the stable defect luminescence (DL) region, where all peaks were observed on the same positions, clearly indicating the stable DL. The peak at 426 nm could be due to sulphur vacancy or oxygen vacancy, the peak at 446 nm can be assigned to the interstitial zinc, peak at 489 nm can be due to the zinc interstitial or transition of an excited electron to the zinc vacancy level. The peak at 535 nm may be attributed to either transition to deep level or transitions from interstitial zinc to oxygen vacancy level [4, 5].



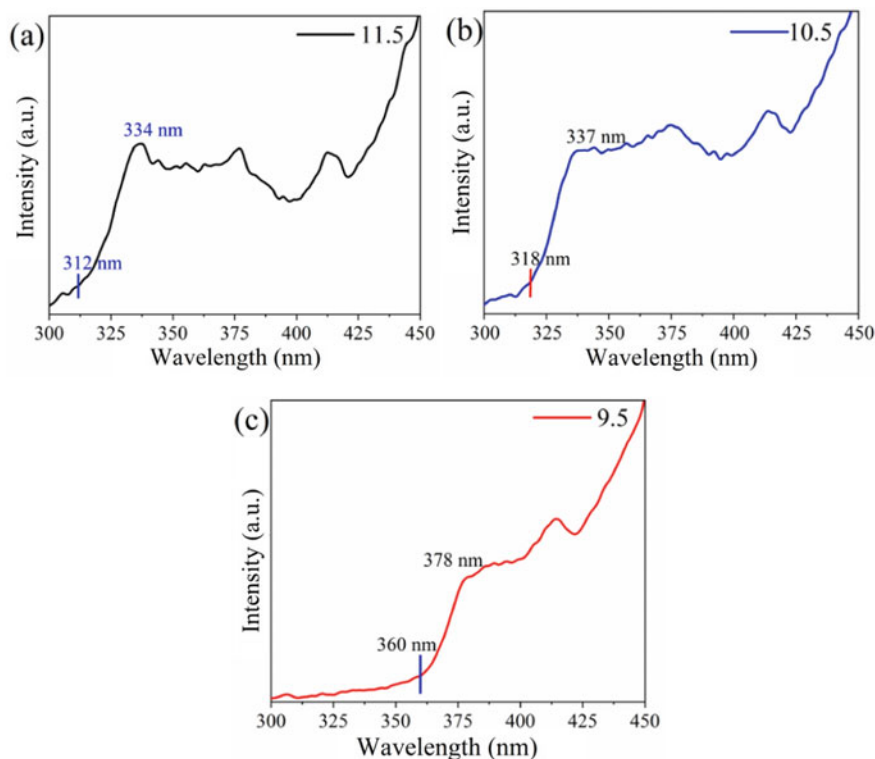
**Fig. 1** Photoluminescence (PL) spectra recorded at fixed excitation wavelength of 300 nm for samples prepared for pH value at, **a** 11.5 [5], **b** 10.5, and **c** 9.5

Figure 2a–c represents the PLE spectra where excitation peak values were observed at 334, 337, and 378 nm for samples prepared at pH 11.5, 10.5, and 9.5, respectively. The band gap of the synthesized samples can also be calculated from the PLE spectra. Generally, excitation processes can only start when the electron absorbs enough photons from the valance band to excite itself. Thus, an immediate change in the starting of excitation spectra just before the first excitation peak can be considered an absorption peak value, where electrons have enough energy to excite to the conduction band. These peak values were observed at 312, 318, and 360 nm in Fig. 2a–c, corresponding to the band gap value of 3.96, 3.88, and 3.43 eV for the samples at 11.5, 10.5, and 9.5 pH, respectively. The structural phase of the prepared samples can also be interpreted from the band gap value. Since a band gap was observed after 3.77 eV for samples prepared at 11.5 and 10.5 pH values, this may be due to the hexagonal phase of the ZnS formed in the structure. Similarly, the band gap value for the prepared sample at 9.5 was observed after 3.37 eV [6]; it can be due to the hexagonal phase of ZnO if formed in the structure, which can be verified through the XRD spectrum and ongoing possible chemical reactions discussed in the following sections.

### 3.2 Structural Study (XRD)

The initial study, which was optical characterization, resulted in a minor change in PL from 338 to 341 nm for samples synthesized at 11.5 and 10.5. However, it shows a drastic shift in PL from 338 to 391 nm for prepared samples at 11.5 and 10.5 pH values. Therefore, only the sample synthesized at 9.5 was characterized for XRD to compare the structural information for the sample already synthesized at 11.5 [5], so that conclusion can be made for this drastic change based on structure, if possible.

Figure 3a, b represents the XRD spectra for samples synthesized at pH values 11.5 and 9.5, and shows the mixed phase of ZnO and ZnS in the prepared samples (JCPDS file number-#80-0074 and #72-0162, respectively). In Fig. 3a, a broad peak of ZnS was observed at  $2\theta$  value of  $29.22^\circ$  [showing plane (1 0 4)], having full width at half maxima (FWHM) value of 0.054 radians, giving out the crystallite size of 2.77 nm according to Scherer's formula. This shows the formation of nanoparticles with confinement effect. Also, small peak at  $11.47^\circ$  confirms the formation of ZnS-10H polytype [5]. ZnO peaks were also observed at  $2\theta$  values of  $31.70^\circ$ ,  $34.32^\circ$ ,  $36.14^\circ$ ,  $47.48^\circ$ ,  $56.53^\circ$ ,  $62.61^\circ$ , and  $67.86^\circ$ . However, the broadening of ZnS at  $29.22^\circ$  represents its dominance in structural property since smaller nanoparticles were formed for ZnS compared to the ZnO phase, which may be responsible for the PL emission peak at 338 nm. It verifies the possible reason for the BEE peak observed at 338 nm mentioned in the PL section. Figure 3b also shows the mixed phase of ZnS and ZnO at 9.5 pH. However, more polytype ZnS-10H phase peaks were observed at  $20.19^\circ$ ,  $27.26^\circ$ ,  $39.41^\circ$ ,  $42.22^\circ$ ,  $52.57^\circ$ , and  $60.48^\circ$ . Using the aqueous-based method, it confirms the reproducibility of ZnS-10H polytype at other pH values, i.e. 9.5. ZnO peaks were observed at the same positions stated above. There was no broadening in



**Fig. 2** Photoluminescence excitation (PLE) spectra recorded at fixed emission wavelength of 500 nm for samples prepared for pH value at, **a** 11.5 [5], **b** 10.5, and **c** 9.5

any peak, showing bigger particle size at this particular pH. This can be the reason behind the significant shift ( $\sim 50$  nm) in the BEE peak observed in PL spectra at 9.5 pH. Therefore, BEE peak at 391 nm shows the dominance of the ZnO phase in the formed structure in the XRD. It could also be due to the polytype structure of ZnS and ongoing chemical reactions during the synthesis, which diminishes its optical property. The possible chemical reactions are discussed in the next section.

### 3.3 Reaction Kinetics

The generalized possible reaction mechanism for both pH values, i.e. 9.5 and 11.5, is shown in Fig. 4 and is as follows:

Step 1: Zinc acetate dihydrate in distilled water will slow the release of zinc ions because of its low solubility in water, i.e. 43 g/100 ml, which will also signify the less formation of zinc hydroxide and acetic acid. Also, simultaneously added hydrazine

**Fig. 3** XRD spectra for prepared samples for pH value at, **a** 11.5 [5], and **b** 9.5

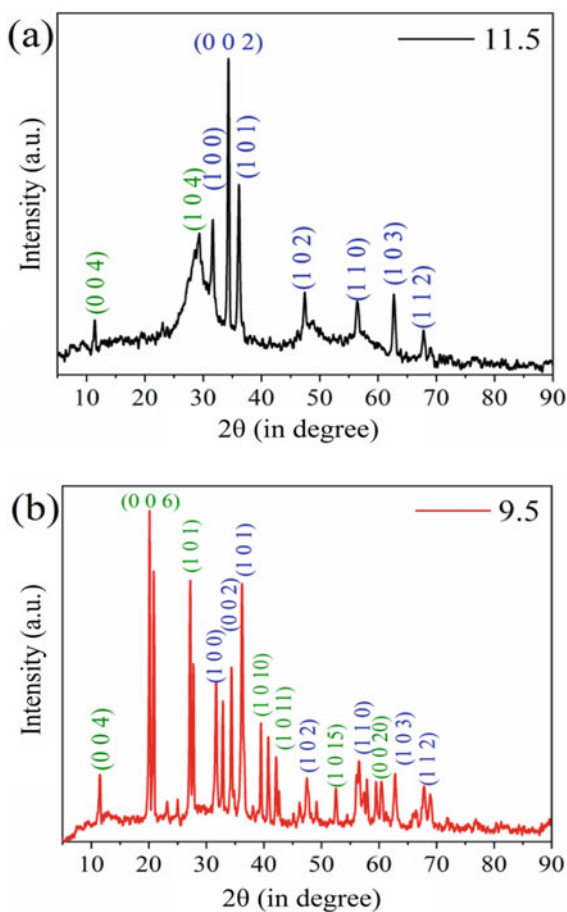
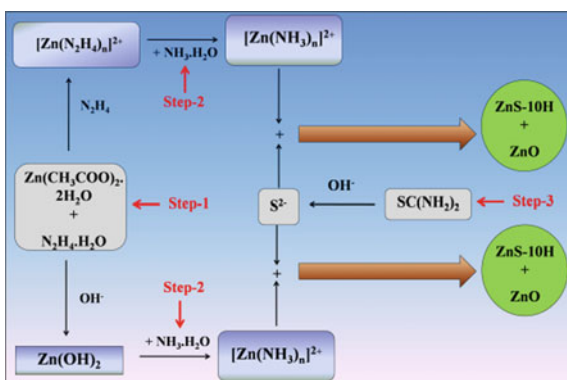
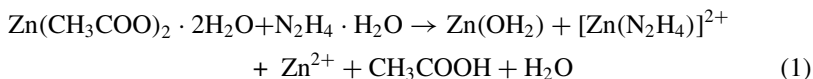


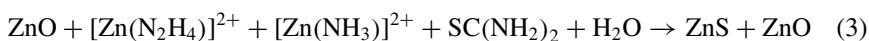
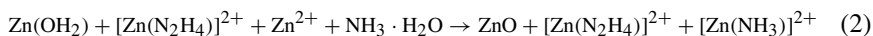
**Fig. 4** The schematic diagram of the chemical reaction for ZnS-polytype and ZnO at pH values of 11.5 and 9.5



hydrate will only result in less formation of zinc-hydrazine complex because of acid–base theory since hydrazine is a strong base and will react with weaker conjugate acid, i.e. acetic acid. Therefore, later on there will be an increment in the zinc hydroxide formation.



Step 2: Ammonia was added to the solution for pH adjustment and as a co-complexing agent, where it will also form zinc-ammonia complexes along with increased  $\text{OH}^-$  ions. Since pH plays a vital role during the ongoing synthesis it; (i) controls the rate of release of sulphur ions from the thiourea; (ii) and it increases the stability of zinc-ammonia complexes by decreasing the release of metal ions from the complexes by increasing the  $\text{OH}^-$  ions in the solution. At 11.5 pH,  $\text{OH}^-$  ion's concentration is high; hence the release of both sulphur ion and zinc ion will be slow, which will result in slow reaction kinetics, thus forming small nanoparticles of ZnS along with the formed ZnO particles, which is also observed in XRD (smaller crystallite size of 2.77 nm) and also resulted in PL emission peak at 334 nm. A similar process can also be stated for the sample prepared at pH 10.5. However, at a pH value of 9.5, the concentration of  $\text{OH}^-$  ions is very low compared to 11.5, resulting in fast reaction kinetics for nanoparticle formation and large-sized nanoparticles.



## 4 Conclusion

Samples were prepared at different pH values of 10.5 and 9.5, which were analysed for optical and structural studies. PL and PLE resulted in the BEE peaks at 334, 337, and 391 nm for samples prepared at 11.5, 10.5, and 9.5 pH values. XRD resulted in the mixed phase of ZnS and ZnO in both samples prepared at pH 11.5 and 9.5. The pH value has affected the reaction kinetics during the ongoing synthesis. Thus, at a particular pH value (< 10.5), i.e. for pH value 9.5, optical properties were changed where the dominance of the ZnO phase was observed, which was due to the presence of lesser zinc-ammonia complexes and faster growth rate resulted in bigger particle. Also, at higher pH values ( $\geq 10.5$ ), i.e. at 10.5 and 11.5, the growth rate was independent of the pH value, resulting in smaller particles size and a higher amount of zinc-ammonia complexes, thus dominated by the ZnS phase giving emission peaks at 337 and 334 nm, respectively. At 9.5 pH value, polytype of ZnS, i.e. was observed



again with more diffraction peaks indicating the successful synthesis method for ZnS-10H. Initial studies have revealed that only samples prepared at pH values 10.5 and 11.5 can have application in QDSSC as a passivation layer since emission peaks are similar to ZnS.

**Acknowledgements** The authors want to acknowledge JUIT Solan for PL and JIIT Noida, India, for the XRD characterization.

## References

1. Song H, Lin Y, Zhang Z, Rao H, Wang W, Fang Y, Pan Z, Zhong X (2021) Improving the efficiency of quantum dot sensitized solar cells beyond 15% via secondary deposition. *J Am Chem Soc* 143:4790–4800
2. Markna JH, Rathod PK (2022) Review on the efficiency of quantum dot sensitized solar cell: insights into photoanodes and QD sensitizers. *Dyes Pigments* 199:110094
3. Chebrolu VT, Kim H-J (2019) Recent progress in quantum dot sensitized solar cells: an inclusive review of photoanode, sensitizer, electrolyte, and the counter electrode. *J Mater Chem C* 7:4911–4933
4. Singh R, Singh RR (2022) Optical properties of ZnS quantum dots: applications in solar cells and biomedicine. *Biointerf Res Appl Chem* 13:158
5. Singh R, Raj Singh R (2022) Unmediated one-step synthesis of novel ZnSO for photovoltaic and electronic applications. *Mater Lett* 324:132651
6. Sakellis E, Markopoulos A, Tzouvelekis C, Chatzigeorgiou M, Travlos A, Boukos N (2021) Low-cost electrodeposition of size-tunable single-crystal ZnO nanorods. *Fibers* 9:38

# Thermal and Anti-Leakage Performance of PCM for Thermal Energy Storage Applications



J. S. Aulakh and D. P. Joshi

**Abstract** Phase change materials (PCMs) are capable of melting and solidifying at nearly a fixed temperature. However, PCM leakage issues limit its application in thermal energy storage (TES). In order to overcome these issues, a leakage-resistant composite has been prepared using a combination of paraffin and styrene-*b*-(ethylene-*ran*-butylene)-*b*-styrene (SEBS) copolymer. The effectiveness of composites against paraffin leakage is investigated using different mass fractions of SEBS, i.e. 10, 15, and 20 wt%. There was no paraffin leakage when SEBS reached 20 wt% mass fractions. In addition, from DSC results it was found that the composite sample exhibit excellent average storage capacity of about ~ 165.25 J/g. Experiments have also been conducted to observe heat transfer performance (storage/release) of composite PCM.

**Keywords** Phase change material · Paraffin · SEBS · Thermal conductivity · Heat transfer

## 1 Introduction

The increasing environmental pollution caused by the use of petrochemical fuels has prompted the development of new technologies that can help to address the issue of sustainable energy and reduce the greenhouse gas emissions [1]. One of the most important factors that has attracted the attention of the industry is the high energy storage density of PCMs. Among numerous types of PCM (hydrate salts, paraffin, esters, fatty acids, etc.), paraffin is the most promising one because of its ‘high storage capability, non-toxicity, non-corrosiveness, low supercooling, and vapour pressure’ [2]. Apart from the various mentioned advantages, the application of paraffin is limited due to leakage issues during phase transformation. To address this problem,

---

J. S. Aulakh (✉) · D. P. Joshi  
Department of Physics, CBSH, G.B. Pant University of Agriculture and Technology,  
Pantnagar 263145, Uttarakhand, India  
e-mail: [aulakh.jaspreet94@gmail.com](mailto:aulakh.jaspreet94@gmail.com)

mainly three approaches have endeavoured—(i) direct incorporation of porous materials into paraffin, (ii) micro-encapsulation of paraffin, and (iii) shape stabilization technique of paraffin with polymeric matrices [3]. However, the direct incorporation of porous materials did not fully solve the leakage issue or may interact with a base material, while micro-encapsulation of PCM is a complex and costlier process. According to review studies, the shape stabilization method has grown significantly over the past few years. PCM that are shape stabilized do not require encapsulation or containment, thereby reducing cost [4]. Therefore, this study introduced a leakage-proof PCM for TES application. For this, composites based on SEBS incorporated with paraffin have been prepared. Paraffin served as PCM and SEBS as the supporting, reinforcing matrix. We also attempted to study the thermal properties of PCM in the polymer matrix. The leakage of paraffin inside the composites has been examined through the leakage test.

## 2 Materials and Methods

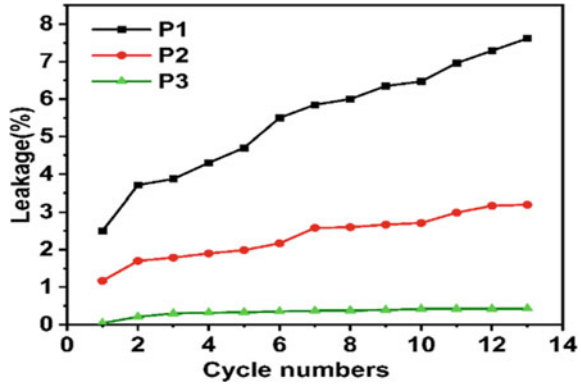
The selected PCM and polymer in this study were paraffin (m.p. = 55–60 °C) and SEBS copolymer purchased from Sigma Aldrich. The samples have been prepared by the melt-mixing method [3, 4]. The paraffin is first fully melted at 70 °C, then SEBS is slowly added into it with constant stirring for 2 h to make a homogeneous mixture. After mixing, the blend was taken into a cylindrical mould (20 mm in diameter) for hot pressing. For compression, 2 bar of pressure was applied for half an hour. In this way, three samples, named P1, P2, and P3 having 10, 15, and 20 wt% of SEBS, have been synthesized in this process.

## 3 Results and Discussion

### 3.1 Paraffin Leakage

The paraffin leakage test method was adopted from our previous study [5]. Results obtained from the leakage test revealed that the composites P1 and P2 perform worse performance and leakage of paraffin increases with increasing the cycle number, while the sample P3, in which SEBS content was 20 wt% shows negligible leakage of paraffin (shown in Fig. 1). The leakage rate for this sample stabilizes at about 0.38%. This low leakage may be ascribed due to the reason that paraffin in a liquid phase is successfully entered in the ethylene–butylene (EB) blocks of the SEBS polymer matrix, and the styrene blocks cover the EB block from both the end, hence forming a crosslinked network, which gives certain strength to the material and restricts the chain movement of paraffin inside it, therefore minimizes the leakage issue [4].

**Fig. 1** Leakage rate graph of samples (P1–P3)



### 3.2 Phase Transition Characteristics and Latent Heat Enthalpy

The phase transition properties of paraffin and P3 composite have been determined by differential scanning calorimetry (DSC, Perkin Elmer) under an N<sub>2</sub> atmosphere. Only P3 has been taken for DSC analysis because of its excellent leakage-bearing properties. The incorporation rate (wt%) of paraffin in the framework of selected SEBS has been calculated using the following formula [5]:

$$\text{Incorporated rate(wt\%)} = \left[ \frac{\Delta H_{\text{impregnated PCM}}}{\Delta H_{\text{pure PCM}}} \right] \times 100$$

where  $\Delta H_{\text{impregnated PCM}}$  is the enthalpy change of shape-stable PCM including paraffin ( $\text{Jg}^{-1}$ ) and  $\Delta H_{\text{pure PCM}}$  is the enthalpy change of paraffin without a framework ( $\text{Jg}^{-1}$ ). The melting and crystallization parameters of the paraffin and P3 composite, including  $T_1$ ,  $T_2$ , and  $\Delta H$ , which have been determined from DSC thermograms, are tabulated in Table 1. Due to the incorporation of SEBS content, the melting and crystallizing peaks of the paraffin in the P3 composite slightly shift to higher and lower temperatures side. Two reasons may explain this behaviour. First, all the paraffin molecules precisely embed in EB-rich microdomains of SEBS, which confines their phase transition to a certain amount. Second, it may be described by the ‘Clapeyron-Clausius equation’ [6, 7]:

$$\ln \frac{T_2}{T_1} = \frac{\Delta_{\alpha}^{\beta} V_m}{\Delta_{\alpha}^{\beta} H_m} (p_2 - p_1)$$

where  $T_2$  and  $T_1$  denote the phase transition temperature  $\Delta_{\alpha}^{\beta} V_m$  and  $\Delta_{\alpha}^{\beta} H_m$  are the change in volume and enthalpy during the phase transition from solid-state ( $\alpha$ -phase) to the liquid state ( $\beta$ -phase). Also,  $p_1$  and  $p_2$  are the ambient pressure during the phase transition process. ‘During the melting of paraffin, the enthalpy ( $\Delta H$ ) and volume of

the paraffin will increase and pressure ( $p_2 > p_1$ ) also increases, resulting in an increase in its melting temperature’.

From the DSC thermogram results (Fig. 2a, b), the latent heat enthalpy of paraffin ( $\Delta H_{\text{paraffin}}$ ) is  $\sim 221.85$  J/g and that of composite P3 is  $\Delta H \sim 165.25$  J/g. The endothermic enthalpy of P3 shape-stable PCMs drops with the increase of SEBS amount. This can be ascribed to the introduction of SEBS causing a corresponding decrease in paraffin content. Also, as shown in Fig. 2a, the SEBS doesn’t contribute to latent heat in their P3 composite.

### 3.3 Thermal Conductivity and Heat Transfer Performance

The thermal conductivity of pure paraffin and P3 sample was  $0.22$  and  $0.177$   $\text{Wm}^{-1} \text{K}^{-1}$ , respectively. The lower conductivity may be due to the confinement of paraffin in the EB block of SEBS copolymer, which increases the thermal resistance on the surface. Further, the temperature changes of paraffin and P3 composite during the charging/discharging process are displayed in Fig. 3a, b. A thermal charging/discharging test has been carried out by using a self-made constant temperature water bath technique to examine the heat transfer ability of paraffin and P3 composite [8]. Prior to the examination, the 20 g sample is filled in a 25 ml beaker and placed into a water bath at room temperature for 2 h to unify its temperature. Afterwards, thermocouples were inserted in the centre of the samples without touching the beaker walls. The heating process was carried out by placing the beaker into the homothermal water bath at  $90^\circ\text{C}$ , and the cooling process was done at room temperature. During heating and cooling, the temperature changes in samples are recorded by the data acquisition system. During the charging process, there is no phase change in paraffin and P3 within the temperature range of  $35\text{--}55^\circ\text{C}$  and the temperature of these two samples rises gradually. When the temperature approaches to the melting point of paraffin, heat is soaked as latent heat; resulting, the temperature increases very slowly. Moreover, a moving solid–liquid interface can be observed in this stage after solid paraffin has been converted into a liquid phase. As paraffin melts, its buoyancy force causes ‘natural convection’ in the liquid region to participate in heat transfer. On the contrary, P3 composite is able to preserve the solidity at the macro level even after the complete melting of paraffin, demonstrating the excellent form stability of composite material. Consequently, natural convection significantly endorses the phase transition and improves the heat transfer, which results in pure paraffin reaching completion of melting more quickly than P3 composite. After melting, the temperature again rises quickly due to the loss of the LHS capacity of paraffin. The time taken by the paraffin and P3 to reach the temperature from  $40$  to  $90^\circ\text{C}$  was  $\sim 972$  and  $\sim 4930$  s. The discharging process took about  $\sim 4371$  and  $\sim 4082$  s to cool their temperature to the same low point. The larger time of paraffin than its composite (P3) is due to its larger latent heat. In the light of the aforementioned findings, it can be said that ‘thermal conduction’, ‘natural convection’, and ‘latent heat absorption’ have the most effect over heat storage/release processes.

**Table 1** DSC data of paraffin and P3 sample

Sample	Melting process		$\Delta H_m$ (J/g)	Solidification process		$\Delta H$ (J/g)	$\Delta H_{p, \text{Theoretical}}$	$\Delta H_{\text{loss}}$ (%)	Incorporation rate (wt%)
	$T_{s-s}$ (°C)	$T_1$ (°C)		$T_{s-s}$ (°C)	$T_2$ (°C)				
Paraffin	46.54	63.41	225.50	40.21	52.52	221.85	–	–	100
P3	46.77	63.56	167.91	39.69	48.70	165.25	177.85	25.51	74.48

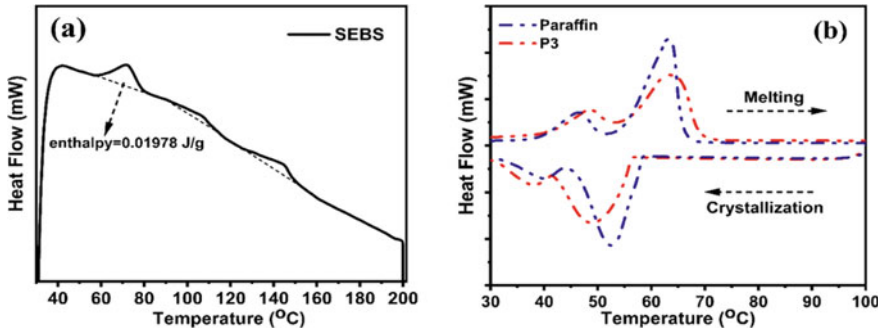


Fig. 2 DSC thermograms of a SEBS, paraffin and b paraffin/20%SEBS (P3) sample

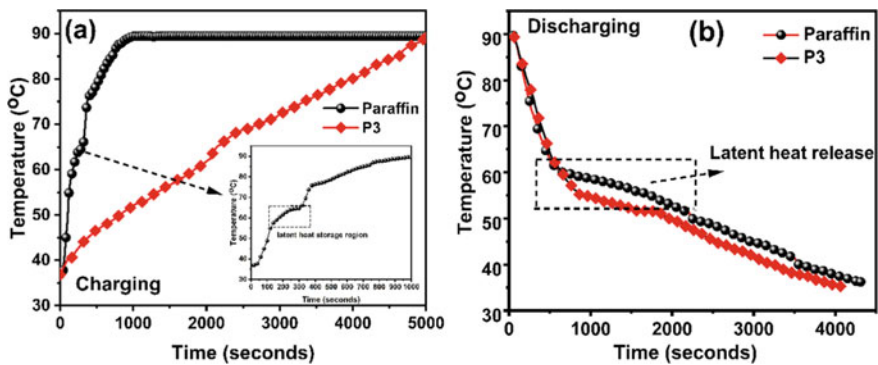


Fig. 3 a Charging and b Discharging of paraffin and paraffin/20% SEBS (P3)

### 4 Conclusion

In this paper, a kind of leakage-proof SEBS/Paraffin composite-based PCM has been prepared by the melt-mixing method. DSC results confirmed that the SEBS slightly shifts the melting peaks of the paraffin and P3 composite to higher temperatures, while the crystallizing peaks shift to lower temperatures. Moreover, the paraffin leakage has been determined through a leakage test in which composites are subjected to repeated heating and cooling cycles at 75 °C. Interestingly, the weight percentage of paraffin can reach ~ 80% with good shape fixing in our exploration, suggesting that high-efficiency shape-stable PCMs possess excellent LHS capacity. In addition, the heat storage/retrieval performance of composite has been studied and it can be concluded that thermal conduction, natural convection, and latent heat absorption have the most effect on paraffin heating and cooling processes. Therefore, this composite has the potential to expand its application to TES.

**Conflict of Interest** The authors declare that they have no conflict of interests.

## References

1. Zhang Y, Li W, Huang J, Cao M, Du G (2020) Expanded graphite/paraffin/silicone rubber as high temperature form-stabilized phase change materials for thermal energy storage and thermal interface materials. *Materials* 13(4):894
2. Mishra DK, Bhowmik C, Bhowmik S, Pandey KM (2022) Property-enhanced paraffin-based composite phase change material for thermal energy storage: a review. *Environ Sci Pollut Res* 15:1–32
3. Wu T, Hu Y, Rong H, Wang C (2021) SEBS-based composite phase change material with thermal shape memory for thermal management applications. *Energy* 221:119900
4. Wu W, Wu W, Wang S (2019) Form-stable and thermally induced flexible composite phase change material for thermal energy storage and thermal management applications. *Appl Energy* 236:10–21
5. Aulakh JS, Joshi DP (2022) Thermal and morphological study of paraffin/SEBS/expanded graphite composite phase change material for thermal energy storage. *Energy Sour A Recov Utiliz Environ Effects* 44(1):986–1003
6. Chriaa I, Trigui A, Karkri M, Jedidi I, Abdelmouleh M, Boudaya C (2020) Thermal properties of shape-stabilized phase change materials based on low density polyethylene, hexadecane and SEBS for thermal energy storage. *Appl Thermal Eng* 171:115072
7. Zhang B, Tian Y, Jin X, Lo TY, Cui H (2018) Thermal and mechanical properties of expanded graphite/paraffin gypsum-based composite material reinforced by carbon fiber. *Materials* 11(11):2205
8. Li C, Zhang B, Liu Q (2020) N-eicosane/expanded graphite as composite phase change materials for electro-driven thermal energy storage. *J Energy Storage* 29:101339



# Molecular Hydrogen Storage in Stone–Wales Defected Single-Walled Carbon Nanotubes Using Molecular Dynamics Simulation



Saurabh Mishra and S. I. Kundalwal

**Abstract** The physisorption of molecular hydrogen ( $H_2$ ) in Stone–Wales defected single-walled carbon nanotubes (D-SWCNTs) is investigated using molecular dynamics simulations (MDS). The interatomic and pairwise interactions between atoms and molecules are described by the AIREBO and Lennard–Jones (LJ) potentials. The effects of defect concentration, temperature, and pressure on hydrogen adsorption metrics have been thoroughly investigated. The findings reveal that (1) the existence of defective sites has a considerable impact on the gravimetric  $H_2$  uptake of large-sized D-SWCNTs and (2) only a trivial difference in hydrogen adsorption is observed on increasing the defect concentration. However, the hydrogen storage capacity of D-SWCNTs exhibits a noticeable advantage over that of pristine SWCNTs as temperature decreases. The maximum  $H_2$  uptake of D-SWCNTs is 9.11 and 1.33 wt% at 77 and 300 K, respectively. Besides, as compared to the requirement for reversible adsorption kinetics, the average binding energy of  $H_2$  molecule in D-SWCNTs is quite low. The average binding energy ranges from 0.021 to 0.052 eV. While the adsorption capacity increases with increasing defect concentration, the mechanical stability of SWCNTs decreases, preventing the utilization of nanotubes for hydrogen storage with a higher defect concentration. We expect that the current studies will encourage researchers to put more effort into efficiently utilizing large-sized D-SWCNTs as a potential hydrogen storage medium.

**Keywords** Stone–wales defect · SWCNT · Gravimetric density · Hydrogen adsorption · Molecular dynamics simulation · Binding energy

---

S. Mishra (✉) · S. I. Kundalwal (✉)

A.T.O.M. Laboratory, Discipline of Mechanical Engineering, Indian Institute of Technology Indore, Simrol, Indore 453552, India

e-mail: [phd2201103002@iiti.ac.in](mailto:phd2201103002@iiti.ac.in)

## 1 Introduction

Energy storage devices based on renewable energy sources may aid in the transition to a more environmentally friendly and sustainable energy economy. One potential option is to use hydrogen as an energy carrier that can be stored, transferred, and retrieved [1]. The establishment of a sustainable hydrogen economy, however, faces few techno-economic challenges. Solid-state storage system based on nanomaterials offers a variety of advantages over traditional storage, including safety, greater accessibility, ease of transportation, and improved thermo-economic kinetics [2].

Carbon nanotubes (CNTs), which have excellent physical properties, porosity, an ideal binding energy, and a higher surface area to density ratio, have shown their distinct benefits as a solid-state hydrogen storage medium [3]. Hydrogen storage in CNTs is primarily caused by the physisorption process, in which hydrogen molecules bind with CNTs via a weak Van der Waals force. Preliminary experimental and theoretical investigations into CNTs' hydrogen storage capability have pointed to the influence of both internal and external parameters, including tube curvature, inter-tube space, structural defects, CNT pre- and post-processing, temperature, pressure, and functionalization [4]. CNTs often contain a wide variety of structural defects as a result of limitations imposed by the synthesis and purifying procedures [5]. These defective sites demonstrated increased  $H_2$  molecule binding strength and considerably improved hydrogen uptake [3, 6, 7].

The present work aims to investigate the effect of di-vacancy defected large-sized SWCNTs (D-SWCNTs) employing molecular dynamics simulations (MDS). Additionally, given a range of defect concentrations, hydrogen adsorption metrics have been determined. An innovative potential energy distribution (PED) [8] technique is employed to estimate the adsorbed molecules on the surface of CNTs.

## 2 Computational Methods

We have implemented classical MDS using LAMMPS software package to investigate the energetics and  $H_2$  physisorption in CNTs. Firstly, the atomistic structure of CNTs was generated and further double vacancy (DV) defects, comprising pentagon and octagon rings, were incorporated into the SWCNT structure based on the defect concentration. The defect concentration is expressed as the removed atoms as a percentage of the total atoms in the structure without defects. The structural schematics of D-SWCNT is depicted in Fig. 1a. In this paper, we have analyzed large-sized (25, 25) armchair SWCNT of diameter 33.9 Å. AIREBO and Lennard–Jones (LJ) potential force fields were applied to capture the interatomic and non-bonded interactions in the CNTs and  $H_2$ . Arbitrarily chosen three thousand  $H_2$  in a spherical configuration were added in the simulation box, as illustrated in Fig. 1b. Finally, the long equilibration was performed to reach desired pressure and temperature applying NVT and NPT ensemble for 5 ns, as illustrated in Fig. 1d, e. Furthermore, the adsorbed  $H_2$  are shown in Fig. 1c.

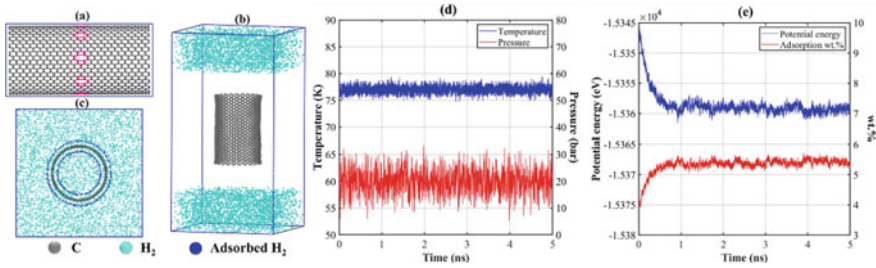


**Fig. 1** a D-SWCNT b initial state c adsorbed H<sub>2</sub>; d, e Equilibration at 77 K and 20 bar

The physisorption of H<sub>2</sub> is evaluated by applying the novel PEDs [8] approach. The adsorption metrics (wt% and  $E_b$ ) can be calculated as:

$$\text{wt}\% = \frac{w_{\text{H}_2}}{w_{\text{H}_2} + w_{\text{C}}}; E_b = \frac{E_{\text{Sys}} - (E_{\text{CNT}} + E_{\text{H}_2})}{n} \quad (1)$$

where  $w_{\text{H}_2}$  and  $w_{\text{C}}$  denotes the weight of adsorbed H<sub>2</sub> and CNTs, respectively.  $E_{\text{Sys}}$ ,  $E_{\text{CNT}}$ , and  $E_{\text{H}_2}$  represents the potential energy (PE) of system, CNT, and H<sub>2</sub>, whereas  $n$  is the number of adsorbed H<sub>2</sub>.

### 3 Results and Discussion

The impact of structural defects in CNTs is inevitable, and this fact must be considered during analysis. The effect of defect concentration on gravimetric H<sub>2</sub> uptake is depicted in Fig. 2a, b. Figure 2a depicts that the adsorption capacity of D-SWCNTs increases significantly compared to the pristine SWCNTs for all the pressures at 77 K. In addition, at 300 K, we have observed an increment in adsorption capacity when the defect concentration is increased up to 2%, stabilizes at 4%, and subsequently declines, as shown in Fig. 2b. At 77 K and 100 bar, the maximum H<sub>2</sub> uptake for D-SWCNT is 9.11 wt%. On the other hand, storage capacity is drastically reduced to 1.33 wt% on raising the temperature from 77 to 300 K due to increased thermally induced motion of the molecules, causing frequent desorption of hydrogen. Notably, both large-sized defected and pristine SWCNTs have achieved the US DOE's target at 50 bar and 77 K. Moreover, the adsorption pattern surrounding pristine SWCNTs and D-SWCNTs at a pressure of 100 bar is displayed in Fig. 2c–f. In addition, Table 1 presents the average binding energies of the CNTs per H<sub>2</sub>, which were calculated at 77 and 300 K.

Figure 3a illustrates the adsorption isotherms for the D-SWCNT containing 4% DV defects at 77 and 300 K. The variation in H<sub>2</sub> uptake at 300 K is depicted in the inset figure. Besides, Fig. 3b reveals the limitations on the incorporation of the higher defect concentration due to the lower mechanical stability of the SWCNTs.

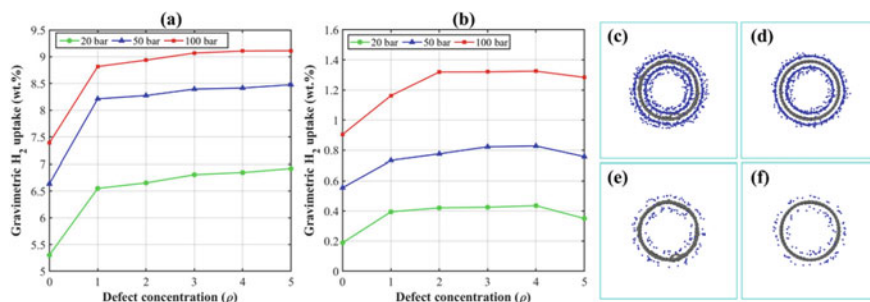


**Fig. 2** Adsorption capacities **a** at 77 K, and **b** 300 K; multilayer adsorption in **c** D-SWCNT at 77 K, **d** pristine CNT at 77 K, **e** D-SWCNTs at 300 K, and **f** pristine CNT at 300 K

**Table 1** Average H<sub>2</sub> binding energy for pristine and defected-SWCNTs at 77 and 300 K

Average binding energy (eV)	Defect concentration ( $\rho$ )					
	0	1	2	3	4	5
$-E_b$ , 77 K	0.021	0.0241	0.0237	0.0229	0.0224	0.0224
$-E_b$ , 300 K	0.0521	0.044	0.0416	0.0396	0.0378	0.0414

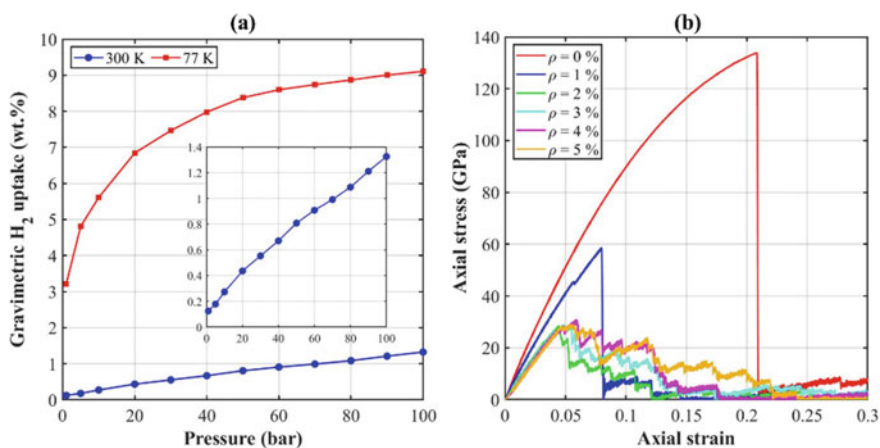


**Fig. 3** **a** H<sub>2</sub> adsorption isotherms, **b** mechanical stability of the D-SWCNTs

## 4 Conclusion

In this study, we employed systematic and extensive MDS to calculate adsorption metrics of large-sized (25, 25) SWCNTs incorporating DV defects employing an innovative PED technique. For all temperature and pressure conditions, we achieved a substantial improvement in the adsorption capacity of D-SWCNTs compared to

pristine SWCNTs. The resultant binding energy, however, reveals a weaker interaction between H<sub>2</sub> molecules and CNTs. Furthermore, the findings demonstrate that increasing the defect concentration in SWCNTs beyond a specific limit would no longer be effective for hydrogen adsorption, but would instead decrease their mechanical stability, resulting in an early fracture.

## References

1. Tarhan C, Çil MA (2021) A study on hydrogen, the clean energy of the future: hydrogen storage methods. *J Energy Storage* 40:102676
2. Moradi R, Groth KM (2019) Hydrogen storage and delivery: review of the state of the art technologies and risk and reliability analysis. *Int J Hydrogen Energy* 44:12254–12269
3. Mishra S, Luhadiya N, Kundalwal SI (2023) Atomistic insights into the H<sub>2</sub> adsorption and desorption behavior of novel Li-functionalized polycrystalline CNTs. *Carbon* 207:23–35
4. Lyu J, Kudiiarov V, Lider A (2020) An overview of the recent progress in modifications of carbon nanotubes for hydrogen adsorption. *Nanomaterials* 10:100217
5. Bhatt MD, Kim H, Kim G (2022) Various defects in graphene: a review. *RSC Adv* 12:21520–21547
6. Lugo G, Cuesta IG, Sánchez Marín J, Sánchez de Merás A (2016) MP2 study of physisorption of molecular hydrogen onto defective nanotubes: cooperative effect in stone–wales defects. *J Phys Chem A* 120:4951–4960
7. Mishra S, Kundalwal SI (2022) Topological defects embedded large-sized single-walled carbon nanotubes for hydrogen storage: a molecular dynamics study. *Int J Hydrogen Energy* 47:36605–36621
8. Luhadiya N, Kundalwal SI, Sahu SK (2021) Investigation of hydrogen adsorption behavior of graphene under varied conditions using a novel energy-centered method. *Carbon Lett* 31:655–666

# 0.9 V Graphene Transistor Based Triple Cascode Operational Transconductance Amplifier: A Comparative Analysis



Faraz Hashmi, M. Nizamuddin, and Adil Zaidi

**Abstract** The design and modeling of a triple cascode operational transconductance amplifier (TCOTA) are presented in this study. These proposed TCOTAs are constructed utilizing 45 nm MOSFETs and carbon nanotube field effect transistors (CNTFETs). Since the suggested architectures are hybrid in nature, they make use of both traditional MOSFETs and CNTFETs. According to the simulation analysis of the suggested TCOTAs, the suggested hybrid devices perform noticeably better than the suggested conventional devices. When compared with traditional devices, the suggested hybrid devices' DC gain, bandwidth, and power consumption have been found to significantly improve. The performance of the suggested TCOTAs can be further customized by altering the amount of CNTs.

**Keywords** OTA · CMOS · CNTFET · Carbon nanotube (CNT) · DC gain

## 1 Introduction

In analog systems, the operational transconductance amplifier is both the most crucial and commonly utilized element. The ratio between the input voltage and output current is referred to as the gain in OTA. Because the transconductance amplifier transforms an input voltage into a current at the output terminal, OTA is a voltage-controlled current source [1]. Compared with an operational amplifier (OP-AMP), OTAs have certain advanced features such as a broader bandwidth, a more fantastic dynamic range, a higher output resistance, a wider bandwidth, and no extra phase difficulties [1–3, 6]. To keep linearity and increase output impedance without sacrificing bandwidth, these OTAs incorporate a directional cascode design. Due to the extremely high output impedance node ( $R_{out} = R_{ocasn} || R_{ocasp}$ ) depicted in Fig. 2a,  $I_{out}$

---

F. Hashmi (✉) · M. Nizamuddin · A. Zaidi  
Department of Electronics and Communication Engineering, Faculty of Engineering and Technology, Jamia Millia Islamia, New Delhi, India  
e-mail: [farazhashmi16@gmail.com](mailto:farazhashmi16@gmail.com)

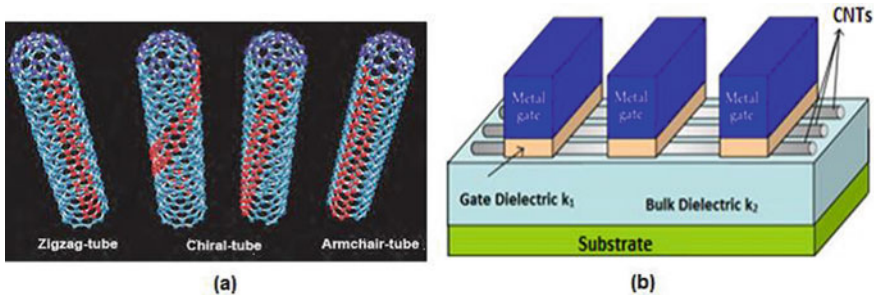


**Fig. 1** a SWCNTs and MWCNTs, b Schematic diagram of a CNTFET

almost entirely flows through external load capacitance  $C_L$ . To get a higher gain, we have added more cascoded devices and placed them in the lower and upper branches [6–8].

## 2 Triple Cascode Operational Transconductance Amplifier Based on Carbon Nanotube Field Effect Transistors

One of the potential replacements for non-silicon electronics is carbon nanotubes, which were discovered in 1991 by Ijima of NEC Japan. They have greater tensile strength, electrical conductivity, thermal conductivity, and almost 1D ballistic transport capability compared with steel. Figure 1 demonstrates how the chirality vector, also known as the roll-up vector or as a pair of indices  $(n, m)$ , can demonstrate the wrapping of graphite sheets in CNT. Using the chiral angle  $(\theta)$  and chiral vector, there are two different types of SWCNTs. If  $n = m = 0$ , SWCNT is an armchair type and lies between  $0^\circ$  and  $30^\circ$ , if  $n = m = 0$ , SWCNT is a zigzag type and lies between  $0^\circ$  and  $30^\circ$  [4, 6, 7].

A CNTFET's channel is built by a parallel combination of SWCNTs, just like a conventional MOSFET. The circuit topology used for the proposed and standard CNTFET-based triple cascode OTAs (TCOTAs) are seen in Fig. 2a, b, respectively. Two different CNTFET-based triple cascode types have been designed and simulated, but only one, the NCNTFET-PMOS-triple cascode, is shown in Fig. 2b.

## 3 Results and Discussion

As illustrated in Fig., the CNT's diameter ( $D_{CNT}$ ) and pitch ( $S$ ) can be preserved while changing the number of CNTs ( $N$ ). Figure 3a illustrates that in both NCNTFET-PMOS-TCOTA and PCNTFET-NMOS-TCOTA circuits, it may be observed as a change in DC gain with the number of CNTs. Then, as  $N$  is increased, raise DC gain

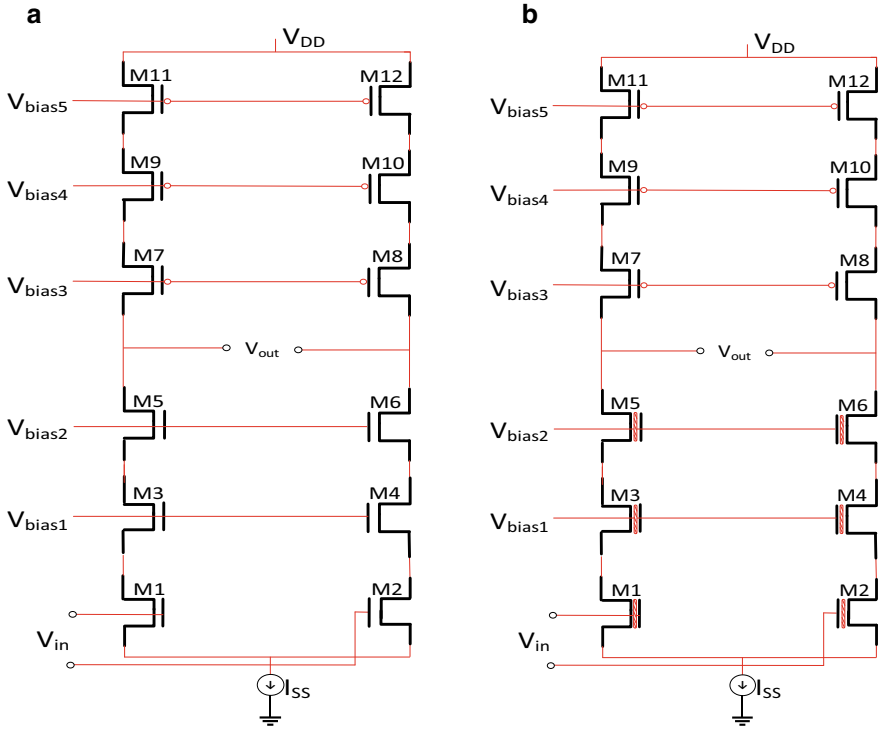


**Fig. 2** **a** Conventional CMOS-triple cascode topology, **b** NCNTFET-PMOS-triple cascode topology

since a CNTFET’s current and conductance will grow. The output resistance does, however, also drop as  $N$  is increased [3]. Because of this,  $N$  grows in both cases with more or less constant DC gain [1, 2]. The following equation provides the gain formula.

$$\text{DC gain}(A_V) = g_{mn}(R_{out}) = g_{mn}(R_{ocasn}|R_{ocasp}) \tag{1}$$

As a result, NCNTFET-NMOS-TCOTA has a greater DC gain than PCNTFET-NMOS-TCOTA.

Figure 3b demonstrates that in both NCNTFET-NMOS-TCOTA and PCNTFET-NMOS-TCOTA circuits, bandwidth improves with the number of CNTs. Nevertheless, for PCNTFET-NMOS-TCOTA circuits, it increases linearly and is more significant than NCNTFET-PMOS-TCOTA.

Figure 3c demonstrates how significantly more CNTs added to CNTFETs result in a significant decrease in output resistance. This is the innovative and outstanding CNT transport-related property. The W/L ratio of a CNTFET increases as the number of CNTs increases, which also increases the channel width ( $W$ ), and the output resistance reduces [5–8].



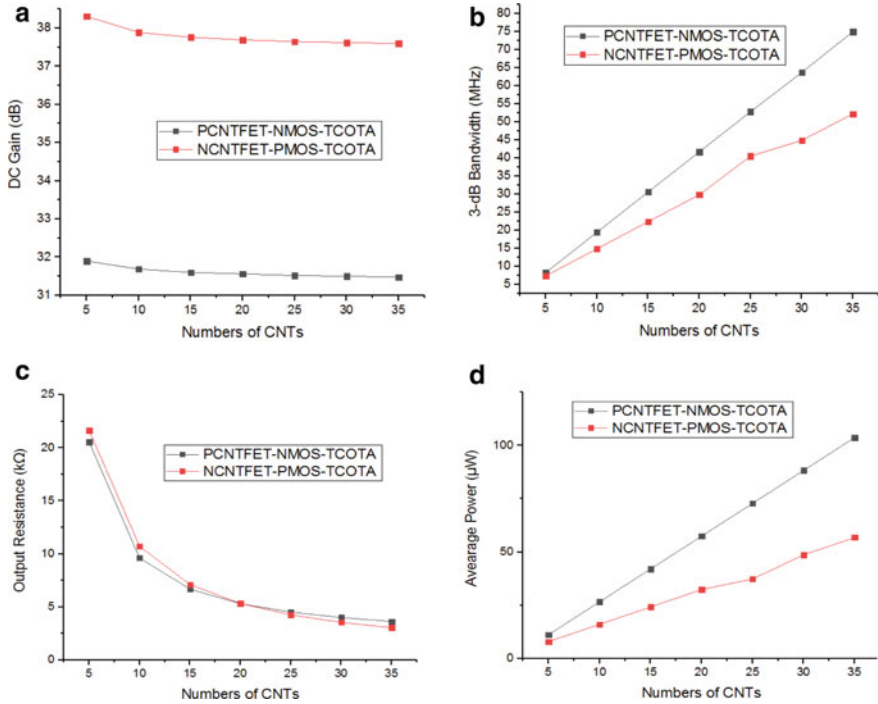


**Fig. 3** a CNT count’s impact on DC gain, b CNT count’s impact on 3-dB bandwidth, c CNT count’s impact on output resistance, d CNT count’s impact on average power

Both NCNTFET-PMOS-TCOTA and PCNTFET-NMOS-TCOTA circuits exhibit an increase in average power as the number of CNTs rises, as seen in Fig. 3d. Due to a significant output current, PCNTFET-NMOS-TCOTA has higher power dissipation (Table 1).

**Table 1** Comparison of the operation and performance of TCOTA circuits based on CNT and on conventional CMOS technology at power supply  $V_{DD} = 0.9$  V, load capacitance  $C_L = 1$  pF,  $W_N = 381.5$  nm, and  $W_P = W_N$  at technology node of 45 nm [9]

Parameters	NCNTFET-PMOS-TCOTA	PCNTFET-NMOS-TCOTA	CMOS-TCOTA
DC gain (dB)	37.69	31.56	28.13
Bandwidth (kHz)	29.84	41.73	37.22
Output Resistance (KΩ)	5.33	5.31	6.18
Average power (μW)	32.39	57.45	59.58

## 4 Conclusion

The design and simulation of three OTA circuits have been shown in this work, while the other two use hybrid technology. Conventional MOSFETs and CNTFETs are used in proposed hybrid structures. The two hybrid structures that have been proposed are known as PCNT-NMOS-TCOTA and NCNT-PMOS-TCOTA. In modeling and comparison investigations of these circuits, the exceptional and unique characteristics of CNTFETs have contributed in a notable improvement in OTA performance. The results for circuits have been observed that are compared with the traditional bulk CMOS-TCOTA, NCNT-PMOS-TCOTA has a DC gain that is 33% higher, an output resistance that is 13% lower, and a power dissipation that is 45% lower. Compared with the traditional bulk CMOS-TCOTA, NCNT-PMOS-TCOTA exhibits a 33% improvement in DC gain, a 13% drop in output resistance, and a 45% reduction in power dissipation. Consequently, employing HSPICE and altering the number of CNTs (N) at a power supply of 0.9 V, the operational performance of CNT-based OTAs is examined.

## References

1. Baker RJ (2000) CMOS circuit design, layout and simulation, 3rd edn. PHI, New Delhi
2. Razavi B (2002) Design of analog CMOS integrated circuits. Tata-McGraw Hill, New Delhi
3. Nizamuddin M, Loan SA, Alamoud AR, Abbasi SA (2015) Design, simulation and comparative analysis of CNT based cascode operational transconductance amplifiers. *Nanotechnology* 26:12
4. Sumio I (1991) Helical microtubules of graphitic carbon. *Nature* 14:354
5. Appenzeller J (2008) Carbon nanotubes for high performance electronics. *Proc IEEE* 96(2):206
6. Yao Zhijian Y, Chengyan M, Tianchun Y, Taishan M (2008) Design and analysis of a gain-enhanced fully differential telescopic operational transconductance amplifier. *J Semicond* 29(2):269
7. Cen M, Song S, Cai C (2017) A high performance CNFET-based operational transconductance amplifier and its applications. *Analog Integr Circ Sig Process* 9:463–472
8. Tomar MK, Singh V, Laxya L (2021) A study on development of CNTFET based analog and digital circuits. *IEEE* 14:9633592
9. A Quick User Guide on Stanford University Carbon Nanotube Field Effect Transistors (CNFET) HSPICE Model V. 2.2.1

# Enhanced Photocatalytic Activity of Hydrothermally Synthesized Nanostructured Monoclinic BiVO<sub>4</sub> Nanosheets



Farheen Jahan, Waseem Ashraf, A. M. Siddiqui, and Manika Khanuja

**Abstract** In this study, we report the synthesis of visible light active monoclinic structured bismuth vanadate (m-BiVO<sub>4</sub>) nanosheets (2D) by facile hydrothermal method. The morphology of the synthesized sample was governed by sodium dodecyl benzene sulfonate (SDBS) surfactant. Prepared samples were investigated by the characterization techniques such as ultraviolet visible (UV–Vis.) spectroscopy, fourier transform infra-red (FTIR) spectroscopy, x-ray diffraction (XRD), field emission scanning electron microscopy (FESEM), and Raman spectroscopy. Monoclinic scheelite structure (m-BiVO<sub>4</sub>) was confirmed by XRD studies. The estimated direct band gap energy ( $E_g$ ) 2.38 eV and monoclinic crystalline phase (XRD) clearly demonstrates a good visible light driven photocatalytic activity. The two-dimensional (2D) nanosheets of m-BiVO<sub>4</sub> showed enhanced photocatalytic activity as studied by degradation efficiency (96% in 150 min) towards malachite green (MG) dye under natural sunlight irradiation in comparison with the synthesized BiVO<sub>4</sub> nanoparticles. The analysis of all the measurements proposed that the nanosheets morphology with large surface area is an important factor in the amplification of photocatalytic reactions in m-BiVO<sub>4</sub> nanosheets.

**Keywords** m-BiVO<sub>4</sub> · Photocatalysis · FESEM · Malachite green (MG)

## 1 Introduction

The most common organic dyes such as methyl orange; malachite green; rhodamine blue; and methylene blue; are heavily employed in textile, cosmetic, leather, food, drug, and plastic industries. However, they are toxic, indissoluble, and harmful for the health of environment and humans. Malachite green is a basic green dye,

---

F. Jahan · A. M. Siddiqui  
Department of Physics, Jamia Millia Islamia, New Delhi 110025, India

W. Ashraf · M. Khanuja (✉)  
Centre for Nanoscience and Nanotechnology, Jamia Millia Islamia, New Delhi 110025, India  
e-mail: [manikakhanuja@gmail.com](mailto:manikakhanuja@gmail.com)

readily soluble in water and has been used as an antimicrobial agent, antifungal medication, and a topical antiseptic since 1930. But it has been classified as carcinogenic [1, 2]. The photocatalysis is the most widely used process, for resolving these types of environmental contaminations. Photocatalysis is the low-cost, sustainable, and ecofriendly technique for wastewater and other polluted water treatment. The photocatalytic materials have enormous potential to treat environmental problems by photocatalytic degradation of dyes and organic pollutants [3].

Monoclinic structured Bismuth vanadate ( $m\text{-BiVO}_4$ ) is a kind of photocatalytic material which shows excellent photocatalytic activity in the visible region for degradation of organic dyes and organic materials along with splitting of water for hydrogen and oxygen evolution due to its comparatively narrow band gap of  $< 2.4$  eV, when compared with tetragonal phase (band gap about 3.1 eV) of  $\text{BiVO}_4$  [4, 5]. The hydrothermal synthesis has been considered a one-step convenient method of preparing metal oxides owing to its numerous benefits, namely particle size management, high purity, and high crystallinity [6].

In addition, the morphology-directing agents utilized in the synthesis method are considered as an imperative factor in varying morphology and improving surface area, which can enhance the photocatalytic activity of  $m\text{-BiVO}_4$ . The presence of SDBS contributed to the crystal structure of  $\text{BiVO}_4$  and improved the photocatalytic activity for the degradation of RhB (N, N, N', N'-tetraethylated rhodamine). The study of Lei et al. revealed the influence of pH in improving the phase and morphology of pure  $\text{BiVO}_4$ . The monoclinic structured  $\text{BiVO}_4$  was fabricated at a low pH, while on increasing the pH value, the mixed phase containing monoclinic and tetragonal structured  $\text{BiVO}_4$  was obtained. The maximum activity of Rhodamine B (RhB) under visible light was shown by  $m\text{-BiVO}_4$  formed at pH 3.0 [7, 8].

2D (nanosheets, nanoplates, etc.) materials describe a developing class of materials that have sheet (or plate)-like structures containing the layer of only single or few atoms. The effort was shined by the invention of graphene, a single-layer carbon material with best thermal, electrical, and mechanical properties in 2004. Later, many graphene-like 2D photocatalyst materials became interesting topics in the photocatalysis field. 2D (sheets or plates-like) structures are described by weak van der Waals interaction between the planes, better electronic properties, strong in-plane bonds, and a large surface area [9–12].

In the present work, we report the hydrothermal synthesis of highly crystalline two-dimensional (2D)  $m\text{-BiVO}_4$  nanosheets and nanoparticles. The crystal structure, functional group, band gap, morphology, and photocatalytic activity were investigated. The toxic malachite green (MG) dye was used for studying the comparative photocatalytic efficiency of  $\text{BiVO}_4$  nanosheets and nanoparticles. The  $m\text{-BiVO}_4$  nanosheets showed higher photocatalytic activity (efficiency 96%) and purified water by degrading hazardous malachite green (MG) dye in water bodies.

## 2 Synthesis Method

All chemicals used for synthesis of pure bismuth vanadate were of scientific grade and were used as received without any alternation. The  $m\text{-BiVO}_4$  nanosheets were prepared by one-step hydrothermal technique. In this procedure, 5 mM of  $\text{Bi}(\text{NO}_3)_3 \cdot 5\text{H}_2\text{O}$  (bismuth nitrate penta hydrate) procured from (Central Drug House Pvt. Ltd., New Delhi) was added to 10 mL of 4 M  $\text{HNO}_3$  (nitric acid) solution, and 5 mM of  $\text{NH}_4\text{VO}_3$  (ammonium vanadate) also procured from (Central Drug House Pvt. Ltd., New Delhi). All these were dissolved into 10 mL of 2 M sodium hydroxide (NaOH) solution. In the next step, 0.25 g of sodium dodecyl benzene sulphonate (SDBS) (Central Drug House Pvt. Ltd., New Delhi) was added to both the solutions and continuously stirred for 30 min separately. After 30 min the two solutions were mixed to get uniform yellow suspension and the pH value of the mixed solution was confirmed as 4.0 by adding 2 M NaOH solution and again stirred for 30 min. The solution was then shifted into a 50 mL teflon-lined hydrothermal autoclave and kept in the furnace at 200 °C for 1.5 h. After that the hydrothermal autoclave was left undisturbed to cool down at room temperature under natural conditions. The precipitate was subjected to filtration and washed with DI water several times and allowed to dry at 100 °C for 4 h in a vacuum oven. Finally collected sample was grinded using mortar and pestle.

## 3 Characterization

The crystal structure and phase determination of the powder samples was determined by using Smart Lab Guidance, Rigaku x-ray diffractometer instrument with X-ray source of  $\text{Cu K}_\alpha$  radiation ( $\lambda = 1.540 \text{ \AA}$ ) with monitoring interval of 0.5 and the scan  $2\theta$  ranging between 10° and 90°. Functional groups and bond structure on the surface of the sample were studied using fourier transform infrared (FTIR) spectroscopy from Bruker Tensor 37 FTIR spectrometer (range 400–4000  $\text{cm}^{-1}$ ). Raman spectrum was measured using HR800 JY, Lab RAM HR in the region from 100 to 1200  $\text{cm}^{-1}$  (Agilent Technologies). To investigate the morphology of the as-synthesized nanostructures, field emission scanning electron microscope (Zeiss, Sigma, FESEM) was used. UV–visible spectrometer (Cary 100 series, Agilent Technologies) was employed to analyze the optical absorption spectra at room temperature.

## 4 Results and Discussion

XRD pattern of the powder material is shown in Fig. 1a. The observed diffraction peaks are perfectly matched with (ICDD file No. 14-0688) [13]. The peaks indicate that the as-synthesized material has the structure of the phase-pure monoclinic

scheelite  $\text{BiVO}_4$  ( $m\text{-BiVO}_4$ ) with high crystallinity. The high-intensity diffraction peak at  $28.9^\circ$  shows the specific orientation of (112) plane in the sample. No extra peaks are detected, inferred hence no impurities are present in the sample.

The diverse functional groups associated to pure  $\text{BiVO}_4$  was studied by FTIR measurements, as shown in Fig. 1b. In  $\text{BiVO}_4$  spectrum, the weak absorption at  $1092\text{ cm}^{-1}$  is referred to the  $\text{V}=\text{O}$  stretching vibrations. The bands at  $721\text{ cm}^{-1}$  is referred to the  $\text{V}-\text{O}-\text{V}$  stretching vibrations and band positioned at  $617\text{ cm}^{-1}$  shows the absorption peak matching to the  $\text{V}-\text{O}-\text{V}$  stretching mode. The wavenumber of FTIR band vibration of  $\text{Bi}-\text{O}$  bending mode was recorded at  $467\text{ cm}^{-1}$  [14, 15].

Raman spectroscopy is a useful tool for investigating the structure and bonding in materials by their vibrational features. In the  $m\text{-BiVO}_4$  nanosheets, the Raman spectrum as shown in Fig. 1c reveals six observable peaks at  $124, 208, 324, 363, 708,$  and  $823\text{ cm}^{-1}$  which are associated with the vibrational features of  $\text{VO}_4$  tetrahedron. The peak at  $823\text{ cm}^{-1}$  is specified to symmetric stretching  $\nu_s$  ( $\text{VO}$ ), with a weak shoulder peak at  $708\text{ cm}^{-1}$  which is attributed to asymmetric stretching  $\nu_{as}$  ( $\text{V}-\text{O}$ ). The asymmetric deformation modes  $\delta_a$  ( $\text{VO}_4^{-3}$ ) and  $\delta_{as}$  ( $\text{VO}_4^{-3}$ ) bands are observed

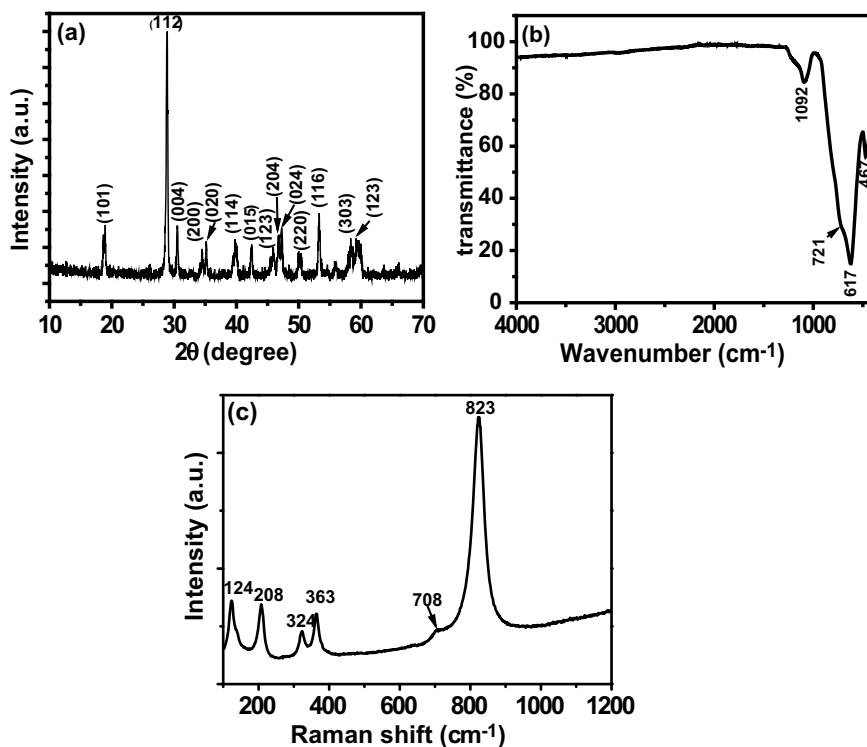


**Fig. 1** a XRD pattern, b FTIR spectrum of  $m\text{-BiVO}_4$  nanosheets, c Raman spectrum of  $m\text{-BiVO}_4$  nanosheets

at 324 and 363  $\text{cm}^{-1}$ . The rotational or translational bands are at about 213 and 124  $\text{cm}^{-1}$  [16].

FESEM is used to examine the morphology of the powder sample. Figure 2a–d shows the FESEM images of m-BiVO<sub>4</sub> nanoparticles and nanosheets at magnifications of 1  $\mu\text{m}$  and 500 nm. Figure 2a, c demonstrated that m-BiVO<sub>4</sub> is an agglomeration of nanoparticles, and Fig. 3b, d depicted m-BiVO<sub>4</sub> clusters of well-defined nanosheets with a smooth, asymmetrical, and dense pattern, and a surface layer containing multiple folds of 2D nanosheets. The optical characteristics of the as-synthesized m-BiVO<sub>4</sub> nanosheets were characterized by using the UV–visible absorbance spectroscopy. Figure 3a shows the absorption spectra. In the nanosheets, band gap energy ( $E_g$ ) was successfully calculated with help of tauc plot (Fig. 3b), which is found to be 2.38 eV ( $E_g$ ) [16]. This band gap lies in the absorption range of visible light, supporting the hypothesis that the sample is in fact photoactive in the visible light range [6].

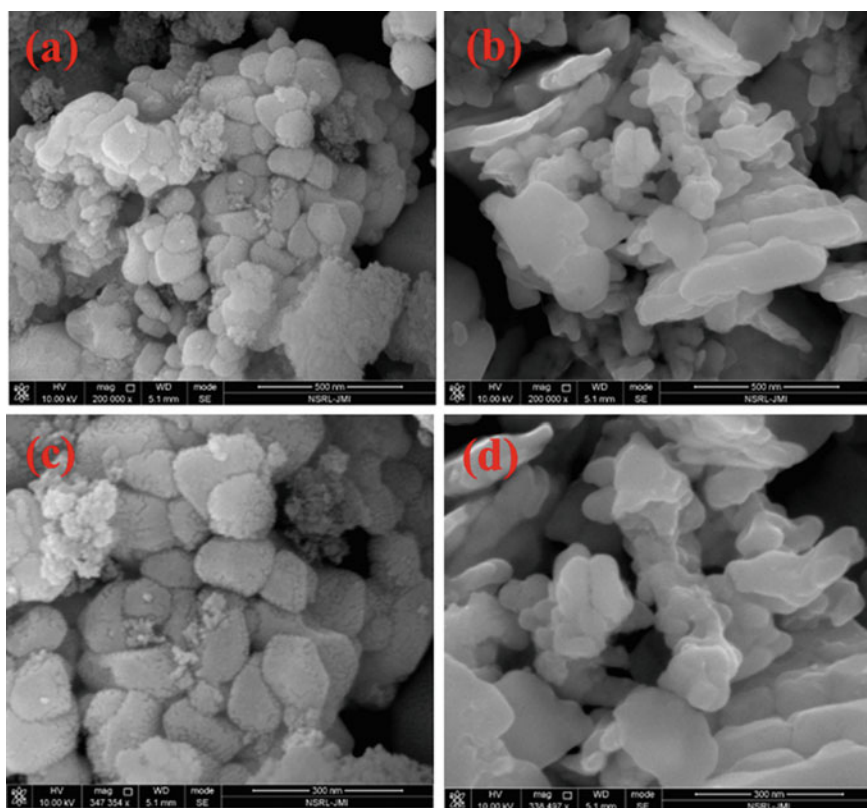


Fig. 2 a, c FESEM images of m-BiVO<sub>4</sub> nanoparticles, and b, d m-BiVO<sub>4</sub> nanosheets

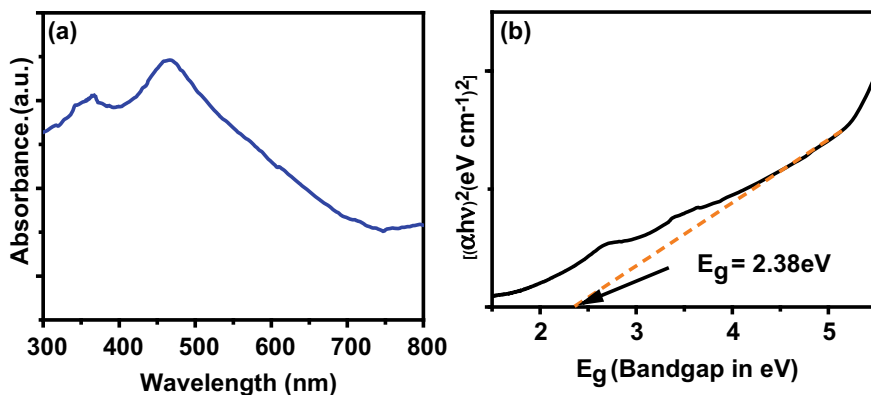


Fig. 3 a UV-visible absorbance spectrum and b Tauc plot of m-BiVO<sub>4</sub> nanosheets

## 5 Photocatalytic Activity Test

The photocatalytic activity experiment was carried out using synthesized nanosheets under sunlight irradiation. For the performance of tests for photocatalysis, 0.025 g photocatalyst was added to 100 ml of aqueous solution of malachite green (10 mg/L). The solution was stirred in dark chamber for half an hour to establish uniform equilibrium between the molecules of dye and the surface of as-synthesized sample. Then, the solution was irradiated under solar light. The photocatalytic behaviour was studied by taking 1 mL solution from MG mixture solution at interval of 30 min for 2 h and 30 min and the collected samples were analyzed using UV-visible spectrometer. The relative absorbance curve of BiVO<sub>4</sub> nanospheres and BiVO<sub>4</sub> nanosheets at UV-visible range wavelengths are depicted in Fig. 4a, b, respectively. Figure 4c the relative absorbance plot  $C/C_0$  versus time are shown in Fig. 4c. It is observed that m-BiVO<sub>4</sub> nanosheets are more efficient in degradation when compared with BiVO<sub>4</sub> nanoparticles. The steep  $C/C_0$  curve is the result of enhanced photocatalytic degradation of MG solution. The degradation efficiency of photocatalyst is shown in Fig. 4d which was evaluated by using relation (1) [17]. It is observed that m-BiVO<sub>4</sub> nanosheets show more photodegradation efficiency ( $\eta = 96\%$  in 150 min) when compared with m-BiVO<sub>4</sub> nanoparticles ( $\eta = 53\%$  in 150 min). It can be suggested that the BiVO<sub>4</sub> nanosheets have a good ability for the purifying water by removing toxic dye (MG) in water bodies. The photodegradation efficiency (%) of the nanosheets (2D) and nanoparticles (3D) were calculated with the help of equation:

$$\eta = (1 - C/C_0) \times 100\% \quad (1)$$

where  $C$  and  $C_0$  denote the concentration at time  $t$  and initial concentrations of MG solution, after visible light irradiation.

The mechanism of photodegradation of malachite green dye solution under the influence of BiVO<sub>4</sub> nanosheets can be attributed to the following equations [1, 18].



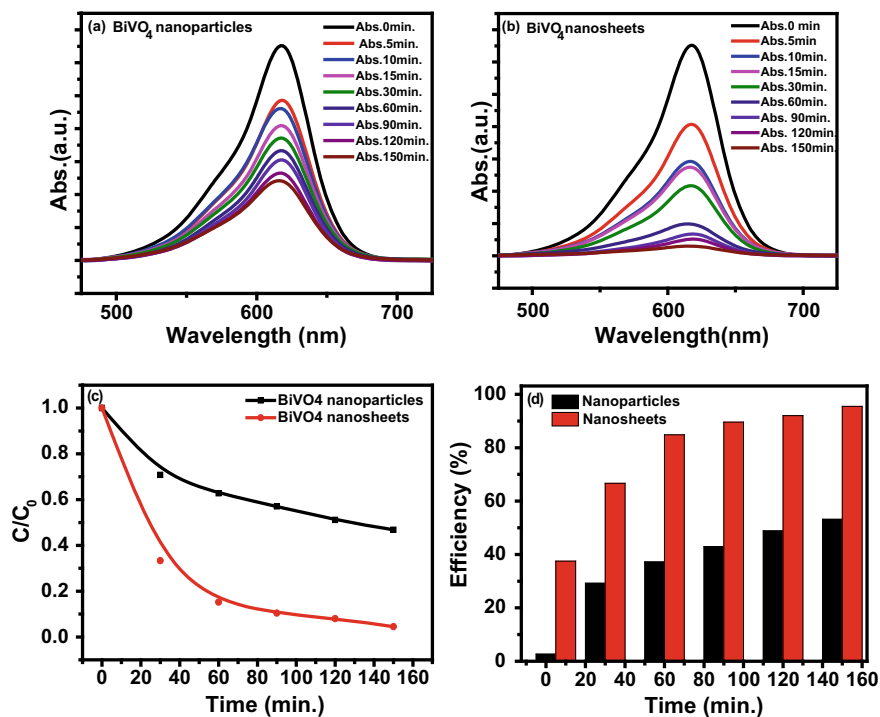
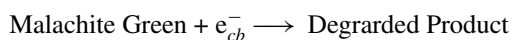
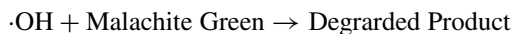
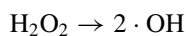
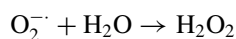
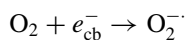
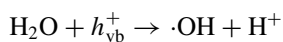
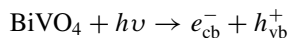


**Fig. 4** UV-visible absorbance characteristics of **a** BiVO<sub>4</sub> nanoparticles, **b** BiVO<sub>4</sub> nanosheets, **c**  $C/C_0$  versus time plot and **d** Photodegradation efficiency (%) versus time



## 6 Conclusion

Two-dimensional (2D) monoclinic-BiVO<sub>4</sub> nanosheets have been prepared by facile hydrothermal technique with the help of the morphology-directing agent SDBS, for the photocatalytic degradation of organic water pollutant. The morphology of the as-synthesized material is well-defined nanosheets clearly observed by FESEM images. The nanosheets are monoclinic structured with a preferred (112) plane orientation. UV-visible absorption spectra determine the band gap 2.38 eV indicating that m-BiVO<sub>4</sub> nanosheets have good capacity to consume sunlight in the range of visible light region. The results revealed that 2D m-BiVO<sub>4</sub> nanosheets ( $\eta = 96\%$  in 150 min) exhibits enhanced photocatalytic activity than the m-BiVO<sub>4</sub> nanoparticles ( $\eta = 53\%$  in 150 min) for the photodegradation of malachite green (MG) dye. The increased efficiency of nanosheets (2D) over nanoparticles (3D) is due to large surface area, higher number of active sites, and good absorption of visible light when compared with nanoparticles. This study presents an excellent visible light induced photocatalytic activity of 2D m-BiVO<sub>4</sub> nanosheets for purification of water.

**Acknowledgements** Dr. Manika Khanuja (one of the authors) is appreciative of Science and Engineering Research Board [(SERB) (No. ECR/2017/001222)] for their support. The use of characterization facility at Centre for Nanoscience and Nanotechnology, Jamia Millia Islamia, New Delhi, is gratefully acknowledged.

## References

1. Ashraf W, Bansal S, Singh V, Barman S, Khanuja M (2020) BiOCl/WS<sub>2</sub> hybrid nanosheet (2D/2D) heterojunctions for visible-light-driven photocatalytic degradation of organic/inorganic water pollutants. *RSC Adv* 10(42):25073–25088
2. Mittal H, Khanuja M (2020) Nanosheets-and nanourchins-like nanostructures of MoSe<sub>2</sub> for photocatalytic water purification: kinetics and reusability study. *Environ Sci Pollut Res* 27(19):23477–23489
3. Kumar A, Singh S, Khanuja M (2020) Temperature based morphological study of graphitic carbon nitride for photocatalytic application. *AIP Conf Proc* 2276(1):020029
4. Pookmanee P, Paosorn S, Phanichphant S (2020) Chemical synthesis and characterization of bismuth vanadate powder. *Adv Mater Res* 93:153–156
5. Singh S, Ruhela A, Rani S, Khanuja M, Sharma R (2018) Concentration specific and tunable photoresponse of bismuth vanadate functionalized hexagonal ZnO nanocrystals based photoanodes for photoelectrochemical application. *Solid State Sci* 76:48–56
6. Xi G, Ye J (2010) Synthesis of bismuth vanadate nanoplates with exposed 001 facets and enhanced visible-light photocatalytic properties. *Chem Commun* 46(11):1893–1895
7. Zhang A, Zhang J, Cui N, Tie X, An Y, Li L (2009) Effects of pH on hydrothermal synthesis and characterization of visible-light-driven BiVO<sub>4</sub> photocatalyst. *J Mol Catal A Chem* 304(1–2):28–32
8. Lei B-X, Zeng L-L, Zhang P, Sun Z-F, Sun W, Zhang X-X (2014) Hydrothermal synthesis and photocatalytic properties of visible-light induced BiVO<sub>4</sub> with different morphologies. *Adv Powder Technol* 25(3):946–951
9. Trinh DTT, Khanitchaidecha W, Channei D, Nakaruk A (2019) Synthesis, characterization and environmental applications of bismuth vanadate. *Res Chem Intermed* 45(10):5217–5259

10. Tan C, Cao X, Wu X-J, He Q, Yang J, Zhang X, Chen J et al (2017) Recent advances in ultrathin two-dimensional nanomaterials. *Chem Rev* 117(9):6225–6331
11. Novoselov KS, Geim AK, Morozov SV, Jiang D, Zhang Y, Dubonos SV, Grigorieva IV, Firsov AA (2004) Electric field effect in atomically thin carbon films. *Science* 306(5696):666–669
12. Low J, Cao S, Yu J, Wageh S (2014) Two-dimensional layered composite photocatalysts. *Chem Commun* 50(74):10768–10777
13. Sharma R, Singh S, Verma A, Khanuja M (2016) Visible light induced bactericidal and photocatalytic activity of hydrothermally synthesized BiVO<sub>4</sub> nano-octahedrals. *J Photochem Photobiol B Biol* 162:266–272
14. Sivakumar V, Suresh R, Giribabu K, Narayanan V (2015) BiVO<sub>4</sub> nanoparticles: preparation, characterization and photocatalytic activity. *Cogent Chem* 1(1):1074647
15. Sajid MM, Amin N, Shad NA, Javed Y, Zhang Z (2019) Hydrothermal fabrication of monoclinic bismuth vanadate (m-BiVO<sub>4</sub>) nanoparticles for photocatalytic degradation of toxic organic dyes. *Mater Sci Eng B* 242:83–89
16. Zhang A, Jiezhong Z (2009) The effect of hydrothermal temperature on the synthesis of monoclinic bismuth vanadate powders. *Mater Sci Poland* 27:14573
17. Ashraf W, Khan A, Bansal S, Khanuja M (2022) Mechanical ball milling: a sustainable route to induce structural transformations in tungsten disulfide for its photocatalytic applications. *Phys E Low-Dimens Syst Nanostruct* 140:115152
18. Aslam Z, Rahman RS, Shoab M, Khan ZMSH, Zulfequar M (2022) Photocatalytic response of CuCdS<sub>2</sub> nanoparticles under solar irradiation against degradation of methylene blue dye. *Chem Phys Lett* 804:139883

# Biomass Derived Fluorescent Nanocarbon Sensor for Effective Sensing of Toxic Cadmium Metal Ions



Joseph Neethu , Mathew Aleena Ann , and Balachandran Manoj 

**Abstract** Cadmium ion ( $\text{Cd}^{2+}$ ) is common in our surroundings and may readily bioaccumulate into the organism following passage through the respiratory and digestive systems. Chronic exposure to  $\text{Cd}^{2+}$  can lead to considerable bioaccumulation in an organism because of its longer biological high life (10–30 years), which permanently harms the health of humans and animals. Considering this hazardous effect of toxic  $\text{Cd}^{2+}$  metal ions, there is a need to develop a toxic-free and simple sensor synthesized from easily available and biocompatible biomass or natural precursor. Herein we report the effective synthesis and development of a fluorescence sensor from *Indigofera tinctoria* (L.), a well-known medicinal plant via one step green, hydrothermal synthesis method. The remarkable fluorescence and larger stokes shift make it ideal for fluorescence sensing strategy. This sensor detects potentially toxic  $\text{Cd}^{2+}$  assisting fluorescence sensing strategy in the metal ion concentration range from 1 nM to 1 M. The Stern–Volmer plot exhibits a remarkable linear detection range exhibiting limit of detection (LOD) as 14.74 nM.

**Keywords** Green synthesis · Nanocarbon sensor · Fluorescence sensing

## 1 Introduction

Heavy metal eutrophication has become a significant issue that has had significant negative consequences on people all over the world. The accelerated release of inorganic pollutants into the environment, particularly aquatic bodies, is one of the primary environmental problems. This is mostly caused by the fast-paced industrialization, improper and illegal garbage disposal, fertilizers, and pesticides. Among many toxic heavy metal ions present in our environment, the hazardous metal cadmium ( $\text{Cd}^{2+}$ ) damages the skeletal and respiratory systems over time, is associated with renal illness, and accumulates in the environment [1, 2]. Therefore, a critical problem that is now being confronted is the requirement to detect  $\text{Cd}^{2+}$ . Because to

---

J. Neethu (✉) · M. A. Ann · B. Manoj

Department of Physics and Electronics, CHRIST (Deemed to Be University), Bengaluru, India  
e-mail: [neethu.joseph@res.christuniversity.in](mailto:neethu.joseph@res.christuniversity.in)

their high sensitivity and selectivity, traditional analytical procedures must be used among the various sensing techniques in order to assist nanoparticles in detecting harmful pollutants at low concentrations. Several analytical approaches do, however, have certain disadvantages, such as time-consuming sample preparation, sophisticated technology, preconcentration processes, and the need for competent employees [3, 4]. Compared with other approaches, the optical spectrophotometry-based sensing strategy has shown to be very advantageous for metal ion sensing due to its excellent sensitivity, selectivity, and low procedural cost.

Biomass is a ubiquitous and renewable resource that is derived from a variety of sources, such as forests, agricultural operations, food waste, etc. Around 140 Gt of biomass waste are produced globally each year, which poses serious environmental problems. Numerous scientists have used a one-pot synthesis of CDs to create nanomaterials from biomass using the green way. In the development of carbon-based nanomaterials, many material scientists' resort to biomass, which is a significant source of carbon because of its environmental friendliness, durability, accessibility, biocompatibility, cheap cost, and relatively high carbon content. It is recognized that CDs made from biomass have several advantages over those made from organic materials, including excellent biocompatibility, cheap cost, selectivity in sensing, and photostability [5, 6].

## 2 Materials and Methods

### 2.1 IBLH-CD Synthesis from Leaf Extract

*Indigofera tinctoria* (L.) was homegrown and is sourced from Bangalore, Karnataka. Treating at 180 °C for 10 h in a teflon-lined autoclave, carbon nanomaterials from the medicinal plant *Indigofera tinctoria* (L.) were created using hydrothermal synthesis process assisting chemical free, one-pot synthesis strategy. The sample was labeled and kept as IBLH for additional characterizations after 0.1 m nylon membrane filter paper (CAT No. 170013 P) obtained from Merck India Ltd., was used for the filtering process after centrifuging the mixture at 10,000 rpm for 20 min.

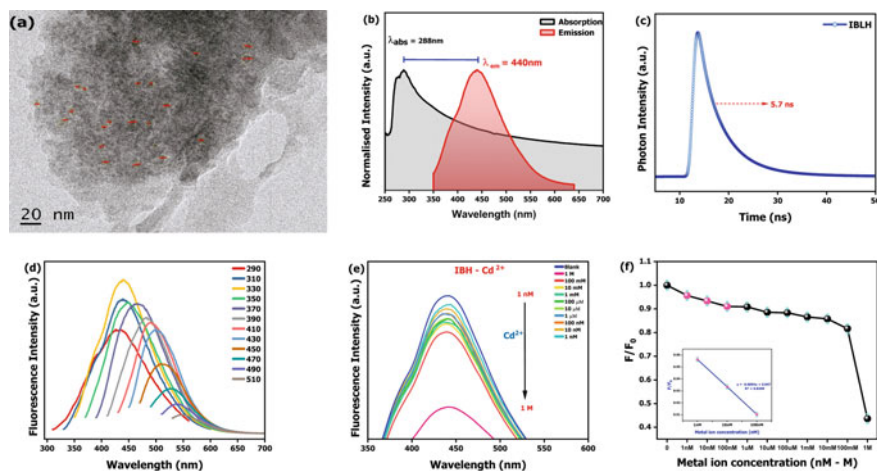


**Fig. 1** IBLH sample displaying its **a** HRTEM images of IBLH-CDs **b** Stokes shift spectra indicating large Stokes shift **c** fluorescence decay lifetime **d** photoluminescence (PL) emission spectra **e** fluorescence quenching with the interaction of various concentrations of  $\text{Cd}^{2+}$  **f** Stern–Volmer plot showing linear response for IBLH-CDs sensor for various concentration  $\text{Cd}^{2+}$

### 3 Results and Discussions

#### 3.1 Structural and Optical Characteristics of the Synthesized IBLH Sample

Figure 1a the 20 nm magnification photograph of the TEM results reveals the formation of clustered spherical nanodots from IBLH via hydrothermal synthesis. The size distribution of these carbon dots (CDs) is heterogeneous and ranges from 3 to 10 nm particle size. TEM results show that carbon dots were successfully generated from IBLH, making this material a suitable probe for fluorescence-based sensing, considering the unique properties of carbon dots in fluorescence sensing strategy [7].

#### 3.2 Optical Analysis and Fluorescence Quenching of IBLH-CDs Sensor by $\text{Cd}^{2+}$

The spectra exhibiting Stokes shift between the fluorescence emission and absorption of the IBLH sample are displayed in Fig. 1b. Due to the large Stokes shift (152 nm) present in this sample, self-absorption is avoided, and the fluorophore's emission and absorption spectra overlap is reduced. Considering the greater Stokes shift value of the IBLH-CDs material, it can be inferred that the carbon nanomaterial synthesized is ideal for fluorescence-based sensing [8].

Fluorescence decay curve of IBLH at wavelength 450 nm recorded using TCSPC, excited at 340 nm. The decay of fluorescence intensity occurs through three distinct relaxation mechanisms, one of which is triggered by the intrinsic state while the remaining two by surface states according to triple-exponential function that was used to model the decay curve as shown in Fig. 1c. IBLH's typical fluorescence lifespan was estimated to be 5.7 ns. This relatively lengthy fluorescence is in favor of making the synthesized IBLH-CDs an excellent probe for fluorescence sensing application in comparison with the previously reported values.

The fluorescence spectra of the synthesized IBLH-CDs recorded at room temperature and neutral pH for excitation wavelengths ( $\lambda_{\text{ex}}$ ) ranging from 290 to 510 nm are shown in Fig. 1. The fluorescence emission intensity of IBLH-CDs rises as the excitation wavelength increases, with an emission maxima at around 441 nm ( $\lambda_{\text{em}}$ ) for excitation at 330 nm ( $\lambda_{\text{ex}}$ ). Following that, with a bathochromic shift in the emission peak, the fluorescence emission decreases as the excitation wavelength increases. In other words, IBLH displays emission behavior that is excitation wavelength dependent. This phenomenon explains why fluorescence emits distinct colors at various excitation wavelengths [9, 10].

The fluorescence response of the IBLH-CDs sensor to  $\text{Cd}^{2+}$  concentrations that vary from 1 M to 1 nM is being conducted to analyze the fluorescence sensing efficacy of IBLH with  $\text{Cd}^{2+}$  (see Fig. 1e). The IBLH fluorescence sensor, whose PL emission exhibits its emission maxima at 330 nm ( $\lambda_{\text{em max}}$ ), was used to record the corresponding fluorescence spectra after adding various quantities of chosen metal ions over time. The Stern–Volmer plot of IBLH-CDs fluorescence sensor reveals a linear response to samples degradation in fluorescence intensity with an appreciably lower detection limit of 14.47 nM, as shown in Fig. 1f. Hence, the linear response exploits the dynamic quenching mechanism, which may be ascribed to the resonance energy transfer or electron transfer [11, 12] between the analyte material  $\text{Cd}^{2+}$  and the fluorophores present in IBLH-CDs material.

## 4 Conclusion

Using an easy and adaptable methodology, biomass-based nanocarbon sensor (IBLH-CDs) was successfully developed from an abundant medicinal plant. To detect the potentially lethal metal ion  $\text{Cd}^{2+}$ , the IBLH-CDs sensor was deployed. The limit of detection (LOD) for the sensor is appreciably low with 14.74 nM as the detection limit, with a wide and linear response spanning from 1 nM to 1 M  $\text{Cd}^{2+}$  concentration range. The developed IBLH-CDs sensor acts as a reliable and easily synthesized fluorescence probe which can be assisted for the sensing of dangerous heavy metal ions and other toxicities.

## References

1. Johri N, Jacquillet G, Unwin R (2010) Heavy metal poisoning: the effects of cadmium on the kidney. *Biometals* 23(5):783–792
2. Hayat MT, Nauman M, Nazir N, Ali S, Bangash N (2019) Environmental hazards of cadmium: past, present, and future. In: *Cadmium toxicity and tolerance in plants*. Elsevier, pp 163–183
3. Arthy M et al (2022) Detection of  $\text{Ag}^+$  by synthesizing fluorescent copper nanoparticles through ultrasensitive free label approach. *J Nanomater* 2022
4. Ramya AV, Joseph N, Balachandran M (2021) Facile synthesis of few-layer graphene oxide from cinnamomum camphora. *Nanobiotechnol Rep* 16(2):183–187
5. Abbas A, Mariana LT, Phan AN (2018) Biomass-waste derived graphene quantum dots and their applications. *Carbon N Y* 140:77–99
6. Iravani S, Varma RS (2020) Green synthesis, biomedical and biotechnological applications of carbon and graphene quantum dots. A review. *Environ Chem Lett* 18(3):703–727
7. Joseph N, Manoj B (2022) Nanomaterials-based chemical sensing. *Nanotechnol Electron Appl* 131–147
8. Sreehari KS, Namratha WN, Joseph N, Balachandran M (2023) Toxic heavy metal ion detection by fluorescent nanocarbon sensor derived from a medicinal plant. *Results Chem* 5:100720
9. Saji M, Elsa Saji B, Joseph N, Mathew AA, Daniel EC, Balachandran M (2022) Investigation of fluorescence enhancement and antibacterial properties of nitrogen-doped carbonized polymer nanomaterials (N-CPNs). *Int J Polym Anal Charact* 27(7):464–476
10. Saji BE, Saji M, Joseph N, Balachandran M (2021) Nitrogen-doped carbonized polymer dots (CPDs) and their optical and antibacterial characteristics: a short review. *Biointerface Res Appl Chem* 12:4662–4674
11. Joseph N (2022) Green synthesized fluorescent nano-carbon derived from *Indigofera tinctoria* (L.) leaf extract for sensing of  $\text{Pb}^{2+}$  ions. *ECS Trans* 107(1):15255
12. Yin H et al (2023) Ultra-sensitive detection of multiplexed heavy metal ions by MOF-derived carbon film encapsulating BiCu alloy nanoparticles in potable electrochemical sensing system. *Anal Chim Acta* 1239:340730



# Design, Simulation, and Comparative Study of CNTFET-Based Folded Cascode Op-Amp with Class AB Output Buffer and Gain Enhancement



Zoya Ali, M. Nizamuddin, and Dinesh Prasad

**Abstract** In this research, Folded Cascode Op-Amp (FCOA) is designed as well as simulated using technologies like pure CNTFET, hybrid CNTFET CMOS, also compare characteristics with CMOS circuit at a 45 nm technology node. It has been noted that unexplored CNTFET-based circuit outshines conventional CMOS technology. DC gain in dB of pure CNTFET-based circuit is improved by 99.6%, the standard power consumption of purely CNTFET circuit is reduced by 10.75%, and the slew rate is improved by 81.38% as compared to CMOS technology circuit at 0.9 V. Stability analysis is also performed and it has been found that the Phase and Gain margin of pure CNTFET circuit are improved by 34.75% and 115.6%, respectively, which makes the system stable. The behavior of CNT and hybrid CNT-CMOS-based FCOA are also studied by varying CNTs Number ( $N$ ), CNT pitch ( $S$ ), and CNT diameter ( $D_{CNT}$ ). The characteristics of CNTFET-based circuits can be enhanced more by changing the number of CNTs, inter-CNT pitch, and CNT diameter.

**Keywords** Carbon nanotubes · CNTFET · CMOS

## 1 Introduction

Folded Cascode Op-Amp (FCOA) is used in analog integrated circuits to achieve high gain and slew rate [1]. It provides higher gain than ordinary Op-Amp. As channel length reduces, the gain of Op-Amp also reduces. So, two stage Op-Amps in which gain enhancement is used to compensate low gain [2] is discussed in this paper using CNTFET and hybrid technology. With scaling of device size, CMOS-based devices are facing challenges of high leakage current and various short channel effects. So, researchers are actively looking for alternatives of MOSFET devices and they can be overcome by replacing MOSFET with carbon nanotube FET (CNTFET) [3, 4].

---

Z. Ali (✉) · M. Nizamuddin · D. Prasad  
Department of ECE, Jamia Millia Islamia, New Delhi, India  
e-mail: [zoya178@gmail.com](mailto:zoya178@gmail.com)

In this work, FCOA is analyzed using CNTFET (pure), hybrid CNTFET CMOS, and traditional CMOS technology at 45 nm node using HSPICE. The CNTFET model by Stanford and Berkeley Predictive Technology model BSIMv4.6.1 is used in simulation analysis. Various performance characteristics and their dependence on CNT pitch ( $S$ ), CNT number ( $N$ ) and CNT diameter ( $D_{CNT}$ ) are studied [4, 5].

There are 5 segments in this paper, second segment describes CNT as well as CNTFET, third segment shows the proposed circuit and its sub-parts shows simulation study, segment 4 shows comparative results and segment 5 is the conclusion.

## 2 Carbon Nanotube Field Effect Transistor (CNTFET)

Carbon nanotube was discovered by Sumio Iijima in 1991. It is formed when graphene sheet is rolled up in the form of tube [3]. Single-walled Nanotube and Multi-walled Nanotube are the two types of CNT. The Silicon channel in conventional MOSFET can be replaced by CNT because of its exceptional electrical properties. The CNTFET is formed when Si channel in conventional MOSFET is replaced by CNT [4]. The working principles of both devices are same. In CNTFET also, gate voltage is capacitively coupled with CNT channel to turn the device ON and OFF. Due to 1-D ballistic transport of charge carriers, CNTFET have improved mobility and higher drive current as compared to conventional MOSFET [4, 5].

## 3 Proposed CNTFET-Based Circuit

Three FCOA circuits based on CNTFET are simulated here, (a) CNT-FCOA, which uses  $P$  type and  $N$  type CNTFETs only, (b) NCNT-PMOS-FCOA, which uses  $N$  type CNTFETs and PMOS and (c) PCNT-NMOS-FCOA, which uses  $P$  type CNTFETs and NMOS. NCNT-PMOS-FCOA and PCNT-NMOS-FCOA circuits are called hybrid structures as they use both CNTFETs and conventional MOSFETs devices. Here, ' $N$ ' and ' $P$ ' blocks in circuit diagram, which provides gain enhancement, are differential amplifier circuits with source follower level shifter stages, which consists of  $N$  type and  $P$  type devices, respectively. NCNT-PMOS-FCOA circuit is shown here, PCNT-NMOS-FCOA is designed by replacing all PMOS transistors by  $P$ -CNTFETs and  $N$ -CNTFETs by NMOS transistors [6] (Fig. 1).

### 3.1 Circuit Analysis by Varying CNT Diameter ( $D_{CNT}$ )

The diameter of ( $n, m$ ) CNT in CNTFET is given by;

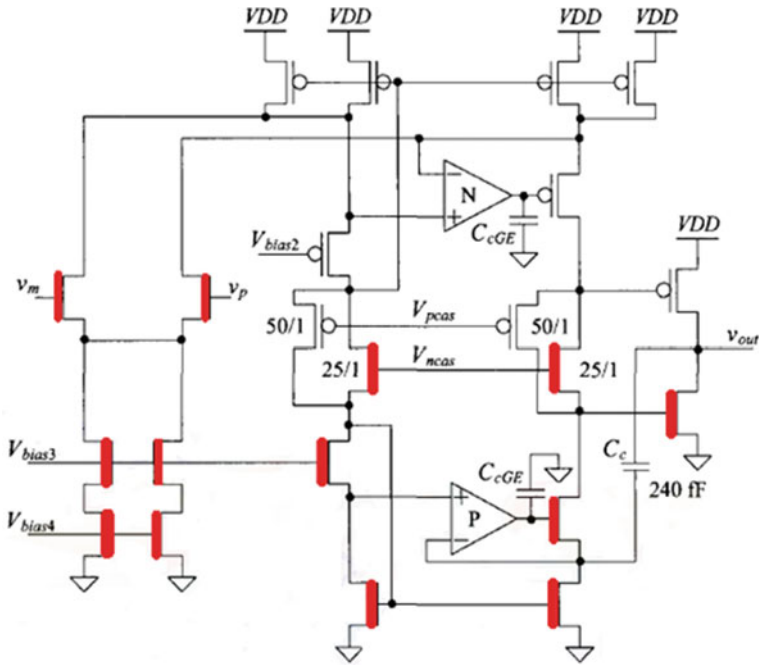


Fig. 1 Proposed NCNT-PMOS-FCOA circuit

$$D_{CNT} = \sqrt{3}a_{C-C}\sqrt{(n^2 + m^2 + n.m)}/\pi \tag{1}$$

$a_{C-C}$  is the carbon atoms distance in the arrangement.

$$E_g = 0.84 \text{ eV}/D_{CNT} \tag{2}$$

$$V_{th} = E_g/(2e) \tag{3}$$

Figure 2 shows that Power dissipation in CNT-FCOA increases with diameter due to increase in charge screening and scattering effect in CNTs [4, 6]. Also, bandgap ( $E_g$ ) and threshold voltage ( $V_{th}$ ) decreases with diameter increment which results in increase in leakage and static power. Gain-Bandwidth product of the circuit is constant, so as diameter of CNT increases, bandwidth increases because of increase in its transconductance [3]. Increment in  $D_{CNT}$  decreases DC gain of circuit, this is due to increase in charge screening and scattering effects in CNT-based circuit.

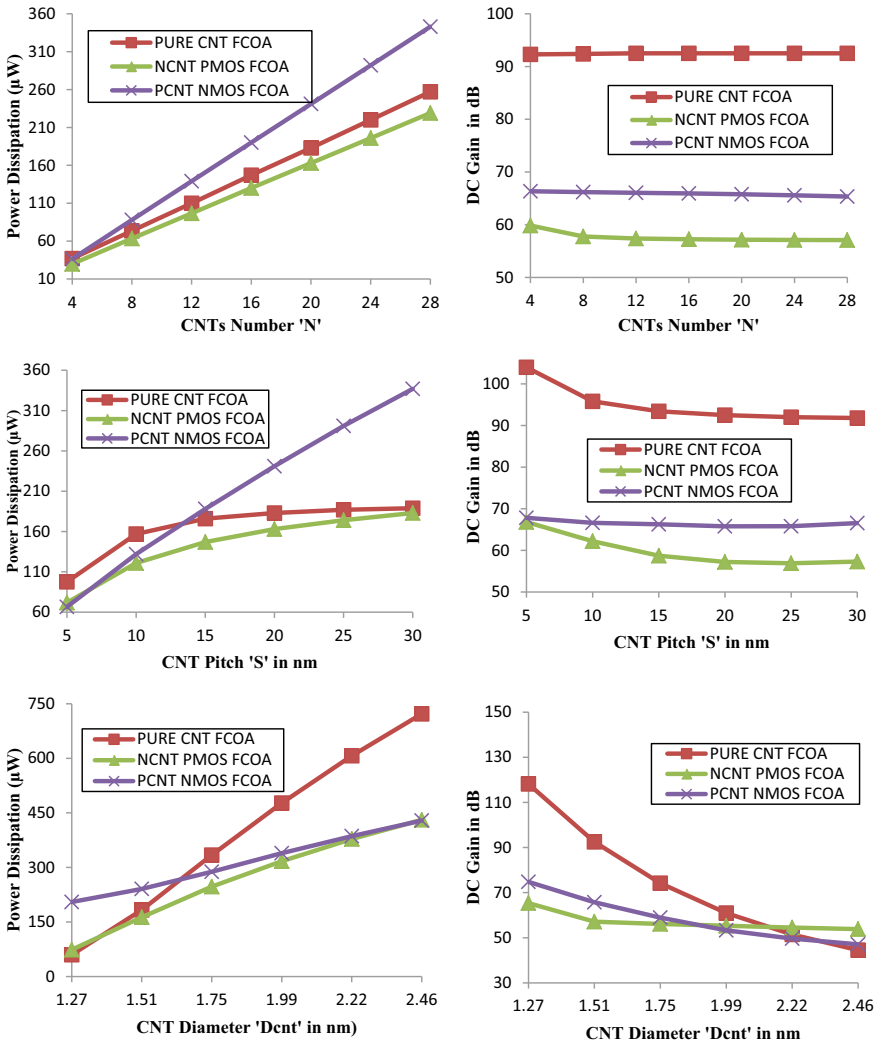


**Fig. 2** Variation of performance parameter with Number of CNTs 'N', Inter-CNT pitch 'S' and CNT Diameter ' $D_{CNT}$ '

### 3.2 Circuit Analysis by Varying Inter-CNT Pitch (S)

Inter-CNT pitch (S) is the distance between centers of two nearby CNTs in CNTFET. Initially, charge screening effect decreases which enhances drive current of CNT [4, 6], hence power consumption increments with increment in Inter-CNT pitch upto 20 nm, then it saturates because drive current is almost constant for larger values of

' $S$ ' as seen in Fig. 2. The DC gain is highest for CNT-FCOA, it slightly decreases with increase in ' $S$ ' because of improvement in circuit bandwidth.

### 3.3 Circuit Analysis by Varying Number of CNTs ( $N$ )

The current flow through carbon nanotube is approximated as;

$$I_{\text{CNTFET}} \approx \frac{Ng_{\text{CNT}}(V_{\text{dd}} - V_{\text{th}})}{1 + g_{\text{CNT}}L_S\rho_S} \quad (4)$$

where  $N$  is number of CNTs,  $g_{\text{CNT}}$  defines transconductance per nanotube, doped CNT length is  $L_S$  and  $\rho_S$  is source resistance/length [5].

From Fig. 2 power dissipation enhances with increment in number of CNTs, this is due to increase in drive current of CNTs. DC gain is highest for CNT-FCOA because of more value of transconductance as well as drive current of carbon nanotubes in both  $N$  type and  $P$  type CNTFETs.

## 4 Comparison Analysis of CNT-FCOA, NCNT-PMOS-FCOA, PCNT-NMOS-FCOA, and CMOS-FCOA

Table 1 shows that DC gain, phase margin, gain margin, and slew rate are best in PURE-CNT-based circuit, also power dissipation and output resistance are least.

## 5 Conclusion

Here CNTFET circuits that is CNT-FCOA, NCNT-PMOS-FCOA, and PCNT-NMOS-FCOA are designed and simulated as well as results are compared to CMOS-FCOA. Simulation results disclosed that CNT circuits based on CNT outshines traditional CMOS circuit. Enhancement is depicted in DC gain, slew rate, power dissipation, GM and PM. Bandwidth of CNT-based circuit is less as compared to CMOS circuit which can be upgraded by optimizing  $N$ ,  $S$ , and  $D_{\text{CNT}}$  values.

**Table 1** Performance comparison at  $V_{dd} = 0.9$  V,  $S = 20$  nm,  $N = 20$ ,  $D_{CNT} = 1.5$  nm at 45 nm tech node

S. No.	Parameter	CMOS-FCOA	PURE-CNT-FCOA	NCNT-PMOS-FCOA	PCNT-NMOS-FCOA
1	DC Gain in dB	46.33	92.48	57.15	65.76
2	Bandwidth KHz	551.2	0.065	175.2	78.2
3	Output Resistance ohm	90.07	3.809	38.3	49.7
4	Average power $\mu$ W	205.5	183.4	163.02	241.4
5	Phase Margin in deg	71	95.7	68	90
6	Gain Margin in dB	22.3	48.1	21.5	43.1
7	Slew rate (V/ $\mu$ s)	62.64	113.6	60.68	111.6

## References

1. Nakamura K, Carley LR (1992) An enhanced fully differential folded-cascode op amp. *IEEE J Solid-State Circuits* 27(4):563–568
2. Baker RJ (2000) CMOS circuit design, layout and simulation, 2nd edn. PHI New Delhi
3. Iijima S (2002) Carbon nanotubes: past, present, and future. *Phys B* 323(1–4):1–5
4. Loan SA, Nizamuddin M, Alamoud AR, Abbasi SA (2015) Design and comparative analysis of high performance carbon nanotube-based operational transconductance amplifiers. *NANO* 10(03):1550039
5. Prakash P, Sundaram KM, Bennet MA (2018) A review on carbon nanotube field effect transistors (CNTFETs) for ultra-low power applications. *Renew Sustain Energy Rev* 89:194–203
6. Jogad S, Afzal N, Loan SA (2019) Sinusoidal oscillator using 32-nm CNTFET-OTA. In: 2019 International conference on electrical, electronics and computer engineering (UPCON). IEEE, pp 1–6

# Photoelectrochemical Response of Titania Photoanode Fabricated via Microwave Irradiation



Asmat Hassan, Arshid Mir, Asif Majeed, Reyaz Ahmad, Malik Aalim, Aamir Sohail, Ab Mateen, and M. A. Shah

**Abstract** TiO<sub>2</sub> nanostructures are prudent in photo applications like photocatalytic water splitting due to their high ability to absorb light. TiO<sub>2</sub> nanostructures were successfully synthesized via microwave-assisted hydrothermal method using Degussa P25 powders (titanium precursor) and aqueous NaOH. The nanostructures were fabricated at low temperatures for about 30 min in aqueous conditions without using hazardous chemicals. The obtained sample was characterized by XRD, FESEM, and UV–VIS–NIR spectrophotometer, FESEM validated the formation of TiO<sub>2</sub> nanotubes. The absorbance edge was observed around 400–425 nm, corresponding to the band gap being 3.02 eV. The sample showed an enhanced photocurrent density with excellent photostability.

**Keywords** Titania photoanode · Microwave irradiation · PEC water-splitting

## 1 Introduction

There are several potential applications for nanostructured titanium dioxide (TiO<sub>2</sub>), including dye-sensitized solar cells, photocatalysis, photoelectrochemical applications, and water splitting. The large surface area and charge transfer capability of TiO<sub>2</sub> nanotubes provide remarkable advantages over other types of morphologies of TiO<sub>2</sub> in these applications [1]. This has led to the emergence of TiO<sub>2</sub> nanotube synthesis. As a result, the fabrication of TiO<sub>2</sub> nanotubes has become a promising area of study. In recent years, several different approaches have been demonstrated for the fabrication of TiO<sub>2</sub> nanotubes. These approaches include anodic oxidation, template-based method, and hydrothermal method. Hydrothermal synthesis has emerged as

---

A. Hassan · A. Mir (✉) · A. Majeed · R. Ahmad · M. Aalim · A. Sohail · M. A. Shah  
Laboratory for Multifunctional Nanomaterials (LMN), P.G. Department of Physics, National Institute Technology Srinagar, Hazratbal, Srinagar, Jammu and Kashmir 190006, India  
e-mail: [arshidphy56@gmail.com](mailto:arshidphy56@gmail.com)

Ab Mateen  
Department of Physics, Islamic University of Science and Technology, Awantipora, Jammu and Kashmir, India

one of the most efficient methods due to its ease of use and capacity for large-area nanotubes [2–5].  $\text{TiO}_2$  nanoparticles are the primary reactants in this process, and they are generally exposed to a concentrated NaOH aqueous solution before undergoing further processing, such as calcination, etc. The traditional hydrothermal synthesis process, however, has drawbacks of longer reaction time (24–72 h) and high energy requirements. There are some reports that  $\text{TiO}_2$  nanotubes can grow directly on other conductive substrates such as the FTO substrate, but this is far from conclusive. With its high conductivity, thermal stability, and strong mechanical properties, FTO has the potential to be used as catalyst support. Despite reports of  $\text{TiO}_2$  nanotubes developed on conducting surfaces such as FTO, it would be worthwhile to investigate the feasibility of developing a more efficient method for synthesizing  $\text{TiO}_2$  nanotubes directly on such surfaces as FTO. The benefits of microwave heating over traditional heating methods include increased efficiency, shorter reaction times, higher yields, and greater repeatability of results [6–8]. This paper presents the successful use of a microwave-assisted hydrothermal technique to fabricate  $\text{TiO}_2$  nanotubes on an FTO substrate. X-ray diffraction and field-emission scanning electron microscopy confirmed the development of  $\text{TiO}_2$  nanotubes. The absorbance edge was observed at around 410 nm corresponding to which a bandgap of 3.02 was estimated. Photoelectrochemical studies demonstrated a 7.12  $\text{mA}/\text{cm}^2$  photocurrent density with good photostability.

## 2 Materials and Method

Direct synthesis of  $\text{TiO}_2$  nanotubes on the FTO substrate was achieved by irradiating it with microwaves. To begin, any impurities like grease, etc. on the surface of the FTO were removed by ultrasonication in acetone, ethanol, and DI water for 10 min. After that, 0.25 g of  $\text{TiO}_2$  powder was added to 10 M NaOH and sonicated for 15 min to prepare a homogeneous mixture which was eventually transferred to a Teflon vessel containing an FTO and was finally exposed to 750 W of microwave radiation for 30 min. The sample was then collected and rinsed with ethanol and DI water several times, dried, and annealed at 450 °C.

## 3 Characterizations

We analyzed the sample's crystal structure and phase purity using an XRD (RIGAKU Instrument) and a Raman spectrometer (RENISHAW Instrument). Field-emission scanning electron microscope was used for the surface morphological analysis (FESEM, ZEISS GEMINI 500). While investigating the sample's optical properties, a (SHIMADZU) UV–VIS–NIR spectrophotometer was used. Photoelectrochemical measurements were carried out using the CH instrument (CHI6005E).



## 4 Results and Discussions

Figure 1a demonstrates the amorphous nature verified by the absence of diffraction peaks in the XRD spectrum of the pre-annealed sample, whereas the appearance of these peaks in the XRD spectrum of the annealed sample (Fig. 1b) reveals the formation of the crystalline TiO<sub>2</sub>'s anatase phase during the annealing process at 450 °C. The emergence of prominent peaks at 25.23°, 37.71°, 47.99°, 53.77°, 55.02°, 62.66°, and 68.73°, corresponding to the (101), (004), (200), (105), (211), (204), and (116) planes of the tetragonal structure of the anatase phase of TiO<sub>2</sub>, corroborated this. Strong diffraction peaks reveal the crystalline nature and the lack of any additional diffraction peaks showed the phase purity of the sample. We employed electron microscopy (FESEM imaging) for analyzing the surface morphology of the TiO<sub>2</sub> sample. Figure 1c reveals the scanning asserting the genesis of the tubular morphology of TiO<sub>2</sub> of an internal diameter of 60 ± 10 nm and tube length of 1.5 ± 0.2 μm. TiO<sub>2</sub> nanotubes have a high specific surface area, which boosts their photocatalytic capability by facilitating the surface adsorption/desorption process due to their broad electrode/electrolyte interface [9, 10].

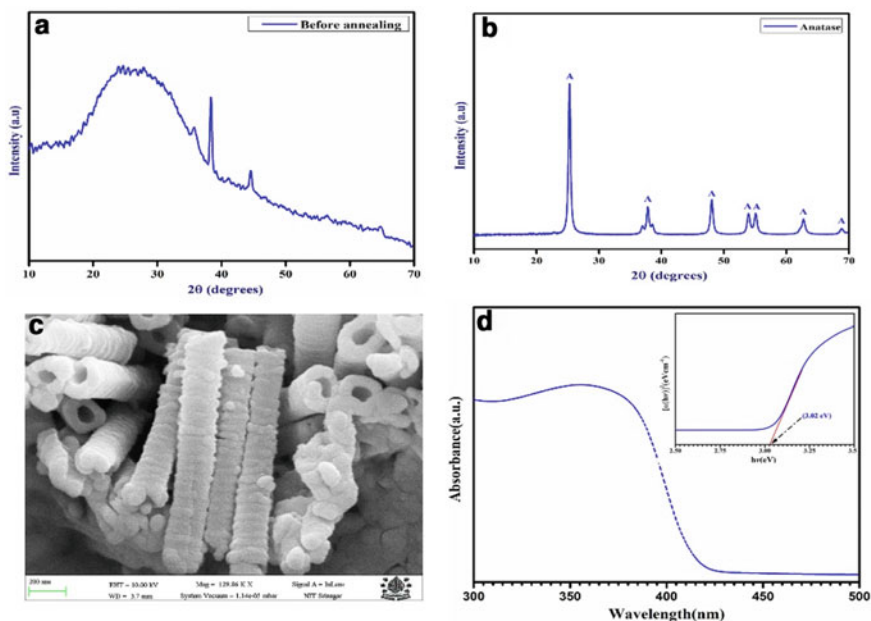


**Fig. 1** a XRD of annealed TiO<sub>2</sub> sample b XRD of annealed TiO<sub>2</sub> sample c FESEM of TiO<sub>2</sub> nanotubes d absorbance spectrum and Tauc plot of TiO<sub>2</sub> sample

Figure 1d depicts the absorbance spectrum of the annealed TiO<sub>2</sub> sample, which exhibits an absorbance edge between 400 and 425 nm; this absorbance edge corresponds to the optical band gap, which was determined using the Tauc plot depicted in the inset of Fig. 1d, for which we employed the Tauc Mott Davisson equation [11, 12].

$$\alpha h\nu = [A(h\nu - E_g)]^n \quad (1)$$

where  $\alpha$ ,  $h\nu$ , and  $A$  is the coefficient of absorption, incident photon energy, and material-dependent constant, respectively, and  $n = 2, 1/2$  for direct, and indirect energy bandgap, respectively, and  $2/3$  for forbidden energy. It was found that the sample exhibited an optical bandgap of 3.02 eV.

Photoelectrochemical measurements were performed in an electrochemical cell containing 1 M aqueous KOH solution as electrolyte using the fabricated sample, platinum, and Ag/AgCl as working electrode, counter, and reference electrodes, respectively. The linear sweep voltammogram recorded under AM 1.5 G illumination (100 mW/cm<sup>2</sup>) shown in Fig. 2a depicts the progressive increase in photocurrent density at lower potentials signifying the electron–hole separation. As the potential increases, the photocurrent reaches a maximum, revealing the distribution of the field over nanotubes. Further investigation on the photo-response of the prepared TiO<sub>2</sub> sample was carried out by analyzing the photocurrent density when exposed to recurring irradiation at 0.2 V versus Ag/AgCl (Fig. 2a). An instantaneous reaction to light exposure indicates that the sample has excellent switching properties. The sample showed a high photocurrent density of 7.12 mA/cm<sup>2</sup> which as per the literature is the highest achieved for pristine TiO<sub>2</sub>. It is vital to keep in mind that photostability under continuous illumination for an extended duration is needed for the actual photoelectrochemical water-splitting application and that this is a fundamental requirement for the application. The sample's photostability was evaluated by measuring the photocurrent stability during prolonged irradiation at 0.2 V versus Ag/AgCl, and the findings are depicted in the inset of Fig. 2a. The sample showed outstanding stability as the current did not show any significant decay during the test period of 4.5 h. The enhanced photocurrent density and excellent photostability suggest TiO<sub>2</sub> is an efficient electrode material for photoelectrochemical water splitting [13].

To investigate the flow of charges and their interactions at the electrode–electrolyte interface, electrochemical impedance spectra (EIS) were used. The Nyquist plot together with an analogous circuit model is shown in Fig. 3b. This model worked well with the sample. The charge transfer resistance  $R_{ct}$  of 15.89 K was observed reflecting a better charge transfer and carrier (e–h) separation.

The Mott–Schottky plot shown in Fig. 3a shows the positive slope identifying TiO<sub>2</sub> as an *N*-type semiconductor. Furthermore, the slopes being smaller indicate a higher charge density. The potential of the flat band was determined by extending the linear portion of the Mott–Schottky plot and was found to be 0.37 which is smaller

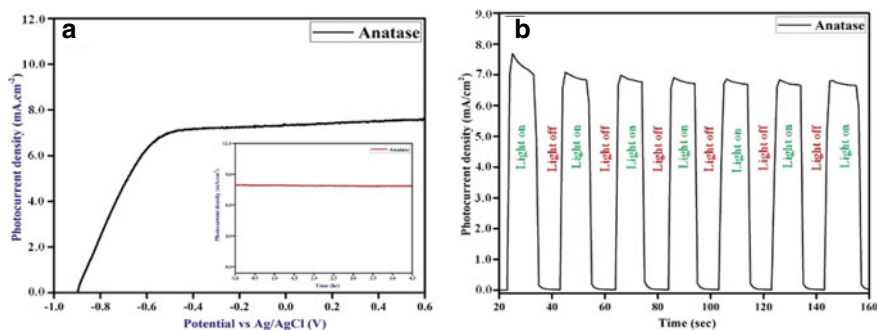


**Fig. 2** **a** LSV and photostability of TiO<sub>2</sub> sample **b** transient photocurrent density of TiO<sub>2</sub> sample

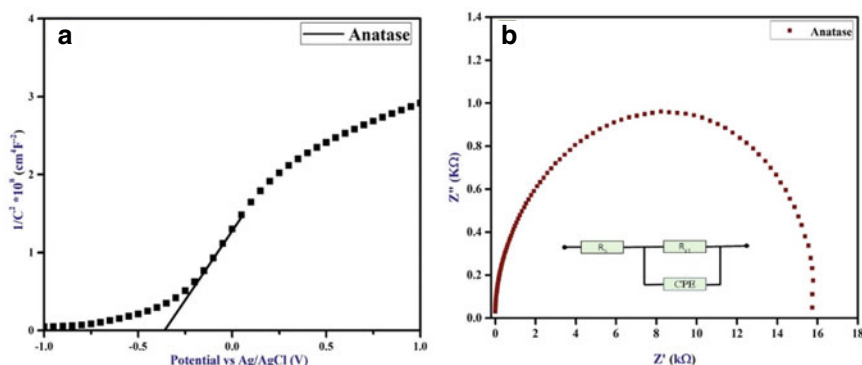


**Fig. 3** **a** Mott-Schottky plot and **b** Nyquist plot of TiO<sub>2</sub>

than earlier reports indicating the conduction band's shifting. The increased charge density as a result of this band shifting is attributable to improved PEC performance [2, 13].

## 5 Conclusion

The microwave technique was employed to successfully fabricate TiO<sub>2</sub> nanotubes on the FTO substrate. XRD spectra confirmed the formation and amorphous TiO<sub>2</sub> which upon annealing at 450 °C leads to the development of the TiO<sub>2</sub>'s anatase phase. FESEM verified the tubular morphology with an internal diameter of 60 ± 10 nm and a tube length of 1.5–2 μm. The absorbance spectrum showed an absorbance edge at around 410 nm corresponding to the bandgap being 3.02 eV. Photoelectrochemical studies demonstrated a 7.12 mA/cm<sup>2</sup> photocurrent density with good photostability.

**Acknowledgements** The authors would like to express their appreciation to the Department of Science and Technology for funding the Nano-mission project that led to the establishment of the laboratory for multifunctional nanomaterials (LMN) at NIT Srinagar. Thanks, are also due to NIT Srinagar and IIT Delhi for providing the necessary research facilities, as well as to Mr. Nayeem for his time and effort in characterizing the samples.

## References

1. Arifin K, Yunus RM, Minggu LJ, Kassim MB (2021) Improvement of TiO<sub>2</sub> nanotubes for photoelectrochemical water splitting: review. *Int J Hydrogen Energy* 46(7):4998–5024
2. Mir A, Shah MA (2022) Fabrication of highly stable Titania photoanode with enhanced photocurrent density. *Appl Phys A* 128(12):1105
3. Mir A, Ahmad R, Majeed A, Sohail A, Aalim M, Farooq J, Shah MA (2023) Microwave-assisted hydrothermal synthesis of Fe-doped TiO<sub>2</sub> photoanode for photocatalytic hydrogen evolution. *ECS J Solid State Sci Technol* 12(2):021007
4. Lin X et al (2021) Hydrothermally regulating phase composition of TiO<sub>2</sub> nanocrystals toward high photocatalytic activity. *J Alloys Compd* 850:156653
5. Ismael M (2020) A review and recent advances in solar-to-hydrogen energy conversion based on photocatalytic water splitting over doped-TiO<sub>2</sub> nanoparticles. *Sol Energy* 211:522–546
6. Cui L et al (2012) Facile microwave-assisted hydrothermal synthesis of TiO<sub>2</sub> nanotubes. *Mater Lett* 75:175–178
7. Qiu Q, Li S, Jiang J, Wang D, Lin Y, Xie T (2017) Improved electron transfer between TiO<sub>2</sub> and FTO Interface by N-doped anatase TiO<sub>2</sub> nanowires and Its applications in quantum dot-sensitized solar cells. *J Phys Chem C* 121(39):21560–21570
8. Asif Javed HM et al (2021) Hydrogen treated TiO<sub>2</sub> nanoparticles onto FTO glass as photoanode for dye-sensitized solar cells with remarkably enhanced performance. *Int J Hydrogen Energy* 46(27):14311–14321
9. Mir A, Shah MA (2022) Cyclic voltammetry response of TiO<sub>2</sub> nanostructures prepared via fast and facile microwave irradiation. *Bull Mater Sci* 29 45(3):119
10. Mir A, Iqbal K, Rubab S, Shah MA (2023) Effect of concentration of Fe-dopant on the photoelectrochemical properties of Titania nanotube arrays. *Ceram Int* 1 49(1):677–682
11. Aalim M, Mir A, Mir JF, Ahmad R, Suhail A, Shah MA (2023) Morphologically tunable fabrication of hematite nanostructures for enhanced photoelectrochemical performance. *ECS J Solid State Sci Technol* 12(2):021002
12. Mir A et al (2023) Microwave-assisted hydrothermal synthesis of Fe-doped TiO<sub>2</sub> photoanode for photocatalytic hydrogen evolution. *ECS J Solid State Sci Technol* 12(2):021007
13. Mir A, Ahmad R, Aalim M, Sohail A, Shah MA (2023) Photoelectrochemical study of Ti<sup>3+</sup> self-doped Titania nanotubes arrays: a comparative study between chemical and electrochemical reduction. *Chem Phys Lett* 811:140219

# Study of Interaction Between Insulin and ZnO Micro-nano Particles Using Dielectric Characterization



Urvashi Singh, Zeeshan Saifi, Mridul Kumar,  
and Soami Daya Krishnananda

**Abstract** Dielectric characterization in the microwave region is a useful approach for analyzing biological systems due to the resonance of free water, which is a major constituent of biological systems. Here, dielectric properties have been calculated using cavity perturbation method to understand the interaction between protein and nanoparticles. The simulation studies of the cavity were carried out using CST microwave studio and the first Eigen mode was observed at 3.234 GHz with the maximum electric field of  $1.28 \times 10^8$  V/m. In our experiment, the cavity mode was observed at 3.236 GHz with a quality factor of 4840 U. The dielectric constant was determined after calibrating the system for the unknown constants using polycarbonate disk. Experimental studies were carried out on commercial Insulin and ZnO (Tetrapods) of various concentrations. Our results show that variation of dielectric constant with respect to Insulin concentration was higher on Day2 than on Day1 suggesting its time decay activity. As we increased the concentration of ZnO (Tetrapods) in buffer, the dielectric constant of the solution decreased. Notably, on mixing ZnO (Tetrapods) of concentration 2.2 and 4 g/l with Insulin of concentration 18 and 24 mg/l did not show any significant variation. We have also performed the zeta potential measurements and our results show that zeta potential of Insulin becomes more negative on Day2 than on Day1 and contrary behavior was observed while mixing it with ZnO (Tetrapods). However, there was no variation in zeta potential of ZnO (Tetrapods) with time which shows its high colloidal stability as compared to protein.

**Keywords** Dielectric characterization · Resonance · ZnO (Tetrapods) · Eigen mode · Quality factor

---

U. Singh · Z. Saifi · M. Kumar · K. Soami Daya (✉)  
Department of Physics and Computer Science, Dayalbagh Education Institute, Agra, Uttar Pradesh, India  
e-mail: [sdayak@gmail.com](mailto:sdayak@gmail.com)

## 1 Introduction

The role of electrical properties of biological systems play a crucial role in understanding their functions, bio-reactivity, stability and interactions with other molecules [1, 2]. It is because, most of the biomolecules carry a net surface charge which depends on the physico-chemical properties of the surrounding medium [3]. In addition, nanoparticles in the biological medium can easily adsorb protein due to size and large surface-to-mass-ratio, which can perturb the electrical interaction of nano-bio complexes [3, 4]. The study of this electrical interaction of nano-bio complexes is important in the biomedical field and can be understood using dielectric characterization. It is reported that the variation in dielectric constant reflects the physical nature and functionality of the biomolecules [1, 5]. Since dielectric properties are dispersive in nature, therefore, appropriate frequency range has to be selected for dielectric characterization. Dielectric characterization in microwave range is of particular interest due to resonance of water, which is a main constituent of biological systems [6–9]. There are various methods such as waveguide transmission, cavity perturbation, free space transmission and reflection-based methods to calculate the dielectric constant [10]. Above all, the cavity perturbation method gives accurate results due to the closed system and narrow frequency bandwidth, which enhances the quality factor of the resonance peak, therefore, increases the sensitivity [10, 11].

In this paper, the dielectric parameters have been calculated using a cavity designed at 3.236 GHz. For increasing the sensitivity of the method, sapphire puck has been used as a dielectric resonator. Using the cavity, the dielectric properties of Insulin and ZnO (Tetrapods) and their mixtures of different concentrations are analyzed. Furthermore, we have used the electrophoretic technique to investigate the zeta potential of the molecules. Zeta potential and dielectric parameters both depend on surface charge interaction of molecules, therefore, the correlation shows another validation of the results. Using this analysis, time decay activity of Insulin, colloidal stability and complex permittivity of nano-bio complex have been discussed in this paper, which makes an apt direction for biological sample studies without any rigorous preparation of the samples.

## 2 Materials and Methods

### 2.1 Material

Commercial Insulin Humalog 100 U is used in experiment and diluted in distilled water at five different concentrations 6, 12, 18, 24 and 30 mg/L. For studying the nanoparticle-protein interaction, ZnO (Tetrapods) have been used and were prepared in distilled water for five different concentrations 0.4, 1.3, 2.2, 3.1 and 4 g/L. ZnO

(Tetrapods) were synthesized using flame transport method by Functional Nano-material group, Kiel University, Germany [12]. For all techniques, the mixing ratio was 2:1 for Insulin and ZnO. All samples were freshly prepared when used for all measurements.

## 2.2 Methods

Cavity was simulated on the CST software as shown in Fig. 1. By optimizing the cavity parameters, the fundamental mode of the cavity is reported at 3.234 GHz (shown in Fig. 1). The schematic of the experimental set-up is shown in Fig. 1. Experiment has been performed using resonant cavity in which sapphire puck as dielectric resonator of 8 mm height and 20 mm diameter is mounted concentrically on cylindrical Teflon spacer of 4 mm diameter and 5 mm height, which is glued to center of the bottom plate of cavity. Cavity is coated with aluminum to minimize conductor losses. The cavity is connected to a loop antenna for microwave feeding. Measurements are carried out using Rohde and Schwarz ZVA 50 vector network analyzer. Resonance frequency and quality factor of single crystal sapphire were 3.236025 GHz and 4840, respectively. Shifting in resonance frequency and quality factor has been observed by placing Sample-Holding Disk (SHD) concentrically on the sapphire puck. In this case, the resonating frequency and quality factor shifted to 3.198225 GHz and 3154 KU.

## 2.3 Dielectric Measurements

The method of calculating the dielectric parameters using cavity perturbation method is already reported and the final equations are as follows [13].

$$\frac{f_{DR} - f_{SHD}}{f_{DR}} = A(\epsilon'_{SHD} - 1) \frac{V_{SHD}}{V_{DR}} \quad (1)$$

$$\frac{f_{SHD} - f_{soln}}{f_{SHD}} = A(\epsilon''_{Soln} - 1) \frac{V_{Soln}}{V_{Soln} + V_{DR}} \quad (2)$$

$$\frac{1}{Q_{SHD}} - \frac{1}{Q_{DR}} = B \epsilon''_{SHD} \frac{V_{SHD}}{V_{DR}} \quad (3)$$

$$\frac{1}{Q_{Soln}} - \frac{1}{Q_{SHD}} = B \epsilon''_{Soln} \frac{V_{Soln}}{V_{SHD} + V_{DR}} \quad (4)$$

where  $f_{DR}$ ,  $f_{SHD}$  and  $f_{soln}$  are resonant frequency and  $Q_{DR}$ ,  $Q_{SHD}$  and  $Q_{Soln}$  are quality factor of the cavity when loaded with dielectric resonator, SHD and solution, respectively.  $V_{DR}$ ,  $V_{SHD}$  and  $V_{Soln}$  are volume of the dielectric resonator, SHD and

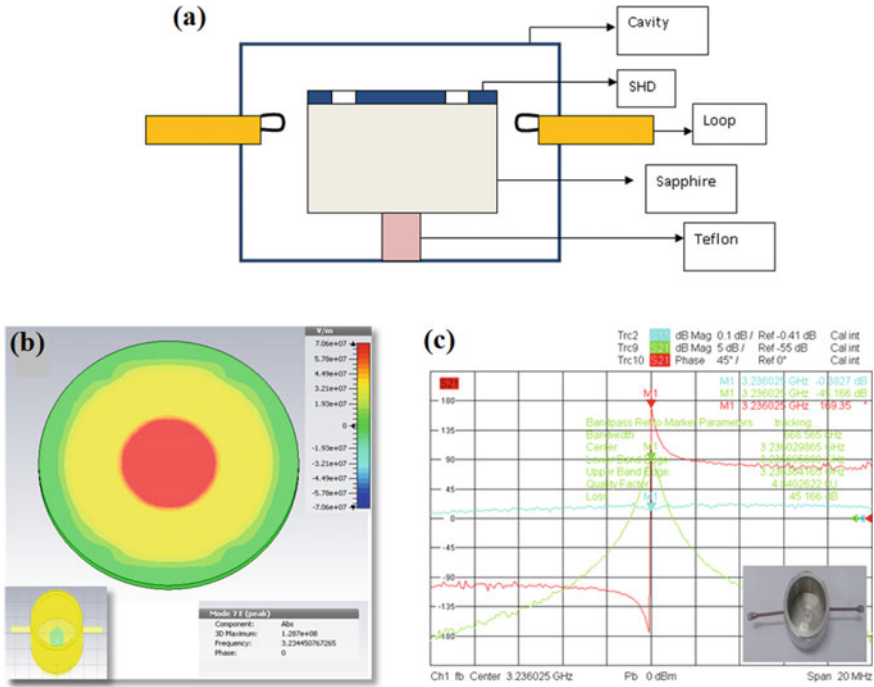


**Fig. 1** a Experiment set-up. b Fundamental Eigen mode of cavity. c S11 and S21 response of cavity measured using vector network analyzer

solution, respectively.  $\epsilon'_{SHD}$  and  $\epsilon'_{Soln}$  are real part and  $\epsilon''_{SHD}$  and  $\epsilon''_{Soln}$  are imaginary part of complex permittivity of SHD and solution, respectively.  $A$  (0.00761) and  $B$  (0.013) are the constant calculated using the known value of dielectric resonator and SHD. In our case the value of  $V_{Sol} = 20 \mu\text{l}$ , hence  $\frac{V_{Sol}}{V_{SHD} + V_{DR}}$  is  $7.0771408 \times 10^{-3}$ . Furthermore, the relaxation time ( $\tau$ ) of the sample can be calculated using equation  $Q_{Soln} = 2\pi\tau f_{soln}$  [13] (Fig. 2).

### 3 Results and Discussion

The complex dielectric constant has been obtained using the formula given in Sect. 2.3. The real part of permittivity depicts the storage of electrical energy, whereas the imaginary part shows the dissipation of electrical energy. In our experiment, we studied the dielectric behavior of Insulin over two days. On the first day, permittivity is nearly constant with an increasing concentration of Insulin. However, the next day, the standard variation in permittivity is observed with varying concentrations even maintaining the Insulin at 4 °C. Furthermore, we have calculated the standard deviation of the real part of permittivity of Insulin and it has found 0.47 and 6.60 in



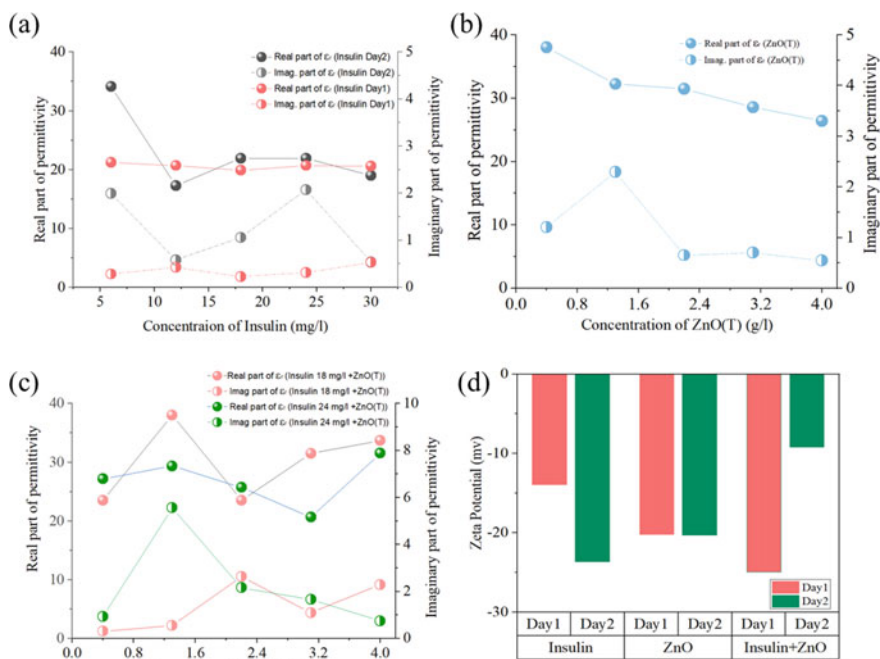


**Fig. 2** **a** Real and imaginary part of permittivity for various concentration of Insulin and **b** ZnO (Tetrapods) and **c** Insulin mixed with ZnO (Tetrapods) **d** Two day variation of Zeta potential of Insulin, ZnO (Tetrapods) and Insulin mixed with ZnO (Tetrapods)

day1 and day2, respectively. The change in permittivity is related to the change in the activity of the biological molecule. These results can help in finding the activity time of biological molecules.

Furthermore, we have studied the dielectric behavior of ZnO (Tetrapods) and by increasing the concentration of ZnO (Tetrapods), the real part of permittivity decreases, which shows that non-polar molecules dominate in polar solvents (i.e., water).

Additionally, intermediate Insulin concentrations of 18 and 24 mg/l are chosen to study how they interact with ZnO (Tetrapods) at all concentrations. Results suggest that the interaction depends on the concentration of the selected sample. In our case, even with a high concentration of polar molecules, the ZnO concentration of 1.2, 3.2 and 4 g/l when mixed with insulin 18 mg/ml has more permittivity (real part) than when it is mixed with 24 mg/ml. When mixed with Insulin at concentrations of 18 and 24 mg/l, it was observed that the ZnO (Tetrapods) at concentrations of 2.2 and 4 g/l did not show any appreciable permittivity change. The results might be the consequence of a change in the protein's dipole orientation in the presence of micro-nano particles.

We have also examined the correlation between these dielectric characteristics and the zeta potential of colloidal particles in a solution. The zeta potential of ZnO

(Tetrapods) was found to be almost constant on days 1 and 2. Result indicates that ZnO (Tetrapods) has a good colloidal stability. Insulin's zeta potential changed from being more positive on day 1 to being more negative on day 2, and when it was mixed with ZnO (Tetrapods), the contrary pattern was observed, showing that non-polar molecules strongly influenced the polar solution.

## 4 Conclusion

In addition to examining how biological samples interact with micro-nanoparticles, which are vital for the designing of drugs, this work also examines how electrical interactions between biological samples change over time. Dielectric characteristics are studied, and the findings suggest that these properties can be employed as biomarkers to study biological samples.

**Acknowledgements** Authors acknowledge the support from Prof. Rainer Adelung, Functional Nano Materials group, Kiel University, Germany for providing us the ZnO Tetrapods.

## References

1. Li L, Li C, Zhang Z, Alexov E (2013) On the dielectric “constant” of proteins: smooth dielectric function for macromolecular modeling and its implementation in DelPhi. *J Chem Theory Comput* 9(4):2126–2136
2. Cottet J, Caselli F (2022) Single-cell electrical characterization. In: *Biosensors for single-cell analysis*. Academic Press, pp 71–99
3. Saptarshi SR, Duschl A, Lopata AL (2013) Interaction of nanoparticles with proteins: relation to bio-reactivity of the nanoparticle. *J Nanobiotechnol* 11(1):1–12
4. Singh U, Saifi Z, Kumar M, Reimers A, Krishnananda SD, Adelung R, Baum M (2021) Role of structural specificity of ZnO particles in preserving functionality of proteins in their corona. *Sci Rep* 11(1):1–9
5. Simonson T, Brooks CL (1996) Charge screening and the dielectric constant of proteins: insights from molecular dynamics. *J Am Chem Soc* 118(35):8452–8458
6. Basey-Fisher TH, Hanham SM, Andresen H, Maier SA, Stevens MM, Alford NM, Klein N (2011) Microwave Debye relaxation analysis of dissolved proteins: towards free-solution biosensing. *Appl Phys Lett* 99(23):233703
7. Wolf M, Gulich R, Lunkenheimer P, Loidl A (2012) Relaxation dynamics of a protein solution investigated by dielectric spectroscopy. *Biochim Biophys Acta (BBA) Proteins Proteomics* 1824(5):723–730
8. Nakanishi M, Sokolov AP (2015) Protein dynamics in a broad frequency range: dielectric spectroscopy studies. *J Non-Cryst Solids* 407:478–485
9. Verma R (2014) Microwave studies of insulin as a bio molecule for application in medical diagnostics. Ph.D. thesis
10. Urvashi Z, Daya KS, Doneria P (2019) Measurement of dielectric properties of biological materials using co-axial fork-type probe. *IEEE Sens J* 19(22):10482–10489
11. Saifi Z, Kumar M, Singh U, Daya KS (2021) Microwave cavity perturbation with 3-D printed sample holders for detection of counterfeit drugs. *IEEE Trans Microw Theory Tech* 70(3):1832–1840

12. Mishra YK et al (2013) Part Part Syst Charact 30:775
13. Verma R, Daya KS (2017) Understanding the decay of proteins: a method to study time dependent response of pM concentration of insulin at microwave frequencies. MethodsX 4:35–41

# Simulation of Highly Effective Eco-Friendly Inorganic Perovskite Solar Cell Using SCAPS-1D



Vaibhava Srivastava, R. K. Chauhan, and Pooja Lohia

**Abstract** Perovskite solar cells (PSCs) are the most appropriate thin film emerging solar device. Conventional perovskite ground on lead has a great challenge because of its short-term stability and toxic behavior. Thus, it is necessary to emerge lead-free perovskite in current era. In this article, simulation of perovskite solar device is handled by SCAPS-1D software. Herein lead free stable and eco-friendly inorganic perovskite solar cell has been proposed. For high carrier mobility, ETL has been introduced along with replacement of PCBM with niobium pentoxide ( $\text{Nb}_2\text{O}_5$ ) which reduces the effective cost of the device. Solar cell limiting factor such as thickness of perovskite layer has been investigated. Using  $\text{Nb}_2\text{O}_5$  as ETL layer, the optimized performance parameters are as following:  $\text{PCE} = 25.02\%$ ,  $V_{oc} = 1.052 \text{ V}$ ,  $J_{sc} = 34.2683 \text{ mA/cm}^2$ , and  $\text{FF} = 64.98\%$ . The proposed model of lead-free perovskite solar cell has potential to revoke stability and toxicity issue and which help to enhance the performance of PSCs.

**Keywords** SCAPS-1D · Perovskite solar cell · PCBM · PCE ·  $\text{Nb}_2\text{O}_5$

## 1 Introduction

Renewable energy like solar cell is one of the most optimistic energy sources to overcome the conventional energy resources. These material shows outstanding physical and chemical properties such as direct and tunable bandgap, ambipolar carrier transport ability, and excellent carrier mobilities. PSCs can be fabricated as regular nip and inverted pin type of the inorganic organic metal halides [4, 10]. The structure of PSCs formula is  $\text{AMX}_3$ , where A denotes to inorganic–organic cation ( $\text{Rb}^+$ ,  $\text{Cs}^+$ ,  $\text{CH}_3\text{NH}^+$ ,  $\text{CH}_3\text{CH}_2\text{NH}^+$ ), M denotes to inorganic cation (Sn, Ge, Pb, etc.), and X is the halides ion ( $\text{I}^-$ ,  $\text{BF}_4^-$ ,  $\text{Br}^-$ ,  $\text{Cl}^-$ ,  $\text{SCN}^-$  etc.) [8]. These materials are frequently used in optoelectronic device like neuromorphic computing, photodetectors, LASERS,

---

V. Srivastava · R. K. Chauhan · P. Lohia (✉)

Department of Electronics and Communication Engineering, Madan Mohan Malaviya University of Technology, Gorakhpur 273010, India

e-mail: [lohia.pooja6@gmail.com](mailto:lohia.pooja6@gmail.com)

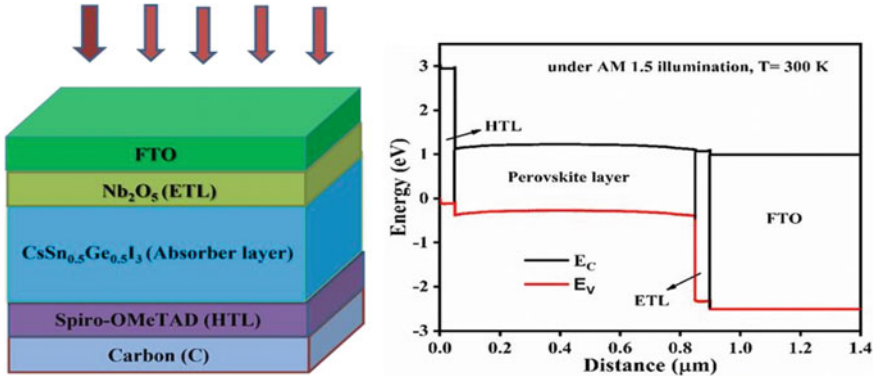


Fig. 1 Device configuration and energy band diagram of PSCs

Humidity Sensor, Field Effect Transistors, etc. [9] In this work,  $\text{CsSn}_{0.5}\text{Ge}_{0.5}\text{I}_3$ -based PSCs have been analyzed the effect of thickness of perovskite layer. The primary objective of this study is to precisely optimize the PSCs' properties so that the final device provides improved PCE while reducing the manufacturing cost.

## 2 Device Architecture and Material Parameters

SCAPS-1D is a simulation tool developed at the University of Ghent, Belgium. It solves fundamental semiconductor equation for Poisson equation and continuity equation for electron and hole [1]. The device structure and energy band diagram used for simulated solar cell  $\text{C}/\text{Spiro-OMeTAD}/\text{CsSn}_{0.5}\text{Ge}_{0.5}\text{I}_3/\text{Nb}_2\text{O}_5/\text{FTO}$  is shown in Fig. 1. The simulation parameters and interface defect density are recorded in Tables 1 and 2. The work function of C and FTO is set to 5.0 and 4.3 eV, respectively.

## 3 Results and Discussion

### 3.1 Absorber Thickness Variation

As shown in Fig. 2a, b, the device performance parameters are estimated using the SCAPS-1D programmed as a function of the active layer thickness in the span of 200–900 nm. The study showed that  $J_{sc}$  rises as the thickness of the active layer increases, reaching at approximately  $26.10 \text{ mA}/\text{cm}^2$  at 900 nm. This indicates that a thicker absorber layer can absorb more photons and greater excess carrier concentration at higher wavelength, allowing for the formation of electron–hole pairs. As per Fig. 2a,  $V_{oc}$  notable drops while a thickness of the active layer increases. The reduction in  $V_{oc}$

**Table 1** Physical material parameters used in simulations [2, 5]

Parameters	Spiro-OMeTAD	CsSn <sub>0.5</sub> Ge <sub>0.5</sub> I <sub>3</sub>	Nb <sub>2</sub> O <sub>5</sub>	FTO
Thickness (nm)	50	600	50	500
Electron affinity ( $\chi$ )	2.2	3.9	3.9	4.0
Bandgap, $E_g$ (eV)	2.9	1.5	3.4	3.5
Relative dielectric permittivity	3.0	28	9	9.0
Conduction band effective density of states ( $1/\text{cm}^3$ ), $NC$	$2.5 \times 10^{18}$	$2.2 \times 10^{18}$	$3.7 \times 10^{18}$	$2.2 \times 10^{18}$
Valence band effective density of states ( $1/\text{cm}^3$ ), $NV$	$1.8 \times 10^{19}$	$1.8 \times 10^{18}$	$1.8 \times 10^{19}$	$2.2 \times 10^{18}$
Mobility ( $\mu_e$ ) $\text{cm}^2/\text{Vs}$	$2.0 \times 10^{-4}$	974	100	20
Mobility ( $\mu_h$ ) $\text{cm}^2/\text{Vs}$	$2.0 \times 10^{-4}$	213	25	10
Donor density ( $1/\text{cm}^3$ ), $ND$	-	$1.0 \times 10^{14}$	$1.0 \times 10^{18}$	$1.0 \times 10^{15}$
Acceptor density ( $1/\text{cm}^3$ ), $NA$	$1.0 \times 10^{17}$	-	-	-
Defect density ( $1/\text{cm}^3$ ), $Nt$	$1.0 \times 10^{13}$	$1.0 \times 10^{15}$	$1.0 \times 10^{15}$	$1.0 \times 10^{18}$

**Table 2** Photovoltaic properties of interface [3]

Parameters	Spiro-OMeTAD/absorber	Absorber/Nb <sub>2</sub> O <sub>5</sub>
Type of defect	Neutral	Neutral
Capture cross-sectional for hole and electron ( $\text{cm}^2$ )	$1.00 \times 10^{-19}$	$1.00 \times 10^{-19}$
Energetic distribution	Single	Single
Defect energy level above EV (eV)	0.60	0.60
Total density ( $\text{cm}^{-2}$ )	$1.00 \times 10^{10}$	$1.00 \times 10^{10}$

makes the PCE similar to  $J_{sc}$ ; with increasing layer thickness, the device efficiency increases until it approaches saturation at a thickness of 600 nm. Hence, we take the ideal thickness of CsSn<sub>0.5</sub>Ge<sub>0.5</sub>I<sub>3</sub> as 500 nm for further simulation [6, 7]. The model outcome is as follows:  $V_{oc} = 1.052$  V,  $J_{sc} = 34.2683$  mA/cm<sup>2</sup>, FF = 64.98%, and PCE = 25.02%.

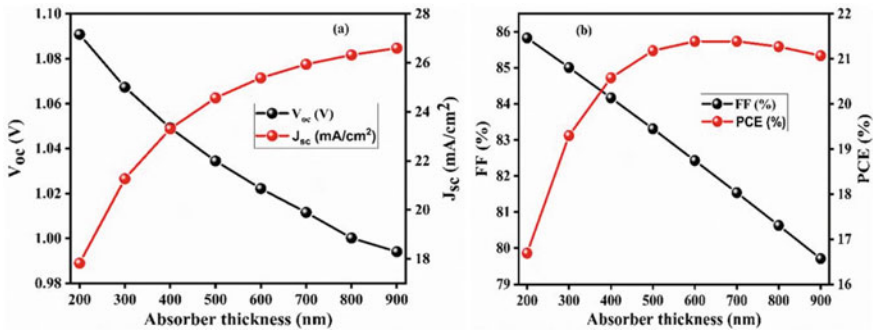


Fig. 2 Variation of photovoltaic parameters with CsSn<sub>0.5</sub>Ge<sub>0.5</sub>I<sub>3</sub> thickness

## 4 Conclusion

In this work, the performance of architecture FTO/Nb<sub>2</sub>O<sub>5</sub>/CsSn<sub>0.5</sub>Ge<sub>0.5</sub>I<sub>3</sub>/Spiro/Au is numerically examined through SCAPS-1D tool. The impact of the absorber thickness has been studied. Using Nb<sub>2</sub>O<sub>5</sub> as ETL layer, the optimized performance parameters are as following: PCE = 25.02%, V<sub>oc</sub> = 1.052 V, J<sub>sc</sub> = 34.2683 mA/cm<sup>2</sup>, and FF = 64.98%. The simulation results are useful for enhancing the efficacy of CsSn<sub>0.5</sub>Ge<sub>0.5</sub>I<sub>3</sub>-based all-inorganic PSCs and for understanding the mechanism clearly.

**Acknowledgements** The author is very thankful to MMMUT, Gorakhpur, to provide research cum teaching fellowship to continue my research work. I am also grateful to Prof. Dilip Kumar Dwivedi for his valuable suggestion.

## References

1. Patel AK, Mishra R, Soni SK (2022) Performance enhancement of CIGS solar cell with two dimensional MoS<sub>2</sub> hole transport layer. *Micro Nanostruct* 165:207195
2. Raghvendra, Kumar RR, Pandey SK (2019) Performance evaluation and material parameter perspective of eco-friendly highly efficient CsSnGeI<sub>3</sub> perovskite solar cell. *Superlattices Microstruct* 135
3. Rai N, Rai S, Singh PK, Lohia P, Dwivedi DK (2020) Analysis of various ETL materials for an efficient perovskite solar cell by numerical simulation. *J Mater Sci: Mater Electron* 31(19):16269–16280
4. Rai S, Pandey BK, Dwivedi DK (2020) Modeling of highly efficient and low cost CH<sub>3</sub>NH<sub>3</sub>Pb(I<sub>1-x</sub>Cl<sub>x</sub>)<sub>3</sub> based perovskite solar cell by numerical simulation. *Opt Mater* 100
5. Rai S, Pandey BK, Dwivedi DK (2021) Designing hole conductor free tin-lead halide based all-perovskite heterojunction solar cell by numerical simulation. *J Phys Chem Solids* 156
6. Sadanand, Dwivedi DK (2019) Theoretical investigation on enhancement of output performance of CZTSSe based solar cell. *Sol Energy* 193:442–451

7. Srivastava V, Chauhan RK, Lohia P (2022) Lead free perovskite solar cell using  $\text{TiO}_2$  as an electron transport materials and  $\text{Cu}_2\text{O}$  as a hole transport materials. Lect Notes Electr Eng 305–311
8. Srivastava V, Chauhan RK, Lohia P (2022) Highly efficient cesium-based halide perovskite solar cell using SCAPS-1D software: theoretical study. J Opt (India) 0123456789
9. Srivastava V, Pooja RKC (2022) Investigating the performance of lead—free perovskite solar cells using various hole transport material by numerical simulation 0123456789
10. Yadav S, Lohia P, Sahu A (2022) Enhanced performance of double perovskite solar cell using  $\text{WO}_3$  as an electron transport material. J Opt (India)



# Photonic Crystal Fiber-Based Biosensor for Sensitive Detection of Breast Cancer Cells in THz Regime



Sapana Yadav, Pooja Lohia, and D. K. Dwivedi

**Abstract** A hollow-core photonic crystal fiber-based THz sensor that enables to detect analytes at terahertz frequencies is presented in this study, which is characterized by its robustness. An analyte gets inserted in an asymmetrical rectangular hollow core with perfectly matched layer absorbent boundary condition. The efficiency of proposed sensor is evaluated utilizing COMSOL multiphysics (v5.5a) simulation technology based on the finite element technique. The proposed sensor's design simplicity makes things a lot easier. Fabrication, on the other side, makes it appropriate for a broad range of biological and industrial applications. A photonic crystal fiber biosensor has been studied for detecting cancerous cells. The proposed model's efficiency has been evaluated using MATLAB (v.2018a) software. The proposed sensor may work in the frequency range of 1.0–2.0 THz. Simulation results have been found to be good enough, with highly birefringence (0.0020) and lower confinement loss ( $17.33 \times 10^{-9} \text{ cm}^{-1}$ ). The proposed sensor's fabrication capabilities are further secured by its simplicity of implementation and can be utilized in bio-sensing application.

**Keywords** Confinement loss · THz frequency · Photonic crystal fiber · Birefringence

---

S. Yadav · D. K. Dwivedi (✉)

Photonics and Photovoltaic Research Lab (PPRL), Department of Physics and Material Science, Madan Mohan Malaviya University of Technology, Gorakhpur 273010, India  
e-mail: [tokd Dwivedi@gmail.com](mailto:tokd Dwivedi@gmail.com)

P. Lohia

Department of Electronics and Communication Engineering, Madan Mohan Malaviya University of Technology, Gorakhpur 273010, India

## 1 Introduction

Due to their diverse applications, photonic crystal fiber (PCF)-based sensors attained lot of interest from researchers all over the world in the recent years. It has ignited a large amount of curiosity due to its unique light guiding characteristics and the potential of light interaction involving gases or liquids. It is important to note that PCFs have been used not only for communication but also for sensing. PCF-based sensors (PbS) are becoming more popular due to their compact size, affordable, solidity, and potential to operate in adverse conditions like high electromagnetic and chemically affected fields [11]. Sensors based on PCF find various applications such as vapor and gas sensing, biochemical sensing and medicinal analysis, factory output monitoring, ocean and atmospheric study, automotive control, and bio-process control [10]. THz radiation analysis has been a priority for researchers over the last decade, as its applications expand in exciting fields such as medical imaging, spectroscopy, drug testing, communication, security, biomedical sensing applications, and so on. THz signals belong to the electromagnetic frequency range, which covers a frequency regime of 0.1–10 THz [7]. Due to the extremely low energy of each photon, THz-based sensors have potential to penetrate porous samples without damaging the sample layer. Terahertz radiation is a useful tool for sensing applications as it can penetrate many materials, such as plastics, paper, and clothing, allowing for non-invasive sensing of objects and materials. Furthermore, PCF which operates at THz frequency has a larger filling region by detecting analyte because the air hole and diameter of fiber have increased than PCF that performs in the mid-infrared range. Adamgil and Haxha et al. [1] modeled a PCF-based liquid sensor inside a circularly micro-fabricated arrangement, with a relative sensitivity of 8% and  $10^{-1}$  dB/m confinement loss for ethanol. Asaduzzaman et al. [3] designed a Hybrid PCF (H-PCF) with micro-fabricated core and cladding areas of elliptical and circular air holes, achieving 48% ethanol sensitivity. Paul et al. [8] proposed a folded-porous cladding of PCF at 1480 nm, which produces confinement loss of  $2.07 \times 10^{-5}$  dB/m and relative sensitivity of 64.19%. Similar number of cladding layers has been used by [2] but for H-PCF [1] et al. have studied large number of air holes [1]. A H-PCF for detecting these important chemical analytes and identified relative sensitivity of 61.05, 60.03, and 63.24% at 1.8 THz for ethanol, water, and benzene correspondingly has been suggested by Hasan et al. [6].

The manufacturing method is crucial for any constructed PCF structure because complicated manufacturing methods would limit the acceptability of the sensor. Sol-gel [4], extrusion, capillary stacking, stack and drilling, and 3D printing [9, 12] are some popularly used manufacturing techniques. The 3D printing technique can be used to create irregular structured PCFs [9]. Recently, the Max Plank Institute created few complicated fabricated PCFs in elliptical and rectangular designs. Because studied PCF has only been made up of air holes, rectangular-shaped, manufacturing employing extrusion, or 3D-printing technology has been possible.

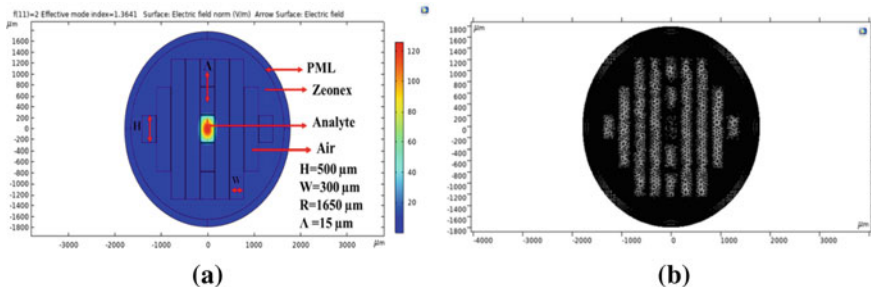


**Fig. 1** **a** Graphical representation of the studied PCF sensor and **b** mesh resolution of proposed photonic crystal fiber model

## 2 Materials and Methods

The present study has been performed in two basic steps: The first involves the configuration of the design in COMSOL multiphysics (v5.5a), which evaluates optical properties using finite element methods, and another is the configuration of pictured observations in MATLAB (v.2018a) for the objective of multiple optical properties observations. With a total fiber radius of 1650 μm, a width of 132 μm is assigned to the perfectly matched layer (PML) employing boundary conditions. In this case, perfectly matched layer detects an electromagnetic signal traveling closer to the surface. Eight rectangular holes (R1–R8) have been created around the core, which allow air injection for analysis. The rectangular air holes have the same width ( $W$ ) but not the same length as 500 μm.  $R_1$  and  $R_2$ ,  $R_3$  and  $R_4$ ,  $R_5$ , and  $R_6$  all have the same lengths of 2700, 1800, and 1200 μm. The spacing between the two holes in the cladding portion has been kept constant. The PCF sensor has a pitch of 15 μm (the distance between two adjacent rectangles). As a fiber background material, Zeonex has been used. Zeonex has a lower absorption loss in the terahertz band than a few other substances such as Topas, silicon, and others. Figure 1a, b shows the graphical representation and mesh resolution of the studied PCF sensor.

## 3 Results and Discussion

Using FEM in 1.0–2.5 THz frequency range, the optimum MRC-PCF has been proposed. To analyze the performance of the model, implementing the material to be examined into the core, various performance parameters such as confinement loss (CL) and birefringence ( $B$ ) have been calculated.

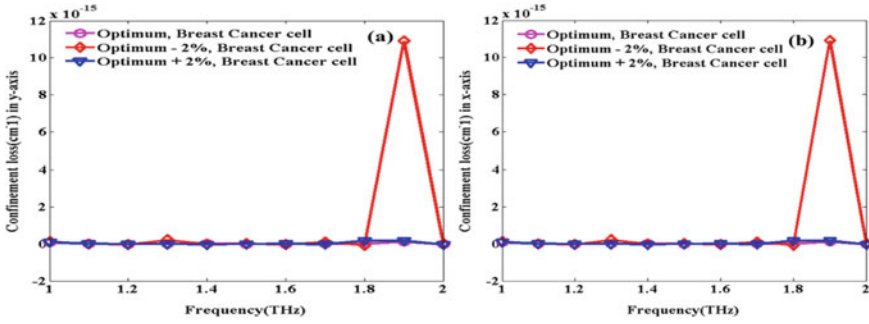


**Fig. 3** **a** Confinement loss for breast cancer cells and **b** normal cells

### 3.1 Confinement Loss

The confinement loss (CL) of a photonic crystal fiber determines its capability to restrict light within the core area and prevent its leakage. It is determined by the amount of light that escapes from the core area. A lower confinement loss indicates more light present within the core or sample. Using the imaginary value of the effective refractive index, the optical parameters can be evaluated. This type of loss can be reduced by suitable alignment of core and cladding holes. The mathematically of CL is calculated using Eq. (1) [5].

$$CL = 418.879 \times f \times \text{Img}(n_{\text{eff}}), \text{ cm}^{-1} \tag{1}$$

here  $f$  and  $n_{\text{eff}}$  denote the THz frequency and effective refractive index in that particular frequency range, correspondingly.

Figure 3a, b represents the confinement loss of  $17.3328 \times 10^{-9}$ ,  $14.5444 \times 10^{-10}$ , and  $66.844 \times 10^{-9}$  for cancer cells and for normal cells  $8.3649 \times 10^{-8}$ ,  $29.5411 \times 10^{-10}$ , and  $24.26592 \times 10^{-10}$  for optimum + 2%, optimum - 2%, and optimum % case correspondingly. It shows that wavelengths have been lowered as frequency rises which decreases confinement loss.

### 3.2 Birefringence

Birefringence calculates the quantity of the uneven structure of core’s air holes and cladding area. It represents a PCF’s ability to maintain polarization. The refractive index (RI) disparity between the  $x$  ( $n_{x\text{plane}}$ ) and  $y$  ( $n_{y\text{plane}}$ ) plane is represented in Eq. (2) [5]. This differential response can be detected by calculating variation in the phase or polarization of the light that propagates through the fiber.

$$B = |n_{x\text{plane}} - n_{y\text{plane}}| \tag{2}$$

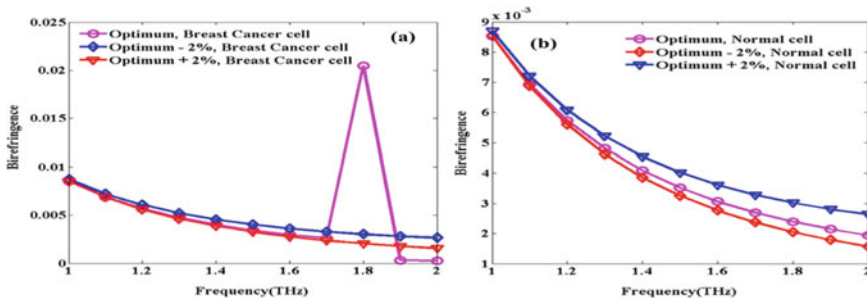


Fig. 4 a Birefringence for breast cancer cells and b normal cells

Figure 4a, b represents that birefringence is 0.00205, 0.000194, 0.02048 for cancerous cells and 0.00205, 0.00302, and 0.00233 for normal cells for optimum + 2%, optimum - 2%, and optimum % case correspondingly. The graph shows that rise in frequency refractive index difference between the polarizing modes rises so birefringence is reduced.

## 4 Conclusion

For identification of breast cancer cells, the studied photonic crystal fiber-based sensor shows propagated mode for optical properties. At the 1.8 THz frequency, the studied PCF shows optical characteristics confinement loss of  $17.33 \times 10^{-9} \text{ cm}^{-1}$  and birefringence of 0.0020.

**Acknowledgements** The author expresses gratitude to MMMUT, Gorakhpur, for awarding research cum teaching fellowship that has enabled the continuation of my research work. I also acknowledge the valuable suggestions provided by Prof. D. K. Dwivedi.

## References

1. Ademgil H, Haxha S (2016) Highly birefringent nonlinear PCF for optical sensing of analytes in aqueous solutions. *Optik* 127(16):6653–6660
2. Ahmed K, Ahmed F, Roy S, Paul BK, Aktar MN, Vigneswaran D, Islam MS (2019) Refractive index-based blood components sensing in Terahertz spectrum. *IEEE Sens J* 19(9):3368–3375
3. Asaduzzaman S, Ahmed K, Bhuiyan T, Farah T (2016) Hybrid photonic crystal fiber in chemical sensing. *SpringerPlus* 5(1)
4. Bise RT, Trevor DJ (2005) Sol–gel derived microstructured fiber: Fabrication and characterization. *Conf Opt Fiber Commun Tech Dig Ser* 3:269–271
5. Bulbul AAM, Kouzani AZ, Mahmud MAP, Nahid AA (2021) Design and numerical analysis of a novel rectangular PCF (R-PCF)-based biochemical sensor (BCS) in the THz regime. *Int J Opt*

6. Hasan MM, Sen S, Rana MJ, Paul BK, Habib MA, Daiyan GM, Ahmed K (2019) Heptagonal photonic crystal fiber based chemical sensor in THz regime. In: 2019 joint 8th international conference on informatics, electronics and vision, ICIEV 2019 and 3rd international conference on imaging, vision and pattern recognition, ICIIVPR 2019 with international conference on activity and behavior computing. ABC 2019, pp 40–44
7. Islam MS, Sultana J, Ahmed K, Islam MR, Dinovitser A, Ng BWH, Abbott D (2018) A novel approach for spectroscopic chemical identification using photonic crystal fiber in the terahertz regime. *IEEE Sens J* 18(2):575–582
8. Paul BK, Ahmed K, Asaduzzaman S, Islam MS (2017) Folded cladding porous shaped photonic crystal fiber with high sensitivity in optical sensing applications: design and analysis. *Sens Bio-Sens Res* 12:36–42
9. Sen S, Abdullah-Al-Shafi M, Sikder AS, Hossain MS, Azad MM (2021) Zeonex based decagonal photonic crystal fiber (D-PCF) in the terahertz (THz) band for chemical sensing applications. *Sens Bio-Sens Res* 31:100393
10. Shephard JD, MacPherson WN, Maier RRJ, Jones JDC, Hand DP, Mohebbi M, George AK, Roberts PJ, Knight JC (2005) Single-mode mid-IR guidance in a hollow-core photonic crystal fiber. *Opt Express* 13(18):7139
11. Wang XD, Wolfbeis OS (2016) Fiber-optic chemical sensors and biosensors (2013–2015). *Anal Chem* 88(1):203–227
12. Yadav S, Singh S, Lohia P, Umar A, Dwivedi DK (2022) Delineation of profoundly birefringent nonlinear photonic crystal fiber in terahertz frequency regime. *J Opt Commun*

# Performance Evaluation of Eco-Friendly $(\text{FA})_2\text{BiCuI}_6$ Double Perovskite Solar Cell for High Efficiency



Shivangi Yadav, Anupam Sahu, and Pooja Lohia

**Abstract** Double perovskite solar cell with FTO/SnS<sub>2</sub>/(FA)<sub>2</sub>BiCuI<sub>6</sub>/CuI/Se structure has been proposed in the present work. Perovskite materials are used for absorber layer to achieve high efficiencies in solar cells. For *n-i-p* planar perovskite solar cells, SnS<sub>2</sub> is preferred material for electron transport layer due to its high charge extraction at interface. CuI as hole-transporting material exhibits high transmittance, carrier mobility, wide bandgap (2.98 eV) and offers high conductivity. Proposed cell structure exhibits high performance with a fill factor of 84.95% and power conversion efficiency of 19.79%. The toxic-free perovskite layer (FA)<sub>2</sub>BiCuI<sub>6</sub> is better substitute for lead-based perovskite solar cells. Optimum thickness of absorber layer for defect density of  $1.0 \times 10^{13} \text{ cm}^{-3}$  and dopant density of  $1.0 \times 10^{16} \text{ cm}^{-3}$  is estimated to be 0.9  $\mu\text{m}$ . The device thickness and working temperature are varied to find the optimum value, and corresponding *J-V* characteristic and quantum efficiency are studied. The device works at 300 K and AM 1.5G. SCAPS-1D software is used for estimation of all parameters. The results show that material (FA)<sub>2</sub>BiCuI<sub>6</sub> is better substitute for lead-based perovskite solar cell.

**Keywords** Double perovskite solar cell · Absorber layer · Photovoltaic performance · SCAPS-1D

## 1 Introduction

The third-generation-based thin-film technologies attract as it shows better efficiencies and stability along with cost efficiency [1]. Perovskite solar cell shows promising characteristics but stability and toxicity is main concern [2]. A new class of emerging double perovskite drawn the attention of researcher.  $\text{A}_2\text{B}(\text{I})\text{B}'(\text{III})\text{X}_6$  or  $\text{A}_2\text{B}(\text{IV})\text{X}_6$  is the typical cell formula for the creation of double perovskite solar cell (DPSC). When monovalent and trivalent ions are injected together, or when a tetravalent ion

---

S. Yadav · A. Sahu · P. Lohia (✉)

Department of Electronics and Communication Engineering, Madan Mohan Malaviya University of Technology, Gorakhpur, Uttar Pradesh 273010, India  
e-mail: [lohia.pooja6@gmail.com](mailto:lohia.pooja6@gmail.com)

is added to replace divalent ions in  $AMX_3$ , double perovskites are generated [3]. It has stability in oxidizing and reducing environment too. It shows tunability, higher charge carrier mobility, and absorption of photon in visible range [4, 5].

The present simulation study is calibrated and examined with the SCAPS-1D tool, and very few experimental works related to double perovskites material are introduced so far. Architecture of solar cell FTO/SnO<sub>2</sub>/((FA)<sub>2</sub>BiCuI<sub>6</sub>)/NiO/Au shows 15.49% efficiency and fill factor 85.84% [6].

In this paper, the simulation study of double perovskite solar cell model FTO/SnS<sub>2</sub>/((FA)<sub>2</sub>BiCuI<sub>6</sub>/CuI/Se has been studied. The presented solar cell is stable and lead free. For *n-i-p* planar perovskite solar cells, SnS<sub>2</sub> is preferred material for electron transport layer due to its high charge extraction at interface. It demonstrates excellent bandgap, strong conductivity, and optical transparency at visible light. CuI as hole transporting material exhibits high transmittance, carrier mobility, wide bandgap (2.98 eV) and is transparent in nature, all of which contribute to its strong conductivity in the visible spectrum. Fluorine tin oxide (FTO) is used as transparent conducting oxide. Organic–inorganic-based absorber layer (FA)<sub>2</sub>BiCuI<sub>6</sub> has high charge carrier mobility along with superior optoelectronic properties. High optical conductivity, promising dielectric characteristics (5.27), and a high absorption coefficient are all present. It is a possible contender to create the next generation of non-toxic, Pb-free materials for photovoltaics and optoelectronics because it spans the entire visible light spectrum [7–9].

## 2 Device Model

Figure 1 shows the schematic device model and the band diagram. Band diagram insights about the flows of charge carrier within the junction. Modeling and simulation software SCAPS-1D [10] has been used for computational study. Table 1 shows input variable for layers.

## 3 Results and Discussion

The solar cell parameter is optimized by varying the layer thickness and its working temperature. The configurations exhibit optimum performance by varying thickness of (FA)<sub>2</sub>BiCuI<sub>6</sub> layer and device temperature. The best performance after device optimization displays fill factor 84.95% and power conversion efficiency 19.79%. The impact of changing the device temperature and absorber layer thickness on photovoltaic characteristics is covered in the remaining section of this study.

Figures 2a, b indicate variation of absorber layer thickness and its impact on solar cell performance, namely  $V_{OC}$ ,  $J_{SC}$ , FF, and PCE. The optimum thickness obtained is 900 nm at which the efficiency is maximum, at lower thickness less amount of absorption of photon occurs that leads to poor performance of the device,



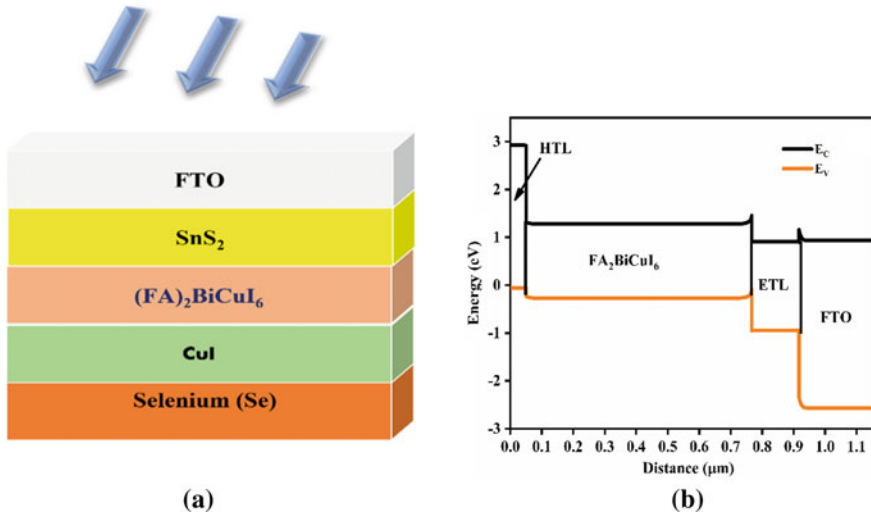


**Fig. 1** Proposed double perovskites solar cell (DPSC) model and **b** band diagram

**Table 1** Input variable for layers [11, 12]

Parameters	CuI	(FA) <sub>2</sub> BiCuI <sub>6</sub>	SnS <sub>2</sub>	FTO
Thickness (nm)	50	900	150	500
Bandgap $E_g$ (eV)	2.98	1.55	1.85	3.5
Electron affinity $\chi$ (eV)	2.1	3.7	4.26	4
Absolute permittivity $\epsilon$	6.5	5.27	17.7	9
Density state of CB $N_c$ (cm <sup>-3</sup> )	$2.8 \times 10^{19}$	$1 \times 10^{22}$	$7.3 \times 10^{18}$	$2.2 \times 10^{18}$
Density state of VB $N_v$ (cm <sup>-3</sup> )	$1.0 \times 10^{19}$	$1 \times 10^{21}$	$1 \times 10^{19}$	$1.8 \times 10^{19}$
Electron mobility $\mu_e$ (cm <sup>2</sup> V <sup>-1</sup> s <sup>-1</sup> )	$1.7 \times 10^{-4}$	2	50	20
Holes mobility $\mu_h$ (cm <sup>2</sup> V <sup>-1</sup> s <sup>-1</sup> )	$2.0 \times 10^{-4}$	1	25	10
Donor density $N_D$ (cm <sup>-3</sup> )	0	0	$1 \times 10^{20}$	$1 \times 10^{15}$
Acceptor density $N_A$ (cm <sup>-3</sup> )	$1 \times 10^{18}$	$1 \times 10^{16}$	0	0
Defect density $N_t$ (cm <sup>-3</sup> )	$1 \times 10^{15}$	$1 \times 10^{13}$	$1 \times 10^{15}$	$1 \times 10^{15}$

and at a same time higher thickness of absorber layer contributes to high charge recombination rate that in returns degrade the performance. Figures 3a, b shows the temperature variation with performance parameter. Above 300 K temperature the device performance mainly degrades only  $J_{SC}$  increased. It is due to the stress-induced ohmic resistance and higher recombination rate. Figures 4a, b show the  $J-V$  characteristics and quantum efficiency of the device with a  $V_{OC}$  of 0.893 V and a bandgap of 1.55 eV. Higher values of  $J_{SC} = 26.09 \text{ mA cm}^{-2}$  are associated with higher solar spectrum absorption. The 100% absorption rate of the proposed DPSC results in high electron-hole pairs and negligible reflection loss at the front contact,

which impacts the electrical and optical properties. Because of recombination loss, QE curve returns to zero after 800 nm. Across the visible and near-infrared spectra, the design exhibits a robust QE.

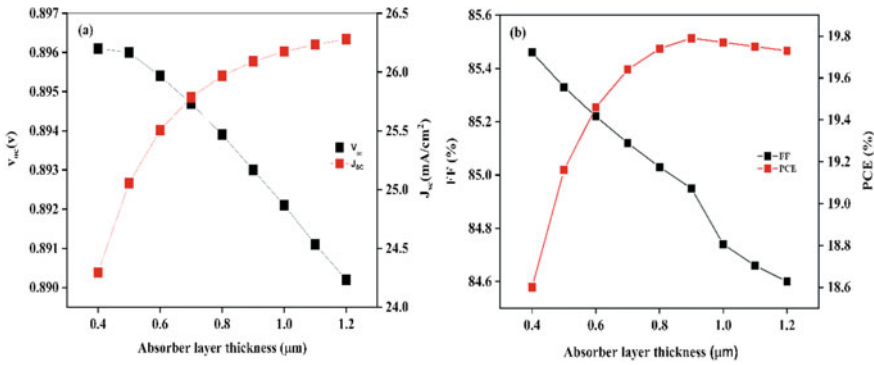


Fig.2 Effect of altering absorber layer thickness on a  $J_{sc}$  and  $V_{oc}$  b FF and PCE

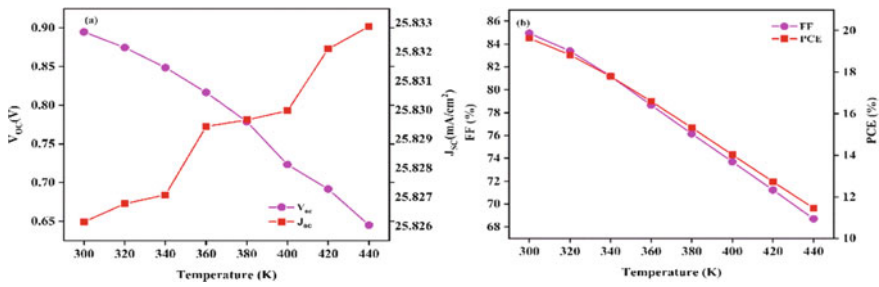


Fig.3 Effect of altering temperature on a  $J_{sc}$  and  $V_{oc}$  b FF and PCE

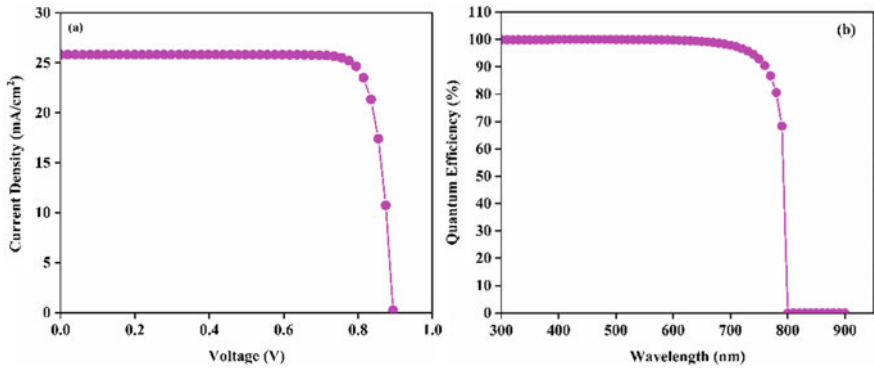


Fig. 4 a  $J-V$  characteristic and b quantum efficiency

## 4 Conclusion

High performance is demonstrated by the proposed double perovskite-based *n-i-p* planar solar cell structure FTO/SnS<sub>2</sub>/(FA)<sub>2</sub>BiCuI<sub>6</sub>/CuI/Se, which has fill factor 84.95% and power conversion efficiency of 19.79%. Optimum thickness of (FA)<sub>2</sub>BiCuI<sub>6</sub> layer for defect density of  $1.0 \times 10^{13} \text{ cm}^{-3}$  and dopant density of  $1.0 \times 10^{16} \text{ cm}^{-3}$  is estimated to be 0.9  $\mu\text{m}$ . The device thickness and working temperature are varied to find the optimum value, and corresponding *J-V* characteristic and quantum efficiency are studied. The device works at 300 K and AM 1.5G. SCAPS-1D software is used for estimation of all parameters. The results show that (FA)<sub>2</sub>BiCuI<sub>6</sub> is better substitute for lead-free perovskite solar cell. Interfacial engineering may be used to improve the device's performance even more. Current study might open up an entirely new avenue for the development of double perovskites solar cells.

**Acknowledgements** We are thankful to Dr. Burgelman and his team, Department of Electronics and Information Systems, University of Gent, Belgium, for developing SCAPS-1D tool.

**Declaration of Interest Statement** The authors declare that they have no conflict of interest.

## References

1. Kojima A, Teshima K, Shirai Y, Miyasaka T (2009) J Am Chem Soc 131:6050–6051. <https://doi.org/10.1021/ja809598r>
2. Manser JS, Christians JA, Kamat PV (2016) Chem Rev 116:12956–13008. <https://doi.org/10.1021/acs.chemrev.6b00136>
3. Wu Y, Li X, Zeng H (2021) Small Struct 2:2000071. <https://doi.org/10.1002/sstr.202000071>
4. Bhorde A, Waykar R, Rondiya SR, Nair S, Lonkar G, Funde A, Dzade NY (2021) ES Mater Manufact 12:43–52. <https://doi.org/10.30919/esmm5f1042>
5. Faizan M, Xie J, Murtaza G, Echeverría-Arroondo C, Alshahrani T, Bhamu KC, Laref A, Mora-Seró I, Khan SH (2021) Phys Chem Chem Phys 23:4646–4657. <https://doi.org/10.1039/D0CP05827K>
6. Rana AD, Pharne ID, Bhargava K (2023) Numerical simulation of highly efficient double perovskite solar cell using SCAPS-1D. Mater Today Proc 73:584–589
7. Roknuzzaman M, Zhang C, Ostrikov KK, Du A, Wang H, Wang L, Tesfamichael T (2019) Electronic and optical properties of lead-free hybrid double perovskites for photovoltaic and optoelectronic applications. Sci Rep 9(1):1–7
8. Srivastava V, Chauhan RK, Lohia P (2022) Highly efficient cesium-based halide perovskite solar cell using SCAPS-1D software: theoretical study. J Opt 1–8
9. Yadav S, Lohia P, Sahu A (2022) Enhanced performance of double perovskite solar cell using WO<sub>3</sub> as an electron transport material. J Opt. <https://doi.org/10.1007/s12596-022-01035-3>
10. Mandadapu U, Vedanayakam SV, Thyagarajan K et al (2017) Design and simulation of high efficiency tin halide perovskite solar cell. Int J Renew Energy Res 7:1604–1612
11. Jayan KD et al (2021) Enhancement of efficiency of (FA)<sub>2</sub>BiCuI<sub>6</sub> based perovskite solar cells with inorganic transport layers. Opt Mater 122:111671
12. Rai N et al (2020) Analysis of various ETL materials for an efficient perovskite solar cell by numerical simulation. J Mater Sci Mater Electron 31(19):16269–16280

# Effect of NiO Hole Transport Layer Thickness on the Power Conversion Efficiency of Perovskite Solar Cell: A Numerical Simulation Study



Saumya Vaish and Shiv Kumar Dixit

**Abstract** Perovskite solar cells (PSCs) have grabbed much attention due to their low cost, simple fabrication techniques and high efficiency. It has been observed that in order to improve the device's efficiency, much attention has to be laid on thickness of absorber layer, doping density and total defect density. There is a strong need to optimize these parameters so as to improve the device performance. Here, in this work  $J$ - $V$  characteristics of the proposed structure are measured along with the effect of nickel oxide (NiO) HTL layer thickness on PCE. The  $p$ - $i$ - $n$  structure simulated using SCAPS-1D simulator under AM1.5G spectrum has the following layers: ITO/HTL/perovskite/ETL/metal contact. The maximum power conversion efficiency (PCE) of the simulated structure with HTL material NiO having layer thickness of 440 nm is 53.76%, and the value of  $V_{OC}$  and FF is 1.80 V and 0.52, respectively. It has been observed that on increasing the HTL layer thickness from 20 to 440 nm, the value of efficiency and  $V_{OC}$  is increasing, but there is a significant drop in the fill factor of the device. The maximum value of fill factor (0.84) is reported for the HTL layer thickness of 20 nm.

**Keywords** PCE ·  $J$ - $V$  characteristics · Fill factor

## 1 Introduction

Methylammonium lead iodide ( $\text{CH}_3\text{NH}_3\text{PbI}_3$ ) perovskite absorbing layer has interesting optical and electronic properties that are under the investigation of the scientific community. It is a semiconductor pigment with a direct bandgap of 1.55 eV, thus an efficient light sensitizer over the whole visible solar spectrum. Perovskite solar cells (PSCs) are known as the solid-state version of the dye-sensitized solar cells (DSSCs) as mentioned in the literature [1]. Experimentally reported, various methods such as

---

S. Vaish (✉) · S. K. Dixit

Department of Electronics and Communication Engineering, Manav Rachna University,  
Faridabad, Haryana 121004, India

e-mail: [svaish91@gmail.com](mailto:svaish91@gmail.com)

vacuum deposition, inkjet printing, spin coating and spray pyrolysis have been used to deposit perovskite films [2]. The inverted planar structure (*p-i-n*) has grabbed attention because it is simple, requires low processing temperature and possess extremely less hysteresis effect [3]. It has been reported that PEDOT: PSS is used as HTM while PCBM as ETM for the for *p-i-n* device. But these materials effect the cell performance due to their poor carrier mobility and higher processing cost. Alternatives to these materials are inorganic compounds like  $\text{TiO}_2$ ,  $\text{SnO}_2$  for ETM and  $\text{NiO}_x$ ,  $\text{Cu}_2\text{O}$  for HTM [4]. Among the various inorganic compounds used as HTM, the devices with a power conversion efficiency exceeding 20% have utilized  $\text{NiO}_x$  as the HTL due to the following advantages: (a) A work function of about 5.0 eV, a band gap of 3.5 eV, a deep-lying valence band (around 5.4 eV) and high optical transparency that aligns well with absorber layers. (b) The efficient hole extraction capability and low electrode polarization of  $\text{NiO}_x$  in inverted PSCs. According to Xu et al. [3],  $\text{NiO}_x$  is expected to play an important role in the development of PSCs for improved performance and stability in the near future.

## 2 Methodology

The SCAPS-1D simulation software has been used to study the optoelectronic performance of the PSC having the configuration as  $\text{ITO}/\text{NiO}_x/\text{CH}_3\text{NH}_3\text{PbI}_3/\text{TiO}_2/\text{Al}$  as shown in Fig. 1. Various material properties of absorbing layer, HTM and ETM used for simulating the structure are reported in Table 1. We have simulated the structure reported by Rahman et al. [4] to compute the value of  $V_{\text{OC}}$ , FF and PCE. All the different parameters of the layers were entered into the working panel window. The flat band condition of the front and back contacts is taken. The defect in the absorber layer lies in center and is Gaussian. The NiO layer thickness was varied from 20 to 590 nm to obtain the maximum value of efficiency. The  $J-V$  curve obtained is shown in Fig. 2.

**Fig. 1** Simulated device structure

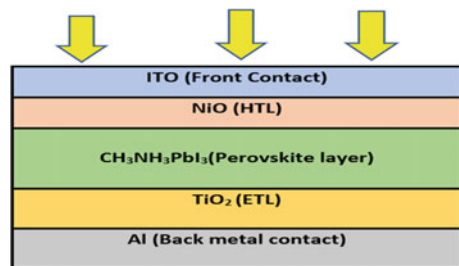
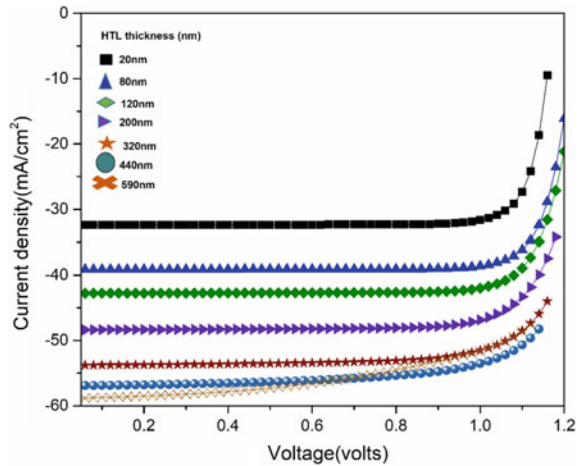


**Table 1** Optoelectronic properties of materials used in simulated structure

Properties	NiO	CH <sub>3</sub> NH <sub>3</sub> PbI <sub>3</sub>	TiO <sub>2</sub>
Thickness (nm)	80	320	80
Bandgap (eV)	3.750	1.560	3.300
Electron affinity (eV)	2.100	3.900	4.200
Dielectric permittivity (relative)	10.700	10.000	10
CB effective DOS (cm <sup>-3</sup> )	$2.8 \times 10^{19}$	$2.76 \times 10^{18}$	$2.5 \times 10^{18}$
VB effective DOS (cm <sup>-3</sup> )	$1.8 \times 10^{19}$	$3.9 \times 10^{18}$	$1 \times 10^{18}$
Electron thermal velocity (cm/s)	$1 \times 10^7$	$1 \times 10^7$	$1 \times 10^7$
Hole thermal velocity (cm/s)	$1 \times 10^7$	$1 \times 10^7$	$1 \times 10^7$
Electron mobility (cm <sup>2</sup> /Vs)	$1.2 \times 10^2$	$1.5 \times 10^1$	$1.0 \times 10^{-1}$
Hole mobility (cm <sup>2</sup> /Vs)	$2.5 \times 10^2$	$1.5 \times 10^1$	$1.0 \times 10^{-1}$
ND (donor density) (cm <sup>-3</sup> )	0	0	$1 \times 10^{19}$
NA (acceptor density) (cm <sup>-3</sup> )	$1 \times 10^{15}$	$1 \times 10^{11}$	0
<i>N<sub>t</sub></i> (total defect density) (cm <sup>-3</sup> )	$1 \times 10^{17}$	$1 \times 10^{15}$	$1 \times 10^{17}$

**Fig. 2** *J-V* curve of the simulated structure for different HTL thickness



### 3 Results and Discussion

Maximum  $V_{oc}$ ,  $J_{sc}$ , fill factor and efficiency of 1.80 V, 57.07 mA/cm<sup>2</sup>, 0.52 and 53.76%, respectively, were obtained at HTL thickness of 440 nm. The maximum PCE at 440 nm is due to an effective charge transport within the solar cell. It was also observed that the value of efficiency increased to a maximum of about 53.76% at a layer thickness of about 440 nm, but afterward it began to decline. The reason could be that, as the HTL layer thickness increases beyond a certain value, the number of photons absorbed by HTL began to decrease resulting in loss of efficiency. Our results showed that a very thin (< 20 nm) or thick HTL (> 440 nm) is not suitable for high efficiency. Above 500 nm, the reduction in fill factor to about 0.442 is observed. A thin HTL (< 20 nm) is not suitable for complete absorption of light photons; therefore, generation will be less and recombination may be high. Figure 2 shows the trend of  $J-V$  curve at varying thickness of HTL. All the results are given in Table 2. Rahman et al. [4] used NiO<sub>x</sub> as the HTL material and compared the lead halide absorber layer with three different ETLs, namely TiO<sub>2</sub>, ZnO and SnO<sub>2</sub>. The maximum efficiency reported in their work is 16.87% for TiO<sub>2</sub> ETL.

**Table 2** Various parameters with the variation of thickness of HTL

Thickness (nm)	$V_{oc}$ (V)	$J_{sc}$ (mA/cm <sup>2</sup> )	FF	PCE (%)
20	1.17	32.37	84.54	32.12
50	1.18	35.97	83.93	35.63
80	1.18	39.13	82.81	38.56
110	1.20	41.91	40.98	40.98
140	1.24	44.36	77.63	42.97
170	1.27	46.49	75.40	44.69
200	1.35	48.36	70.72	46.25
230	1.39	50.19	68.60	47.87
260	1.51	51.62	62.88	49.25
290	1.55	52.88	61.48	50.51
320	1.58	53.97	60.41	51.61
350	1.76	54.92	54.19	52.50
380	1.78	55.75	53.40	53.16
410	1.79	56.46	52.73	53.58
440	1.80	57.07	52.18	53.76
470	2.02	57.59	46.14	53.71
500	2.01	58.03	45.70	53.42
530	2.00	58.39	45.26	52.90
560	1.98	58.69	44.79	52.17
590	1.96	58.91	44.27	51.24

## 4 Conclusion

It has been observed that PCE is HTL thickness dependent that varies from 20 to 590 nm. The maximum PCE achieved is 53.76% and fill factor 0.52 at 440 nm HTL thickness. After 440 nm up to 590 nm thickness, PCE is reducing. Therefore, optimization of HTL thickness is also important for the commercialization of perovskite solar cells.

**Acknowledgements** I would like to thank Dr. Marc Burgelman for providing the SCAPS-1D software.

## References

1. Grätzel M (2014) The light and shade of perovskite solar cells. *Nat Mater* 13(9):838–842
2. Bag A, Radhakrishnan R, Nekovei R, Jeyakumar R (2020) Effect of absorber layer, hole transport layer thicknesses, and its doping density on the performance of perovskite solar cells by device simulation. *Sol Energy* 196:177–182
3. Xu L, Chen X, Jin J, Liu W, Dong B, Bai X, Reiss P et al (2019) Inverted perovskite solar cells employing doped NiO hole transport layers: a review. *Nano Energy* 63:103860
4. Rahman MS, Miah S, Marma MSW, Sabrina T (2019) Simulation based investigation of inverted planar perovskite solar cell with all metal oxide inorganic transport layers. In: International conference on electrical, computer and communication engineering (ECCE). IEEE, Feb 2019, pp 1–6



# Visible-Light-Assisted Photocatalytic Degradation of Methyl Orange Using La–Ag<sub>3</sub>PO<sub>4</sub>/ZnO as Photocatalyst



Neenamol John, P. S. Samjeev, Bony K. John, and Beena Mathew

**Abstract** Photocatalytic degradation is an advanced oxidation processes (AOP) in which the photosensitized molecular entity alters the photochemical reaction by the initial absorption of radiation. Heterogeneous photocatalysis has demonstrated significant promise as a low-cost, sustainable, and environmentally friendly wastewater treatment technology. In this work, a heterogeneous photocatalyst ZnO/Ag<sub>3</sub>PO<sub>4</sub> has been prepared and modified by doping with lanthanum to enhance its photocatalytic activities under light irradiation. The morphology and structure of La–Ag<sub>3</sub>PO<sub>4</sub>/ZnO were characterized by Fourier transform infrared (FT-IR), scanning electron microscopy (SEM), transmission electron microscopy (TEM), and UV–vis diffuse reflectance spectroscopy. Under visible light, the synthesized La–Ag<sub>3</sub>PO<sub>4</sub>/ZnO has shown an excellent activity towards the degradation of methyl orange (MO). The degradation studies revealed that the modified photocatalyst shows confounded degradation efficiency than unmodified Ag<sub>3</sub>PO<sub>4</sub>/ZnO. The radical trapping experiments evidence that the main species reasoning for photodegradation was hydroxyl ( $\cdot$ OH) radicals. The mechanism of photocatalytic degradation of MO over the La–Ag<sub>3</sub>PO<sub>4</sub>/ZnO photocatalyst surface was also described.

**Keywords** Photocatalysis · Methyl orange · Semiconductor

## 1 Introduction

Agricultural and industrial effluents are considered to be the major pollutants of consanguineous habitats. In particular, colour-producing substances such as dyes and pesticides used in agriculture are aesthetically objectionable when they are present in water supplies. Not only can these toxic and non-toxic chemicals disrupt the ecological balance in the receiving water, but they may also threaten the health of the animals and humans who will have to use the contaminated water for drinking.

---

N. John · P. S. Samjeev · B. K. John · B. Mathew (✉)  
School of Chemical Sciences, Mahatma Gandhi University, Kottayam, Kerala 686 560, India  
e-mail: [beenamathew@mgu.ac.in](mailto:beenamathew@mgu.ac.in)

In the field of environmental cleaning, photocatalysis is a sustainable and energy-efficient method. Photocatalytic degradation is an AOP in which the photosensitized molecular entity alters the photochemical reaction by the initial absorption of radiation. Specific heterogeneous metal oxide semiconductor materials were developed and gained substantial interest due to their photocatalytic potential when subjected to ultraviolet irradiation. These photocatalysts can turn the contaminants directly in wastewater into harmless substances. When these semiconductors are exposed to a specific light source, electron–hole pairs are created, with the positive holes remaining in the valence band and the electrons moving to the conduction band. Vestigial dye contaminants that are adsorbed on the surface of the semiconductors are involved in a complex series of chemical reactions that are activated by the electron–hole pairs that have been formed. Recently reported  $\text{Ag}_3\text{PO}_4$ -based ternary composites such as  $\text{C}_3\text{N}_4/\text{MoS}_2/\text{Ag}_3\text{PO}_4$  and  $\text{BiVO}_4/\text{RGO}/\text{Ag}_3\text{PO}_4$  show good degradation activity [1, 2].

Zinc oxide is a possible semiconductor with a large band width (3.2 eV). When it hodgepodge with silver phosphate ( $\text{Ag}_3\text{PO}_4$ ) and lanthanum (La), ZnO's photocatalytic activity can be increased. Research suggest that the photogenerated electrons in  $\text{Ag}_3\text{PO}_4$  may be coupled with surface adsorbed oxygen and hydrogen ions to shape  $\text{H}_2\text{O}_2$  and coupled with another electron to create active hydroxyl radicals to kill organic pollutants. The conductive band of ZnO is thus deemed more negative than that of  $\text{Ag}_3\text{PO}_4$ , and the valence band of  $\text{Ag}_3\text{PO}_4$  is more favourable than that of ZnO. They developed the  $\text{Ag}_3\text{PO}_4/\text{ZnO}$  hybrid photocatalyst by integrating  $\text{Ag}_3\text{PO}_4$  and ZnO. Photogenerated electrons are required to be moved from ZnO to  $\text{Ag}_3\text{PO}_4$ , thus supporting the multi-electron-involved reduction cycle and improving the photodegradation efficiencies in  $\text{Ag}_3\text{PO}_4$  [3, 4]. The amount of reactive  $\cdot\text{OH}$  radical species is further increased by lanthanum present in the system. Photocatalytic decomposition of methyl orange was studied with lanthanum-doped  $\text{Ag}_3\text{PO}_4/\text{ZnO}$  in the present study.

## 2 Materials and Instrumentation

All the chemicals and reagents used in this experiment are analytically pure. Zinc oxide (ZnO), disodium hydrogen phosphate (anhydrous) ( $\text{Na}_2\text{HPO}_4$ ), silver nitrate ( $\text{AgNO}_3$ ), lanthanum nitrate hexahydrate ( $\text{LaN}_3\text{O}_9 \cdot 6\text{H}_2\text{O}$ ), methyl orange ( $\text{C}_{14}\text{H}_{14}\text{N}_3\text{NaO}_3\text{S}$ ), ethylene diaminetetra acetic acid (EDTA) ( $\text{C}_{10}\text{H}_{16}\text{N}_2\text{O}_8$ ), isopropanol ( $\text{C}_3\text{H}_8\text{O}$ ), and benzoquinone ( $\text{C}_6\text{H}_4\text{O}_2$ ) were purchased from Merck, India, and used as received. The Fourier transform infrared spectroscopy (FT-IR) was studied using Perkin–Elmer spectrometer between 400 and  $4000\text{ cm}^{-1}$  range. Scanning electron microscopy was carried out using JEOL-JSM-6390. UV–vis spectral analysis was recorded on a Shimadzu UV-3600 plus UV–visible spectrophotometer. TEM analysis was carried out using JEOL-JEM 2100 microscope.

### 3 Experimental

An in-situ precipitation technique was used to deposit  $\text{Ag}_3\text{PO}_4$  nanoparticles onto the commercial ZnO surface. Commercial ZnO particles weighing 0.1628 g (0.002 mol) were sonicated for 5 min after being dissolved in 20 mL of deionized water. About 0.7163 g (0.002 mol) of  $\text{Na}_2\text{HPO}_4$  was immediately added to the solution following the sonication. A 20 mL (0.3 M)  $\text{AgNO}_3$  solution with a pH of 7 was added dropwise after being magnetically stirred for 10 min. The colour of the solution changed from white to yellow. After being magnetically stirred for 4 h, the photocatalyst  $\text{Ag}_3\text{PO}_4/\text{ZnO}$  ( $\text{Ag}_3\text{PO}_4$ -to-ZnO molar ratio = 1:1) was filtered, then washed, and dried. In order to prepare 2% of La- $\text{Ag}_3\text{PO}_4/\text{ZnO}$ , 0.3 g of the  $\text{Ag}_3\text{PO}_4/\text{ZnO}$  catalyst was weighed and dissolved in 150 mL deionized water and sonicated for 30 min and magnetically stirred. About 30 mL of deionized water was used to dissolve 0.006 g of  $\text{LaN}_3\text{O}_9 \cdot 6\text{H}_2\text{O}$ , which was then added dropwise to the sonicated sample and stirred for 1 h. The photocatalyst was centrifuged, then washed, and dried. Then, 1 and 3 percentage of lanthanum-doped  $\text{Ag}_3\text{PO}_4/\text{ZnO}$  were prepared under the same condition.

### 4 Results and Discussion

The FT-IR spectra of  $\text{ZnO}/\text{Ag}_3\text{PO}_4$  with and without doping of lanthanum are shown in Fig. 1a. A strong peak that observed at  $535\text{ cm}^{-1}$  is attributed to the Zn-O stretching frequency which is found almost close to the actual one. The asymmetric O=P-O bending vibration modes are responsible for the absorption band near  $639\text{ cm}^{-1}$ , while the ones that appeared at  $954\text{ cm}^{-1}$  is assigned to the asymmetric stretching vibrations of P-O-P bonds in phosphate ( $\text{PO}_3^{-4}$ ). The stretching vibrations of O-H after La doping are responsible for the extensive absorption that appeared between  $3000$  and  $3500\text{ cm}^{-1}$ . So it is expected that lanthanum present in the system as its hydroxide. SEM was used to investigate the morphologies of the sample. It is observed that the morphology of La-ZnO/ $\text{Ag}_3\text{PO}_4$  is agglomerate grains composed of rod-shaped ZnO and clusters of  $\text{Ag}_3\text{PO}_4$  particles. It was noticed that the surfaces of the ZnO particles were “studded” with a number of  $\text{Ag}_3\text{PO}_4$  particles (Fig. 1b). The TEM analysis illustrates the internal morphology of the photocatalyst. On the surface of the ZnO rod,  $\text{Ag}_3\text{PO}_4$  and  $\text{La}(\text{OH})_3$  nanoparticles are deposited. The SAED pattern depicts the crystal planes in the form of circular rings. (Fig. 1c, d). Diffuse reflectance spectroscopy is used to evaluate the photocatalytic activity of the synthesized composite. The binding energy is decreased by the La-ZnO/ $\text{Ag}_3\text{PO}_4$  composite catalysts, according to the Tauc plot derived from the DRS spectra. The decrease in bandgap after doping also indicates the enhanced photocatalytic activity of the synthesized photocatalyst (Fig. 1e, f) [5].

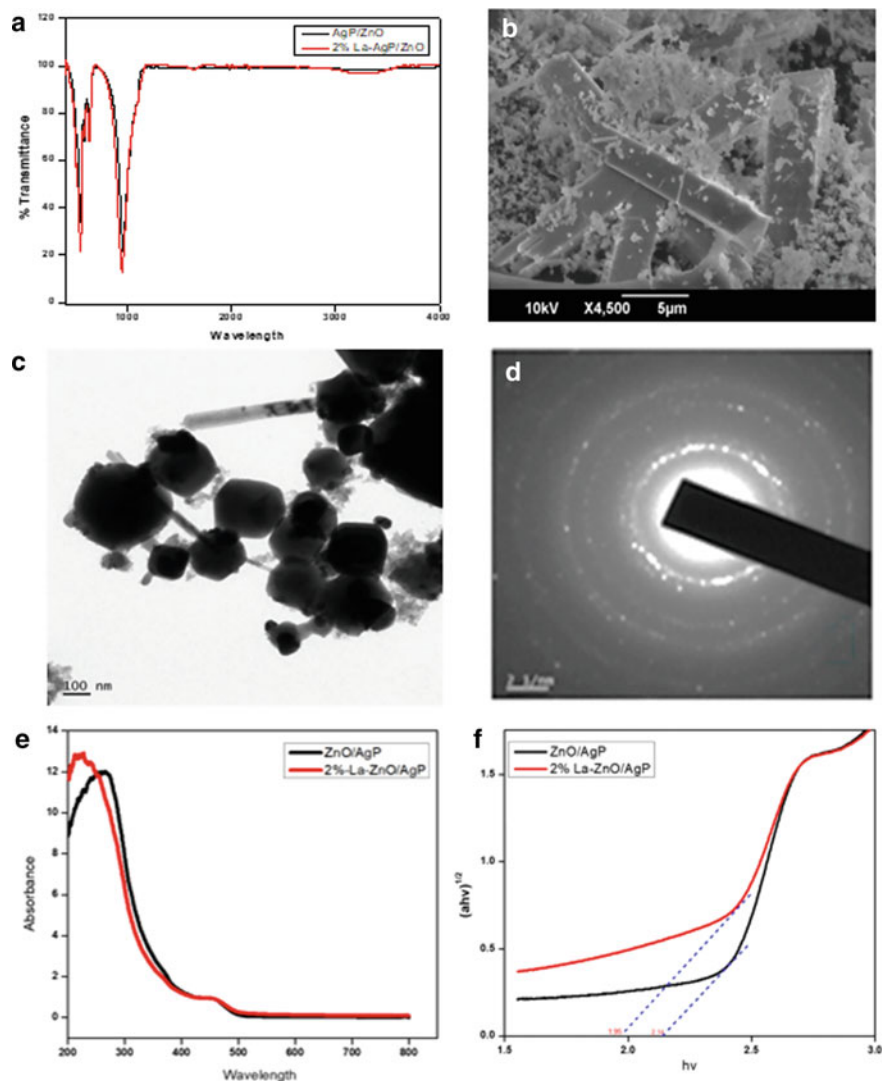


**Fig. 1** a, b FT-IR and SEM, c, d TEM and SAED pattern, e, f absorbance and Tauc plot of La-ZnO/Ag<sub>3</sub>PO<sub>4</sub>

To explore the photocatalytic activity, we choose methyl orange as a model compound since it is a notable water pollutant which is carcinogenic and mutagenic. Hence, photodegradation of methyl orange is extremely relevant. Figure 2a, b shows the time dependent UV-vis. spectra of methyl orange (MO) dye during photo irradiation with pure ZnO/Ag<sub>3</sub>PO<sub>4</sub> and La-ZnO/Ag<sub>3</sub>PO<sub>4</sub> respectively. When the irradiation time was increased from 1, 2, and 5 min, the prominent peak at  $\lambda_{\max}$ , i.e. 464 nm, gradually decreased, indicating that the dye had been degraded.

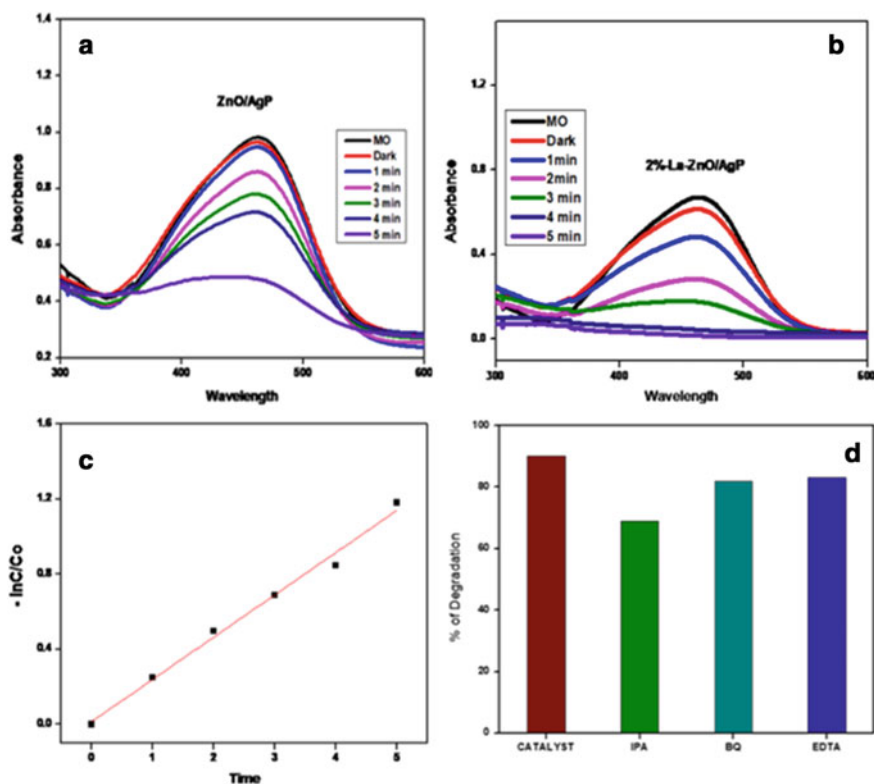


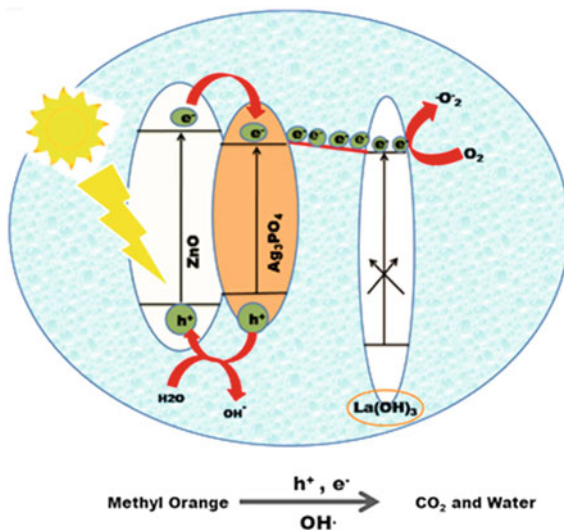
**Fig. 2** a, b Photodegradation of MO using ZnO/Ag<sub>3</sub>PO<sub>4</sub> and La-ZnO/Ag<sub>3</sub>PO<sub>4</sub>, c kinetic study, and d scavenger study

Though ZnO/Ag<sub>3</sub>PO<sub>4</sub> shows better degradation for the dye, it has been improved when La-ZnO/Ag<sub>3</sub>PO<sub>4</sub> is used. However, when La-ZnO/Ag<sub>3</sub>PO<sub>4</sub> was used, 98% of the methyl orange was degraded in 5 min. The optimization study reveals that about 2 wt% of La-ZnO/Ag<sub>3</sub>PO<sub>4</sub> results in the augmented degradation of MO within 5 min. Figure 2c depicts the  $-\ln C/C_0$  versus time plot of La-ZnO/Ag<sub>3</sub>PO<sub>4</sub> photocatalyst. The rate constant value of this reaction is  $0.222 \text{ min}^{-1}$ , and the  $R^2$  value is 0.989. From Fig. 2d, it is clear that the active species in the photocatalysis using La-ZnO/Ag<sub>3</sub>PO<sub>4</sub> was hydroxyl ( $\cdot\text{OH}$ ) radical, then comes  $\cdot\text{O}_2^-$  and  $\text{h}^+$ .

## 5 Mechanism

A proposed mechanism can help to explain the photodegradation efficiency of the catalyst. When we consider the surface of ZnO and Ag<sub>3</sub>PO<sub>4</sub> as an example, electrons in the valence band of ZnO and Ag<sub>3</sub>PO<sub>4</sub> are transferred to its conduction band

**Scheme 1** Proposed mechanism of photodegradation



and then these electrons are shifted to the conduction band of  $\text{La(OH)}_3$ . At the same time, holes in  $\text{Ag}_3\text{PO}_4$  will be transported to the VB of  $\text{ZnO}$  conveniently. The photogenerated electrons convert  $\text{O}_2$  molecule into superoxide radical, and the holes generated after irradiation react with water molecule forming hydroxyl radical. These active species react with MO and forming  $\text{CO}_2$  and water. The schematic representation of mechanism is shown in Scheme 1.

## 6 Conclusions

The novel  $\text{La-ZnO/Ag}_3\text{PO}_4$  photocatalyst was successfully synthesized by simple precipitation method. The synthesized photocatalyst was characterized by IR, SEM, TEM, and UV-vis. DRS spectroscopy.  $\text{La-ZnO/Ag}_3\text{PO}_4$  displayed maximum photocatalytic efficiency, 98% of MO was degraded within minutes, and the hydroxyl ( $\cdot\text{OH}$ ) radicals played the major role in the degradation which was significantly suppressed in the presence of isopropyl alcohol (IPA). Other strategies, such as charge carrier separation and energy band modification, could be applied in future works to enhance their photocatalytic activity. Researchers may be encouraged to use the existing and improved photocatalytic approaches to remediate other industrial effluents.

## References

1. John N, Priyanka RN, Abraham T, Punnoose MS, John BK, Mathew B (2022) Rational design of  $\text{Ag}_2\text{CO}_3$ -loaded SGO heterostructure with enhanced photocatalytic abatement of organic pollutants under visible light irradiation. *Environ Sci Pollut Res* 29(35):53225–53237
2. Abraham T, Priyanka RN, Joseph S, Chacko AR, Mathew B (2021) Fabrication of  $\text{La}_2\text{O}_3/\text{Bi}_2\text{O}_3$ /silver orthophosphate heterojunction catalyst for the visible light mediated remediation of refractory pollutants. *Mater Res Bull* 140:111299
3. Lee KM, Lai CW, Ngai KS, Juan JC (2016) Recent developments of zinc oxide based photocatalyst in water treatment technology: a review. *Water Res* 88:428–448
4. Rauf MA, Ashraf SS (2009) Fundamental principles and application of heterogeneous photocatalytic degradation of dyes in solution. *Chem Eng J* 151(1–3):10–18
5. Luo Y, Xu N, Liu X, Yang L, Wu H, Qin Y (2015) Photoactivity enhanced and photo-corrosion inhibited  $\text{Ag}_3\text{PO}_4/\text{ZnO}$  visible light photocatalyst for the degradation of rhodamine B. *Energy Environ Focus* 4(2):121–127

# CNTFET Folded Cascode Operational Transconductance Amplifier: Design and Comparative Analysis



Mir Bintul Islam and M. Nizamuddin

**Abstract** The purpose of this study is to design a folded cascode operational transconductance amplifier (FC-OTA). The simulation was carried out with HSPICE software on a 45 nm technology node at a supply voltage of 0.9 V. FC-OTA circuits are built using both traditional CMOS and pure CNTFETs. The suggested CNT-based circuits were compared to traditional CMOS-based circuits. The suggested circuits outperformed traditional devices in terms of many metrics such as DC gain and output resistance.

**Keywords** Carbon nanotube (CNT) · OTAs · Gain · Output resistance

## 1 Introduction

Analog circuits use operational transconductance amplifier (OTA), as they provide versatility owing to an additional control input. In sub-micron technology domains, OTA suffers from gain deterioration [1–3]. Many approaches have been used to combat gain deterioration, but the cascoding methodology has shown superior results [4–6]. Folded cascode is a key configuration in cascoding OTAs because it improves gain.

## 2 Proposed CNTFET-Based Folded Cascode Operational Transconductance Amplifier

A CNTFET, like a regular MOSFET, has four terminals: gate, source, drain, and substrate. The gate controls the channel properties of a CNTFET, and its operating characteristics are comparable to those of a MOSFET. Verilog-A Stanford model was

---

M. B. Islam (✉) · M. Nizamuddin  
Department of Electronics and Communication Engineering, Jamia Millia Islamia, New Delhi 110025, India  
e-mail: [mir1909967@st.jmi.ac.in](mailto:mir1909967@st.jmi.ac.in)



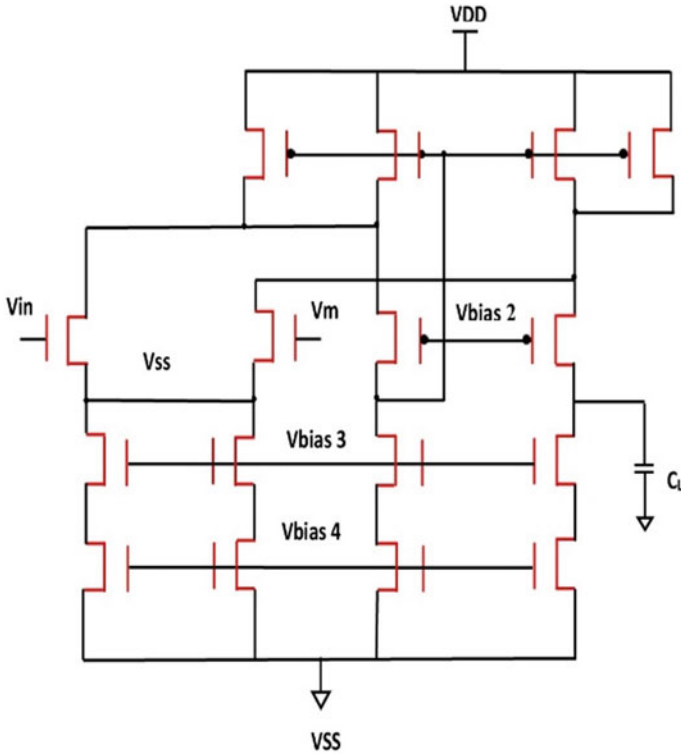


**Fig. 1** Conventional CMOS-based folded cascode OTA

utilized for CNTFET simulation, while PTM 45 nm model was used for conventional *n*- and *p*-channel MOSFETS [7]. Figure 1 shows the circuit of bulk CMOS-based FC-OTA which has been simulated in HSPICE at a supply voltage of 0.9 V. The proposed CNFET-based circuit has been formed by replacing conventional NMOS and PMOS transistors by *n*-CNFETs and *p*-CNFETs, respectively. The suggested architecture's performance was evaluated by altering the diameter of the CNTs.

### 3 Results and Discussion

The CNT-based OTA's performance was evaluated by computing performance measurement parameters such as DC gain, output resistance, average power, and 3-dB bandwidth by altering the diameter of the CNTs. Figure 2a shows that as CNT diameter increases, DC gain decreases. This is because RO increases as CNT diameter increases. Increased RO enhances the screening and scattering effects, lowering the gain. Figure 2a illustrates that as CNT diameter rises, DC gain drops. The bandgap lowers as  $D_{CNT}$  rises, lowering the threshold voltage and raising leakage but also

static power dissipation [1, 8, 9]. The relationship of output resistance with 3-dB bandwidth is provided by

$$f_{3\text{-dB}} = 1/2\pi R_O C_L \tag{1}$$

Figure 2c demonstrates that when  $D_{\text{CNT}}$  grows, output resistance falls. This is because rising  $D_{\text{CNT}}$  increases transconductance, which increases output current, resulting in a drop in output resistance [10, 11]. Figure 2d illustrates that when  $D_{\text{CNT}}$  grows, 3-dB bandwidth increases, which is attributable to the parameter  $R_O$ . Because bandwidth and output resistance are connected by Eq. (1), as output resistance reduces, 3-dB bandwidth increases (Table 1).

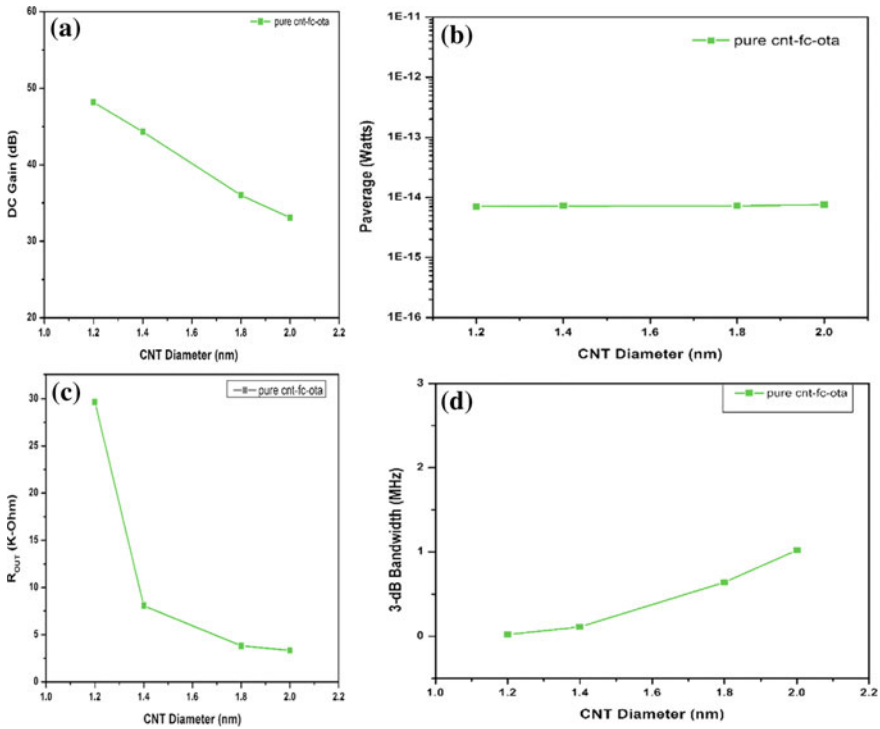


**Fig. 2** Effect of change in  $D_{\text{CNT}}$  on **a** DC gain **b** average power dissipation **c** output impedance **d** bandwidth

**Table 1** Comparative analysis of CMOS and CNTFET-based FC-OTA at  $N = 20$ ,  $S = 20$  nm,  $CL = 1$  pF

S. no.	Parameters	CMOS-based OTA	CNT-based OTA
1	DC gain (dB)	14	44
2	Rout (KΩ)	5	6

## 4 Conclusion

In this study, it was discovered that the performance of carbon nanotube-based folded cascode OTA was superior to the CMOS-based folded cascode OTA in terms of parameters: DC gain and output impedance. The impact of changing the diameter of the CNTs was also noted, and an optimal value is necessary for the best performance.

## References

1. Nizamuddin M, Loan SA, Alamoud AR, Abbassi SA (2015) Design, simulation and comparative analysis of CNT based cascode operational transconductance amplifiers. *Nanotechnology* 26(39):395201
2. Li T, Ye B, Jiang J (2009) A novel fully differential telescopic operational transconductance amplifier. *J Semicond* 30(8):085002
3. Amlani I, Lee KF, Deng J, Wong H-SP (2009) Measuring frequency response of a single-walled carbon nanotube common-source amplifier. *IEEE Trans Nanotechnol* 8(2):226–233
4. Chatterjee S, Tsvividis Y, Kinget P (2005) 0.5-V analog circuit techniques and their application in OTA and filter design. *IEEE J Solid-State Circuits* 40(12):2373–2387
5. Ren MY, Wu T, Song MX, Zhang CX (2012) Design procedures for a fully differential telescopic cascode two-stage CMOS operational amplifier. *Proc Eng* 29:4030–4034
6. Redouane D, Bougachel NE (2008) Design choices for folded cascode operational transconductance amplifiers. *Afr Phys Rev* 2 82–4 Special Issue (Microelectronics):0039
7. [https://stanford.edu/group/nanoelectronics/model\\_downloads.html](https://stanford.edu/group/nanoelectronics/model_downloads.html)
8. Usmani FA, Hasan M (2010) *Microelectron J* 41:395
9. Sun Y, Kursun V (2011) *Trans Electr Electron Mater* 12:43
10. Ajit JS, Kim Y-B, Choi M (2010) Performance assessment of analog circuits with carbon nanotube FET (CNFET). In: *Proceedings of the 20th symposium on Great lakes symposium on VLSI*
11. Deng J, Wong HSP (2007) *IEEE Trans Electron Devices* 54:2377

# Antibacterial Effect of Phosphorous-Doped Carbon Nanomaterial Derived from *Alstonia Venenata*



Meera Varghese , Kaviya Parambath Kootery , Suma Sarojini ,  
and Manoj Balachandran 

**Abstract** Antibiotics have been widely used as fundamental medicine for several decades to treat various bacterial infections. However, bacteria develop different mechanisms to defeat the action of antibiotics, which has become a significant issue that endangers infectious therapy. To reduce the consumption of antibiotics and thus combat the increasing antibiotic resistance, it is necessary to implement safe and effective alternatives to conventional antibiotics. Though nanomaterials have become an emerging hope in infectious treatments, they have limited application due to aggregation, toxicity issues, and problems related to their dispersibility. However, carbon nanomaterials (CNMs) offer high solubility, biocompatibility, and minimum toxicity with their inherent antibacterial properties. The selection of natural precursors as the carbon source is an eco-friendly and economical route for synthesizing antibacterial carbon nanomaterials. In the present work, fluorescent CNMs have been synthesized by the hydrothermal treatment of *Alstonia venenata* leaf extract. The antibacterial capability of the bare extract (AVE), hydrothermally treated extract (AVH), AVH doped with nitrogen (N-AVH), and AVH doped with phosphorous (P-AVH) are tested against gram-positive *Staphylococcus aureus* (*S. aureus*) and gram-negative *Escherichia coli* (*E. coli*) bacteria. Except for P-AVH, all other samples showed nontoxicity towards the tested bacterial species. In contrast, P-AVH inhibited bacterial growth with minimum inhibitory concentration (MIC) values of 2.5 and 2 mg/ml on *S. aureus* and *E. coli*, respectively.

**Keywords** Carbon nanomaterials · Antibiotic resistance · Antibacterial

---

M. Varghese · M. Balachandran (✉)  
Department of Physics and Electronics, Christ University, Bengaluru, India  
e-mail: [manoj.b@christuniversity.in](mailto:manoj.b@christuniversity.in)

K. P. Kootery · S. Sarojini  
Department of Life Sciences, Christ University, Bengaluru, India

## 1 Introduction

The invention of antibiotics and their extensive use in infectious treatment have saved millions of lives from morbidity and mortality caused by various pathogens. However, imprudent usage of antibiotics has resulted in antibiotic resistance that requires the immediate attention of the medical and scientific community, or else it may lead to the loss of millions of lives [1]. Replacing conventional antibiotics with alternative strategies is the fastest and most effective means of eliminating antibiotic resistance. With their excellent physio-chemical properties, CNMs have been widely studied for various applications in diverse fields [2–6]. The emergence of CNMs in the medical field has changed the face of antibacterial therapies. CNMs possess less toxicity and high biocompatibility with unique antibacterial mechanisms that are less likely to develop antibiotic resistance.

Various types of CNMs, such as carbon nanotubes, graphene, graphene oxide, carbon dots etc., have been widely experimented against different microorganisms [7]. Carbon dots possess inherent antibacterial properties, and hetero atom doping of carbon dots has been reported as introducing enhanced antibacterial effects [8–10]. Chai et al. hydrothermally synthesized phosphorous-doped carbon quantum dots using m-aminophenol and phosphoric acid, which inhibited the growth of *Escherichia coli* and *Staphylococcus aureus* with MIC of 1.23 and 1.44 mg/mL, respectively [11]. Lin et al. reported that onion-derived carbon dots prepared by a facile hydrothermal method could inactivate *Pseudomonas fragi* with a MIC of 2 mg/mL [12]. Chai et al. tested the antibacterial activity of carbon quantum dots derived from valine, in which triethylamine and phosphoric acid were used as nitrogen and phosphorus sources, respectively. The authors observed an increment in the antibacterial activity of the sample against *E. coli* and *S. aureus*, along with increased phosphorous content [13]. Herein, a facile hydrothermal route is followed to obtain phosphorous-doped CNMs from *Alstonia venenata* leaf extract, using phosphoric acid as the phosphorous precursor. The antibacterial response of the derived CNMs was studied against *S. aureus* and *E. coli* bacteria which showed MIC values of 2.5 and 2 mg/ml, respectively.

## 2 Materials and Methods

The synthesis of CNMs was achieved by a facile hydrothermal method. 10 g of clean *A. venenata* leaves were ground with 100 ml of distilled water and heated under 60 °C for 3 h. The extract was allowed to cool to room temperature and then filtered through a home-use tea filter. 30 ml of the extract was then hydrothermally re-acted at 180 °C temperature for 10 h in a 50 ml autoclave. The obtained solution was allowed to cool down to room temperature which is then centrifuged at 10,000 rpm for 30 min. The supernatant was separated carefully and filtered through a 0.22 µm nylon membrane. The final solution in which CNMs were dispersed in water was

labelled as AVH. The leaf extract was magnetically stirred with 1 ml of ammonia and phosphoric acid, respectively, followed by the same procedures to obtain N-AVH and P-AVH samples. Chemicals used for bacterial culture (peptone, sodium chloride, yeast extract, and agar) were obtained from Sigma-Aldrich. The bacteria were cultured overnight in Luria–Bertani broth (LB) media at 37 °C.

### 3 Results and Discussion

The x-ray diffraction (XRD) profile of P-AVH is shown in Fig. 1a. The XRD pattern shows a broad (002) diffraction peak approximately at  $2\theta = 23.8^\circ$  with an interlayer spacing of  $d = 0.374$  nm. The nature of the peak suggests the formation of graphitic structures with weak crystallinity. The difference in the interlayer spacing of P-AVH and that of graphite (0.33 nm) indicates the occurrence of specific functional groups on the surface of the graphitic structures within the sample [14].

The optical properties of P-AVH have been studied from the UV–vis absorption spectra (Fig. 1b) and photoluminescent spectra (Fig. 2) of the material. The absorption spectra show a strong absorbance in the ultraviolet region, peaking approximately at 271.21 nm, indicating the  $\pi - \pi^*$  transitions of aromatic carbon. The fluorescence spectra of P-AVH have been obtained for excitation ranges from 270 to 450 nm. The spectra show an excitation-dependent emission characteristic with a maximum emission approximately at 455.79 nm, corresponding to the 350 nm excitation. The excitation-dependent nature of photoluminescent spectra can be attributed to the involvement of functional groups [15].

The antibacterial activity of the obtained CNMs has been tested against gram-positive *S. aureus* and gram-negative *E. coli* bacteria using an agar well diffusion method (Fig. 3). 20  $\mu$ l of CNMs (40 mg/ml) and 100  $\mu$ l of Amp (100 mg/ml) were used to analyze the antibacterial activity. After 24 h of incubation at 37 °C

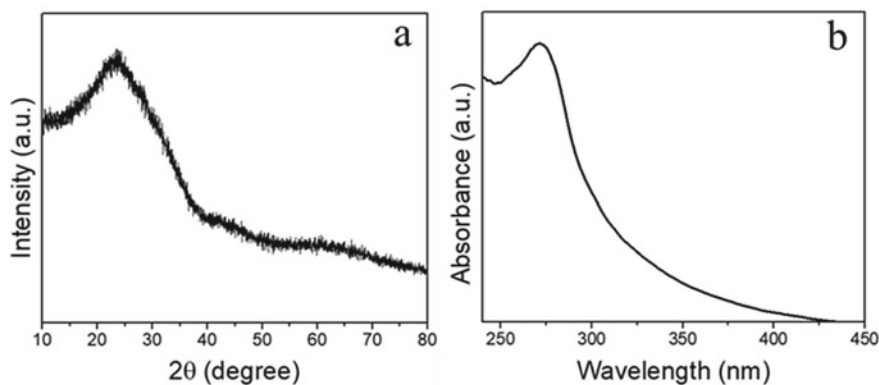


**Fig. 1** XRD profile (a) and UV–Vis absorption spectrum (b) of P-AVH

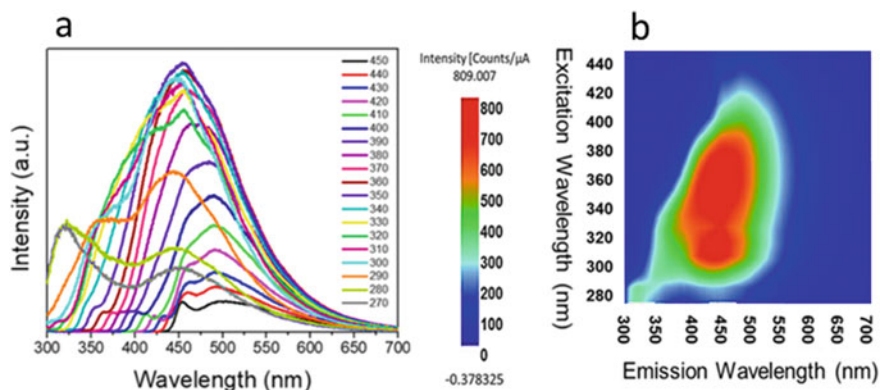


**Fig. 2** Photoluminescent spectra (a) and Excitation—emission matrix (b) of P-AVH

temperature, no zones of inhibitions were observed with AVE, AVH, and N-AVH samples. In contrast, P-AVH exhibited clear zones with 24 and 25 mm diameters, corresponding to *E. coli* and *S. aureus*, respectively. The inhibition zones of AMP were 26 mm on *E. coli* and 27 mm on *S. aureus*. The MIC of P-AVH analyzed with a broth dilution method and obtained 2.5 and 2 mg/ml MIC values on *S. aureus* and *E. coli*, respectively. The antibacterial properties of P-AVH can be attributed to the electrostatic interaction between bacteria and positively charged phosphorous-doped CNMs [11].

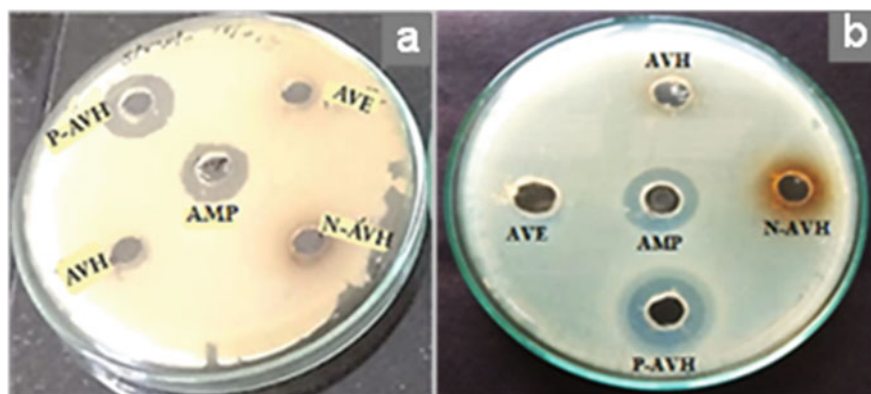


**Fig. 3** Antibacterial activity of P-AVH on *S. aureus* (a) and *E. coli* (b) bacteria

## 4 Conclusion

Fluorescent CNMs from *A. venenata* leaf extract have been synthesized via a simple hydrothermal method. The XRD profile shows the carbonaceous structure of the sample. Among the synthesized samples, the phosphorous-doped sample showed antibacterial effects on *E. coli* and *S. aureus* bacteria with MIC values of 2 and 2.5 mg/ml, respectively. The antibacterial activity may be attributed to the electrostatic interaction of the sample with negatively charged bacterial cells.

## References

1. Yin R, Agrawal T, Khan U, Gupta GK, Rai V, Huang YY et al (2015) Antimicrobial photo-dynamic inactivation in nanomedicine: small light strides against bad bugs. *Nanomedicine* 10(15):2379–2404
2. Razack IJ, Thomas A, Kota S, Varghese M, Chiriyankandath JS, Nair AS (2020) Graphene based materials for supercapacitors. *Mapana J Sci* 19(1):87–137
3. Saikia M, Singh A, Dihingia A, Khare P, Kalita J, Saikia BK (2022) Scalable production, cell toxicity assessment, and plant growth promotion activities of carbon quantum dots derived from low-quality coal feedstock. *Chem Eng J* 433:133633
4. Luan X (2022) Heating properties of graphene oxide nanosheets and their application in clothing design. *Adv Mater Sci Eng* 2022:1457
5. Rao AA, Joseph AP, Balachandran M (2022) An outlook on zero-dimensional nanocarbons as components of DSSC. *Biomass Convers Biorefinery* 14:1–23
6. Venkatesan RA, Balachandran M (2020) Novel carbon nano-onions from paraffinum liquidum for rapid and efficient removal of industrial dye from wastewater. *Environ Sci Pollut Res* 27(35):43845–43864
7. Varghese M, Balachandran M (2021) Antibacterial efficiency of carbon dots against gram-positive and gram-negative bacteria: a review. *J Environ Chem Eng* 9(6):106821
8. Zhou LJ, Chi YT, Chen LS, Pei SC, Chai SQ (2022) One-step synthesis of Si-doped carbon dots with antibacterial activities. *Russ J Gen Chem* 92(11):2363–2369
9. Travlou NA, Giannakoudakis DA, Algarra M, Labella AM, Rodríguez-Castellón E, Bandoz TJ (2018) S- and N-doped carbon quantum dots: surface chemistry dependent antibacterial activity. *Carbon* 135:104–111
10. Ezati P, Rhim JW, Molaei R, Priyadarshi R, Roy S, Min S et al (2022) Preparation and characterization of B, S, and N-doped glucose carbon dots: antibacterial, antifungal, and antioxidant activity. *Sustain Mater Technol* 32:e00397
11. Chai S, Zhou L, Pei S, Zhu Z, Chen B (2021) P-doped carbon quantum dots with antibacterial activity. *Micromachines* 12(9):1116
12. Lin R, Cheng S, Tan M (2022) Green synthesis of fluorescent carbon dots with antibacterial activity and their application in Atlantic mackerel (*Scomber scombrus*) storage. *Food Funct* 13(4):2098–2108
13. Chai S, Zhou L, Chi Y, Chen L, Pei S, Chen B (2022) Enhanced antibacterial activity with increasing P doping ratio in CQDs. *RSC Adv* 12(43):27709–27715
14. Başoğlu A, Ocak Ü, Gümrükçüoğlu A (2020) Synthesis of microwave-assisted fluorescence carbon quantum dots using roasted-chickpeas and its applications for sensitive and selective detection of Fe<sup>3+</sup> ions. *J Fluoresc* 30(3):515–526
15. Kalaiyaran G, Joseph J, Kumar P (2020) Phosphorus-doped carbon quantum dots as fluorometric probes for iron detection. *ACS Omega* 5(35):22278–22288



# Comparative Study for Supercapacitive Performance of Polypyrrole Matrix Reinforced with Different Organic Fillers



Sarfراز Ansari , Gobind Mandal , Debashish Nayak ,  
Sanjeev Kumar , Jayanta Bauri , and Ram Bilash Choudhary 

**Abstract** Like other intrinsic conducting polymers (ICPs), polypyrrole (PPy) also suffers from its inferior cyclic behavior due to its fragile polymeric backbone. However, the cycling capability can be greatly enhanced by a suitable selection of organic fillers. Herein, we have synthesized PPy via in-situ chemical oxidative polymerization method with different organic fillers including reduced graphene oxide (rGO), activated carbon (sugarcane bagasse), carbon nanotubes (CNTs) and graphitic carbon nitride ( $g\text{-C}_3\text{N}_4$ ). Morphological studies of the as-synthesized polymeric composite materials were done by using field emission scanning electron microscopy (FESEM) analysis. For structural and elemental analysis, X-ray diffraction (XRD) spectroscopy, Raman spectroscopy and energy dispersive X-ray (EDX) analysis techniques were employed. The electrochemical performance of the polymeric electrode materials was evaluated with cyclic voltammetry (CV), galvanostatic charge–discharge (GCD) and electrochemical impedance spectroscopy (EIS) performed in a three-electrode symmetric system with 1 M potassium chloride (KCl) electrolyte. Resultant polymeric composites exhibited well-improved cyclic behavior due to sublime synergistic interaction between the polymer and the filler materials.

**Keywords** Polypyrrole (PPy) · Activated carbon ·  $g\text{-C}_3\text{N}_4$  · Pseudocapacitor

## 1 Introduction

PPy being possessed high electrical conductivity ( $7000\text{ S cm}^{-1}$ ), large electrical conductivity ( $620\text{ F g}^{-1}$ ), facile synthesis process and high redox activity is considered excellent pseudocapacitive material [1]. However, its inferior cyclic stability curtails most of electrochemical implication. The best strategy to overcome this obstacle is—using PPy in form of composites with some suitable filler materials. Metal oxides/sulfides (MO/MS), metal organic frameworks (MOFs), MXenes,

---

S. Ansari · G. Mandal · D. Nayak · S. Kumar · J. Bauri · R. B. Choudhary (✉)  
Nanostructured Composite Materials Laboratory (NCML), Department of Physics, Indian  
Institute of Technology (Indian School of Mines), Dhanbad 826004, India  
e-mail: [rbcism@gmail.com](mailto:rbcism@gmail.com)

carbonaceous materials are most widely used fillers in polymeric composites. However, carbonaceous materials seem to be most logical candidate due to multiple reasons: (1) Being EDLC materials, carbonaceous materials can provide advantages of dual charge storage mechanism, and (2) Carbonaceous materials also provide stable surface for growth of polymeric chains and supply a firm supportive network to fragile polymeric backbone. Several researches have been performed to study electrochemical performance of PPy/carbon composites [2–4]. However, all of these studies were performed at non-identical conditions and hence uncomparable. Herein, we have synthesized composites of PPy with four carbon materials, viz., graphene oxide (GO), carbon nanotubes (CNTs), sugar bagasse derived activated carbon (SBAC) and graphitic carbon nitride (g-C<sub>3</sub>N<sub>4</sub>) and studied their electrochemical performance over identical environmental and electrolytical conditions. The result so obtained were compared and concluded. It is expected that the composite materials acquired ameliorated electrochemical as well as cyclic performance.

## 2 Materials and Method

Exfoliated graphene oxide (GO) sheets were prepared by well-known and facile modified Hummer's method similar to our previous research work [5]. Sugarcane bagasse activated carbon (SBAC) was synthesized via hydrothermal treatment of sugarcane bagasse followed by pyrolysis as shown in Fig. 1a [6]. g-C<sub>3</sub>N<sub>4</sub> was synthesized from thermal condensation of melamine [7]. PPy and its composites with GO, CNT, SBAC and g-C<sub>3</sub>N<sub>4</sub> (10% by mass of pyrrole) were synthesized by in-situ chemical oxidative polymerization of pyrrole monomers in presence of APS, as shown in Fig. 1b [5]. The composites were named as PGO, PCNT, PAC and PGCN, respectively.

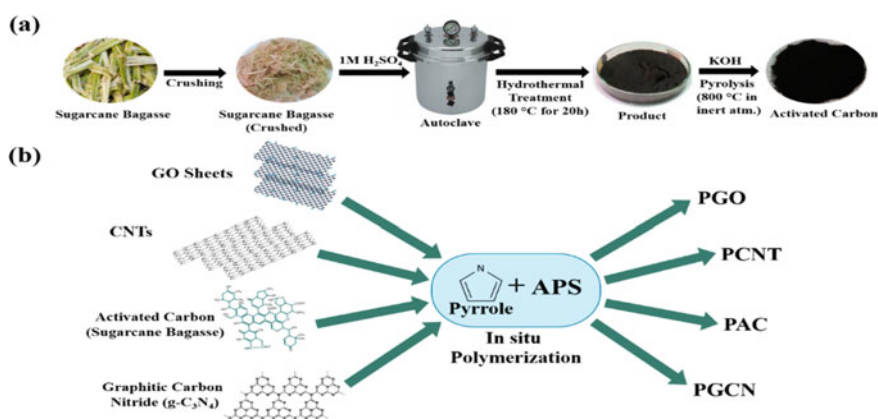


**Fig. 1** Schematic diagram for synthesis of **a** SBAC; **b** PGO, PCNT, PAC and PGCN

### 3 Results and Discussion

Morphological and elemental studies of the materials were carried out with field emission electron microscope (FESEM) and energy dispersive X-ray (EDX) analysis (Supra-55, Carl Zeiss, Germany) as shown in Fig. 2. FESEM image of PPy exhibited its renowned agglomerated globular structures as shown in Fig. 2a. The images of PGO, PCNT, PAC and PGCN composites showed the presence of PPy particles anchored over organic filler materials—crumpled rGO sheets (Fig. 2b), tubular structure of CNT (Fig. 2c), flake-like AC (Fig. 2d) and sheets of g-C<sub>3</sub>N<sub>4</sub> (Fig. 2e) [8]. Thus, FESEM established the interactive behavior between polymer and filler materials. Figure 2f represents weight and atomic composition of C, N, O and S in PPy and its composites deduced from EDX analysis. The result showed that the polymeric composites mainly comprised of C, N and O with trace amount of S due to APS.

Crystallinity of electrode materials were investigated via X-ray diffraction (XRD) spectroscopic technique (Smartlab, Rigaku, Cu-K $\alpha$  X-ray) and shown in Fig. 2g. The spectrum of PPy possessed two broad peaks centered around 2 $\theta$  angles of 8° and 23°. XRD pattern of PGO possessed a small bulge over the broad peak of PPy at ~ 26° which revealed the presence of reduced form of graphene oxide in the composite. XRD spectrum of PCNT and PGCN possessed characteristic peaks of CNT (at ~ 26°) and g-C<sub>3</sub>N<sub>4</sub> (at ~ 27.6°) fused into the broad peaks of PPy [7]. The XRD spectrum of PAC appeared similar to that of PPy due to absence of any sharp peaks in activated carbon (AC). Therefore, the spectra confirmed that the electrode materials were mostly amorphous with characteristic peaks of filler components.

Electrochemical performance of the electrode materials was evaluated with three different methods, viz., cyclic voltammetry (CV), galvanostatic charge discharge

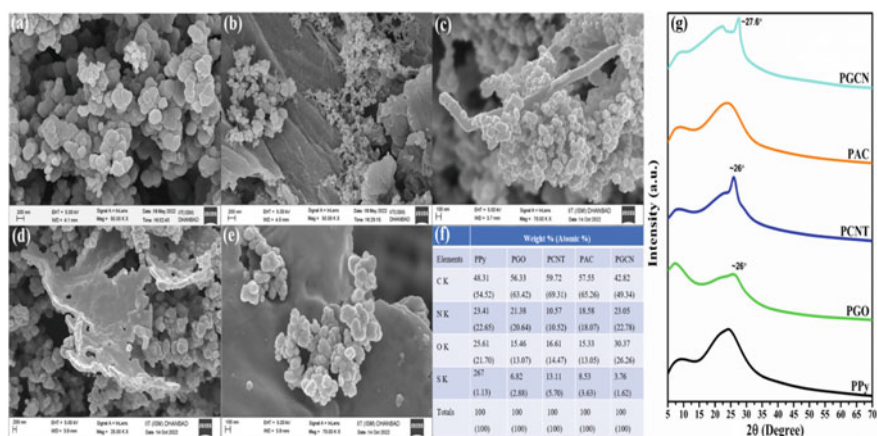


**Fig. 2** FESEM images of **a** PPy; **b** PGO; **c** PCNT; **d** PAC; **e** PGCN; **f** weight and atomic composition of PPy, PGO, PCNT, PAC and PGCN; **g** XRD spectra of PPy, PGO, PCNT, PAC and PGCN

(GCD) and electrochemical impedance spectroscopy (EIS), performed in two-electrode symmetric system with 1 M KCl electrolyte. Specific capacitance of materials from CV curves and GCD curves were evaluated using Eqs. (1) and (2), respectively.

$$C_{\text{sp}} = \frac{2 \int IV dV}{m S_R \Delta V} \quad (1)$$

$$C_{\text{sp}} = \frac{4I \Delta t}{m \Delta V} \quad (2)$$

where  $I$  is currently density,  $V$  is applied potential across the electrodes,  $m$  is the total active-mass of materials loaded over the electrodes,  $S_R$  is scan rate,  $\Delta V$  is potential window and  $\Delta t$  is discharging time. Figure 3a showed CV curves of electrode materials at the scan rate of 100 mV s<sup>-1</sup>. The deviation of the shape of the curves from rectangular justify the presence of pseudocapacitive material, i.e., PPy. Area enclosed within CV curve become optimal for PGO composite and hence PGO also possessed highest specific capacitance (148.6 F g<sup>-1</sup>) among all synthesized samples as shown in Table 1. Figure 3b represented GCD curves of the electrode materials at current density of 1 A g<sup>-1</sup> over potential window of 0–0.8 V. The quasi-triangular GCD curves revealed the presence of both pseudocapacitive and EDLC charge storage mechanism. It is observed that the discharging time increased with inclusion of organic filler into the polymeric matrix. PGO composite showed largest discharging times and highest specific capacitance (176.6 F g<sup>-1</sup>) at the current density of 1 A g<sup>-1</sup> as shown in Table 1. At higher current densities of 3 and 5 A g<sup>-1</sup> the specific capacitance became maximum for PGCN as shown in Fig. 3c and Table 2, showing its remarkable electrochemical performance at higher voltages. However, PCNT showed shortest discharging time as well as specific capacitance. This behavior observed as the presence of CNTs reduced the surface area accessible for insertion of electrolytic ions. Improved specific capacitance of PGO is due to dual charge storing mechanism and enhanced active surface area for electrolyte anchoring.

Energy density ( $E_d$ ) and Power density ( $P_d$ ) of samples were evaluated from Eqs. (3) and (4) and summarized in Table 2.

$$E_d = \frac{1}{2} C_{\text{sp}}^2 V \quad (3)$$

$$P_d = \frac{E_d}{\Delta t} \quad (4)$$

From the table it is clearly depicted that PGO exhibited high energy density of 15.7 Wh kg<sup>-1</sup> at current density of 1 A g<sup>-1</sup> which is almost 1.5 times higher than that of PPy and highest among all the binary composites. However, at higher current densities PGCN overstriped PGO and showed better energy storing capability with energy density of 10.4 Wh kg<sup>-1</sup>. All the materials exhibited a decline in energy density with current density. PAC and PGCN showed decline in energy density by

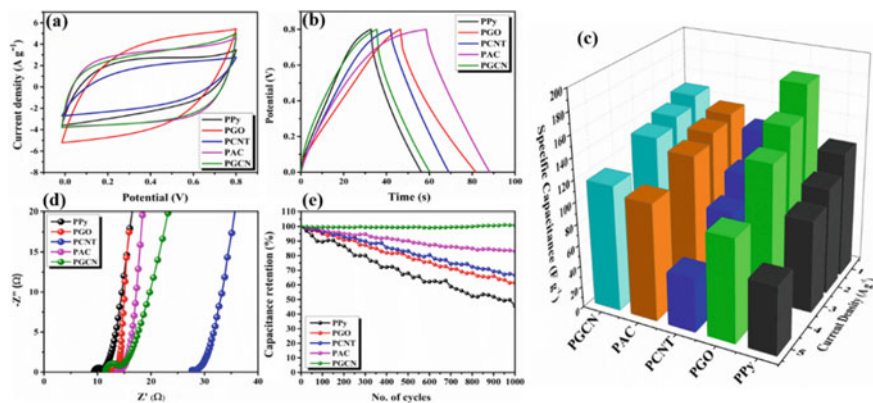


**Fig. 3** a CV curves; b GCD curves; c Bar graph; d Nyquist plots; e Cyclic stability plots of PPy, PGO, PCNT, PAC and PGCN

**Table 1** Electrochemical performance of PPy, PGO, PCNT, PAC and PGCN

Electrode materials	Specific capacitance (F g <sup>-1</sup> ) @ 100 mV s <sup>-1</sup>	Specific capacitance (F g <sup>-1</sup> ) @ 1 F g <sup>-1</sup>	Equivalent series resistance (R <sub>ESR</sub> ) (Ω)	Charge transfer resistance (R <sub>CT</sub> ) (Ω)	Capacitance retention (%)
PPy	93.5	118.3	9.35	1.64	45.6
PGO	148.6	176.6	12.50	0.81	61.5
PCNT	72.0	124.5	27.68	0.47	66.7
PAC	124.1	136.5	13.66	0.40	83.1
PGCN	121.5	148.3	11.49	2.76	100.9

**Table 2** Specific capacitance and energy density of PPy, PGO, PCNT, PAC and PGCN at various current densities and power densities

Electrode materials	Specific capacitance (C <sub>s</sub> ) (F g <sup>-1</sup> ) [Current density (A g <sup>-1</sup> )]				Energy density (E <sub>d</sub> ) (Wh kg <sup>-1</sup> ) [Power density (P <sub>d</sub> ) (W kg <sup>-1</sup> )]			
	(1)	(2)	(3)	(5)	(444.4)	(888.8)	(1333.2)	(2222)
PPy	118.3	100.2	86.7	64.3	10.5	8.9	7.7	5.7
PGO	176.6	150.1	130.2	96.5	15.7	13.3	11.6	8.6
PCNT	124.5	96.9	76.4	50.2	11.1	8.6	6.8	4.5
PAC	136.5	131.1	122.7	109.2	12.1	11.7	10.9	9.7
PGCN	148.3	139.9	132.4	116.7	13.2	12.4	11.8	10.4

the factor of 1.25 and 1.27, respectively. The small decline in energy density of PAC and PGCN suggested its stable charge storage properties over wide range of current density.

Capacitive behavior and charge mobility of the electrode materials were studied with EIS performed over 0.1 Hz to 100 kHz as shown in the *Nyquist plot*, Fig. 3d. It has been observed that PCNT possessed highest equivalent series resistance ( $R_{ESR}$ ) while PAC possessed low charge transfer resistance as shown in Table 2. Cyclic stability of the electrode materials were examined as capacitance retention as shown in Fig. 3e and Table 2. Pristine PPy exhibited capacitance retention of 45.6% after 1000 GCD cycles. Insertion of carbon material successfully ameliorated the cyclic stability by providing a stable and rigid support to the polymeric chains. PGCN exhibited significantly improved cyclic behavior with almost constant specific capacitance upto 1000 cycles. The results showed wonderful synergistic compatibility between PPy and g-C<sub>3</sub>N<sub>4</sub>.

## 4 Conclusion

For comparative study of electrochemical performance of carbon materials embedded PPy composites, four different composites of PPy, viz., PGO, PCNT, PAC and PGCN were synthesized via in-situ oxidative polymerization technique. Their structural and morphological properties were studied with XRD, FESEM and EDX spectroscopy. Electrochemical evaluation revealed that PGO exhibited best electrochemical performance with highest specific capacitance (148.6 F g<sup>-1</sup> at 100 mV s<sup>-1</sup> and 176.6 F g<sup>-1</sup> at 1 A g<sup>-1</sup>) and energy density (15.7 Wh kg<sup>-1</sup>). However, at higher current densities PGCN overstripped PGO and showed better energy storing capability and energy density. Moreover, PGCN also showed excellent cyclic characteristics with almost uniform capacitance retention up to 1000 GCD cycles. The remarkable result suggests that PGCN could be an excellent filler material to enhance cyclic performance of PPy.

**Acknowledgements** The authors express their gratitude to Indian Institute of Technology (Indian School of Mines) Dhanbad for providing the essential facilities, characterization, and instrumental support.

**Conflict of Interest** The authors declare that there is no conflict of interest.

## References

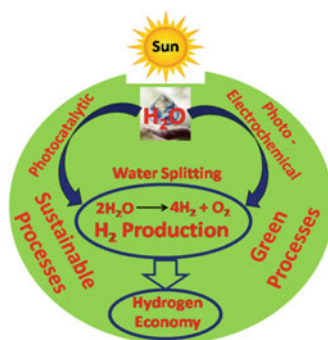
1. Kumar S, Choudhary RB (2022) Influence of MnO<sub>2</sub> nanoparticles on the optical properties of polypyrrole matrix. *Mater Sci Semicond Process* 139:106322
2. Liu G, Shi Y, Wang L, Song Y, Gao S, Liu D, Fan L (2020) Reduced graphene oxide/polypyrrole composite: an advanced electrode for high-performance symmetric/asymmetric supercapacitor. *Carbon Lett* 30:389–397
3. Arora R, Nehra SP, Lata S (2022) In-situ composited g-C<sub>3</sub>N<sub>4</sub>/polypyrrole nanomaterial applied as energy-storing electrode with ameliorated super-capacitive performance. *Environ Sci Pollut Res* 2022:1–12
4. Pan H, Li J, Feng YP (2010) Carbon nanotubes for supercapacitor. *Nanoscale Res Lett* 5:654–668
5. Ansari S, Choudhary RB, Gupta A (2023) Nanoflower copper sulphide intercalated reduced graphene oxide integrated polypyrrole nano matrix as robust symmetric supercapacitor electrode material. *J Energy Storage* 59:10066
6. Wahid M, Puthusseri D, Phase D, Ogale S (2014) Enhanced capacitance retention in a supercapacitor made of carbon from sugarcane bagasse by hydrothermal pretreatment. *Energy Fuels* 28:4233–4240
7. Nayak D, Choudhary RB (2023) Tuning the optical properties of high quantum-yield g-C<sub>3</sub>N<sub>4</sub> with the inclusion of ZnS via FRET for high electron–hole recombination. *Spectrochim Acta A Mol Biomol Spectrosc* 289:122162
8. Bauri J, Choudhary RB (2023) Thermal and electronic states of exfoliated g-C<sub>3</sub>N<sub>4</sub>-based nanocomposite with ZrO<sub>2</sub> nanoparticles as a robust emissive layer. *Mater Sci Semicond Process* 154:107205

# Sustainable Water Splitting Using Nanotechnology for Hydrogen Production: A Review



Md. Merajul Islam , Neha Saxena , and Amina Nafees 

**Abstract** Hydrogen may be produced simply and cheaply by splitting water. Hydrogen generation from water and sunshine is a popular, demanding, and crucial topic. Researchers are trying to construct water-splitting devices that use sunlight's visible light. Future energy demands require large-scale hydrogen production using novel materials and technologies. Nanotechnology and nanoparticles make solar water-splitting materials. High surface-to-volume ratios enhance visible light absorption, segregate charges, and limit electron–hole recombination. In solar water-splitting systems to create hydrogen, photocatalysts with the aforementioned qualities are more efficient. Photocatalytic and photoelectrochemical approaches for creating green hydrogen are reviewed. Nanotechnology improves a photocatalyst's water-splitting efficiency. Clean and efficient hydrogen fuel's economics is also dealt.



Md. M. Islam (✉) · N. Saxena

School of Basic Sciences and Technology, IIMT University, Meerut, Uttar Pradesh 250001, India  
e-mail: [merajchem29@gmail.com](mailto:merajchem29@gmail.com)

A. Nafees

Department of Physics, IIT Delhi, New Delhi 110016, India



**Keywords** Nanotechnology · Water splitting · Photocatalysis · Renewable and sustainable energy · Hydrogen economy

## 1 Introduction

As the worldwide energy turmoil increases, hydrogen counts as one of the finest viable and wholesome energy alternatives to replace fossil fuels [1]. Hydrogen's high energy density and renewability make it a feasible energy source in minimal greenhouse gas (GHG) circumstances [2]. Hydrogen generated from water doesn't produce harmful pollutants, but it requires more energy. Hydrogen can fuel everything from laptops to submarines when manufactured using renewable energy like sunlight.

Water is often divided into oxygen (O<sub>2</sub>) and hydrogen (H<sub>2</sub>) using electric current as a supplementary power source. Through a process known as electrolysis, water is split into oxygen and hydrogen when subjected to an electric current as:



Electrolysis wastes energy since it needs an external power source to drive H<sub>2</sub>O oxidation and/or reduction processes. Alternatively, electrolysis may be performed with very little external power by receiving, storing, and transforming energy from the environment, mainly solar energy.

## 2 Role of Nanotechnology in Water Splitting

In order to efficiently create the hydrogen, nanomaterials and nanotechnology play a crucial role. As a result of their high absorption coefficients, nanomaterials significantly enhance the conversion efficacy of photocatalytic water splitting. As the diameter of a nanoparticle is almost equal to the scattering length of a carrier, the scattering rate is drastically lowered and the collecting efficiency of the carriers is substantially enhanced. Theoretically, the entire solar spectrum could be absorbed if the nanomaterials' band gap could be tuned to absorb light only at specific wavelengths by varying their size. The photocatalyst's electrical band structure can be modified further by doping. To generate an adequate overpotential for water splitting, photocatalysts must rely on an essential phenomenon known as the modification of the electrical band structure. The catalyst's overall effectiveness hinges on this bandgap engineering.

Nanomaterial photocatalysts' photocatalytic activity is very sensitive to a number of variables that can significantly alter its efficiency. Nanomaterials' crystallinity, morphology or dimensionality, and band gap significantly affect how well they work

as photocatalytic water splitters [3]. In addition to comminution, regulating the form and structure is essential for an efficient water-splitting process.

### 3 Sustainable Green Processes for Water Splitting

#### 3.1 Photocatalytic Hydrogen Generation

Solar energy is a persuasive way to reduce GHG emissions and provide a stable future energy supply. The photocatalytic hydrogen generating system is cheap, has simple infrastructure, and is scalable [4]. Equation (2) reveals photocatalytic hydrogen synthesis requires a  $\Delta G^\circ$  change of 237 kJ/mol (1.23 eV) [4]. Figure 1 shows how photocatalytic subdividing water works using photocatalysts built on semiconductors in three steps. (i) Photons having more energy than the photocatalyst's band gap make electrons move to the conduction band, creating a hole in the valence band. (ii) Electrons and holes produced by photons migrate and spread out after surpassing coulombic affinity. (iii) Electrons and holes produced by photons interact with species adsorbing to the photocatalyst's edge while reducing or oxidizing a material.

The sum of the three phases' performances indicates the effectiveness of solar energy generation.

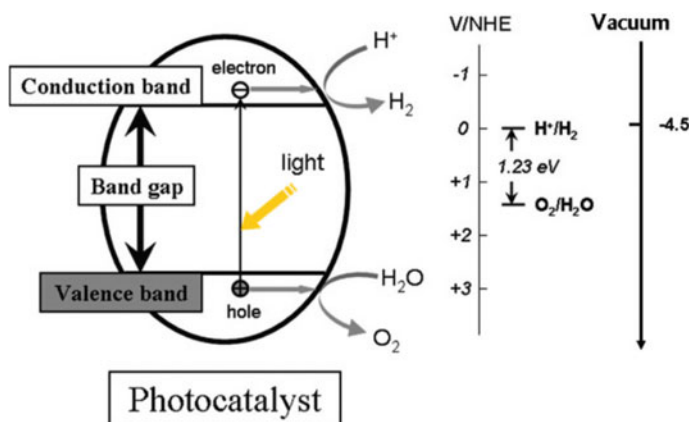
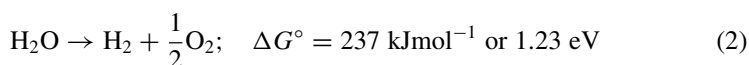
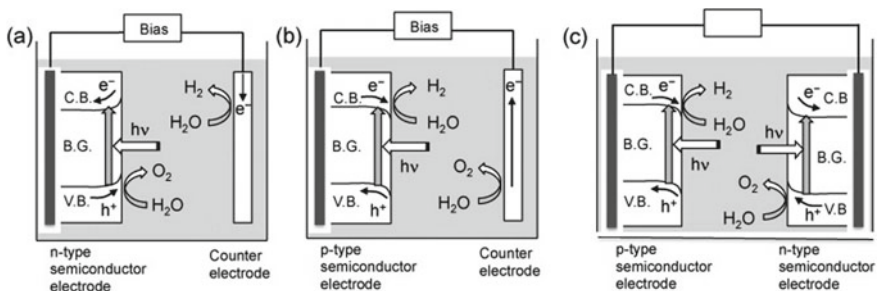
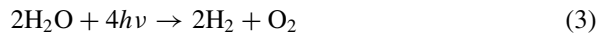


Fig. 1 Schematic of photocatalytic splitting of water [4]

### 3.2 Photoelectrochemical (PEC) Hydrogen Generation

PEC cell to split water utilizes photoelectrolysis to create hydrogen fuel. In PEC cells, photoelectrode and counter electrode are submerged in electrolyte. A photoelectrode is an electrode where sunlight can cause desired responses. Semiconductor layers on photoelectrode substrates oxidize or reduce water. Photoanode and photocathode accomplish water oxidation and reduction. PEC water splitting can be achieved with just the right amount of overpotential if the sun and an applied bias (using electrochemical methods) work in tandem. As a result, PEC is a more effective method of producing hydrogen than photocatalysis.

Figure 2 depicts three fundamental layouts of a PEC cell that may divide water photoelectrochemically [5] and illustrates PEC's functioning principles and operations. Figure 2a displays a submerged n-type semiconductor photoelectrode (TiO<sub>2</sub>) and metal electrode (Pt). Electrons and holes are created when sunlight with energy over the band gap hits a photoelectrode. The external circuit transfers energized electrons to the metal counter electrode, which converts water to H<sub>2</sub>. As holes are transmitted to the photoelectrode's exterior, water is converted to oxygen. An external bias between the electrodes allows greater charge separation and overcomes solution and electrode resistance. Figure 2b displays a p-type photoelectrode and auxiliary electrode composed of metal in electrolyte. On the photoelectrode semiconductor, water is reduced to H<sub>2</sub> while oxidized at the counter electrode. Figure 2c displays p-type and n-type photoelectrodes immersed in an electrolyte, a "tandem" system. Tandem technology captures a broad spectrum of visible light in a PEC device instead of an outer bias. In coupled framework, photoelectrodes are biased by a solar cell. The second system may be created using an n-type semiconductor electrode and a p-type semiconductor electrode. This leads to the following summary of the overall water-splitting (OWS) reaction:



**Fig. 2** Schematic of PEC cell: n-type semiconductor photoanode, p-type semiconductor photocathode, and tandem system (a–c) [5]

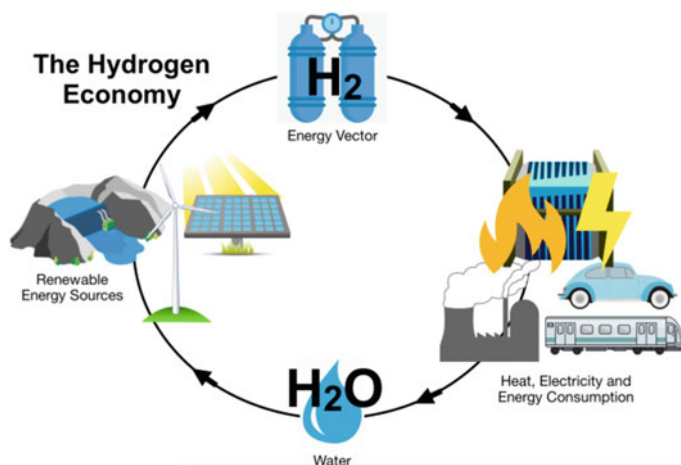


**Fig. 3** Schematic of a hydrogen-based economy [7]

To electrolyze water, a thermodynamic potential of  $\Delta E^\circ = -1.23$  V, or  $\Delta G^\circ = +237$  kJmol<sup>-1</sup>, is needed at the very least. In actuality, the separation of water needs hundreds of millivolts (mV) overpotential due to overpotentials caused by water oxidation, the auxiliary electrode overpotential, carrier mobility in the analyte and photoelectrode substrate, proximity between electrodes, and device architecture [6].

## 4 Hydrogen Economy

Hydrogen's adaptability might unleash an economic revolution. As a green power source, hydrogen reduces emissions in transportation, residential, economic, and associated industries. Hydrogen works well with low-carbon solutions and may make greener, carbon-free power sources more accessible (Fig. 3).

## 5 Conclusion

Solar hydrogen is a potential storage material for a sustainable civilization. Nanotechnology's importance in creating hydrogen with solar energy is highlighted. The utilization of electrochemical bias combined with sunlight, a PEC technique, is becoming increasingly practical. The importance of hydrogen economy in various sectors is also highlighted.

## References

1. Hu E, Feng Y, Nai J, Zhao D, Hu Y, Lou XWD (2018) Construction of hierarchical Ni–Co–P hollow nanobricks with oriented nanosheets for efficient overall water splitting. *Energy Environ Sci* 11(4):872–880
2. Muradov NZ, Veziroğlu TN (2008) “Green” path from fossil-based to hydrogen economy: an overview of carbon-neutral technologies. *Int J Hydrog Energy* 33(23):6804–6839
3. Joy J, Mathew J, George SC (2018) Nanomaterials for photoelectrochemical water splitting—review. *Int J Hydrog Energy* 43(10):4804–4817
4. Chen X, Shen S, Guo L, Mao SS (2010) Semiconductor-based photocatalytic hydrogen generation. *Chem Rev* 110(11):6503–6570
5. Abe R (2010) Recent progress on photocatalytic and photoelectrochemical water splitting under visible light irradiation. *J Photochem Photobiol C* 11(4):179–209
6. Smith WA (2016) Photoelectrochemical cell design, efficiency, definitions, standards, and protocols. In: Giménez S, Bisquet J (eds) *Photoelectrochemical solar fuel production: from basic principles to advanced devices*. Springer International Publishing, Cham, pp 163–197
7. Grahame A, Aguey-Zinsou KF (2018) Properties and applications of metal (M) dodecahydro-closo-dodecaborates ( $M_{n=1,2}B_{12}H_{12}$ ) and their implications for reversible hydrogen storage in the borohydrides. *Inorganics* 6(4):106

# Effect of Different Current Collectors on Electrochemical Performance of Activated Carbon-Based Supercapacitor



Ritu Jangra, Manoj Karakoti, Poonam Mahendia, N. G. Sahoo, O. P. Sinha, and Suman Mahendia

**Abstract** A supercapacitor is an emerging field of energy storage and each component of a supercapacitor, i.e. current collector, electrode, and electrolyte has a significant effect on its charge storage capacity. The power delivery rate, efficiency, and extraction of stored energy depend upon the interaction of the electrode material/electrolyte with current collector. Therefore, in the present work, we endeavour to study the electrochemical performance of supercapacitors of activated carbon-based electrode with three different current collectors [Aluminium (Al) sheet, Graphite sheet, and Indium Tin Oxide (ITO)]. A significant difference in the specific capacitance is observed and is found to have a maximum value of 103.42 F/g for ITO-based device, 70.81 F/g for Graphite, and 23.61 F/g for Al-based supercapacitive device.

**Keywords** Supercapacitor · Current collector · Power density

## 1 Introduction

Supercapacitors are one of the latest research hotspot and have been widely considered as a substitute for batteries and capacitors [1]. This is owing to their rapid charging rate, superior power density, outstanding cyclic performance, and high

---

R. Jangra · S. Mahendia (✉)

Department of Physics, Kurukshetra University, Kurukshetra, Haryana, India  
e-mail: [smahendia@kuk.ac.in](mailto:smahendia@kuk.ac.in)

M. Karakoti · N. G. Sahoo

Department of Chemistry, DSB Campus, Kumaun University, Nainital, India

M. Karakoti

Department of Materials Engineering and Convergence Technology and Research Institute for Green Energy Convergence Technology (RIGET), Gyongsang National University, Jinju, South Korea

P. Mahendia · O. P. Sinha

Amity Institute of Nanotechnology, Amity University UP, Noida, India

safety [2–4]. There are two classes of supercapacitors: *Electric Double Layer Capacitors* (EDLC) and *Pseudo capacitors*. EDLC have been used on a commercial scale due to their very long cycle life, very high power density, environment friendliness, and low cost [5, 6]. An EDLC is composed of current collector, porous carbon materials, an insulated ion-permeable separator, and an electrolyte [3]. The most commonly used electrode material is activated form of carbon attributed to its very high specific surface area and good porosity [7, 8]. Another important part of the EDLC supercapacitor is the current collector. It collects and conducts current from these carbon materials to external electrical loads [3]. The interaction of the current collector with carbon materials and electrolyte decides the power delivery rate of the supercapacitor. Therefore, it is necessary to study the interaction between current collectors with electrode material and electrolyte. For this purpose, different type of current collectors such as Indium Tin Oxide (ITO), Graphite sheet, and Aluminium (Al) are used with activated carbon as active electrode material for EDLC application.

## 2 Experimental Section

In the present work, Activated carbon (AC) and Phosphoric acid ( $\text{H}_3\text{PO}_4$ ) were procured from SD Fine-chem. Ltd. Polyvinylidene fluoride (PVDF) binder and ITO sheets were purchased from Sigma Aldrich. Aluminium (Al) sheets were purchased from Nice chemicals ltd. and Graphite (Gr) sheets from Nickunj Eximp Entp. For device fabrication, first two cleaned  $1 \times 1 \text{ cm}^2$  area electrodes were cut down from ITO, Al, and Gr sheets. Thereafter, to make slurry of AC, 10 wt% of PVDF binder was mixed with the help of acetone in a pistol mortar. The prepared slurry was brush-coated over each of two electrodes of different types. The prepared electrodes were then allowed to dry overnight at 60–70 °C. Afterward, a filter paper dipped in 1 M  $\text{H}_3\text{PO}_4$  electrolyte was used as separator. Figure 1a represents the schematic representation of steps used for device fabrication. The electrochemical performance of as-fabricated devices was tested using Cyclic Voltammetry (CV), Galvanostatic charge–discharge (GCD), and Electrochemical Impedance Spectroscopy (EIS) using CHI660E Instruments, Inc.

## 3 Results and Discussion

### 3.1 Cyclic Voltammeter (CV)

Figure 1b represents the CV curves for all three fabricated devices at a scan rate of 10 mV/sec. For ITO (curve ‘a’) and Graphite paper (curve ‘b’)-based devices, quasi-rectangular shaped CV curves without any specific oxidation/reduction peak can be clearly seen depicting EDLC type behaviour. Whereas for Al-based device

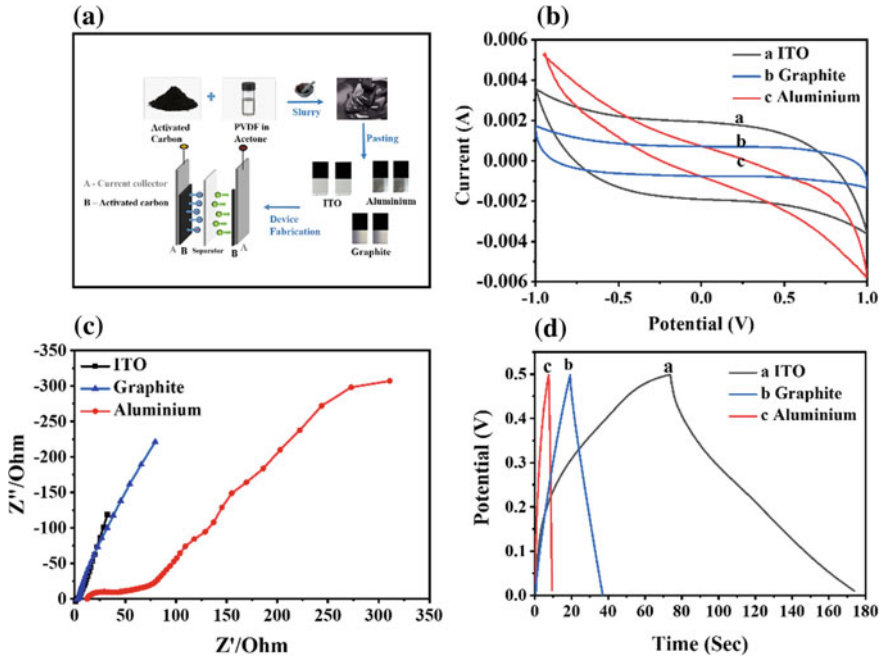


**Fig. 1** a Schematic for the device fabrication, b Cyclic voltammery curves, c Nyquist plots, and d Charge–discharge curves for ITO, Aluminium, and Graphite-based supercapacitive devices at 1 A/g

(curve ‘c’) spike end distorted shaped curve is observed with relatively small area this may be because of poor interaction of Al-based current collector with AC and acidic electrolyte. Further, the specific capacitance is examined using the area under the CV curve using the formula  $C_s = \frac{\int IdV}{2 \times s \times m \times \Delta V}$  here,  $\int IdV$  is the area under CV curve,  $s$  is scan rate,  $m$  is mass of activated carbon on single electrode, and  $\Delta V$  is potential window [8]. It is observed that the area under the CV curve is found to be highest for ITO-based device and minimum for Al-based device. This means that specific capacitance ( $C_s$ ) is highest for ITO (103.42 F/g) current collector compared to Gr (70.81 F/g) and Al (23.61 F/g) current collector-based supercapacitive devices.

### 3.2 Electrochemical Impedance Spectroscopy (EIS)

The electrochemical performance for different types of current collector-based EDLC devices was also studied in a frequency range of 0.01–10<sup>5</sup> Hz and recorded Nyquist plots are shown in Fig. 1c. The intercept at the X-axis in the high-frequency region gives an idea about the equivalent series resistance (ESR) of the device. While the semicircle in lower frequency region is linked to the charge transfer resistance ( $R_{ct}$ )



and capacitance. ESR of the device is a sum of resistances of electrode material, electrolyte, current collector, and interface resistance of current collector and electrode material [7]. The lower value of ESR is suggested for better device performance and is found to be small for ITO (1.89  $\Omega$ ) and Gr (2.60  $\Omega$ )-based device as compared to Al-based device. This clearly suggests the good transportation of electrolyte ions from active electrode material to current collectors, i.e. ITO and Gr type. However, for Al-based device, the value of ESR is found to be very high (12.39  $\Omega$ ). This may be due to poor interaction of Al with acidic electrolyte and AC. The middle-frequency region of these plots gives identification about the Warburg resistance which is due to the electrolyte ions diffusion to current collector from active electrode materials. For ITO (curve 'a') and Gr (curve 'b')-based device more inclined line towards the  $Y$ -axis is observed depicting excellent electrochemical performance in these supercapacitive devices. However, this inclined line is quite away from the vertical axis in the case of an Al (curve 'c')-based device, representing poor diffusion of electrolyte ions. This is because of corrosive redox reactions which occur during the interaction between aluminium and acidic electrolyte. Further, the value of specific capacitance can also be estimated from imaginary part ( $|Z''|$ ) of impedance in low-frequency region of such plots, i.e. ( $C_s = 2/2 \times \Pi \times m \times f \times |Z''|$  here  $f$  is the lowest given frequency (0.01 Hz),  $m$  is mass of activated carbon on single electrode) [8]. The highest specific capacitance of 89.50 F/g is observed for ITO-based device; for Gr (72.08F/g)-based device it lies in between and is lowest for Al (34.57F/g)-based device. These observations are in accordance with that of CV measurements.

### 3.3 Galvanostatic Charge–Discharge (GCD)

The GCD curves for different types of current collector (ITO, Al, and Gr)-based supercapacitive devices are shown in Fig. 1d. Nearly triangular-shaped curves are observed for all type of devices depicting EDLC behaviour [8]. For ITO-based device, area under the GCD curve is much higher than that of other devices depicting the longer charging/discharging. This show high charge adsorption/desorption from electrolyte to current collector through active electrode material for ITO-based device whereas Gr and Al-based devices showed a smaller charge/discharge time. From the charging/discharging time we can also estimate the charge storage capability of these devices. The value of specific capacitance can be calculated using  $C_s = (4 \times I \times \int V dt)/(m \times V^2)$  here,  $I$  is current,  $\int V dt$  is area under discharge curve,  $m$  is mass of activated carbon, and  $V$  is charging/discharging potential. It is found to be highest for ITO-based device (105.97 F/g) and minimum for Al-based device (21.06 F/g). Using these GCD curves, the energy density,  $E_D = I \times \int V dt/2 \times m$ ; here  $R = dV/2I$ ,  $dV$  is voltage drop when device switches charging to discharging and  $I$  is current), and power density ( $P_D = V^2/8 \times m \times R$ ) of fabricated devices are also calculated. A maximum  $E_D$  of 6.62 Wh/Kg is observed at a  $P_D$  of 12.62 kW/Kg for ITO-based device whereas a minimum  $E_D$  of 0.65 Wh/Kg at a  $P_D$  of 1.28 kW/Kg is obtained

for Al-based device. This low value of power density is due to the poor adhesion of AC with Al which increased the resistance of the device.

## 4 Conclusion

Three different materials (ITO, Al, and Gr) were used as current collectors for the fabrication of AC-based supercapacitive devices. The interaction between ITO with electrolyte and AC was found to be superior which was reflected in small ESR value (1.89  $\Omega$ ), leading to highest  $C_s$  of 103.42 F/g with  $E_D$  of 6.62 Wh/Kg at a  $P_D$  of 12.62 kW/Kg.





**Acknowledgements** Authors from KUK are highly thankful for the Seed Money Grant, under RUSA 2.0, KUK. One of the authors, Ritu Jangra, SRF is thankful to CSIR, New Delhi.

## References

1. Yadlapalli RT (2022) Super capacitors for energy storage: progress, applications and challenges. *J Energy Storage* 49:104194
2. Saikia BK (2020) A brief review on supercapacitor energy storage devices and utilization of natural carbon resources as their electrode materials. *Fuel* 282:118796
3. Liu J (2021) Flexible antifreeze zn-ion hybrid supercapacitor based on gel electrolyte with graphene electrodes. *ACS Appl Mater Interf* 13(14):16454–16468
4. Olabi AG (2022) Supercapacitors as next generation energy storage devices: properties and applications. *Energy* 248:123617
5. Jiang Y (2019) Definitions of pseudocapacitive materials: a brief review. *Energy Environ Mater* 2(1):30–37
6. Samantara AK, Ratha S (2018) Materials development for active/passive components of a supercapacitor. Springer, Singapore
7. Taberna PL (2003) Electrochemical characteristics and impedance spectroscopy studies of carbon-carbon supercapacitors. *J Electrochem Soc* 150(3):A292
8. Yadav N (2020) Ionic liquid incorporated redox-active blend polymer electrolyte for high energy density quasi-solid-state carbon supercapacitor. *J Power Sourc* 451:227771

# Polymer-Based Nanomaterial as a Bacteriostatic Agent on Gram-Positive Bacteria



Sooraj Anto Dennis, A. V. Sudhamshu, Aleena Ann Mathew ,  
Joselyn Elizabeth Abraham , Elcey C. Daniel ,  
and Balachandran Manoj 

**Abstract** The colonization of surfaces by bacteria is a widespread phenomenon that affects environmental processes and human health. Bacterial growth can also be found in materials used in the textile industries, food packaging, and wearable electronics. Moreover, the necessity for replacing traditional antibiotics is relevant due to the increased health risks of antimicrobial resistance from the excessive use of antibiotics. Recently, research is focused more on developing polymer-based antibacterial materials critical to preventing bacterial proliferation. The use of some nanomaterials appears to be very promising in this regard. This work reports the synthesis of a polymer-based nanomaterial derived from polyvinyl alcohol (PVA) via the hydrothermal method and studies its structural and optical properties. It is also observed that these nanoparticles (NPs) display the highest antibacterial potency against gram-positive (*Bacillus subtilis*) bacteria than their bulk counterpart.

**Keywords** Nanomaterial · Fluorescence · Antibacterial

## 1 Introduction

Infectious diseases continue to be a major global health threat and have become a health concern. Antibiotics are used to treat bacterial infections, but when they are overused, bacteria can become resistant. This resistance can spread, leading to the development of multidrug-resistant bacteria, which can cause infections that are difficult to treat. Materials scientists must explore the development of new materials that can help reduce and combat the spread of antimicrobial resistance (AMR). Nanotechnology has the potential to revolutionize the treatment of AMR. These

---

S. A. Dennis · A. V. Sudhamshu · A. A. Mathew · J. E. Abraham · B. Manoj (✉)  
CHRIST (Deemed to Be University), Bengaluru 560029, India  
e-mail: [manoj.b@christuniversity.in](mailto:manoj.b@christuniversity.in)

E. C. Daniel  
Kristu Jayanti College (Autonomous), Bengaluru 560077, India

materials have the potential to penetrate bacterial cell walls, inhibit the growth of resistant strains, and even enhance the effectiveness of antibiotics [1].

Zero-dimensional (0-D) nanomaterials have recently gained much attention among the different dimensional materials. They are spherical-like materials with good dispersibility and stability. A major topic of interest in the 0-D world is polymer NPs. Polymer nanoparticles have emerged as a potential substitute to antibiotics. They have been studied as a potential means of combating AMR. Research has been conducted to understand how nanoparticles interact with bacteria, and how they can be used to reduce the activity and spread of antibiotic-resistant bacteria. Polymer nanoparticles can accumulate onto the cell membranes of bacteria and interact with them in such a way that it can cause disruption of the membrane integrity, leading to the destruction of the entire bacteria cell. This can be achieved through the formation of reactive oxygen species (ROS) on the surface of the nanoparticles, which can then be transferred to the bacterial cell membrane and induce oxidative damage. Additionally, the increased surface area of the nanoparticles can also lead to increased adsorption of the cell membrane components, thus resulting in the breakdown of the membrane structure [2, 3]. Polymer architecture also influences bactericidal activity. Hyperbranched polymers show no hemagglutination activity, which makes them suitable for use in medical applications [4].

This paper discusses the preparation of PVA NPs as well as the optical and antibacterial properties of the NPs formed. Polyvinyl alcohol (PVA) is a non-toxic, water-soluble polymer with high chemical and mechanical resistance and good hydrophilicity. PVA is used in synthetic organs, implants, pharmaceuticals, contact lenses, cosmetics, fibers, films, and other applications [5]. Herein, pure PVA was hydrothermally treated at different timings keeping the temperature constant. The as-synthesized NPs displayed more antibacterial potency against gram-positive (*Bacillus subtilis*) bacteria than their bulk counterpart.

## 2 Materials and Methods

PVA was purchased from Sigma Aldrich. 0.2 g of PVA was dissolved in 40 mL of deionized water and stirred until completely dissolved. The PVA solution was poured into a 50 mL Teflon-lined autoclave and kept for hydrothermal synthesis at a temperature of 220 °C at three different timings (6, 9, and 12 h). The resultant solution after the reaction was dried at 80 °C to obtain in powdered form. The polymer NPs thus obtained were characterized further to study their properties.

### 3 Results and Discussion

#### 3.1 UV Analysis

UV–Visible spectroscopy technique measures the extinction of light passing through a material. Due to the distinctive optical characteristics of NPs, which depend on their size, shape, concentration, and aggregation state close to the surface, UV–Visible spectroscopy is a beneficial tool for recognizing, describing, and investigating nanomaterials. The UV–Visible spectra of PVA and its nanomaterials are plotted from 200 to 600 nm shown in Fig. 1a. The maximum absorption wavelengths of PVA, PVA-6, PVA-9, and PVA-12 are at 239, 254, 283, and 290 nm, respectively. The PVA nanomaterials have a sharp UV absorption peak compared to pure PVA. These peaks correspond to the aromatic carbon's  $\pi - \pi^*$  transition and is speculated to be the formation of graphite structure [6]. The absorption intensity peaks of PVA and their nanomaterials have increased with increasing reaction time. The improved carbonization in the nanomaterials with reaction time may be the reason for the absorption intensity enhancement. A significant red shift is observed in the absorbance peaks from a PVA to its nanomaterials. This can be ascribed to the reduction in the size of nanomaterials with the growth time. The samples were transparent under visible light and UV light. It indicates that the bulk system holds its transparent optical property at its nanomaterial state.

The extrapolation of fit in the photon energy axis can theoretically calculate the optical bandgap energy of synthesized particles. The bandgap energy of PVA and its nanomaterials are plotted in Fig. 1b. The optical energy bandgap of PVA, PVA-6, PVA-9, and PVA-12 are calculated by Tauc plots are 3.21, 3.17, 3.13, and 2.95 eV, respectively. The bulk PVA shows higher band gap energy than its nanomaterials and the band gap energies of nanomaterials decrease with increasing reaction time. The decrease in the band gap with increasing reaction time can be attributed to the nanomaterial's particle size reduction.

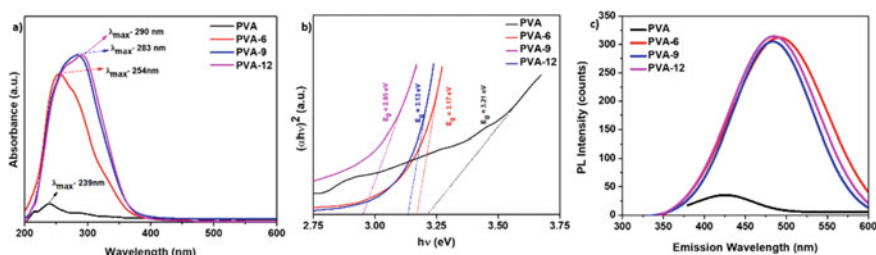


**Fig. 1** a UV–visible spectrum, b Optical bandgap, and c Maximum excitation spectra of polymer and polymer NPs at different reaction times

### 3.2 Luminescence Analysis

The luminescence emission spectrum provides an idea of excited states and emission intensity of corresponding exciting photons. Non-conjugated PVA is non-fluorescent due to the lack of an emission center in its structure. The PL emission spectra of PVA and its nanomaterials corresponding to their excitation wavelengths were plotted in the 300–700 nm range. The maximum excitation wavelengths of synthesized samples are plotted together for a comparative study plotted in Fig. 1c. The PL spectra display an excitation-dependent behavior, indicating the presence of NPs with different sizes. A prominent bathochromic shift is observed between bulk and its nanomaterials, and a slight hyperchromic shift is observed in the luminescence spectra of nanomaterials [7].

### 3.3 Antibacterial Analysis

The antibacterial activity of the synthesized samples was tested against four organisms from two groups with distinct cell wall character traits. *S. aureus* and *B. subtilis* were chosen as gram-positive organisms. Gram-negative bacteria *E. coli* and *P. fluorescens* were chosen. To test the antibacterial activity, cultures were spread out on sterile Mueller Hinton agar medium in sterile Petri plates. On the plates, there were evenly distributed liquid cultures that had grown overnight in a nutrient broth medium, and 3 mm diameter wells were punched on it, and 30  $\mu$ l of the appropriate test samples were added. Depending on the growth characteristics of each organism, *B. subtilis*, *S. aureus*, and *E. coli* were incubated at 37 °C, whereas *P. fluorescens* was incubated at 28 °C [8].

The compounds PVA-6 and PVA-9 inhibited the tested organisms and showed an evident zone of inhibition against *B. subtilis* (Fig. 2). PVA-6 and PVA-9 had the most impact on *B. subtilis*, however (i.e., 8 mm) indicating the selectivity of the antibacterial action. The other set of samples lacked antibacterial activity against gram-positive and gram-negative bacteria (Table 1). To compare the efficacy of synthesized samples, the microbial activity against gram-negative and gram-positive bacteria were tested using Ampicillin as a positive control. But the positive control showed more effective antibacterial activity against the bacteria. This initial study requires further antibacterial investigations for more clarification.

## 4 Conclusion

Bacterial infections result in significant sickness, and antibiotics are used as a general strategy to treat bacterial infections. Antibiotic misuse, however, causes the development of microbes that are resistant to a broad range of drugs and poses a major threat

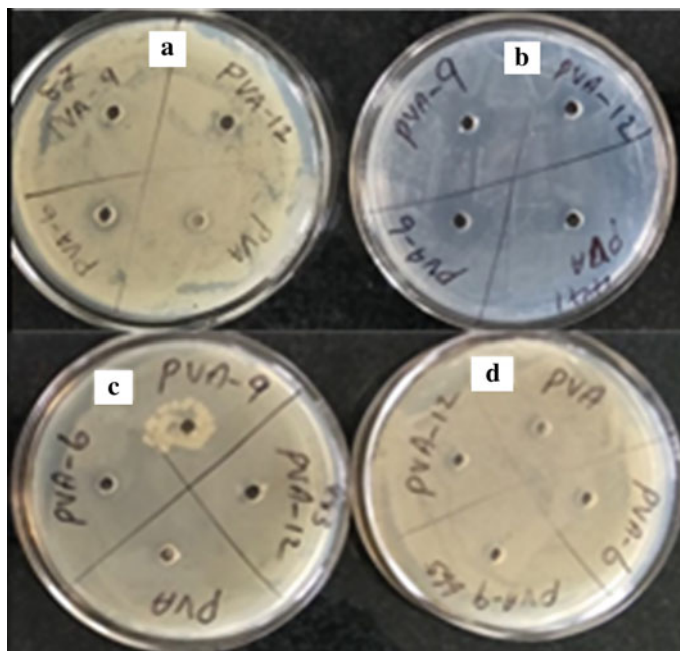


**Fig. 2** Antibacterial activity of polymer NPs

**Table 1** Zone of inhibition of samples against bacteria

Sample	<i>Staphylococcus aureus</i> A	<i>Bacillus subtilis</i> B	<i>Escherichia coli</i> C	<i>Pseudomonas fluorescens</i> D
PVA	0	0	0	0
PVA6	0	8	0	0
PVA-9	0	8	0	0
PVA-12	0	1	0	0

to human life. Therefore, the development of new antibacterial materials is a critical need in the modern world. Herein we synthesized polymer NPs from PVA via the hydrothermal method and investigated their optical and antibacterial analyses. Reaction time-dependent antibacterial properties were observed and the polymer NPs can be developed for more biological applications.

## References

1. Gao W, Chen Y, Zhang Y, Zhang Q, Zhang L (2018) Nanoparticle-based local antimicrobial drug delivery. *Adv Drug Deliv Rev* 127:46–57
2. Judzewitsch PR, Nguyen T, Shanmugam S, Wong EHH, Boyer C (2018) Towards sequence-controlled antimicrobial polymers: effect of polymer block order on antimicrobial activity. *Angew Chem* 130(17):4649–4654
3. Mathew AA, Antony M, Thomas R, Sarojini S, Balachandran M (2022) Fluorescent PVDF dots: from synthesis to biocidal activity. *Polym Bull* 167:1–18
4. Namivandi-Zangeneh R et al (2018) The effects of polymer topology and chain length on the antimicrobial activity and hemocompatibility of amphiphilic ternary copolymers. *Polym Chem* 9(13):1735–1744
5. Mostafa AM, Menazea AA (2020) Polyvinyl alcohol/silver nanoparticles film prepared via pulsed laser ablation: an eco-friendly nano-catalyst for 4-nitrophenol degradation. *J Mol Struct* 1212:128125
6. Saji M, Elsa Saji B, Joseph N, Mathew AA, Daniel EC, Balachandran M (2022) Investigation of fluorescence enhancement and antibacterial properties of nitrogen-doped carbonized polymer nanomaterials (N-CPNs). *Int J Polym Anal Charact* 1587:1–13
7. Abraham JE, Balachandran M (2022) Fluorescent mechanism in zero-dimensional carbon nanomaterials: a review. *J Fluoresc* 56:1–20
8. Joseph N, Mathew AA, Daniel EC, Balachandran M (2023) Polymer-carbon nanocomposite: synthesis, optical and biocidal properties. *Results Chem* 897:100826



# Nanotechnology for Water Treatment and Filtration



Mehreen Shah

**Abstract** Nanotechnology is fast gaining popularity and attention of scientists and research groups worldwide as a promising tool for remediation of polluted and contaminated wastewater. Economically, nanoparticles can be made from carbon-based or carbon-based materials such as graphene. It can also be made from metals. They have highly effective adsorbent/absorbate mechanisms that help in uptake of contaminants from the wastewater such as synthetic dyes or heavy metals which cause damage to human health if found present in water.

**Keywords** Nanoparticles · Graphene nanotubes · Carbon nanotubes

## 1 Nanoparticles for Water Decontamination

### 1.1 Carbon Nanoparticles

Activated carbon had been used for decades for water purification technologies even at municipal level. Treatment with carbon helps in removal of odor and gives clarity to water by removal of suspended soils in it by adsorption. Carbon is highly cost-effective too and offers promising results for water purification goals. Fard et al. [1] used carbon nanotubes (CNTs) for adsorption of heavy metal, cadmium(II). Fard et al. [1] were able to achieve simultaneous removal of  $Pb^{2+}$  and  $Cd^{2+}$  ion from water using carbon walled nanotubes.

---

M. Shah (✉)

Department of Environment Science and Engineering, Jamia Millia Islamia, New Delhi, India  
e-mail: [Meishah666@gmail.com](mailto:Meishah666@gmail.com)

**Table 1** Graphene nanoparticles for water decontamination

Adsorbent used	Adsorbance (mg/L)	Adsorbance %	Reference
Graphene nanosheets with zero valent Fe	15–35	70	Li et al. [3]
Spinel Ni–Fe based on graphene oxide	45	80	Lingamdinne et al. [4]
Modified graphene (GN) with CTAB	21.57	98	Wu et al. [5]
Graphene sand composite	43	93	Dubey et al. [6]

## 1.2 Graphene Nanoparticles

Graphene and graphene-based nanoparticles are common nanomaterial choices for water pollution and metal removal. Graphene is a 2D structure of carbon. It has high efficiency rates. It helps to absorb heavy metals on its surface. The adsorption process is highly rapid and spontaneous. Gopalakrishna et al. [2] achieved a 100% removal of chromium using only 70 mg of graphene oxide at an optimum pH of 8. This method involved addition of functional groups on the surface such as  $-\text{COOH}$ ,  $-\text{OH}$ , and  $-\text{C}=\text{O}$ . This is a breakthrough advancement in the field of nanotechnology for wastewater decontamination of heavy metals such as chromium. Graphene oxide-based nanofilters are now being increasingly used by scientists for water purification purposes. They have high hydrophilicity and an anti-microbial nature that prevents biofouling which is frequently seen in biomembrane filtration (Table 1).

## 2 Metallic Nanoparticles

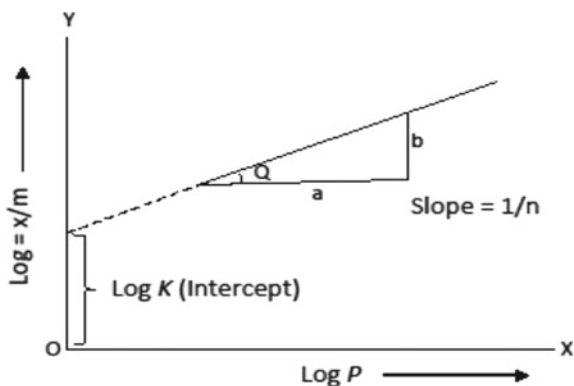
### 2.1 Nickel Oxide Nanoparticles

Song et al. [7] could remove 100 mg/L reactive dye completely after a contact period of 6 h using nickel oxide nanosheets. Nickel oxide and nanoparticles derived from it are essential to nanotechnology owing to their high surface to volume ratio hence having numerous sites that are available for bulk adsorption of the contaminants and effect rapid degradation of the synthetic colorant in the wastewater.

### 2.2 Ferrous Nanoparticles

Vasiljevic et al. [8] used iron titanate ( $\text{Fe}_2\text{TiO}_5$ ) nanoparticles for photodegradation of Methylene Blue (MB) dye in water where both photodegradation of the dye occurred after a 4 H exposure with mineralization into end products  $\text{H}_2\text{O}$  and  $\text{CO}_2$ . Iram et al.

**Fig. 1** Representation of the slope of a typical Freundlich isotherm



[9] used  $\text{Fe}_3\text{O}_4$  hollow nanospheres for removal of Neutral Red dye from water via adsorption on the nanosphere and magnetism for a 90% dye removal. Carbon nanotubes containing  $\text{Fe}_2\text{O}_3$  particles are effective for adsorption of Methylene Blue and Neutral Red that were adsorbed in quantities as 42.3 and 77.5 mg/g, respectively, by Song et al. [7].

#### *Adsorbance Mechanism for Nanoparticles*

##### *Adsorption*

Majority of nanoparticles are able to effect water remediation by their ability to adsorb the contaminants onto their surface. The high surface/volume ratio of nanoparticles due their extremely small size aids them in this process. An adsorption isotherm is a graphical representation of the relationship between the adsorbate that is remaining in liquid phase and the amount absorbed by the adsorbent in equilibrium. Freundlich and Langmuir isotherm are the most studied models to explain the mechanism of metal ion uptake by the adsorbent system. Langmuir isotherm is based on assumptions such as there is a monolayer at surface; each site only holds one single molecule, and there are no intermolecular interactions [10]. Freundlich isotherm involves multilayer adsorption for heterogeneous molecular systems and as cations and anions both are adsorbed simultaneously (Fig. 1).

## References

1. Fard EM, Parvareh A, Moravaji MK (2022) Optimization of removal of lead and cadmium from industrial wastewater by ethylenediamine-modified single-walled carbon nanotubes. *Int J Environ Sci Technol* 19(4):2747–2760
2. Gopalakrishnan AT, Venugopal G (2016) Kim S-J (2015) Removal of heavy metal ions from pharma-effluents using graphene-oxide nanosorbents and study of their adsorption kinetics. *J Ind Eng Chem J* 2(5):99–110

3. Li X, Ai L, Jiang J (2016) Nanoscale zerovalent iron decorated on graphene nanosheets for Cr (VI) removal from aqueous solution: surface corrosion retard induced the enhanced performance. *Chem Eng J* 288:789–797
4. Lingamdinne LP, Koduru JR, Choi YL, Chang YY, Yang JK (2015) Studies on removal of Pb(II) and Cr(III) using graphene oxide based inverse spinel nickel ferrite nano-composite as sorbent. *Hydrometallurgy* 165:64–72
5. Wu Y, Luo H, Wang H, Wang C, Zhang J, Zhang Z (2013) Adsorption of hexavalent chromium from aqueous solutions by graphene modified with cetyltrimethylammonium bromide. *J Colloid Interface Sci* 394:183–191
6. Dubey R, Bajpai J, Bajpai AK (2015) Green synthesis of graphene sand composite (GSC) as novel adsorbent for efficient removal of Cr (VI) ions from aqueous solution. *J Water Process Eng* 5:83–94
7. Song Q, Fei H, Shaoning Y, Gang C, Jilie K (2008) Magnetic removal of dyes from aqueous solution using multi-walled carbon nanotubes filled with Fe<sub>2</sub>O<sub>3</sub> particles. *J Hazard Mater* 160(2–3):643–647
8. Vasiljevic ZZ, Dojcinovic MP, Vujancevic JD, Jankovic-Castvan I, Ognjanovic M, Tadic NB, Stojadinovic S, Brankovic GO, Nikolic MV (2020) Photocatalytic degradation of methylene blue under natural sunlight using iron titanate nanoparticles prepared by a modified sol–gel method. *R Soc Open Sci* 157:7200708200708
9. Iram M, Chen G, Yueping G, Ahmad I, Huizhou L (2008) Adsorption and magnetic removal of neutral red dye from aqueous solution using Fe<sub>3</sub>O<sub>4</sub> hollow nanospheres. *J Hazard Mater* 160(2–3):643–647. <https://doi.org/10.1016/j.jhazmat.2008.03.037>
10. Yadav KK, Singh JK, Gupta N, Kumar V (2017) A review of nanobioremediation and its technologies for environmental cleanup: a novel biological approach. *J Mater Environ Sci* 8:740–757

# Evaluation of Treatment Performance and Development of Aerobic Granular Sludge in A/O/A Mode Sequencing Batch Reactor Fed with Sewage



Mohd Rayaz, Mohammad Waqqas Mirza, Fehmeeda Khatoon,  
and Abid Ali Khan

**Abstract** This study was designed to explore the rapid aerobic granular sludge (AGS) formation and treatment performance of sequencing batch reactor (SBR). The SBR was operated in anaerobic, oxic (aerobic), and anoxic (A/O/A) cycle—i.e., anoxic phase—5% of the total cycle duration for complete nutrients removal. After 20 days of operation, growth in biomass was observed. Complete granulation was achieved within 35 days of operational studies. Visible outlines and clear boundaries, regular-shaped, and compact granules become dominant inside the system, with an average particle size of 220  $\mu\text{m}$ . The A/O/A system achieved averages  $70.02 \pm 5.98\%$ ,  $78.21 \pm 18.66\%$ ,  $60.62 \pm 9.69\%$ , and  $53.49 \pm 8.14\%$  COD,  $\text{NH}_4^+\text{-N}$ , TN, and  $\text{PO}_4^{3-}\text{-P}$  removal efficiency, respectively. Poor COD and  $\text{PO}_4^{3-}\text{-P}$  removal performance was caused by a short anaerobic phase (25% of the total cycle duration of 6 h) and higher biomass concentration, whereas a long aerobic phase (60% of the total cycle duration of 6 h) with an anoxic phase led to outstanding (100%) ammonium removal efficiency after the system reached steady state. Moreover, results indicate that partial denitrification and higher nitrate concentrations in sewage were responsible for the low TN removal efficiency. Results further demonstrated that AGS formation and development within an A/O/A cycle SBR reactor is accelerated by sewage with a high COD loading rate. The rapid granulation and simultaneous removal of organics and nutrients by the A/O/A mode SBR without any support materials provide a viable option for medium-strength wastewater treatment.

**Keywords** Sequencing batch reactor · Anaerobic · Oxic · Anoxic · Sewage

---

M. Rayaz (✉) · F. Khatoon  
Department of Applied Sciences and Humanities (Environmental Science Lab), Jamia Millia  
Islamia (A Central University), New Delhi 110025, India  
e-mail: [mohdrayazpaswal@gmail.com](mailto:mohdrayazpaswal@gmail.com)

M. W. Mirza · A. A. Khan  
Department of Civil Engineering, Jamia Millia Islamia (A Central University), New  
Delhi 110025, India

## 1 Introduction

Aerobic granular sludge (AGS) is one of the best alternative technology for the treatment of low-strength as well as high-strength wastewater. Several biological wastewater treatment technologies have already been used at full scale in the field and in the laboratory to treat industrial and municipal wastewater [1, 2]. Long start-up periods and instability during long-term operation are some of the major factors that bring barrier in the wide application of AGS-based wastewater treatment plants (WWTPs). High operation and maintenance costs hindered the growth of AGS technology [3]. It is important to search how to accelerate the granulation system, which is mostly concerned with cost savings and resource consumption [1]. Cycle type and distribution of cycle time duration play a critical role in treatment performance, sludge growth rate, and system stability [4]. Therefore, in this experimental work, we investigate granules start-up time, overall system stability, and treatment performance in an A/O/A cycle SBR reactor without sludge discharge over the study period. We propose a novel A/O/A mode SBR reactor strategy in which the aeration period is fixed at 60% of the total cycle duration of 6 h for complete nitrification and phosphorous sequestration. The remaining times were adjusted in the anaerobic and anoxic phases.

## 2 Materials and Methods

A rectangular reactor was set up for the cultivation of AGS, with a total volume of 20 L and a working volume of 14 L. Figure 1 shows the reactor setup. The current study lasted 60 days, whereby an alternating A/O/A mode SBR reactor was fed with sewage collected from the partition chamber of STP Bahadurgarh, Haryana, India. Cycle time was adjusted to 6 h, including a filling phase of 20 min (5% of the total cycle duration of 6 h), anaerobic phase of 90 min (25% of the total cycle duration of 6 h), oxic phase (aerobic phase) of 216 min (60% of the total cycle duration of 6 h), and anoxic phase of 18 min (5% of the total cycle duration), followed by settling and decanting (10 and 6 min, respectively). The influent (sewage) was pumped into the A/O/A SBR reactor by a peristaltic pump. An aquarium air pump was used to deliver aeration into the SBR reactor, which was dispersed by the four diffusers located at the base of the reactor. The whole automatic cyclic operation was controlled by the laptron timers (Fig. 1).

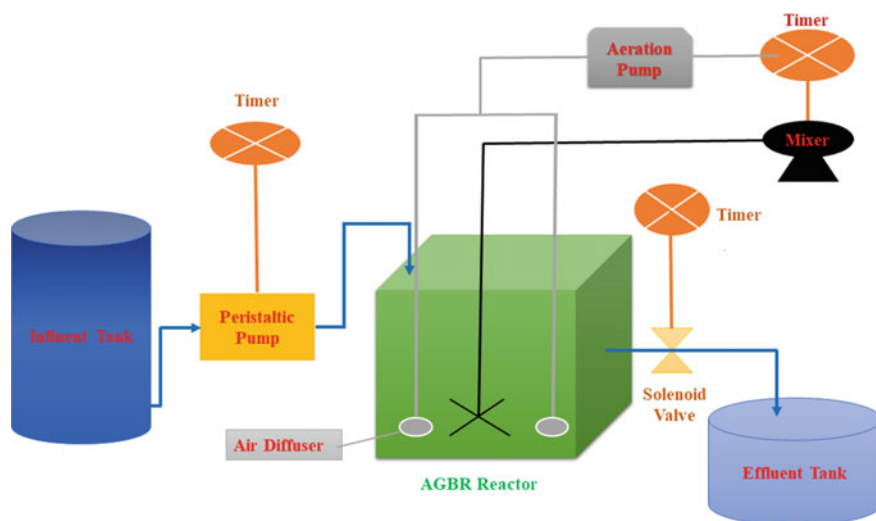
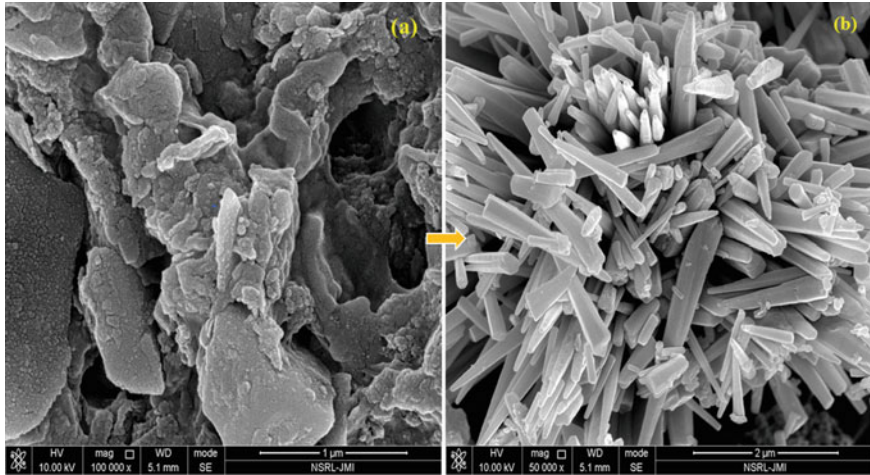


Fig. 1 Schematic flow diagram of A/O/A SBR

### 3 Results and Discussion

Granules start growing after the 20 day of the study, which points out that medium-strength wastewater reduced the long start-up time of AGS. On day 0, the average size of the AGS was determined to be  $150.10 \mu\text{m}$  on day (0). At the end of the study, regular round-shaped granules with good settling ability were observed in A/O/A SBR containing an average particle size of  $220 \mu\text{m}$ . Average COD removal was  $70.02 \pm 5.98\%$ . The results obtained from this study differ from those presented by de Sousa Rollemberg et al. [4], in which COD removal efficiency was achieved at 90% in A/O/A cycle SBR reactor. However, in this study the reactor was fed with medium-strength sewage containing COD  $818.01 \pm 121.98 \text{ mg/L}$ , including filling + anaerobic phase (30%) and aerobic phase (60%) over a 6 h cycle. On the other hand, De Sousa Rollemberg et al. [4] used low-strength synthetic wastewater (COD-550 mg/L) as a substrate, along with filling + anaerobic phase (35%) and aerobic phase (55%), from a 6-h cycle. Short anaerobic phase was the reason of poor COD removal performance. At the stabilization period (after 35 days of experimental studies), the system achieved 100% ammonium removal efficiency. The findings of this study differed from those of Alattabi et al. [5], who observed that increasing the MLSS concentration from 4000 to 6000 mg/L reduced the (11%) ammonium removal percentage. However, in this study, the results reveal that ammonium removal efficiency increased (20%) with the accumulation of biomass (3000–7000 mg/L) inside the reactor. These findings showed that increasing the biomass concentration had no effect on  $\text{NH}_4^+\text{-N}$  removal performance. The average nitrite concentration was also very low (1.42 mg/L) in



**Fig. 2** SEM images of (a) seed sludge on day 0 and (b) mature aerobic granules on day 60

the treated effluent, which indicates that complete nitrification had been done. The present results are in agreement with the results reported by de Sousa Rollemberg et al. [4], who observed that a minimum 50% aerobic phase is required for complete nitrification during the treatment of medium-strength wastewater. On the other hand, denitrification did not occur completely, as a high amount of nitrate was detected in the treated effluent. This accumulation of nitrate concentrations in the treated effluent could be due to a higher nitrate concentration in the sewage. The average removal of total nitrogen over the experimental studies was measured  $60.62 \pm 9.69\%$ . Results reveal that complete nitrification and partial denitrification occurred after the stabilization period in the A/O/A cycle SBR reactor. SEM results show that the seed sludge (Fig. 2a) used to start the study on day 0 had an irregular, fluffy structure, and *Cocci*, *Coccolbacillus*, and *Bacillus rod-like* bacteria were dominant. At the end of the study, mature AGS was found, which indicates the compact and regular structure of the granules; a group of *rod-shaped* bacteria compacted with each other were clearly visible in the single granules (Fig. 2b).

## 4 Conclusions

- A long aerobic phase (60%) with a short anoxic phase (5%) improved the nitrification process but was insufficient for denitrification.
- When the nitrate concentration in the influent (sewage) is high, the anoxic phase (10%) is required for complete denitrification.



- Medium-strength wastewater, in which  $\text{PO}_4^{3-}$ -P content is high (15–17 mg/L) and COD is (800–1200 mg/L), the anaerobic phase (25% of the total cycle duration) is not enough for the outstanding removal of  $\text{PO}_4^{3-}$ -P and COD.

**Conflict of Interest** The authors declare that they have no conflict of interests.

## References

1. Tanavarotai K, Kamyab H, Anuar AN, Khademi T, Yuzir A, Ashokkumar V, Rezanian S (2022) Storage and reactivation of aerobic granular sludge: a review. *Fuel* 330:125536
2. Zhang Y, Dong X, Nuramkhaan M, Lei Z, Shimizu K, Zhang Z et al (2019) Rapid granulation of aerobic granular sludge: a mini review on operation strategies and comparative analysis. *Bioresour Technol Rep* 7:100206
3. Bengtsson S, de Blois M, Wilén BM, Gustavsson D (2019) A comparison of aerobic granular sludge with conventional and compact biological treatment technologies. *Environ Technol* 40(21):2769–2778
4. de Sousa Rollemberg SL, Ferreira TJJ, Firmino PIM, Dos Santos AB (2020) Impact of cycle type on aerobic granular sludge formation, stability, removal mechanisms and system performance. *J Environ Manag* 256:109970
5. Alattabi AW, Harris CB, Alkhaddar RM, Ortoneda-Pedrola M, Alzeyadi AT (2019) An investigation into the effect of MLSS on the effluent quality and sludge settleability in an aerobic-anoxic sequencing batch reactor (AASBR). *J Water Process Eng* 30:100479
6. de Sousa Rollemberg SL, de Oliveira LQ, Barros ARM, Melo VMM, Firmino PIM, Dos Santos AB (2019) Effects of carbon source on the formation, stability, bioactivity and biodiversity of the aerobic granule sludge. *Bioresour Technol* 278:195–204
7. Iorhemen OT, Hamza RA, Sheng Z, Tay JH (2019) Submerged aerobic granular sludge membrane bioreactor (AGMBR): organics and nutrients (nitrogen and phosphorus) removal. *Bioresour Technol Rep* 6:260–267

# First and Second Law Analyses of an Organic Rankine Cycle to Recover the Waste Heat from the Solar-Operated Combined Cycle Power Plants with Grid



Wasim Akram, Mohd Parvez, Khwaja M. Rafi, and Osama Khan

**Abstract** The waste heat being released into the environment from power plants and industries is a serious issue for scientists and researchers. Therefore, the current study mainly focused on recovering the waste heat which is obtained from the exit of a steam generator and uses it to operate the organic Rankine cycle by using the refrigerants R-113. The analysis predetermines the effects of solar irradiance and turbine inlet temperature on first and second law efficiencies in the combined power plants. The computed results show that as the direct normal irradiation (DNI) increases from (600–1000 W/m<sup>2</sup>), first-law efficiency is obtained in the range of (35.81–40.34%) and second law efficiency from (22.96–25.36%) after employing the organic Rankine cycle. Further, the result indicates that maximum exergy destruction that occurs in the central receiver is around 42.18%, heliostat is 31.15%, HRSG is 10.15%, a heat exchanger is 3.57%, etc.

---

W. Akram

Department of Mechanical Engineering, Mewat Engineering College, Palla, District Nuh, Mewat, Haryana, India

M. Parvez (✉)

Department of Mechanical Engineering, Al-Falah University, Faridabad, Haryana, India  
e-mail: [mparvezalig@rediffmail.com](mailto:mparvezalig@rediffmail.com)

K. M. Rafi

Department of Electrical and Electronics Engineering, Mewat Engineering College, Palla, District Nuh, Mewat, Haryana, India

O. Khan

Department of Mechanical Engineering, Jamia Millia Islamia, New Delhi, India

**Keywords** HRSG · Steam generator · Waste heat recovery · HRVG · Organic Rankine cycle

## Abbreviations

$A_{\text{app}}$	Aperture area (m <sup>2</sup> )
$\dot{A}_{\text{field}}$	Area of heliostat field (m <sup>2</sup> )
$\dot{E}$	Exergy (kW)
$\Delta \dot{E}$	Exergy destruction (kW)
$h$	Enthalpy (kJ/Kg)
$\dot{m}$	Mass flow rate (Kg/s)
$\dot{Q}_{\text{CR}}$	Heat energy of the central receiver (kW)
$\dot{Q}_{\text{E}}$	Energy of the evaporator (kW)
$s$	Specific entropy (kJ/K)
$\eta_{\text{I}}$	Primary (first) law efficiency
$\eta_{\text{II}}$	Secondary (second) law efficiency

## 1 Introduction

Over the past few years, a significant amount of waste heat has been discharged into the environment from various sources such as conventional power plants, solar tower power plants, and industrial facilities, resulting in severe environmental contamination. In order to utilize this waste heat, the organic Rankine cycle (ORC) plays an important role to recover this heat and improving overall energy conversion efficiency by using different working fluids. In recent years, researchers are more interested in solar tower power plants [1, 2]. The system is an integration of the Rankine power cycle and ORC cycle for a combined power generation energy system [3].

Yağlı et al. [4] presented an ORC system to improve the entire performance of a gas turbine used in wood production. In addition to ORC, a steam boiler cycle is integrated with the gas turbine to produce steam to run the cycle. More recently, Martínez-Sánchez et al. [5] explored the patents based on solar energy technologies by using the organic Rankine cycle and its applications. Bellos et al. [6] examined a solar-driven power cycle that is operated by evacuated tube collectors. This ORC worked with cyclopentane and use reheating to enhance its thermodynamic efficiency.

Therefore, the objective of this study is to examine the first and second law analyses of the ORC-driven combined power cycle, with input energy as waste heat available at the exit of the steam generator that receives energy from a solar power tower that uses molten salt as a heat transfer fluid. The present study further includes the various numerical calculations which formed the basis of graphs plotted to understand the relationship between various properties and hence commented upon.

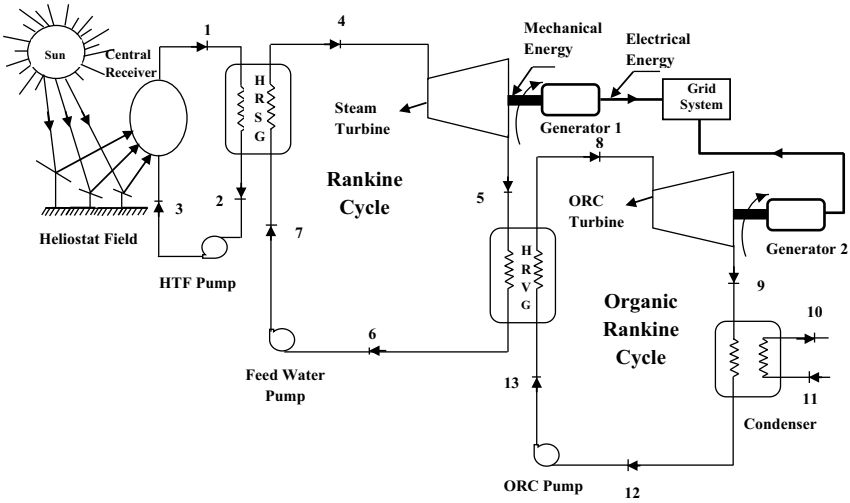


Fig. 1 Schematic diagram of solar-operated ORC combined cycle power plant with grid

## 2 System Description of a Proposed Cycle

The solar-operated system contains the steam Rankine cycle and the ORC with the aid of solar energy to generate electricity as highlighted in Fig. 1. As far as the solar components are concerned, it comprises a set of heliostats that collect and concentrate sunlight onto the receiver, which captivates the focused sunlight and transfers the heat energy to working fluid [7]. The power transformation system comprises a steam generator, turbine generator, organic Rankine system, and supplies different types of apparatus which convert the thermal energy into electric power and further supply it to the utility grid.

## 3 Thermodynamic Modelling for a Combined Power Cycle

This study mainly focuses on the primary model of a cascade system which is based on the integration of two varying models into one another. The important energy and exergy equations are expressed as:

$$\dot{Q}_{\text{solar}} = A_{\text{field}}q \tag{1}$$

$$\dot{Q}_{\text{solar}} = \dot{Q}_{\text{CR}} + \dot{Q}_{\text{lost, heliostat}} \tag{2}$$

$$\eta_{\text{energy, heliostat}} = \frac{\dot{Q}_{\text{CR}}}{\dot{Q}_{\text{solar}}} \quad (3)$$

$$\dot{Q}_{\text{CR}} = \dot{Q}_{\text{moltensalt}} + \dot{Q}_{\text{lost, CR}} = \dot{m}_{\text{moltensalt}}(h_2 - h_1) + \dot{Q}_{\text{lost, CR}} \quad (4)$$

$$\eta_{\text{energy, CR}} = \frac{\dot{Q}_{\text{moltensalt}}}{\dot{Q}_{\text{CR}}} \quad (5)$$

$$\Delta \dot{E}_{\text{CR}} = \dot{m}_{\text{moltensalt}}[(h_2 - h_1) - T_0(s_2 - s_1)] \quad (6)$$

$$\dot{m}_{\text{moltensalt}}(h_2 - h_3) = \dot{m}_{\text{st}}(h_4 - h_7) \quad (7)$$

$$\Delta \dot{E}_{\text{SG}} = T_0[\dot{m}_{\text{moltensalt}}(s_2 - s_3) + \dot{m}_{\text{st}}(s_4 - s_7)] \quad (8)$$

$$\dot{W}_T = \dot{m}_{\text{st}}(h_4 - h_5) \quad (9)$$

$$\Delta \dot{E}_{\text{st}} = \dot{m}_{\text{st}}[(h_4 - h_5) - T_0(s_4 - s_5)] - \dot{W}_T \quad (10)$$

$$\dot{W}_{T, \text{RT}} = \dot{m}_{\text{vapour}}(h_8 - h_9) \quad (11)$$

$$\Delta \dot{E}_{\text{RT}} = \dot{m}_{\text{RT}}[(h_8 - h_9) - T_0(s_8 - s_9)] - \dot{W}_{T, \text{RT}} \quad (12)$$

$$\eta_I = \frac{\dot{W}_{\text{ST}} + \dot{W}_{\text{RT}} - \dot{W}_{\text{HP}} - \dot{W}_{\text{FP}} - \dot{W}_{\text{ORC}, P3} - \dot{W}_{c, \text{ORC}}}{\dot{Q}_{C, R}} \quad (13)$$

$$\eta_{II} = \frac{\dot{W}_{\text{ST}} + \dot{W}_{\text{RT}} - \dot{W}_{\text{HP}} - \dot{W}_{\text{FP}} - \dot{W}_{\text{ORC}, P3} - \dot{W}_{c, \text{ORC}}}{\dot{E}_{x, \text{in}}} \quad (14)$$

## 4 Results and Discussion

The novel investigation has been supported to ascertain the effect of one of the influencing variables like DNI and turbine inlet temperature on primary-law and secondary-law efficiencies of the solar-based combined power plant cycle.

Figures 2 and 3 illustrate the impact of changes in direct normal irradiance (DNI) on the first and second law efficiencies of a combined power plant cycle. The results indicate that a minor improvement in the first law efficiency is observed following a significant upsurge in DNI. This can be attributed to the fact that DNI is linked to the external temperature of the absorber, and a slight increment in the absorber

temperature is detected with a substantial rise in DNI. However, the exergy linked with the heat of the receiver is less than its energy content, and the increase in the second law efficiency of the system is less than the increase in DNI [8].

Figures 4 and 5 displayed the variations of the first and second law efficiencies of the entire system performance while varying turbine inlet temperature (TIT) for production of power. It can be noted that both the efficiencies of the entire system increase appreciably with an increase in TIT of the entire combined power cycle. This increase was noted since an increase in the refrigeration output of ORC and power output from the steam turbine cycle. The results findings justify the benefits of the integration of ORC with RC, showing a significant increment in both the efficiencies of the combined-cycles system [9].

**Fig. 2** Variation of first law efficiency with the change in DNI of a combined power cycle

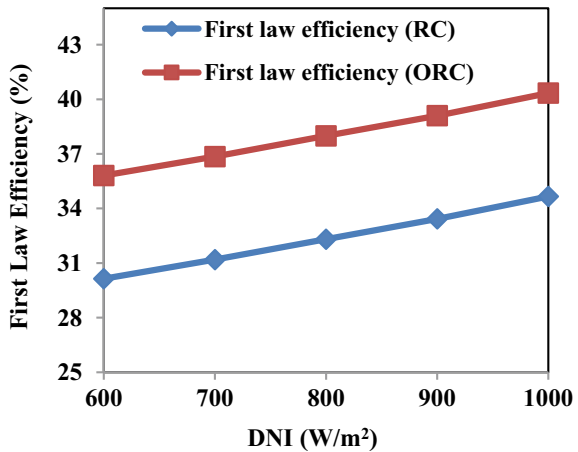


**Fig. 3** Variation of second law efficiency with the change in DNI of a combined power cycle

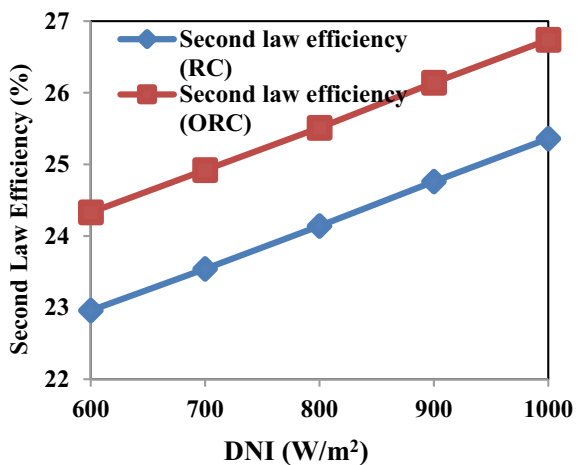


**Fig. 4** Variation of first law efficiency with the change in turbine inlet temperature

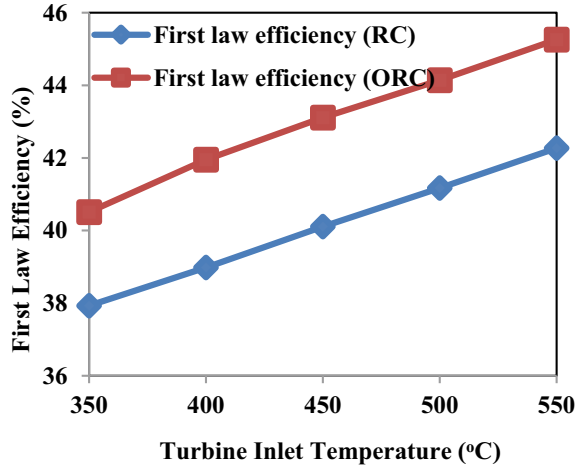
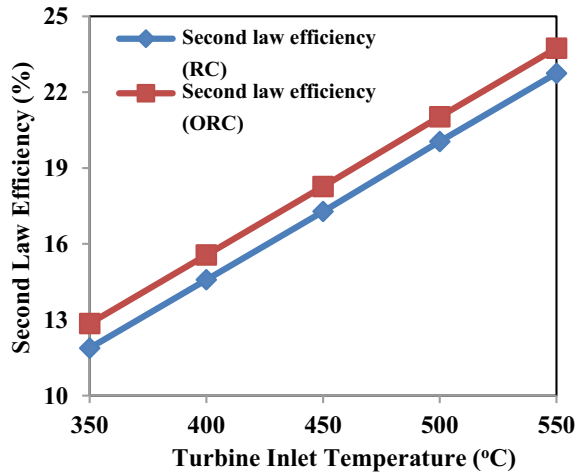
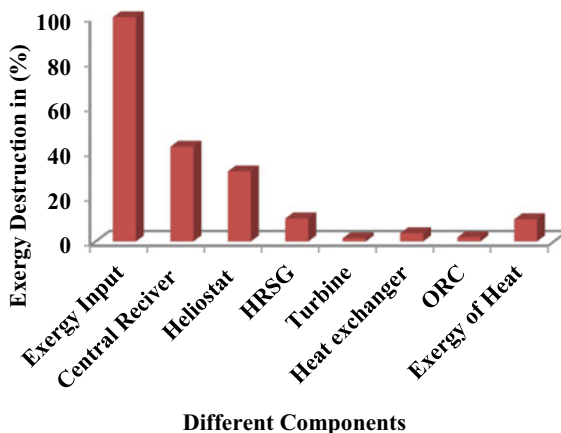


**Fig. 5** Variation of second law efficiency with the change in turbine inlet temperature



enlargethispage-20ptThe degree of thermodynamic irreversibility in each component was determined by calculating the exergy destruction in relation to the exergy input to the cycle, which was then expressed as a percentage. The results are presented in Fig. 6, which shows that the central receiver and heliostat in the solar field contribute significantly to the higher thermodynamic irreversibility of 42.28% and 31.15%, respectively, in the overall combined power cycle. Additionally, a considerable amount of exergy destruction occurs in the HRSG, at around 10.15%, and other components of the cycle.

**Fig. 6** Exergy destruction in each component in the combined power cycle



## 5 Conclusions

The following concluding remarks are coined from the research below:

- A slight gain in the first and second law efficiencies was observed after a considerable increase in the value of DNI at different operating conditions.
- The first law efficiency at mean operating conditions of DNI is lying in the range of 35.81%–40.34%, and the second law efficiency lies in the range of 22.96%–25.36% when the ORC was employed to produce power.
- Out of 100% exergy input of the cycle, the highest exergy destruction is found to be about 42.18% in the central receiver, 31.15% in heliostat, 10.15% in HRSG, 3.57% in the heat exchanger, 1.81% in ORC, etc.

## References

1. Assad M, Rosen M (2021) Design and performance optimization of renewable energy systems, 1st edn. Academic Press Elsevier, Cambridge
2. Haq MZ (2021) Optimization of organic Rankine cycle (ORC) based waste heat recovery (WHR) system using a novel target-temperature-line approach. *J Energy Resour Technol* 143(9):092101
3. Loni R, Mahian O, Markides CN, Bellos F, le Roux WG, Kasaeian A, Najafi G, Rajaei F (2021) A review of solar-driven organic Rankine cycles: recent challenges and future outlook. *Renew Sustain Energy Rev* 150:111410
4. Yağlı H, Koç Y, Kalay H (2021) Optimisation and exergy analysis of an organic Rankine cycle (ORC) used as a bottoming cycle in a cogeneration system producing steam and power. *Sustain Energy Technol Assess* 44:100985
5. Martínez-Sánchez RA, Rodríguez-Resendiz J, Álvarez-Alvarado JM, Macías-Socarrás I (2022) Solar energy-based future perspective for organic Rankine cycle applications. *Micromachines* 13(6):944



6. Bellos E, Lykas P, Tzivanidis C (2022) Investigation of a solar-driven organic rankine cycle with reheating. *Appl Sci* 12(5):2322
7. Caraballo A, Galán-Casado S, Caballero A, Serena S (2021) Molten salts for sensible thermal energy storage: a review and an energy performance analysis. *Energies* 14:1197
8. Parvez M, Khalid K, Khan O (2020) Thermodynamic performance assessment of solar based combined power and absorption refrigeration cycle. *Int J Exergy* 31(3):232–248
9. Ahmad S, Parvez M, Khan TA, Siddiqui SA, Khan O (2022) Performance comparison of solar powered cogeneration and trigeneration systems via energy and exergy analyses. *Int J Exergy* 39(4):395–409

# Nanotechnological Advancements in Sports Rehabilitation to Elevate Athletic Performance Levels



Adil Ali Ansari

**Abstract** The incorporation and evolution of nanoscience and technology is set to have an overwhelming impact on human society, solving numerous obstacles being faced by the human race specifically in the field of sports medicine and rehabilitation. With the advancements of nanotechnology and other branches, the athletic rehabilitation and training after injuries can be achieved in a much more efficient and rewarding manner. By incorporating a mixture of nanomaterials, it is possible to enhance local blood circulation in injured patients, reduce pain, increase muscle flexibility and strength, improve balance and coordination, facilitate the recovery of joint function, and enhance athletic performance. The nanotechnological application can also be adapted in evolving the sporting environment and utilities which can aid in boosting the athletic performance. The increasing demand and enthusiasm of people in sports revealing their ‘unmatched talents and potential’ extensively puts up the need of these nanotechnological advancements, which can raise the benchmark of the human performance to greater heights globally. This review paper studies the application of nanotechnology combined with sports rehabilitation training in the treatment and rehabilitation of athletes as well as multiple ways to improve their performance in the game.

**Keywords** Nanotechnology · Sports performance · Nanoscience · Human · Skeletal muscles performance · Nanomedicine · Nanomaterials · Sports equipment · Athletes · Nano-enhancement

## 1 Introduction

The expanding use of nanotechnology in modern times has led to its implementation in several aspects of sports, such as stadiums, gear, training, flooring, and apparel. Sports accessories that incorporate diverse nanoparticles exhibit enhanced performance, greater flexibility, improved durability, and reduced weight. Moreover, these

---

A. A. Ansari (✉)  
Sharda University, Greater Noida, Uttar Pradesh, India  
e-mail: [adil.ali@sharda.ac.in](mailto:adil.ali@sharda.ac.in)

© The Author(s), under exclusive license to Springer Nature Singapore Pte Ltd. 2023  
Z. H. Khan et al. (eds.), *Recent Advances in Nanotechnology*, Springer Proceedings  
in Materials 28, [https://doi.org/10.1007/978-981-99-4685-3\\_54](https://doi.org/10.1007/978-981-99-4685-3_54)

377

equipment items have an impact on an athlete's performance and serve as protective measures against potential injuries. In recent years, a number of studies have explored the potential applications of nanotechnology in sports rehabilitation. These studies have demonstrated the potential for nanomaterials to enable more precise targeting of therapeutic agents, create scaffolds for tissue engineering, and incorporate sensors for real-time monitoring of athlete performance. For instance, nanotechnology is used to create high-speed and lightweight boats with decreased flow resistance through the application of nanoparticle coatings. Other applications of nanotechnology in sportswear include odor-resistant and waterproof insoles in athletic shoes, water-resistant swimsuits, and protective sports clothing with high-impact resistance [1]. Wearing sportswear that has been modified with nanotechnology can enhance the safety and physical comfort of athletes. This literature studies the application of nanotechnology and nanomaterials in the treatment and rehabilitation of athletes as well as multiple ways to improve their performance in training and game.

## **2 Methodology**

Various databases and search engines were utilized to conduct a search for pertinent articles published from 2014 to 2021. The specific search terms used in isolation and/or combination were 'nanotechnology', 'sports performance', 'nanoscience', 'human', 'skeletal muscles performance', 'nanomedicine', 'nanomaterials', 'sports equipment', 'athletes', and 'nano-enhancement'. In addition to that, the reference lists of the articles obtained from the search were scrutinized to identify any other relevant articles. The criteria for including or excluding studies were determined by their potential relevance to the utilization of nanotechnology in sports to improve athletic performance.

## **3 Results and Discussion**

The use of nanotechnology in sports performance has countless advantages, including improved sports facilities and equipment, increased equipment and facility durability, improved sportsman performance, increased comfort and safety for athletes, decreased risk of injury, increased controllability over earlier equipment, and athletes who are more agile than ever. Some of the benefits of using nanotechnology in sports gear include: greater endurance, increased hardness, decreased weight, wear resistance, resilience, reduced friction, improved strength to weight ratio, it's safer, and it raises the level of competition in sports.

Sports medicine uses nanotechnology in a broad sense to adapt all types of nanoscale developments into medical treatments for injuries sustained in athletic competition. The modified developments may be directly connected to treatment options like tissue regeneration, implantation, and pharmacological therapies or

they may be tied to supportive components like screening, bracing, and taping. With the aid of nanotechnology-based approaches, the advancements in the textile industry, imaging, tissue engineering, and drug delivery demonstrate new goods and procedures for the medical sector, and they develop daily (Table 1).

Functional sportswear that provides therapeutic benefits can aid in the recovery of muscles that have been strained, injured, or fatigued from physical activity, particularly in intense sports such as bodybuilding, arm-wrestling, and powerlifting. By combining textile materials that come into contact with the skin with germanium and ceramic nanoparticles possessing far-infrared radiation properties, such as alumina, titanium dioxide, and silicon dioxide, it is possible to create versatile products that can be used for therapeutic purposes, including knee bands, elbow bands, and back belts [2]. Materials that give off far-infrared radiation take in heat or sunlight from the human body, transform this energy into far-infrared rays with wavelengths ranging from approximately 6 to 14 mm, and then return the energy to the body, resulting in better blood circulation and metabolism. In addition, these materials aid in the recuperation of tired muscles [3] (Fig. 1).

**Table 1** Application of nanotechnological properties in different sports fields

Materials	Properties	Applications in sports
Metal nanoparticles, such as silver (Ag), palladium (Pd), copper (Cu), nickel (Ni)	Antibacterial	Variety of sports wears
Clay nanoparticles	UV protection, protection from cold and heat	Clothing for outdoor sports like skiing, snowboard, high altitude sports, canoeing, and cycling clothes
Metal oxide nanoparticles such as TiO <sub>2</sub> , ZnO, and CuO	Waterproof, self-cleaning	Swimsuit, diving, canoeing, sport shoes, sailing
Carbon nanotubes	Electrical and thermal conductivity	Improved blood flow and faster muscle recovery by therapeutic knee bands, elbow bands, and back belts, particularly when weightlifting

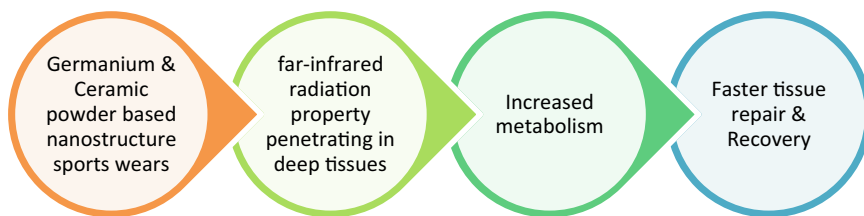


**Fig. 1** Mechanism of enhancing tissue recovery to increase performance

A study done in 2017 discusses the use of nanotechnology in various aspects of sports rehabilitation, such as drug delivery, tissue engineering, and biomechanics where it has been suggested that nanomaterials can be used to create scaffolds that support the growth of new tissue, such as muscle or bone, or to deliver therapeutic agents directly to injured tissue. The authors also highlighted the potential of nanosensors for monitoring athlete performance and detecting injuries [4]. For example, nanosensors embedded in wearable devices or sports equipment could provide real-time feedback on an athlete's performance, as well as alert them to potential injuries before they become more serious. In a separate study that explored the use of nanotechnology in physiotherapy, the authors identified shortcomings of conventional drug delivery methods in this field, such as the inability to target specific body parts and the occurrence of adverse side effects. The study suggests that nanotechnology-based drug delivery systems could address these issues by allowing for more precise drug targeting and reducing the likelihood of side effects. The study also highlights the various types of nanomaterials that can be used for drug delivery in physiotherapy, such as liposomes, dendrimers, and carbon nanotubes in the form of conductive materials in electrotherapeutic modalities [5].

## 4 Conclusion

To summarize, the application of nanotechnology in sports injury management and performance enhancement in athletes has shown great promise in recent years. Various nanomaterials, including nanoparticles, nanofibers, and nanocomposites, have been explored for their potential in enhancing tissue repair and regeneration, controlling inflammation, and improving athletic performance. Nanotechnology has various benefits for athletic performance sections compared to conventional sports applications, such as

- Lightweight and stronger accessories
- Better athletic comfort
- Better athletic safety
- Better athletic performance and confidence
- Better flexibility of sports wears
- Better breathability

Moreover, nanotechnology-based drug delivery systems have the potential to enable targeted delivery of drugs to specific areas of the body, thereby improving the efficacy of treatments and minimizing side effects. However, the numerous benefits associated with nanotechnology, several challenges remain to be addressed. These include safety concerns associated with the use of nanomaterials and the need for

more robust clinical studies to establish the safety and efficacy of nanotechnology-based interventions. Furthermore, the high cost of nanotechnology-based interventions may limit their widespread adoption in sports injury management and performance enhancement. Nanotechnology holds great potential in sports injury management and performance enhancement in athletes. While there are challenges that must be addressed, the continued exploration and development of nanotechnology-based interventions in sports medicine are likely to lead to significant advancements in the field, benefiting athletes and sports enthusiasts alike.

## References

1. Harifi T, Montazer M (2017) Application of nanotechnology in sports clothing and flooring for enhanced sport activities, performance, efficiency and comfort: a review. *J Ind Text* 46(5):1147–1169
2. Chung J, Lee S (2014) Development of nanofibrous membranes with far-infrared radiation and their antimicrobial properties. *Fibers Polymers* 15:1153–1159
3. Meoli D, May-Plumlee T (2002) Interactive electronic textile development: a review of technologies. *J Text Apparel, Technol Manage* 2(2):1–12
4. Singh M, Singh N (2017) Nanotechnology in sports medicine: a perspective on latest developments. *Int J Nanomed* 12:871–881
5. Mohammadi A, Alijani SS, Vahabi S (2016) Nanotechnology-based approaches in physiotherapy: a focus on drug delivery systems. *J Med Signals Sens* 6(4):211–220

# An Electrochemical Ascorbic Acid Sensor Constructed by Ferrocene Palladium Nanoparticles Modified Graphite



Kulveer Singh, Chitra Singh, and Manisha Malviya

**Abstract** This paper discusses how palladium affects the redox electrochemistry of ferrocene. The amount of palladium present, as well as its geometrical distribution, has been found to have a significant impact on the redox electrochemistry of ferrocene. Significant results were obtained with the Fc-based electrode, and startling results were obtained with the Pd-modified Fc-based electrode, as confirmed by amperometry titration which demonstrated a significantly higher current when using palladium nanoparticles modified ferrocene-based electrode. Electrochemical impedance spectroscopy has also been investigated, which confirms that a PdNPs modified Fc-based electrode with low charge transfer resistance and fast electron transfer, and high sensitivity toward ascorbic acid. Cyclic voltammetry and transmission electron microscopy have been used to characterize the nanomaterial. For the purpose of detecting ascorbic acid, the impact of palladium nanostructures on the oxidation and reduction electrochemistry of Fc is investigated.

**Keywords** Cyclic voltammetry (CV) · Ferrocene (Fc) · Electrochemical impedance spectroscopy (EIS)

## 1 Introduction

Ascorbic acid (AA), which is easily converted to dehydroascorbic acid, is well known for its reductive characteristics. It functions as a potent antioxidant that combats diseases brought on by free radicals [1]. Collagen is a protein that gives structure

---

K. Singh (✉) · C. Singh · M. Malviya  
Department of Chemistry, Indian Institute of Technology (B.H.U.), Varanasi 221005, Uttar Pradesh, India  
e-mail: [kulveersingh.rs.chy19@itbhu.ac.in](mailto:kulveersingh.rs.chy19@itbhu.ac.in)

C. Singh  
e-mail: [chitrasingh.rs.chy19@itbhu.ac.in](mailto:chitrasingh.rs.chy19@itbhu.ac.in)

M. Malviya  
e-mail: [manisha.apc@iitbhu.ac.in](mailto:manisha.apc@iitbhu.ac.in)

to muscles, bones, and blood vessels. It is formed when the water-soluble vitamin ascorbic acid is present in the body. It is possible to use the AA content as a health indicator. In general, AA shortage frequently results in anemia, scurvy, and premature aging. But too much AA always causes diarrhea and stomach irritability [2, 3]. The methods for finding ascorbic acid that has been generally discussed include fluorimetry [4], oxidation-reduction titration [5], electrochemistry [6], HPLC [7], and chromatography [8]. Due to its great sensitivity, ease of use, and low cost, electrochemistry is one of these methods that is seen to be appealing. Here, the role of palladium nanoparticles has been studied for the oxidoreduction electrochemistry of ferrocene, and the modified fabricated electrode was found more active for ascorbic acid sensing

## 2 Materials and Methods

### 2.1 Materials

Ferrocene (Fc), graphite powder (particles size < 20  $\mu\text{m}$ ), Nujol oil (density 0.838  $\text{g}/\text{ml}^{-1}$ ),  $\text{K}_2\text{PdCl}_4$ , and Polyvinylpyrrolidone (PVP) were purchased from Sigma Aldrich Chemical co. India. Ascorbic acid, anhydrous sodium phosphate ( $\text{Na}_2\text{HPO}_4$ ), and dihydrogen sodium phosphate mono hydrates ( $\text{NaH}_2\text{PO}_4 \cdot \text{H}_2\text{O}$ ) were obtained from HiMedia Chemicals, India. 3-Aminopropyltrimethoxysilane(3-APTMS) was purchased from TCI India. The usage of all other compounds was without additional purification, and they were all of the analytical grade.

### 2.2 Synthesis

The PdNPs have been synthesized by the previously reported method [9], which involves mixing of methanolic solution of  $\text{K}_2\text{PdCl}_4$  (20 mM) 50  $\mu\text{l}$ , polyvinyl pyrrolidone (PVP, 1% aqueous solution) 20  $\mu\text{l}$ , and 3-APTMS (15 mM) 10  $\mu\text{l}$ . Stirred the solution on cyclo mixture and kept for 5–10 min for incubation at ambient temperature. The brownish-black colloidal solution is obtained and represented as PdNPs.

## 3 Electrochemical study and Characterization-

Using a Tecnai G2 20 TWIN, pictures from transmission electron microscopy (TEM) were captured (FEI Electron Optics). Model CHI 660B TX, USA, a computer-controlled electrochemical workstation was used to record the electrochemical tests.



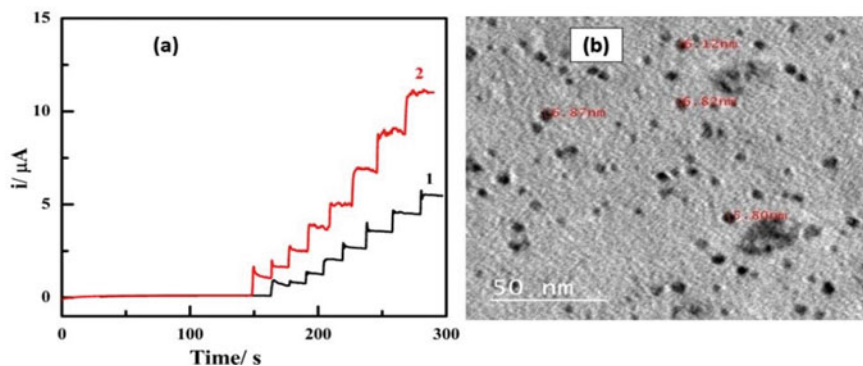


**Fig. 1** Amperometry response (a) 1—CPE/Fc, 2—CPE/Fc-PdNPs and (b) TEM image of PdNPs, having an average particle size of  $6 \pm 2$  nm

Using an experimental setup where the resistance was gradually compensated for the uncompensated state, each CV was recorded many times. Using a three-electrode cell setup with a working capacity of 3 ml, the measurements were performed. A Pt foil electrode and Ag/AgCl electrode (RE1B, ALS co.-Japan) are used as counter and reference electrodes. All potentials given below were relative to the Ag/AgCl. The modified carbon paste electrode was used as a working electrode. In a 0.1M phosphate buffer (pH 7.0) with 0.5M KCl, ascorbic acid (AA) was identified using cyclic voltammetry (CV), amperometry, and EIS. All studies used freshly produced AA. The same condition and ambient temperature were used for all the experiments. The  $N_2$  gas is purged to the electrochemical cell before running each electrode studied (Fig. 1).

The CPE/Fc-PdNPs modified electrode reveals a higher current response with ascorbic acid than CPE/Fc electrode during amperometric and cyclic voltammetry measurement under similar conditions.

As shown in Fig. 2, how the decrease in cathodic ( $E_{pc}$ ) and anodic ( $E_{pa}$ ) peak potentials is clearly explained. Additionally, under similar conditions, both cathodic and anodic peak currents steadily rise, showing a reduction in charge transfer resistance as a result of the palladium nanoparticle. Impedance spectroscopy is used to confirm these findings. The results shown in Fig. 3 convincingly support a substantial increase in anodic current due to the electrochemical transformation of ascorbic acid, further demonstrating how palladium nanoparticle modified electrode reduces charge transfer resistance.

### 3.1 EIS Measurement

One of the most effective electrochemical techniques is electrochemical impedance spectroscopy (EIS), which uses a Nyquist plot with a semi-circular region at

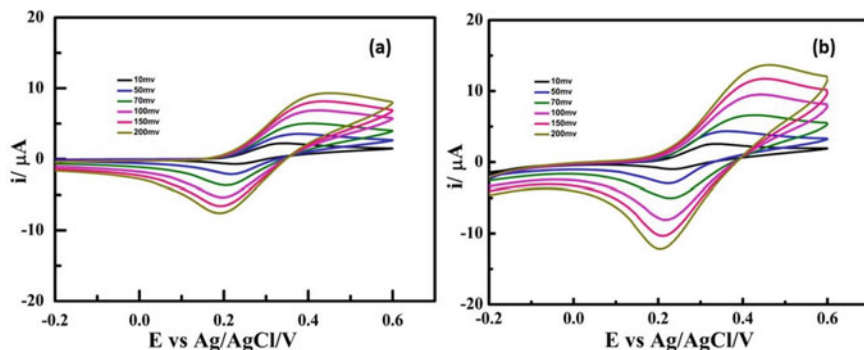


**Fig. 2** Cyclic voltammetry of (a) CPE/Fc and (b) CPE/Fc-PdNPs in 0.1 M phosphate buffer (0.5M KCl) between  $-0.2$  and  $0.6$  V versus Ag/AgCl at differ scan rates starting at  $0.01$ – $0.2$   $\text{Vs}^{-1}$

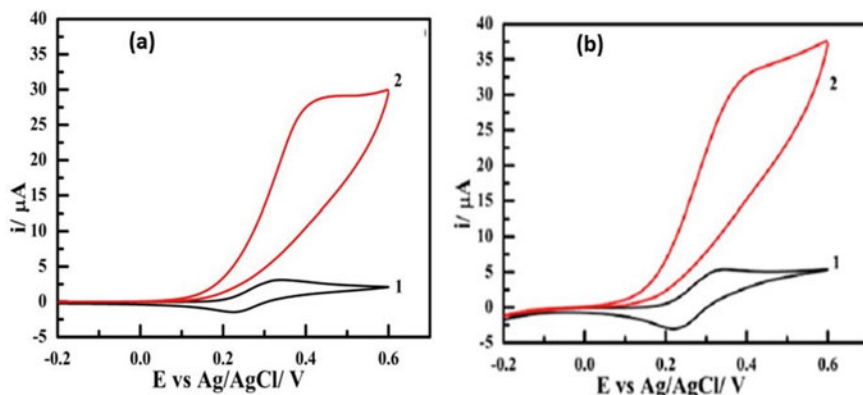


**Fig. 3** Cyclic voltammograms at  $10$  mV/s before (curve 1) and after (curve 2) addition of ascorbic acid ( $10$  mM) for (a) CPE/Fc, (b) CPE/Fc-PdNPs electrodes

higher frequencies representing charge transfer resistance and a straight line at lower frequencies, the diffusion control process. CPE/Fc-PdNPs have a lower  $R_{ct}$  ( $7.4 \text{ K}\Omega\text{cm}^2$ ) than CPE/Fc ( $14.4 \text{ K}\Omega\text{cm}^2$ ), revealing that the system CPE/Fc-PdNPs has the highest charge transfer and  $0.1$  M phosphates (with  $0.5$  M KCl) buffer between  $1$  Hz and  $1000$  kHz, and  $0.23$  V potential was used as shown in Fig. 4.

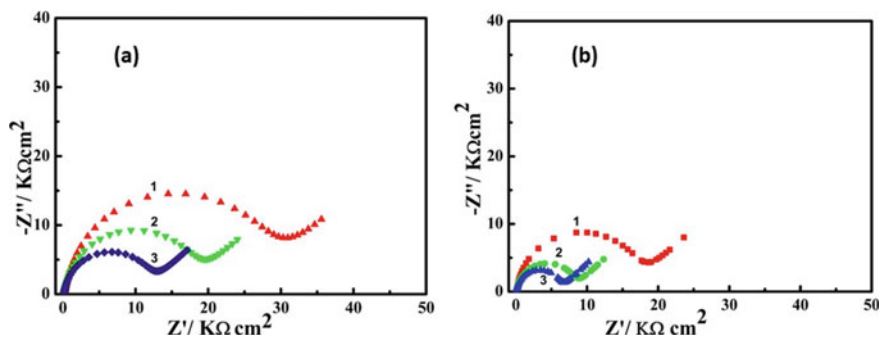


**Fig. 4** Nyquist plot of CPE/Fc (a), CPE/Fc-PdNPs (b), 1—without adding AA, with AA- 2—2 mM, and 3—4 mM

## 4 Conclusion

The results of the experiments reveal that Pd nanoparticles help in improving the sluggish electrochemistry of ferrocene in ascorbic acid (AA) sensing. The sluggish electrochemistry of the Fc-modified electrode accelerates in the presence of palladium, and the peak current gradually rises as a function of the palladium nanoparticles. These results show that the CPE/Fc-PdNPs modified electrode exhibits excellent reproducible and stable electrochemical behavior while detecting AA. The linear ranges of AA under ideal circumstances were 50–400  $\mu\text{M}$ . For AA, the detection limit was 20  $\mu\text{M}$ .

## References

1. Erdurak-Kiliç CS et al (2006) Anodic voltammetric behavior of ascorbic acid and its selective determination in pharmaceutical dosage forms and some Rosa species of Turkey. *J Anal Chem* 61(11):1113–1120
2. Massey LK, Liebman M, Kynast-Gales SA (2005) Ascorbate increases human oxaluria and kidney stone risk. *J Nutr* 135(7):1673–1677
3. Padayatty SJ et al. (2003) Vitamin C as an antioxidant: evaluation of its role in disease prevention. *J Am College Nutr* 22(1):18–35
4. Wu X et al. (2003) Fluorimetric determination of ascorbic acid with o-phenylenediamine. *Talanta* 59(1):95–99
5. Suntornsuk L et al. (2002) Quantitation of vitamin C content in herbal juice using direct titration. *J Pharm Biomed Anal* 28(5):849–855
6. Wen D et al. (2010) Ultrathin Pd nanowire as a highly active electrode material for sensitive and selective detection of ascorbic acid. *Biosens Bioelectr* 26(3):1056–1061
7. Abad K et al. (2011) A new HPLC method for the simultaneous determination of ascorbic acid and amino thiols in human plasma and erythrocytes using electrochemical detection. *Talanta* 84(3):789–801
8. Tai A, Gohda E (2007) Determination of ascorbic acid and its related compounds in foods and beverages by hydrophilic interaction liquid chromatography. *J Chromatogr B* 853(1–2):214–220

9. Maurya KK, Singh K, Malviya M (2023) Effect of palladium and its nanogeometry on the redox electrochemistry of tetracyanoquinodimethane modified electrode; application in electrochemical sensing of ascorbic acid. *J Appl Electrochem* 53:1–12

# Bimetallic Heterogeneous Catalysis for Oxygen Evolution Reaction with Varying Concentrations of Silica



Chitra Singh and Kulveer Singh

**Abstract** Although the effectiveness of noble metal nanocatalysts per noble metal atom is currently low, they are frequently used in heterogeneous catalysis. Nanostructured silica is necessary for the recyclability of nanocatalysts, the synergistic interaction of bimetallic components during OER, and the much enhanced palladium nanogeometry. Co-NTA nanowires were used as a precursor in the synthesis of Co@Pdnpns, which was mediated by organotrialkoxysilane to regulate the existence of nanostructured silica after calcination that is helpful in OER, Co@Pdnpns were created employing a variable amount of organotrialkoxysilane in an N-doped carbon matrix. They were then examined by XRD, TEM, and EDX. With a small Tafel slope of  $39 \text{ mV dec}^{-1}$ , a catalyst loading of  $2 \text{ mg cm}^{-2}$ , and a nanostructured silicon-derived thin film constituted of Co@Pdnpns, a very high current density was obtained at a low overpotential. In the absence of silica, the nanocatalysts are somewhat bigger and exhibit a lower current density ( $20.5 \text{ mA cm}^{-2}$ ) than those that were seen with a high silica concentration.

**Keywords** Oxygen evolution reaction (OER) · Tafel slope · Linear sweep voltammetry (LSV)

## 1 Introduction

The world's need for energy has grown as a result of the direct usage of fossil fuels and global industrialization. A considerable amount of greenhouse gases are also released when fossil fuels are burned often, which contributes to global warming. In this sense, replacing fossil fuel resources with electrochemical energy conversion is a great idea. This is why electrochemical water splitting is crucial for creating clean,

---

C. Singh (✉) · K. Singh  
Department of Chemistry, Indian Institute of Technology (B.H.U.), Varanasi 221005, Uttar Pradesh, India  
e-mail: [chitrasingh.rs.chy19@itbhu.ac.in](mailto:chitrasingh.rs.chy19@itbhu.ac.in)

K. Singh  
e-mail: [kulveersingh.rs.chy19@itbhu.ac.in](mailto:kulveersingh.rs.chy19@itbhu.ac.in)

environmentally responsible energy [1]. The hydrogen evolution reaction (HER) and the oxygen evolution reaction (OER) are two half-cell processes involved in electrochemical water splitting [2]. The OER occurs at the anode, while the HER occurs at the cathode. The total reaction requires a typical value of 1.23 V potential to be driven electrochemically. OER is the slower of the two half-cell reactions because it involves a multistep electron transfer that involves a number of high-energy intermediates. In addition, OER is easier to carry out in an alkaline medium than an acidic one [3]. HER is less deep than in an alkaline media because to the concentration of protons in an acidic medium. The entire OER and HER reaction is significantly impacted by the pH of the electrolyte. Noble metal-based catalysts with strong OER catalytic activity such as  $\text{IrO}_2$  and  $\text{RuO}_2$ , provide quicker kinetics and greater electrochemical water splitting efficiency [4]. In HER, Pt-based noble metals perform well. The primary obstacles preventing noble metal-based catalysts from being widely used are their rarity and high price.[5] For the past 20 years, transition metal-based electrocatalysts have been employed as a substitute for noble metal catalysts because of their increased activity, low price, and availability [6]. Examples of electrocatalysts based on transition metals include layered double hydroxides, metal oxides, and metal nitrides [7]. Here we have synthesized the Co@PdNps which is showing the best oxygen evolution reaction activity in basic medium with the small Tafel slope.

## 2 Materials and Synthesis

### 2.1 Synthesis of Co-NTA

0.002 mol of  $\text{CoCl}_2 \cdot 6\text{H}_2\text{O}$  was dissolved in 15 mL of deionized water and stirred for 20 min. 15 mL of isopropyl alcohol were swirled with 0.005 mol of NTA for 30 min. The cobalt chloride solution was mixed with the NTA solution for 30 min. In a Teflon line autoclave, the resulting mixture was transferred for 6 h at 180 °C (50 mL capacity). The autoclave has to be allowed to cool to room temperature. The pink precipitate was collected, centrifuged with ethanol at 8000 rpm for ten minutes, and then repeatedly cleaned with deionized water. The recovered solid was dried for 6 h at 600 °C in a hot air oven [8].

### 2.2 Synthesis of Co@NC

Co-NTA fine powder (100 mg) was placed in a crucible boat and pyrolyzed for 3 h at 600 °C in an  $\text{N}_2$  environment. The tubular furnace was let to cool naturally at ambient temperature. Co@NC was used to represent the black powder that was collected [9].

### 2.3 Synthesis of Co@Pdnp<sub>s</sub>

Palladium nanoparticles were synthesized utilizing a wet chemical reduction method using EETMS. First, we made a methanolic solution of PVP (1%, 1 mL) and K<sub>2</sub>PdCl<sub>4</sub> (10 mM, 1 mL). Then, a methanolic solution of EETMS was produced with a concentration range of 0.1–4.32 M. The appropriate concentration of EETMS (15 μL) was added to the solution of K<sub>2</sub>PdCl<sub>4</sub> (80 μL) and PVP (15 μL), which was then agitated for 2 min and incubated at 40 °C for 10–15 min. The black colloidal solution was obtained. Now this black colloidal solution was adsorbed on pre synthesized Co-NTA powder and then calcined at 600 °C in an N<sub>2</sub> environment for 3 h. The obtained material is represented as Co@Pdnp<sub>s</sub>.

## 3 Results and Discussion

The XRD data offered a deeper understanding of the crystalline characteristics of the nanoparticle catalysts Fig. 1. The XRD pattern was used to index the selected region electron diffraction pattern, then indexed for cubic cobalt's (111) plane. Pd (200) nanoparticles are bimetallic. Figure 2, TEM image, SAED pattern, and particle size distribution of Co@Pdnp<sub>s</sub>1 (a, b) and Co@Pdnp<sub>s</sub>2. It is clear that the Co@Pdnp<sub>s</sub>1 and Co@Pdnp<sub>s</sub>2 particle sizes are  $20 \pm 5$  and  $25 \pm 5$ , respectively, Fig. 3, (a) Co@NC and Co@Pdnp<sub>s</sub> increased OER, with Co@Pdnp<sub>s</sub> exhibiting substantial catalytic activity. Co@Pdnp<sub>s</sub>1, Co@Pdnp<sub>s</sub>2, Co@Pdnp<sub>s</sub>3, and Co@NC modified electrodes, the overpotentials corresponding to current density on the order of 5 mA/cm<sup>2</sup> are 0.98 V, 1.03 V, 1.06, and 1.10 V, respectively. Figure 3, (b) from cyclic voltammetry of a blank CC, Co@NC, and Co@Pdnp<sub>s</sub> modified electrode, demonstrating a several-fold increase in the catalytic activity of Co@Pdnp<sub>s</sub> when palladium concentration is 4.3% in the cobalt-based heterogeneous catalyst. Figure 3, (c) Nyquist Plot reveals a semicircle section of the impedance spectra depicted in Fig. 3c corresponds to charge transfer resistance, whereas a linear portion corresponds to diffusion-limited processes. As semicircle decrease the charge transfer increase. Figure 3d shows a Tafel plot that confirms the low slope value of 39 mV/decade, showing the benefits of low palladium concentration in cobalt-based catalysts.

## 4 Conclusion

The recording result indicates the following significant finding (a) Polycrystallinity decreases as a function of different content of silica, increased nanogeometry Pd nanoparticle with an increase in silica concentration, which improves the rate of OER. (b) In the presence of silica, Pdnp<sub>s</sub>3 transitions from hexagonal to a circular and triangular shape. The interaction of different forms of silica residue with as-synthesized

**Fig. 1** XRD pattern of synthesized Co@Pdnpns

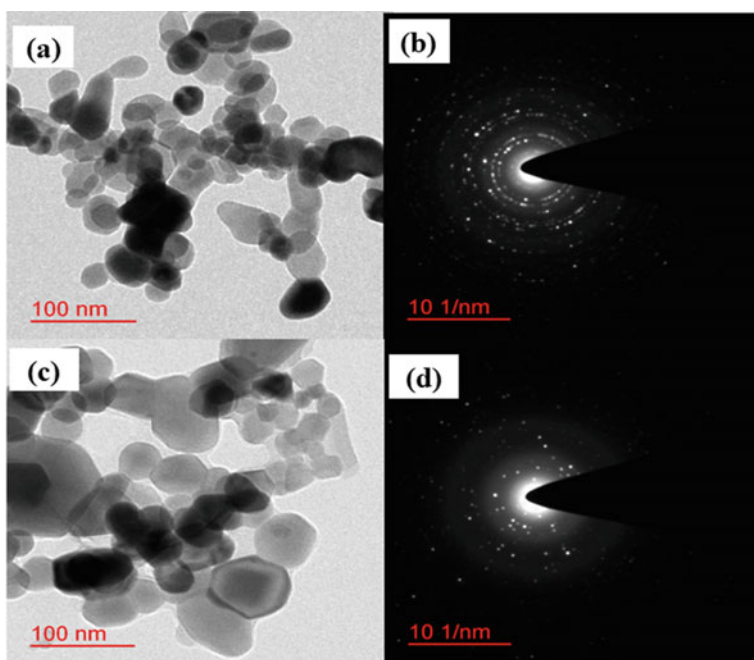
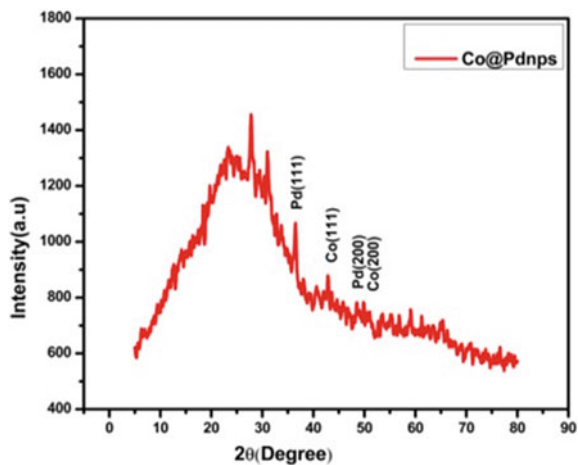


**Fig. 2** TEM image (a, c) and SAED pattern (b, d) of Co@Pdnpns

Pd resulted in such diversity in polycrystallinity and microstructure of Pdnpns Co-NTA nanowires were used as a precursor in the creation of Co@Pdnpns through organotrialkoxysilane. In order to regulate the presence of nanostructured silica following calcinations, representing a carbon-free nanocatalyst in OER, Co@Pdnpns



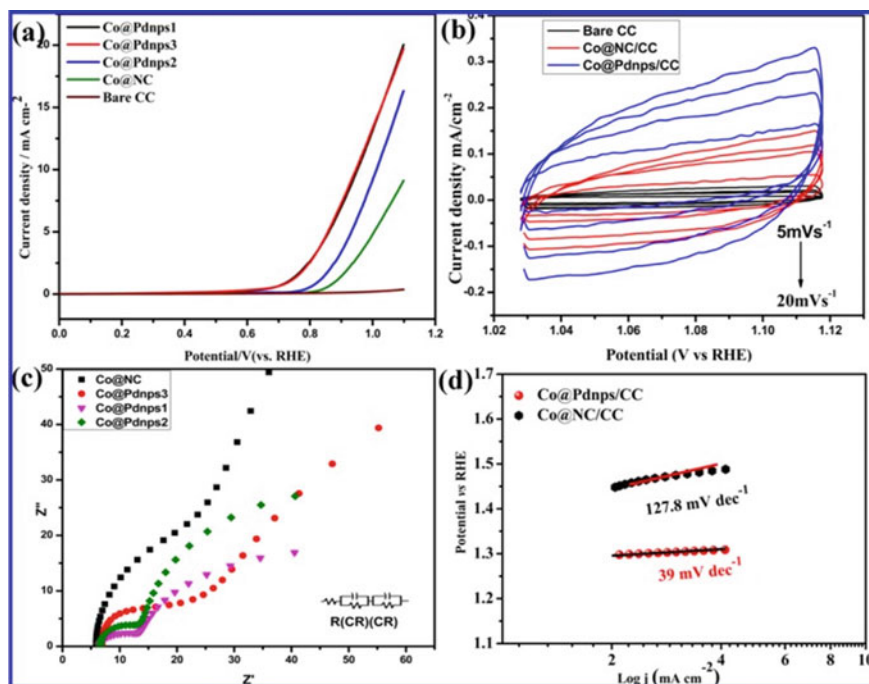


**Fig. 3** Electrochemical study (a) LSV with different conc. of silica in Co@Pdnp, (b) Cyclic voltammetry, (c) Electrochemical impedance spectroscopy (EIS), Nyquist plot, (d) Tafel plot

were produced employing a variable amount of organotrialkoxysilane in an N-doped carbon matrix. After calcination, several systems of bimetallic nanocatalysts with diverse compositions—(i) Co@Pdnp1, (ii) Co@Pdnp2, and (iii) Co@Pdnp3—are created to support the influence of nanostructured silica with varying silica concentrations and palladium nanogeometries on OER. Nanostructured silica greatly increases the palladium nanogeometry, the recyclability of nanocatalyst, and the synergistic interaction of bimetallic components during OER.

## References

1. Ling T, Yan DY, Wang H, Jiao Y, Hu Z, Zheng Y, Zheng L, Mao J, Liu H, Du XW, Jaroniec M (2017) Activating cobalt (II) oxide nanorods for efficient electrocatalysis by strain engineering. *Nat Commun* 8(1):1–7
2. Gerken JB, McAlpin JG, Chen JY, Rigsby ML, Casey WH, Britt RD, Stahl SS (2011) Electrochemical water oxidation with cobalt-based electrocatalysts from pH 0–14: the thermodynamic basis for catalyst structure, stability, and activity. *J Am Chem Soc* 133(36):14431–14442
3. Jiao Y, Zheng Y, Jaroniec M, Qiao SZ (2015) Design of electrocatalysts for oxygen- and hydrogen-involving energy conversion reactions. *Chem Soc Rev* 44(8):2060–2086

4. Li X, Hao X, Abudula A, Guan G (2016) Nanostructured catalysts for electrochemical water splitting: current state and prospects. *J Mater Chem A* 4(31):11973–20000
5. Song F, Bai L, Moysiadou A, Lee S, Hu C, Liardet L, Hu X (2018) Transition metal oxides as electrocatalysts for the oxygen evolution reaction in alkaline solutions: an application-inspired renaissance. *J Am Chem Soc* 140(25):7748–7759
6. Jin H, Wang J, Su D, Wei Z, Pang Z, Wang Y (2015) In situ cobalt–cobalt oxide/N-doped carbon hybrids as superior bifunctional electrocatalysts for hydrogen and oxygen evolution. *J Am Chem Soc* 137(7):2688–2694
7. Wang J, Li K, Zhong HX, Xu D, Wang ZL, Jiang Z, Wu ZJ, Zhang XB (2015) Synergistic effect between metal–nitrogen–carbon sheets and NiO nanoparticles for enhanced electrochemical water-oxidation performance. *Angew Chem* 27(36):10676–10680
8. Wang B, Chen K, Wang G, Liu X, Wang H, Bai J (2019) A multidimensional and hierarchical carbon-confined cobalt phosphide nanocomposite as an advanced anode for lithium and sodium storage. *Nanoscale* 11(3):968–985
9. Wang Y, An C, Wang Y, Huang Y, Chen C, Jiao L, Yuan H (2014) Core–shell Co@C catalyzed  $\text{MgH}_2$ : enhanced dehydrogenation properties and its catalytic mechanism. *J Mater Chem A* 2(38):16285–16291

# Rational Designing of Ni-Ag/C Bimetallic Nanoparticles



Samika Anand and K. R. Sunaja Devi 

**Abstract** Bimetallic nanoparticles have been found to show improved properties due to the synergistic effect between the incorporated metals as a result of electronic charge transfer between them. The importance of using bimetallic particles lies in the high selectivity that they offer. Ni being a reactive metal, was doped with Ag, a highly selective host. In this study, Ni-Ag bimetallic nanoparticles supported on carbon have been synthesized by co-impregnation by using nickel (II) nitrate and silver nitrate as precursors. The catalyst is characterized using XRD, FTIR, DLS, Zeta potential, EDX, SEM, and TEM. The scope of this synthesized catalyst can be extended to several reactions like CO<sub>2</sub> reduction reaction, hydrogenation, and industrially important organic reactions.

**Keywords** Bimetallic · Ni-Ag nanoparticles · Organic synthesis

## 1 Introduction

Metal nanoparticles have been known to catalyze reactions remarkably for a few decades. After extensive use of monometallic catalysts, recently, bimetallic catalysts have gained significance [1]. Bimetallic catalysts mainly show synergistic effects, which lead to their properties being much different than that of their monometallic counterparts. This is majorly attributed to the electronic charge transfer between two metals [2]. Bimetallic nanoalloys consist of a reactive dopant added to a selective host. This not only aids in boosting the catalytic activity but also the selectivity of the product obtained [3]. Conventional catalysts function by lowering the energy of LUMO of the reacting species. The mechanism of action of bimetallic catalysts proceeds via decreasing the energy of LUMO and increasing the energy of HOMO in the reacting species, thereby decreasing the energy gap between the two [4]. Chan-Lam coupling reactions are simplified carbon-heteroatom bond forming reactions utilizing aryl boronic acids and nucleophiles containing heteroatoms [5]. Such

---

S. Anand · K. R. Sunaja Devi (✉)  
Department of Chemistry, CHRIST (Deemed to Be University), Bengaluru 560029, India  
e-mail: [sunajadevi.kr@christuniversity.in](mailto:sunajadevi.kr@christuniversity.in)

reactions required harsh conditions in presence of copper as a catalyst. Moreover, the reaction scope was limited to a few substrates. This led to use of copper-ligand systems as catalysts which favored coupling in mild conditions [6].

However, synthesis of ligand systems follows complex synthesis procedures. Due to the presence of too many entities in the catalyst, there is a decrease in the number of active sites. The presence of only metal sites leads to higher active sites, thereby boosting the catalytic activity [7]. Sharma and co-workers demonstrated an enhancement in catalytic activity of monometallic Ni by forming nano-rod like supported  $\text{NiFe}_2\text{O}_4$  having greater surface area, pore volume, and active sites. Ni was added to  $\text{Fe}_3\text{O}_4$ -N doped carbons (NDCs) by a reduction method and  $\text{Ni@Fe}_3\text{O}_4$ -NDCs. Due to an impressive interaction between Ni and Fe,  $\text{NiFe}_2\text{O}_4$  was formed, which was proved by HRTEM, XPS, and XRD [8]. Sharma et al. reported a synergistic effect between Ag and Cu supported on modified graphene.  $\text{Cu@Ag-TiO}_2$ -NGO was synthesized by using the respective nitrates as precursors, followed by reduction using  $\text{NaBH}_4$ . Graphene oxide was first doped with nitrogen, followed by  $\text{TiO}_2$  as this led to a support with higher surface area [9]. Thus from the literature reports it is evident that bimetallic nanocatalysts result in high reactivity and selectivity [10]. Herein, we report the synthesis of Ni-Ag nanoparticles supported on activated carbon via a simple and efficient co-impregnation method. Ni being a reactive dopant, when combined with Ag, a selective host, showed an enhancement in catalytic activity. The synthesized catalyst showed efficient activity and recyclability in Chan-Lam coupling reaction.

## 2 Materials and Methods

### 2.1 Synthesis of Ni-Ag/C Bimetallic Nanoparticles

A co-impregnation technique was employed to synthesize Ni-Ag bimetallic nanoparticles supported on activated carbon. 2 g carbon black, from Sigma Aldrich was activated using 100 mL, 9 M  $\text{HNO}_3$  by keeping it under reflux for 3 h at 90 °C. The solution was heated until a 50% reduction in volume was obtained. This was followed by addition of 0.12 g of  $\text{Ni}(\text{NO}_3)_2$  and  $\text{AgNO}_3$ , one after the other, respectively. The mixture was allowed to stir under warm conditions for 12 h. The mixture was centrifuged, and the residue was allowed to dry. The obtained residue was then pyrolyzed at 900 °C under nitrogen atmosphere for 1 h to obtain Ni-Ag/C nanoparticles. A similar method was used by Zheng et al. to synthesize Ni single atom catalyst [7]. Figure 1 shows a schematic illustration for the synthesis of Ni-Ag/C bimetallic nanocatalyst.

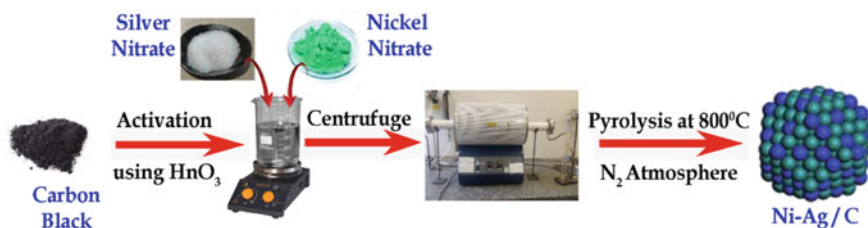


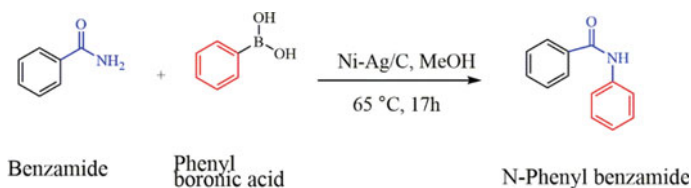
**Fig. 1** Scheme for the synthesis of Ni-Ag/C

## 2.2 Characterization of the Catalyst

The X-ray Diffraction (XRD) plot of the bimetallic nanocatalyst was analyzed for its crystalline nature using Bruker AXS X-ray diffractometer having Cu-K $\alpha$  radiation ( $\lambda = 0.154$  nm) in the  $2\theta$  range of  $5^\circ$  to  $80^\circ$  with the scan rate of  $2^\circ \text{ min}^{-1}$ . Fourier Transform Infrared (FTIR) spectrometer was employed to obtain the IR spectrum in the wavelength range of  $400\text{--}4000 \text{ cm}^{-1}$  using Shimadzu spirit QATR-S instrument. Particle size and zeta potential were obtained using Malvern ZEN3600. HRTEM analysis was done using JEOL/JEM 2100 transmission electron microscope.

## 2.3 Catalytic Activity Toward Chan-Lam Coupling

To study the effectiveness of the catalyst, Chan-Lam coupling was carried out between phenylboronic acid and benzamide with methanol as a solvent (Scheme 1). In a 50 mL round bottom flask, 1 eq. of phenylboronic acid was added to 1.5 eq. of benzamide and dissolved in a minimum quantity of methanol. To this mixture, 6 mol % of the catalyst was added and stirred for 17 h. The reaction was continuously monitored using thin-layer chromatography using ethyl acetate and hexanol (1:1) solvent system [6]. The product obtained was separated using column chromatography.



**Scheme 1** Chan-Lam coupling between benzamide and phenylboronic acid

### 3 Results and Discussion

#### 3.1 Characterization of Ni-Ag/C

Ni-Ag/C was characterized in order to understand the surface morphology and composition. From the XRD pattern, (Fig. 2a), the peak at  $26.5^\circ$  corresponds to carbon [11]. The absence of any metal peak in the XRD pattern reveals that the concentration of both Ni and Ag in the catalyst is less than 3% [11]. From the IR spectrum (Fig. 2b), the presence of bands at 1050, 1701, 1524,  $3648\text{ cm}^{-1}$  correspond to metal-metal stretching, O-H bending, C-C stretching, and O-H stretching, respectively [12]. The absence of IR peak in the range of  $500\text{--}600\text{ cm}^{-1}$  proves the absence of metal-oxide bonding [13, 14]. The surface charge of the catalyst was revealed from the zeta potential and was found to be  $-19.4\text{ mV}$ , which indicated that the catalyst had a negative surface charge and could be employed as a base. The size of the nanoparticles formed was confirmed by DLS analysis and found to be 310 d.nm. The SAED pattern obtained confirmed the crystalline nature of the sample (Fig. 2c). EDX analysis (Fig. 2d) confirmed the presence of Ni (0.29 at.%), Ag (2.86 at.%), and C (96 at.%). Thus, from IR and EDX spectrum, it is clear that the nanoparticles exist as metals and not as oxides. TEM image at magnifications 5 nm is as shown in Fig. 2e. The existence of metal nanoparticles on the carbon support is clearly visible from the TEM images, and it is seen that the particles are spherical in shape [15].

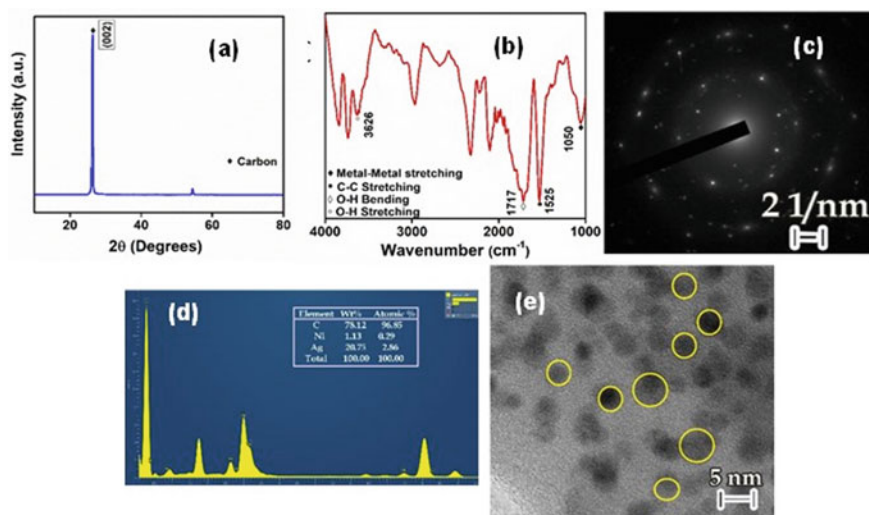


**Fig. 2** a X-ray diffraction, b IR spectrum, c SAED pattern, d EDS spectrum, e TEM images of Ni-Ag/C

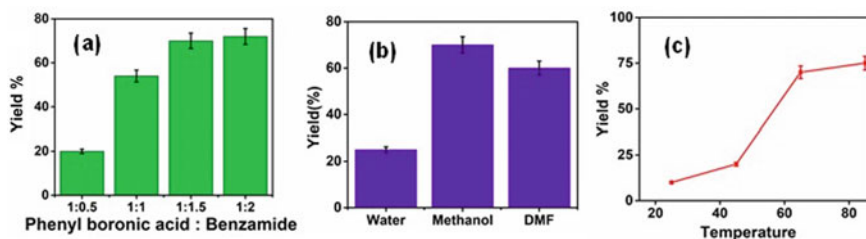


**Fig. 3** Effect of **a** Atomic ratio of reactants, **b** Solvent, **c** Temperature, on yield of N-Phenyl benzamide

### 3.2 Chan-Lam Coupling Reaction

Optimization studies for coupling of benzamide and phenyl boronic acid were carried out by studying the effect of temperature and initial concentration of reactants. Figure 3a shows the effect of varying concentration of reactants. Phenyl boronic acid and benzamide in the ratio 1:0.5, 1:1, 1:1.5, and 1:2 gave 20, 54, 70, and 72% yields, respectively. Hence it was inferred that a slight excess of nucleophile was necessary for good yields of the final product. With further increase in concentration of nucleophile (1:2), no major change in yield was seen. Thus atomic ratio of phenyl boronic acid and benzamide was optimized as 1:1.5. A Cu-based USY zeolite reported by Garnier et al. with 10 mol % catalyst concentration in presence of pyridine gave similar yields of the product [6].

The choice of solvent also played a major role in deciding the yield of the reaction. Water, methanol, and DMF were tested for the above reaction, and methanol proved to show a maximum yield of the product probably due to greater solubility of reactants in methanol (Fig. 3b). The effect of temperature was studied by carrying out the reaction at 25, 45, 65, and 85 °C (Fig. 3c). It was seen that at room temperature, very less conversion of the reactants was obtained. As the temperature increased from 45 °C to 65 °C, the yield obtained increased from 20 to 70%. However, with a further increase in temperature to 85 °C, a slight increase in yield was seen. Hence it was inferred that 65 °C was the optimized temperature for coupling of benzamide and phenyl boronic acid. In 2 h, no conversion of the reactants occurred. As time increased from 10 to 17 h, yield of N-Phenyl benzamide increased from 30 to 70%. On increasing the reaction time to 30 h, there was a slight increase in yield from 70 to 75%. Hence, at 17 h, maximum yield was obtained.

### 3.3 Characterization of N-phenyl Benzamide

The purified product obtained after column chromatography was a white solid with a melting point of 160–162 °C. The product was subjected to  $^1\text{H}$  NMR,  $^{13}\text{C}$  NMR,

and mass spectrometry. The following results were obtained which confirmed the formation of N-Phenyl benzamide.

$^1\text{H}$  NMR (300 MHz,  $\text{CDCl}_3$ ):  $\delta$  = 7.90 (s, 1 H), 7.86 (d, 2 H), 7.80 (br s, 1 H), 7.66–7.63 (m, 2 H), 7.53 (t, 1 H), 7.35 (t, 2 H), 7.19–7.13 (t, 1 H)

$^{13}\text{C}$  NMR NMR (75 MHz,  $\text{CDCl}_3$ ):  $\delta$  = 166.1, 137.9, 135.3, 131.8, 129.1, 129.0, 127.0, 124.9, 120.6 MS (DCI, +):  $m/z$  (%) = 198 (100)  $[\text{M} + \text{H}]^+$ , 215 (25)  $[\text{M} + \text{NH}_4]^+$

## 4 Conclusion

Ni-Ag bimetallic nanoparticles on carbon substrate were synthesized successfully using a simple and efficient procedure. The procedure used is a simple technique and gives no oxide particles. It can be extended to other bimetallic as well as trimetallic catalysts. The catalyst was employed in Chan-Lam coupling as a model reaction using benzamide and phenylboronic acid. The key feature of this synthesis involves simple synthesis of catalyst, mild reaction conditions, and fairly good selectivity. The development of such catalysts opens a new dimension for organic synthesis. The applicability of several such bimetallic and trimetallic catalysts can be tested in other organic transformations as well.

## References

1. Sankar M, Dimitratos N, Miedziak PJ, Wells PP, Kiely CJ, Hutchings GJ (2012) Designing bimetallic catalysts for a green and sustainable future. *Chem Soc Rev* 41:8099–8139. <https://doi.org/10.1039/c2cs35296f>
2. Anand S, Pinheiro D, Sunaja Devi KR (2021) Recent advances in hydrogenation reactions using bimetallic nanocatalysts: a review. *Asian J Org Chem* 10:3068–3100. <https://doi.org/10.1002/ajoc.202100495>
3. Hannagan RT, Giannakakis G, Flytzani-Stephanopoulos M, Sykes ECH (2020) Single-atom alloy catalysis. *Chem Rev* 120:12044–12088. <https://doi.org/10.1021/acs.chemrev.0c00078>
4. Allen AE, MacMillan DWC (2012) Synergistic catalysis: a powerful synthetic strategy for new reaction development. *Chem Sci* 3:633. <https://doi.org/10.1039/c2sc00907b>
5. Chen JQ, Li JH, Dong ZB (2020) A review on the latest progress of Chan-Lam coupling reaction. *Adv Synth Catal* 362:3311–3331. <https://doi.org/10.1002/adsc.202000495>
6. Garnier T, Sakly R, Danel M, Chassaing S, Pale P (2017) Chan-Lam-type C-N cross-coupling reactions under base- and ligand-free CuI-zeolite catalysis. *Synth* 49:1223–1230. <https://doi.org/10.1055/s-0036-1588652>
7. Zheng T, Jiang K, Ta N, Hu Y, Zeng J, Liu J, Wang H (2019) Large-scale and highly selective  $\text{CO}_2$  electrocatalytic reduction on nickel single-atom catalyst. *Joule* 3:265–278. <https://doi.org/10.1016/j.joule.2018.10.015>
8. Sharma C, Sharma N, Sharma S, Sharma S, Paul S (2021) Nano-rod like morphology of Ni@ $\text{Fe}_3\text{O}_4$ -NDCs on interaction of NDC-supported  $\text{Fe}_3\text{O}_4$  with nickel NPs: an efficient catalyst for ligand free Chan-Lam coupling reaction in aqueous medium. *Curr Res Green Sustain Chem* 4:100133. <https://doi.org/10.1016/j.crgsc.2021.100133>



9. Sharma N, Choudhary A, Kaur M, Sharma C, Paul S, Gupta M (2020) Modified graphene supported Ag-Cu NPs with enhanced bimetallic synergistic effect in oxidation and Chan-Lam coupling reactions. *RSC Adv* 10:30048–30061. <https://doi.org/10.1039/d0ra01540g>
10. Arora N, Thangavelu K, Karanikolos GN (2020) Bimetallic nanoparticles for antimicrobial applications. *Front Chem* 8:1–22. <https://doi.org/10.3389/fchem.2020.00412>
11. Zhou S, Shang L, Zhao Y, Shi R, Waterhouse GIN, Huang YC, Zheng L, Zhang T (2019) Pd single-atom catalysts on nitrogen-doped graphene for the highly selective photothermal hydrogenation of acetylene to ethylene. *Adv Mater* 31:1–7. <https://doi.org/10.1002/adma.201900509>
12. Sudhasree S, Banu AS, Brindha P, Kurian GA (2014) Synthesis of nickel nanoparticles by chemical and green route and their comparison in respect to biological effect and toxicity. *Toxicol Environ Chem* 1:12. <https://doi.org/10.1080/02772248.2014.923148>
13. Hwang SW, Umar A, Dar GN, Kim SH, Badran RI (2014) Synthesis and characterization of iron oxide nanoparticles for phenyl hydrazine synthesis and characterization of iron oxide nanoparticles for phenyl hydrazine sensor applications. <https://doi.org/10.1166/sl.2014.3224>
14. Sharma A, Dixit R, Sharma S, Dutta S, Yadav S, Arora B, Gawande MB, Sharma RK (2021) Efficient and sustainable Co<sub>3</sub>O<sub>4</sub> nanocages based nickel catalyst: a suitable platform for the synthesis of quinoxaline derivatives. *Mol Catal* 504:111454. <https://doi.org/10.1016/j.mcat.2021.111454>
15. Chau JLH, Chen C, Yang C (2017) Facile synthesis of bimetallic nanoparticles by femtosecond laser irradiation method. *Arab J Chem* 10:S1395–S1401. <https://doi.org/10.1016/j.arabjc.2013.04.014>

# Fabrication of Two-Dimensional MoS<sub>2</sub> Thin Film Using Chemical Vapor Deposition (CVD) for Gas Sensing Application



Priyanka Berwal, Paul Singh, Suman Rani, Smriti Sihag, Sunil Kumar, Anushree Jatrana, Amit Kumar Gangwar, and Vinay Kumar

**Abstract** MoS<sub>2</sub> in two dimensions (2D) has gained intensive interest as it has wide range of uses in diverse sectors like catalysis, gas sensing field, supercapacitor, hydrogen storage, optoelectronics, and transistors. In this work, the MoS<sub>2</sub> thin film has been grown via a chemical vapor deposition (CVD) approach. The fabricated thin layer of MoS<sub>2</sub> was investigated using various methods such as XRD and FE-SEM. The microstructural and compositional studies were conducted using these techniques to identify the quality and characteristics of the developed MoS<sub>2</sub> thin layer. The XRD results revealed the crystalline nature of the sample, having 44 nm of crystallite size and FE-SEM data showed nano-flakes like structure of MoS<sub>2</sub> grown on the glass substrate which provided active sites for NO<sub>2</sub> molecule to adsorbed and desorbed and quick charge transfer of gas molecules. The outcomes demonstrated the ability of such a MoS<sub>2</sub> nanostructure for creating an effective NO<sub>2</sub> gas sensor.

**Keywords** MoS<sub>2</sub> · Chemical vapor deposition (CVD) · Gas sensing

---

P. Berwal · P. Singh · S. Rani · S. Sihag · S. Kumar · V. Kumar (✉)  
Department of Physics, COBS&H, CCS Haryana Agricultural University, Hisar, Haryana 125004, India  
e-mail: [vinay23@hau.ac.in](mailto:vinay23@hau.ac.in)

A. Jatrana  
Department of Chemistry, COBS&H, CCS Haryana Agricultural University, Hisar, Haryana 125004, India

A. K. Gangwar  
CSIR-National Physical Laboratory, Dr. K.S.Krishnan Marg, New Delhi 110012, India  
Academy of Scientific and Innovative Research (AcSIR), Ghaziabad 201002, India

## 1 Introduction

Due to rapid population increase, development in the industrial sector, motor fuel combustion, poisonous gas emissions from chemical industries, and gas explosion incidents, the environmental condition is getting worse every day [1]. Due to continual exposure to harmful gases, such as CO, NO<sub>2</sub>, H<sub>2</sub>S, NH<sub>3</sub>, present in the environment, humans, and animals suffer a lot, including health problems such as cancer, heart disease, and lung illness. Therefore, the early recognition of these diseases needs sensing of toxic gases to monitor the healthcare systems [2]. Nitrogen oxide gases (NO<sub>x</sub> = NO<sub>2</sub>, NO) are the most toxic and frequent contaminating gases among all poisonous and hazardous gases, generally resulting from exhaustion. Due to the excessive exposure of NO<sub>2</sub> gas to human beings, may lead to respiratory issues [3]. So, to protect human health and indoor and outdoor surroundings, there is a need of sensitive and specific NO<sub>2</sub> gas sensors [4]. Recently, various nano-materials, such as 2D materials, metal oxide, polymers, have been employed as gas sensors. Due to their atomically thin layered structures produced by Vander Waals forces, two-dimensional (2D) materials based on graphene and transition metal dichalcogenides (TMDs) have recently gained much interest in the field of gas sensing. These materials are considered to be ideal for the adsorption and desorption of gas molecules at an ambient temperature [5]. Among them, MoS<sub>2</sub> is a popular two-dimensional (2-D) layered material that offers considerable promise for gas sensors because of its exceptional features like a high surface-to-volume ratio and adequate gas sensitivity. Additionally, MoS<sub>2</sub> thin film's remarkable mechanical flexibility and tunability of their wide intrinsic band gap (1.2–1.8 eV) promote its usage as a semiconductor for flexible electronic devices [6]. Researchers are now emphasizing more on the scalable synthesis of high-quality MoS<sub>2</sub> layers via chemical vapor deposition (CVD) technology to develop and improve the performance of electronic devices [7]. The current study used chemical vapor deposition to manufacture MoS<sub>2</sub> thin films on a glass substrate for gas sensing applications.

## 2 Experimental Details

### 2.1 Materials and Methodology

Sigma Aldrich provided Molybdenum trioxide (MoO<sub>3</sub>) and sulfur powder (99.99% purity) with an average particle size of less than 150 μm. Glass substrate was purchased from the local market. The Silver paste was purchased from Sigma Aldrich (99.99% purity) for thin film contacts.

A MoS<sub>2</sub> thin film was made on a glass substrate by employing a chemical vapor deposition technique. A two zone tube furnace was used for the CVD of MoS<sub>2</sub>. Before deposition, the ultrasonic cleaning of the glass substrate in acetone and distilled (DI) water was done. A quartz boat containing 250 mg of S powder was placed in the

first zone and the other boat containing the 20 mg of MoO<sub>3</sub> powder was located in the center of the tube (high temperature zone). The glass substrate was used for deposition on another boat next to MoO<sub>3</sub>. Before the temperature operation, 200 sccm of Argon gas was pumped into the tube and monitored by a mass flow controller to eliminate the hosting gases. The reaction chamber was enclosed and heated to 800 °C (MoO<sub>3</sub> zone) having the rate of 10 °C/min. The argon gas having flow rate of 70 sccm passed through the furnace during this temperature which was sustained for 10 min. After the reaction was ended, the furnace allowed to cool naturally.

## 2.2 Characterizations

The analysis of the structural properties of the as-prepared MoS<sub>2</sub> film were investigated using a Rigaku diffractometer having Copper K $\alpha$  radiation with a wavelength of 1.54 Å and to examine the morphological properties of fabricated MoS<sub>2</sub> on a glass substrate, field emission scanning electron microscope (FE-SEM) technique was used.

## 3 Results and Discussion

The observed XRD spectra of MoS<sub>2</sub> film grown on a glass substrate shows significant peaks at 14.1°, 37.11°, 44.3°, and 60.34° corresponding to (002), (100), (006), (110). Figure 1a shows all XRD diffraction peaks in XRD spectra attributed to hexagonal MoS<sub>2</sub>, and no impurity phase diffraction peaks can be identified, proving that only one phase of MoS<sub>2</sub> was produced. The strong diffraction peak corresponds to the (002) crystal plane. Using the formula proposed by Debye Scherrer

$$D = \frac{K\lambda}{\beta \cos \theta} \quad (1)$$

where  $D$  is the crystallite size,  $K = 0.9$  denotes the shape factor,  $\lambda = 1.54$  Å is the wavelength of X-rays used,  $\beta$  denotes the full width of half maxima, the crystallite size of the material was evaluated. The estimated average crystallite size for the developed MoS<sub>2</sub> layer is 44 nm.

The morphology of the as-prepared material captured by FE-SEM have shown in Fig. 1b. The nano-flakes-like structure of grown MoS<sub>2</sub> thin film on a glass substrate at various magnifications have shown.

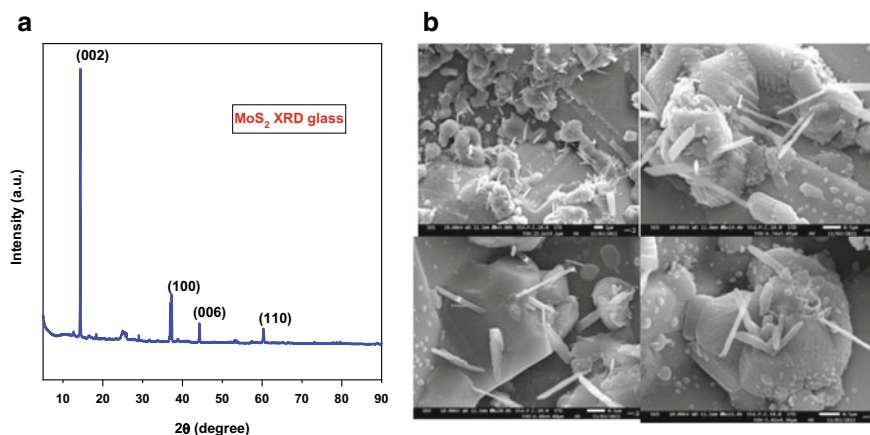


**Fig. 1** a XRD pattern of grown MoS<sub>2</sub> layer on a glass substrate b FE-SEM images of as-prepared MoS<sub>2</sub>

### 3.1 Gas Sensing Performance

The gas sensing parameters of MoS<sub>2</sub> film analyzed in terms of the % response, response time, and recovery time. The silver paste was deposited on grown thin film of MoS<sub>2</sub> for electrode contacts. All electrical evaluations and the device's gas sensing parameters were conducted in a sealed vacuum environment at air temp. The current versus time measurements were recorded using the Keithley 2450 source-meter. NO<sub>2</sub> gas of 200 ppm concentration (sigma gas 99% pure) was employed as the test-gas source. The Target gas and N<sub>2</sub> gas were supplied into the chamber having fixed value of 100 sccm. To control and vary the amount of flow of the gas, two mass flow controllers (MFC) were used and software measuring panels were used to capture all of the data. The formula for calculating the as-prepared gas sensor's percentage response in terms of current is shown in Eq. 2:

$$\%R = \frac{|I_a - I_g|}{I_a} \times 100 \quad (2)$$

where  $I_a$  and  $I_g$  denotes the measuring currents of the sensor during air and of the analyte gas, respectively. The time needed to reach 90% of its maximum current value during target gas presence is known as the response time. The duration of time required to achieve 10% of the air current baseline is known as recovery time.

At room temperature (RT), the synthesized MoS<sub>2</sub> sensor presents linear plot of current (I) versus voltage (V) in Fig. 2a, demonstrating an Ohmic contact between the MoS<sub>2</sub> and the electrodes. Figure 2b illustrates the MoS<sub>2</sub> film's current response at room temperature, where the current decreased after introduction to 200 ppm of NO<sub>2</sub> gas. The sensor displayed a 15.3% response for 200 ppm of NO<sub>2</sub> at room temperature with a response time of 120 s; however, recovery was poor (25 min) due to a tight

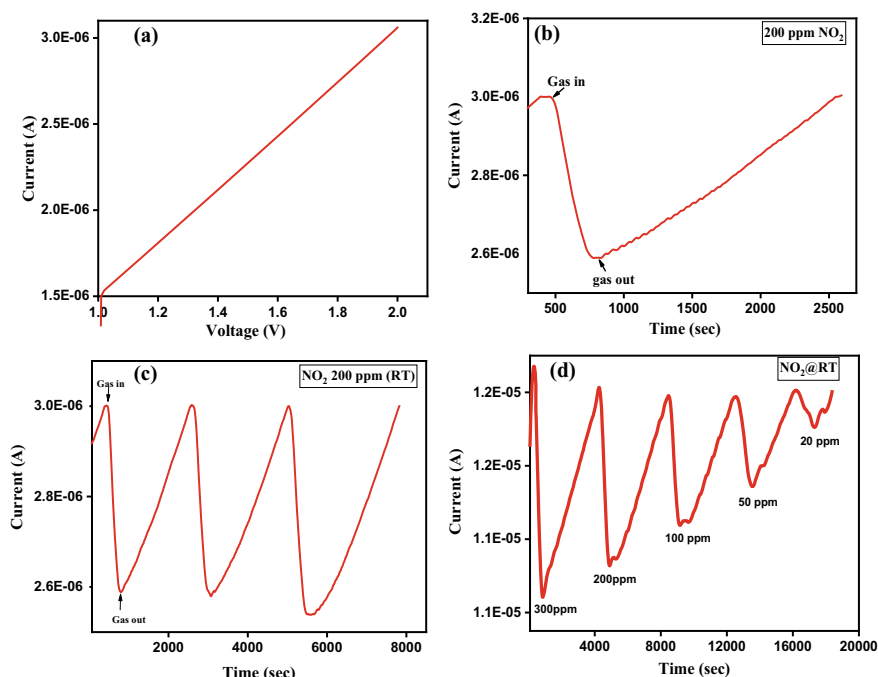


**Fig. 2** **a** Voltage versus current graph of prepared MoS<sub>2</sub> layer at room temp, **b** Current response curve of fabricated MoS<sub>2</sub> sensor for NO<sub>2</sub> at 200 ppm, **c** Repeatability cycle of the sensor for NO<sub>2</sub> gas at 200 ppm, **d** The sensor's current response curve to various NO<sub>2</sub> concentrations at room temperature

binding between MoS<sub>2</sub> and NO<sub>2</sub> gas molecules. Figure 2c displays the repeatability curve of the MoS<sub>2</sub> sensor for 200 ppm at RT. Figure 2d depicts the typical dynamic response curve of the as-prepared MoS<sub>2</sub> sensor for various concentrations of NO<sub>2</sub>. The sensitivity decreases as the concentration of NO<sub>2</sub> decreases from 300 to 20 ppm.

Here, the sensor's lower detection limit for NO<sub>2</sub> gas with a sensitivity of 0.86% can be defined as 20 ppm.

## 4 Conclusion

The fabrication of the MoS<sub>2</sub> thin layer in a tube furnace using a single CVD method involved the sequential deposition of MoO<sub>3</sub> and sulfur powder successfully. The chemiresistive gas sensor based on as-prepared MoS<sub>2</sub> films demonstrated a sensitivity of 15.3% to 200 ppm NO<sub>2</sub> at environment temperature, with quick response time (120 s) and have a lowest detection limit of 20 ppm. By optimizing their structural design and interdigitated kind of connections, these sensors' gas sensing performance can be improved.

## References

1. Shokri A (2016) Gas sensor based on MoS<sub>2</sub> monolayer. *Sens Actuators B Chem* 236:378–385
2. Joshi N (2018) A review on chemiresistive room temperature gas sensors based on metal oxide nanostructures, graphene and 2D transition metal dichalcogenides. *Microchim Acta* 185:213
3. Laera AM (2020) Synthesis of nanocrystalline ZnS/TiO<sub>2</sub> films for enhanced NO<sub>2</sub> gas sensing. *Thin Solid Films* 709:138–190
4. Shendage SS (2017) Sensitive and selective NO<sub>2</sub> gas sensor based on WO<sub>3</sub> nanoplates. *Sens Actuators B* 240:426–433
5. Yang S (2017) Gas sensing in 2D materials. *Appl Phys Rev* 4:021304
6. Kumar S (2022) Sustainable and scalable approach for enhancing the electrochemical performance of molybdenum disulfide (MoS<sub>2</sub>). In: *Advances in materials science and engineering*
7. Liu KK (2012) Growth of large-area and highly crystalline MoS<sub>2</sub> thin layers on insulating substrates. *Nano Lett* 12(3):1538–1544

# Performance Evaluation of CNT FET with High-K Dielectric



Md Akram Ahmad and Jitendra Kumar

**Abstract** In this article, the quantum transport properties of carbon nanotube (CNT)-based field-effect transistors (FETs) with the effect of different gate-oxide dielectric strength are deliberate through non-equilibrium Green's function (NEGF) formalism in the real space approach. All the simulations are done using the atomistic device simulator, NanoTCAD ViDES, under the NEGF framework. It is observed from the device simulator results that with the increase in dielectric strength, the ON-current ( $I_{ON}$ ) of the device increased and the leakage current ( $I_{OFF}$ ) reduced; also, drain-induced-barrier-lowering decreased. It is also observed that the two significant analog figures-of-merit (FOM), transconductance ( $g_m$ ) and transconductance generation factor (TGF) of CNT FET is also increased with an increase in gate dielectric strength, which indicates that CNT FETs have significant reliance on the dielectric strength of the gate-oxide materials.

**Keywords** Carbon nanotube (CNT) · Field-effect transistors (FETs) · Non-equilibrium Green's function (NEGF)

## 1 Introduction

The recent development in technology has forced device sizes into the nanoscale range, which is the key to advancing the efficiency of digital circuits. However, shrinking CMOS devices poses difficulties such as drain-induced-barrier-lowering (DIBL), subthreshold slope (SS), velocity saturation, and leakage current; as a result, maintaining Moore's Law is intriguing given the multiple restrictions on Si-based transistors. In order to replace the current silicon-based technology, scholars are looking for alternatives to these devices [1–3]. Due to their outstanding qualities, carbon nanotubes (CNTs) have emerged as a strong contender for silicon-based device integration. When compared to CMOS devices, CNT-based devices produce a decent ON-current ( $I_{ON}$ ) because of their high mobility and velocity saturation [3,

---

M. A. Ahmad (✉) · J. Kumar

Department of Electronics Engineering, IIT (ISM), Dhanbad, India

e-mail: [akram14407@gmail.com](mailto:akram14407@gmail.com)



4]. Additionally, CNTs with tunable bandgaps that are smaller in diameter reveal less OFF-current ( $I_{OFF}$ ) [4, 5]. In the context of this, CNT recommends a high current ON/OFF ratio ( $I_{ON}/I_{OFF}$ ) without experiencing short-channel effects (SCEs), which are detrimental in traditional metal oxide semiconductor field-effect transistors (MOSFET). Therefore, to create CNTFET in modern times, CNT is used as a channel material in a field-effect transistor (FET) [6].

This study proposes a double-gated carbon nanotube field-effect transistor (CNTFET) using several gate insulator high-k dielectric materials and analyses the performance parameters for each material.

## 2 Device Structure and Simulation Methodology

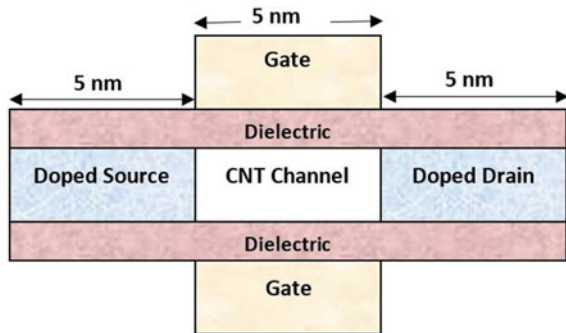
Figure 1 shows the double-gated CNT FET that we employed in our simulation. The device structure features a band gap of 0.75 eV and chirality of (13, 0) with a channel length of 5 nm. The drain and source, which are extensions of channel length, are of 5 nm size. To create an n-type extension of the CNT channel, a donor with a 5 mM fraction is doped into the source and drain regions. All simulations were performed using the atomistic device simulator NanoTCAD ViDES at 298 K with the drain biased at 0.5 V voltage.

The non-equilibrium Green’s function (NEGF) framework and a tight-binding model method were used to simulate CNT FETs [7]. In order to derive the retarded Green’s function, the model must first determine the suitable Hamiltonian matrix for the channel [7] in real space.

$$G(E) = \left[ EI - H - \sum_D - \sum_S \right]^{-1}$$

where  $E$ ,  $I$ ,  $H$ ,  $\sum_D$ , and  $\sum_S$  are the energy, identity matrix, Hamiltonian of CNT, self-energy matrix of the drain, and self-energy of source, respectively. The atomic

Fig. 1 The simulated CNTFET structure



cooperation between carbon–carbon (C–C) atoms is described by the first closest neighbor tight-binding approximation. The hole and electron concentrations can be computed as [8] once  $G(E)$  has been determined. In order to obtain electrostatic potential self-consistently after that, the Newton–Raphson iteration approach is used. As mentioned in [8], drain current is finally attained.

### 3 Results and Discussion

Using the method described above, the performance evaluation of CNTFETs with different gate insulator dielectric materials is presented in the section below. Here, we evaluate the devices using criteria like transfer properties, transconductance, transconductance generation factor (TGF), DIBL, ON-current ( $I_{ON}$ ), and OFF-current ( $I_{OFF}$ ) of the device.

The transfer characteristics of the device with various dielectric constants are shown in Fig. 2a. The graph demonstrates that when  $k$  values rise, the drain current also rises. It happens because, as illustrated in Fig. 2b, as the dielectric constant rises, the energy bandgap expands, however, the declining transmission coefficient, Fig. 2c, caused the  $I_{OFF}$  to drop which is observed in Fig. 2d. It is worth mentioning that the ON-current and OFF-current are set at  $I_{DS}$  ( $V_{DS} = 0.5$  V,  $V_{GS} = 0.8$  V) and  $I_{DS}$  ( $V_{DS} = 0.5$  V,  $V_{GS} = 0$  V), respectively. Furthermore, the band-to-band tunneling currents decrease as the dielectric constant increases, whereas the thermionic emission current, the thermally induced movement of charge carriers from a potential-energy barrier, grows. In contrast, increasing thermionic emission current causes more  $I_{ON}$  as shown in Fig. 2d.

Additionally, decreasing band-to-band tunneling current results in a decrease in  $I_{OFF}$ . As a result, the  $I_{ON}/I_{OFF}$  ratio is raised [9, 10], which is observed in Fig. 2e. Figure 2f demonstrates how  $g_m$  first rises with  $V_{GS}$  with different gate-oxide materials before reaching its highest point. It is observed that the  $g_m$  is maximum for the  $HfO_2$  gate-oxide materials and the minimum is for  $SiO_2$  gate-oxide material, it is due to the proportionality relation of  $g_m$  with the drain current. It is also observed that once it reaches the peak value, then the  $g_m$  decreases with  $V_{GS}$ , because of decreased mobility of the device with high  $V_{GS}$ . The TGF denotes the effectiveness of using the drain current to derive a recognized value of  $g_m$ . The larger value of TGF promises that the device is appropriate for amplifier designs, especially for low-power operation. It is observed from Fig. 2f that the device with high dielectric materials exhibits higher TGF as compared to lower dielectric materials. It is witnessed that, at low  $V_{GS}$ , the maximum value of TGF is attained, and it degrades severely as  $V_{GS}$  increases, which implies a high gain at low-power dissipation.

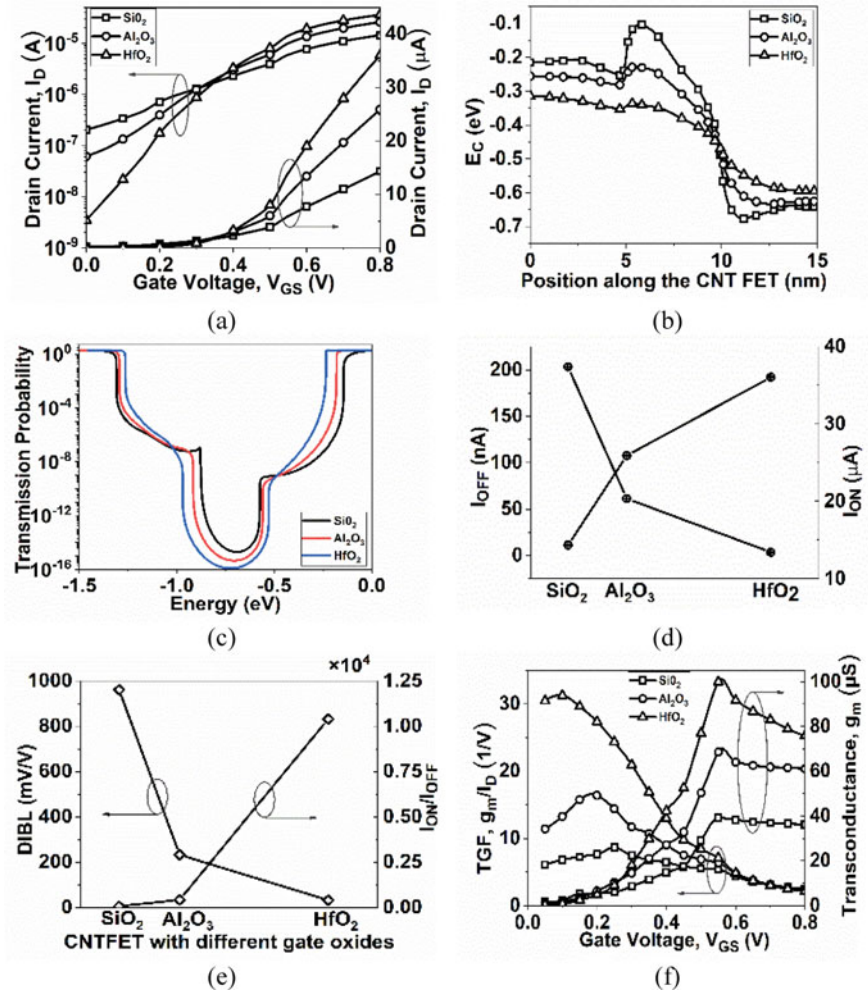


**Fig. 2** **a** Transfer characteristics at  $V_{DS} = 0.5$  V, **b** CB profile of the CNT FETs at ON-state, **c** Variation of transmission probability with energy, **d** Variation of ON-current and OFF-current with different dielectric gate-oxide, **e** Variation of current ON/OFF ratio and DIBL, **f** Variation of  $g_m$  and TGF as a function of  $V_{GS}$  at  $V_{DS} = 0.5$  V

### 4 Conclusion

The optimization of the gate dielectric material for the device has been done through an atomistic device simulator, NanoTCAD ViDES. Both static and dynamic performances of CNT FET have been analyzed by varying gate dielectric materials. A study is made for SCEs like DIBL and also for important analog/RF figures-of-merit (FOMs) like  $g_m$  and TGF by changing the gate dielectric materials for double gate

CNT FET configurations. It is observed that devices that have  $\text{HfO}_2$  as a gate-oxide dielectric have 39.1 and 151% raised values of ON-current compared to devices with  $\text{Al}_2\text{O}_3$  and  $\text{SiO}_2$  as the dielectric, respectively. However, the off-current of the device with  $\text{HfO}_2$  as a gate-oxide dielectric is a decreased value of 94.3 and 98.3% compared to the device with  $\text{Al}_2\text{O}_3$  and  $\text{SiO}_2$  as the dielectric, respectively. Moreover, the DIBL of the device with  $\text{HfO}_2$  as a gate-oxide layer is decreased by 86 and 96.6% compared to the device with  $\text{Al}_2\text{O}_3$  and  $\text{SiO}_2$  as the gate-oxide layer. For analog performances the  $g_m$  of the device with  $\text{HfO}_2$  is increased by 45.8 and 155%, however, TGF is raised by 90.7 and 261.8%, compared to the device with  $\text{Al}_2\text{O}_3$  and  $\text{SiO}_2$  as the gate-oxide layer. So the proposed CNT FET structure with a high-k dielectric as a gate-oxide layer has much better performance than the device with a low-k dielectric and may be considered a suitable candidate for high-speed low-power switching devices for the design of analog and RF circuits.

## References

1. Skotnicki T, Hutchby JA, King T-J, Wong H-SP, Boeuf F (2005) The end of CMOS scaling: toward the introduction of new materials and structural changes to improve MOSFET performance. *IEEE Circuits and Dev Magaz* 21:16–25
2. Rabaey JM, Malik S (2008) Challenges and solutions for late-and postsilicon design. *IEEE Design and Test of Comp* 25:296–302
3. Usmani FA, Hasan M (2010) Carbon nanotube field effect transistors for high performance analog applications: an optimum design approach. *Microelect J* 42:395–402
4. Banerjee S, Chaudhuri A, Chakrabarty K (2020) Analysis of the impact of process variations and manufacturing defects on the performance of carbon-nanotube FETs. *IEEE Trans Very Large Scale Integr Syst* 28:1513–1526
5. Tamersit K, Madan J, Kouzou A, Pandey R, Kennel R, Abdelrahem M (2022) Role of junctionless mode in improving the photosensitivity of sub-10 nm carbon nanotube/nanoribbon field-effect phototransistors: quantum simulation, performance assessment, and comparison. *Nanomaterials* 5:1639
6. McEuen PL, Fuhrer MS, Park H (2002) Single-walled carbon nanotube electronics. *IEEE Trans Nanotechnol* 1:78–85
7. Djamil R, Aicha K, Cherifa A, Djeflal F (2016) Impacts of high-k gate dielectrics and low temperature on the performance of nanoscale CNTFETs. *J Comput Electron* 15:1308–1315
8. Information on <http://vides.nanotcad.com/vides>
9. Fallah M, Faez R, Jafari AH (2013) Simulation of carbon nanotube field-effect transistor with two different gate insulator. *Scientia Iranica* 20:2332–2340
10. Owlia H, Keshavarzi P (2014) Investigation of the novel attributes of a double-gate graphene nanoribbon FET with  $\text{AlN}$  high-K dielectrics. *Superlattices Microstruct* 75:613–620

# Employing Temperature-Dependent Photoluminescence of Tin Oxide (SnO<sub>2</sub>) Nanostructures for Designing of Efficient Light-Emitting Diodes



Mohd Azharuddin and Rana Tabassum

**Abstract** The temperature influenced photoluminescence property of any material is an efficient way to analyze the thermal transport behavior of the charge carriers within that material. The measurement of photoluminescence intensity is one of the methods to predict the excitation of charge carrier over the metastable states within the materials. In this paper, we explained the temperature variable photoluminescence of tin oxide (SnO<sub>2</sub>) nanostructures fabricated via a hydrothermal approach. The optics and photonic-based properties of the fabricated SnO<sub>2</sub> nanostructures was studied using absorption spectra by which its bandgap was measured. At the same time, by careful evaluation of the XRD peaks, the presence of SnO<sub>2</sub> in the nanostructures was confirmed. Using scanning electron microscopy (SEM), it was confirmed that the synthesized SnO<sub>2</sub> nanoflower structures was in the size range of 200–500 nm. The reported results suggest that the trapping of the electrons over the defects level at higher temperature regime were measured by temperature variable photoluminescence intensity. With the findings of the peaks in the photoluminescence spectra, we have discussed various types of defects found within the fabricated SnO<sub>2</sub> nanostructures and hence provide the mechanism of the excitation of charge carriers from the valence band to the conduction band of the SnO<sub>2</sub> nanostructures. Using the temperature variable photoluminescence property of the synthesized SnO<sub>2</sub> nanostructures, the possible device applications was employed via Commission International de l'Eclairage (CIE) diagram which is very useful method for fabrication and designing of light-emitting diodes (LEDs).

**Keywords** Tin oxide (SnO<sub>2</sub>) · Temperature variable photoluminescence · Metastable states · Light-emitting diodes (LEDs)

---

M. Azharuddin · R. Tabassum (✉)

Centre for Nanoscience and Nanotechnology, Jamia Millia Islamia (A Central University), New Delhi 110025, India

e-mail: [rtabassum1@jmi.ac.in](mailto:rtabassum1@jmi.ac.in)

## 1 Introduction

From the past decades, nanostructured materials attracted much attention in designing, modeling, and fabrications /characterizations of various devices for diversified applications. These nanostructures were used as detecting materials for several electrical, electronic, optical, and photonic devices [1–5]. These nanostructures possess several favorable properties which can be used further so as to obtain improved performance of the devices. Due to the improved response of nanomaterials-based fabricated devices, researchers have been indulged in carrying out work on the development of nanostructured materials with several diversified morphologies and sizes. These synthesized nanostructures may be in the form of 0D, 1D, and 2D dimensions nanomaterial or may be mixed phase materials such as nanoflowers, core–shell nanostructures, nanobelts, nanowires [6–11]. These several types of nanostructures possess their own tailored properties, merits/demerits as well as limitations. The main motive of each fabricated nanostructure is to improve their physical, chemical, thermal, and optical properties so as to get improved performances of the devices fabricated for a particular application. For instance, nanostructures of semiconductors oxides such as  $\text{SnO}_2$  possess lots of favorable properties in optics and photonics applications [12]. These properties may further be tuned to make it more useful by adopting particular fabrication methods and trained personals. There are various methods of fabrication of various types of nanostructures such as via chemical route [13], sol–gel method [14], thermal evaporation method [15], chemical route [16], and hydrothermal methods [17]. Using the chemical route, the prepared nanostructures may possess several byproducts which would reduce the yields of nanostructures. The hydrothermal method is found to be one of the most easy, most simple, most cost-effective, and most useful methods to fabricate nanostructures in the form of nanoflowers. Reports have been found in the fabrication of nano-sheets, nanorods, and nanospheres of  $\text{SnO}_2$  via different synthesis methods. [10, 18, 19]. The reports are also available for the fabrication of combinational nanostructures using a hydrothermal approach where one material may be semiconductor oxides and the other may be metal or carbon-based materials [20, 21]. Tin oxide ( $\text{SnO}_2$ ), one of the useful and optically active materials possesses several favorable properties for various optic and photonic devices. The tin oxide nanostructure can be fabricated using various experimental techniques to use them further for various applications. [20] Since one of the prominent applications of the prepared  $\text{SnO}_2$  nanostructure is in the fabrication, characterization, and designing of light-emitting diodes therefore in the present study, we have paid much attention in making a detailed study of the optical behavior of the synthesized  $\text{SnO}_2$  nanoflower structures. The researches have already been done on the fabrication and characterization of  $\text{SnO}_2$  using several methods so as to understand the behavior of its photoluminescence (PL) spectrum [21]. Since one can study the optical properties of a material using their absorption and photoluminescence spectrum therefore researchers have extensively evaluated the bandgap and photoluminescence spectrum of several nanostructures. They have performed experiments to obtain the lifetimes of the photoluminescence of several

semiconductor oxides such as  $\text{TiO}_2$ ,  $\text{ZnO}$ , and  $\text{SnO}_2$ . Furthermore, the photoluminescence intensity of the semiconductor oxides can also be tuned by varying their temperatures. Therefore, temperature-dependent photoluminescence is found to be a very useful technique to evaluate the thermal transport behavior in any material so as to use them further for optics and photonic applications [22].

This work is based on the synthesis and characterization of tin oxide ( $\text{SnO}_2$ ) nanoflower structures in an aqueous medium using the hydrothermal techniques to use them further in fabricating light-emitting diodes (LEDs). The main motive of fabricating such  $\text{SnO}_2$  nanostructures is to obtain temperature variable photoluminescence (PL) spectra of the synthesized  $\text{SnO}_2$  nanoflower structures for designing efficient LEDs. Apart from temperature-dependent PL, the several diversified properties of prepared  $\text{SnO}_2$  nanoflower structures were analyzed using different characterization techniques. Using SEM images, fabricated nanoflower structures of  $\text{SnO}_2$  were justified and then employing the absorption spectroscopic technique and the mathematical formulation termed as Tauc's formula, the bandgap of prepared  $\text{SnO}_2$  nanoflower structures was measured. The XRD in conjunction with SEM results gives the structural and morphological study while absorption spectra and temperature variable PL measurements gives the detailed information of the photonic application of the aforesaid  $\text{SnO}_2$  nanoflower structures. Then, hydrothermally fabricated and structurally, morphologically, and optically characterized  $\text{SnO}_2$  nanoflower structures were used in designing of efficient light-emitting diodes employing the Commission International de l'Eclairage (CIE) diagram.

## 2 Materials and Methods

### 2.1 Materials Used

Here, we have to fabricate  $\text{SnO}_2$  nanoflower structures for experimentation purpose, therefore bulk powder of  $\text{SnO}_2$  along with a solvent to dissolve  $\text{SnO}_2$  which is *N*-Methyl-2-pyrrolidone (NMP) were procured commercially from Sigma Aldrich. Both the materials were used in their pure form as obtained from the company. In addition, in the experimentation process of fabrication, we have also used de-ionized (DI) water which was obtained from in house Millipore system ( $\sim 18.2 \text{ M}\Omega$ ) planted in our university. Here, we trying to fabricate  $\text{SnO}_2$  nanoflower structures via hydrothermal route so, we also used a hydrothermal autoclave having an inbuilt facility of varying high temperatures and pressure so as to use them together while experimentation.



## 2.2 Fabrication of SnO<sub>2</sub> Nanoflower Structures Using a Hydrothermal Approach

In the present work, we have employed a hydrothermal route to fabricate the SnO<sub>2</sub> nanoflower structures. The detailed steps for the fabrication of SnO<sub>2</sub> nanoflower structures are shown Fig. 1. These SnO<sub>2</sub> nanoflower structures were fabricated using a hydrothermal approach by undergoing three steps shown in Fig. 1. In experimental method to fabricate the SnO<sub>2</sub> nanoflower structures, first of all, dispersion of a particular concentration of SnO<sub>2</sub> was prepared by continuous magnetic stirring and the addition of de-ionized water and NMP solution followed by ultra-sonication. This stirring and sonication process completes Step-I of Fig. 1. Now, in step-II, we put the already prepared SnO<sub>2</sub> dispersion solution in a hydrothermal autoclave at 120 °C temperature for approximately 10 h. Now the final suspension of the SnO<sub>2</sub> nanoflower structures was obtained. Once, the final suspension of SnO<sub>2</sub> nanoflower was obtained, we characterize it to observe its various properties by scanning electron microscopy, X-ray diffraction, absorption, and temperature variable photoluminescence measurements. Employing aforesaid characterization techniques, the morphological, structural, thermal, and optical properties were evaluated. These spectroscopic techniques were performed either in SnO<sub>2</sub> nanoflower dispersion depicted in step-II or on glass slides. To get the glass slides which possess SnO<sub>2</sub> nanoflower, we drop-casted the prepared SnO<sub>2</sub> suspension shown in step-III of Fig. 1. To perform SEM and XRD, we need SnO<sub>2</sub> nanoflower coated glass slide while absorption and temperature-dependent photoluminescence measurements were carried out in SnO<sub>2</sub> nanoflower dispersion solutions.

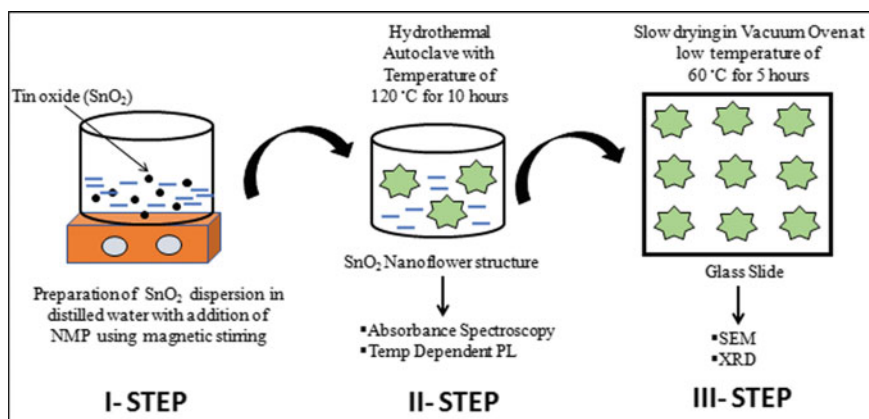


**Fig. 1** Schematic of the fabrication of SnO<sub>2</sub> nanoflower structures using the hydrothermal approach



### 3 Results and Discussion

#### 3.1 Scanning Electron Microscopy (SEM) Analysis

Since the present study is to fabricate the nanoflower structures of  $\text{SnO}_2$ , so first of all, we carried out the morphological characterization of the fabricated samples of  $\text{SnO}_2$  which has been carried out using scanning electron microscopy (SEM). The fabricated  $\text{SnO}_2$  nanoflower structures at various magnifications have been displayed in Fig. 2a–d. In Fig. 2a, b, the SEM images at  $1\ \mu\text{m}$  and  $500\ \text{nm}$ , respectively, has been shown where it has been clearly noticeable bunches of nanoflowers at two different magnifications. As the magnifications change and reaches to  $300$  and  $200\ \text{nm}$ , the bunches of nanoflower get more magnified and it has been shown petal-like nanostructures which has been depicted clearly in Fig. 2c, d. These SEM images given from  $1$  to  $200\ \text{nm}$  justified the formation of nanoflowers structures of  $\text{SnO}_2$  fabricated via hydrothermal route. We have chosen the magnification from  $1$  to  $200\ \text{nm}$  so that we can make a guess of the dimension of the fabricated nanoflower. From the magnification scale of the SEM images of Fig. 2a–d, it may be noticeable that the fabricated  $\text{SnO}_2$  flowers are nano-dimension. Further, the evaluation of crystallite size was done via X-ray diffraction technique (XRD) which is going to discuss in the next section and depicted well in Fig. 3.

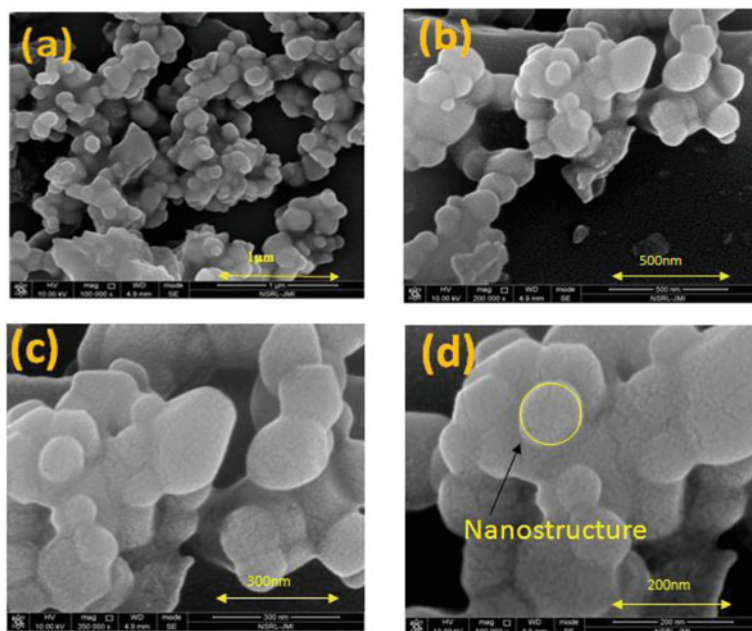


Fig. 2 SEM micrograph of the fabricated  $\text{SnO}_2$  nanoflower structure

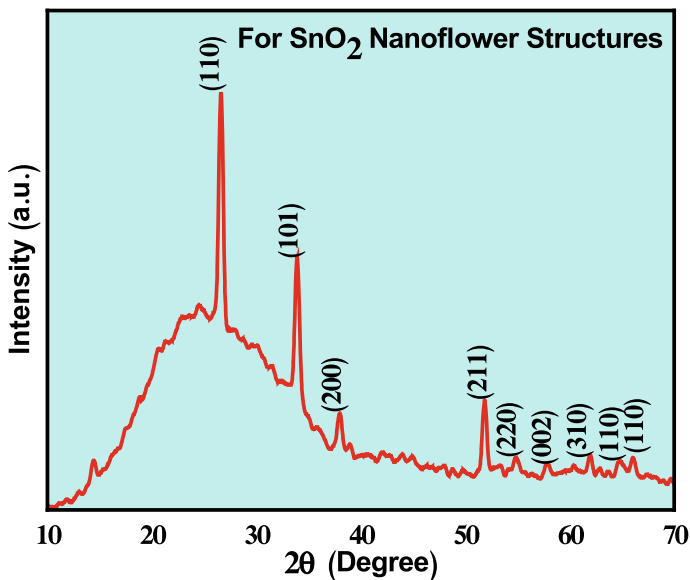


Fig. 3 XRD spectra of the fabricated SnO<sub>2</sub> nanoflower structures

### 3.2 X-Ray Diffraction (XRD) Analysis

The XRD pattern of fabricated SnO<sub>2</sub> nanostructures has been displayed well in Fig. 3. In this XRD patterns of SnO<sub>2</sub> nanostructures belong to the standard pattern found in the literature and belongs to JCPDS #006 0097. In the typical XRD pattern shown in Fig. 3, it may be noticeable that the maximum intensity was seen for the (110) peak but the peaks of (101) and (200) planes are found to be less intense in comparison to the (110) planes. All the other peaks are found to be lesser intense and are due to the synthesized nanosized structures. The XRD pattern of Fig. 3 which is obtained for SnO<sub>2</sub> nanostructures is used to analyze their phase structure and is formed in a hexagonal structure. The careful investigation of the present XRD patterns of SnO<sub>2</sub>, it may be observed that the highest diffraction peak of the fabricated SnO<sub>2</sub> nanostructures is measured at ca. 26.68°. Hence, the obtained XRD patterns confirm the formation of SnO<sub>2</sub> nanostructures.

### 3.3 Absorption-Based Characterization and Evaluation of Bandgap of Prepared SnO<sub>2</sub> Nanoflower Structures

Here, the main application of this work was guessed to design the efficient LEDs so it is useful to first investigate the optical properties of the prepared SnO<sub>2</sub> nanoflower structures. To measure basic property of the structure such as 'bandgap',

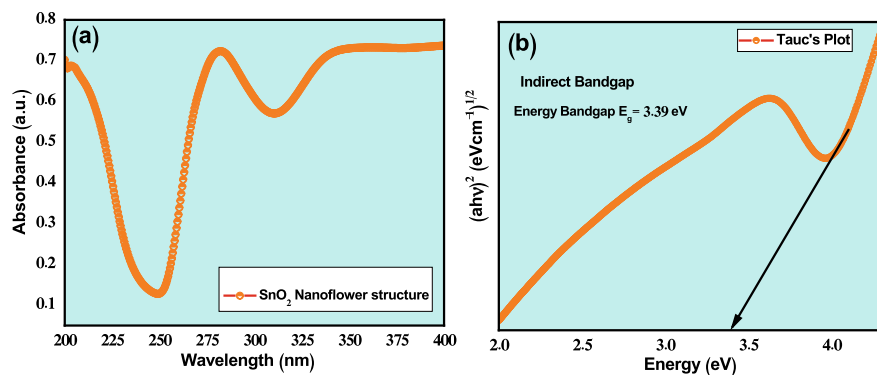


**Fig. 4** a Absorption spectra, b Tauc's plot and bandgap measurement of the fabricated SnO<sub>2</sub> nanoflower structures

we performed experiments to obtain the absorption spectra of the synthesized SnO<sub>2</sub> nanoflower structures. The findings via absorption spectra in coordination with Tauc's relationship, we evaluate its 'bandgap'. For the evaluation of the bandgap of the fabricated SnO<sub>2</sub> nanoflower structures, we employed the Tauc's formula. In Fig. 4a, the absorption spectrum of the synthesized SnO<sub>2</sub> nanoflower structures was displayed, and its corresponding Tauc's relationship and obtained value of the bandgap and is shown in Fig. 4b. It is clearly visible from Fig. 4a that two absorbance peaks were obtained at ~285 and ~340 nm wavelengths in the UV-Vis spectra of the SnO<sub>2</sub> nanoflower structures to evaluate their bandgaps using the basic mathematical relationship of the light energy,  $E_g = 1240/\lambda$ . In this work, the bandgap of the synthesized SnO<sub>2</sub> nanoflower structures were measured to be ~3.39 eV and is given in Fig. 4b.

### 3.4 Temperature Varied Photoluminescence Measurements and Commission International de l'Eclairage (CIE) Chromaticity Diagram

To further discuss the temperature influenced properties of the synthesized SnO<sub>2</sub> nanoflower structures, we have first performed the measurements for the temperature-dependent photoluminescence. Using this experimental technique, we have obtained temperature variable photoluminescence spectra of the fabricated SnO<sub>2</sub> nanoflower structures were obtained by irradiating it with laser light of wavelength typically 315 nm where the varied temperature range from 5 to 85 °C, such curves have been depicted well in Fig. 5a. In the given Fig. 5a, it is clearly noticeable that as the temperature varies from 5 to 85 °C, the PL intensity decreases continuously which is observed for all temperatures and the nature of curves of the PL intensities are nearly same. This similar trend in the PL spectra is found to be such that two peaks are observed for all the temperature ranges from 5 to 85 °C. It means that for all the

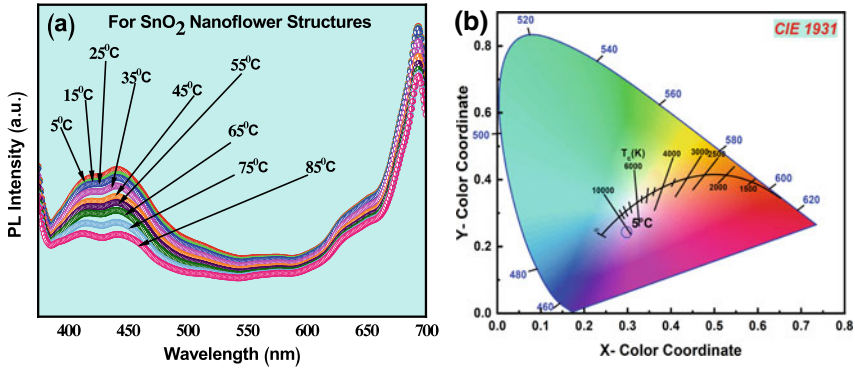


**Fig. 5** **a** Temperature-dependent photoluminescence spectrum, **b** Commission International de l’Eclairage (CIE) chromaticity diagram of the fabricated SnO<sub>2</sub> nanoflower structures

values of temperature, the nature of the curves of the PL intensity is almost same but is found to be gradually increasing in nature as the temperature changes from 5 to 85 °C that reflects the anomalous behavior. This anomalous behavior is understood by the excitation of the charge carrier from valence band to the conduction band as well as between different localized states.

Finally, we have explored the application of such fabricated SnO<sub>2</sub> nanoflower structures in several optical applications such as in fabrication of light-emitting diodes. To obtain such application, we have plotted Commission International De l’Eclairage diagram [22] using the temperature-dependent photoluminescence spectra shown in Fig. 5a. The CIE diagram is displayed in Fig. 5b where the color chromaticity coordinates ( $x, y$ ) were calculated for all the PL spectra shown in Fig. 5a. As depicted in Fig. 5b, the position of such chromaticity coordinates for the temperatures ranges from 5 to 85 °C are mainly found in the light pink region which indicates that careful fabrication of SnO<sub>2</sub> nanoflower structures may be appropriate nanostructured materials to fabricate and used as pink LEDs.

## 4 Conclusion

To conclude, we successfully synthesized SnO<sub>2</sub> nanoflower structures to study its various useful properties for optics and photonic applications. The main application of the fabricated SnO<sub>2</sub> nanoflower structures was evaluated from temperature influenced PL measurements. From the basic characterization, it may be observed that SnO<sub>2</sub> nanostructures were prepared using hydrothermal method under controlled experimental conditions. From the experimentally observed results, it is found that XRD and SEM are in accordance with each other. From the UV–Vis absorption spectra, the bandgap were measured and hence used to guess the application in various optical applications. From temperature influenced PL measurements, it may

be found that there are a sufficient amount of defects levels in the fabricated SnO<sub>2</sub> nanoflower structures and an abnormal increment was shown in the temperature varied PL intensity where the highest increment in PL intensity was found to be at  $T = 5\text{ }^{\circ}\text{C}$ . Using the optical property, i.e., bandgap and, i.e., temperature varied photoluminescence spectra, we are successful in using these SnO<sub>2</sub> nanoflower structures in several the possible device applications. The experimental results and their analysis reveals that the performed characterizations as well as CIE diagram of the fabricated SnO<sub>2</sub> nanoflower structures possess all the favorable properties which can further be used in various light-emitting diodes (LEDs).

**Acknowledgements** Dr. Rana Tabassum is grateful to the Department of Science and Technology (DST) for INSPIRE Faculty scheme and Science and Engineering Research Board for SERB-Research Scientist fellowships and Research grants.

**Declaration of Interest Statement** The authors declare that they have no conflict of interest.

## References

1. Medhi R, Li C-H, Lee SH, Marquez MD, Jacobson AJ, Lee T-C, Lee TR (2019) Uniformly spherical and monodisperse antimony and zinc-doped tin oxide nanoparticles for optical and electronic applications. *ACS Appl Nano Mater* 2(10):6554–6564
2. Wang Y, Zhu X, Xue X, Chi X, Wang R, Ji W (2022) Electron transport mechanism in colloidal SnO<sub>2</sub> nanoparticle films and its implications for quantum-dot light-emitting diodes. *J Phys D Appl Phys* 55(37):374004
3. Azharuddin M, Tabassum R (2022) Nanophotonics and optical fibers: new avenues for sensing and active devices. *Results Opt* 9:100321
4. Dalapati GK, Sharma H, Guchhait A, Chakrabarty N, Bamola P, Liu Q, Saianand G, Krishna AMS, Mukhopadhyay S, Dey A (2021) Tin oxide for optoelectronic, photovoltaic and energy storage devices: a review. *J Mater Chem A* 9(31):16621–16684
5. Tabassum R, Gupta BD (2015) Performance analysis of bimetallic layer with zinc oxide for SPR-based fiber optic sensor. *J Lightwave Technol* 33:4565–4571
6. Viana ER, González JC, Ribeiro GM, de Oliveira AG (2013) Photoluminescence and high-temperature persistent photoconductivity experiments in SnO<sub>2</sub> nanobelts. *J Phys Chem C* 117(15):7844–7849
7. Mishra SR, Ahmaruzzaman M (2022) Tin oxide based nanostructured materials: synthesis and potential applications. *Nanoscale* 14(5):1566–1605
8. Aslam M, Mahmood T, Naeem A, Ali R (2021) Investigation of HDTMA mediated sol gel synthesis of N-doped SnO<sub>2</sub> nanoparticles: studies of their electrical and optical properties. *Mater Technol* 36(3):169–178
9. Periyasamy M, Kar A (2020) Modulating the properties of SnO<sub>2</sub> nanocrystals: morphological effects on structural, photoluminescence, photocatalytic, electrochemical, and gas sensing properties. *J Mater Chem C* 8(14):4604–4635
10. Wan W, Li Y, Ren X, Zhao Y, Gao F, Zhao H (2018) 2D SnO<sub>2</sub> nanosheets: synthesis, characterization, structures, and excellent sensing performance to ethylene glycol. *Nanomaterials* 8(2):112
11. Zhao Y-F, Sun Y-P, Yin X, Yin G-C, Wang X-M, Jia F-C, Liu B (2018) Effect of surfactants on the microstructures of hierarchical SnO<sub>2</sub> blooming nanoflowers and their gas-sensing properties. *Nanoscale Res Lett* 13(1):1–11

12. Senthil S, Srinivasan S, Thangeeswari T, Madhu BJ, Silambarasan M (2020) Enhanced dielectric, EMI shielding effectiveness, linear and nonlinear optical properties of CdO/SnO<sub>2</sub> nanocomposites. *Nano-Struct Nano-Objects* 24:100554
13. Tabassum R, Gupta BD (2017) Simultaneous tuning of electric field intensity and structural properties of ZnO: graphene nanostructures for FOSPR based nicotine sensor. *Biosens Bioelectron* 91:762–769
14. Alagiri M, Ponnusamy S, Muthamizhchelvan C (2012) Synthesis and characterization of NiO nanoparticles by sol–gel method. *J Mater Sci: Mater Electron* 23:728–732
15. Tabassum R, Gupta BD (2016) Simultaneous estimation of vitamin K1 and heparin with low limit of detection using cascaded channels fiber optic surface plasmon resonance. *Biosens Bioelectron* 86:48–55
16. Manawi YM, Ihsanullah SA, Al-Ansari T, Atieh MA (2018) A review of carbon nanomaterials' synthesis via the chemical vapor deposition (CVD) method. *Materials* 11:822
17. Cai H, Qiao X, Chen M, Feng D, Alghamdi AA, Alharthi FA, Pan Y, Zhao Y, Zhu Y, Deng Y (2021) Hydrothermal synthesis of hierarchical SnO<sub>2</sub> nanomaterials for high-efficiency detection of pesticide residue. *Chin Chem Lett* 32(4):1502–1506
18. Hussain N, Zulfiqar S, Khan T, Khan R, Khattak SA, Ali S, Khan G (2020) Investigation of structural, optical, dielectric and magnetic properties of SnO<sub>2</sub> nanorods and nanospheres. *Mater Chem Phys* 241:122382
19. Singh GV, Singh RC (2019) Highly sensitive gas sensor based on Er-doped SnO<sub>2</sub> nanostructures and its temperature dependent selectivity towards hydrogen and ethanol. *Sens Actuators B: Chem* 282:373–383
20. Tian X, Zhou F, Liu X, Zhong H, Wen J, Lian S, Ji C, Huang Z, Chen Z, Peng H (2019) Enhanced photoluminescence and high-temperature sensitivity from a novel Pr<sup>3+</sup> doped SrSnO<sub>3</sub>/SnO<sub>2</sub> composite phosphor. *J Solid State Chem* 280:120997
21. Ahmad F, Azharuddin M, Bansal J, Tabassum R, Hafiz AK (2022) Understanding of temperature-dependent photoluminescence in graphite and SixZnO<sub>(1-x)</sub> tri-composite nanostructure. *Opt Mater* 134:113165
22. Rahman S, Azharuddin M, Bansal J, Bilal M, Tabassum R, Hafiz AK (2023) Role of temperature on CdS and MoS<sub>2</sub> doped SnO<sub>2</sub> nanostructures: Potential applications in photodetection and temperature dependent current-voltage characteristics. *J Alloy Compd* 941:168901

# Improvement of Thermal Resistivity of Brick/AAC Block Wall Using Air Encapsulated Clay Tile



Sabista Siddiqui, Mohammad Danish, and Ibrar Ahmed

**Abstract** Previous few years have seen unprecedented crisis of climate change. The recent Heatwaves of Europe and fatal flooding of Pakistan, all point toward the looming perils. The root cause of these crises is the rapid warming of the Earth. Buildings and related activities consume a substantial amount of energy, approximately 40%. Green building technologies, such as insulation materials, offer a viable solution to this issue. They can reduce the operational energy load of buildings by regulating internal temperatures, thus eliminating the need for external appliances for cooling and heating. This paper proposes the use of AAC block wall, half barrel clay tile and rice husk plaster to improve thermal resistivity of buildings. These materials are not only eco-friendly as they include waste material such as rice husk ash, but also have a lower environmental impact. The only downside is the increase in installation cost, but it is likely to be compensated in a short period of time by minimizing the heating and cooling loads for HVAC equipment inside a building. The combination of AAC block wall, half barrel clay tile and rice husk plaster results in an achievable  $U$  Value of the system around  $0.021 \text{ Wm}^{-2} \text{ K}^{-1}$  with a system or wall thickness of around 275 mm, which is far better than the brick and cement plaster which is around  $2.103 \text{ Wm}^{-2} \text{ K}^{-1}$ . The suggested solution offers an eco-friendly and efficient approach that not only decreases energy consumption but also enhances the building's thermal resistance.

**Keywords** Thermal insulation · Thermal resistivity · Energy efficient buildings · Environment friendly bricks · Design builder software V6.1.0.006 (Simulation)

---

S. Siddiqui (✉) · M. Danish

Department of Applied Sciences and Humanities, Faculty of Engineering and Technology, Jamia Millia Islamia University, New Delhi, India

e-mail: [sabistasiddiqui@gmail.com](mailto:sabistasiddiqui@gmail.com)

I. Ahmed

Department of Computer Science and Engineering, Faculty of Engineering and Technology, NIET, Greater Noida, India

## 1 Introduction

As people's living standards have improved over time, it has led to increased energy consumption, necessitating building energy efficiency [1]. Within the European Union, various new building designs have emerged in recent years, including Zero Carbon Buildings, Zero Emission Buildings and Net Zero Source/Site Buildings [2]. It is projected that buildings will account for one-third of global energy and water consumption and generate 40 billion tons of carbon emissions annually by the 2030s [3]. Improving the thermal performance of building envelopes is imperative due to the significant energy consumption caused by inadequate thermal insulation [3]. Agriculture covers about 1.5 billion ha of the world's land area [4] with rice being the most productive crop in the world [5]. However, straws are burned in the fields in many developing countries after the harvest season; producing numerous greenhouse gases and air pollutants [5]. According to previous studies [5, 6], it is possible to replace some amount (safely 10%) of silica in cement with rice husk ash (RHA) as they possess cementitious properties. Moreover, RHA has been found to possess exceptional thermal insulation properties, as well as sound insulation capabilities [5, 6] and robust shear performance, according to several researchers [6]. Research has revealed that Autoclaved Aerated Concrete (AAC) is an environmentally sustainable structural material that is derived from modern waste and created using non-harmful and non-poisonous ingredients. It has been found that AAC surpasses traditional bricks in terms of thermal insulation, porosity, constructability, accessibility and cost-effectiveness [7]. In this study, the possibility of improving thermal resistivity of building by using AAC block wall, half barrel clay tile and rice husk plaster is explored. By using design builder software simulation is done and a high thermal resistivity of the proposed system is achieved.

## 2 Materials and Methods

### 2.1 Materials

(1) Autoclaved Aerated Concrete Block, (2) Half Barrel Ceramic/Clay Tile, (3) Rice Husk Plaster.

### 2.2 Methods

In this experiment, the  $U$  Value of the insulation system (wall) comprising of AAC Block, Hollow Ceramic/Clay Tile and Rice Husk Plaster is simulated with the help of software, i.e., Design Builder V6.1.0.006. The layer-wise organization of the



**Table 1** Layer details of the insulation system

Layer	Material	Thickness (mm)
1	Rice husk plaster	10
2	AAC block	125
3	Rice husk plaster	10
4	Ceramic/clay tile	120
5	Rice husk plaster	10

**Fig. 1** Structural details of insulation system (Wall)



materials is shown in the Table 1, the pictorial view of the same is shown in the Fig. 1 and 2. Figure 1 is obtained from the design builder software itself.

The simulation of the insulation system is carried out under the construction tab of the Design Builder by creating a new wall. Material for each layer is selected from the Design Builder Library. The thicknesses for each layer are entered manually. After the layer detailing the bridging is un-tick.

The *U* Value calculation is done under the calculation tab of the software, the calculated *U* Value of the Insulation System is  $0.021 \text{ Wm}^{-2} \text{ K}^{-1}$ . The screenshot of the calculated *U* Value from the Design Builder is shown in Fig. 3.

### 3 Results and Discussion

The *U* Value and *R* Value of the new insulation system (wall) is obtained as  $0.021 \text{ Wm}^2 \text{ K}^{-1}$  and  $46.537 \text{ m}^2\text{KW}^{-1}$ , respectively, by the simulation with the help of Design Builder 6.1.0.006. The *U* Value and *R* Value of the conventional

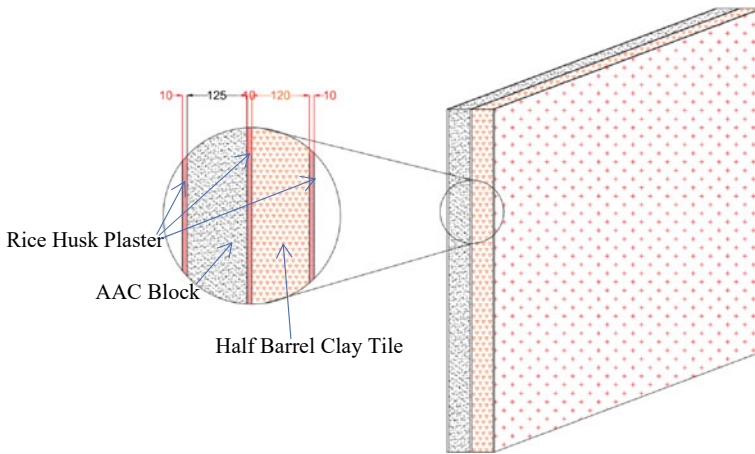


Fig. 2 Arrangement of the layers in the insulation system (Wall)

<b>Inner surface</b>		<<
Convective heat transfer coefficient (W/m <sup>2</sup> -K)	2.152	
Radiative heat transfer coefficient (W/m <sup>2</sup> -K)	5.540	
Surface resistance (m <sup>2</sup> -K/W)	0.130	
<b>Outer surface</b>		<<
Convective heat transfer coefficient (W/m <sup>2</sup> -K)	19.870	
Radiative heat transfer coefficient (W/m <sup>2</sup> -K)	5.130	
Surface resistance (m <sup>2</sup> -K/W)	0.040	
<b>No Bridging</b>		<<
U-Value surface to surface (W/m <sup>2</sup> -K)	0.022	
R-Value (m <sup>2</sup> -K/W)	46.537	
<b>U-Value (W/m<sup>2</sup>-K)</b>	<b>0.021</b>	
<b>With Bridging (BS EN ISO 6946)</b>		<<
Thickness (m)	0.2750	
Km - Internal heat capacity (KJ/m <sup>2</sup> -K)	0.0000	
Upper resistance limit (m <sup>2</sup> -K/W)	46.537	
Lower resistance limit (m <sup>2</sup> -K/W)	46.537	
U-Value surface to surface (W/m <sup>2</sup> -K)	0.022	
R-Value (m <sup>2</sup> -K/W)	46.537	
<b>U-Value (W/m<sup>2</sup>-K)</b>	<b>0.021</b>	

Fig. 3 Calculated U value of the insulation system (Wall)

insulation system (wall) is around 2.103 Wm<sup>-2</sup> K<sup>-1</sup> and 0.476 m<sup>2</sup>KW<sup>-1</sup>, respectively. Design Builder follows “EN ISO 6946: Building components and building elements—Thermal resistance and thermal transmittance—Calculation method” [8].

## 4 Conclusion

Comparing both the systems, we can conclude that the thermal insulation properties of the new insulation system (wall) is much better than the conventional insulation system (wall) which can result in the better energy performance of the building. Contributing toward the greener environment thereby reducing the carbon footprints. The practicability of the new insulation system (wall) can be worked out further for the installation feasibility. The pay-back periods for the different type of structures can be calculated hereby giving the detailed analysis of the cost savings.

## 5 Declaration of Interest Statement

The authors declare that they have no conflict of interests or personal connections that may have cropped up and caused biases in the research outlined in this paper.

## References

1. Kazmi SMS, Munir MJ, Patnaikuni I, Wu Y-F, Fawad U (2018) Thermal performance enhancement of eco-friendly bricks incorporating agro-wastes. *Energy Build* 158:1117–1129
2. Wang J, Liu SH, Meng X, Gao WJ, Yuan JH (2021) Application of retro-reflective materials in urban buildings: a comprehensive review. *Energy Build* 247:111137
3. United Nation Environment Program. Environment for Development; United Nation Environment Program: Nairobi, Kenya, 1 July 2016. [Google Scholar]
4. Gao YN, He F, Meng X, Wang ZY, Zhang M, Yu HT, Gao WJ (2020) Thermal behaviour analysis of hollow bricks filled with phase-change material (PCM). *J Build Eng* 31:101447
5. Ruff-Salís M, Calvo MJ, Petit-Boix A, Villalba G, Gabarrell X (2020) Exploring nutrient recovery from hydroponics in urban agriculture: an environmental assessment. *Resour Conserv Recy* 155:104683
6. Amin M, Abdelsalam BA (2019) Efficiency of rice husk ash and fly ash as reactivity materials in sustainable concrete. *Sustain Environ Res* 29(1)
7. Arif K (July 2020) Analysis of autoclaved aerated concrete (AAC) blocks with reference to its potential and sustainability
8. EN ISO 6946 Building components and building elements—Thermal resistance and thermal transmittance—Calculation method

# Structural and Electrochemical Characterizations of Sodium Doped Bimetallic Layered Nanocomposite for Sodium-Ion Capacitors



Yamini Gupta, Poonam Siwath, Shweta Rana, Reetika Karwasra, Kriti Sharma, and S. K. Tripathi

**Abstract** Sodium-ion capacitors have received consideration due to the abundance of sodium reserves and the collective characteristics of high energy and power density derived from the capacitor-type cathode and battery-type anode. Herein, layered sodium doped bimetallic (Nickel and Manganese)-nanocomposite has been synthesized using the solid-state method. The structural characterization of the synthesized material has been evaluated using X-ray diffraction (XRD). The sharp peaks of the XRD pattern reveal the crystalline nature of the material. The crystallite size confirming the construction of nanocomposite is calculated which comes out to be  $\sim 32$  nm corresponding to the (002) plane. Electrochemical characterizations are studied using galvanostatic charge–discharge methods and cyclic voltammetry. Further research is done using electrochemical impedance spectroscopy to identify the numerous resistances connected to the electrochemical process. The layered nanocomposite has an energy and power density of  $5.78 \text{ Whkg}^{-1}$  and  $14.87 \text{ Wkg}^{-1}$ , respectively, and a specific capacitance of  $29 \text{ Fg}^{-1}$  at the current density of  $0.025 \text{ Ag}^{-1}$ . The results show that the nanocomposite can be an electrode candidate with great potential for sodium-ion capacitors.

**Keywords** Layered transition metal oxides · Bimetallic doping · Sodium nickel manganese oxide · Sodium-ion capacitors

---

Y. Gupta · R. Karwasra · K. Sharma (✉)

Department of Physics, Goswami Ganesh Dutta Sanatan Dharma College, Sector 32-C, Chandigarh 160030, India  
e-mail: [kriti.sharma@ggdsd.ac.in](mailto:kriti.sharma@ggdsd.ac.in)

P. Siwath

Department of Physics, Arya Kanya Mahavidyalaya, Shahbad (M), Haryana 136135, India

S. Rana

Department of Chemistry, Panjab University, Chandigarh 160014, India

S. K. Tripathi (✉)

Department of Physics, Centre for Advanced Study in Physics, Panjab University, Chandigarh 160014, India  
e-mail: [surya@pu.ac.in](mailto:surya@pu.ac.in)

## 1 Introduction

To maintain a balance between the production of electrical energy during off-peak and peak hours, grid-scale energy storage devices have grown in popularity due to the tremendous demands of viable energy usage. A major problem nowadays is the development of inventive electrochemical energy storage (EES) devices as energy demands increase and we transit from convenient electronics to renewable energy [1–3]. Due to the faradaic charge storage mechanism on the anode side (battery-type) and electrical double layers on the cathode side (capacitor-type) of hybrid energy storage devices, such as Hybrid-ion capacitors, they are regarded as the most promising [4, 5]. As a result, they offer classic supercapacitors with better cycle life and power density with an enriched energy density [6–9]. In comparison to lithium-ion capacitors (LICs), sodium-ion capacitors (SICs) have become an innovative recent variety of energy storage technology. Due to their low cost, easy access to resources for manufacturing, and potential for extensive energy storage, SICs are greatly favored over LICs [10–13]. Despite this, a significant kinetic gap exists between the cathode and anode of SICs because the anode side (battery-type) typically experiences the slow kinetics of ions in the Faradaic reaction. This issue can be addressed by assembling a high pseudocapacitance anode to address the kinetics of redox reactions. In this regard, it is necessary to incorporate battery-type anode materials with outstanding rate performance, superior specific capacitance, and low redox voltage [14, 15].

Layered sodium transition metal oxides are generally formulated as  $\text{Na}_x\text{TMO}_2$  (where  $x = 0-1$ , TM refers to transition metals such that V, Cr, Co, Fe, Ni, Cu, Mn, Ti, or an arrangement of two or three of them) that are composed of repeating  $\text{TMO}_6$  octahedral sheets with Na-ions sandwiched in between the layered oxides. These layered transition metal oxides are considered promising candidates due to their feasible synthesis, low production cost, and enhanced electrochemical performance. They also possess high specific capacitance and high potential windows [16]. So in this study, the thin films of layered nanocomposite have been arranged which can be used as electrodes for SICs. Layered composite is structurally characterized by X-ray diffraction (XRD). Cyclic voltammetry (CV), galvanostatic charge–discharge (GCD), and electrochemical impedance spectroscopy (EIS) methods are employed to explore the electrochemical behavior.

## 2 Materials and Methods

Sodium acetate trihydrate ( $\text{CH}_3\text{COONa}\cdot 3\text{H}_2\text{O}$ ), manganese acetate tetrahydrate ( $\text{CH}_3\text{COOMn}\cdot 4\text{H}_2\text{O}$ ), nickel acetate tetrahydrate ( $\text{CH}_3\text{COONi}\cdot 4\text{H}_2\text{O}$ ), activated carbon (AC), and polyvinylidene fluoride (PVDF) are used as precursors. Layered sodium nickel manganese oxide nanocomposite is synthesized using a solid-state route followed by calcination. The stoichiometric amounts of  $\text{CH}_3\text{COONa}\cdot 3\text{H}_2\text{O}$ ,  $\text{CH}_3\text{COONi}\cdot 4\text{H}_2\text{O}$ , and  $\text{CH}_3\text{COOMn}\cdot 4\text{H}_2\text{O}$  are weighed and mixed using a mortar

and pestle for half an hour. The complete mixture is further stirred in a beaker in an ethanol solution for 2 h. The subsequent powder is dried for 5 h at 80 °C. The end product is then calcined in a muffle furnace for 8 h at 850 °C [16, 17].

The active material, AC, and PVDF are weighed in a ratio of 80:10:10 and carefully combined to create the material's working electrode. The combination is dissolved in N-Methyl-2-pyrrolidone (NMP) as a solvent, resulting in a homogeneous slurry. The slurry is then dropped and cast onto an FTO substrate that has earlier been cleaned (by sonicating in distilled water and ethanol for 20 min each) and dried. The electrodes are dried in an oven at 60 °C for 8 h which is further employed as the working electrodes. A mass loading of about 2 mg is found [16, 17].

Using an Auto-Lab potentiostat/galvanostat multichannel apparatus, the electrochemical performance has been evaluated. Using this apparatus, measurements are made using CV, GCD, and EIS with the prepared material acting as the working electrode, Ag/AgCl electrode acting as the reference electrode, platinum wire acting as the counter electrode, and 1M aqueous NaClO<sub>4</sub> as an electrolyte. The following formula can be used to calculate the value of specific capacitance from the GCD results [18]:

$$C_S = (\Delta t \times I) / (\Delta V \times m) \quad (1)$$

The given equation can be used to get the energy density ( $E_D$ ):

$$E_D = C_S V^2 / (2 \times 3.6) \quad (2)$$

The given equation can be used to compute the power density ( $P_D$ ):

$$P_D = (E_D / \Delta t) \times 3600 \quad (3)$$

where  $I$  (A) is the discharge current,  $m$  (g) is the mass of the active materials, and  $\Delta V$  (V) is the discharge potential window.  $C_S$  (Fg<sup>-1</sup>) is the specific capacitance of the electrodes.

### 3 Results and Discussion

By utilizing Panalytical X'Pert Pro XRD, the crystallinity and phase purity of the layered nanocomposite have been determined. The prepared material's crystalline XRD patterns are displayed in Fig. 1. The high-temperature solid-state produced material is characterized by the crystalline quality of the patterns. The JCPDS card number 54-0894 is compatible with the diffraction peaks of material, which are situated at the (002), (004), (100), (102), (103), (104), (106), (110), and (112) planes. This shows that hexagonally symmetric P2-type layered material is created. The trigonal prismatic shape of sodium-ions with six O atoms and the TMO<sub>6</sub> octahedral layers are combined to form the P2-type structure [16]. To define the average crystallite

sizes ( $D$ ) of the samples, the Debye Scherer formula has been applied. The equation is expressed as  $D = k\lambda/\beta\cos\theta$ , where  $D$ ,  $k$ ,  $\lambda$ ,  $\beta$ , and  $\theta$  and is the crystallite size, Scherer's constant, X-ray wavelength, full-width half maxima, and diffraction angle, respectively. The crystallite size is found to be 32 nm corresponding to the (002) plane for synthesized material. There are also some additional weakly intensified peaks that are visible, indicating that the nanocomposite contains some impurities or unreacted components [19].

Utilizing the CV procedure and a three-electrode setup with a 1 M NaClO<sub>4</sub> aqueous electrolyte solution, the capacitive phenomena of multilayer nanocomposite have been investigated. The aqueous NaClO<sub>4</sub> is taken as an electrolyte due to its low cost, excellent solubility, superior electrochemical activity, and wider potential window in comparison to other aqueous-based electrolytes. For the high value of  $E_D$ , the potential window plays an important role as  $E_D$  has twice the power of the potential window in its formula. So, choosing an electrolyte plays a crucial role in enhancing the electrochemical performance of SICs. The CV pattern of layered nanocomposite is shown in Fig. 2a at several scan rates ranging from 10, 20, 30, 40, 50, and 100 mVs<sup>-1</sup>. The values of  $C_S$  to be calculated comes out to be 11, 7, 6, 5, 4, and 3 Fg<sup>-1</sup> corresponding to different scan rates. With an increase in scan rate, the value of  $C_S$  decreases due to rapid movement of electrolyte ions which prevents them from penetrating into the surface area of the electrode. There is also an increment in peak current with the increase of scan rates that shows better reversibility in the charge–discharge phenomenon. Additionally, due to the polarization of the electrodes, the potential difference between the peaks consistent with the cathode and anode grows at high scan rates. Because CV curves formed are mostly unaffected by changes in scan rate, they can also accurately depict capacitive behavior. With higher scan rates, ions may diffuse into the polymer matrix, which would explain why the area under CV curves increases [20].

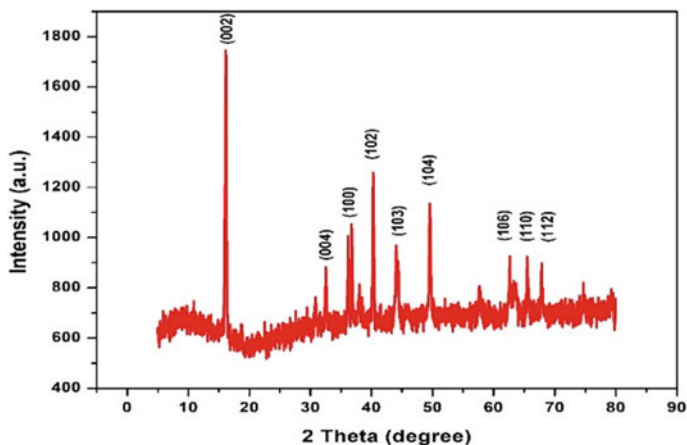


**Fig. 1** XRD pattern of the layered nanocomposite

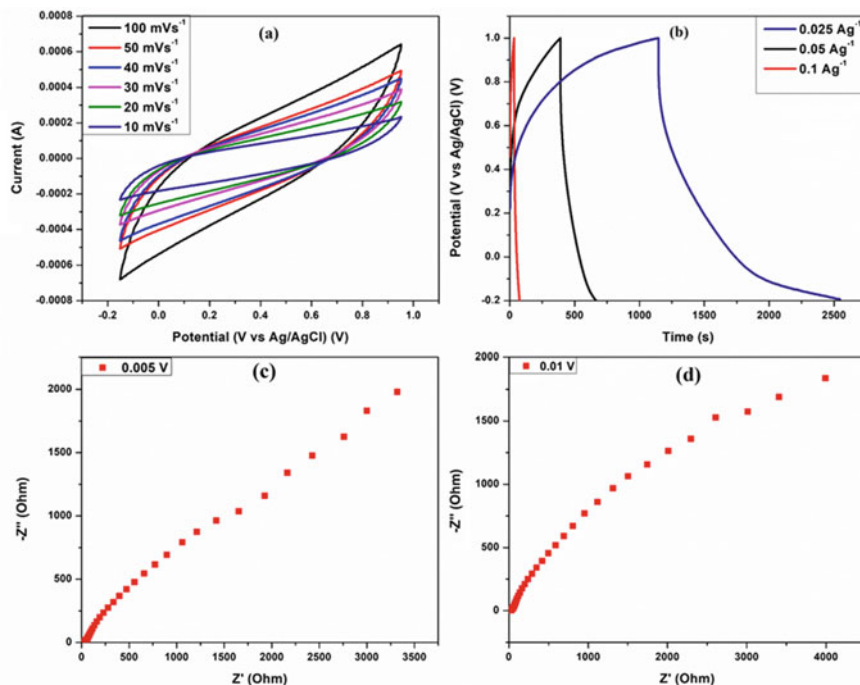


**Fig. 2** **a** CV curves, **b** GCD curves, **c** Nyquist plot at 5 mV, and **d** Nyquist plot at 10 mV of layered nanocomposite

To determine the nanocomposite's capacity for charge storage and rate capability, GCD behavior is investigated at several current rates. The GCD behavior of a nanocomposite with greater rate capability is shown in Fig. 2b when taken in the voltage plateau of  $-0.2$ – $1$  V at different current densities of  $0.025$ ,  $0.05$ , and  $0.1$   $\text{Ag}^{-1}$ . Its pseudocapacitive character is indicated by the sloped deviation in discharge curves, which may be initiated by an electrochemical adsorption–desorption route at the electrode–electrolyte interface. Due to the ohmic resistance of the electrolyte and internal resistance of ion diffusion into the holes of the electrode substance, there is a rapid potential drop at the start of the discharge. Equation (1) is employed to derive the  $C_S$  of the layered nanocomposite, which at current densities of  $0.025$ ,  $0.05$ , and  $0.1$   $\text{Ag}^{-1}$  corresponds to  $29$ ,  $12$ , and  $4$   $\text{Fg}^{-1}$ . Due to its symmetrical form and better reaction kinetics, the GCD curve advises great electrochemical reversibility. The  $C_S$  decreases with the increase of current density which can be due to insufficient faradaic redox reactions at higher rates and a rise in the potential drop. Equations (2) and (3) are used, respectively, to compute the  $E_D$  and  $P_D$  of the nanocomposite. The layered nanocomposite films show  $E_D$  of  $5.78$   $\text{Whkg}^{-1}$  at  $14.87$   $P_D$  of  $\text{Wkg}^{-1}$ , which corresponds to a current density of  $0.025$   $\text{Ag}^{-1}$ . According to the measured  $E_D$  and  $P_D$ , the produced nanocomposite can be a good electrode material for sodium-ion capacitors [21].



At a potential of 5 and 10 mV, EIS data are attained in the frequency series of  $0.01\text{--}10^5$  Hz. A semicircle in the high-frequency part of a Nyquist plot (Fig. 2c, d) shows a high charge transfer resistance, whereas an approximately vertical line in the low-frequency zone recommends capacitance due to ion diffusion. The total resistance of the electrode, electrolyte, and contact resistance is given by the left intersect on the  $Z'$  axis. The charge transfer resistance created by the electronic and ionic resistance at the electrode–electrolyte contact is indicated by the width of the semicircle. Warburg diffusion resistance is represented by a non-vertical line with a  $45^\circ$  slope. This resistance can be ascribed to the electrical double layer's diffuse layer or the electrolyte's ion-transport restriction in porous electrodes. Less internal resistance is advantageous for charge storage because the pseudocapacitance is heavily dependent on electron–ion transportation in electrodes and at the electrode–electrolyte contact [22]. All the electrochemical characterizations prove that the synthesized material can be used as an electrode material for SICs.

## 4 Conclusion

The layered sodium nickel manganese oxide has been synthesized by using a solid-state technique and characterized structurally using XRD. The XRD pattern's multiple peaks confirm that a nanocomposite has been synthesized. Using XRD analysis, crystallite size has been calculated whose value is  $\sim 32$  nm corresponding to the (002) plane. Electrochemical characterizations prove the synthesized material is a suitable candidate for sodium-ion capacitor electrodes. At the current density of  $0.025\text{ Ag}^{-1}$ , the value of the specific capacitance is  $29\text{ Fg}^{-1}$ .  $E_D$  and  $P_D$  are determined to be  $5.78\text{ Whkg}^{-1}$  and  $14.87\text{ Wkg}^{-1}$ , respectively. The outcomes demonstrate that sodium-ion capacitors made of the nanocomposite have great potential.

## References

1. Yang S, Jiang J, He W, Wu L, Xu Y, Ding B, Zhang X (2023) Nitrogen-doped carbon encapsulating Fe<sub>7</sub>Se<sub>8</sub> anode with core-shell structure enables high-performance sodium-ion capacitors. *J Colloid Interface Sci* 630:144–154
2. Lee SY, An JH, Park YI (2023) Synergistic effect of NaTi<sub>2</sub>(PO<sub>4</sub>)<sub>3</sub> and MXene synthesized in situ for high-performance sodium-ion capacitors. *Appl Surf Sci* 612:155960
3. Jo A, Lee B, Kim BG, Lim H, Han JT, Jeong SY, Park JH (2023) Ultrafast laser micro-machining of hard carbon/fumed silica anodes for high-performance sodium-ion capacitors. *Carbon* 201:549–560
4. Zhang X, Chen S, Cai J, King S, Liu C, Yuan W, Wang G (2023) Pre-strain accommodation enabled multi-dimensionally and hierarchically elastomeric MoSe<sub>2</sub>/MXene and AC/MXene electrodes for stretchable sodium ion capacitors. *J Alloys Compd* 935:168065
5. Maurya DK, Dhanusuraman R, Guo JZ, Angaiah S (2023) Na-ion conducting filler embedded 3D-electrospun nanofibrous hybrid solid polymer membrane electrolyte for high-performance Na-ion capacitor. *Adv Compos Mater* 6(1):45

6. Zhang Y, Jiang J, An Y, Wu L, Dou H, Zhang J, Guo Z (2020) Sodium-ion capacitors: materials, mechanism, and challenges. *Chemsuschem* 13(10):2522–2539
7. Cai P, Zou K, Deng X, Wang B, Zheng M, Li L, Ji X (2021) Comprehensive understanding of sodium-ion capacitors: definition, mechanisms, configurations, materials, key technologies, and future developments. *Adv Energy Mater* 11(16):2003804
8. Wang H, Zhu C, Chao D, Yan Q, Fan HJ (2017) Nonaqueous hybrid lithium-ion and sodium-ion capacitors. *Adv Mater* 29(46):1702093
9. Zhang H, Hu M, Lv Q, Huang ZH, Kang F, Lv R (2020) Advanced materials for sodium-ion capacitors with superior energy–power properties: progress and perspectives. *Small* 16(15):1902843
10. Ding J, Hu W, Paek E, Mitlin D (2018) Review of hybrid ion capacitors: from aqueous to lithium to sodium. *Chem Rev* 118(14):6457–6498
11. Zhu J, Roscow J, Chandrasekaran S, Deng L, Zhang P, He T, Huang L (2020) Biomass-derived carbons for sodium-ion batteries and sodium-ion capacitors. *Chemsuschem* 13(6):1275–1295
12. Zhang T, Wang R, He B, Jin J, Gong Y, Wang H (2021) Recent advances on pre-sodiation in sodium-ion capacitors: a mini review. *Electrochem Commun* 129:107090
13. Han D, Zhang J, Weng Z, Kong D, Tao Y, Ding F, Yang QH (2019) Two-dimensional materials for lithium/sodium-ion capacitors. *Mater Today Energy* 11:30–45
14. Wang B, Gao X, Xu L, Zou K, Cai P, Deng X, Ji X (2021) Advanced carbon materials for sodium-ion capacitors. *Batteries Supercaps* 4(4):538–553
15. Deng X, Zou K, Cai P, Wang B, Hou H, Zou G, Ji X (2020) Advanced battery-type anode materials for high-performance sodium-ion capacitors. *Small Methods* 4(10):2000401
16. Chen Y, Su G, Cheng X, Du T, Han Y, Qiang W, Huang B (2021) Electrochemical performances of P2-Na<sub>2</sub>/3Ni<sub>1</sub>/3Mn<sub>2</sub>/3O<sub>2</sub> doped with Li and Mg for high cycle stability. *J Alloys Compd* 858:157717
17. Nti F, Han JI (2017) Layered Na<sub>2</sub>/3Ni<sub>1</sub>/3Mn<sub>2</sub>/3O<sub>2</sub> as electrode material with two redox active transition metals for high performance supercapacitor. *J Alloys Compd* 728:78–87
18. Siwatch P, Sharma K, Tripathi SK (2020) Facile synthesis of NiCo<sub>2</sub>O<sub>4</sub> quantum dots for asymmetric supercapacitor. *Electrochim Acta* 329:135084
19. Siwatch P, Sharma K, Tripathi SK (2022) Electrochemical behavior of nickel cobalt oxide micro-flowers in different electrolytic systems. *Mater Today: Proc* 48:709–712
20. Siwatch P, Sharma K, Manyani N, Tripathi SK (2022) Synthesis of nickel cobalt oxide-reduced Graphene Oxide Nanocomposite using ammonia for supercapacitor. *ECS Trans* 107(1):11697
21. Siwatch P, Sharma K, Manyani N, Kang J, Tripathi SK (2021) Characterization of nanostructured nickel cobalt oxide-polyvinyl alcohol composite films for supercapacitor application. *J Alloys Compd* 872:159409
22. Siwatch P, Sharma K, Singh N, Manyani N, Tripathi SK (2021) Enhanced supercapacitive performance of reduced graphene oxide by incorporating NiCo<sub>2</sub>O<sub>4</sub> quantum dots using aqueous electrolyte. *Electrochim Acta* 381:138235

# Dynamics of Double Nitrogen-Vacancy Centre in a Photonic Crystal Nanocavity: Optical Bistability and Four-Wave Mixing



Tarun Kumar, Samantha Rath, and A. B. Bhattacharjee

**Abstract** Over the past decade, confinement of light to microscales has produced fruitful advancements in quantum optics. Cavity resonators are convenient tools of Cavity Quantum Electrodynamics (CQED) to study interaction of light and matter. Large number of studies have been carried out on nitrogen-vacancy (NV) centre coupled with photonic crystal nanocavities. On the nanoscale level, the coupling of NV centre to cavities has been extensively studied (Vahala in *Nature* 424:839–846, 2003). These include microtoroids (Vuckovic in *Quantum Optics and Nanophotonics*. Oxford University Press, pp. 365–403, 2014), microdisks (Aspelmeyer et al. *J Opt Soc Am B* 27: 189, 2010), microsphere resonators (Aspelmeyer et al. in *Phys Today* 65:29, 2012), and PC nanocavities. In this article, we investigate the dynamics of hybrid optical system consisting of photonic crystal nanocavity having double NV centre in it. We look into the bistability and four-wave mixing of the system. In this study, it is shown that the system exhibits the phenomena of optical bistability, which can be achieved for some different combinations of system parameters, at a lower power. The system under consideration finds application in all optical switches and memory devices used in quantum information processing where system requires low power. We also find that the system under consideration exhibits four-wave mixing due to nonlinear behaviour of the system. The results so obtained can be employed to further understand the solid-state CQED. Since the NV centre has well-defined quantum states with well-defined bandgap, which can be easily initialised by optical pumping mechanism thereby making them a potential candidate in quantum information processing.

**Keywords** Nitrogen-vacancy centre · Bistability · Four-wave mixing

---

T. Kumar (✉)  
Ramjas College, University of Delhi, Delhi 110007, India  
e-mail: [tarunrawat@ramjas.du.ac.in](mailto:tarunrawat@ramjas.du.ac.in)

S. Rath  
Department of Physics and Astrophysics, University of Delhi, Delhi 110007, India

A. B. Bhattacharjee  
Department of Physics, Birla Institute of Technology and Science, Pilani, Hyderabad Campus, Telangana State 500078, India

## 1 Introduction

Over the past decade, confinement of light to microscales has produced fruitful advancements in quantum optics. Cavity resonators are convenient tools in Cavity Quantum Electrodynamics (CQED) to study the synergy of light and matter [1, 2]. A transition from classical to quantum level can be achieved by direct coupling of different quantum systems such as mechanical resonators to quantum systems like optical cavities [3, 4], superconducting qubit circuits [5–7], quantum dots [9, 10], and nitrogen-vacancy centres. Specifically, the coupling of mechanical resonators with microwave cavities forms a cavity electro-optomechanical system. Such systems are particularly useful in attaining a quantum regime for mechanical motion [11–13]. For example, two-phonon blockade mechanism for a quadratically coupled system has been found to have potential application in quantum information processing [14]. Recently, Kerr nonlinearities in an optomechanical system were also studied for performance enhancement of quantum systems by noise suppression [15]. Therefore, cavity optomechanics has been studied extensively [16–21], thereby producing intriguing results. Of these, the current favourites are nanoscale photonic crystal cavities. Their promising attributes are cubic wavelength mode volume and high-quality factor [22–24]. Further, the idea that complex systems on-a-chip [25, 26] can be fabricated by the integration of waveguides into PCs makes waveguide-coupled nanocavity systems an area of thriving research. Specifically, these devices find applications in communication, sensing, and information processing. Further, a large number of studies have been carried out on nitrogen-vacancy centres coupled with photonic crystal nanocavities. In a host lattice of diamond, nitrogen vacancies are point defects consisting of a substitutional nearest-neighbour nitrogen pair for carbon atom, and a lattice vacancy. Due to the simultaneous occurrence of three characteristics, namely, spin coherence in the ground state, structure and stability of diamond lattice in NV's level. The nitrogen centres have gained attention in quantum information processing. On the nanoscale level, the coupling of NV centres to cavities has been extensively studied [27–29]. These include microtoroids [29], microdisks [30], microsphere resonators [31, 32], and PC nanocavities [33–39]. Yang et al. considered the quantum dynamics and showed the preservation of quantum correlation for different nitrogen-vacancy centres in photonic crystals and plasmonic waveguide [39]. Ali et al. reported analytical results for the transfer of quantum states among coupled nitrogen-vacancy centres and photonic crystal molecule. Their results were valid for strong coupling, comparable coupling-hopping and high hopping [40]. Recently, the dynamics of quantum correlation were studied for two nitrogen-vacancy centres by mathematically modelling the time-dependent Schrödinger equation and obtaining their analytical solutions [41]. Heisenberg–Langevin (HL) equations are used to investigate the cavity-coupled NV centre powered by a driving field [46]. This has been extended to the case for two NV centres coupled to PC nanocavity. As these equations are highly nonlinear, analytic solutions are hard to obtain. Therefore, they are explored in the weak-field regime. Within this approximation,  $\hat{\sigma}_{11}(t) \approx 1$  is the ground state and  $\hat{\sigma}_{22}(t) \approx 0$  is the excited states of the emitter. Further,

$\hat{\sigma}_z(t) = [\hat{\sigma}_{22}(t) - \hat{\sigma}_{11}(t)]/2$  is the population inversion operator relating the two states. The equations are then linearised to obtain solutions for the steady-state case. However, for moderate driving power, it is imperative to consider the nonlinear terms as the weak-field approximation fails. This paper is written in following manner. We have discussed and solved the Hamiltonian describing our model and thus obtained the equations showing the evolution of our system in Sect. 2. This is followed by analysis of the bistable behaviour in Sect. 3. In Sect. 4, we discuss the four-wave mixing phenomena. Results and discussions have been presented finally.

## 2 Theoretical Framework

In the proposed model (Fig. 1), we consider a double NV centre which is captured in a PC nanocavity composed of single-mode radiation field. The nanocavity is also coupled to a waveguide optically. The waveguide is required for in and out coupling of light field in the cavity as proposed in [42–44]. The system is obtained by introducing spatial point defects in the photonic crystal. The single-mode cavity frequency that can only couple to the forward coupling fields [45] can also be tuned by the geometrical parameters of the defect. The NV centre is a point defect in the diamond crystal, having a nitrogen atom with a vacancy. In our proposed system, we have two such point defects, which are coupled through single-mode optical field. In rotating wave and dipole approximation, the Hamiltonian becomes.

$$\begin{aligned}
 H = & \hbar\omega_1\sigma_{22}(1) + \hbar\omega_2\sigma_{22}(2) + \hbar\omega_{\text{cav}}c^\dagger c \\
 & + i\hbar g_1(c\sigma_{21}(1) - c^\dagger\sigma_{12}(1)) \\
 & + i\hbar g_2(c\sigma_{21}(2) - c^\dagger\sigma_{12}(2)) + i\hbar\sqrt{\kappa_e}(S_{\text{in}}(t)c^\dagger - S_{\text{in}}^*(t)c)
 \end{aligned} \quad (1)$$

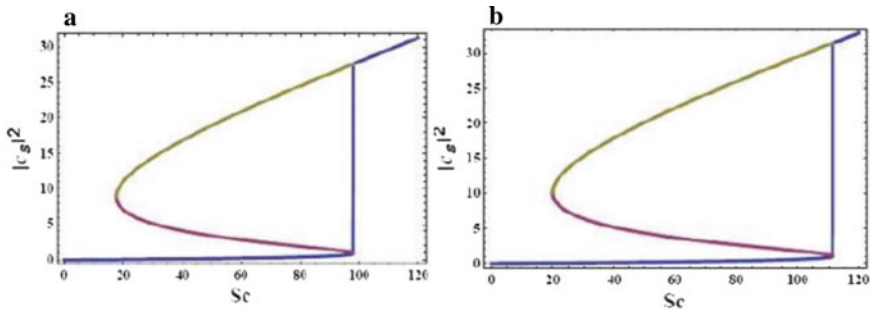


**Fig.1** Plot of  $|c_s|^2$  versus probe power for  $g_1$  **a**  $g_1 = 3.2$  and **b**  $g_2 = 3.0$ . The other constants are  $\kappa_i = 1$ ,  $\kappa_e = 5$ ,  $g_2 = 3.2$ ,  $\gamma_{\text{spon}}(1) = 0.008125$ ,  $\gamma_{\text{spon}}(2) = 0.008125$ ,  $\Delta_1 = 5.0625$ ,  $\Delta_2 = 5.0625$ , and  $\Delta_3 = 5.0625$

In Eq. 1, the first and the second terms are the energies of the NV centres, third term is the cavity field energy, and fourth and fifth terms represent the cavity field interaction with the NV centres. The sixth term is driving term for cavity field. Here,  $\omega_1$  and  $\omega_2$  represent the optical transition frequencies  $|1\rangle$  (lower state) and  $|2\rangle$  (upper state) of the NV centres.  $\sigma_{ij}$  ( $i, j = 1, 2$ ) is the projection operator between the states  $|i\rangle$  and  $|j\rangle$  and  $\sigma_{jj}$  ( $j = 1, 2$ ) is the population operator of the NV centre of  $j$ th state.  $\omega_c$  is the single-mode intracavity resonance frequency being driven by the external laser.  $g_1$  and  $g_2$  represent coupling strengths of the two NV centres with the intracavity field. Equation 1 Hamiltonian can be transformed in rotating frame of the input laser frequency  $\omega_l$  as

$$\begin{aligned}
 H = & \hbar\Delta_1\sigma_{22}(1) + \hbar\Delta_2\sigma_{22}(2) + \hbar\Delta_3c^\dagger c \\
 & + i\hbar g_1(c\sigma_{21}(1) - c^\dagger\sigma_{12}(1)) \\
 & + i\hbar g_2(c\sigma_{21}(2) - c^\dagger\sigma_{12}(2)) + i\hbar\sqrt{\kappa_e}(S_{\text{in}}(t)c^\dagger - S_{\text{in}}^*(t)c)
 \end{aligned} \tag{2}$$

where  $\Delta_1 = \omega_1 - \omega_l$ ,  $\Delta_2 = \omega_2 - \omega_l$ , and  $\Delta_3 = \omega_{\text{cav}} - \omega_l$  are respectively the detunings of two NV centres from intracavity fields and cavity resonance frequency  $\omega_{\text{cav}}$  from external laser frequency  $\omega_l$ .

To solve the Hamiltonian in Eq. 2, we consider a driving field consisting of two parts (bichromatic) [46], namely a probe field and a control field, which can be written as  $S_{\text{in}} = S_p \exp^{-i\omega_p t} + S_c \exp^{-i\omega_c t}$ ,  $\omega_p, \omega_c$  being the carrier frequencies for probe and control fields, with field amplitudes  $S_p$  and  $S_c$ , respectively. Under rotating frame of the  $\omega_c$ , we choose  $\omega_l = \omega_c$ . Under above transformations, Hamiltonian in Eq. 2 can be re-written as

$$\begin{aligned}
 H = & \hbar\Delta_1\sigma_{22}(1) + \hbar\Delta_2\sigma_{22}(2) + \hbar\Delta_3c^\dagger c + i\hbar g_1(c\sigma_{21}(1) - c^\dagger\sigma_{12}(1)) \\
 & + i\hbar g_2(c\sigma_{21}(2) - c^\dagger\sigma_{12}(2)) + \hbar\omega_D(\sigma_{21}(1)\sigma_{12}(2) + \sigma_{21}(2)\sigma_{12}(1)), \\
 & + i\hbar\sqrt{\kappa_e}(S_c + S_p \exp^{-i\Omega t})c^\dagger - H.C.)
 \end{aligned} \tag{3}$$

where  $\Delta_1 = \omega_1 - \omega_c$ ,  $\Delta_2 = \omega_2 - \omega_c$ ,  $\Delta_3 = \omega_{\text{cav}} - \omega_c$ , and  $\Omega = \omega_p - \omega_c$ . Also, the field amplitudes  $S_p$  and  $S_c$  are normalised with respect to photon flux. The field amplitudes and the power in the waveguide have the relation  $P_p = \hbar\omega_p S_p^2$  and  $P_c = \hbar\omega_c S_c^2$ , respectively.

### 3 Heisenberg–Langevin Equations (QL)

QL eqns. describe the system dynamics given by Eq. 3. The nonlinear QL eqns. having noise damping terms are written as

$$\dot{c} = -\left[\iota\Delta_3 + \frac{\kappa_i}{2} + \frac{\kappa_e}{2}\right]c - g_1\hat{\sigma}_{12}(1) - g_2\hat{\sigma}_{12}(2) + \sqrt{\kappa_e}(S_c + S_p \exp^{-i\Omega t})c + \hat{f}_c, \tag{4}$$

$$\dot{\hat{\sigma}}_{11}(1) = \gamma_{\text{spon}}(1)\hat{\sigma}_{11}(1) - g_1\hat{c}\hat{\sigma}_{21}(1) - g_1\hat{c}^\dagger\hat{\sigma}_{12}(1) + \hat{f}_{11}(1), \quad (5)$$

$$\dot{\hat{\sigma}}_{22}(1) = \gamma_{\text{spon}}(1)\hat{\sigma}_{22}(1) + g_1c\hat{\sigma}_{21}(1) + g_1c^\dagger\hat{\sigma}_{12}(1) + \hat{f}_{22}(1), \quad (6)$$

$$\dot{\hat{\sigma}}_{11}(2) = -\gamma_{\text{spon}}(2)\hat{\sigma}_{11}(2) - g_2c\hat{\sigma}_{21}(2) - g_2\hat{c}^\dagger\hat{\sigma}_{12}(2) + \hat{f}_{11}(2), \quad (7)$$

$$\dot{\hat{\sigma}}_{22}(2) = -\gamma_{\text{spon}}(2)\hat{\sigma}_{22}(2) + g_2\hat{c}\hat{\sigma}_{21}(2) + g_2\hat{c}^\dagger\hat{\sigma}_{12}(2) + \hat{f}_{22}(2), \quad (8)$$

$$\dot{\hat{\sigma}}_{12}(1) = -[\iota\Delta_1 + \gamma_{\text{spon}}(1)]\hat{\sigma}_{12}(1) - 2g_2\hat{c}\hat{\sigma}_z(1) + \hat{f}_{12}(1), \quad (9)$$

$$\dot{\hat{\sigma}}_{12}(2) = -[\iota\Delta_2 + \gamma_{\text{spon}}(2)]\hat{\sigma}_{12}(2) - 2g_2\hat{c}\hat{\sigma}_z(2) + \hat{f}_{12}(2). \quad (10)$$

Here,  $\hat{\sigma}_z(i) = (\hat{\sigma}_{22}(i) - \hat{\sigma}_{11}(i))/2$  ( $i = 1, 2$ ) represents population inversion operator for  $i$ th NV centre. The system under consideration is open, and hence, it is dissipative. Therefore,  $\kappa_e$  and  $\kappa_i$  are the intracavity decay constant and coupling rate of the waveguide cavity. Also,  $\gamma_{\text{spon}(1)}$  and  $\gamma_{\text{spon}(2)}$  give the decay rate of the two NV centres.  $f_c$  is the cavity input noise and  $f_{11}(i)$ ,  $f_{22}(i)$ ,  $f_{12}(i)$  ( $i = 1, 2$ ) are the quantum noise operators of the NV centres. Since we are looking for the solutions of the steady state of QL Eqs. 4–10, therefore under mean field response, the average value of the noise operators reduces to zero ( $\langle f_c \rangle = \langle f_{11}(i) \rangle = \langle f_{22}(i) \rangle = \langle f_{12}(i) \rangle = 0$ ), and all operators are replaced by their steady-state values, i.e.  $\langle \hat{c}(t) \rangle = c(t)$ ,  $\langle \hat{\sigma}_{11}(i) \rangle = \sigma_{11}$ ,  $\langle \hat{\sigma}_{22}(i) \rangle = \sigma_{22}$ ,  $\langle \hat{\sigma}_{ij} \rangle = \sigma_{ij}$ , where ( $i = 1, 2$ ). Under above approximations and the  $\langle XY \rangle = \langle X \rangle \langle Y \rangle$ ,  $\sigma_z(i) = (\sigma_{22}(i) - \sigma_{11}(i))/2$ , the Quantum Langevin equations give:

$$\dot{c} = -\left[\iota\Delta_3 + \frac{\kappa_i}{2} + \frac{\kappa_e}{2}\right]c - g_1\sigma_{12}(1) - g_2\sigma_{12}(2) + \sqrt{\kappa_e}(S_c + S_p\exp^{-\iota\Omega t}), \quad (11)$$

$$\dot{\sigma}_{11}(1) = \gamma_{\text{spon}}(1)\sigma_{11}(1) - g_1c\sigma_{21}(1) - g_1c^\dagger\sigma_{12}(1), \quad (12)$$

$$\dot{\sigma}_{22}(1) = \gamma_{\text{spon}}(1)\sigma_{22}(1) + g_1c\sigma_{21}(1) + g_1c^\dagger\sigma_{12}(1) + f_{22}(1), \quad (13)$$

$$\dot{\sigma}_{11}(2) = -\gamma_{\text{spon}}(2)\sigma_{11}(2) - g_2c\sigma_{21}(2) - g_2c^\dagger\sigma_{12}(2) + f_{11}(2), \quad (14)$$

$$\dot{\sigma}_{12}(2) = -[\iota\Delta_2 + \gamma_{\text{spon}(2)}]\sigma_{12}(2) - 2g_2c\sigma_z(2) + f_{12}(2), \quad (15)$$

$$\dot{\sigma}_{12}(1) = -[\iota\Delta_1 + \gamma_{\text{spon}(1)}]\sigma_{12}(1) - 2g_1c\sigma_z(1) + f_{12}(1), \quad (16)$$

$$\dot{\sigma}_{22}(2) = -\gamma_{\text{spon}}(2)\sigma_{22}(2) + g_2c\sigma_{21}(2) + g_2c^\dagger\sigma_{12}(2) + f_{22}(2). \quad (17)$$

### 4 Bistability

Assuming strong pump field and weak laser probe field, perturbation theory can be used further to study the bistability of the photons inside the cavity. To study the bistability, we treat probe laser as perturbation, whereas the control laser field provides the steady-state solutions corresponding to  $c$ ,  $\sigma_z(i)$  and  $\sigma_{12}(i)$  ( $i = 1, 2$ ) as

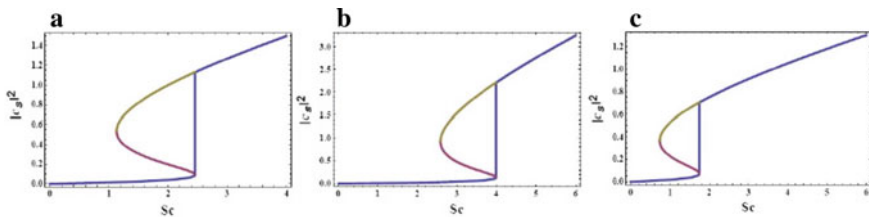
$$\bar{c} = \frac{F_1 F_2 \sqrt{\kappa_e} S_c}{F_1 F_2 F_3 - 2g_1^2 \sigma_z(1) F_2 - 2g_2^2 \sigma_z(2) F_1}, \tag{18}$$

$$\bar{\sigma}_z(1) = \frac{-\frac{\gamma_1}{2}}{\gamma_1 + 2g_1^2 \left( \frac{1}{F_1} + \frac{1}{F^*} \right)} |\bar{c}|^2, \tag{19}$$

$$\bar{\sigma}_z(2) = \frac{-\frac{\gamma_2}{2}}{\gamma_2 + 2g_2^2 \left( \frac{1}{F_2} + \frac{1}{F^*} \right)} |\bar{c}|^2, \tag{20}$$

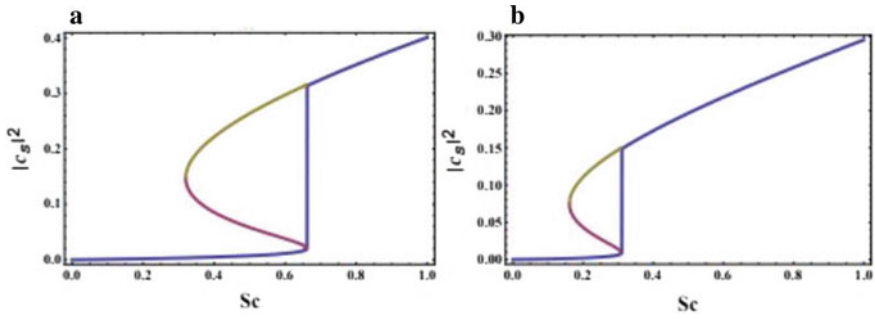
where  $F_1 = \iota \Delta_1 + \gamma_{\text{spon}}(1)/2$ ,  $F_2 = \iota \Delta_2 + \gamma_{\text{spon}}(2)/2$  and  $F_3 = \iota \Delta_3 + \kappa_e/2 + \kappa_i/2$ . Equations 18–20 are coupled equations, which we solve for photon numbers under steady state in the cavity. We find that for certain parameter range, our system shows optical bistability, which we demonstrate in Figs. 2, 3, 4, and 5. The parameters used are well within the experimental range. Optical bistability so obtained proves that our system finds application as an all optical switch, which can be used in quantum information platforms and quantum communication.

Figure 1 depicts that as we increase the cavity photons and one of the NV centres coupling strength say ( $g_1$ ), optical bistability shifts from higher pump power to lower pump power. Same pattern is also observed when we increase the detuning  $\Delta_3$  (Fig. 2), decrease the detuning of probe laser–cavity photon  $\Delta_1$  (Fig. 3), and increase the decay constant of one of the NV centres (Fig. 4). We find that for some particular combination of different system parameters, optical bistability at a lower power can be achieved. That means the optical bistability behaviour can be controlled via different system parameters, thus making the proposed system a handy tool to be used for all optical switch, logic gates, and memory where low power is required.



**Fig.2** Plot of  $|c_s|^2$  versus probe power for detuning  $\Delta_3$ , **a**  $\Delta_3 = 5.0525$ , **b**  $\Delta_3 = 2.0625$  and **c**  $\Delta_3 = 7.0625$ .  $g_2 = 3.2$ ,  $\gamma_1 = 0.08125$ . The other constants are same as in Fig. 1





**Fig.3** Plot of  $|c_s|^2$  versus probe power for different detunings  $\Delta_1$ , **a**  $\Delta_1 = 0.008125$  and **b**  $\Delta_1 = 0.08125$ .  $g_1 = 3.2$ . The other constants are same as in Fig. 1

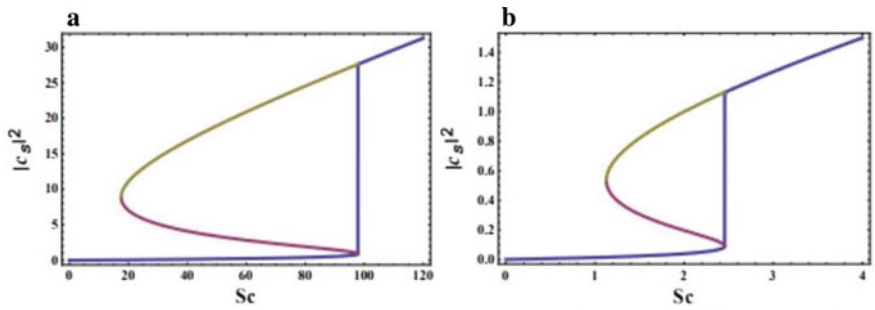
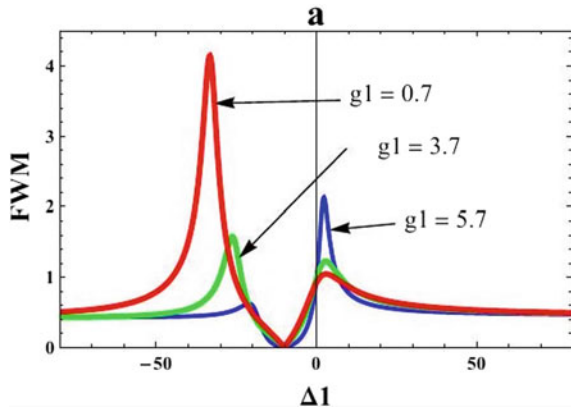


**Fig.4** Plot of  $|c_s|^2$  versus probe power for  $\gamma_1$ , **a**  $\gamma_1 = 0.008125$  and **b**  $\gamma_1 = 0.08125$ .  $g_1 = 3.2$ . The other constants are same as in Fig. 1

**Fig.5** Plot of  $|c_s|^2$  versus detuning  $\Delta_1$  for different values of coupling constant  $g_1$ ,  $g_1 = 0.7, 3.7$  and  $5.7$ .  $g_2 = 5.7$ .  $\sigma_{zs} = -1$ ,  $\sigma_{12s} = 0.5$ . The other constants are same as in Fig. 1



## 5 Four-Wave Mixing

To study small fluctuation dynamics, QL eqns. are linearized about their steady-state values. For doing so, we substitute  $c \rightarrow \bar{c} + \delta c$ ,  $\sigma_{12} \rightarrow \bar{\sigma}_{12}(i) + \delta\sigma_{12}(i)$  and  $\sigma_z \rightarrow \bar{\sigma}_z(i) + \delta\sigma_z(i)$ , ( $i = 1, 2$ ). Also, we only retain first-order terms in the fluctuation, i.e. in  $\delta c$ ,  $\delta\sigma_z(i)$ , and  $\delta\sigma_{12}(i)$ . This gives

$$\delta\dot{c} = -\left[\iota\Delta_3 + \frac{\kappa_i}{2} + \frac{\kappa_e}{2}\right]\delta c - g_1\delta\sigma_{12}(1) - g_2\delta\sigma_{12}(2) + \sqrt{\kappa_e}S_p\exp^{-\iota\Omega t}, \quad (21)$$

$$\delta\dot{\sigma}_z(1) = -\gamma_{\text{spn}}(1)\delta\sigma_z(1) + g_1\bar{c}^*\delta\sigma_{12}(1) + g_1\delta c^*\sigma_{12}^-(1) + g_1\bar{c}\delta\sigma_{12}^*(1) + g_1\delta c\sigma_{12}^*(1), \quad (22)$$

$$\delta\dot{\sigma}_z(2) = -\gamma_{\text{spn}}(2)\delta\sigma_z(2) + g_2\bar{c}^*\delta\sigma_{12}(2) + g_2\delta c^*\sigma_{12}^-(2) + g_2\bar{c}\delta\sigma_{12}^*(2) + g_2\delta c\sigma_{12}^*(2), \quad (23)$$

$$\delta\dot{\sigma}_{12}(1) = -\left[\iota\Delta_1 + \frac{\gamma_{\text{spn}}(1)}{2}\right]\delta\sigma_{12}(1) - 2g_1\bar{c}\delta\sigma_z(1) - 2g_1\delta c\bar{\sigma}_z(1), \quad (24)$$

$$\delta\dot{\sigma}_{12}(2) = -\left[\iota\Delta_2 + \frac{\gamma_{\text{spn}}(2)}{2}\right]\delta\sigma_{12}(2) - 2g_2\bar{c}\delta\sigma_z(2) - 2g_2\delta c\bar{\sigma}_z(2). \quad (25)$$

Next, to further analyse the problem, we use the rotating wave approximation on the driving field given by  $\delta S_{\text{in}} = S_p\exp(-\iota\Omega t)$ , ( $\Omega = \omega_p - \omega_c$ ) and using the following ansatz

$$\delta c = c_+\exp^{-\iota\Omega t} + c_-\exp^{\iota\Omega t}, \quad (26)$$

$$\delta\sigma_{12}(1) = \sigma_{12+}(1)\exp^{-\iota\Omega t} + \sigma_{12-}(1)\exp^{\iota\Omega t}, \quad (27)$$

$$\delta\sigma_{12}(2) = \sigma_{12+}(2)\exp^{-\iota\Omega t} + \sigma_{12-}(2)\exp^{\iota\Omega t}, \quad (28)$$

$$\delta\sigma_z(1) = \sigma_{z+}(1)\exp^{-\iota\Omega t} + \sigma_{z-}(1)\exp^{\iota\Omega t}, \quad (29)$$

$$\delta\sigma_z(2) = \sigma_{z+}(2)\exp^{-\iota\Omega t} + \sigma_{z-}(2)\exp^{\iota\Omega t}. \quad (30)$$

On equating the coefficients with same frequencies, i.e. equating the terms with  $\exp(\pm\iota\Omega t)$ , we get following equations:

$$D1\sigma_{12+}(1) + 2g_1c_s\sigma_{z+}(1) + 2g_1c_+\sigma_{zs}(1) = 0, \quad (31)$$

$$D2\sigma_{12-}(1) + 2g_1c_s\sigma_{z-}(1) + 2g_1c_-\sigma_{zs}(1) = 0, \quad (32)$$

$$D3\sigma_{12+}(2) + 2g_2c_s\sigma_{z+}(2) + 2g_2c_+\sigma_{zs}(2) = 0, \quad (33)$$

$$D4\sigma_{12-}(2) + 2g_2c_s\sigma_{z-}(2) + 2g_2c_-\sigma_{zs}(2) = 0, \quad (34)$$

$$g_1\sigma_{12+}(1) + g_2\sigma_{12+}(2) + D5c_+ - \sqrt{\kappa_e}S_p = 0, \quad (35)$$

$$g_1\sigma_{12+}(1) + g_2\sigma_{12+}(2) + D6c_+ - \sqrt{\kappa_e}S_p = 0, \quad (36)$$

$$-(\gamma_1 - i\Omega)\sigma_{z+}(1) + g_1c_s^*\sigma_{12+}(1) + g_1c_-^*\sigma_{12s}(1) + g_1c_s\sigma_{12+}(1) + g_1c_+\sigma_{12s}^*(1) = 0, \quad (37)$$

$$\gamma_1 + (2) + g_2c_s^*\sigma_{12-}(2) + g_2c_+\sigma_{12s}(2) + g_2c_s\sigma_{12-}(2) + g_2c_-\sigma_{12s}^*(2) = 0, \quad (38)$$

where  $D1 = (i\Delta_1 + \gamma_1/2 + i\Omega)$ ,  $D2 = (i\Delta_1 + \gamma_1/2 - i\Omega)$ ,  $D3 = (i\Delta_2 + \gamma_2/2 + i\Omega)$ ,  $D4 = (i\Delta_2 + \gamma_2/2 - i\Omega)$ ,  $D5 = (i\Delta_3 + \kappa_a/2 + \kappa_e/2 + i\Omega)$ , and  $D6 = (i\Delta_3 + \kappa_a/2 + \kappa_e/2 - i\Omega)$ . Now making use of the usual input–output relation,  $S_{\text{out}} - S_{\text{in}} = \sqrt{\kappa_e}c$ ,

where  $S_{\text{out}}$  is the output field, and we get

$$S_{\text{out}}(t) = \sqrt{\kappa_e}c_- \exp(-i(\omega_c - \Omega)t) + (S_c + \sqrt{\kappa_e}c_s) \exp(-i\omega_c t) \\ + (S_p + \sqrt{\kappa_e}c_+) \exp(-i(\omega_c + \Omega)t) \quad (39)$$

which can be written as

$$S_{\text{out}}(t) = \sqrt{\kappa_e}c_- \exp(-i(2\omega_c - \omega_p)t) \\ + (S_c + \sqrt{\kappa_e}c_s) \exp(-i\omega_c t) \\ + (S_p + \sqrt{\kappa_e}c_+) \exp(-i\omega_p t) \quad (40)$$

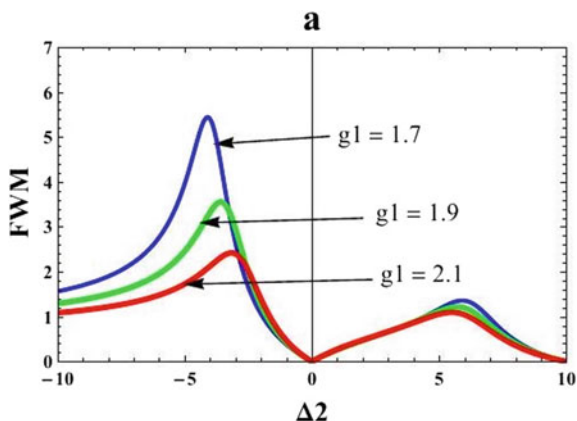
In above equation, coefficients of  $\exp(-i(2\omega_c - \omega_p)t)$ ,  $\exp(-i\omega_c t)$  and  $\exp(-i\omega_p t)$  represent the optical responses at the generated frequency  $2\omega_c - \omega_p$ , probe frequency  $\omega_p$ , and control frequency  $\omega_c$ , respectively. The normalised four-wave mixing (FWM) intensity, with reference to probe field is defined as

$$I_{\text{FWM}} = \left| \frac{\sqrt{\kappa_e}c_-}{S_p} \right|^2 \quad (41)$$

Solving Eqs. 31–38 and using the relation 41, we further obtain

$$I_{\text{FWM}} = \left| \frac{\kappa_e}{T_{21}} \right|^2, \quad (42)$$

**Fig.6** Plot of  $|c_s|^2$  versus detuning  $\Delta_2$  for different values of coupling constant  $g_1$ ,  $g_1 = 1.7, 1.9$  and  $2.1$ .  $\sigma_{z,s} = -1, \sigma_{12s} = 0.5$ . The other constants are same as in Fig. 1



where  $T_{21} = \frac{T_{17}T_{20}^*}{T_{19}^*} + T_{18}^*$ ,  $T_{17} = \frac{T_1T_{12}^*}{T_{11}^*} + \frac{T_2T_{13}^*}{T_{14}^*} + T_3$ ,  $T_{18} = \frac{T_1T_{13}^*}{T_{11}^*} + \frac{T_2T_{16}}{T_{14}^*}$ ,  $T_{19} = \frac{T_4T_{12}^*}{T_{11}^*} + T_5$ ,  $T_{20} = T_6 - \frac{T_4T_{13}^*}{T_{11}^*}$ ,  $T_1 = \frac{2g_1^2c_s}{D_1}$ ,  $T_2 = \frac{2g_2^2c_s}{D_3}$ ,  $T_3 = \frac{2g_1^2\sigma_{zs}(1)}{D_1} + \frac{2g_2^2\sigma_{zs}(2)}{D_2} - D_5$ ,  $T_4 = -(\gamma_1 - i\Omega) - \frac{2g_1^2|c_s|^2}{D_1} - \frac{2g_1^2c_s^2}{D_1}$ ,  $T_5 = -\frac{2g_1^2c_s^*\sigma_{zs}(1)}{D_1} - \frac{2g_1^2c_s\sigma_{zs}(1)}{D_1} + g_1\sigma_{12s}^*(1)$ ,  $T_6 = g_1\sigma_{12s}(1)$ ,  $T_7 = -(\gamma_1 - i\Omega) - \frac{2g_2^2|c_s|^2}{D_3} - \frac{2g_2^2c_s^2}{D_3}$ ,  $T_8 = -\frac{2g_2^2c_s^*\sigma_{zs}(2)}{D_3} - \frac{2g_2^2c_s\sigma_{zs}(2)}{D_3}$ ,  $T_9 = g_1\sigma_{12s}^*(2)$ ,  $T_{10} = g_1\sigma_{12s}(2)$ ,  $T_{11} = \frac{-2g_1c_s^*D_2}{D_1^*} + 2g_1c_s$ ,  $T_{12} = \frac{2g_1\sigma_{zs}^*(1)D_2}{D_1^*}$ ,  $T_{13} = 2g_1\sigma_{zs}(1)$ ,  $T_{14} = \frac{-2g_2c_s^*D_4}{D_3^*} + 2g_2c_s$ ,  $T_{15} = \frac{-2g_2\sigma_{zs}^*(2)D_4}{D_3^*}$ , and  $T_{16} = 2g_2\sigma_{zs}(2)$ .

Next, we discuss the plots of Eq. 42 and discuss about the intensity of four-wave mixing  $I_{\text{FWM}}$ . In Figs. 5 and 6, the variations of four-wave mixing intensity with respect to detuning parameters  $\Delta_1$  and  $\Delta_2$ , respectively, for different values of coupling constant are displayed. In Fig. 5, it is noticed that with the change in  $\Delta_1$ , two sets of peaks in  $I_{\text{FWM}}$  arise. The first set of peaks are observed at negative values of  $\Delta_1$ , the heights of which are inversely proportional to the coupling strength  $g_1$ . The second set of peaks are observed around  $\Delta_1 = 0$ , a fact that is preserved from the plot of single cavity centre.

Interestingly, the peaks are now directly proportional to the coupling strength. In Fig. 6, the behaviour of  $I_{\text{FWM}}$  is quite different from that of Fig. 5. While two sets of peaks are still observed, their positions are confined around  $\Delta_2 = \pm 5$ . The heights of the peaks are inversely proportional to the coupling strength.

## References

1. Vahala KJ (2003) Nature (London) 424:839–846
2. Vuckovic J (2014) Quantum optics and nanophotonics. Oxford University Press 8:365–403
3. Aspelmeyer M, Gr\*oblacher S, Hammerer K, Kiesel N (2010) J Opt Soc Am B 27:189
4. Aspelmeyer M, Meystre P, Schwab K (2012) Phys Today 65:29
5. Zhang P, Wang YD, Sun CP (2005) Phys Rev Lett 95:097204
6. Xue F, Wang YD, Sun CP, Okamoto H, Yamaguchi H, Semba K (2007) New J Phys 9:35

7. LaHaye MD, Suh J, Echternach PM, Schwab KC, Roukes ML (2009) *Nature (London)* 459:960
8. Arcizet O, Jacques V, Siria A, Poncharal P, Vincent P, Seidelin S (2011) *Nat Phys* 7:879
9. Bennett SD, Yao NY, Otterbach J, Zoller P, Rabl P, Lukin MD (2013) *Phys Rev Lett* 110:156402
10. Kippenberg TJ, Vahala KJ (2008) *Science* 321:1172
11. Chan J, Alegre TPM, Safavi-Naeini AH, Hill JT, Krause A, Groblacher S, Aspelmeyer M, Painter O (2011) *Nature (London)* 478:89
12. Dong CH, Fiore V, Kuzyk MC, Wang H (2012) *Science* 338:1609
13. Li ZY, Jin GR, Yin TS, Chen A (2022) *Photonics* 9:70
14. Bothner D, Rodrigues IC, Steele GA (2022) *Commun Phys* 5:33
15. Sun CP, Wei LF, Liu YX, Nori F (2006) *Phys Rev A* 73:022318
16. Marquardt F, Girvin SM (2009) *Trend: Optomechanics. Physics* 2:40
17. Gao M, Liu YX, Wang XB (2011) *Phys Rev A* 83:022309
18. Verhagen E, Deleglise S, Weis S, Schliesser A, Kippenberg TJ (2012) *Nature (London)* 482:63
19. Treutlein P, Genes C, Hammerer K, Poggio M, Rabl P (2014) *Cavity Optomech* 327–351
20. Meystre P (2013) A short walk through quantum optomechanics. *Ann Phys* 525:215–233
21. Akahane Y, Asano T, Song BS, Noda S (2003) *Nature (London)* 425:944–947
22. Song BS, Noda S, Asano T, Akahane Y (2005) *Nat Mater* 4:207–210
23. Noda S, Fujita M, Asano T (2007) *Nat Photonics* 1:449–458
24. Pan J, Huo Y, Sandhu S, Stuhmann N, Povinelli ML, Harris JS, Fejer MM, Fan S (2010) *Appl Phys Lett* 97:101102
25. Pan J, Sandhu S, Huo Y, Stuhmann N, Povinelli ML, Harris JS, Fejer MM, Fan S (2010) *Phys Rev B* 81:041101(R)
26. Manson NB, Harrison JP, Sellars MJ (2006) *Phys Rev B* 74:104303
27. Huck A, Kumar S, Shakoor A, Andersen UL (2011) *Phys Rev Lett* 106:096801
28. Chen Q, Yang WL, Feng M, Du JF (2011) *Phys Rev A* 83:054305
29. Barclay PE, Santori C, Fu KM, Beausoleil RG, Painter O (2009) *Opt Express* 17:8081–8097
30. Park YS, Cook AK, Wang H (2006) *Nano Lett* 6:2075–2079
31. Yang WL, Yin ZQ, Xu ZY, Feng M, Du JF (2010) *Appl Phys Lett* 96:241113
32. Tomljenovic-Hanic S, Steel MJ, Martijn de Sterke C, Salzman J (2006) *Opt Express* 14:3556–3562
33. Barclay PE, Fu KM, Santori C, Beausoleil RG (2009) *Opt Express* 17:9588–9601
34. Wolters J, Schell AW, Kewes G, Nusse N, Schoengen M, Doscher H, Hannappel T, ochel BL, Barth M, Benson O (2010) *Appl Phys Lett* 97:141108
35. Englund D, Shields B, Rivoire K, Hatami F, Vuckovic J, Park H, Lukin MD (2010) *Nano Lett* 10:3922–3926
36. Yang WL, Yin ZQ, Xu ZY, Feng M, Oh CH (2011) *Phys Rev A* 84:043849
37. Faraon A, Santori C, Huang Z, Acosta VM, Beausoleil RG (2012) *Phys Rev Lett* 109:033604
38. Yang WL, An JH, Zhang C, Feng M, Oh CH (2013) *Phys Rev A* 87:022312
39. Ali H, Basit A, Badshah F, Ge G-Q (2018) *Physica E* 104:261–267
40. Abdel-Aty AH, Kadry H, Mohamed ABA et al (2020) *Sci Rep* 10:16640
41. van der Sar T, Hagemeyer J, Pfaff W, Heeres EC, Thon SM, Kim H, Petroff PM, Oosterkamp TH, Bouwmeester D, Hanson R (2011) *Appl Phys Lett* 98:193103
42. Englund D, Shields B, Rivoire K, Hatami F, Vukovi J, Park H, Lukin MD (2010) *Nano Lett* 10:39223926
43. Barth M, Nsse N, Lchel B, Benson O (2009) *Opt Lett* 34:11081110
44. Faraon A, Fushman I, Englund D, Stoltz N, Petroff P, Vuckovic J (2008) *Opt Express* 16:1215412162
45. Waks E, Vuckovic J (2006) *Phys Rev Lett* 96:153601
46. Li J, yu R, Ding C, Wu Y (2014) *Opt Express* 22(12):15025

# Exploitation of *Carica papaya* Seeds for the Fabrication of Titanium Dioxide Nanoparticles and Determination of Their Antibacterial and Antidiabetic Potential



Tabassum Siddiqui, Nida Asif, and Nida Jamil Khan

**Abstract** Synthesis of nanoparticles via biological approach is fast gaining momentum. The use of TiO<sub>2</sub>NP as a potential nanomedicine is a relatively unexplored avenue. In this study, biofabrication of TiO<sub>2</sub>NP was done using the aqueous extract of the seeds of *Carica papaya* for the evaluation of their antibacterial and antidiabetic properties. Synthesis was followed by optimization of various reaction parameters to obtain nanosized particles. The characterization of the bioengineered TiO<sub>2</sub>NP was done by UV–Visible Spectroscopy, XRD, FTIR, and HR-FESEM to analyze their physical and chemical properties. Results of XRD analysis revealed peaks confirming the synthesis of TiO<sub>2</sub>NP, while comparison of the spectrums of FTIR analysis of salt, extract and nanoparticles confirmed the possible interaction between salt and extract, resulting in the synthesis. The antibacterial potential of the biogenic TiO<sub>2</sub>NP against *Escherichia coli* was evaluated at different concentrations by the disk diffusion method. Streptomycin was used as a standard drug in antibacterial studies. Antidiabetic activity of the *C. papaya*-mediated TiO<sub>2</sub>NP showed promising results paving the way for diabetic care. This study, thus, established an environment-friendly, cost-effective, and facile method for the synthesis of TiO<sub>2</sub>NP from the *C. papaya* seeds for the first time and also revealed their antibacterial and antidiabetic potential of medical significance.

**Keywords** Titanium dioxide nanoparticles · Antibacterial · Antidiabetic · *Carica papaya*

---

T. Siddiqui (✉) · N. Asif · N. J. Khan  
Department of Biosciences, Jamia Millia Islamia, New Delhi 110025, India  
e-mail: [tabassum169253@st.jmi.ac.in](mailto:tabassum169253@st.jmi.ac.in)

## Highlights

- Phytofabrication of TiO<sub>2</sub>NP was achieved via a novel source—*Carica papaya* seeds.
- UV–Vis, XRD, and SEM–EDX analysis were done for the biosynthesized nanoparticles.
- Biofabricated TiO<sub>2</sub>NP possessed significant antibacterial activity against *Escherichia coli*.
- Antidiabetic potential of TiO<sub>2</sub>NP was established by suppression of glucosidase.

## 1 Introduction

Nanotechnology is the field which deals with the design, characterization, production, and application of nanoparticles and structures. It is the manipulation of matter at nanoscale. The synthesis of metallic nanoparticles is an active area of academic interest owing to their wide range use across multiple fields. Titanium dioxide nanoparticles (TiO<sub>2</sub>NP) exude unique properties when compared to other nanomaterials. TiO<sub>2</sub>NP also possesses different physicochemical properties in comparison with its fine particles. These properties likely influence their bioactivity [1]. Expanding need to forge alternate drugs against disease causing bacteria and lack of biocompatible antidiabetic medications gave us necessary impetus to utilize a waste product to engineer green-TiO<sub>2</sub>NP. To the best of our knowledge, papaya seeds have not been explored yet for the synthesis of the TiO<sub>2</sub>NP.

## 2 Materials and Methods

Papaya seeds were washed, dried, and pulverized [2]. Aqueous extract preparation was achieved by mixing 5 g of powdered seeds with 100 ml of water. This mixture was then heated to 60 °C for 15 min. Finally, it was centrifuged at 5000 rpm. The supernatant was then filtered using Whatman 1 paper to obtain extract. Synthesis of TiO<sub>2</sub>NP was done by mixing equal amounts of papaya seeds extract and precursor salt. This reaction mixture was then subjected to incubation at 30 °C for 24 h in an incubator shaker. Formation of TiO<sub>2</sub>NP was indicated by change in color of the reaction mixture and by measuring absorbance spectrophotometrically [3]. To determine the impact of various reaction parameters on the reduction process for the synthesis of TiO<sub>2</sub>NP, optimization of different reaction parameters was done. For this purpose, “one factor-at-a time” method was followed. So, the investigational factor was changed one at a time, and remaining factors were kept constant. UV–Vis analysis was done in the range of 200–500 nm (Shimadzu’s UV-1280 UV–visible spectrophotometer). Crystallinity of the bioengineered nanoparticles was evaluated by XRD analysis in the  $2\theta$  range of 10–80° (CubiX3). Involvement of the functional groups of the reducing agents in the reduction process was determined using

FTIR (Agilent Technologies Cary 630 FTIR). Finally, confirmation of biosynthesis of nanoparticles was done using HRSEM (JSM-7610FPlus Schottky). It also gave information about size, texture, and morphology of TiO<sub>2</sub>NP. EDX analysis further confirmed the elemental composition of the biosynthesized TiO<sub>2</sub>NP.

In vitro antibacterial activity was evaluated for the phytosynthesized TiO<sub>2</sub>NP using disk diffusion method. Muller Hinton Agar plates were used for this study. Bacterial culture of *E. coli* was grown overnight and its absorbance was adjusted according to McFarland 0.5 standard. The biosynthesized TiO<sub>2</sub>NP was impregnated on discs and was placed on the plates with appropriate controls. Antidiabetic activity of the TiO<sub>2</sub>NP was determined via  $\alpha$ -glucosidase assay. In order to evaluate  $\alpha$ -glucosidase activity, 100 ml solution of  $\alpha$ -glucosidase was prepared. 100  $\mu$ l of nanoparticles were mixed with 200  $\mu$ l of enzyme and incubated at 37 °C for 60 min. This was then treated with 100  $\mu$ l of p-nitrophenyl- $\alpha$ -d-glucopyranoside and incubated again at 37 °C for 10 min. Termination of the reaction was done by mixing 2 ml Na<sub>2</sub>CO<sub>3</sub> (0.1 M). Optical density was then measured (405 nm) to calculate the percentage inhibition [4].

Statistical analysis: Experiments were performed in triplicates, and final results were represented as means  $\pm$  SD.

### 3 Results and Discussion

The present study focused on the green synthesis of TiO<sub>2</sub>NP from *C. papaya* seeds extract. This facile method has successfully reduced TiO<sub>2</sub> to TiO<sub>2</sub>NP. The optimization results were analyzed using UV–Vis spectroscopy revealed that the optimum amount of seeds biomass needed for the synthesis of TiO<sub>2</sub>NP was 50 mg ml<sup>-1</sup>, and the optimum conditions for the preparation of extract were 100 °C for 10 min. Similarly, optimization of reaction conditions revealed the best temperature was 60 °C, salt concentration was 0.1 mM, pH was 7, salt to extract ratio was 1:3, and reaction time was 6 h. Roopan et al. [5] reported the synthesis of rutile TiO<sub>2</sub>NP using *Annona squamosa* at the temperature of 60 °C and time 6 h. In order to confirm the presence of nanoparticles, the UV–Vis spectrum was analyzed, and absorption spectrum was observed at 252 nm (Fig. 1a). FTIR spectrum was done from 650 to 4000 cm<sup>-1</sup>. It was done for the extract, salt, and the reaction mixture (Fig. 2e–g). The FTIR analysis of the seed extract suggested the involvement of a range of phytochemicals that could have played a crucial role in the synthesis process. The FTIR analysis of the salt solution gave the information of the characteristic bonds present in the salt. Various functional groups present in the nanoparticles confirmed the role of both salt and extract in the reducing process. The spectra revealed the functional groups at 3272, 2127, 1639, 1546, and 1048 cm<sup>-1</sup>. They are related to primary alcohol, aliphatic nitro compounds, and azo compounds. The XRD graph of TiO<sub>2</sub>NP is shown in Fig. 1b. The result indicated the synthesis of anatase form of TiO<sub>2</sub>NP. Four distinct peaks were absorbed at 25°, 49°, 62°, and 77° corresponding to Miller indices values (1



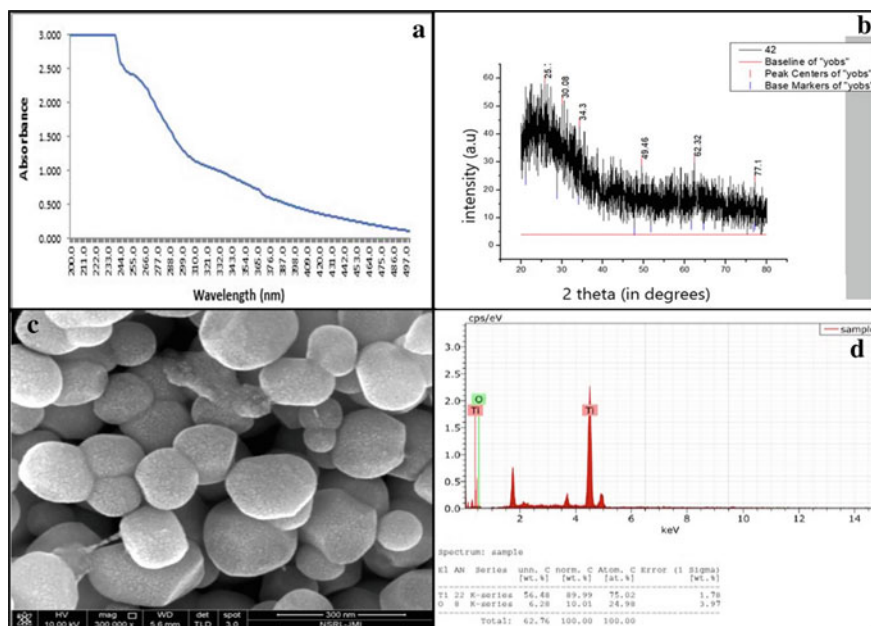


**Fig. 1** a UV spectra; b XRD graph; c SEM micrograph; d EDX spectra

0 1), (2 0 0), (2 0 4), and (2 1 5), respectively [6]. SEM analysis of TiO<sub>2</sub>NP was performed to reveal their size and structure (Fig. 1c). The phytosynthesized TiO<sub>2</sub>NP was polydisperse and spherical with an average size of 80 nm. To gain an insight into the elemental composition, EDX analysis was performed (Fig. 1d). It revealed strong signals in the titanium region and in the oxygen region confirming the formation of TiO<sub>2</sub>NP.

### 3.1 Antibacterial Activity

The antibacterial activity of TiO<sub>2</sub>NP was determined using disk diffusion (Fig. 3h). Streptomycin was used as a control. The synthesized TiO<sub>2</sub>NP displayed antibacterial activity against pathogenic bacteria—*E. coli*. The zone of inhibition was measured. The results are depicted in Table 1.

### 3.2 Antidiabetic Activity

Significant carbohydrate metabolism enzyme— $\alpha$ -glucosidase is used for the treatment of diabetes. Inhibition of this and similar enzymes delay carbohydrate ingestion

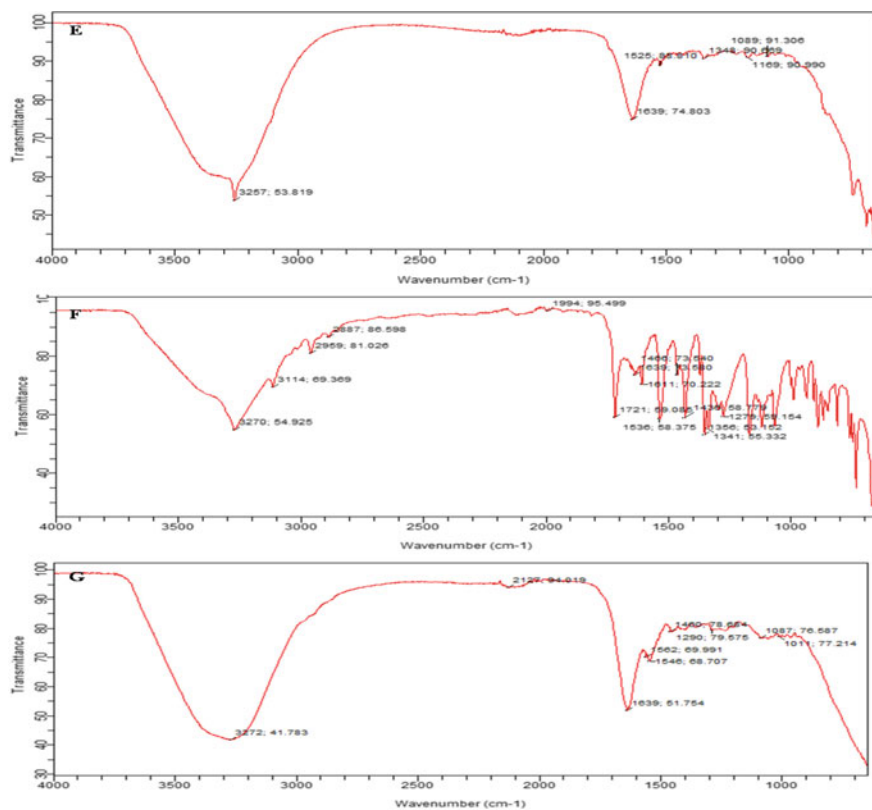


**Fig. 2** FTIR spectra of **e**  $\text{TiO}_2$  salt; **f** extract; **g**  $\text{TiO}_2\text{NP}$

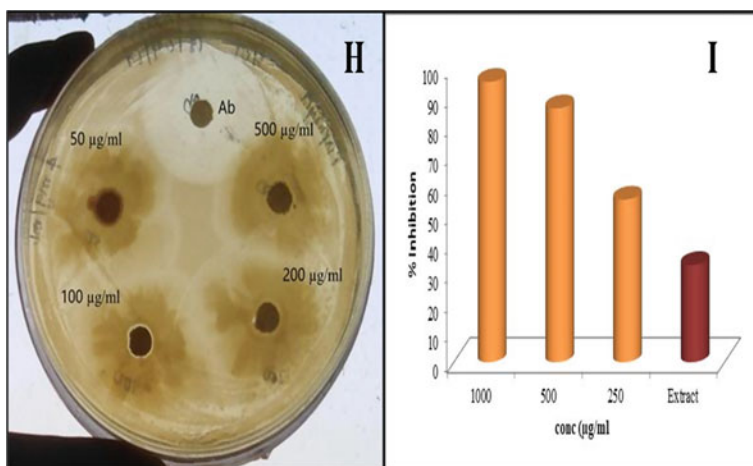


**Fig. 3** **h** Antibacterial activity; **i** antidiabetic activity

**Table 1** Antibacterial activity of TiO<sub>2</sub>NP

TiO <sub>2</sub> NP concentration (μg/ml)	Zone of inhibition (in mm)
50	10
100	11
200	15

and glucose absorption in the body. The papaya seed extract-mediated nanoparticles greatly reduced  $\alpha$ -glucosidase activity with increasing dose (Fig. 3h). The results showed that with increase in concentration of nanoparticles (250, 500 and 1000  $\mu\text{g/ml}$ ), the activity of the  $\alpha$ -glucosidase decreased. Highest percentage inhibition was achieved at 1000  $\mu\text{g/ml}$  by TiO<sub>2</sub>NP.

## 4 Conclusion

In the present times, there is a growing need to innovate biocompatible treatment options as the existing ones are expensive, noxious, and cause side-effects. Titanium, as a metal, already possess versatile characteristics. Its use for the synthesis of nanoparticles further accentuates its properties. Exploitation of papaya seeds for this purpose is not only novel but also cost effective and environment-friendly.

## References

1. Shi H, Magaye R, Castranova V, Zhao J (2013) Titanium dioxide nanoparticles: a review of current toxicological data. Part Fibre Toxicol 10:15
2. Ravindra K, Sangeeta B, Prerana K, Sandeep M (2018) Green synthesis of silver nanoparticles using papaya seed and its characterization. Int J Res Appl Sci Eng Technol 6(2):168–174
3. Thirunavukkarasu S, Abdul AR, Chidambaram J, Govindasamy R, Sampath M, Arivarasan VK, Kanayairam V, John T, Jayachandran V, Se-Kwon K (2013) Green synthesis of titanium dioxide nanoparticles using *Psidium guajava* extract and its antibacterial and antioxidant properties. Asian Pac J Trop Med 7(12):968–976
4. Sanap SP, Ghosh S, Jabgunde AM, Pinjari RV, Gejji SP, Singh S, Chopade BB, Dhavale DD (2010) Synthesis, computational study and glycosidase inhibitory activity of polyhydroxylated conidine alkaloids—a bicyclic iminosugar. Org Biomol Chem 8:3307–3315
5. Roopan SM, Bharathi A, Prabhakar A, Rahuman AA, Velayutham K, Rajakumar G, Madhumitha G (2012) Efficient phyto-synthesis and structural characterization of rutile TiO<sub>2</sub> nanoparticles using *Annona squamosa* peel extract. Spectrochim Acta A Mol Biomol Spectrosc (SAA) 98:86–90
6. Siddiqui T, Khan NJ, Asif N, Ahamad I, Yasin D, Fatma T (2022) Screening, characterisation and bioactivities of green fabricated TiO<sub>2</sub> NP via cyanobacterial extract. Environ Sci Pollut Res 1–15

# Development of a Nanocarrier for Plant-Derived Drug



Tajunisa Munasuddin and Reshmi Nair

**Abstract** Herbal medicines and formulations have been used since time immemorial and have been recognized to have fewer adverse effects as compared to modern medicine, but have been limited due to their volatility, instability and poor solubility. To overcome this complication, the authors proposed that encapsulation of therapeutic phytocompounds in a suitable biomatrix. These designs of nano-systems can deliver the active compounds in desired quantity with controlled release directed toward specific tissue or organ and protect it against thermal or photo-degradation. The strategy of integrating nanotechnology and plant extracts has revolutionized the drug delivery and also improves formulation's most desirable property. In this research, the possibility of integrating biopolymer nanoparticles like chitosan and alginate posing as nano-vehicle for plant-derived hydrophobic drug is being explored, while probing into its drug loading capacity and further evaluation based on its efficacy, done using different assays. The novelty of this project lies in the choice of naturally derived compounds to fabricate a combination that constitutes the formation of novel drug delivery system. Synthesis of chitosan-alginate nanoparticles loaded with quinones had the size  $260 \pm 20$  nm. The encapsulation efficiency of nanoparticulate system was found to be 56%. Cytotoxic activity of the sample was observed at 24 h and at 48 h was 70% and 78%, respectively, similar to the clonogenic assay results that depicted that higher concentration of nanoparticles showed lesser colony formation while the microbial analysis showed positive outcome. These promising results pave the way to the possibility of the prepared formulation to have anti-microbial and anti-cancerous property.

**Keywords** Herbal medicine · Nano-systems · Encapsulation · Drug delivery

---

T. Munasuddin · R. Nair (✉)  
Amity University Dubai, Dubai International Academic City, Dubai, UAE  
e-mail: [mair@amityuniversity.ae](mailto:mair@amityuniversity.ae)

## 1 Introduction

Cancer is a very common malignant disease that leads to deaths worldwide. Current modes of treatment are based on synthetic drugs or radiation which cannot tell the difference between normal and cancerous cells resulting in many side effects. These agents that deal with tumor have restricted effects during chemotherapy because of its poor solubility in the aqueous environment, cytotoxicity and side effects to healthy tissues as it cannot always eradicate the tumor cells and multidrug resistance problems. As a substitute to these therapies, large number of plants have been used widely to put brakes on several chronic diseases including various types of cancer. Despite the benefits they offer, using molecules that are larger in size have posed to have major challenges. The employment of materials in the production of nano-sized entities broadens the possibility to improve, control and change their properties by modifying the overall system using certain variables; like the size, surface charge, encapsulation efficiency and drug release when formulating the nanoparticles as its crucial for nanoparticles to reach the site. By designing a novel drug delivery system (NDDS), the therapeutic value and bioavailability of the corresponding herbal constituent are increased. Additionally, bulk dosing and decreased absorption of the drug can be apprehended and overcome by incorporating these herbal extracts into nano-formulation systems.

*Nigella sativa* or the black cumin is a most popularly grown annual herbaceous plant widely distributed in the Middle East and Southeast Asia. Its seed oil is extensively studied as a natural remedy in treating a variety of ailment and chronic diseases [1]. The chemical composition of volatile oil from its seed is very diverse with the main active component Thymoquinone (TQ), and its anti-cancerous activity is exhibited through various mechanisms both in vivo and in vitro [2, 3]. Different formulations, which included nanostructured carriers, of TQ nanoparticles were tested against various types of cancer and studies show greater effectiveness of these particles when compared with free TQ [4]. The selection of a suitable matrix for the current intended use is of prime importance since it will affect the efficiency of encapsulation of the therapeutic molecules including its release profile where biodegradable polymeric materials have gained more popularity [5]. The two naturally occurring polysaccharides or polyelectrolyte polymers of opposite charges chosen were chitosan and alginate that are extensively exploited and show promising results [6, 7]. Chitosan has been the choice of compound to prepare mucoadhesive formulations, boost the dissolution of poorly soluble drugs, its targeting with improved absorption. Alginate is a linear hydrophilic anionic copolymer extracted from brown algae or bacteria. It is capable of forming hydrogels by chelating with divalent cations such as calcium. Alginate nanoparticles may be easily created by gelation with calcium ions, and this property can be leveraged to create a pre-gel consisting of small gel particles, which can then be followed by the addition of a polycation to form a polyelectrolyte complex reducing its porosity and preventing leakage like in the case of liposomes. These biopolymers are considered as Generally Recognized as Safe (GRAS) by the Food and Drug Administration (FDA). The controlled and combined use of calcium

alginate and chitosan compounds can lead to novel ways of delivering drugs with considerable effects [8]. The ideal range of particle size must be between 100 and 800 nm as the structural variation caused due to the formation of tumor cells has pores within that range. A novel approach with an all-natural combination is contemplated to overcome drawbacks of traditional drug delivery systems, and the strategies of synthesizing such nanocarriers are that higher concentration of drugs can be delivered due to unique size and loading capacities of the nano-systems, enhanced surface area of drugs that aid in quicker dissolution in blood, persisting at sites for longer durations. Without the addition of any ligand, it is assumed to exhibit the enhanced permeation and retention (EPR) effect or passive targeting. Subsequently, it has decreased side effects since the dosage of drug formulation is also minimal.

## **2 Materials and Methods**

### **2.1 Chemicals Required**

Cold pressed *Nigella Sativa* seed oil (purity-100%) was obtained from a commercial supplier, Aswar Elite factory FZE. Chitosan, from Shrimp shells (MW is 750,000, degree of deacetylation is 75%) purchased from Himedia Laboratories Pvt. Ltd. (India). Sodium alginate (purity-91%, food grade) and calcium chloride (extra pure-95%) purchased from Loba Chemie Pvt. Ltd. All other chemicals and reagents used were of analytical grade.

### **2.2 Sample Preparation**

Cold pressed oil was subjected to liquid–liquid extraction [9]. This method involved extracting the oil with an ethanol–water solution and determining the best ethanol concentration and extraction time. After 12 h of equilibrium, two distinct layers were observed (oil and hydroalcoholic phases). These were separated using a Pasteur pipette and subsequently analyzed by FTIR spectroscopy. This was followed by preparation of blank Chitosan-Alginate nanoparticles. Chitosan solution (0.8 mg/ml in acetic acid) was added to the pre-gel composed of aqueous sodium alginate (3 mg/ml) and calcium chloride (3.35 mg/ml) where pH was adjusted to 5.1 using HCl and was stirred for an hour. The opalescent suspension after the addition of alginate pre-gel indicated the formation of nanoparticles and was equilibrated overnight to allow formation uniformly sized nanoparticles.

A constant volume of quinones solution (300  $\mu$ l) obtained from the liquid–liquid extraction procedure mixed with equal volumes of dehydrated alcohol was incorporate in the aqueous alginate solution prior to the formation of pre-gel using calcium

chloride solution. The following steps were the same as preparation of blank nanoparticles. Prior to characterization of the blank and thymoquinone loaded nanoparticles, the sample was sonicated for one hour at 30 °C. With the literature, opalescent color was observed. This method of preparation is also termed as ionotropic pre-gelation followed by polyelectrolyte complexation. The calcium ions react with guluronic acid structures on alginate. It is proposed that the formation of nanoparticles takes place by the interaction of negatively charged calcium alginate complex with the cationic polymer, chitosan. The pre-gel state is necessary to enable ionic interactions between calcium, alginate and chitosan to form nanoparticles.

### 3 Results and Discussion

#### 3.1 Characterization

The process of extracting quinones involved formation of two easily separable layers observed in the cold pressed nigella sativa seed oil that contained 80% ethanol and both were analyzed using FTIR spectroscopy. The characteristic strong stretching band of carbonyl group present in the sample is observed at the wavenumber 1743  $\text{cm}^{-1}$  which is in resemblance to the peak reported for thymoquinone. The intense band present at 2922  $\text{cm}^{-1}$  corresponds to the C–H stretching of aliphatic groups, and the weaker band that was obtained at higher wavenumber (3008  $\text{cm}^{-1}$ ) was allocated to the stretching observed in the vinylic C–H in the C=C–H groups. The few extra peaks that were observed toward the fingerprint region accounts for the fatty acids which include flavonoids, saponins and tannins present in the quinones rich extract. The optimized size of the thymoquinone loaded nanocarrier was found to be approximately 289 nm when tested under dynamic light scattering (DLS) equipment.

#### 3.2 Encapsulation Efficiency

Ensuring effective encapsulation of drugs into the nanoparticulate delivery systems could increase the efficacy of therapeutic effects by the respective bioactive component in prevention and treatment of diseases. This analysis was calculated by comparing the difference in absorbance of the compound that was encapsulated in the solution to that of the unencapsulated compound [10]. Different concentrations varying from 0.5 to 2.5 g/ml of free drug nanoparticles and 0.6 mg quinones rich extract loaded polymer nanoparticles were prepared using ethanol as the solvent. Using a UV–vis spectrophotometer, the absorbance was measured at wavelength 258 nm for the bioactive compound, and the wavelength at maximum absorbance after encapsulation was considered.

**Fig. 1** Standard plot represents the absorbance of nano-formulated drug in the nanocarrier at different concentrations

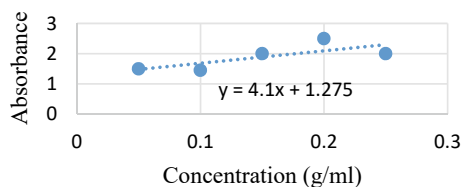
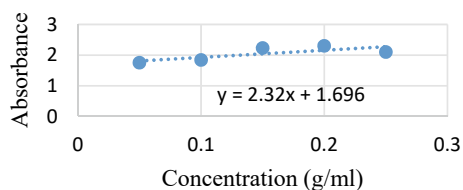


**Fig. 2** Standard plot represents the absorbance of nano-formulated encapsulated in the nanocarrier at different concentrations



A graph was plotted as shown in Figs. 1 and 2, with absorbance on the vertical axis and the concentration in g/ml on the horizontal axis whose slope of the best line fit determined the average values required for calculation according to Eq. (1).

$$\text{Encapsulation efficiency (\%)} = (\text{weight of drug in nanoparticle} / \text{initial weight of drug}) * 100 \quad (1)$$

The absorbance values from the slopes of the graphs plotted in accordance with values obtained from the standard plot of drug nanoparticles before encapsulation or weight of the drug initially fed to the system and the encapsulated forms or weight of the drug in the nanoparticle are 2.66 and 1.89, respectively. The encapsulation efficiency of the nanoparticulate system thus formed was found to be 56%.

### 3.3 Biological Assays

The prepared quinones loaded chitosan-alginate nanoparticles were screened for in vitro anticancer activity by MTT assay against MCF-7 breast cancer cell lines. The difference in substrate to chromogenic product conversion by live cells is determined by this viability assay. The graph is based on the percentage of live cells in the positive and negative controls, as well as the samples submitted for testing. According to the two plots, data was obtained after 24 h (Fig. 3) and 48 h (Fig. 4). It is quite evident that the sample with higher concentration of nanoparticles had greater cytotoxic affect; it destroyed 70% and 78% cancer cells at time intervals of 24 and 48 h, respectively, which showed a promising result.

To test the anti-microbial properties of the synthesized nanoparticulate carrier system, Minimum Inhibitory Concentration (MIC) and Minimum Microbicidal Concentration (MMC) evaluations of the prepared herbal compound loaded nanoparticles against antibiotic sensitive and resistant *Staphylococcus aureus* bacterial and



**Fig. 3** Cytotoxic activity of quinones loaded chitosan-alginate nanoparticles on MCF-7 cancer cell lines after 24 h

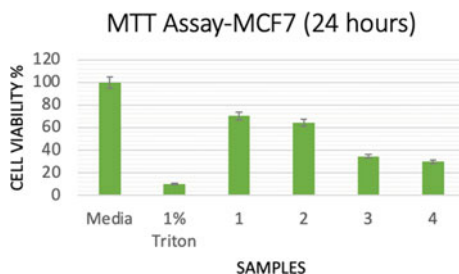
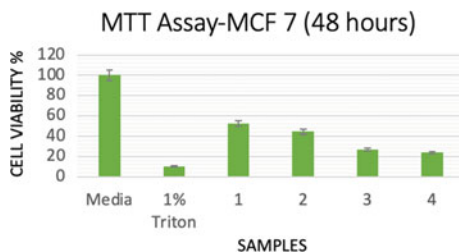


**Fig. 4** Cytotoxic activity of quinones loaded chitosan-alginate nanoparticles on MCF-7 cancer cell lines after 48 h



*Candida auris* fungal species were done. Both Minimum Inhibitory Concentration (MIC) and Minimum Microbicidal Concentration (MMC) are complementary to each other. The results obtained as illustrated in Table 1 indicate that less concentration of the nanoparticulate system is required to inhibit the growth of the respective bacteria and fungi.

The clonogenic assay effectively checks each cell in the population's ability to divide indefinitely, which can be used to assess the efficacy of cytotoxic medicinal drugs. The results obtained were compared with controls positive and negative which clearly indicated that the formation of colonies decreased as the concentration of drug encapsulated nanoparticles increased, there was reduction in the number of colonies formed.

**Table 1** MIC and MMC values obtained from agar and broth method using bacterial and fungal species

Sample	<i>Staphylococcus aureus</i>		<i>Candida auris</i>	
	MIC	MMC	MIC	MMC
1	3.12	25.4	4.7	24.6
2	3.61	22.1	4.2	23.5
3	3.11	20.3	4.8	22.8
4	3.17	21.6	4.3	23.7

## 4 Conclusion

Chitosan nanoparticles have the desired effects and have prompted accelerated research activities as a pharmaceutical excipient or drug delivery material. Such systems have immense utility in targeting and controlled release of a wide range of bioactive molecules. In this study, the best and simple ionotropic gelation method was used to prepare and combine chitosan with alginate to synthesize nanoparticles, and its efficiency was evaluated. The procedure for the synthesis of these nanoparticles was optimized to obtain minimum particle size by varying different parameters. The nanoparticles had a diameter of  $260 \pm 20$  nm. The encapsulation efficiency of nanoparticulate system was found to be 56%. Cytotoxic activity of the sample was observed at 24 h and at 48 h was 70% and 78%, respectively, similar to the clonogenic assay results that depicted that higher concentration of nanoparticles showed lesser colony formation while the microbial analysis showed positive outcome. Therefore, taking these factors into consideration, it can be derived that the fabricated drug delivery system depicted to have anti-microbial and anti-cancerous property. In conclusion, this novel nano-system may offer interesting potential for the transportation and controlled release of hydrophobic compounds.

## References

1. Büyük Nİ, Arayıcı PP, Derman S, Mustafaeva Z, Yücel S (2020) An optimization study for chitosan nanoparticles: synthesis and characterization. *Celal Bayar Univ J Sci* 16(2):119–127
2. Caban S, Aytakin E, Sahin A, Capan Y (2014) Nanosystems for drug delivery. *OA Drug Des Delivery*. <http://www.oapublishinglondon.com/article/1191>
3. Kumar KS, Kumar PS, Vijayalakshmi S (2011) Anticancer studies of drug encapsulated polyethylene terephthalate-co-poly(lactic acid) nanocapsules. *J Pharm Bioall Sci* 3(2):286
4. Elkady AI, Abu-Zinadah OA, El Hamid Hussein RA (2017) Crude flavonoid extract of the medicinal herb *nigella sativa* inhibits proliferation and induces apoptosis in breast cancer cells. *J Biomater Tissue Eng* 7(12):1235–1249
5. Bashandy AES (2006) Effect of fixed oil of *nigella sativa* on male fertility in normal and hyperlipidemic rats. *Int J Pharmacol* 3(1):27–33
6. Almajali B et al (2021) Thymoquinone, as a novel therapeutic candidate of cancers. *Pharmaceuticals* 14(4)
7. Bhattacharya S et al (2015) PEGylated-thymoquinone-nanoparticle mediated retardation of breast cancer cell migration by deregulation of cytoskeletal actin polymerization through miR-34a. *Biomaterials* 51:91–107
8. Panyam J, Labhasetwar V (2003) Biodegradable nanoparticles for drug and gene delivery to cells and tissue. *Adv Drug Delivery Rev* 55(3):329–347
9. Manickam B, Sreedharan R, Elumalai M (2014) ‘Genipin’—the natural water soluble cross-linking agent and its importance in the modified drug delivery systems: an overview. *Curr Drug Delivery* 11(1):139–145
10. Urbanova K, Kloucek P, Havlik J, Valterova I, Kokoska L (2020) Fast and ecological liquid-liquid separation method for preparing quinones enriched extract from *nigella sativa* oil. *J Braz Chem Soc*

# Recombination Analysis of $\text{CH}_3\text{NH}_3\text{PbI}_3$ Perovskite Solar Cell for Optimized Device Structure



Mohd Amir, Mukesh Pratap Singh, and Iram Masood

**Abstract** In this work, we have designed a conventional perovskite solar cell (PSC) with the structure “FTO/TiO<sub>2</sub>/CH<sub>3</sub>NH<sub>3</sub>PbI<sub>3</sub>/Spiro-OmeTAD/Au” using general-purpose photovoltaic device model (OghmaNano). With this primary design, 13.88% power conversion efficiency (*PCE*) has been obtained. In order to enhance the performance of this device, the thicknesses of each layer and the doping concentrations of transport layers (ETL and HTL) are optimized with respect to the characteristic parameters of the solar cell, namely the open-circuit voltage ( $V_{OC}$ ), short circuit current density ( $J_{SC}$ ), and fill factor (*FF*). The optimized thickness of active/perovskite layer, electron and hole transport layers (ETL and HTL), and cathode are obtained as 240, 20, 100, and 20 nm, respectively. The optimized value of dopant concentrations for HTL and ETL is obtained as  $2 \times 10^{25}$  and  $4 \times 10^{25} \text{ m}^{-3}$ , respectively. Furthermore, the effect of carrier recombination on the performance of the device has also been studied. We have achieved 24.18% of *PCE* with the optimized design of this conventional structure.

**Keywords** Perovskite solar cells · Simulation · Optimization · Layer thicknesses · Transport layers doping · Recombination

## 1 Introduction

The perovskite solar cell (PSC) has competed the star candidates of PV industry such as silicon (Si) and gallium arsenide (GaAs) in term of power conversion efficiency (*PCE*) at a very fast rate. The research in the field of PSCs, during a short span of past ten years, has gradually increased their *PCE* from 3.8 to ~ 25% [1].

To further improve the *PCE*, the better understanding of operational physics of such devices is required, unfortunately no enough information is available in the literature about this. The numerical experiments using computer-aided tools provides a

---

M. Amir (✉) · M. P. Singh · I. Masood

Department of Applied Sciences and Humanities, Jamia Millia Islamia, New Delhi 110025, India  
e-mail: [mohd169066@st.jmi.ac.in](mailto:mohd169066@st.jmi.ac.in)

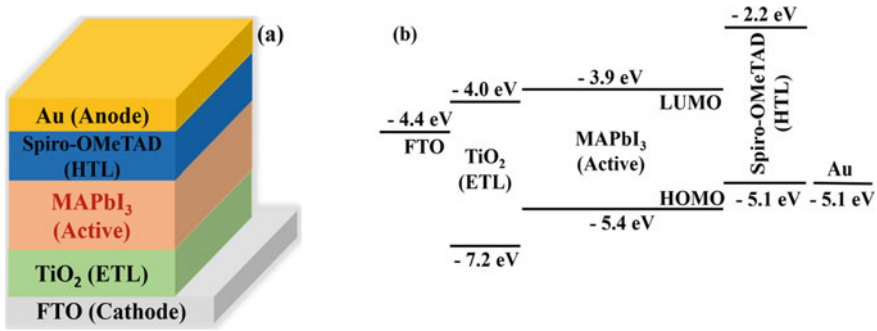


**Fig. 1** Schematic of the designed device (a) and the band diagram (b)

cost effective and efficient alternative to the experiments to detail inside the fundamental physics of such devices, to identify the *PCE* limiting factors, and to study the effect of several parameters upon the device performance [2–4]. Herein, we have performed numerical experiments, in order to optimize the thicknesses of all the layers in the device stack, and to optimize the doping levels of the transport layers. We have also studied; how does the recombination affect the device performance.

## 2 Device Structure and Band Diagram

The device structure and the energy band alignment of the device are depicted in Fig. 1a, b. The FTO,  $\text{TiO}_2$ ,  $\text{CH}_3\text{NH}_3\text{PbI}_3$  ( $\text{MAPbI}_3$ ), Spiro-OMeTAD, and Au are used as a cathode, ETL, active layer, HTL, and anode, respectively.

## 3 Simulation Details

To carry out all the numerical experiments, we have used an open-source simulation tool, i.e., OghmaNano. To simulate the electrical response of the device, the program solves Poisson, continuity, and the drift diffusion equations numerically by finite element method. The transfer matrix method is been utilized in the program to record the optical behavior of the device. The detailed description of the program can be found in Refs. [5, 6]. The material parameter used in the simulation is given in Table 1.

**Table 1** Parameter of the materials used in the simulation [3]

Parameter	TiO <sub>2</sub>	CH <sub>3</sub> NH <sub>3</sub> PbI <sub>3</sub>	Spiro-OMeTAD
Electron mobility (m <sup>2</sup> /Vs)	6e-07	0.005	1e-08
Hole mobility (m <sup>2</sup> /Vs)	6e-07	0.005	1e-08
Effective DOS for free electrons (m <sup>-3</sup> )	1.0e27	2.0e26	2.5e26
Effective DOS for free holes (m <sup>-3</sup> )	2.0e26	2.5e26	2.5e26
Electron affinity (eV)	4.0	3.93	2.2
Band-gap (eV)	3.2	1.5	2.91
Relative permittivity	100	30	3

## 4 Results and Discussion

### 4.1 Optimization of Layers Thicknesses

The thickness of one layer is varied at a time, by fixing the thickness of remaining layers. To obtain the optimized value of layer thickness, the effect of its variation on the characteristic parameters of the device, namely open-circuit voltage ( $V_{OC}$ ), short-circuit current density ( $J_{SC}$ ), fill factor ( $FF$ ), and the power conversion efficiency ( $PCE$ ), has been studied for the considered PSC. The obtained results are plotted in Fig. 2.

The results reveal that the variation in active layer, transport layers, and the cathode thicknesses majorly influences the  $J_{SC}$  in the device along with  $FF$ . However, no significant change is observed in the  $V_{OC}$  with respect to the change in particular layer thickness. A number of simulations has run with different values of thicknesses, for a considered layer under investigation. The value of thickness providing maximum  $PCE$  is considered as the optimized. On the basis, the obtained optimized value of thicknesses for the active layer, ETL, HTL, and cathode are 240, 20, 100, and 20 nm, respectively. The  $PCE$  of 18.31% has been obtained with the optimized values of considered layers thicknesses.

### 4.2 Optimization of Transport Layers Doping Levels

It has been observed in the results that the variation of doping concentrations  $N_A$  and  $N_D$  in the HTL and ELT, respectively, majorly affects the series resistance ( $R_S$ ) of the device which in turn severely changes the fill factor, and hence the  $PCE$  as shown in Fig. 3. At the optimized doping concentration of  $2 \times 10^{25}$  and  $4 \times 10^{25}$  m<sup>-3</sup> in HTL and ETL, respectively, the maximum value of  $PCE$  (18.38) is achieved.

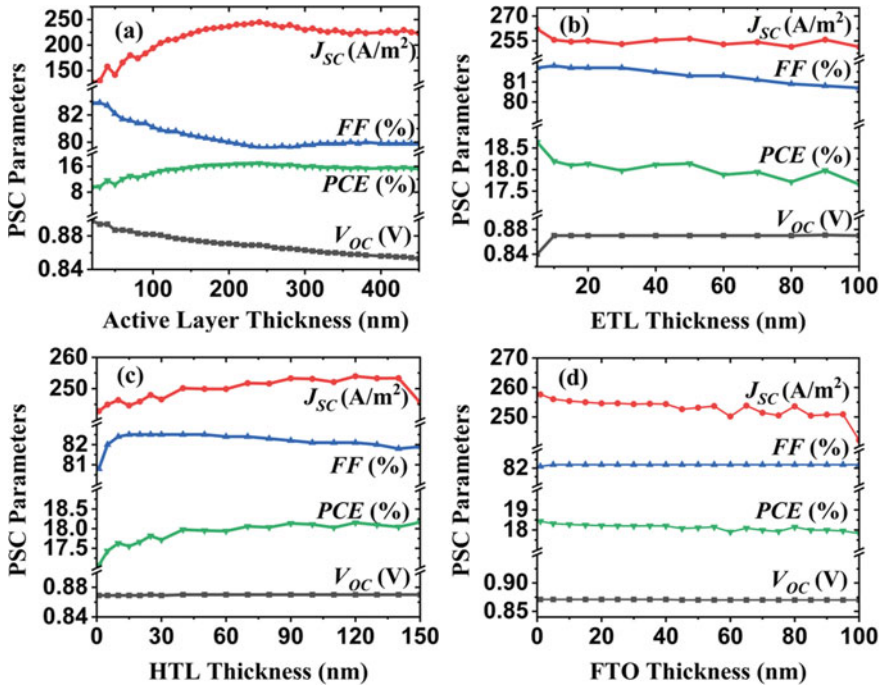


Fig. 2 Observed changes in the characteristics parameters of the device with the variation in **a** active layer thickness, **b** ETL thickness, **c** HTL thickness, and **d** FTO thickness

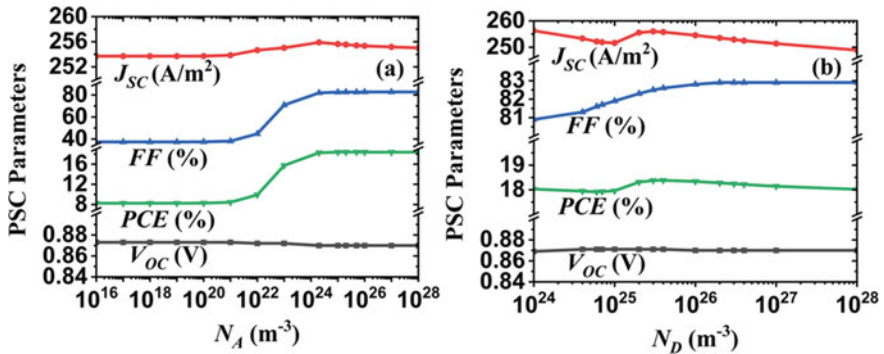
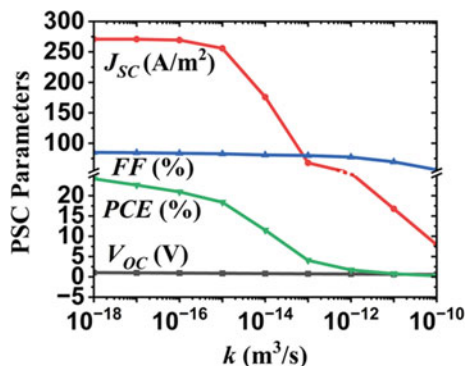


Fig. 3 Observed changes in the characteristics parameters of the device by varying the doping concentration in **a** HTL and **b** ETL

### 4.3 Effect of Recombination

The  $PCE$  of 24.18% is obtained with  $1 \times 10^{-18} m^3/s$  of recombination coefficient ( $k$ ). Onwards, it has observed as the value of  $k$  increases the free carrier concentration

**Fig. 4** Effect of recombination coefficient on the characteristic parameters



in the active layer starts decreasing. Hence, the  $J_{SC}$  continually decreases as the  $k$  increases as shown in Fig. 4. The decline in  $J_{SC}$  degrades the  $PCE$  of the device. However, the variation of  $k$  does not result in any significant change in the other characteristic parameters of the device.

## 5 Conclusion

This study concludes, after optimizing the thicknesses of the active layer, transport layers and cathode to 240, 20, 100, and 20 nm, respectively, the  $PCE$  of 18.38% can be obtained. Further, improvement in  $PCE$  is obtained by optimizing the doping concentrations of the transport layers. It has also been observed in this study that suppression of carrier recombination can lead the  $PCE$  up to 24.18%.

## References

1. Zhang J, Li X, Wang L et al (2021) Enhanced performance of  $\text{CH}_3\text{NH}_3\text{PbI}_3$  perovskite solar cells by excess halide modification. *Appl Surf Sci* 564:150464
2. De Los M, Santos I, Cortina-Marrero HJ, Ruíz-Sánchez MA et al (2020) Optimization of  $\text{CH}_3\text{NH}_3\text{PbI}_3$  perovskite solar cells: a theoretical and experimental study. *Sol Energy* 199:198–205
3. Taheri S, Ahmadkhan Kordbacheh A, Minbashi M, Hajjiah A (2021) Effect of defects on high efficient perovskite solar cells. *Opt Mater (Amst)* 111:110601
4. Karthick S, Velumani S, Bouclé J (2020) Experimental and SCAPS simulated formamidinium perovskite solar cells: a comparison of device performance. *Sol Energy* 205:349–357
5. MacKenzie RCI, Shuttle CG, Chabinye ML, Nelson J (2012) Extracting microscopic device parameters from transient photocurrent measurements of P3HT:PCBM solar cells. *Adv Energy Mater* 2:662–669
6. MacKenzie RCI, Kirchartz T, Dobb GFA, Nelson J (2011) Modeling nongeminate recombination in P3HT:PCBM solar cells. *J Phys Chem C* 115:9806–9813

# Comparative Analysis on Crystallographic Presentation of WS<sub>2</sub> Polymorphs by VESTA Software



Somveer, Davender Singh, and Dharamvir Singh Ahlawat

**Abstract** Here in this work, we carried out a comparative analysis of different crystallographic properties of WS<sub>2</sub> polymorphs for the monoclinic (m-WS<sub>2</sub>) and hexagonal (h-WS<sub>2</sub>) structures. Due to advancement of nanoscience and nanotechnology, this work comprises of crystallographic representation of WS<sub>2</sub> polymorphs nanomaterial's using VESTA software. Lattice parameters for m-WS<sub>2</sub>:  $a = 3.270 \text{ \AA}$ ,  $b = 5.717 \text{ \AA}$ ,  $c = 12.309 \text{ \AA}$  and for h-WS<sub>2</sub>:  $a = b = 3.1530 \text{ \AA}$ ,  $c = 12.343 \text{ \AA}$  with bond length between tungsten (W) and sulfur (S) atoms in angstrom unit for both structural models have been reported. Moreover, we have compared the bond lengths of the studied polymorphs with the previously reported crystals.

**Keywords** Polymorphs · WS<sub>2</sub> · VESTA · Lattice parameters

## 1 Introduction

The area of material science has progressed to a greater extent in the last decade and a half. The discovery of the two-dimensional (2D) materials like carbon nanotubes (graphene) and inorganic nanotubes (transition metal dichalcogenides) has been very significant compared to their bulk materials. These 2D materials are very useful in developing metallic (graphene) and insulating devices and heavy metal detoxification (boron-nitride, copper selenides) [1–5]. The monolayer metal dichalcogenides such as MoS<sub>2</sub>, WS<sub>2</sub>, and WSe<sub>2</sub> have been vastly explored in the recent times as a 2D semiconductor material as they possess direct gap in the visible and near infrared region [6–10]. Among the 2D materials, WS<sub>2</sub> has gained a lot of interest due to its simple preparation technique [11–13] and having large spin–orbit coupling value ( $\approx 420 \text{ meV}$ ) [14]. Moreover, they depict high emission quantum yield and are

---

Somveer (✉) · D. S. Ahlawat

Department of Physics, Chaudhary Devi Lal University, Sirsa, Haryana 125055, India  
e-mail: [gandashsomveer@gmail.com](mailto:gandashsomveer@gmail.com)

D. Singh

Department of Physics, RPS Degree College, Balana, Mahendergarh 123029, India



characterized by a large exciton/trion binding energy. The 2H-WS<sub>2</sub> possessing the hexagonal space group (P6<sub>3</sub>/mmc) is reported to be the most stable form of WS<sub>2</sub> [15]. The bulk layer of WS<sub>2</sub> is reported to be an indirect gap semiconductor (1.3 eV gap), and as the thickness of the material is continued to be reduced toward the monolayer formation, then it slowly converts to a direct gap semiconductor (2 eV gap) [16]. Gutiérrez et al. have also proved the transition of indirect semiconductor gap of bulk material WS<sub>2</sub> to direct gap semiconductor of monolayer WS<sub>2</sub> by theoretical study [17]. In case of bulk WS<sub>2</sub>, the d-orbitals of W and p<sub>z</sub>-orbitals of sulfur play a combined effect in the electronic states because they are found to be involved in the indirect transition. For the monolayer WS<sub>2</sub>, the indirect gap involved in the electronic transition is higher than the direct transition band. The direct transition band occurring in the case of monolayer WS<sub>2</sub> involves only the d-orbitals of W [15]. WS<sub>2</sub> exists in different polymorphic forms such as monoclinic, rhombohedral, and hexagonal [13, 16]. The varied crystal forms give rise to multiple electronic properties mainly in topological states, valley polarization, and superconductivity. In this context, it will be very significant to explore this area and discover other polymorphs of the WS<sub>2</sub>, so that we may come across better applications of this material and further reconstruct devices with higher efficiency and utility.

In this work, we are reporting two new polymorphs of WS<sub>2</sub> (m-WS<sub>2</sub> and h-WS<sub>2</sub>) and have represented it in various models such as ball-and-stick model, polyhedral, space-fill, stick, and wireframes using VESTA software. We have also reported its crystal parameters (bond lengths, bond angles, and volume) and highlighted important bond distances and angles.

## 2 Electronic and Structural Visualization

VESTAs are 3D visualization software for the analysis of crystal structures of molecules, volumetric type of data, and various crystal morphologies. It is a versatile tool where we can visualize the metallic, organic, and inorganic crystal. Moreover, it helps us to visualize the 3D images of the crystal in different styles and also has many more options which we can explore according to our requirements. It also helps to measure the bond distances and angles in the crystal and to generate high resolution graphic images.

## 3 Results and Discussion

### 3.1 Structural Models of m-WS<sub>2</sub> and h-WS<sub>2</sub>

The structures of the two polymorphs of WS<sub>2</sub>, viz. m-WS<sub>2</sub> and h-WS<sub>2</sub> have been analyzed and curated by using VESTA software. The structures of the studied polymorphs have been displayed in different styles (ball-and-stick, polyhedral, space-filling, stick, and wireframe) that are available in the software, and important lattice parameter, bond distance, and angles are also reported in this study.

#### 3.1.1 Structural Model of m-WS<sub>2</sub>

The crystallographic representation of m-WS<sub>2</sub> in different styles has been shown in Fig. 1. The unit cell in each of the representation is outlined by a solid line. It is evident from Fig. 1 that they adopt monoclinic phase. The cell parameters for the system have been provided in Table 1, which depict P21/c space group. The axial length of m-WS<sub>2</sub> as shown in Table 1 is  $a = 3.27 \text{ \AA}$ ,  $b = 5.717 \text{ \AA}$ ,  $c = 12.309$ . The inter-axial angles of the crystal were determined to be  $\alpha = \gamma = 90^\circ$ ,  $\beta = 88.48^\circ$ , and volume ( $V$ ) was found to be  $230.030738 \text{ \AA}^3$ . The W–W bond distance in the crystal was measured to be  $4.11 \text{ \AA}$  which is little higher than the literature reported data [7]. The W–S (at one end) bond distance and  $\angle$ SWS angle of the m-WS<sub>2</sub> were observed to be  $2.44 \text{ \AA}$  and  $130.16^\circ$ , respectively, and are in accordance with the literature reported data. However, the other end W–S bond distance was found to be  $4.66 \text{ \AA}$  and is quite higher than the reported value [8]. A study by Schutte was done on the crystal structure of 2H-WS<sub>2</sub> and 3R-WS<sub>2</sub>. The space group parameter of the two models of 2H-WS<sub>2</sub> and 3R-WS<sub>2</sub> was reported to be P6<sub>3</sub>/mmc and R<sub>3</sub>m, respectively. The unit cell parameters are  $a = 3.153 \text{ \AA}$ ,  $b = 12.323 \text{ \AA}$ ,  $c = 3.908 \text{ \AA}$  for the 2H-WS<sub>2</sub>, whereas the parameter for 3R-WS<sub>2</sub> is  $a = 3.158$ ,  $b = 18.49$ , and  $c = 5.855$  are found to be respectively. It was observed that the result of 2H-WS<sub>2</sub> is well agreed with our study. The 2H-WS<sub>2</sub> possessing the hexagonal space group (P6<sub>3</sub>/mmc) is reported to be the most stable form of WS<sub>2</sub> [13].

#### 3.1.2 Structural Model of h-WS<sub>2</sub>

The different crystallographic representative model of h-WS<sub>2</sub> has been shown in Fig. 2, and its related cell parameters have been listed in Table 1. The unit cell in each of the representation is outlined by a solid line. The experimentally observed space group of the system is P6<sub>3</sub>/mmc, and unit cell volume was found to be  $106.267227 \text{ \AA}^3$ . The related axial length of the system as shown in Table 1 is  $a = 3.153 \text{ \AA}$ ,  $b = 3.153 \text{ \AA}$ ,  $c = 12.343 \text{ \AA}$ . The inter-axial angles  $\alpha$ ,  $\beta$ , and  $\gamma$  of the crystal system in h-WS<sub>2</sub> phase were observed to  $90^\circ$ ,  $90^\circ$ , and  $120^\circ$ , respectively. The W–W bond distance in the crystal was measured to be  $3.14 \text{ \AA}$  and correlates well with the previously reported

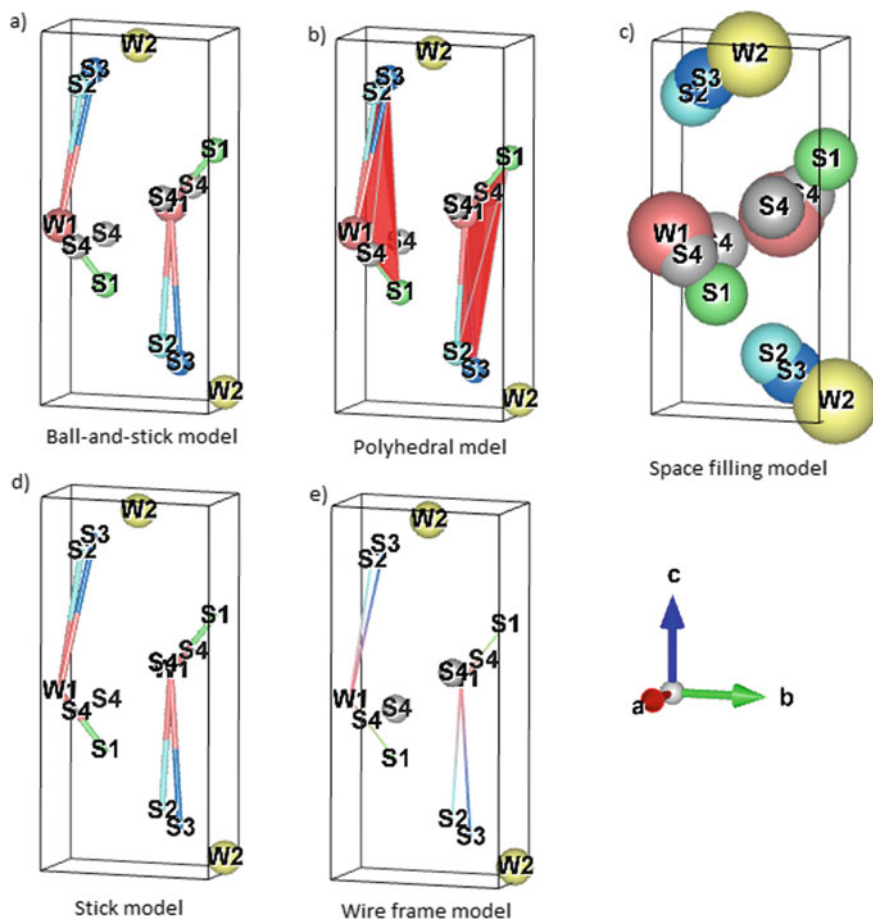


**Fig. 1** Crystallographic representation of structural models of m-WS<sub>2</sub> a ball-and-stick, b polyhedral, c space-filling, d stick, and e wire-frame model

**Table 1** Structural characteristics of the monoclinic and hexagonal WS<sub>2</sub> polymorphs

Phase-WS <sub>2</sub>	Space group	Lattice parameters (Å)	V (Å <sup>3</sup> )
m-WS <sub>2</sub>	P21/c	$a = 3.270, b = 5.717, c = 12.309$ $\alpha = 90^\circ, \beta = 88.48^\circ, \gamma = 90^\circ$	230.030738
h-WS <sub>2</sub>	P6 <sub>3</sub> /mmc	$a = 3.153, b = 3.153, c = 12.343$ $\alpha = 90^\circ, \beta = 90^\circ, \gamma = 120^\circ$	106.267227

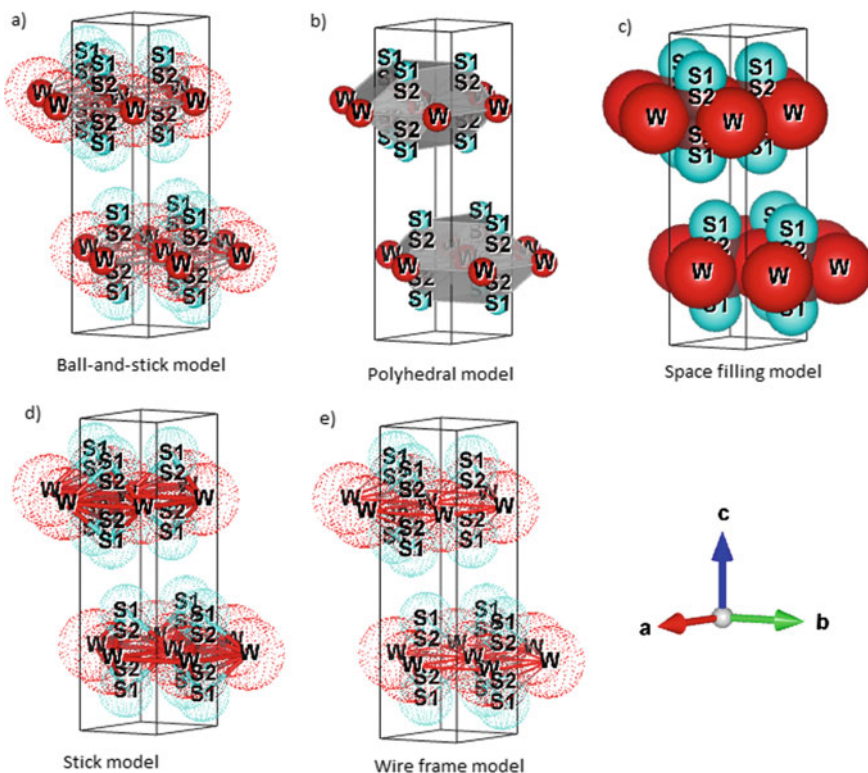


**Fig. 2** Crystallographic representation of structural models of h-WS<sub>2</sub> a ball-and-stick, b polyhedral, c space-filling, d stick, and e wire-frame model

value [8]. The W–S (2.41 Å) bond distance and  $\angle$ SWS (81.69°) angle were also found well agreed with the previously reported data in literature.

## 4 Conclusion

The observed cell parameters of WS<sub>2</sub> clearly depict the formation of two polymorphs of WS<sub>2</sub> (m-WS<sub>2</sub> and h-WS<sub>2</sub>). The crystallographic representation of the two polymorphs in 5 different styles such as ball-and-stick, polyhedral, space-fill, stick as well as wireframe has been featured. The W–W bond distance and  $\angle$ SWS bond angles of the two polymorphs (m-WS<sub>2</sub> and h-WS<sub>2</sub>) were measured and compared with the literature reported value. The h-WS<sub>2</sub> polymorphs parameters were found to be in accordance with the previous values, but h-WS<sub>2</sub> polymorphs possess has slightly different bond parameters than the reported ones. The observed polymorphs may have a future application in enhancing the lubricity of the wet lubricants such as oil and grease and in optoelectronics.

## References

1. Novoselov KS, Geim AK, Morozov SV, Jiang D, Katsnelson MI, Grigorieva I, Dubonos S, Firsov A (2005) Two-dimensional gas of massless Dirac fermions in graphene. *Nature* 438:197–200
2. Neto AC, Guinea F, Peres NM, Novoselov KS, Geim AK (2009) The electronic properties of graphene. *Rev Mod Phys* 81:109
3. Geim AK, Novoselov KS (2007) The rise of graphene. *Nat Mater* 6:183–191
4. Jin C, Lin F, Suenaga K, Iijima S (2009) Fabrication of a freestanding boron nitride single layer & its defect assignments. *Phys Rev Lett* 102:195505
5. Chalana A, Karri R, Mandal S, Pathak B, Roy G (2019) Chemical degradation of mercury alkyls mediated by copper selenide nanosheets. *Chem Asian J* 14:4582–4587
6. Pumera M, Loo AH (2014) Layered transition-metal dichalcogenides (MoS<sub>2</sub> and WS<sub>2</sub>) for sensing and biosensing. *Trends Anal Chem* 61:49–53
7. Ramakrishna Matte HSS, Gomathi A, Manna AK, Late DJ, Datta R, Pati SK, Rao CNR (2010) MoS<sub>2</sub> and WS<sub>2</sub> analogues of graphene. *Angew Chem Int Ed* 49:4059–4062
8. Zhao W, Ghorannevis Z, Chu L, Toh M, Kloc C, Tan PH, Eda G (2013) Evolution of electronic structure in atomically thin sheets of WS<sub>2</sub> and WSe<sub>2</sub>. *ACS Nano* 7:791–797
9. Wang X, Yasuda K, Zhang Y, Liu S, Watanabe K, Taniguchi T, Hone J, Fu L, Jarillo-Herrero P (2022) Interfacial ferroelectricity in rhombohedral-stacked bilayer transition metal dichalcogenides. *Nat Nanotechnol* 17(4):367–371
10. Su M, Sun H, Tian Z, Zhao Z, Li P (2022) Z-scheme 2D/2D WS<sub>2</sub>/Bi<sub>2</sub>WO<sub>6</sub> heterostructures with enhanced photocatalytic performance. *Appl Catal* 63:118485
11. Huang F, Jian J, Wu R (2016) Few-layer thick WS<sub>2</sub> nanosheets produced by intercalation/exfoliation route. *J Mater Sci* 51:10160–10165
12. Cong C, Shang J, Wang Y, Yu T (2018) Optical properties of 2D semiconductor WS<sub>2</sub>. *Adv Opt Mater* 6:1700767
13. Schutte WJ, De Boer JL, Jellinek F (1987) Crystal structures of tungsten disulfide and diselenide. *J Solid State Chem* 70:207–209
14. Zeng H, Liu GB, Dai J, Yan Y, Zhu B, He R, Xie L, Xu S, Chen X, Yao W, Cui X (2013) Optical signature of symmetry variations and spin-valley coupling in atomically thin tungsten dichalcogenides. *Sci Rep* 3:1–5
15. Gutiérrez HR, Perea-López N, Elías AL, Berkdemir A, Wang B, Lv R, López-Urías F, Crespi VH, Terrones H, Terrones M (2013) Extraordinary room-temperature photoluminescence in triangular WS<sub>2</sub> monolayers. *Nano Lett* 13:3447–3454
16. Fang Y, Pan J, Zhang D, Wang D, Hirose HT, Terashima T, Uji S, Yuan Y, Li W, Tian Z, Xue J (2018) Coexistence of intrinsic superconductivity and topological insulator state in monoclinic phase WS<sub>2</sub>. *arXiv preprint arXiv:1808.05324*
17. Kim, JY, Gelczuk Ł, Polak MP, Hlushchenko D, Morgan D, Kudrawiec R, Szlufarska I (2022) Experimental and theoretical studies of native deep-level defects in transition metal dichalcogenides. *npj 2D Mater Appl* 6(1):75

# Titanium Dioxide Nanofillers Incorporated Glass Ionomer Cement with Carboxymethyl Chitosan for Superior Mechanical Properties



Preety Kumari Kashyap, Jyoti Gupta, Bharath Govind, and Sunita Rattan

**Abstract** Glass ionomer cement (GIC) has become a popular choice for dental restorations because of its biocompatibility, capacity to bond to calcium in oral tissues, and protracted fluoride release that enhances its anticariogenic behaviour. Nevertheless, due to their low compressive and flexural strengths, which cause microleakage that and detach the restoration from the tooth, these are inappropriate for high-stress locations. The breakdown of the binding between the glass powder and polymer during protracted water absorption, leading to in surface/bulk cracks, is one of the causes of dental composites collapsing. Among the various investigated methods till date, utilization of nanofillers to make GIC applicable for areas of high masticatory stress has also been studied. In the present study, a dental cement with high mechanical strength was prepared using titanium dioxide nanofillers. Titanium dioxide nanofillers (5%) were added homogeneously to previously prepared carboxymethyl chitosan-functionalized glass powder (CMC-f-Glass) to form titanium dioxide-incorporated glass powder (Glass-TiO<sub>2</sub>/nF). It was used to form a dental cement (DC/Glass-TiO<sub>2</sub>/nF) on mixing with the polyelectrolyte. Glass-TiO<sub>2</sub>/nF was characterized by FTIR, DLS, and XRD. DC/Glass-TiO<sub>2</sub>/nF yielded a compressive strength of 148.84 MPa and flexural strength of 16.32 MPa which was comparatively higher when compared with standard dental cement (DC/standard). The surface morphology of the GIC was assessed using FESEM. When DC/Glass-TiO<sub>2</sub>/nF was tested for anti-microbial action against *Streptococcus mutans*, it was discovered that the compound suppresses bacterial growth. MTT experiment suggests that DC/Glass-TiO<sub>2</sub>/nF was non-cytotoxic and had no impact on cell viability.

**Keywords** Titanium dioxide · Glass ionomer cement · Compressive strength · Biofilm assay · Carboxymethyl chitosan

---

P. K. Kashyap (✉) · J. Gupta · B. Govind · S. Rattan  
Amity Institute of Applied Sciences, Amity University Uttar Pradesh, Noida, India  
e-mail: [preetykashyap1002@gmail.com](mailto:preetykashyap1002@gmail.com)

## 1 Introduction

The dental materials have proven to be the best methods to repair carious tooth. Thus, dental materials have been studied globally by the researchers for applications as restoration and lining. Among them, glass ionomer cement (GIC) has been the promising biocompatible material in the field of dentistry. The GICs are biocompatible and have high affinity to bind to the calcium in the dental tissues, which has made GICs a widely accepted option for dental restorations. They have also shown remarkable anticariogenic action, owing to the protracted fluoride release [1]. But the poor mechanical stability and microleakage of the GICs make them inappropriate under high masticatory forces [2]. Various techniques have been employed to improve the mechanical strength, e.g. incorporation of metal powders [3], glass fibres [4], reinforcing powders [5], and nanoparticles. Different types of nanoparticles have been utilized as nanofillers, by the researchers to influence the mechanical properties of the GICs, which not only diminished the micropores and cracks, but also offered ease of mixing [6]. Initially, nanoparticles incorporated were alumina, zirconia nanoparticles, etc. [7].

Titanium dioxide has also been explored in various applications owing to its chemical stability and biocompatibility [8].  $\text{TiO}_2$  constantly releases fluoride ions, which are exchanged in the oral cavity, between the tooth and GIC, as a result, it contributes to minimize the recurrent caries lesions [9]. Further, it increases the stability of GICs in the acidic environment produced by the bacteria on the tooth surface. It stabilizes the mineral apatite and favours remineralization of the enamel [10]. In the present study, the glass powder is further functionalized using the  $\text{TiO}_2$  nanofillers (nF) to increase the hardness to improve mechanical properties. The reinforcing filler is added to a unified and amalgamated GIC which minimal microcracks.  $\text{TiO}_2/\text{nF}$  (5%) was added homogeneously to previously prepared carboxymethyl chitosan-functionalized glass powder (CMC-f-Glass) [11] to form  $\text{TiO}_2/\text{nF}$ -incorporated glass powder (Glass- $\text{TiO}_2/\text{nF}$ ). It was used to form a dental cement (DC/Glass- $\text{TiO}_2/\text{nF}$ ) on mixing with the polyelectrolyte.

## 2 Materials and Methods

### 2.1 Materials

The solid component, i.e. the glass powder, was initially synthesized following the procedure as mentioned in our previous studies [11]. Brain Heart Infusion (BHI) Agar and Brain Heart Infusion (BHI) Broth were procured for assessing the antibacterial activity of the GIC. MTT assay for cytocompatibility was tested for which 3-[4,5-Dimethylthiazol-2-yl]-2,5-diphenyltetrazolium bromide (MTT), Foetal Bovine Serum (FBS), Dulbecco's modified Eagle's medium (DMEM), penicillin-streptomycin and trypsin 0.25%, and Dimethyl Sulfoxide (DMSO) were

procured from M/s HiMedia (India). To compare the created GIC with the GIC produced employing commercial liquid and commercial glass powder (Shofu), DC/standard was designated.

## 2.2 Characterization

A Universal ATR was used to study functional groups in the GICs in the range 4000–500  $\text{cm}^{-1}$  over 16 scans with a Universal ATR. GIC specimens were characterized for mechanical strength, as per ISO 9917-1:2007. Three-point bending test was performed in UTM. Using field emission scanning electron microscopy, the fracture morphology of the surface of GICs was examined (FESEM, QUANTA 200 FEG, MIRA3 TESCAN). For assessing the microbial activity, the biofilm was developed according to our previous studies [11]. Cytotoxic studies were undertaken on RAW 264.7 cells through Methyl Tetrazolium (MTT) [11].

## 3 Results and Discussion

The polymeric liquid and the basic powder reacted via an acid–base neutralization reaction. The reaction was followed by the formation of the silica gel which was confirmed by the peaks observed at 3440–3770  $\text{cm}^{-1}$  which corresponded to the Si–OH bonds. The reaction was completed by the generation of metal chelates between the carboxyl groups of the polymeric acid and metal ions, which were observed at 1592  $\text{cm}^{-1}$  (COO). Further, the peaks at 1457 and 1401  $\text{cm}^{-1}$  corresponded to the Al-polyacrylates and Ca-polyacrylates [12]. The intense peak observed at 1094  $\text{cm}^{-1}$  corresponded to the Si–O–Si asymmetric stretching vibration, while at 1043  $\text{cm}^{-1}$  was obtained due to the presence of Si–O stretching mode. The peak at 1726  $\text{cm}^{-1}$  corresponded to the C–O stretching polyacids [13] (Fig. 1).

The morphology of the surface of the glass-TiO<sub>2</sub>/nF and DC/glass-TiO<sub>2</sub>/nF has been shown in Fig. 2. The nanofillers could be seen homogeneously distributed in the glass powder. Further, the GC prepared has been observed with negligible micro-cracks and micropores. The GIC showed a rigid amalgamated matrix. The compact and highly unified microstructure supported the results for mechanical strength due to absence of interparticle spacing, which prevented glass fragments from releasing.

The mechanical strength was assessed by obtaining the compressive and flexural strengths of the experimental GICs which were compared with the DC/standard as shown in Fig. 3. With the increase in the immersion in water from day 1 to day 28, the GICs exhibited a slow increase in both the CS and FS, due to the maturation of the GICs [14]. DC/glass produced CS and FS of 127.38 MPa and 10.24 MPa, whereas DC/glass-TiO<sub>2</sub>/nF produced CS and FS of 157.45 MPa and 16.32 MPa, respectively,



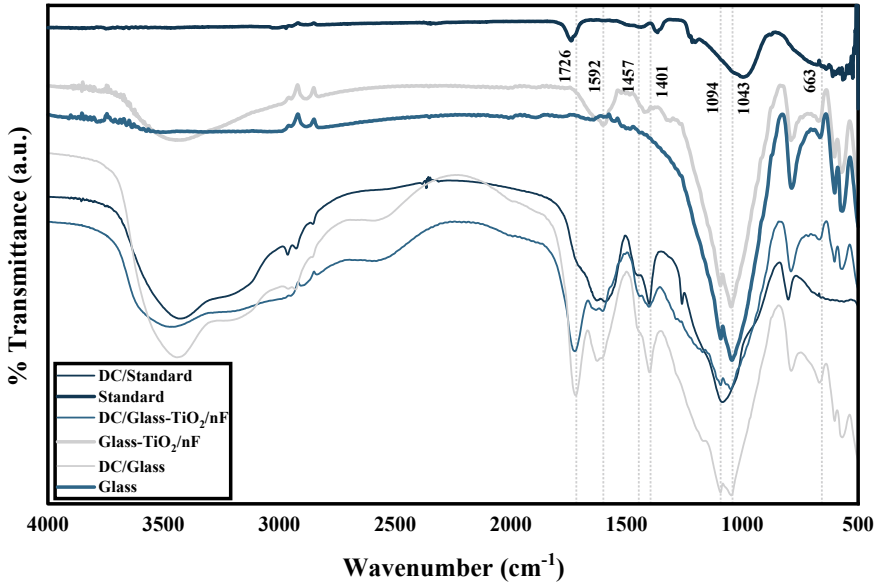


**Fig. 1** FTIR analysis—glass, glass-TiO<sub>2</sub>/nF, standard and dental cements (DC/glass, DC/glass-TiO<sub>2</sub>/nF, DC/standard)

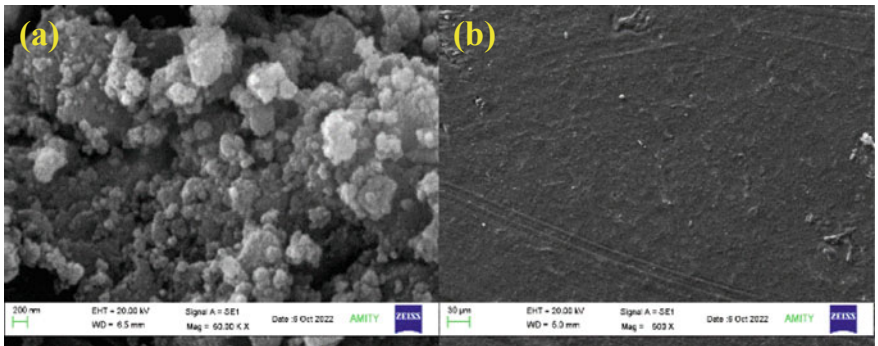


**Fig. 2** SEM image **a** glass-TiO<sub>2</sub>/nF (200 nm, 50 k×), **b** DC/glass-TiO<sub>2</sub>/nF (30 μm, 500×)

which was higher than the DC/standard, which produced CS and FS of 149.64 MPa and 12.62 MPa after 24 h post-maturation. The higher CS and FS of DC/glass-TiO<sub>2</sub>/nF was attributed to incorporation of nanofillers which restricted the micropores and microcracks formation [15].

The results of the spectrophotometric analysis of the biofilm formation assessed via the optical density calculation have been shown in Fig. 4. The observations indicated that the DC/glass has the maximum bacterial growth over it as it had the maximum optical density of the bacterial suspension examined after days 1 and 3.

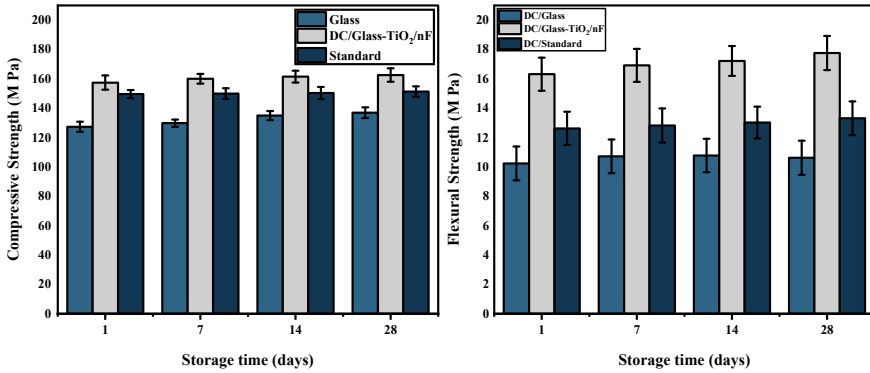


**Fig. 3** Mechanical strength analysis of the GICs (compressive strength and flexural strength)—DC/glass, DC/glass-TiO<sub>2</sub>/nF, DC/standard

However, the other GICs DC/standard and DC/glass-TiO<sub>2</sub>/nF had the lowest optical densities due to lower bacterial growth. The findings showed that from day 1 to day 3, bacteria on all GIC specimens grew more quickly. The results indicated that inhibition against *Streptococcus mutans* biofilm by DC/glass-TiO<sub>2</sub>/nF was significantly higher than other GICs due to TiO<sub>2</sub>/nF, which damage the anionic cell membrane of the bacteria [16].

The in vitro cell viability on RAW 264.7 cells was assessed by MTT assay method. Figure 5 showed that the calculated cell viability for DC/glass was 93.57%, DC/glass-TiO<sub>2</sub>/nF was 97.63%, and DC/standard was 98.84% as compared to untreated cells (100% viability). This indicated that the viability of the cells in conditioned media

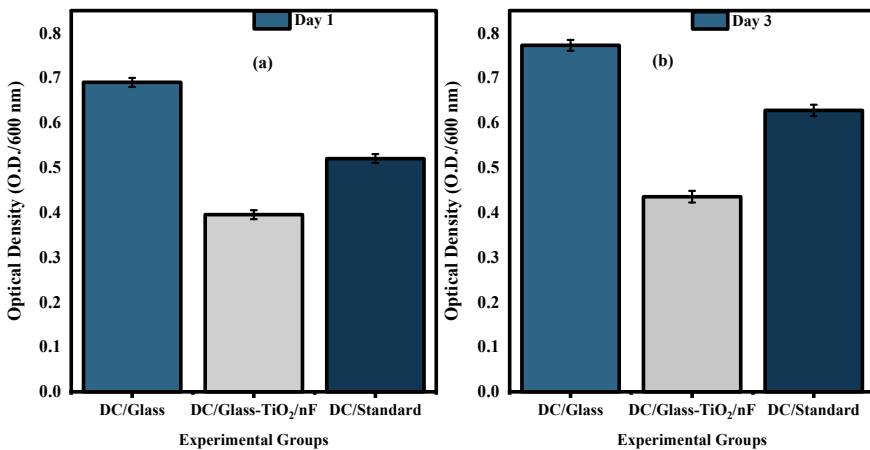
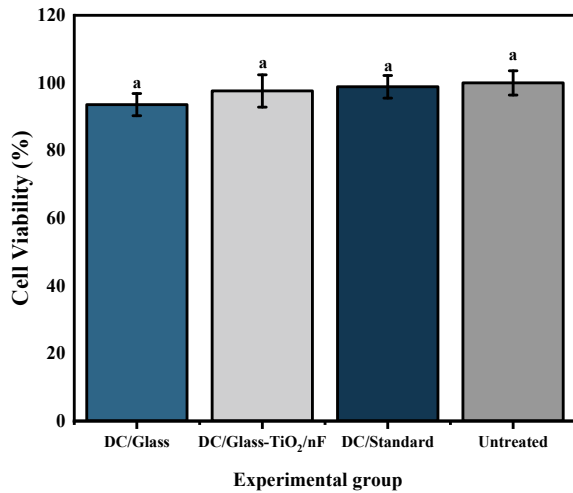


**Fig. 4** Biofilm formation on DC/glass, DC/glass-TiO<sub>2</sub>/nF, and DC/standard maturation times of **a** 1 day and **b** 3 days, calculated using the spectrophotometric analysis

**Fig. 5** Cell viability of RAW 264.7 cell lines on treatment with experimental DMEM from: DC/glass, DC/glass-TiO<sub>2</sub>/nF, DC/standard and untreated. Significance at \* $p < 0.05$ , compared with the standard



slightly reduces that cell viability. However, the decrease in was not significant at  $p < 0.05$ . Thus, GICs were non-cytotoxic [17].

## 4 Conclusion

The TiO<sub>2</sub> nanoparticles incorporation into the GIC yielded higher mechanical strength by forming a rigid and unified GIC matrix. The acid–base reaction was confirmed by FTIR analysis showed which presence of calcium- and aluminium-polyacrylates in the GICs. The surface of the dental cement studied using SEM indicated a uniformly fused and amalgamated matrix. The images showed that the GICs surface was free from cracks and pores. Anti-microbial activity of experimental GIC was assessed against *S. mutans*, which exhibited that the DC/glass-TiO<sub>2</sub>/nF inhibited bacterial growth and thus would prevent secondary caries. MTT assay inferred that DC/glass-TiO<sub>2</sub>/nF was biocompatible.

**Declaration of Interest Statement** There are no conflicts of interest.

## References

1. Chau NPT, Pandit S, Cai JN, Lee MH, Jeon JG (2015) Relationship between fluoride release rate and anti-cariogenic biofilm activity of glass ionomer cements. *Dent Mater* 31:e100–e108
2. Meiers JC, Miller GA (1996) Antibacterial activity of dentin bonding systems, resin-modified glass ionomers, and polyacid-modified composite resins. *Operative Dent* 21(1):257–264

3. Nicholson JW, Sidhu SK, Czarnecka B (2020) Enhancing the mechanical properties of glass-ionomer dental cements: a review. *Materials*. <https://doi.org/10.3390/ma13112510>
4. Garoushi S, He J, Obradovic J, Fardim P, Vallittu PK, Lassila L (2020) Incorporation of cellulose fiber in glass ionomer cement. *Eur J Oral Sci* 128:81–88
5. Simila HO, Karpukhina N, Hill RG (2018) Bioactivity and fluoride release of strontium and fluoride modified Biodentine. *Dent Mater* 34:e1–e7
6. Bin QSS, Ali D, Soliman MS, Zafropoulos GG (2021) The effect of chitosan derived silver nanoparticles on mechanical properties, color stability of glass ionomer luting cements. *Mater Res Express*. <https://doi.org/10.1088/2053-1591/ac1cd5>
7. Beketova A, Theocharidou A, Tsamesidis I et al (2021) Sol-gel synthesis and characterization of YSZ nanofillers for dental cements at different temperatures. *Dent J*. <https://doi.org/10.3390/dj9110128>
8. Ibrahim MA, Meera Priyadarshini B, Neo J, Fawzy AS (2017) Characterization of chitosan/TiO<sub>2</sub> nano-powder modified glass-ionomer cement for restorative dental applications. *J Esthet Restor Dent* 29:146–156
9. Makvandi P, Gu JT, Zare EN, Ashtari B, Moeini A, Tay FR, Niu LN (2020) Polymeric and inorganic nanoscopic antimicrobial fillers in dentistry. *Acta Biomater* 101:69–101
10. Sun J, Xu Y, Zhu B, Gao G, Ren J, Wang H, Lin Y, Cao B (2019) Synergistic effects of titanium dioxide and cellulose on the properties of glass-ionomer cement. *Dent Mater J* 38:41–51
11. Kashyap PK, Chauhan S, Negi YS, Goel NK, Rattan S (2022) Biocompatible carboxymethyl chitosan-modified glass ionomer cement with enhanced mechanical and anti-bacterial properties. *Int J Biol Macromol* 223:1506–1520
12. Kumari P, Singh Y, Kumar N, Kumar R, Rattan S (2022) Chemical initiator-free synthesis of poly (acrylic acid-co-itaconic acid) using radiation-induced polymerization for application in dental cements. *Radiat Phys Chem* 198:110243
13. Loy CW, Whitten AE, de Campo L et al (2018) Investigation of the siliceous hydrogel phase formation in glass-ionomer cement paste. *Phys B Condens Matter* 551:287–290
14. Nicholson JW (2018) Maturation processes in glass-ionomer dental cements. *Acta Biomater Odontol Scand* 4:63–71
15. Elsaka SE, Hamouda IM, Swain MV (2011) Titanium dioxide nanoparticles addition to a conventional glass-ionomer restorative: influence on physical and antibacterial properties. *J Dent* 39:589–598
16. Chen R, Han Z, Huang Z, Karki J, Wang C, Zhu B, Zhang X (2017) Antibacterial activity, cytotoxicity and mechanical behavior of nano-enhanced denture base resin with different kinds of inorganic antibacterial agents. *Dent Mater J* 36:693–699
17. Fuchs M, Gentleman E, Shahid S, Hill RG, Brauer DS (2015) Therapeutic ion-releasing bioactive glass ionomer cements with improved mechanical strength and radiopacity. *Front Mater* 2:1–11
18. Wetzel R, Hupa L, Brauer DS (2019) Glass ionomer bone cements based on magnesium-containing bioactive glasses. *Biomed Glas* 5:1–12

# Synthesis of Curcumin Loaded Mesoporous Silica Nanoparticles for Anti-cancer Drug Delivery



Harsha Gautam, Sameeksha Luthra, Aakanksha Chhokra, Saumya Anand, Prashant Kumar, Reshma Sinha, Sunil Kumar, Ravi Kumar, Manoj Kumar Khanna, and Daya Bhardwaj

**Abstract** In this research, we report the synthesis of amino functionalized mesoporous silica (MSN) nanoparticles as a drug carrier. Furthermore, folic acid was conjugated to MSN for pH-sensitive drug release. MSNs improved the solubility of poorly water-soluble curcumin drug and thus could enhance their absorption. These MSNs have a high-loading affinity toward hydrophobic anti-cancer drugs. In this study, the encapsulation efficiency of curcumin was found to be  $57 \pm 1.9\%$ . The release experiments confirm the ability to deliver the drug in a pH-responsive manner. Curcumin loaded particles exhibited substantial cellular uptake in C6 glioma cell lines. In vitro cytotoxicity study demonstrated that the nanoparticles loaded with curcumin considerably enhanced antitumor activity (85%) against C6 cell line as compared to non-drug loaded nanoparticles, suggest the anti-cancer potential of curcumin loaded nanoparticles.

**Keywords** Cancer · Mesoporous silica nanoparticles · Curcumin · Drug delivery

## 1 Introduction

Cancer is most likely the most lethal disease, and chemotherapy continues to be the used method of treatment but they are not target-specific and kill all the rapidly dividing cells which leads to severe side effects such as a weakened

---

Harsha Gautam, Sameeksha Luthra, Aakanksha Chhokra and Saumya Anand: equally contributed

---

H. Gautam · S. Luthra · A. Chhokra · S. Anand · R. Sinha · S. Kumar · R. Kumar · D. Bhardwaj (✉)

Shaheed Rajguru College of Applied Sciences for Women, University of Delhi, New Delhi, India  
e-mail: [daya.bhardwaj@rajguru.du.ac.in](mailto:daya.bhardwaj@rajguru.du.ac.in)

P. Kumar  
Department of Electronic Science, University of Delhi, South Campus, New Delhi, India

M. K. Khanna  
Ramjas College, University of Delhi, New Delhi, India

immune system [1]. Curcumin (*Curcuma longa*) is a potential phytochemical natural drug with desirable therapeutic attributes such as potent antitumor characteristics, anti-inflammatory, and antioxidant [2].

However, curcumin's therapeutic potential has been constrained by its hydrophobic nature and chemical instability, which are likely to lead to inadequate absorption and bioavailability [3]. Mesoporous silica nanoparticles (MSNs) because of their high biocompatibility, large surface area, porosity, and well-defined and controllable morphology are well suited to solve formulation problems associated with hydrophobic drugs and are especially useful for a targeted and controlled release of drug [4].

In the existing research, we investigated a pH-responsive controlled delivery of drug to enhance the efficacy of curcumin. In particular, MSN was synthesized and functionalized with an amino group for improved curcumin loading followed by further conjugation with folic acid (FA) for cell targeting. Using pH-sensitive Schiff base reactions, curcumin was loaded into the functionalized MSN. Furthermore, the efficiency of the intended controlled release was assessed in-suspension. In contrast to the stability and biocompatibility of free curcumin, results showed that the formulated MSN drug delivery system has some advanced features, including an appropriate loading capacity, pH-controlled release, and active targeting capability. Therefore, this novel drug delivery method offers a viable prospect for clinical cancer treatment.

## 2 Materials and Methodology

### 2.1 Reagents

All chemicals used in this study were analytical grade and used as received. Tetraethyl orthosilicate (TEOS), Cetyltrimethylammonium bromide (CTAB), Diethanolamine (DEA), 3-aminopropyl trimethoxysilane (APTES), Folic acid (FA), Dimethyl sulfoxide (DMSO), ethanol, methanol, Hydrochloric acid, curcumin (cur), deionized (DI) water, ethylene glycol, PBS buffer were locally purchased from Himedia Chem India.

### 2.2 Synthesis of FA Conjugated MSNs

Mesoporous silica nanoparticles were functionalized with an amino group (MSN-NH<sub>2</sub>) using previously reported protocol. Further, the MSN-NH<sub>2</sub> solution dried and dissolved into ethanol. Thereafter, FA was activated by dissolving it into 5.0 mL DMSO which contained 100 mg EDC along with 50 mg NHS and then stirring the solution for 2 h in the dark. The aforementioned solution received 30  $\mu$ L of APTES, which was then agitated for 4 h. After stirring, the mixture was introduced to the

MSN-NH<sub>2</sub> suspension, where it was allowed to react for 24 h at 80 °C. After 24 h, a sample was extracted, and it was reported as FA-MSN-NH<sub>2</sub> [5].

Curcumin loading and release experiments were accomplished by previously reported protocol [6]. The curcumin release experiments were evaluated at three different pH such as pH of 5.0 (acidic), pH of 6.5 (mildly acidic), and pH of 7.4 (physiological) [7]. Assessments of the drug LC and EE (loading capacity and encapsulation efficiency, respectively) were conducted as previously reported [7]. In vitro evaluation of anti-cancer activity of synthesized nanoparticles on glioma cells (C6) was done as previously reported paper by Kumar et al. [8].

### 3 Results and Discussion

XRD patterns established the amorphous nature of mesoporous SiO<sub>2</sub> samples as shown in Fig. 1a. The broad peak centered at 22° shows a complete amorphous structure of mesoporous SiO<sub>2</sub> [8]. Figure 1b exhibits TEM monographs of MSNs, which indicate that the nanoparticle has uniformly sized pores, dispersed on the surface. The silica shell featured mesopores that resembled wormholes and varied in size from 1 to 4 nm [9]. Mesoporous channels and LSMO were clearly observed in the TEM images of the mesoporous silica shell's core. The range of 40–50 nm was discovered to be the average size distribution of MSN.

The DLS pattern (Fig. 1c) of MSNs is depicted in the following graph which concludes that the hydrodynamic particle size range for our particles is 100–180 nm. The average diameter observed by DLS was found to be higher than TEM, and this is possibly due to hydrated adsorbed organic layers present on the surface of MSLN [9]. The zeta potential of MSN (Fig. 1d) increased from – 25.1 to 19.4 mV on amine functionalization (APTES) to obtain MSN-NH<sub>2</sub>. Changing zeta potentials implied the successful synthesis of MSN-NH<sub>2</sub>. Continuous changing of the zeta potential at every step signaled the successful functionalization of MSN and curcumin loading.

The curcumin loading encapsulation efficiency (%EE) and loading capacity (%LC) of FA-MSN-N = C-Cur was observed as  $57 \pm 1.9$  and  $9.8 \pm 0.2\%$ , respectively. According to these findings, curcumin's carbonyl group and MSN's amine group had strong electrostatic interactions and Schiff's base reaction, which was also related to the MSN's mesoporous structure. The curcumin drug release assay was also performed. Figure 2a shows the curcumin release behavior of the FA-MSN-N = C-Cur at 37 °C under various pH conditions (acidic, basic, and physiological). Figure 2a shows that the curcumin release from nanoparticles is pH-dependent, i.e., as the value of pH decreases, the release rate from the particles increases. At neutral pH (7.4), the release rate of curcumin from FA-MSN-N = C-Cur was observed as 23.5% over a period of 10 h. However, a significant increase was observed in the rate of release in presence of an acidic environment (at a decreased pH). During the entire period, approximately 39.3% and 68.5% curcumin release were observed at pH 6.0 and 5.0, respectively. Different release rates have been attributed mainly to pH-dependent cleavage of the C–N bonds in Schiff's base, which is pH-dependent

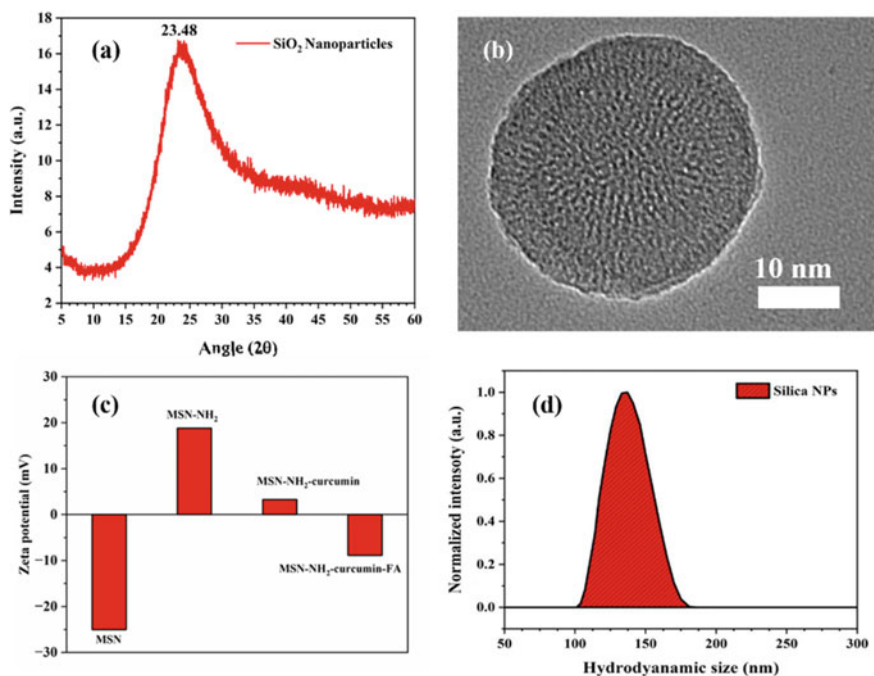


**Fig. 1** a XRD of MSNs, b right filed image of MSNs, c zeta potential of synthesized nanoparticles, d DLS data of MSNs

[6]. Based on these results, it appears that drug bioavailability was improved due to an increase in solubility and the avoidance of premature drug release from the nanoparticles before contacting the target tumor cells.

**In vitro anti-cancer activity:** The anti-cancer effect of cur-FA-NH<sub>3</sub>-MSN was determined on cancer cell C6 using MTT assay. The cell viability results demonstrated that the nanoparticles loaded with curcumin showed a significant increase in cytotoxicity (~85%) over a period of 48 h at a concentration of 1000 μg/ml as compared to non-drug-loaded nanoparticles. The overall result suggests that curcumin loaded nanoparticles showed anti-cancer effect on glioma cells as compared to other particles.



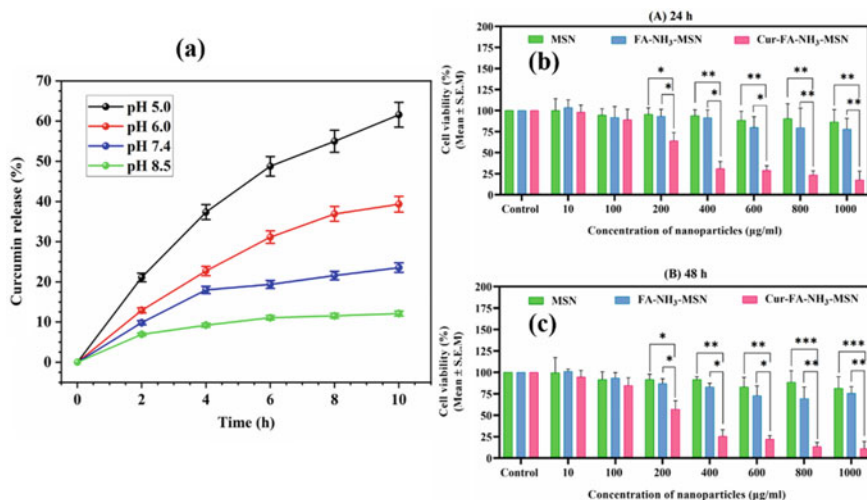


**Fig. 2** a pH-dependent curcumin release behavior of FA-MSN-N = C-Cur. b In vitro biocompatibility study of synthesized nanoparticles

### 4 Conclusion

Curcumin is an antioxidant and a polyphenolic compound found in turmeric. It acts as an effective target-specific anti-cancer agent but the biggest drawback in its therapeutic efficacy is the hydrophobic nature of curcumin which causes poor bioavailability. MSNs are chemically and thermally stable nanomaterials with high biocompatibility, porosity, and well-defined and controllable morphology. They appear to be ideal carriers for hydrophobic drugs like curcumin as they improve solubility and thus enhance absorption. MSNs have been prepared by Stober method, and then, amine functionalization has been done to develop a positive charge on MSN to increase the uptake of curcumin. Folic acid conjugation was done on MSNs to make them specific to target cancerous cells and for pH-sensitive release. XRD and TEM imaging were confirming the proper synthesis of MSN. The worm-like texture confirms formation. DLS was done to observe particle size range, and zeta potential analysis was used to assess the stability of nanoparticle suspension. Maximum curcumin release was observed at pH 6 which is close to our body pH. Cytotoxicity was checked by MTT assay which showed a concentration of 1000 µg/ml as an ideal concentration which caused 85% decrease in cell viability. Thus, MSN has been established as an effective drug delivery agent for cancer therapy by curcumin.

## References

1. Elbially NS, Aboushoushah SF, Sofi BF, Noorwali A (2020) Multifunctional curcumin-loaded mesoporous silica nanoparticles for cancer chemoprevention and therapy. *Microp Mesop Mater* 291:109540
2. Darvesh A, Aggarwal B, Bishayee A (2011) Curcumin and liver cancer: a review. *Curr Pharm Biotechnol* 13:218–228
3. Sohn SI, Priya A, Balasubramaniam B, Muthuramalingam P, Sivasankar C, Selvaraj A, Valliammai A, Jothi R, Pandian S (2021) Biomedical applications and bioavailability of curcumin: an updated overview. *Pharmaceutics* 13:1–33
4. Jafari S, Derakhshankhah H, Alaei L, Fattahi A, Varnamkhasti BS, Saboury AA (2019) Mesoporous silica nanoparticles for therapeutic/diagnostic applications. *Biomed Pharmacother* 109:1100–1111
5. Xiong L, Du X, Kleitz F, Qiao SZ (2015) Cancer-cell-specific nuclear-targeted drug delivery by dual-ligand-modified mesoporous silica nanoparticles. *Small* 11:5919–5926
6. Massaro M, Amorati R, Cavallaro G, Guernelli S, Lazzara G, Milioto S, Noto R, Poma P, RIELA S (2016) Direct chemical grafted curcumin on halloysite nanotubes as dual-responsive prodrug for pharmacological applications. *Colloids Surf B Biointerf* 140:505–513
7. Zhang J, Sun Y, Tian B, Li K, Wang L, Liang Y, Han J (2016) Multifunctional mesoporous silica nanoparticles modified with tumor-shedable hyaluronic acid as carriers for doxorubicin. *Colloids Surf B Biointerf* 144:293–302
8. Kumar R, Chauhan A, Kuanr BK (2021) A robust in vitro anticancer activity via magnetic hyperthermia mediated by colloiddally stabilized mesoporous silica encapsulated La<sub>0.7</sub>Sr<sub>0.3</sub>MnO<sub>3</sub> core-shell structure. *Colloids Surf A Physicochem Eng Asp* 615:126212
9. Kumar R, Chauhan A, Jha SK, Kuanr BK (2019) Encapsulated lanthanum strontium manganese oxide in mesoporous silica shell: Potential for cancer treatment by hyperthermia therapy. *J Alloys Compd* 790:433–446

# Role of Grain Boundaries Governing the Giant Dielectric Constant in Bulk SnO<sub>2</sub>



Shweta Dhiman, Nirmal Manyani, and S. K. Tripathi

**Abstract** In this report, we compare the frequency-dependent dielectric and AC impedance spectroscopy measurements performed on the polycrystalline SnO<sub>2</sub> in bulk (BK) and thin film (TF) grown on the glass substrate. We observe a giant dielectric constant ( $2 \times 10^4$ ) at room temperature and low frequencies in the case of the BK SnO<sub>2</sub> sample, which significantly decreases in the case of the TF sample, indicating the critical role of the grain boundaries in governing the dielectric response of this sample. The imaginary part of the AC impedance ( $Z''$ ) shows a relaxation peak around 2 MHz in the BK SnO<sub>2</sub> sample, which shifts to  $\sim 170$  kHz in the case of TF sample due to a significant reduction in the resistive component. Further, the depressed semicircle in the Nyquist plot indicates the deviation from the ideal capacitive behavior in both BK as well as TF samples and a significant reduction in the grain boundary component in the TF compared to the BK sample. Moreover, a relaxation peak in the loss tangent ( $\tan \delta$ ) has been observed around 100 Hz in BK as well as TF samples. We suggest that the present study can be helpful in further engineering the suitable materials for the high dielectric constant for their potential use in microelectronics and gas sensing applications.

**Keywords** Impedance spectroscopy · Grain boundary · Thin film · Giant dielectric constant

## 1 Introduction

Potential uses for tin oxide (SnO<sub>2</sub>) include transparent electrodes, solar cells, gas sensors, and other photovoltaic devices. With a high binding energy of 130 meV and a constant band gap of 3.6 eV, it is an *n*-type semiconductor [1]. SnO<sub>2</sub> TF is attractive due to its low electrical resistance and optical transparency. They can be used as optoelectronic devices such as solar energy conversion, photo sensors, and conductive

---

S. Dhiman · N. Manyani · S. K. Tripathi (✉)

Department of Physics, Centre for Advanced Studies in Physics, Panjab University,  
Chandigarh 160014, India

e-mail: [surya@pu.ac.in](mailto:surya@pu.ac.in)

electrodes on glass substrates. However, the features of the films are significantly affected by the deposition techniques used [2]. The Maxwell–Wagner effect explains why charges accumulate at interfaces between materials and grains due to variations in the alleviation of the charge carrier times [3]. It is found in various two-material interfaces and primarily concentrates on inhomogeneous structures with multiple phases, structural heterogeneity, and materials with many interfaces and faults. In polycrystalline bulk samples, the charge accumulates near grain boundaries leading to a high dielectric constant [4]. This study characterizes the BK and TF deposition of SnO<sub>2</sub> produced by the thermal evaporation method on glass using X-ray diffraction, UV–Vis and Raman spectroscopy, AFM, AC impedance, and dielectric constant plots. This study is crucial for understanding polarization behavior from a scientific perspective.

## 2 Materials and Methods

SnO<sub>2</sub> nanoparticles were produced by adding SnO<sub>2</sub>·2H<sub>2</sub>O and cellulose to PVDF and CTAB, then heating the mixture in a hydrothermal reactor for 10 h. The resulting powder was ground and calcinated at 500 °C for 5 h [5]. Impedance spectroscopy was conducted on a pellet of the SnO<sub>2</sub> nanoparticles. In order to create an electrical connection between two layers of bismuth, a TF of SnO<sub>2</sub> was sandwiched between them using thermal deposition (see Fig. 1a). The SnO<sub>2</sub> layer was 1.24 kÅ thick, while the bismuth layers were 5.12 kÅ thick. On a glass substrate, an identical SnO<sub>2</sub> TF was produced concurrently.

## 3 Results and Discussion

The crystal forms in the tetrahedral form with the P42/mnm Feredov groups (crystallographic groups) show in Fig. 1b. Rietveld refinement was performed using Fullprof software, and the fitting parameters  $R_p = 4.47$ ,  $R_{wp} = 6.09$ ,  $R_{exp} = 4.26$ , and  $\chi^2 = 2.04$  verified the excellent fitting of the XRD pattern, and there was no extra peak visible. The obtained lattice parameters are  $a = b = 4.7377$  Å,  $c = 3.1867$  Å. The [SnO<sub>6</sub>] forms a distorted octahedron having tetragonal elongation where the four planar (Sn–O) equal bonds have a bond length of 2.02777 Å, and the bond length of two elongated (Sn–O) bonds is 2.09578 Å [6]. Four planar (Sn–O) bonds have different (O–Sn–O) bond angles; two (O–Sn–O) bond angles are 76.4189°, and the other two are 103.5811°. SnO<sub>2</sub> samples' optical transmittance spectra are measured between 300 and 900 nm in wavelength. To determine the band gap of the prepared samples, Fig. 1c is plotted in the shape of the Tauc plot, corresponding to BK and TF (inset of Fig. 1c). Both situations have a computed optical band gap close to the UV spectrum. However, in BK, the band gap calculated from the plot is 3.77 eV and matches well with the literature. TFs have the benefit of having an optical band gap

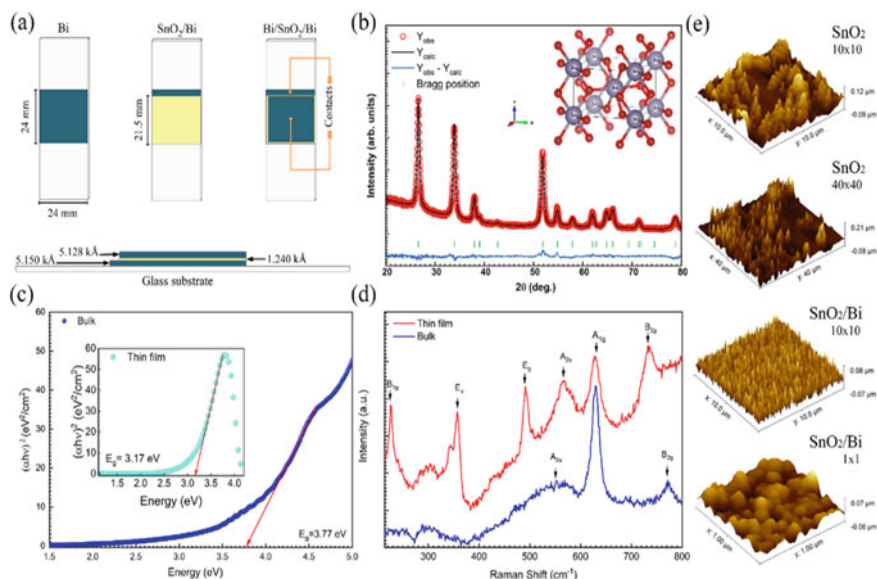


**Fig. 1** a Fabrication process, b XRD and Reitveld refinement, c Tauc plot of the UV–Vis spectra for BK and TF (in inset), d Raman spectra of BK and TF, and e AFM mapping of the fabricated TFs

that changes with film thickness, which is beneficial for altering the optical band gap that decreases in TFs due to an elevation in tensile strain in the structure [7].

Raman spectra (Fig. 1d) of BK SnO<sub>2</sub> show Raman peaks corresponding to the typical lattice vibration modes near the gamma point of the Brillouin zone, specifically the non-degenerated first-order active modes A<sub>1g</sub> and B<sub>2g</sub> at 630 and 772 cm<sup>-1</sup>, respectively. On the other hand, the Raman spectrum of TF SnO<sub>2</sub> (Fig. 1d inset) shows different modes, such as non-degenerated B<sub>1g</sub> and doubly degenerated E<sub>g</sub> fundamental active modes at 628 and 736 cm<sup>-1</sup>, respectively. Additionally, the TFs Raman spectra have triply degraded E<sub>u</sub> mode at 225 cm<sup>-1</sup> and the single A<sub>2u</sub> mode at 491, 357, and 566 cm<sup>-1</sup>, respectively, which are not visible in the Raman spectral data of BK. In summary, a surface-sensitive methodology called Raman spectroscopy may disclose a material's surface characteristics, which may differ from the bulk material's properties [8, 9]. Atomic force microscopy (AFM) was used beforehand to analyze the preparation of SnO<sub>2</sub>/Bi TFs. The RMS roughness determined from the AFM is 32.81 nm on a 10 × 10 μm mapping of bare SnO<sub>2</sub> TF, and the surface distribution of deposition is quite uneven. However, deposition is very uniform when SnO<sub>2</sub> is deposited on Bismuth, and the homogeneity can be seen in even 1 × 1 μm AFM image (Fig. 1e) and an RMS roughness of 17.95 nm only.

The impedance spectroscopy of both BK and TFs samples displays similar characteristics, with a plateau in the real part of the impedance (Z') (as shown in Fig. 2a) and a sharp decay after the critical frequency. The saturation in Z' for BK samples is around 20 Hz, while for TFs, it is visible after 100 Hz. The critical frequency

also differs significantly between the two samples, with a drop for TFs occurring at a much lower frequency than the BK sample. The imaginary impedance ( $Z''$ ) shows a dipolar relaxation peak, with similar peak features for both samples, but at different frequencies: 2 MHz for BK and 170 kHz for TF [10]. The  $\epsilon''$  shows linear behavior with no relaxation peak in both BK and TF samples [11], while  $\epsilon'$  (see Fig. 2b) shows frequency-activated regions at low and high frequencies and a frequency-independent region. The BK sample has a high dielectric constant of  $2 \times 10^4$  at 10 Hz, while TF sample has a much lower value of  $\sim 2$  at 10 Hz, suggesting that the high dielectric constant of BK samples is because of interfacial effects and space charge polarization [12, 13]. The Nyquist plots (as shown in Fig. 2c, d) of both BK and TFs show a typical semicircle, with a depressed semicircle signifying a deviation from ideal capacitor behavior. SnO<sub>2</sub> has given high dielectric loss tangent values ( $\tan \delta$ ), (as shown in Fig. 2e) with an apex centered around 100 Hz, regardless of sample type. Additionally, a sharp peak was observed in BK and a broad peak over a range of frequencies in TFs, which is assumed to be due to intrinsic electrical conduction and non-linear processes in SnO<sub>2</sub>.

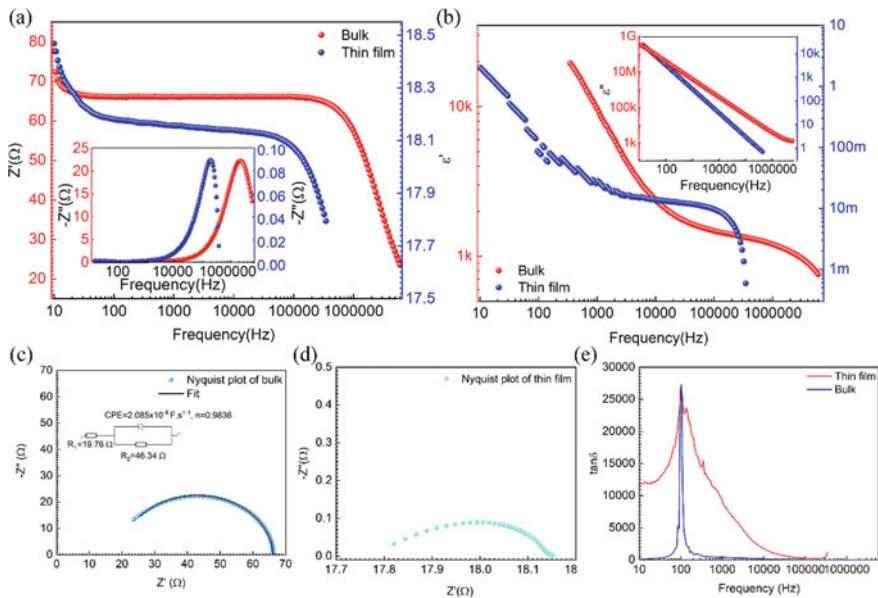


**Fig. 2** Frequency-dependent **a** real and imaginary (in inset) impedance of BK and TF, **b** dielectric response for BK and TF. Nyquist plot of **c** BK and **d** TF. **e** The dielectric loss response for BK and TF

## 4 Conclusion

In conclusion, this paper presents the structural, optical, Raman, AFM, impedance, and dielectric properties of BK and TFs of SnO<sub>2</sub>. The XRD pattern shows that the crystal structure of SnO<sub>2</sub> formed in the tetrahedral forms with the P42/mnm space group. The optical band gap of BK SnO<sub>2</sub> is 3.77 eV, while the optical band gap of TF SnO<sub>2</sub> decreases due to an elevation in tensile strain in the structure. Raman spectra of BK and TF SnO<sub>2</sub> show different modes, such as non-degenerated  $B_{1g}$  and doubly degenerated  $E_g$  fundamental active modes. The AFM mapping of the fabricated TFs shows uniform deposition when SnO<sub>2</sub> is deposited on Bismuth. Lastly, the impedance spectroscopy of both BK and TFs samples displays similar characteristics, with a plateau in the real part of the impedance ( $Z'$ ) and a sharp decay after the critical frequency. The high  $\epsilon'$  values are a property of grain boundaries showing dominance as interfacial contributions, which are absent in TFs. SnO<sub>2</sub> has given high dielectric loss tangent values ( $\tan \delta$ ), with an apex centered around 100 Hz, and assumed to be intrinsic. In summary, this paper provides a comprehensive insight into the structural, optical, Raman, AFM, impedance, and dielectric properties of bulk, and thin film of SnO<sub>2</sub>. Also, we can conclude that being n-type semiconductor of prepared material and having an optical bandgap of 3.6 eV particular material is useful in optoelectronic applications as well as gas sensors.

**Conflict of Interest** The authors declare that they have no conflict of interest.

## References

1. Rouchdi M, Salmani E, El hat A, Nassiri C, Hassanain N, Mzerd A (2017) Synthesis and magnetic properties of Mg doped SnO<sub>2</sub> thin films: experimental and Ab-initio study. *Opt Quant Electr* 49:150
2. Wu S, Chen H, Du X, Liu Z (2016) Effect of deposition power and pressure on rate deposition and resistivity of titanium thin films grown by DC magnetron sputtering. *Spectrosc Lett* 49:514–519
3. Marikkannan M, Vishnukanthan V, Vijayshankar A, Mayandi J, Pearce JM (2015) Maxwell-Wagner polarization in ceramic composites BaTiO<sub>3</sub>–(Ni<sub>0.3</sub>Zn<sub>0.7</sub>)Fe<sub>21</sub>O<sub>4</sub>. *J Appl Phys* 91:794–797
4. Kao KC (2004) Electric polarization and relaxation. *Dielectric phenomena in solids*. Elsevier, Amsterdam, pp 41–114
5. Li L, Yuan Z, Fan R, Luo T, Fan C (2020) Low-temperature synthesis of pyrolytic-PVDF-coated SnO<sub>2</sub>@hard carbon nanocomposite anodes for Li-ion batteries. *J Mater Sci Mater Electr* 31:6449–6460
6. Nirmal S, Kriti S, Poonam Tripathi SK (2020) Synthesis and characterization of Ni-BTC MOF for supercapacitor electrode. *AIP Confer Proc* 2265:030617. <https://doi.org/10.1063/5.0017162>
7. Zhou W, Liu Y, Yang Y, Wu P (2014) Band gap engineering of SnO<sub>2</sub> by epitaxial strain: experimental and theoretical investigations. *J Phys Chem C* 118:6448–6453

8. Diéguez A, Romano-Rodríguez A, Vilà A, Morante JR (2001) The complete Raman spectrum of nanometric SnO<sub>2</sub> particles. *J Appl Phys* 90:1550–1557
9. Mehraj S, Ansari MS, Alimuddin S (2015) Annealed SnO<sub>2</sub> thin films: structural, electrical and their magnetic properties. *Thin Solid Films* 589:57–65
10. Saha BC, Bera AK, Yusuf SM (2021) Mechanism of Na-ion conduction in the highly efficient layered battery material Na<sub>2</sub>Mn<sub>3</sub>O<sub>7</sub>. *ACS Appl Energy Mater* 4:6040–6054
11. Liu J, Duan C-G, Yin W-G, Mei WN, Smith RW, Hardy JR (2003) Dielectric permittivity and electric modulus in Bi<sub>2</sub>Ti<sub>4</sub>O<sub>11</sub>. *J Chem Phys* 119:2812–2819
12. Matysiak W, Tański T, Smok W (2020) Study of optical and dielectric constants of hybrid SnO<sub>2</sub> electrospun nanostructures. *Appl Phys A* 126:115
13. Lunkenheimer P, Fichtl R, Ebbinghaus SG, Loidl A (2004) Nonintrinsic origin of the colossal dielectric constants in CaCu<sub>3</sub>Ti<sub>4</sub>O<sub>12</sub>. *Phys Rev B* 70:172102



# Removal of Cationic and Anionic Dyes from Aqueous Phase by Biosynthesized Nickel Nanoparticles



Harshvardhan Chauhan, Mohd Saquib Tanweer, and Masood Alam

**Abstract** In this study, nickel nanoparticles (BNPs) have been biosynthesized by ethanoic whole plant extract of Brahmadandi plant (*Tricholepis glaberrima*) as a potential and sustainable adsorbent for the elimination of methyl orange (MO) as well as brilliant green (BG) from aqueous solution. The prepared BNPs were characterized using UV–Vis, XRD, FTIR, HR-FESEM. Numerous factors such as pH of the solution, contact time, BNPs dose, and initial dye concentrations were boosted to monitor the adsorption method of MO and BG onto the surface of BNPs. The results equipped well to the Langmuir model. Adsorption isotherm and adsorption kinetics studies were extensively studied. The adsorption kinetics of the adsorption technique originated to understand the pseudo-second-order kinetics. The BNPs uncovered in terms of adsorption capability for the cationic as well as anionic dyes because of its high surface area and enormous number of functional groups.

**Keywords** Ni NPs · Brahmadandi (*Tricholepis glaberrima* DC) ethanoic extract · Dye · Adsorption · Textile water purification

## 1 Introduction

Due to rapid development of industries, public health is in danger. Most predominant worldwide challenges are deficit of fresh, consumable, and healthy water for all living organisms of earth [1, 2]. Discharging of precarious dyes and chemicals from various industries such as fabric, paper, photography, printing, and leather into water bodies is disturbing to both toxicological and esthetical reasons. Such dyes in water bodies diminish light penetration as well as photosynthesis and deteriorate to generate toxic agents like carcinogens [3]. Nanoscale nickel particles (Ni NPs) attracted huge interest in environmental remediation. One of the prominent uses in this regard is

---

H. Chauhan · M. S. Tanweer · M. Alam (✉)

Environmental Science Research Lab, Department of Applied Sciences and Humanities, Faculty of Engineering and Technology, Jamia Millia Islamia, New Delhi 110025, India  
e-mail: [malam@jmi.ac.in](mailto:malam@jmi.ac.in)

the exclusion of organic and inorganic pollutants from aqueous bodies because it has nanoscale size compromises high surface area as well as high surface reactivity.

Chemical and physical route synthesized metallic nanoparticles generally toxic in nature as well as has high cost [4]. Whereas in greener approaches it is more secure, nontoxic, cost effective, and environment friendly [5]. For biosynthesis of metallic nanoparticles, plant extracts are widely used as reducing agent and capping agent because ease of availability, nontoxic, safe, and having broad range of phytochemicals.

Herein, nickel nanoparticles biosynthesized by plant extract of *Tricholepis glaberrima* DC (common name Brahmadandi; Family: Asteraceae). In this study, adsorption of both cationic and anionic dyes has been investigated by using biosynthesized nickel nanoparticles (BNPs).

## 2 Materials and Methods

### 2.1 Preparing Biosynthesized Nickel Nanoparticles (BNPs)

Firstly, the whole plant of Brahmadandi was collected from the nursery of Jamia Millia Islamia and rinsed a few times with tap water to remove its dust particles. Again, it was washed with DDW and dried in shade for one week to eliminate moisture content. Dried leaves of the plant were powdered using grinder mixer and stored in dark at room temperature. 2.5 g air dried powder mixed with ethanol (500 mL) in a flask and kept at room temperature for 5 days. The mixture was heated at low temp for 30 min using water bath to obtain concentrated extract of the plant. Finally, mixture was filtered consuming Whatman filter paper 1 (having pore size 11  $\mu\text{m}$ ) and stored at cool place. 5 mM Ni (NO<sub>3</sub>)<sub>2</sub>·6H<sub>2</sub>O mixed with 100 mL DDW in 250 mL flask. For reduction, 10 mL of plant extract mixed in the previous solution and magnetically stirred for 2 h. at room temperature. Color change was observed from green to pale yellow indicating the formation of Ni NPs. After completion of reaction, precipitate settles down in flask. Finally, mixture was washed and purified by centrifugation for 20 min at 5000 rpm with DDW to obtain BNPs. Then, BNPs were dried at room temperature.

### 2.2 Evaluation of MO and BG Dye Removal

Batch studies were investigated to evaluate the cationic (BG) and anionic (MO) dye's adsorption onto surface of BNPs with continuous agitation by rotary shaker. Typically, adsorbent material (BNPs) was mixed in various 100 mL Erlenmeyer flasks having 30 mL of both MO and BG dyes solution with amount range 10–250 mg L<sup>-1</sup> for 180 min. pH was maintained in between 2 and 10 by adding 0.1N NaOH/HCl.

After equilibrium accomplishment, the finding samples were centrifuged to isolate the aliquots part of dyes. After adsorption process, the residual MO and BG dyes were analyzed by UV–Vis spectrophotometer at  $\lambda_{\max}$  464 and 625 nm, respectively. To estimate dyes uptake and adsorption capacity  $q_e$  (mg g<sup>-1</sup>) of BNPs for MO and BG initial dye concentration  $C_i$  (mg L<sup>-1</sup>) and equilibrium MO and BG dyes concentration  $C_e$  (mg L<sup>-1</sup>), they are given as following expressions [1].

$$R(\%) = \frac{C_i - C_e}{C_i} \times 100 \quad (1)$$

$$q_e = \frac{(C_i - C_e)V}{M} \quad (2)$$

Here,  $M$  (g) is the amount of the BNPs nanomaterial, and ‘ $V$ ’ is the volume of MO and BG dye solution as adsorbate in liter.

### 3 Results and Discussion

#### 3.1 Characterization of BNPs

##### 3.1.1 FTIR

The vibrational spectra of the BNPs are presented in Fig. 1c. In the following, there are three spectra in which Fig. 1c(z) represents BNPs, further Fig. 1c(x), (y) represents FTIR of post adsorption of MO and BG dyes. Spectrum of FTIR of BNPs synthesized by whole plant ethanoic extract of Brahmadandi was reported in the literature and find peaks at 676 cm<sup>-1</sup> because of stretching of the Ni–O of oxidized nickel. In the Fig. 1c(z) depicted characteristic spectral bands of functional groups of several phytochemicals such as phytosterol, i.e., Spinasterol, Stigmasterol, naturally producing triterpene (Betulin), triterpenoid, and flavone Glycoside present in Brahmadandi whole plant extract. The peak at 3640 cm<sup>-1</sup> revealed presence of phenolic hydroxyl groups stretching in flavone Glycoside in all three spectra. The peak at 2916 and 2849 cm<sup>-1</sup> is ascribed to –C–H stretching of –CH<sub>3</sub> and CH<sub>2</sub> of phytochemicals, respectively. The phytochemicals have ethers (–O–) and carbonyl (C=O) functional groups its peak at 1107, 1628 cm<sup>-1</sup>, respectively [5]. In Fig. 1c(x–z), spectra wavenumber from 4000 to 1500 cm<sup>-1</sup> has probably not much changed, but in Fig. 1c(x, y), from 1500 cm<sup>-1</sup> till 500 cm<sup>-1</sup> have many modifications in compare with Fig. 1c(z) that mean adsorption has been take place for both cationic and anionic dyes onto BNPs surface. Hence, this study confirms that the functional groups present on the surface of BNPs participated in dyes adsorption.

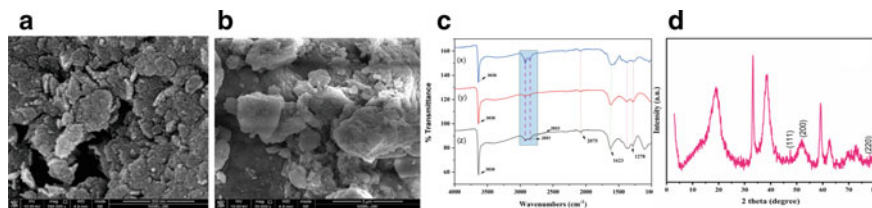


**Fig. 1** Surface morphology of BNPs (a); dye loaded BNPs (b); FTIR spectra of BNPs, MO dye loaded, and BG dye loaded (c); XRD spectra of BNPs (d)

### 3.1.2 XRD Study

The crystallinity and phase structure of the biosynthesized Ni NPs (BNPs) were recorded by X-ray diffraction (XRD) and presented in Fig. 1d. The clear diffraction peaks situated at  $47.5^\circ$ ,  $51.9^\circ$ , and  $77.9^\circ$  have been indexed as face-centered cubical structure, according to the standard JPCDS card number 04-0835 [5]. All three peaks correspond to 111, 200, and 220 crystal planes, respectively.

### 3.1.3 HR-FESEM

HR-FESEM works like a crucial technique to morphological analysis of BNPs. Here, we use HR-FESEM in which two images are used. First image is before adsorption (Fig. 1a), and second is for post adsorption of dyes (Fig. 1b). HR-FESEM image of BNPs sample reveals that the surface of NPs was rough, porous, and cracked type structure. In Fig. 1b, HR-FESEM clearly displayed that rough, porous structure of BNPs gets trapped or blocked by dyes (BG and MO). It is demonstrated that biosorption has been take place between adsorbent surface as well as MO and BG dyes.

## 3.2 Batch Experiment

### 3.2.1 Impact of Contact Time and Kinetic Study

In the Fig. 2, it is clearly shown that MO and BG uptake % onto BNPs adsorbent elevated with rise in the contact time, and after 120 min, the removal was 98 and 96% for both MO and BG dye, respectively. Such adsorption nature was caused by accessibility of active adsorptive sites onto BNPs at primary phase procedure of adsorption. Two kinetic models, i.e., PFO and PSO, were employed to suitable experimental data of MO and BG dye sorption from the aqueous phase to evaluate the adsorption mechanism and kinetics of the adsorption process. PSO kinetic is

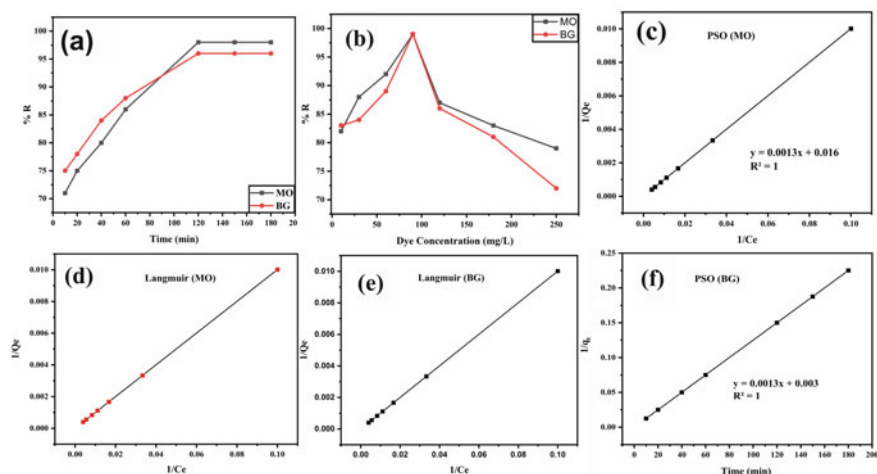


**Fig. 2** Impact of contact time (a); effect of initial concentration of MO and BG (b); pseudo-second order kinetic model for the sorption of MO dye (c) and BG dye (f); Langmuir isotherm onto the BNPs of MO (d) and BG dye (e)

apparent well suited for both dyes as calculated  $q_e$  value and experimental  $q_e$  value are more near which justifies chemisorption is rate determining step [1].

### 3.2.2 Effect MO and BG Concentration and Isotherm Study

The result of the primary amount of MO and BG dye checked with intensity range of 10–250 mg L<sup>-1</sup> on BNPs. It is clear shown in Fig. 2 that the removal efficiency rises from 82 to 99% in case of MO dye and from 83 to 99% of BG dye with increase of both dyes' concentration after 90 mg L<sup>-1</sup>, and after that equilibrium got achieved. Further, as dyes concentration rises, a strong driving force developed that allowed dyes molecules to overwhelm all their resistance to mass sift from the liquid media to the solid matter. Figure 2d, e shows two isotherm model for MO and BG dyes adsorption on the BNPs. Table 1 demonstrations the parameters of selected isotherm models. According to Langmuir model, the maximum adsorption capacities ( $q_m$ ) for BNPs were 312.5 and 370.4 mg g<sup>-1</sup>. Table 2 reveals that the adsorbent materials, BNPs projected good separation factor ( $R_l$ ), i.e., 0.26 for MO and 0.01 for BG dye. The values of  $R_l$  are in between 0 and 1 which confirms favorable adsorption of MO and BG dye and appropriateness of the Langmuir isotherm model [6].

**Table 1** Parameters of PSO model for the sorption of both MO and BG dye on the BNPs

Adsorbent	PSO (MO)				PSO (BG)			
	$q_e$ (exp) (mg g <sup>-1</sup> )	$q_e$ (cal) (mg g <sup>-1</sup> )	$K_2$ (min <sup>-1</sup> )	$R^2$	$q_e$ (exp) (mg g <sup>-1</sup> )	$q_e$ (cal) (mg g <sup>-1</sup> )	$K_2$ (min <sup>-1</sup> )	$R^2$
BNPs	799.59	769.23	$9.7 \times 10^{-5}$	1	799.58	769.23	0.00052	1

**Table 2** Parameters of Langmuir model for the sorption of both MO and BG dye on the BNPs

Adsorbent	Langmuir model (MO)				Langmuir model (BG)			
	$q_{\max}$ (mg g <sup>-1</sup> )	$K_l$ (L mg <sup>-1</sup> )	$R_l$	$R^2$	$q_{\max}$ (mg g <sup>-1</sup> )	$K_l$ (L mg <sup>-1</sup> )	$R_l$	$R^2$
BNPs	312.5	0.031	0.26	1	370.37	1	0.01	1

## 4 Conclusion

In this research work, the biosynthesized nickel nanoparticles have been successfully prepared using ethanoic extract of whole plant, i.e., *T. glaberrima* DC. It was used for decolorization of textile discharges containing MO and BG dye. Biosorption of dyes onto BNPs followed Langmuir isotherm with  $q_{\max}$  of 312.5 mg·g<sup>-1</sup> for MO and 370.37 mg·g<sup>-1</sup> in the case of BG dye. Adsorption kinetics study shows that the uptake of dyes onto BNPs well suited better with pseudo-second order. Thus, it was established that BNPs could be a potential adsorbent material for the deprivation of toxic dyes.

**Conflict of Interest** The authors declare that they have no conflict of interests.

## References

1. Tanweer MS, Iqbal Z, Alam M (2022) Experimental insights into mesoporous polyaniline-based nanocomposites for anionic and cationic dye removal. *Langmuir* 38:8837–8853. <https://doi.org/10.1021/ACS.LANGMUIR.2C00889>
2. Chauhan H, Alam M (2020) Combination of phytochemicals with nanotechnology for targeting GI cancer therapy. *Phytochemicals targeting tumor microenvironment in gastrointestinal cancers*. Springer International Publishing, Cham, pp 141–167
3. Bir R, Tanweer MS, Singh M, Alam M (2022) Multifunctional ternary NLP/ZnO@ <sc>l</sc>-cysteine- grafted -PANI bionanocomposites for the selective removal of anionic and cationic dyes from synthetic and real water samples. *ACS Omega* 7:44836–44850. <https://doi.org/10.1021/acsomega.2c04936>
4. Rathore S, Madhav H, Jaiswar G (2019) Efficient nano-filler for the phase transformation in polyvinylidene fluoride nanocomposites by using nanoparticles of stannous sulfate. *Mater Res Innov* 23:183–190. <https://doi.org/10.1080/14328917.2017.1406572>

5. Din MI, Nabi AG, Rani A et al (2018) Single step green synthesis of stable nickel and nickel oxide nanoparticles from *Calotropis gigantea*: catalytic and antimicrobial potentials. *Environ Nanotechnol Monit Manag* 9:29–36. <https://doi.org/10.1016/j.enmm.2017.11.005>
6. Ali S, Tanweer MS, Alam M (2020) Kinetic, isothermal, thermodynamic and adsorption studies on *Mentha piperita* using ICP-OES. *Surf Interf* 19:100516. <https://doi.org/10.1016/J.SURFIN.2020.100516>

# Comparative Performance Analysis of Lead-Free Perovskite Solar Cell with Different Electron Transport Layer



Jaiswal Vivek, Jha Kaushal, and Rawat Kusum

**Abstract** Lead-free perovskite solar cell has gained tremendous attention due to environment-friendly elements and good stability as compare to Pb-based perovskite solar cells (PSCs). Among various lead-free-based absorber materials,  $\text{Cs}_2\text{BiAgI}_6$  emerged as a potential candidate due to benign elements and ability to match the performance of current leading lead-based PSCs technology. In this paper, lead-free  $\text{Cs}_2\text{BiAgI}_6$ -based PSC has been numerically analyzed using a solar cell capacitance simulator (SCAPS-1D). Detail investigations have been performed on n-i-p structure where  $\text{Cs}_2\text{BiAgI}_6$  acts as an absorber layer and copper(I) oxide ( $\text{Cu}_2\text{O}$ ) as hole transport layer (HTL). A comparative study has been performed with different electron transport layers (ETL) such as zinc magnesium oxide ( $\text{ZnMgO}$ ), tin(IV) oxide ( $\text{SnO}_2$ ), zinc oxide ( $\text{ZnO}$ ), and buckminsterfullerene ( $\text{C}_{60}$ ) while keeping other layers unchanged. All the PSCs structure demonstrated greater than 16% power conversion efficiency. Optimization of the device parameters done through numerical analysis of device parameters with different ETLs, doping density, thickness of various layers and defect density.

**Keywords** SCAPS-1D · Lead-free · Perovskite · ETL ·  $\text{Cs}_2\text{BiAgI}_6$

---

J. Vivek

Department of Electronics and Communication Engineering, Gurukula Kangri University, Haridwar, Uttarakhand 249404, India

J. Kaushal (✉)

Department of Electronic Science, B.R.A. Bihar University, Muzaffarpur, Bihar 842001, India  
e-mail: [kaushaljha096@gmail.com](mailto:kaushaljha096@gmail.com)

R. Kusum (✉)

Department of Electronics, D.D.U. Gorakhpur University, Gorakhpur, Uttar Pradesh 273009, India  
e-mail: [kusum04rawat@gmail.com](mailto:kusum04rawat@gmail.com)



## 1 Introduction

In fourth generation photovoltaic technology, lead-based perovskite solar cell (PSC) has gained significant attention due to its tunable direct bandgap, high absorption coefficient, low exciton binding energy, and high carrier mobility. Although, lead-based perovskite solar cell has demonstrated highest photovoltaic efficiency of 23.7%, however, toxicity nature of lead element and device stability issues cannot be ignored [1]. Hence, an alternative lead perovskite material needs to be explored. Recently, [2] have reported lead-free halide double perovskites and eco-friendly  $\text{Cs}_2\text{BiAgI}_6$  material. A theoretical investigation was performed by [3] and stated theoretical power conversion efficiency (PCE) of 16.23% using PCBM and PTTA as HTL and ETL layer, respectively.

In this present work,  $\text{Cs}_2\text{BiAgI}_6$  is used as an absorber layer in PSC structure. The factors affecting the  $\text{Cs}_2\text{BiAgI}_6$ -based PSCs efficiency are analyzed by SCAPS-1D simulation software under AM1.5G illumination with different ETL materials. Current density versus voltage and quantum efficiency are analyzed for suitable ETL. Optimization of device structure is carried out by varying the thickness and doping levels of different layers with different density of state.

## 2 Device Structure and Simulation Method

### 2.1 Device Structure

The structure of our proposed PSCs is shown in Fig. 1a, and the energy band diagram of the material studied in this work is shown in Fig. 1b. The cell has an *n-i-p* structure consisting of a fluorine coated transparent conductive oxide layer (FTO), electron transporting layer (ETL), a lead-free perovskite (absorber layer), and hole transport layer (HTL) with the layer configuration of FTO/ETL/ $\text{Cs}_2\text{BiAgI}_6$ /HTL/metal contact.

The simulation parameter of each layer is taken from the reported literature. For all layers, the defect type was set to neutral, and the electron and hole capture cross sections were set to  $1 \times 10^{-15} \text{ cm}^{-2}$ .

### 2.2 Simulation Method

The simulation and the calculations carried out in the SCAPS-1D software are mainly based on three basic equations, namely the Poisson's equation, electron continuity equation, and hole continuity. The AM 1.5G sun spectrum used to study the performance of PSC.

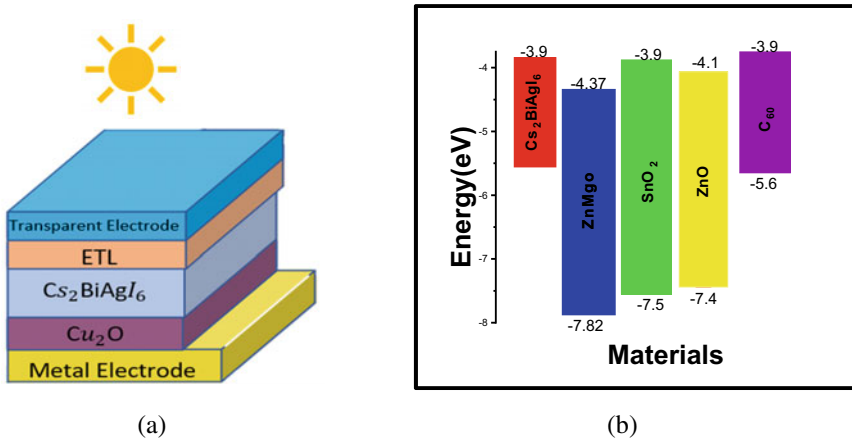


Fig. 1 a Schematic diagram of solar cell, b energy band of different ETLs with respect to PSCs

### 3 Results and Discussions

#### 3.1 Different ETL Materials

Numerical modeling of proposed  $n-i-p$  structure performed using SCAPS-1D simulation tool. Figure 2 shows the  $J-V$  characteristics of the  $Cs_2BiAgI_6$ -based PSC with different ETL layer such as  $SnO_2$ , ZnO,  $C_{60}$ , and zinc magnesium ZnMgO. It is observed that the PSC with  $SnO_2$  ETL layer shows better performance than the other ETLs. Similarly, the power conversion efficiency (PCE) of  $C_{60}$  is a very close to that of  $SnO_2$ . The excellent result of  $SnO_2$  and  $C_{60}$  is due to better band alignment with PSCs. The band alignment of PSCs with respect to ETLs termed as conduction band offset (CBO). Recent study shows that the optimum value of CBO is  $-0.1$  to  $+0.1$  eV for minimum barrier spike and low recombination at interface [4], because of low recombination at interface, the electron has greater probability to reach the heterojunction of cell. Hence,  $SnO_2$  can be used as optimal ETL for proposed structure.

#### 3.2 Thickness Optimization of Absorber Layer

The perovskite material layer acts as an absorbing layer; therefore, its thickness is very important. It should be thick enough to absorb most of incident photons, but not too thick to allow the collection of photogenerated charge carriers before recombination occurs. Figure 3 depicts the simulation results by varying the thickness from 200 to 1000 nm. The optimal thickness chosen is 400 nm, which absorbs the most of incident photons.

**Fig. 2**  $J$ - $V$  characteristics of PSC with different ETL layer

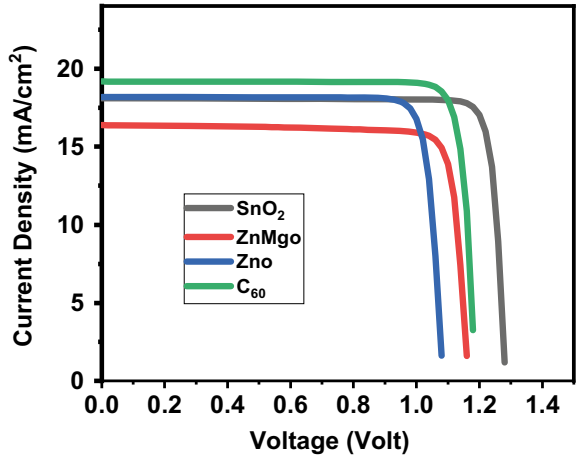


**Fig. 3** Variation in FF,  $J_{sc}$ ,  $V_{oc}$ , and  $\eta$  versus thickness of absorber layer

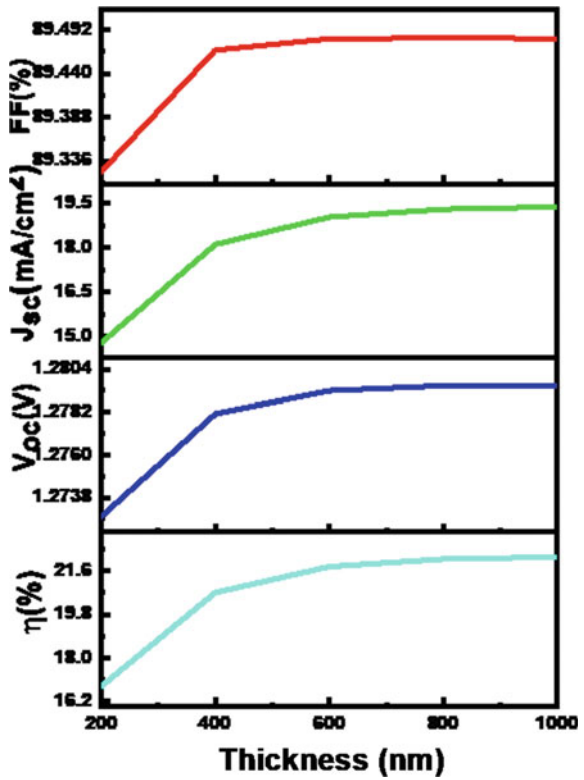
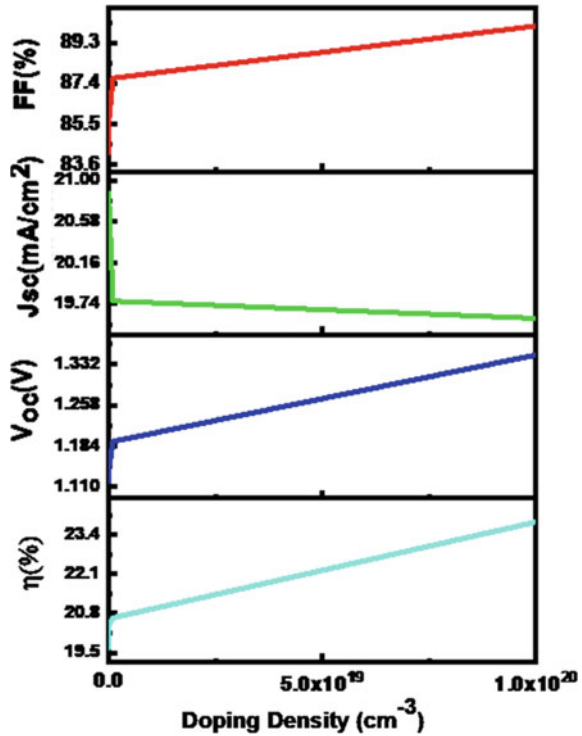


**Fig. 4** Variation in FF,  $J_{sc}$ ,  $V_{oc}$ , and  $\eta$  versus doping density in absorber layer



### 3.3 Doping Optimization of Absorber Layer

Figure 4 shows the absorber layer doping variation from  $N_A = 0.5 \times 10^{15} \text{ cm}^{-3}$  to  $1 \times 10^{20} \text{ cm}^{-3}$ . It is observed that the  $V_{oc}$ , PCE, and FF increased with doping above  $0.5 \times 10^{15} \text{ cm}^{-3}$ , however,  $J_{sc}$  decreased. The open circuit voltage is a function of both  $J_{sc}$  and  $J_{sc}$ . The optimal doping density  $N_A = 1 \times 10^{19} \text{ cm}^{-3}$  has been found to be suitable for high efficiency solar cell. For optimized device parameters, the PSCs with  $\text{SnO}_2$  as ETL have been analyzed, and thickness and doping density of absorber layer are varied. The optimized thickness and doping density of absorber layer are found to be 400 nm and  $N_A = 1 \times 10^{19} \text{ cm}^{-3}$ . The value of optimized characteristics parameter is  $V_{oc} = 1.27 \text{ V}$ , PCE = 20.7%,  $J_{sc} = 18.1 \text{ mA}/\text{cm}^2$  and FF = 89.4%.

## 4 Conclusions

Using SCAPS-1D simulation software, the lead-free  $\text{Cs}_2\text{BiAgI}_6$  and perovskite solar cells with various ETL materials are examined. To maximize efficiency, the effect of absorber layer thickness and doping density is varied. It was observed that ETL

and absorber layer play a significant role in device performance. Among the various ETL materials,  $\text{SnO}_2$  shows maximum PCE of 20.70% and  $V_{oc} = 1.278$  V due to excellent band alignment of  $\text{SnO}_2$  with absorber layer & HTL at optimized thickness of 400 nm and doping density  $N_A = 1 \times 10^{19} \text{ cm}^{-3}$  of absorber layer. Further, this work can be viewed as a guideline for fabricating new efficient non-toxic.

**Acknowledgements** The authors are grateful to acknowledge Department of Science and Technology, SERB (Project No. SPG/2021/000574) for provide financial support and Dr. Marc Burgelman, University of Gent, Belgium, for allowing to use SCAPS simulation software.

## References

1. Green MA, Dunlop ED, Hohl-Ebinger J, Yoshita M, Kopidakis N, Bothe K, Hinken D, Rauer M, Hao X (2022) Solar cell efficiency tables (version 57). *Prog Photovolt Res Appl* 30:687
2. Faghinasiri M, Beheshtian J, Shayeganfar F, Shahsavari R (2020) Phase transition and mechanical properties of cesium bismuth silver halide double perovskites ( $\text{Cs}_2\text{AgBiX}_6$ , X = Cl, Br, I): a DFT approach. *Phys Chem Chem Phys* 22:5959
3. Srivastava S, Singh AK, Kumar P et al (2021) Comparative performance analysis of lead-free perovskites solar cells by numerical simulation. Preprint (Version 1) available at Research Square. <https://doi.org/10.21203/rs.3.rs-583148/v1>
4. Singh N, Agarwal A, Agarwal M (2022) *Opt Mater* 125:112112

# Printed Carbon Film-Based Self-Powered Triboelectric Nanogenerator as Flexible Tactile Sensor



Pramila Viswanathan and Arunkumar Chandrasekhar

**Abstract** With the continued rise in demand for smart devices, most sophisticated features such as wearability, compatibility, flexibility, durability, affordability, and sustainability are anticipated. In this paper, we proposed an activated carbon electrode-based flexible and skin-conformal self-powered tactile sensor that working under the principle of triboelectrification and electrostatic induction (Wu in *Mater Today Energy* 20:657, 2021; Zhao in *Nano Energy* 59:302–310, 2019;). The fabricated sensor can capture the biomechanical signals including touching, muscle bending, walking, and hand gesture and convert them into an electrical signal with high sensitivity in single electrode mode. The proposed work reports the film fabrication and characterization using the stencil printing technique. Additionally, carried out the surface modification of biodegradable triboelectric thin film to enhance device performance (Yang in *ACS Nano* 7:9213–9222, 2013). The change in fabricated device's electrical response which is varied due to the applied force has been studied using a finite element method solver (COMSOL) by coupling electrostatics and solid mechanics. The obtained results providing the potential performance in the field of human motion sensing and tactile sensing.

**Keywords** Tactile sensing · Stencil printing · Biodegradable · Energy harvesting · Flexible · Bio-compatible and sustainability

## 1 Introduction

Due to their accessibility, sustainability, adaptability, triboelectric nanogenerators (TENGs) became an emerging technology in the field of wearable electronics. As a result, it can serve as an energy harvester and tactile sensor using the coupled effect of triboelectrification and electrostatic induction [1]. In accordance with prior

---

P. Viswanathan · A. Chandrasekhar (✉)

Nanosensors and Nanoenergy Lab, Sensor Systems Lab, Department of Sensors and Biomedical Technology, School of Electronics Engineering, Vellore Institute of Technology, Vellore, Tamilnadu 632 014, India  
e-mail: [arunkumar.c@vit.ac.in](mailto:arunkumar.c@vit.ac.in)

research, the polarity and density of the triboelectric charges are typically defined by the functional groups on the main chains of the polymers as the friction layer [4]. In this proposed work, we present skin-conformal surface modified silicone rubber (Ecoflex-biodegradable polymer) as friction layer. Herein, we report a single electrode TENG device for self-powered tactile sensing using an eco-friendly material as printed activated carbon electrode and ecoflex (a biopolymer as dielectric friction layer). This fabricated device can be used in the variety of wearable applications such as gait monitoring, haptic sensing, health monitoring, and biomechanical motion sensing. Self-powered nanosensors exploit the energy harvested by triboelectric nanogenerator, which doesn't need any conventional batteries or other external power supply [3, 5].

## 2 Experimental Section

### 2.1 Fabrication of Ecoflex Friction Layer

A biodegradable silicone rubber (Ecoflex 00-30—Part A Monomer and Part B curing agent) was procured from Smooth-On Inc. The monomer and curing agent or a hardener were taken in the ratio of 1:1 and mixed homogeneously, then the mixture was degassed to remove the air bubbles. The obtained solution was poured onto the mold to solidify it. The fabricated ecoflex film has the fine grain on the surface of very thin film with the thickness of 1.5 mm. The optical image of surface modified ecoflex film with  $5\times$  magnification has been shown in Fig. 2b.

### 2.2 Fabrication of Activated Carbon Electrode and Single Electrode TENG Device for Tactile Sensing

An activated carbon electrode has been fabricated using the stencil printing technology [6]. The PET stencil of dimension  $1\text{ cm} \times 1\text{ cm}$  was prepared with the help of nonmetal laser cutting machine. Here, we prepared an activated carbon ink by probe sonicated the mixture of 1 g activated carbon and 10 ml of 10% polyvinyl alcohol (PVA) together for 1 min. Hydrophilic plasma surface treatment had been carried out on the surface of polyethylene terephthalate (PET) to improve the adhesion of substrate and activated carbon ink. The PET stencils mask was placed on the surface of PET substrate. Finally using a squeegee, multiple coatings of activated carbon ink are applied to the PET substrate. The copper wire was attached to the activated carbon electrode using silver paste for electrical validation.

The single electrode triboelectric nanogenerator device was fabricated by placing printed activated carbon electrode beneath an ecoflex film to collect charge which is induced due to the triboelectric effect which is shown in Fig. 1d. When the human

skin in contact with the fabricated flexible TENG device, the device will act as tactile sensor as well as an energy harvester. Figure 1a–c shows the schematic working mechanism of single electrode tactile sensor and the schematic of printed carbon single electrode triboelectric nanogenerator using stencil printing. Here, the surface modification on the ecoflex surface improves the friction which leads to increase in charge accumulation.

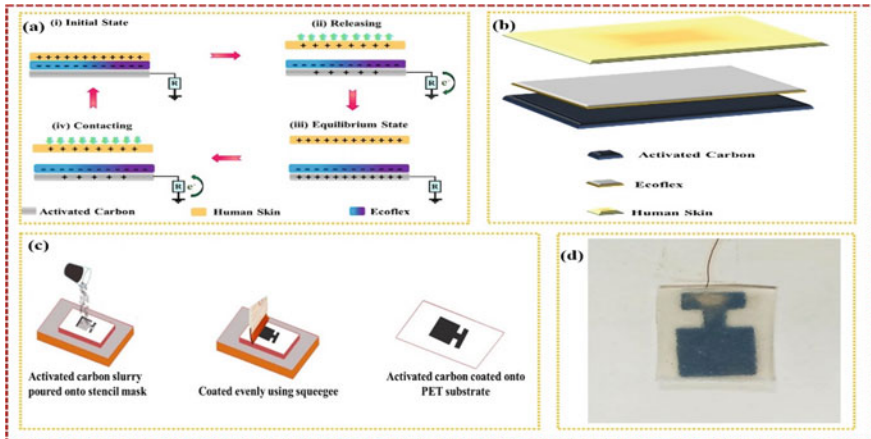


**Fig. 1** a Working mechanism of printed carbon electrode-based single electrode TENG, b schematic working of TENG device, c schematic illustration of stencil printing of activated carbon electrode, d optical image of fabricated TENG device

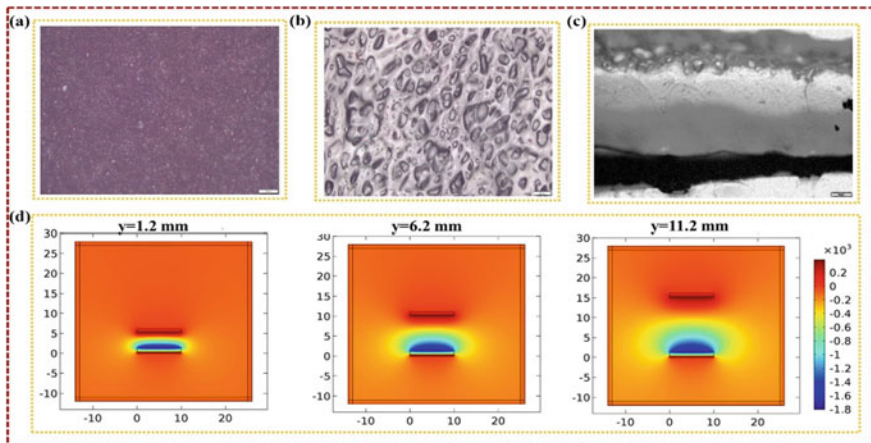


**Fig. 2** a Optical microscopic image of activated carbon film at 5x magnification, b optical microscopic image of surface modified ecoflex film at 5x magnification, c cross-sectional optical image of TENG device at 5x magnification, d COMSOL simulation results: surface electric potentials at  $y = 1.2$  mm,  $y = 6.2$  mm,  $y = 11.2$  mm distance



Figure 2 depicts the optical images of the fabricated device's dimensions, and its electrical performance analysis was verified using finite element method solver by coupling electrostatics and solid mechanics.

### 3 Results and Discussions

In this paper, we report a single electrode triboelectric nanogenerator that comprises the biodegradable materials ecoflex film and printed carbon electrode. When the contact arises between ecoflex and human skin, the change in charge difference occurs which results in driving an electron flow to external load. Due to the surface modified friction layer, more charges are accumulated that improves the TENG performance. The skin and ecoflex surfaces totally enclose one another in their initial state, causing charge transfer between them. The triboelectric series states that the electron transfer occurs from skin to ecoflex since ecoflex silicone rubber is more negative than human skin, as part of the contact electrification. There is no electron transfer between electrode and human skin, because of the equilibrium condition.

Once the separation occurs between human skin and ecoflex friction layer, the negative charges on ecoflex can induce the positive charge in an activated carbon electrode and build the electron flow from activated carbon electrode to ground via external load. This electrostatic induction process produces the open circuit voltage and short-circuit current as shown in Fig. 3.

Figure 3a–c depicts the change in open circuit voltage for various frequencies. The increase in frequency improves the friction between human skin and ecoflex layer, which leads to more charge accumulation as well as electron transfer between

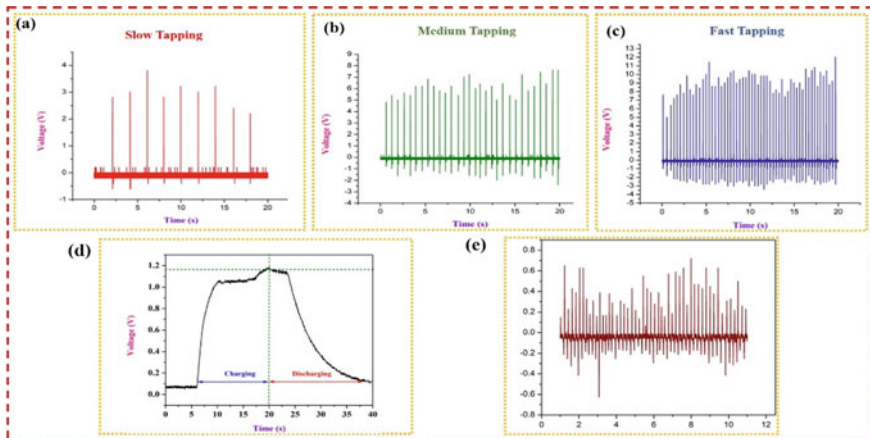


**Fig. 3** a–c Open circuit voltage and frequencies of the tactile sensor for slow, medium, and fast tapping respectively, **d** voltage variation in the charging and discharging of 1  $\mu\text{F}$  capacitor versus time while hand tapping, **e** short-circuited current

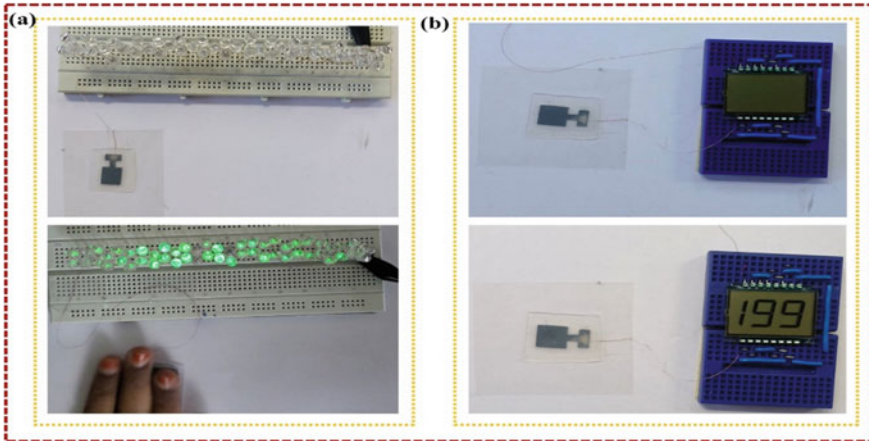


**Fig. 4** **a** LED lit up using tactile sensor, **b** energize an LCD display with tactile sensor

human skin to carbon electrode. The minimum and maximum  $V_{oc}$  of the TENG are reported as 2.5 and 14 V.

As shown in Fig. 3d, the fabricated device can store the charge and discharges when the load connected. Figure 3e shows the short-circuit current of tactile sensor, the maximum  $I_{sc}$  of the device is  $0.8 \mu\text{A}$ . Figure 4a shows that the proposed device can lit up multiple LEDs in a single tapping. The fabricated flexible and durable device can energize the LCD display that is shown in Fig. 4b.

## 4 Conclusion

In this proposed work, we reported the single electrode TENG-based tactile sensor which comprises an eco-friendly materials ecoflex silicone rubber as friction layer and printed carbon electrode to capture charge during contact electrification. The fabricated tactile sensor has high sensitivity, flexibility, and durability. This device possesses the short-circuit current of  $0.8 \mu\text{A}$  and maximum open circuit voltage of 14 V. As well as this tactile sensor has the capability of charge storage that has been examined with charging a  $1 \mu\text{F}$  capacitor. Future work will focus on integrating the array of this flexible tactile sensor and miniaturizing the device with good performance, to implement it as haptic-based assistive device for the people needs visual aid.

**Acknowledgements** This research work was supported by the VIT SEED grant 2021, and the authors would like to thank VIT University for providing research facilities. Also, grateful to Mr. Harish Gnanasambanthan and Mr. V Udayasurian for their lab support.

## References

1. Wu M et al (2021) Thin, soft, skin-integrated foam-based triboelectric nanogenerators for tactile sensing and energy harvesting. *Mater Today Energy* 20:657. <https://doi.org/10.1016/j.mtener.2021.100657>
2. Zhao G et al (2019) Transparent and stretchable triboelectric nanogenerator for self-powered tactile sensing. *Nano Energy* 59:302–310. <https://doi.org/10.1016/j.nanoen.2019.02.054>
3. Yang Y et al (2013) Human skin based triboelectric nanogenerators for harvesting biomechanical energy and as self-powered active tactile sensor system. *ACS Nano* 7(10):9213–9222. <https://doi.org/10.1021/nn403838y>
4. Shao JJ, Jiang T, Wang ZL (2020) Theoretical foundations of triboelectric nanogenerators (TENGs). *Sci China Technol Sci* 63(7):1087–1109. <https://doi.org/10.1007/s11431-020-1604-9>
5. Yu J et al (2019) Highly skin-conformal wearable tactile sensor based on piezoelectric-enhanced triboelectric nanogenerator. *Nano Energy* 64:103923. <https://doi.org/10.1016/j.nanoen.2019.103923>
6. Gnanasambanthan H, Nageswaran S, Maji D (2019) Fabrication of flexible thin film strain sensors using kapton tape as stencil mask. In: Proceedings of the international conference on visual towards the emergy trends communication networking, ViTECoN 2019, pp 3–6. <https://doi.org/10.1109/ViTECoN.2019.8899456>

# Heterogeneous Oxidation of Alcohols Catalyzed by Titania-Supported Palladium Nanoparticles in Aqueous Micellar Solution



Ranjan Kumar Padhy and Sarita Sahu

**Abstract** One of the most fundamental and important chemical processes for the production of fine chemicals in the chemical and pharmaceutical industries that has been studied extensively is the oxidation of alcohols either into carboxylic acids or aldehydes. An efficient, high surface concentration support catalyst from Pd and Titania was prepared, characterized by FTIR, XPS, Magnetic susceptibility and SEM. The catalytic behavior of this material was investigated at room temperature for the oxidation of hydroxy group to carbonyl compounds in the presence of *t*-butylperoxide (*t*-BuOOH) as an oxidant. Intrinsic reusability of the synthesized catalyst, environment-friendly simple procedure and high yield of products are the findings. Synergistic catalytic effect of anionic surfactant, sodium dodecyl sulfate and the metal–support were noticed.

**Keywords** Oxidation · XPS · Amino alcohol · Catalyst · Titania · Palladium

## 1 Introduction

Conversion of hydroxyl group into compounds containing carbonyl group is one of the fundamental reactions in the history of organic synthesis. Oxidative transformation of alcohols in the presence of catalysts is a process of importance for synthesis of chemicals bearing industrial and pharmaceutical importance as well as alcohol-based fuel cells. Moreover, oxidation of alcohols selectively to aldehydes is one of the most challenging jobs for a synthetic organic chemist. The reasons attributed to this are many, viz. the products of the reactions are precursors for large number of medicinal molecules, intermediates for the synthesis of fine chemicals such as vitamins and fragrances [1–6]. Oxides or salts of metals are conventionally used in their stoichiometric ratios for this purpose. Extensive work has been done

---

R. K. Padhy (✉) · S. Sahu  
NIST (Autonomous), Berhampur, Odisha 761 008, India  
e-mail: [rkipadhy@nist.edu](mailto:rkipadhy@nist.edu)

with reagents like Collins's reagent [7, 8] pyridinium chlorochromate [9–11], Dess–Martin periodinane [12],  $\text{CrO}_3/\text{H}_2\text{SO}_4$  [13],  $\text{KMnO}_4$  [14], Ru oxides or salts [15, 16], etc., and there are reports of use of molecular oxygen as the oxidizing agent [17]. In order to achieve high yield and reduced time requirement, suitable catalysts [18–25] including metallic or metal-oxide nanoparticles, supported catalysts or hydrotalcite are used maintaining heterogeneous or homogenous medium. Although some of catalysts being used are regenerated (have high turnover frequency, TOF) and separated, the reactions generate significant number of toxic molecules along with the desired products from the organic precursors. Removal of undesired reagents from the reaction mixtures and the end-product isolation are quite cumbersome, which require lot of labor and time to be invested.

To address this and moreover environmental issues, nowadays, the focus is on the development of green catalysts with high TOF and turnover number (TON) [26–31] with reduced impact on environment. A large chunk of processes of industrial, pharmaceutical and environmental importance focusses on usage of nanoparticles supported over oxide surface as heterogeneous catalysts. The wider acceptance of such biphasic metal-oxide–support system is due to ease of recycling and quite a high turnover [32–34]. The current work aims at synthesis of a support catalyst (titania-supported palladium), its characterization and application for the selective oxidation of amino alcohol (monoethanolamine, MEA) in presence of *t*-butylhydroperoxide (*t*-BuOOH) in *t*-BuOH of alcohols which has not been documented in literature. The preference of support catalysis over homogenous systems is because the catalytic material in heterogeneous conditions can be easily regenerated. Moreover, the solid catalysts can be used in a wider temperature range owing to their higher stability. This can be regarded as a green process since almost 100% conversion occurs of course after removal of the catalyst and evaporation of the solvents from the reaction medium. Metallic nanoparticles well dispersed over the surface of the oxides play vital role in myriad number of catalytic and electrocatalytic process of industrial and pharmaceutical importance. The efficacy of such biphasic materials to some extent depends on the shape, size, composition and the extent of dispersion or distribution of metals over the support.

Surface active agents, surfactants containing hydrophilic head and hydrophobic tail are extensively used as a clean and green sustainable catalyst in a myriad number of industrially and biologically important reactions [35–37]. The hydrophobic part of most of the surfactants associates to form aggregates called “micelles” at a specific narrow concentration of the surfactant in aqueous medium. The process of micellization depends on the properties: dimension of the hydrophobic domain, the size and nature of head groups, concentration, salt, temperature, etc. The concentration range beyond which micellization begins is regarded as critical micelle concentration (cmc) [38]. Micellar effect on reactions that involves metal ions has dragged the attention of researchers due to their importance in physicochemical processes. Hence, it is considered worthy to study the effect of these sustainable catalytic materials on the oxidation of MEA and get the information of the synergistic impact of the catalytic activities of both (surfactant and metal–support pair) on the oxidation process. The substrate, MEA having the presence of amino group (imparts basic

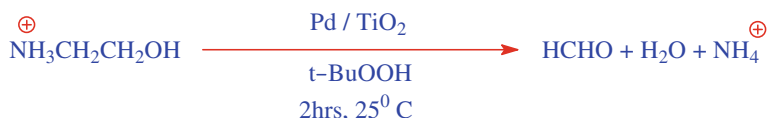
nature) and hydroxyl group, gives the properties of both amines and alcohols. MEA find its use in the emulsifier production, textile chemicals, cement and agrochemical production. Besides, amino alcohols are also used to capture or scrub  $\text{CO}_2$  and  $\text{H}_2\text{S}$  from refinery and natural gas [39]. To get an insight of the micellar medium, three types, viz. sodium dodecyl sulfhate, SDS (anionic), Cetyltrimethylammonium bromide, CTAB (cationic) and Triton X-100 (non-ionic) surfactants, have been used. While monitoring the progress of the reaction, we observed that with rise in SDS concentration, the rate increases and this continues up to about the cmc of SDS. Beyond this [SDS], there is a rapid decrease in rate which was noticed so that the rate—[SDS] profile has resulted in the formation of a maximum.

## 2 Materials and Methods

All the chemicals procured were of AR grade and hence put to use without any subsequent purification. Redistilled solvents were used whenever needed. The IR spectra were recorded in the  $2000\text{--}400\text{ cm}^{-1}$  range using Shimadzu 8400S FTIR spectrophotometer, and 2 MLH magnetic stirrers (Remi Equipment) are used for stirring. The surface morphology and dimension of the catalyst determination were done by SEM using ZEISS Scanning Electron Microscope. The measurement of magnetic susceptibility of the metal–support pair was done with a CTI cryogenic 8200 (Oscillator: voltage = 5 V, frequency = 330 Hz). With X-ray photoelectron spectroscopy, the surface composition of the catalytic material and the oxidation state of metal were investigated by SPECS, X-ray photoelectron spectrometer. The sampling of the specimen was performed as described in [40] and a beam of X-rays of  $\text{MgK}_\alpha/\text{AlK}_\alpha$  was used in fixed analyzer transmission (FAT) mode. A pH meter (Systronics  $\mu\text{-361}$ ) with temperature probe was used to measure and maintain the pH of the medium. The critical micelle concentration values of the surfactant solutions were measured whenever needed using a conductance bridge (Systronics model 306) with cell constant of  $1\text{ cm}^{-1}$ .

### 2.1 Synthesis of Catalyst

Titania-supported Pd(IV) oxide was prepared by stirring  $\text{TiO}_2$  with  $\text{Pd}(\text{NO}_3)_2 \cdot 2\text{H}_2\text{O}$  (in the equimolar ratio) with DCM (dichloromethane) as solvent for 24 h at room temperature, filtered and washed with the solvent. The residue was left to dry at room temperature for 24 h, then calcined at  $250\text{ }^\circ\text{C}$  for 2 h.



**Scheme 1** Oxidation of amino alcohol

## 2.2 Oxidation of Alcohol

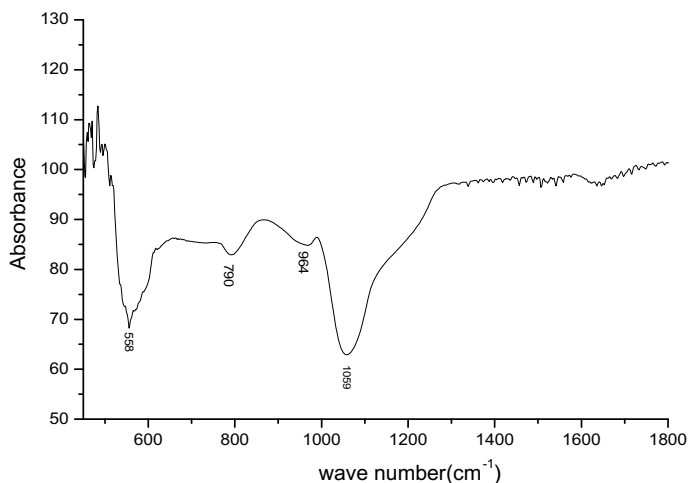
Amino alcohol (1 mmol) and 3.5 mol% of the catalyst in *t*-BuOH were vigorously stirred at 25 °C for half an hour. Two mmol peroxide (*t*-BuOOH) in hexane (10 ml) was added to it and was again stirred at the same rpm using a magnetic stirrer for at least 2 h (Scheme 1). The progress of the conversion process was monitored using chromatography (TLC) with *n*-hexane and ethyl acetate as eluents. The contents in the reaction flask were treated with sodium thiosulfate to remove excess of peroxide and then filtered. A rotary evaporator was used to evaporate the filtrate and get the product. The catalyst was regenerated immediately, preserved for further analysis and re-use.

## 3 Results and Discussion

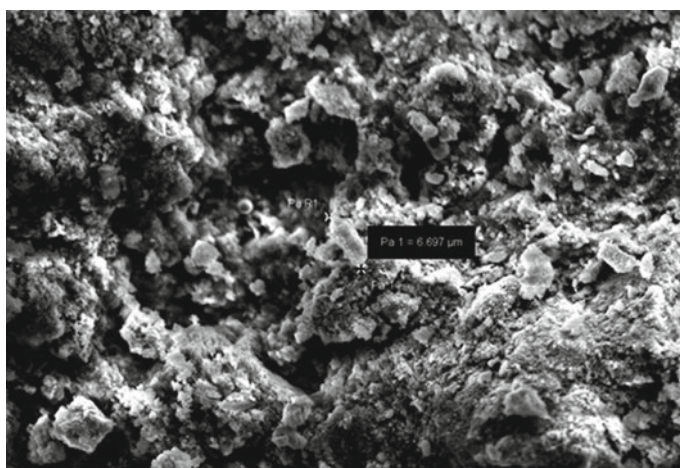
The FTIR spectra of the synthesized catalyst are presented in Fig. 1. The band at 1059 cm<sup>-1</sup> corresponds to transverse vibrational mode of Pd–O–Pd link. Peaks at 588 cm<sup>-1</sup> and 964 cm<sup>-1</sup> may be ascribed, respectively, to the Pd–O symmetric and asymmetric stretching type of vibrations. Owing to the larger dipole change, asymmetric vibration (more intense) is stronger [41] compared to symmetric vibration.

Figure 2 is the scanning electron microscopy (SEM) image of titania-supported palladium particles. The average particle size is found to be nearly 7 μm and is almost uniformly dispersed [40]. Surface morphology of the prepared catalyst is determined using XPS signal of few top layers. From the XPS signals of surface Pd and Ti, the (Pd/Ti)<sub>XPS</sub> was obtained and observed to be higher in comparison to (Pd/Ti)<sub>Bulk</sub> suggesting the wide spread dispersal of Pd over the TiO<sub>2</sub> support. Figure 3 shows the plot of (Pd/Ti)<sub>Bulk</sub> versus (Pd/Ti)<sub>XPS</sub> with slope 6.5. The results of magnetic susceptibility (χ) test are shown in Fig. 4. With the rise in temperature, χ decreases indicating the inverse dependence of χ with temperature. This is indicative of the fact of paramagnetism of the catalyst and is in + 4 oxidation state of Pd.

A support catalyst system consists of an active transition metal like Pt, Pd, Ag, Au, etc. or bimetallic components and a support material. This biphasic metal–support pair having a porous network and appropriate pore dimension constitutes an efficient heterogeneous catalyst for oxidation of organic substrates. The metal–support pair as mentioned with proper pore dimension permits the substrates and the products to the



**Fig. 1** FTIR spectra of titania-supported Pd catalyst



**Fig. 2** SEM image of the Pd supported over titania

active sites present in the catalyst. The initial oxidation was executed using isopropyl alcohol as the substrate to optimize the reaction conditions with *t*-BuOOH as well as H<sub>2</sub>O<sub>2</sub> as the oxidant. The reactions were performed separately with or without the catalyst. Almost about 98% yield was recorded using *t*-butylperoxide as the oxidant and in the presence of the catalytic medium whereas hardly any appreciable conversion was noticed in the absence of it. Moderate-to-nil yields were seen with H<sub>2</sub>O<sub>2</sub> even though its percentage was varied from 20 to 60% and stirred for 6 h in a typical run. The reactivity difference of the substrate with different peroxides is



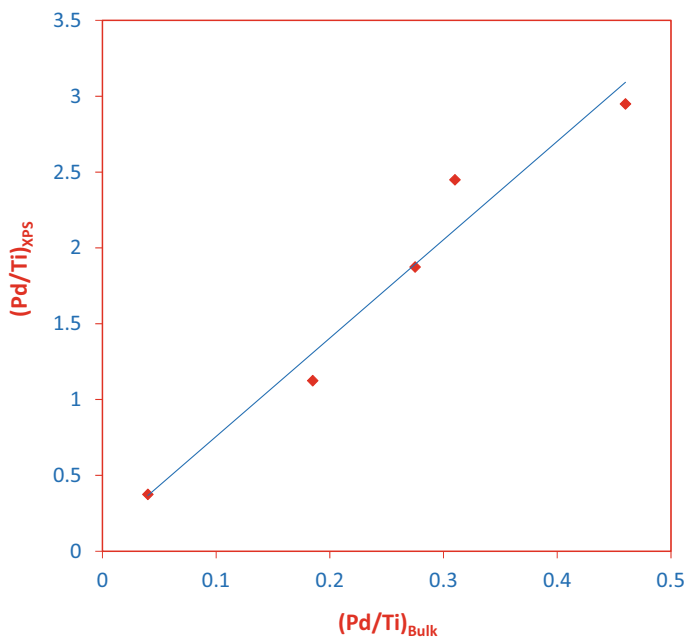


**Fig. 3** Results of XPS analysis of titania-supported Pd catalyst

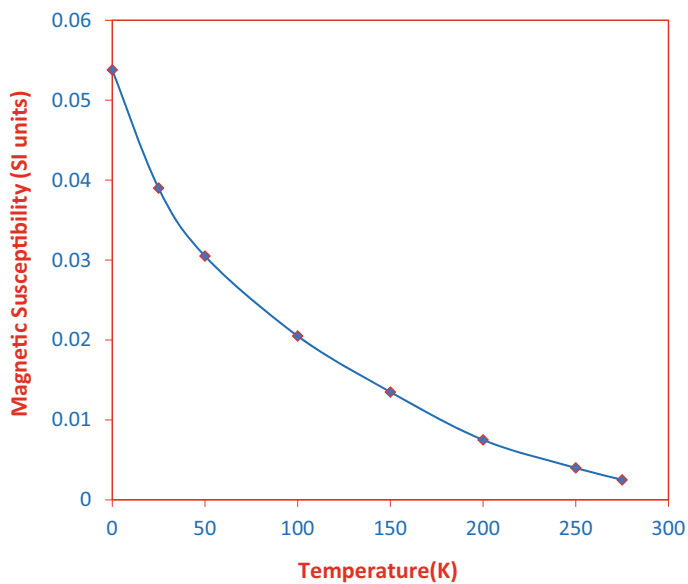
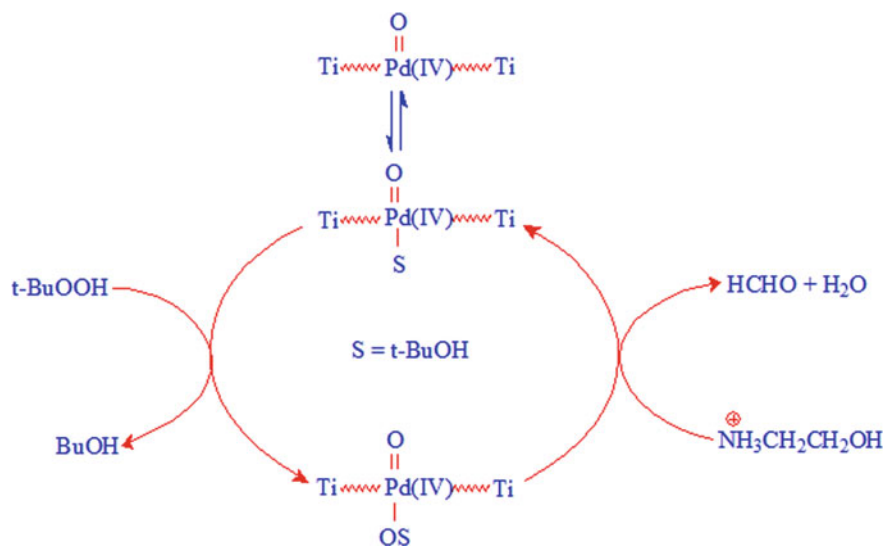


**Fig. 4** Variation of magnetic susceptibility with temperature of the titania-supported Pd catalyst system



**Scheme 2** Mechanism of the catalyzed path

probably due to the different types of peroxy complexes [42] formed in the pH range of 2.17–3.67 with  $\text{H}_2\text{O}_2$  and more acidic pH of 5.47 with *t*-BuOOH as oxidant. The color (gray) of the reaction medium with *t*-BuOOH as oxidant is regained by either the consumption of peroxy species during the progress of the reaction or treatment with  $\text{Na}_2\text{SO}_3$  (in fact the addition of  $\text{Na}_2\text{SO}_3$  was continued till the regeneration of color). The reaction mixture was filtered; the residue containing catalyst was left to dry and preserved for next cycle. The filtrate was taken for claiming the aldehyde by evaporation. The catalysis cycle is described in Scheme 2. The efficacy of the synthesized catalyst is found to be intact for a minimum of four cycles.

Herein, the macro-pores and voids are believed to provide the amino alcohol to reach to the active site, where it undergoes the necessary transformation and subsequently desorbs. The  $\text{TiO}_2$  support materials having high level of porosity (meso- and micro-), i.e., enhanced surface area play an important role in the catalytic performance of the metal–support pair. As the results were promising, we performed the oxidation of the amino alcohols under different concentrations of the anionic surfactant, SDS. The results are mentioned in Table 1 along with the yield% and approximate time of completion of reaction. Each of the oxidation reaction was carried out in absence of the catalyst as well. Either almost nil or very little yield even after 2–3 h of initiation of the process was observed.

Figure 5 shows the product yield with the variation of mol% of the catalyst used during the oxidation process. Maximum conversion was observed with around 3.5 mol% of the catalyst. The sites in the metal–support catalyst system capable of redox process (redox sites) does the conversion to yield the aldehydes. The better catalytic performance of titania-supported Pd may be assigned to enhanced surface

**Table 1** Titania-supported Pd catalyzed multi-component oxidation of amino alcohol

[SDS], mol dm <sup>-3</sup>	Time (Min.)	Yield (%)
0.0	120	96
$2.5 \times 10^{-3}$	108	95
$5.0 \times 10^{-3}$	99	96
$8.0 \times 10^{-3}$	84	97
$10.0 \times 10^{-3}$	104	95
$12.5 \times 10^{-3}$	119	93

area as confirmed from XPS results, efficient dispersion of Pd over the support TiO<sub>2</sub>, thereby increasing the average number of active sites accessible by the amino alcohol. During the investigation of the oxidation process, we have checked whether or not leaching out of the metallic Pd has taken from the support. After nearly about half completion of the reaction, the catalyst was removed from the reaction flask and the filtrate containing all the reagents and expectedly without any Pd particles was subjected back to the reaction condition. TLC was recorded intermittently. The observation of stagnancy of the spot formation of the product (aldehyde) in the TLC plate even after 5 h of mixing confirms the Pd nanoparticle which has not leached out of the support system.

Effect of either cationic or anionic surfactants as an additional component on the oxidation process is an interesting proposition as micelles are known to catalyze [43, 44] or solubilize [45] the reactions strongly modifying the chemical equilibria and reactivity. Hence, oxidation of the amino alcohol in the surfactant medium has constituted the next part of our study of oxidation of the amino alcohol. The solubility and hence the reactivity-related issues in the oxidation of alcohols can suitably be

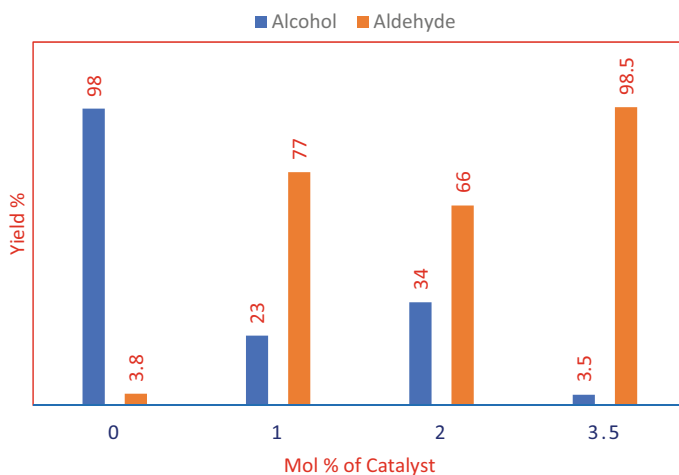
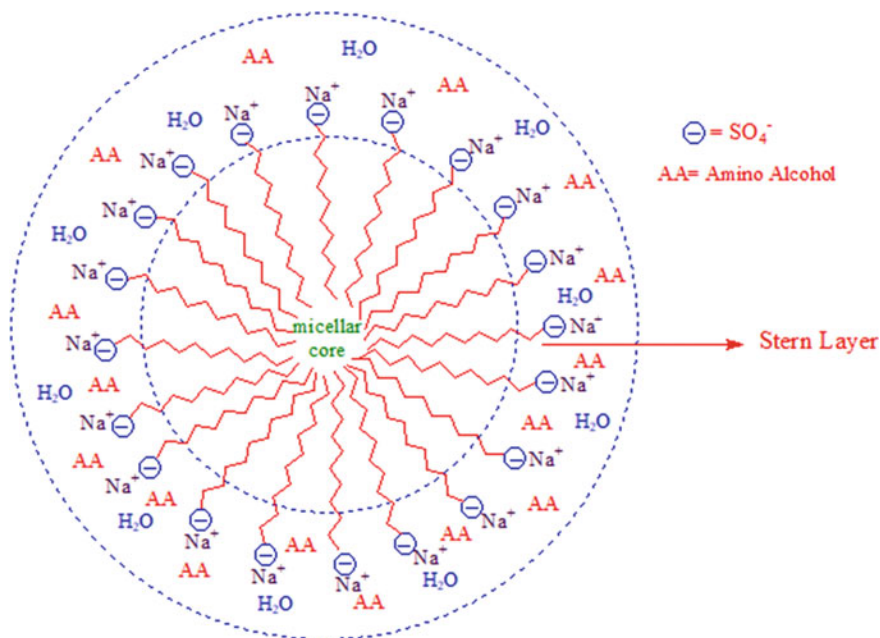


**Fig. 5** Effect of variation of amount of catalyst on the oxidation of alcohol

addressed by the addition of surfactants. Surfactants in fact usually help to solubilize hydrophobic organic substrates in the aqueous medium by forming an organized assembly, micelles. In the presence of SDS medium, time of completion of the reaction goes on decreasing as the concentration of the surfactant increases till about the cmc of SDS, and beyond this concentration, again there is fall in the rate of the reaction (Table 1). This higher rate of reaction in the pre-micellar region of SDS is due to the gathering and forming an active species of the positively charged reactant molecules with the anionic surfactant molecule aggregates. It is worthy to mention here that the surfactant molecules exist as monomers, dimers, trimers, or even higher aggregates before formation of the organized assembly, i.e., micelles. With the rise in [SDS], i.e., on attainment of literature cmc of SDS ( $8 \times 10^{-3}$  mol dm<sup>-3</sup>), the rate of reaction attains the maximum, and hence, the time requirement for the completion of the reaction is the minimum. Beyond the cmc of [SDS], the rate of reaction again falls, and hence, a maximum is observed in the rate-[SDS] profile. This observation can be explained on the basis of formation of micelles by the surfactant molecules when it reaches to the critical concentration which is just enough for the formation of the micelle. The amino alcohol positions itself on the Stern layer of the spherical micelles and are in strongly associated with the SDS head groups through electrostatic forces of attraction. This aggregation of the organic substrate alongside the oxidant (Bu-peroxide) in close proximity of each other facilitates the enhanced oxidation reaction. Beyond the cmc region, i.e., in the post-micellar concentration of SDS, the fall in the rate of reaction in the surfactant medium can be well understood by the dilution effect. Herein, the number of surfactant molecules per the organic substrate increases, and hence, role of the surfactant aggregates as catalyzing moiety is not that appreciable. The oxidation reaction is synergistically catalyzed by heterogeneous support–metal pair and the surfactant medium. However, catalytic effect in the heterogeneous path dominates the corresponding activity of the micelles or the surfactant aggregates in the pre- and post-micellar region of SDS concentration. The distribution of the reagents and the amino alcohol in the surfactant medium can be presented by Scheme 3.

## 4 Conclusion

The structure–reactivity relationship of model palladium catalyst supported on titania was prepared by the method of wet impregnation and characterized using techniques like FTIR spectroscopy, XPS, magnetic susceptibility and SEM. As expected, the inclusion of Pd on to the surface of the titania support has impacted the surface area, pore volume and size resulting in the enhanced activity of the metal–support pair. The catalytic ability of the synthesized catalyst was judged in the oxidation process of amino alcohol to aldehyde. The results indicated greater yield in comparison to the reactions performed without the catalyst. The catalytic activity in the multi-component oxidation of amino alcohol by the heterogeneous catalyst is attributed to the improved surface area besides higher and dispersed presence of Pd on the support



**Scheme 3** Distribution of reactants in the micellar region

material as well as modified redox properties. Introduction of surfactant SDS in the reaction medium in adequate quantity has shown synergistic catalytic effect.

**Acknowledgements** The authors thank NIST (Autonomous), Berhampur-761008, India, for providing the facilities to carry out the work.

**Declaration of Interest Statement** The authors declare that they have no conflict of interests.

## References

1. Sheldon RA, Kochi JK (1981) Metal catalyzed oxidation of organic compounds. Academic Press, New York
2. Mallat T, Baiker A (2004) Oxidation of alcohols with molecular oxygen on solid catalysts. Chem Rev 104:3037–3058
3. Brink GJ, Arends IWCE, Sheldon RA (2000) Green, catalytic oxidation of alcohols in water. Science 287:1636–1639
4. Ahmad JU, Figiel PJ, Raisanen MT, Leskela M, Repo T (2009) Aerobic oxidation of benzylic alcohols with bis (3,5-di-*tert*-butylsalicylaldehyde) copper (II) complexes. Appl Catal A Gen 371:17–21
5. Enache DI, Edwards JK, Landon P, Solsona-Espriu B, Carley AF, Herzing AA, Watanabe M, Kiely CJ, Knight DW, Hutchings GJ (2006) Solvent-free oxidation of primary alcohols to aldehydes using au-Pd/TiO<sub>2</sub> catalysts. Science 311:362–365

6. Zhan BZ, Thompson A (2004) Recent developments in the aerobic oxidation of alcohols. *Tetrahedron* 60:2917–2935
7. Collins JC, Hess WW, Frank FJ (1968) Dipyridine-chromium (VI) oxide oxidation of alcohols in dichloromethane. *Tetrahedron Lett* 9(30):3363–3366
8. Collins JC, Hess WW (1972) Aldehydes from primary alcohols by oxidation with chromium trioxide: heptanal. *Org Synth* 52:5–10
9. Paquette LA, Earle MJ, Smith GF (1996) (4R)-(+)-*tert*-butyldimethylsiloxy-2-cyclopenten-1-one. *Org Synth* 73:36–43
10. Tu Y, Frohn M, Wang ZX, Shi Y (2003) Synthesis of 1,2:4,5-di-*o*-isopropylidene-*d*-erythro-2,3-hexodiulo-2,6-pyranose. A highly enantioselective ketone catalyst for epoxidation. *Org Synth* 80:1–8
11. White JD, Grether UM, Lee CS (2005) (R)-(+)-3,4-dimethylcyclohex-2-en-1-one. *Org Synth* 82:108–114
12. Dess DB, Martin JC (1983) Readily accessible 12-I-5 oxidant for the conversion of primary and secondary alcohols to aldehydes and ketones. *J Org Chem* 48:4155–4156
13. Ishihara K, Mori A, Yamamoto H (1990) Stereoselective reduction of acetals. A method for reductive generation of heterocyclic ring systems. *Tetrahedron* 46:4595–4612
14. Heffner RJ, Jiang J, Joullie MM (1992) Total synthesis of (–)-nummularine F. *J Am Chem Soc* 114:10181–10189
15. Overman LE, Ricca DJ, Tran VD (1997) Total synthesis of (±)-scopadulcic acid B. *J Am Chem Soc* 119:12031–12040
16. Kreutzer JS, Vanoye L, Guichet B, Philippe R, Metay E, Duclos MC, Lemaire M, Bellefont CD, Fongarland P, Réguillon AF (2019) Continuous flow aerobic alcohol oxidation using a heterogeneous Ru<sup>0</sup> catalyst. *React Chem Eng* 4:550–558
17. Xu C, Zhang C, Li H, Zhao X, Song L, Li X (2016) An overview of selective oxidation of alcohols: catalysts, oxidants and reaction mechanisms. *Catal Surv Asia* 20:13–22
18. Muzart J (2003) Palladium-catalysed oxidation of primary and secondary alcohols. *Tetrahedron* 59(31):5789–5816
19. Aldrich KE, Odom AL (2019) A silica-supported titanium catalyst for heterogeneous hydroamination and multicomponent coupling reactions. *Dalton Trans* 48:11352–11360
20. Bauer EB (2017) Recent advances in iron catalyzed oxidation reactions of organic compounds. *Isr J Chem* 57:1131–1150
21. Ballarini AD, Virgens CF, Rangel MC, Miguel SR, Grau JM (2019) Characterization and behaviour of Pt catalysts supported on basic materials in dry reforming of methane. *Braz J Chem Eng* 36(1):275–284
22. Zhu C, Wei Y, Ji L (2010) Catalytic oxidation of alcohols to corresponding aldehydes or ketones with TEMPO-mediated iodobenzene in water in the presence of a surfactant. *Synth Commun* 40(14):2057–2066
23. Zhu J, Carabineiro SAC, Shan D, Faria JL, Zhu Y, Figueiredo JL (2010) Oxygen activation sites in gold and iron catalysts supported on carbon nitride and activated carbon. *J Catal* 274:207–214
24. Mallat T, Baiker A (2012) Potential of gold nanoparticles for oxidation in fine chemical synthesis. *Annul Rev Chem Biomol Eng* 3:11–28
25. Mobley JK, Crocker M (2015) Catalytic oxidation of alcohols to carbonyl compounds over hydrotalcite and hydrotalcite-supported catalysts. *RSC Adv* 5:65780–65797
26. Stevens R, Chapman KT, Weller HN (1980) Convenient and inexpensive procedure for oxidation of secondary alcohols to ketones. *J Org Chem* 45(10):2030–2032
27. Rajabimoghadam K, Darwish Y, Bashir U, Pitman D, Eichelberger S, Siegler MA, Swart M, Bosch IG (2018) Catalytic aerobic oxidation of alcohols by copper complexes bearing redox-active ligands with tunable H-bonding groups. *J Am Chem Soc* 140(48):16625–16634
28. March J (1985) *Advanced organic chemistry: reactions, mechanisms, and structure*. Wiley, New York
29. Stoltz BM (2004) Palladium catalyzed aerobic dehydrogenation: from alcohols to indoles and asymmetric catalysis. *Chem Lett* 33(4):362–367

30. Stahl SS (2004) Palladium oxidase catalysis: selective oxidation of organic chemicals by direct dioxygen-coupled turnover. *Angew Chem Int Ed* 43(26):3400–3420
31. Sigman MS, Schultz MJ (2004) The renaissance of palladium(ii)-catalyzed oxidation chemistry. *Org Biomol Chem* 2(18):2551–2554
32. Astruc D, Lu F, Aranzas JR (2005) Nanoparticles as recyclable catalysts: the frontier between homogeneous and heterogeneous catalysis. *Angew Chem Int Ed* 44:7852–7872
33. Huber GW, Iborra I, Corma A (2006) Synthesis of transportation fuels from biomass: chemistry, catalysts, and engineering. *Chem Rev* 106:4044–4098
34. Besson M, Gallezot P, Pinel C (2014) Conversion of biomass into chemicals over metal catalysts. *Chem Rev* 114:1827–1870
35. Padhy RK, Sahu S (2022) Oxidation of iminodiethanol by Ce (IV) in microheterogeneous system: a comprehensive kinetic analysis. *J Dispers Sci Technol*. <https://doi.org/10.1080/01932691.2022.2026783>
36. Padhy RK, Bhattamisra SD (2021) Surfactant catalyzed oxidation of ethanolamines by Cerium(IV). *Asian J Chem* 33(1):21–25
37. Maiti K, Sen PK, Barik BK, Pal B (2018) Influence of microheterogeneous environments of sodium dodecyl sulfate on the kinetics of oxidation of l-serine by chloro and chlorohydroxo complexes of gold(III). *J Phys Chem A* 122(24):5270–5282
38. Moroi Y (1992) Micelles, theoretical and applied aspects. Plenum Press, New York
39. Kohl K, Nielson R (1997) Gas purification, 5th edn. Gulf Publishing Co., Houston
40. Arora N, Deo G, Wachs IE, Hirt AM (1996) Surface aspects of bismuth-metal oxide catalysts. *J Catal* 159(1):1–13
41. Mitra B, Gao X, Wachs IE, Hirt AM, Deo G (2001) Characterization of supported rhenium oxide catalysts: effect of loading, support and additives. *Phys Chem Chem Phys* 3:1144–1152
42. Crans DC, Smee JJ, Gaidamauskas E, Yang L (2004) The chemistry and biochemistry of vanadium and the biological activities exerted by vanadium compounds. *Chem Rev* 104:849–902
43. Bunton CA, Savelli G (1986) Organic reactivity in aqueous micelles and similar assemblies. *Adv Phys Org Chem* 22:213–309
44. Calvaruso G, Cavasino FP, Didio E (1986) Kinetic investigation of the base hydrolysis of the chloropentaamminecobalt (III) ion in micellar sodium dodecyl sulfate solution. *Inorg Chim Acta* 119(1):29–33
45. Bhattamishra SD, Padhy RK (2009) Estimation of Ibuprofen solubilization in cationic and anionic surfactant media: application of micelle binding model. *Ind J Chem Tech* 16:426–430

# Application of Salts, Alkalis, and Nanoparticles for Reducing Adsorption Loss of Anionic Surfactant for the Application in Enhanced Oil Recovery (EOR)



Neha Saxena  and Md. Merajul Islam

**Abstract** Anionic surfactants have distinctive properties that reduce the tension at the interface of the between the surface-active solution and trapped crude oil and change the hydrophilicity of heterogenous rock of reservoir from oil-wet condition to water-wet condition; these are extensively used chemicals for improved oil recovery. However, a significant issue that lowers the effectiveness of the surfactant flooding process is surfactant losses by adsorption on the rock surface, which must be taken into account when planning the process. The current research focuses on the static and dynamic absorption at equilibrium of surfactant on reservoir minerals such as sandstone, carbonate, and bentonite clay. In group tests, the quantity of surfactant molecules adsorbed on firm rock/clay surfaces was measured using UV–visible spectroscopy. Salt tends to slightly enhance surfactant adsorption on carbonate or clay. It was identified that the presence of alkali and nanoparticles, which has additive effects on IFT reduction, lowers the loss in quantity of surfactant through adsorption and is advantageous for the use of the surface-active agents in oil recovery methods. The present study results are very beneficial for appropriate surfactant flooding design for improved oil recovery.

**Keywords** Natural surfactant · Adsorption · Salt · Nanoparticles · Enhanced oil recovery

## 1 Introduction

Global petroleum and petroleum product demand is rising, while traditional crude oil reserves are decreasing. Oil companies must produce crude oil from mature fields with over 60% reserves after conventional primary and secondary recovery to fulfil energy demand [1, 2]. To boost oil production from matured oil reservoirs, an

---

N. Saxena (✉) · Md. M. Islam  
School of Basic Sciences and Technology, IIMT University, Meerut, Uttar Pradesh 250001, India  
e-mail: [gemini.neha1990@gmail.com](mailto:gemini.neha1990@gmail.com)



inexpensive and effective enhanced oil recovery (EOR) method such thermal, chemical, microbiological, or miscible EOR can create this residual oil. Surfactant-based chemical EOR can rehabilitate in the low-pressure exhausted reservoirs. Surfactant flooding reduces IFT at oil-aqueous interface by adsorbing surfactant molecules, allowing trapped oil droplets to overcome capillary forces and improve mobility [3–5]. For enhanced oil recovery, surfactant changes from oil-soaked to water-soaked reservoirs [5].

Capillary pressure, rock wettability, and interfacial tension determine surfactants' oil recovery capability. Surfactants are surface-active substances used in detergent, cosmetics, paints, adhesives, and oil recovery. Most petroleum surfactants are expensive and harmful. Thus, renewable natural resins oils, rosins, and other surfactants are needed [6]. These compounds make these products eco-friendly, biodegradable, and economically feasible for enhanced oil recovery. Surfactants made from natural oils like *Jatropha*, palm, corn seed, and other vegetable sources can reduce the IFT at the oil-aqueous juncture and change rock wettability from oil soaked to water soaked [7]. The naturally generated surfactants biodegrade, which is anticipated and desirable in the eco-logical system. The present study used fruit-derived anionic surfactant as adsorbate. Salt content, type of rock, alkali, and nanoparticles were examined to see how they affect surfactant adsorption on rock surfaces, making it an inexpensive EOR system.

## 2 Material Required

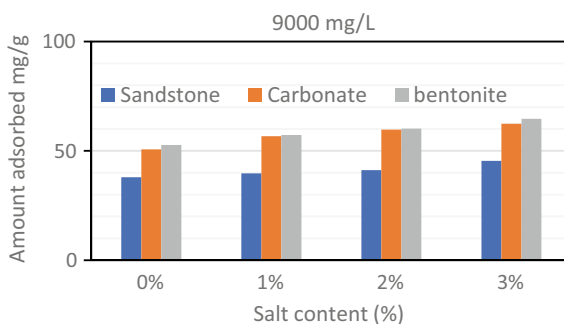
Soap-nut fruit produced the anionic surfactant in the laboratory [8]. Our previous study described surfactant synthesis. SRL supplied sodium chloride and sodium carbonate to examine surfactant adsorption and salinity and alkalinity. SRL supplied 15–20 nm silica and 20–30 nm alumina nanoparticles for adsorption studies. Cambay Basin, India, provided sandstone and carbonate samples. The experiment utilized Loba Chemicals Pvt. Ltd. bentonite clay.

## 3 Result and Discussion

### 3.1 Studies on Adsorption

Grinded adsorbent (rock and clay) samples were mixed to 1000–15,000 mg/L surfactant solutions. Rotospin rotated solutions at 50 rpm for 1 day. After 1 day, centrifuged samples were separated at 3000 rpm for 20 min. After being centrifuged, the top liquid was collected and examined using a spectrophotometer (SHIMADZU UV-1800) to determine concentration at equilibrium. Using aqueous solutions of surfactant with known concentrations, the calibration curve predicted the unknown supernatant

**Fig. 1** Effect of salinity on surfactant adsorption at concentration 9000 mg/L



liquid concentration.  $m$  is the experimental analysis's adsorbent mass ( $g$ ), and  $V$  is the surfactant solution's volume ( $L$ ). It was found the highest absorbance at  $\lambda_{max} = 259$  nm of the solution of different surfactant concentrations.

### 3.2 Effect of Salinity on Surfactant Adsorption

Electrostatic interactions during anionic surfactant adsorption are disrupted by salt. Figure 1 shows how salt affected surfactant concentration above CMC at 9000 mg/L. Figure shows that salt content promotes surfactant adsorption. Dissolved salt ions affect solid chemisorption of ionic surfactants [5]. Salt content increases counterion adsorption on surfactant micelles, reducing electrostatic charge [4]. However, adsorbent surface electrical double layer suppression dominates this behaviour. Contraction of the electrical double layer (EDL) of the adsorptive surface increases surfactant adsorption with salt content [3].

### 3.3 Effect of Alkali on Surfactant Adsorption

Alkalis mainly sodium carbonate are used as sacrificial agents to minimize surfactant adsorption in reservoir rocks [7]. Figure 2 indicates that surfactant adsorption on all samples decreases with sodium carbonate content. Dissociation of  $Na_2CO_3$  into carbonic acid that is weak to produce  $OH^-$  ions upon water molecules decreases surfactant adsorption. This raises system pH and sample surface negative. Surfactant adsorption decreases due to electrostatic repulsion between adsorbed molecule of surfactants and rock surfaces. In situ surfactants from sodium carbonate molecules and naphthenic acids in crude oil help recover stranded oil.

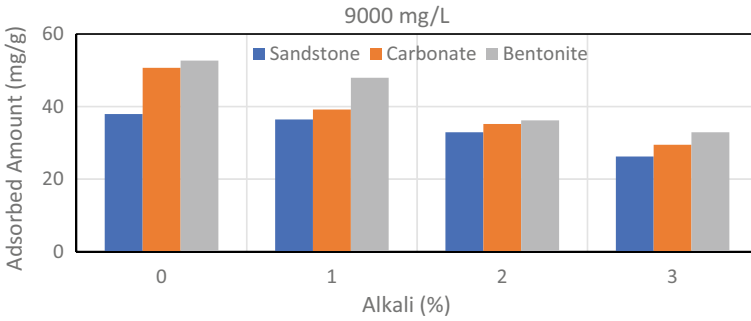
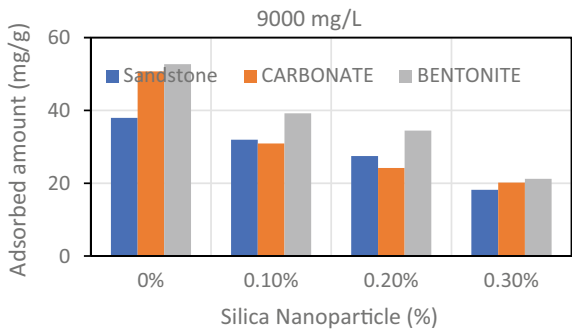


Fig. 2 Impact of 9000 mg/L of alkali on the adsorption of surfactants

### 3.4 Effect of Nanoparticle on Surfactant Adsorption

Figure 3 shows how silica nanoparticles affect synthesized surfactant adsorption on sample surfaces. The graphs illustrate that nanoparticles reduce surfactant absorption. In this investigation, nanoparticle weight percentages ranged from 0.1 to 0.3% for concentration of surface-active agent at 9000 mg/L. Surfactant molecules adsorb on materials without nanoparticles. However, adding nanoparticles functions as an adsorbent causes absorption in a competitive environment of molecules of surfactants onto nanoparticles and rock samples [9]. Due to greater hydrogen bonding, surfactant molecules adsorb more on nanoparticles than on rocks. Nanoparticles and surfactant particles that are bonded persist as in solution, reducing surfactant adsorption on rock surfaces. Most surfactant molecules smash with nanoparticles and not with rock surfaces, reducing adsorption [9].

Fig. 3 Absorption impact of 9000 mg/L of silica nanoparticles



## 4 Conclusions

For surfactant-based chemical enhanced oil recovery, experimental and modelling investigations on reservoir rock surfaces including sandstone, carbonate, and bentonite clay showed surfactant adsorption patterns. Salinity increased surfactant adsorption onto rock surfaces, whereas alkali and nanoparticles reduced it, with silica nanoparticles showing the greatest results.

## References

1. Arabloo M, Ghazanfari MH, Rashtchian D (2016) Wettability modification, interfacial tension and adsorption characteristics of a new surfactant: implications for enhanced oil recovery. *Fuel* 185:199–210
2. Liu Z, Zhao G, Brewer M, Lv Q, Sudhölter EJ (2021) Comprehensive review on surfactant adsorption on mineral surfaces in chemical enhanced oil recovery. *Adv Coll Interface Sci* 294:102467
3. Bournival G, Du Z, Ata S, Jameson GJ (2014) Foaming and gas dispersion properties of non-ionic surfactants in the presence of an inorganic electrolyte. *Chem Eng Sci* 116:536–546
4. Yekeen N, Idris AK, Manan MA, Samin AM, Risal AR, Kun TX (2017) Bulk and bubble-scale experimental studies of influence of nanoparticles on foam stability. *Chin J Chem Eng* 25(3):347–357
5. Saha R, Uppaluri RV, Tiwari P (2018) Effects of interfacial tension, oil layer break time, emulsification and wettability alteration on oil recovery for carbonate reservoirs. *Colloids Surf A* 559:92–103
6. Bera A, Kumar T, Ojha K, Mandal A (2013) Adsorption of surfactants on sand surface in enhanced oil recovery: isotherms, kinetics and thermodynamic studies. *Appl Surf Sci* 284:87–99
7. Liu Y, Grigg RB, Bai B (2005) Salinity, pH, and surfactant concentration effects on CO<sub>2</sub>-foam. In: SPE international symposium on oilfield chemistry
8. Saxena N, Pal N, Ojha K, Dey S, Mandal A (2018) Synthesis, characterization, physical and thermodynamic properties of a novel anionic surfactant derived from *Sapindus laurifolius*. *RSC Adv* 8(43):24485–24499
9. Lorenz PB (1991) The effect of alkaline agents on retention of EOR chemicals (No. NIPER-535). National Institute for Petroleum and Energy Research, Bartlesville, OK, USA

# Cost Optimization of a Hybrid Stand-Alone Renewable Energy System for Remotely Located Areas



Ameer Faisal and Naqui Anwer

**Abstract** Solutions of hybrid energy can be used to reliably meet the energy needs of remote village locations. The subject of the proposed article is the size optimization of a hybrid stand-alone renewable energy system (HSRES) for a collection of villages in the Indian state of Uttarakhand's Dewal Block, District Chamoli. To address the electrical energy needs in the study region, the proposed HSRES combines locally accessible renewable energy resources, such as solar, wind, and bioenergy, with the battery storage system. The paper develops a system operating technique for HSRES size optimization; HOMER Pro software is used to optimize the overall net present cost (NPC) of the system, which came to \$828,917. In this, a combination of wind, solar PV, and bio-generators with battery storage is used. By using renewable energy sources like solar and biogas, NPC and COE will be reduced with no pollution. The obtained microgrids are evaluated to supply at an average cost of \$0.177 per kWh, fully satisfying the annual electricity requirement.

**Keywords** Cost of energy (COE) · Net present cost (NPC) · HOMER Pro · Hybrid stand-alone renewable energy system · Unmet load · Cost optimization

## 1 Introduction

When using stand-alone, adaptable structures, renewable energy resources are subject to several limitations. To address these issues, solar and wind energy sources are combined with other sources to create hybrid renewable energy. Therefore, it is possible to increase power-generating efficiency by making the greatest use of many

---

A. Faisal (✉) · N. Anwer  
TERI School of Advanced Studies, New Delhi, India  
e-mail: [ameerfaisal12@gmail.com](mailto:ameerfaisal12@gmail.com)

N. Anwer  
e-mail: [naqui.anwer@terisas.ac.in](mailto:naqui.anwer@terisas.ac.in)

A. Faisal  
KIET Group of Institutions, Delhi NCR, Ghaziabad, India

benefits to reduce their limitations [1]. Barriers include rough terrain, restricted transmission, and widely dispersed valleys with low populations that are characterized by lower incomes, load density, and education levels which slow down the electrical power supply of isolated communities. To calculate the various costs when creating a hybrid renewable energy system using the HOMER Pro software. Rajanna et al. [1] presented a hybrid system utilizing a genetic algorithm. The electricity requirements of several load sections in the rural Chamarajanagar, State of Karnataka, Southern India, were met using this genetic algorithm. Olatomiwa et al. [2] analysed the statistics of wind and solar energy potentials for distant Nigerian village districts. The most efficient, cost-effective, and technically sound hybrid renewable energy systems are designed and sized using HOMER software. There is also coverage of the two ideal system arrangements: solar photovoltaic, diesel, and battery systems and solar photovoltaic-diesel battery systems combined with the conventional system. Out of the two configurations listed above, configuration one is the more economically viable choice with a COE of \$0.409 and TNPC of \$69,811/kWh. Samy et al. [3] suggested a stand-alone solar photovoltaic-fuel cell hybrid renewable energy system in a techno-economic feasibility analysis for supplying electricity to be isolated from the grid village regions in Egypt.

## 2 About the Study Location

A cluster of 12 numbers of villages in the Dewal block of district Chamoli in Uttarakhand, India, has been selected as the study location. Most people in these regions reside in hilly terrain, and they have ample access to renewable energy resources with sun, wind, biogas, and biomass. The best method to meet the energy needs of these hamlets is by utilizing the potential of renewable energy sources that are already accessible. Figure 1 depicts the location of the chosen place on the map, and Table 1 provides general information about that place [4]. The chosen area's biogas production is from energy resources [5]. Numerous native animals, including buffalo, cows, sheep, and goats, are present in the chosen communities, and their dung may be used to produce biogas to power the biogas generator. A sufficient volume of biogas can be produced and used to produce power depending on the availability of cattle dung in the selected area. 5.04 kWh/m<sup>2</sup> is the average amount of solar radiation that the study region receives each year [6]. The study place experiences low wind speeds (2–18 m/s), which are suited for low values wind turbines (1–25 kW). Given that the Dewal block's site 'Harmal' has a mean annual wind speed of 5.11 m/s at a 20-m height, installing a small wind energy conversion device there is viable [6]. The current study takes into account four different types of energy consumption: domestic, commercial, communal, and agricultural.

The domestic sector required electrical power to run water pumps, fans, LED bulbs, TVs, radios, and other household appliances. Commercial loads include things like small shops, dairy facilities, and flour mills [7, 8]. The estimated daily electrical

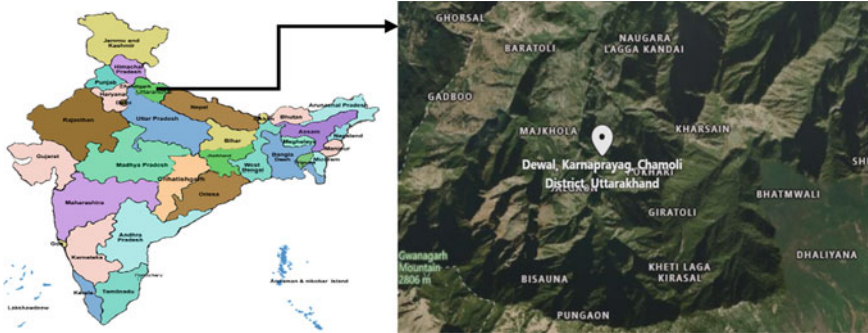


**Fig. 1** Geographical location of the study place (from Google Map)

energy requirement for the chosen location is 727.10 kWh/day. The research region is expected to use 265,391 kWh of electrical energy annually.

### 3 Resource Assessment

The system configuration has a solar system, wind power generation, and a biogas generator with a battery storage system.

#### 3.1 Solar PV System

Solar energy data is all about the solar radiation that in a year, incidents on the Earth’s surface are the total amount of dispersed radiation and beam radiation. The clearness index is another important predictor of data related to solar resources. Solar-related data is collected from the NASA website for Dewal. Figure 2 shows the average monthly clearness index and average solar irradiation. The fifth month has the highest cumulative daily radiation average (6.67 kWh/m<sup>2</sup>/day), while the first month of the year has the lowest cumulative daily radiation average (3.57 kWh/m<sup>2</sup>/day).

#### 3.2 Wind Energy System

The generic 3 kW horizontal axis wind turbines are used for the selected location. The capacity of the wind turbine to produce electrical energy depends on the wind speed availability and its variation. Both the capital cost and the replacement cost are \$850/kW each. The costs of operation and maintenance cost are considered zero.

**Table 1** General information about the selected area [6]

Country/State	District	Block	Latitude	Longitude	Elevation from sea level	Village hamlets	Total population	Households in village hamlets
India/Uttarakhand	Chamoli	Dewal	30° 08' N	79° 37' E	1611 m	12	774	189





Fig. 2 Monthly average solar radiation and clearness



Fig. 3 Monthly average wind speed at the study location

Figure 3 represents the monthly average wind speed in m/sec at the selected location. The height of the hub of the wind turbine under consideration is 20 m, and its lifespan is estimated to be 20 years. The annual average speed of wind is 5.11 m/s.

### 3.3 Biogas System (Bio-Gen)

The biogas generator (Bio-Gen) is a secondary or backup energy source for the planned system. When solar, wind, and battery power are insufficient to meet load demand, the Bio-Gen is employed to handle peak load. Bio-Gen generates electricity using biogas as fuel. This gas generator has a 120 kW biogas-rated capability. The fuel consumption-related quantities are given in Table 2. The transportation, installation, moisture absorber, pipe, valve, distribution, and control system costs are all included in the biogas generator’s capital cost. The gas generator has a total capital expenditure of \$281,621.

Table 2 Fuel summary of the Bio-Gen

Quantity	Consumption of fuel	Input in the form of fuel energy	Consumption of specific fuel	The mean of electrical efficiency
Worth	16,741	1,64,731	0.323	31.5
Units	Litre	kWh per year	Litre/kWh	%

### 3.4 Battery Storage System

When there is a peak load or generating shortfall, the batteries are employed as a backup. A battery bank or string made up of 330 batteries connected in series and parallel is implemented by HOMER Pro in the best possible configuration. The battery bank has the following specs: 12 V each, 165 string, 231 kWh, and a lifetime power of 264,000 kWh when it is in cycle charged. The capital cost, operation, maintenance cost, and replacement cost are \$300, \$5, and \$240, respectively. The properties of a battery storage system having generic 1 kWh lead acid types are listed in Table 3.

## 4 Converter

To ensure the power flow between DC, AC buses, and electrical components during power generation, electronic devices are used which are called converters. It comprises an inverter and a rectifier to convert from AC power to DC power and vice versa. The per kW costs associated with the purchase and replacement are estimated to be \$150 each. The inverter efficiency is 95%, the rectifier efficiency is 90%, and the lifespan of the converter is 25 years.

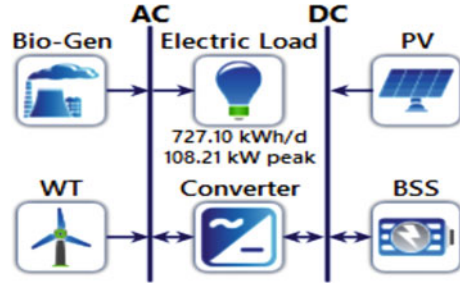
## 5 System Simulation and Optimization

Four important steps are included in the process of organizing and assessing the hybrid system. The first step involves locating the site and assessing its potential for producing renewable energy. In the second step, the electrical energy required for the site is accessed. The energy requirement of the projected model is displayed. The third step is developed using HOMER Pro software to model the hybrid system for the selected area. A schematic of the hybrid energy system is depicted in Fig. 4. A wide range of diverse hybrid system configurations, including various wind turbines, biogas generators, solar PV modules, batteries, and converters are simulated.

**Table 3** Properties of generic 1 kWh lead acid battery

Item	Batteries	Size of string	Strings used in parallel	Voltage of bus
Worth	330	2	165	24
Units	Quantity	Batteries	Strings	Volt

**Fig. 4** Schematic of the hybrid energy system



Optimization Results

Left Double Click on a particular system to see its detailed Simulation Results.

Architecture				Cost				System				Bio-Gen				PV	
PV (kW)	WT	Bio-Gen (kW)	BSS (kW)	Converter (kW)	Dispatch	COE (\$)	NPC (\$)	Operating cost (\$/yr)	Initial capital (\$)	Ren. Fra. (%)	Total Fuel (\$/yr)	Hours	Production (kWh)	Fuel (\$)	O&M Cost (\$/yr)	Fuel Cost (\$/yr)	Capital Cost (\$)
163	95	120	330	105	LF	\$ 0.177	\$ 0.26,918	\$ 29,811	\$ 3,01,459	80.5	16,741	1,039	51,838	16,741	3,740	10,045	81,412
199	116		566	119	CC	\$ 0.193	\$ 0.81,402	\$ 28,026	\$ 3,85,592	100	0						99,282
237		120	350	120	LF	\$ 0.206	\$ 0.67,439	\$ 39,629	\$ 2,66,251	68.3	26,906	1,619	84,640	26,906	5,820	16,144	1,18,633
300			854	108	CC	\$ 0.242	\$ 1.10M	\$ 38,268	\$ 4,22,598	100	0						1,50,179
	223	120	284	48.0	LF	\$ 0.246	\$ 1.16M	\$ 48,039	\$ 3,06,550	63.5	32,272	2,225	96,796	32,272	8,010	19,363	
		542		1,296	CC	\$ 0.351	\$ 1.58M	\$ 39,784	\$ 8,78,357	100	0						
	438	209	120		CC	\$ 0.348	\$ 1.63M	\$ 68,117	\$ 4,28,107	38.1	58,974	4,954	1,64,176	58,974	17,834	35,384	2,14,295
		278	120		CC	\$ 0.363	\$ 1.70M	\$ 81,582	\$ 2,68,900	22.1	73,212	5,951	2,06,647	73,212	21,424	43,827	

**Fig. 5** Optimization results of the hybrid system

## 6 Results and Discussion

### 6.1 Optimization Result

In HOMER Pro, the proposed system follows the user requirements; at the least, NPC is the best optimum or feasible value. It lists the possible solutions according to the overall net present value and presents the possible one with the least NPC as the optimum structure set-up. Among the solutions, the optimal design has minimal NPC. The optimal results of the possible hybrid systems are shown in Fig. 5.

### 6.2 Evaluation of Electrical Load

Throughout the year, the demand for electrical energy is assessed by considering the usage patterns of appliances for residential, business, and community services, as well as energy use for agricultural applications. Figure 6 displays the daily, seasonal, and annual electrical load profiles for the chosen location, which had a peak load demand of 108.21 kW.

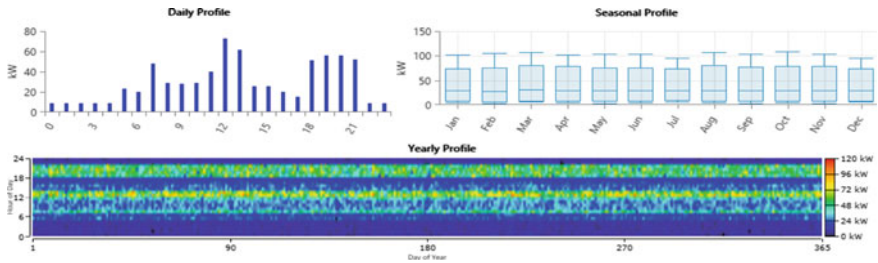


Fig. 6 Electrical load profile of the selected area

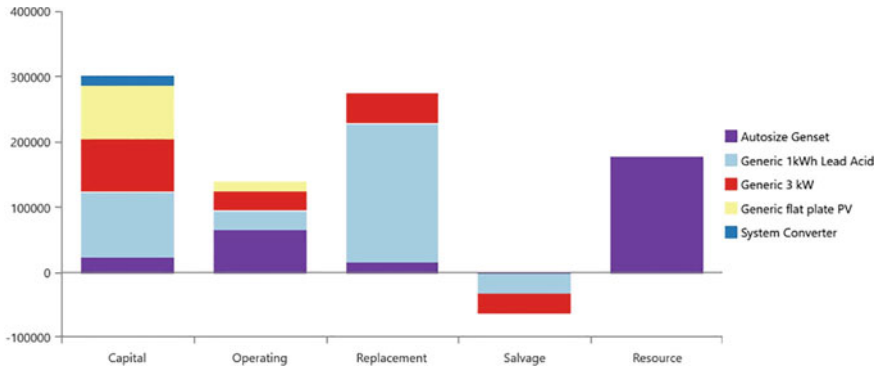


Fig. 7 Summary of the cost assessment of the hybrid energy system

### 6.3 Cost Assessment

A cash flow summary is produced by HOMER Pro to provide a comprehensive understanding of the associated costs. Figure 7 displays a summary of the hybrid energy system’s cost analysis. The capital, replacement, operating, fuel, and salvage expenses for the NPC for the hybrid power system are shown in Fig. 7’s cash flow overview.

### 6.4 Biogas System

In this work, the cost for gas production is considered as \$0.015/kWh. This biogas is used to run the Bio-Gen and modelled in HOMER Pro. And the power obtained from the Bio-Gen throughout the year is shown in Fig. 8.

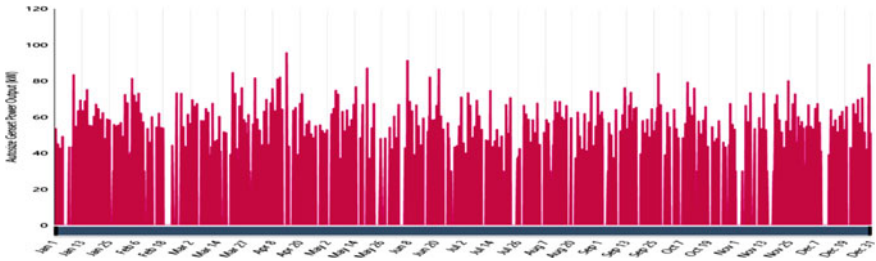


Fig. 8 Output power of Bio-Gen system

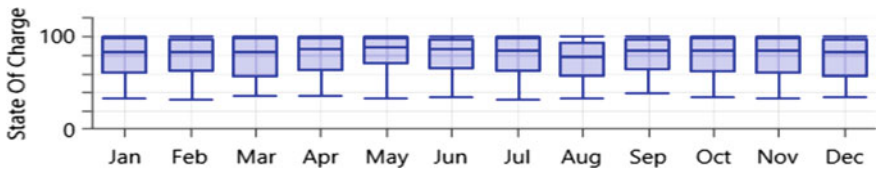


Fig. 9 Monthly state of charge of battery storage system

### 6.5 Battery Storage System

When the total power produced surpasses the amount of electricity needed, the battery begins to charge. The battery storage system functions as a backup power source when the electricity generated is insufficient to meet demand. Based on the power needed for a day, battery efficiency, and energy consumption, the capacity of the battery storage system (BSS) is chosen. The state of charge determines how the battery storage system characterizes its charge and discharge status (SOC). The monthly state of charge of the battery storage system is shown in Fig. 9.

### 6.6 Converter System

The suggested system includes a bidirectional converter, which is a crucial element. This converter’s function is to control the flow of electricity in either direction, while additional power is being added to the battery. The converter’s primary job is to supply the load with the essential power from DC sources. The converter’s size is determined by the system’s minimum or maximum energy level.

## 7 Conclusions

By running the simulation and optimizing the results, it was determined that the 163 kW PV modules, 332 kW wind turbines, 120 kW BDG, 330 kWh storage batteries, and 105 kW converter configuration would be the most reliable and cost-effective configuration for the stand-alone hybrid system. This configuration would be able to produce 526,228 kWh/year, which could make the location autonomous from the main supply grid and would also be able to offer electricity at a suitable price of \$0.177/kWh.

**Declaration of Interest Statement** The authors declare that they have no conflict of interest.

## References

1. Siddaiah R, Saini RP (2016) A review on planning, configurations, modeling and optimization techniques of hybrid renewable energy systems for off grid applications. *Renew Sustain Energy Rev* 58:376–396. <https://doi.org/10.1016/j.rser.2015.12.281>
2. Olatomiwa L, Blanchard R, Mekhilef S, Akinyele D (2018) Hybrid renewable energy supply for rural healthcare facilities: an approach to quality healthcare delivery. *Sustain Energy Technol Assess* 30:121–138. <https://doi.org/10.1016/j.seta.2018.09.007>
3. Samy MM, Barakat S, Ramadan HS (2019) A flower pollination optimization algorithm for an off-grid PV-fuel cell hybrid renewable system. *Int J Hydrogen Energy* 44(4):2141–2152. <https://doi.org/10.1016/j.ijhydene.2018.05.127>
4. <https://chamoli.gov.in/document-category/statistical-report/>, Chamoli, May 2022
5. Chauhan A, Saini RP (2016) Discrete harmony search based size optimization of integrated renewable energy system for remote rural areas of Uttarakhand state in India. *Renew Energy* 94:587–604. <https://doi.org/10.1016/j.renene.2016.03.079>
6. NASA (2022) Surface meteorology and solar energy: a renewable energy resource website. <https://eosweb.larc.nasa.gov>, 19 Jan 2022
7. Thirunavukkarasu M, Sawle Y (2021) A comparative study of the optimal sizing and management of off-grid solar/wind/diesel and battery energy systems for remote areas. *Front Energy Res* 9 (2021). <https://doi.org/10.3389/fenrg.2021.752043>
8. Sawle Y, Gupta SC, Bohre AK (2017) Optimal sizing of standalone PV/wind/biomass hybrid energy system using GA and PSO optimization technique. *Energy Proc* 117:690–698. <https://doi.org/10.1016/j.egypro.2017.05.183>

# Preparation and Energy Storage Assessment of $Ti_3C_2$ 2d MXene and Its Possible Thinning Mechanism



Diya Singh, Pinki Rani, Sayani Biswas, and Prashant S. Alegaonkar

**Abstract** Since after its discovery, MXene has captivated the focus of many researchers. In this work, we report on the low-temperature synthesis of  $Ti_3AlC_2$  MAX phase at 800 °C and its further etching to obtain  $Ti_3C_2$  MXene. Initially, titanium (Ti), aluminium (Al), and graphite (C) precursors were taken in an appropriate volume proportion and add-mixed and grounded well via molten salt technique (Galvin et al. in *J Eur Ceram Soc* 38, 2018 [1]). The characterizations performed on powder such as FTIR, XRD, UV–Visible, SEM, and EDS confirmed  $Ti_3AlC_2$  MAX phase. The MAX phase was subjected to the acid treatment (HF, concentration 40%) for ~ 80 h. The synthesized MXene was separated and investigated using FTIR, XRD, UV–Visible, SEM, and EDS techniques. The MXene was further employed to microwave treatment over the temperature 300–420 K at a discharge of power 120 W for 1 h. Analysis revealed that thickness of  $Ti_3C_2$  layers is observed to be decreased with microwave treatment which can be a possible mechanism to obtain MXene quantum dots. In electrochemical analysis, specific capacitance for two electrode MXene@300 K and @400 K is reported to be 15 and 10 F/g, respectively, showing resistive nature of capacitance coupling for MXene. Analysis of electrochemical impedance spectroscopy together with bode showed the surface passivation effect of MXene layers to achieve different charge dynamics in both the systems.

**Keywords** 2D materials · MXene · Wet chemistry · Vibration spectroscopy · Surface morphology · Energy storage · Supercapacitance

## 1 Introduction

The increasing attention towards 2D nanomaterials has manifested several times as impactful research works over the last few years. Due to their high aspect ratio (surface area to volume ratio) owing to their one atomic layer thickness, they not only

---

D. Singh · P. Rani · S. Biswas · P. S. Alegaonkar (✉)

Department of Physics, School of Basic Sciences, Central University of Punjab, Bathinda 151 401, India

e-mail: [prashant.alegaonkar@cup.edu.in](mailto:prashant.alegaonkar@cup.edu.in)

have contrasting physical differences with bulk materials but also unique combination of properties [2]. The onset of experimental endeavours was triggered by the discovery of Graphene in 2004 and was a pivotal event in the arena of material science [3]. The first instance of MXene synthesis was carried out by Naguib et al. in 2011 via selective etching of ternary 3D layered solid called MAX phase using HF as the etchant [4]. MXenes are synthesized by selective removal of the 'A' layer from MAX phases resulting in accordion like structure of stacked 2D layers with general formula  $M_{n+1}X_nT_x$ . The extension  $T_x$  is the surface termination group (-F, -OH, -O) obtained during the etching process depending on then chemicals used and reaction conditions.

## 2 Experimental

### 2.1 Materials

Titanium powder, Ti, 98% pure of particle grade, aluminium, Al, fine powder, 98%, and graphite fine powder, G, 98% have been taken in a weight proportion of 6:2:2 g. These agents were LR grade. 15 gm each of NaCl and KCl were taken.

### 2.2 Methodology

KCl of 15 gm and NaCl of 15 gm were mixed and crushed using a mortar-pestle to convert into fine powder. In accordance with molten salt route, salts were grounded for 3 h to obtain fine powder. The resultant fine powder was subjected to heating for about 6 h at 800 °C in a blast furnace. The obtained product was ceramic-like hard and jet black in physical appearance. The sample was washed. The obtained sample was subjected to drying in the oven at 60 °C. After this, the MAX phase was subjected to the etching process using HF of concentration 40%. Preparation of  $Ti_3C_2$  powder was done after following the procedure reported by [4]. The resultant mixture was kept as it is for about 70 h soaked in HF. The obtained sedimented product was further washed using ethanol to remove any residual impurities. Finally, the powder thus obtained was MXene confirmed after characterization (Fig. 1).

### 2.3 Fabrication of Electrode Assembly for Ultracapacitor Studies

For electrochemical measurements, a slurry mixture was prepared in the composition, active material: carbon black: PVDF = 70:20:10 ratio. The active material



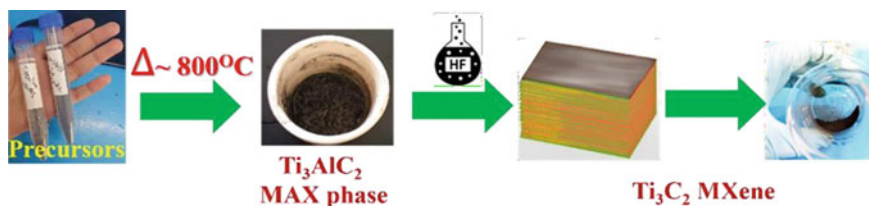


Fig. 1 Involved precursors,  $\text{Ti}_3\text{AlC}_2$  MAX phase synthesis,  $\text{Ti}_3\text{C}_2$  MXene

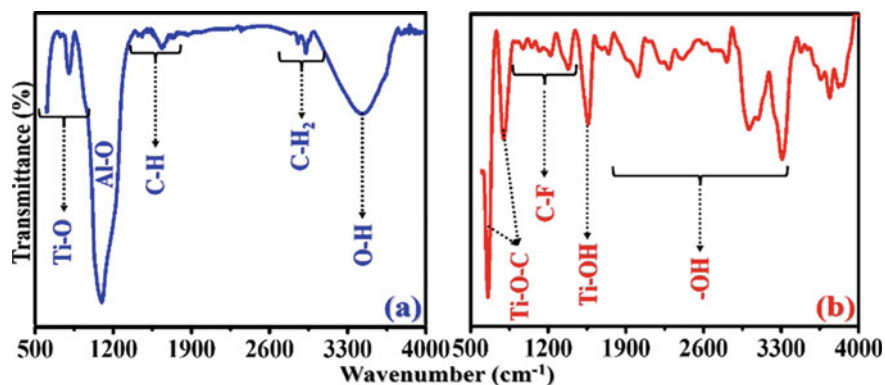


Fig. 2 Recorded FTIR spectra for **a**  $\text{Ti}_3\text{AlC}_2$  and **b** corresponding  $\text{Ti}_3\text{C}_2$  MXene

of MXene 30 and 100 °C was homogeneously mixed with *N*-methyl-2-pyrrolidone (NMP) solution. Two symmetric electrodes have been prepared by coating the slurry onto the nickel foam and subjected to overnight drying.

### 3 Results and Discussion

#### 3.1 FTIR

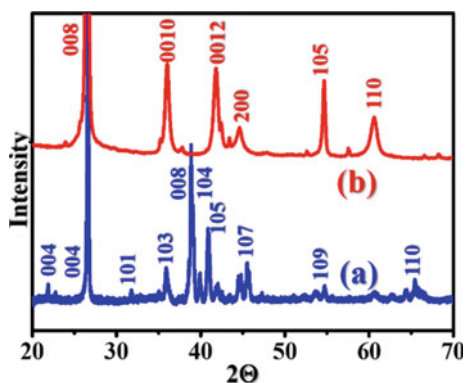
See Fig. 2 and Table 1.

#### 3.2 XRD

In XRD analysis, measurement showed distinct changes in  $\text{Ti}_3\text{AlC}_2$  MAX phase and  $\text{Ti}_3\text{C}_2$  MXene. The obtained peaks are consistent with the literature published in [5]. In general, the peak at  $9.43^\circ$  is the measure of the d-spacing of the  $\text{Ti}_3\text{AlC}_2$  MAX

**Table 1** Assigned vibration peaks for the species present in  $\text{Ti}_3\text{AlC}_2$  MAX phase and  $\text{Ti}_3\text{C}_2$  MXene

S. No.	$\text{Ti}_3\text{AlC}_2$ MAX phase			$\text{Ti}_3\text{C}_2$ MXene		
	Wave number	Assigned band	Type	Wave number	Assigned band	Type
1	605.6	Ti–O	Str.	650–800	Ti–O–C/ Ti–C	Twist./Rock.
2	810	Ti–O	Str.	970–1382	– CF	Bend.
3	1420–1620	– CH	Str.	1550	Ti–OH	Asym. Str.
4	2850–2950	– $\text{CH}_2$	Asym. Str.	1670–2000	OH	Sym. Str.
5	3430	– OH	Asym. Str.	2200–3300	OH	Bend.

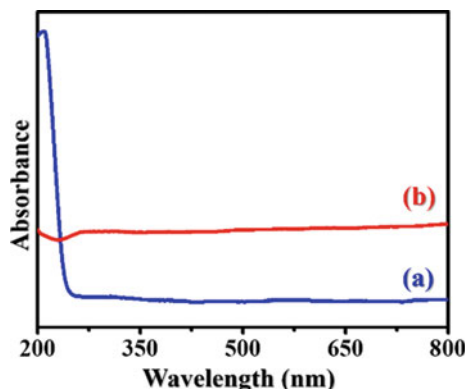
**Fig. 3** Recorded XRD spectra for **a**  $\text{Ti}_3\text{AlC}_2$  and **b**  $\text{Ti}_3\text{C}_2$  MXene

phase, and it corresponds to the (002) miller plane. In our case, no such peak is noted which indicated that the d-spacing in the  $\text{Ti}_3\text{AlC}_2$  MAX phase has not yet exfoliated to the fuller strength. There are many peaks in the  $\text{Ti}_3\text{C}_2$  MXene that got modified with respect to the  $\text{Ti}_3\text{AlC}_2$  MAX phase. The peaks resembled with the data reported for  $\text{Ti}_3\text{C}_2$  MXene literature published in [6] (Fig. 3).

### 3.3 UV–Visible Spectroscopic Interface

The MAX phase  $\text{Ti}_3\text{AlC}_2$  curve indicates lower absorbance as compared to  $\text{Ti}_3\text{C}_2$  MXene. For the  $\text{Ti}_3\text{AlC}_2$  MAX phase, there was a clear absorption edge of  $\sim 250$  nm. However, due to the turbid appearance of the suspension, no clear absorption edge has been noted for MXene. Such flatness in absorption spectra is associated with the localization and delocalization of the surface plasmon (Fig. 4).

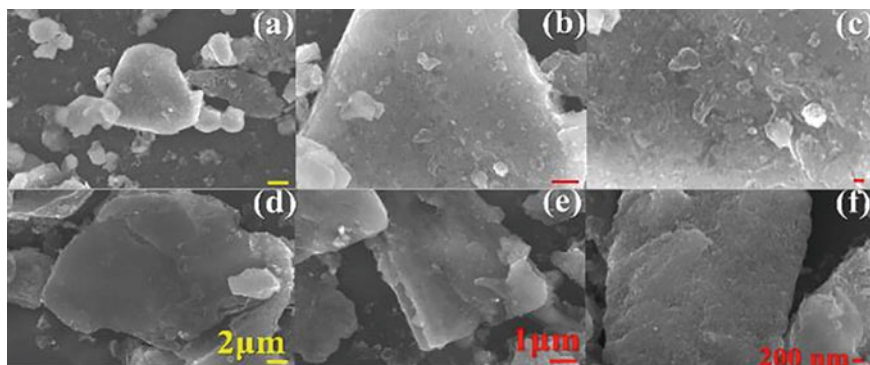
**Fig. 4** Recorded optical response of **a**  $\text{Ti}_3\text{AlC}_2$  MAX phase and **b**  $\text{Ti}_3\text{C}_2$  MXene in UV–Visible wavelength region



### 3.4 FESEM and EDS

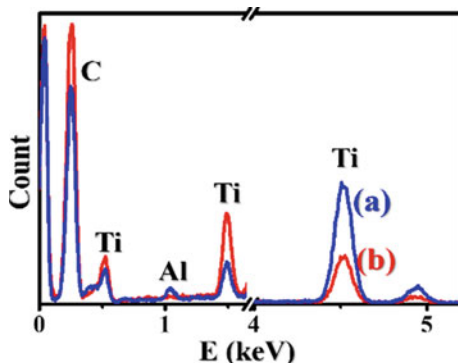
One can see that the  $\text{Ti}_3\text{AlC}_2$  exhibits a thicker structure as compared to  $\text{Ti}_3\text{C}_2$  MXene. The flakes of  $\text{Ti}_3\text{C}_2$  MXene seem to be somewhat tapered at the edges and the corners. At several places, we noted the irregular shaped morphologies of the  $\text{Ti}_3\text{AlC}_2$  MAX phase in contrast to  $\text{Ti}_3\text{C}_2$  MXene, the overall flake size is found to be  $\sim 2\text{--}4 \mu\text{m}^2$ . The flakes were having edges and thickened less. A large amount of carbonaceous deposit has been seen for both the  $\text{Ti}_3\text{AlC}_2$  MAX phase and  $\text{Ti}_3\text{C}_2$  MXene. For  $\text{Ti}_3\text{C}_2$  MXene, the particles are seen to be bigger in size and shape as compared to the  $\text{Ti}_3\text{AlC}_2$  MAX phase. In some places, the scaffolds are clearly visible with exfoliated over layers of  $\text{Ti}_3\text{C}_2$  MXene. At some places, amorphous carbon and Al deposits are seen, however, with data recorded for EDS indicate the presence of C is more probable than that of Al (Fig. 5).

Figure 6 shows recorded EDS spectra for (a)  $\text{Ti}_3\text{AlC}_2$  MAX phase and (b)  $\text{Ti}_3\text{C}_2$  MXene. From profile (a) dominant C and Ti phases can be seen, prominently, together



**Fig. 5** Typical FESEM images recorded for: (upper panel) **a–c** MAX phase, (lower) **d–f**  $\text{Ti}_3\text{C}_2$  MXene. For left vertical panel: image magnifications@10KX, middle@30KX, right@50KX

**Fig. 6** Recorded EDS profiles for **a**  $\text{Ti}_3\text{AlC}_2$  MAX phase and **b**  $\text{Ti}_3\text{C}_2$  MXene



with Al. As discussed, the HF treatment significantly reduces Al and overall contained sacrificial Ti layers and enriches C to form  $\text{Ti}_3\text{C}_2$  MXene. For  $\text{Ti}_3\text{AlC}_2$ , MAX phase presence of Al is through by-products like  $\text{AlF}_3$  which subsequently got etched out during HF treatment. The trace of F in the  $\text{Ti}_3\text{AlC}_2$  MAX phase is not detectable due to its low  $Z$  elemental nature.

#### 4 Microwave Exfoliation

In a study,  $\text{Ti}_3\text{C}_2$  MXene was exposed to microwave power of  $\sim 120$  W and a frequency of 2.45 GHz. The power was delivered to the suspension of  $\text{Ti}_3\text{C}_2$  MXene. The suspension was prepared by dispersing 0.1 mg of  $\text{Ti}_3\text{C}_2$  MXene in DDW and subjected to microwave exposure. The process was carried out for a period of 1 h at various temperatures from 300 to 420 K. The obtained product was characterized using UV–Visible spectroscopy and electron microscopy techniques such as field emission scanning and transmission. As prepared  $\text{Ti}_3\text{C}_2$  MXene consisted of species like  $-\text{F}$ , residual C and terminated H (dangling) on the surface of  $\text{Ti}_3\text{C}_2$  MXene. Microwaves interact with those species and erode them from the surface. While doing so, the connected routes of these species to  $\text{Ti}_3\text{C}_2$  MXene peel off the conjugated layers due to the minimization of surface energy. It seems that this is predominant up to 378 K. Thereafter, further thinning of the layers were annihilate the bipolar charge carriers and results in only the existence of unipolar majority carriers. But it seems that there is an ultimate limit to this exfoliation because of the structure and stoichiometry that competes with surface and edge state energy. This prevents further thinning and microwave-assisted etching of edges takeover to reduce the size of the flake in terms of its area. This is in fact seen in the surface plasmon resonance peak prominently seen for  $\sim 400$  K. It seems that, at higher temperatures, beyond 350 K, microwave-assisted etching of edges initiates, and instead of thinning  $\text{Ti}_3\text{C}_2$  MXene, it reduces particle size. The corresponding band structure for thick  $\text{Ti}_3\text{C}_2$  MXene and etched thin layers is displayed in Fig. 7 by blue arrows.

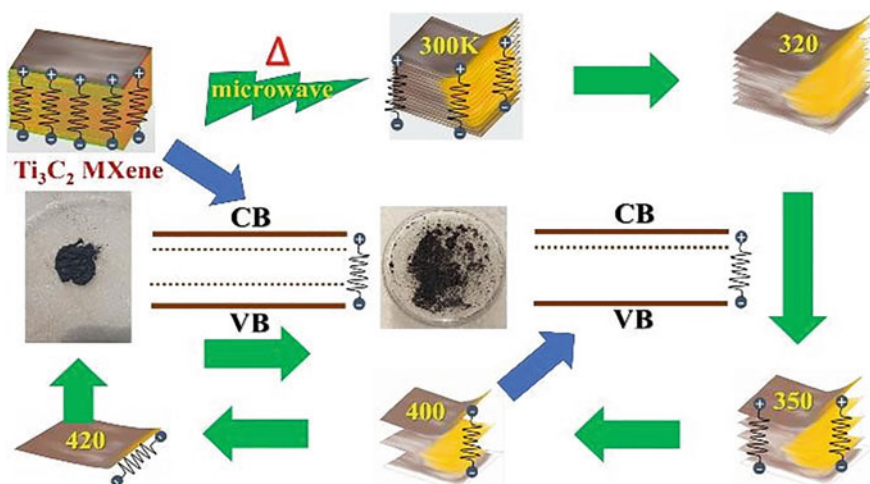


Fig. 7 Schematic diagram of microwave-assisted Ti<sub>3</sub>C<sub>2</sub> MXene thinning from 300 to 420 K

## 5 Electrochemical Application

### 5.1 Electrochemical Performance

The CV measurement was carried out at the different scan rates such as 10, 30, 50, 80, and 100 mV/s. The recorded CV profiles for Ti<sub>3</sub>C<sub>2</sub> MXene at 30 °C and 100 °C have been displayed in Fig. 8a, b. A gradual increase in the CV profile has been observed with respect to the increase in scan rate. The comparative CV plots of both the samples have been shown in Fig. 8c. It is clear that with increasing microwave exfoliation temperature, the overall active area for Ti<sub>3</sub>C<sub>2</sub> MXene is increased with redistribution of F-active surface termination. Further, the specific capacitance ( $C_{sp}$ ) from the CV plots has been determined using the equation

$$C_{sp} = \frac{\text{Area under the curve}}{\text{mass scan rate potetial window}}. \quad (1)$$

From the recorded CV data, it has been observed that Ti<sub>3</sub>C<sub>2</sub> MXene @ 30 °C possess higher  $C_{sp}$  over 100 °C. This behaviour is clearly visible in Fig. 8d.

The value of  $C_{sp}$  is recorded to be 15 F/g and reduced to 11 F/g, respectively, for Ti<sub>3</sub>C<sub>2</sub> MXene @ 30 °C and 100 °C @ scan rate 10 mV/s. Further analysis of GCD is shown in Fig. 9a. It shows similar superior trend for Ti<sub>3</sub>C<sub>2</sub> MXene 30 °C over 100 °C recorded at 1 mA current. The discharging time was observed to be ~ 11 s for Ti<sub>3</sub>C<sub>2</sub> MXene 30 °C and 9 s for Ti<sub>3</sub>C<sub>2</sub> MXene 100 °C. The F surface termination seems to be dominating more by subsequent thinning of Ti<sub>3</sub>C<sub>2</sub> MXene. The fitted Nyquist impedance plot is shown in Fig. 9b. The experimental Nyquist impedance results have been simulated by constructing an equivalent circuit using ZSimpWin

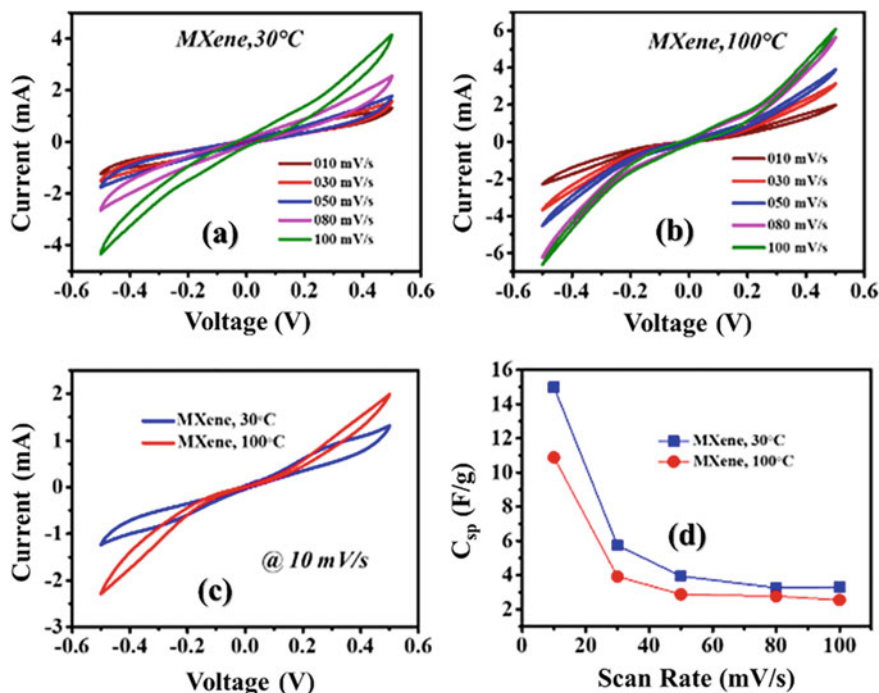


**Fig. 8** Recorded CV profile for **a** MXene, 30 °C, **b** MXene, 100 °C, **c** comparative @ 10 mV/s, **d** specific capacitance versus scan rate plot

software for  $Ti_3C_2$  MXene electrode system. In Fig. 9b, the open circles represent the experimentally obtained result, and the red solid line is corresponding fitted data. The constructed equivalent circuit is shown in Fig. 9c.

The simulated circuitry values are displayed in Table 2. From these values, one can see that the shunt resistance ( $R_s$ ) is dominating over the capacitive mechanism of  $Ti_3C_2$  MXene active material. For low as well as high-temperature microwave exfoliation, the shunt resistance is dominant and almost independent of surface area of MXene. However, magnitude of  $R_s$  is computed to be lower  $\sim 1.88 \Omega$  for 30 °C as compared to 100 °C sample ( $\sim 2.23 \Omega$ ). This shows that the effect is enhanced at higher temperature exfoliation redistributed maximum number of  $F$  moieties at the surface termination. By and large, resistive coupling might have limited the capacitive performance of  $Ti_3C_2$  MXene, thereby achieving smaller values for capacitance and quality factor as displayed in Table 2. This is in fact evident, prominently, in the plotted Bode profiles displayed in Fig. 9d for both the system. The impedance profile shows that at low frequency,  $Ti_3C_2$  MXene phase capacitor offers high amount of impedance for electromigrated charges, and gradually, dominance reduces at high frequency. Among these two systems, thinner specimen, i.e. 100 °C microwave processed sample showed enhanced impedance, which is consistent with the analysis presented above.

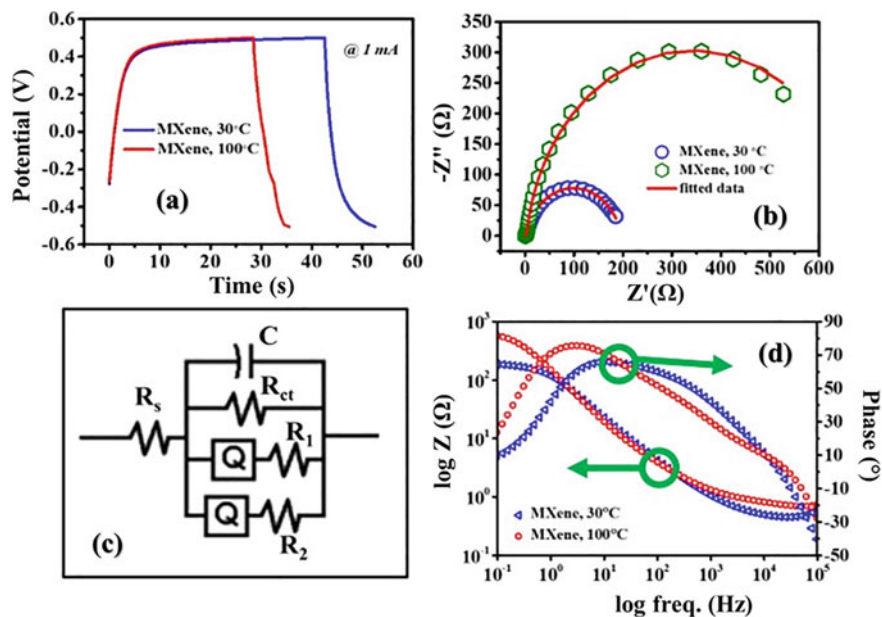


**Fig. 9** Recorded **a** GCD, **b** Nyquist plot, **c** fitted circuit analogues, **d** bode plot

**Table 2** Simulated circuit parameter of Nyquist plot

$\text{Ti}_3\text{C}_2$ MXene ( $^{\circ}\text{C}$ )	Fitting parameter					
	$R_s$ ( $\Omega$ )	$C$ ( $\mu\text{F}$ )	$R_{ct}$ ( $\Omega$ )	$Q$	$R_1$ ( $\Omega$ )	$R_2$ ( $\Omega$ )
30	1.88	0.1	1.88	0.1	1.88	1.88
100	2.23	0.1	2.23	0.1	2.23	2.23

## 6 Conclusion

Attempts were made for the synthesis of  $\text{Ti}_3\text{AlC}_2$  MAX phase at a temperature of  $800^{\circ}\text{C}$  which is lower than the reported values till date. A large amount of graphitic carbon peak was observed in XRD indicating the lack of thorough mixing of the precursor materials. This process can be modified by using ball milling technique prior to the sintering of precursor materials. Although, synthesis of  $\text{Ti}_3\text{C}_2$  MXene was independent of this, and proper 2D lamina sheets of the material were obtained. Microwave-assisted treatment was fruitful in thinning down the layers of  $\text{Ti}_3\text{C}_2$  MXene. Therefore, it can be a possible approach for the synthesis of  $\text{Ti}_3\text{C}_2$  MXene quantum dots. Electrochemical analysis revealed that exfoliation and downsizing of  $\text{Ti}_3\text{C}_2$  MXene altered the specific capacitance. The  $F$  surface termination has played significant role in its distribution over the thin and thick flakes of  $\text{Ti}_3\text{C}_2$  MXene.

## References

1. Galvin T, Hyatt NC, Rainforth WM et al (2018) Molten salt synthesis of MAX phases in the Ti–Al–C system. *J Eur Ceram Soc* 38. <https://doi.org/10.1016/j.jeurceramsoc.2018.06.034>
2. Kang MH, Lee D, Sung J et al (2019) Structure and chemistry of 2D materials. In: *Comprehensive nanoscience and nanotechnology*
3. Novoselov KS, Geim AK, Morozov SV et al (2004) Electric field in atomically thin carbon films. *Science* 306 (1976). <https://doi.org/10.1126/science.1102896>
4. Naguib M, Kurtoglu M, Presser V et al (2011) Two-dimensional nanocrystals: two-dimensional nanocrystals produced by exfoliation of  $\text{Ti}_3\text{AlC}_2$  (*Adv Mater* 37/2011). *Adv Mater* 23. <https://doi.org/10.1002/adma.201190147>
5. Khot AC, Dongale TD, Park JH et al (2021)  $\text{Ti}_3\text{C}_2$ -based MXene oxide nanosheets for resistive memory and synaptic learning applications. *ACS Appl Mater Interfaces* 13. <https://doi.org/10.1021/acsami.0c19028>
6. Iqbal A, Hamdan NM (2021) Investigation and optimization of MXene functionalized mesoporous titania films as efficient photoelectrodes. *Materials* 14. <https://doi.org/10.3390/ma14216292>



# Photocatalytic Approach of *Camellia sinensis* Extract-Mediated Green-Synthesized Magnesium Oxide Nanoparticles



Pinky Yadav , Muskan Batra, Nancy Yadav, and Ayana Bhaduri 

**Abstract** Herein, the synthesis, properties, and photocatalytic performances of nanoparticles of magnesium oxide (MgO NPs) have been reported. By employing magnesium acetate as a precursor salt, *Camellia sinensis* (tea) extract as a precipitating agent, and annealing at 550 °C temperature, MgO NPs were produced using a facile green technique. The prepared MgO NPs are analyzed by X-ray diffraction (XRD) and UV–Visible Spectroscopy, and their photocatalytic studies have been performed using organic dye. The samples' XRD measurements showed that they were cubic, with typical crystallite sizes of less than 10 nm. The absorption was investigated using UV–Visible spectroscopy, and the predicted bandgap was determined to be 4.1 eV using the Tauc relation. The prepared samples showed significant photocatalytic activity in degrading organic dyes which shows that the green method-synthesized MgO NPs are a viable alternative for treating hazardous effluents from textile manufacturers.

**Keywords** Magnesium oxide nanoparticles · Green synthesis · *Camellia sinensis* extract · Photocatalytic dye removal

## 1 Introduction

Lately, research attention has been directed toward the health risks that organic dye effluents from diverse sectors like textile, paper, paints, cosmetics, and food processing cause to mankind and other living things. Because of their color and the potentially harmful by-products created during the wastewater phase of the hydrolysis and oxidation processes, it is not advisable to release effluents with low-biodegradable dyes into aquatic bodies [1, 2]. Of the several methods for the treatment of dye-contaminated water, organic contaminants' photocatalytic degradation has

---

P. Yadav · M. Batra · N. Yadav · A. Bhaduri (✉)  
Department of Physics, Amity School of Applied Sciences, Amity University Haryana,  
Gurugram 122413, India  
e-mail: [ayana.bhaduri@gmail.com](mailto:ayana.bhaduri@gmail.com)

drawn a lot of attention [3, 4]. Traditional wastewater treatment techniques including adsorption, coagulation, flocculation, advanced oxidation, and precipitation produce resultant sludge that is expensive to dispose of and takes longer duration to achieve the desired level [5, 6].

Inorganic materials like metal and metal oxides at the nanoscale have drawn enough interest recently due to their prospective usage in numerous fields, including dye degradation produced by photocatalysis. The effectiveness of a number of transition metal oxide as a photocatalysts, including MO (M=Mn, Ni, Cu, Ag, and Ti), in degrading dyes has been studied [7–11]. Due to its remarkable physico-chemical and optoelectronic properties, earth-abundance, and lack of toxicity, among other things, magnesium oxide (MgO) is appealing for photocatalytic purposes [2, 12]. MgO nanoparticles are employed in a variety of industrial applications, such as coatings, petrochemical products, ceramics, electronics, and catalysis. The highly crystalline MgO NPs have unique crystal morphologies, small electrical conductivity, an elevated melting temperature, significant surface areas. Co-precipitation, sol-gel, hydrothermal, and chemical gas phase processes are just a few of the methods that have been employed to create MgO nanoparticles [13–15]. These methods often involve a multitude of dangerous substances, strong acids, and bases that are harmful to the environment. Hence, creating safe, economical, and environmentally acceptable processes in order to synthesize of MgO nanoparticles continue to be a challenge. Recently, emphasis has switched to the improvement of “green synthesis” methods, which produce nanoparticles utilizing plant extracts, sugars, polymers, organisms such as yeast, bacteria, algae [16–18].

Herein, *Camellia sinensis* (tea) extract was used as a reducing agent to synthesize MgO nanoparticles. Polyphenols found in tea extract aid in reducing the salt precursor for obtaining nanoparticles. In the polyphenols, you can find flavonoids and catechin [17, 19]. The preparation of MgO nanoparticles is attributed to the main catechin, epigallocatechin gallate (EGCG), which participates in the reduction of salt precursors [1]. It is an easy procedure that does not call for complicated equipment or hazardous materials. Several characterization techniques were utilized to systematically characterize the various properties of the obtained MgO nanoparticles. Using Scherrer's formula and the results of XRD, the crystallite size was determined. The energy bandgap and chemical bonds present were analyzed by UV-Visible and FTIR spectroscopy, respectively. When employed as a photocatalyst, MgO nanoparticles demonstrated efficient photocatalytic degradation of crystal violet (CV) and brilliant green (BG) dyes.

## 2 Materials and Methods

Magnesium acetate tetrahydrate was taken as a magnesium precursor material and *Camellia sinensis* (Tea) of the brand: Tata premium was employed as a reducing agent. Deionized water (DIW) was used throughout the whole process.

## 2.1 Preparations of *Camellia sinensis* (Tea) Extract

To prepare the tea extract, 16 g of tea powder was blended with 250 ml of DIW and boiled on a hot plate at 100 °C for an hour. Then, the solution was cooled, strained and the extract was collected.

## 2.2 Synthesis of MgO Nanoparticles

A simple co-precipitation method was employed for obtaining MgO nanoparticles (Fig. 1a). A 2 M solution of magnesium acetate tetrahydrate was prepared in 250 ml of DIW in a beaker. Subsequently, 50 ml of the tea extract was added to the solution by stirring. After 2 h, the solution was washed with water and ethanol several times with centrifugation for removing the excess impurities. Then, the produced nanoparticles were dried at 60 °C followed by annealing at 550 °C for 2 h to get brown-colored MgO nanoparticles and stored in airtight storage vials for further investigations. The obtained MgO nanoparticles were further characterized by XRD (Bruker D-8 Advanced), UV–Visible spectroscopy (Cary 100 from Agilent Technologies), and FTIR spectroscopy (Perkin Elmer).

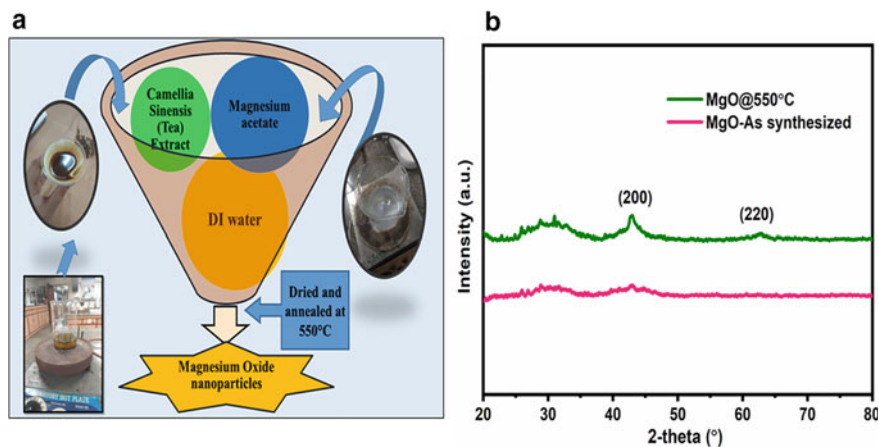


**Fig. 1** a Synthesis process of green extract-mediated MgO nanoparticles and b XRD patterns of synthesized samples

## 2.3 Photocatalytic Studies

By using the model dyes brilliant green (BG) and crystal violet (CV) under visible irradiation at room temperature in a lab-made photoreactor, the photocatalytic performances of the obtained MgO nanoparticles were examined. In the UV–Visible spectrum, the BG and CV dyes exhibit a prominent absorption band at 624 nm and 590 nm, respectively. Initially, 20 mg of photocatalyst in 50 ml dye solution (concentration 10 ppm each for both the dyes) was dispersed and set on stirring in dark for 45 min for the occurrence of adsorption and desorption equilibrium. Thereafter, the suspension was exposed to visible illumination along with agitation. Small volumes (4 ml) of dye solution were drawn out at pre-set time intervals, centrifuged, and analyzed under a Cary 100 UV–Visible Spectrophotometer.

## 3 Results and Discussion

### 3.1 Powder XRD Patterns

The powder XRD technique is employed to determine the crystal structure, phases, and crystallinity of the materials. Figure 1b presents the X-ray diffraction patterns of the prepared samples. The broadbands in the XRD pattern of as-synthesized samples showed the amorphous nature of the nanoparticles. The XRD peaks of prepared MgO nanoparticles annealed at temperature 550 °C observed at  $2\theta = 42.9^\circ$ ,  $62.3^\circ$ , and  $74.5^\circ$  (slight hump) corresponding to the (200), (220), and (311) crystal planes of MgO, respectively, were well-matched to the standard cubic phase of MgO corresponding to ICDD reference number 01-075-0447 [20]. There were no peaks of other phases observed in the XRD patterns of the green extract-mediated prepared samples which revealed the pure phase of MgO nanoparticles. Scherrer's relation is used for evaluating the average crystallite sizes of the samples as given in Eq. (1),

$$D = k * \frac{\lambda}{\beta \cos \theta}. \quad (1)$$

Here,  $D$  is average crystallite size and  $k$ ,  $\lambda$ ,  $\theta$ , and  $\beta$  are Scherrer's shape constant (0.9), source wavelength (X-ray), peak position, and full width at half-maximum intensity, respectively. The calculated sizes for both samples were found to be less than 5 nm using the above equation.

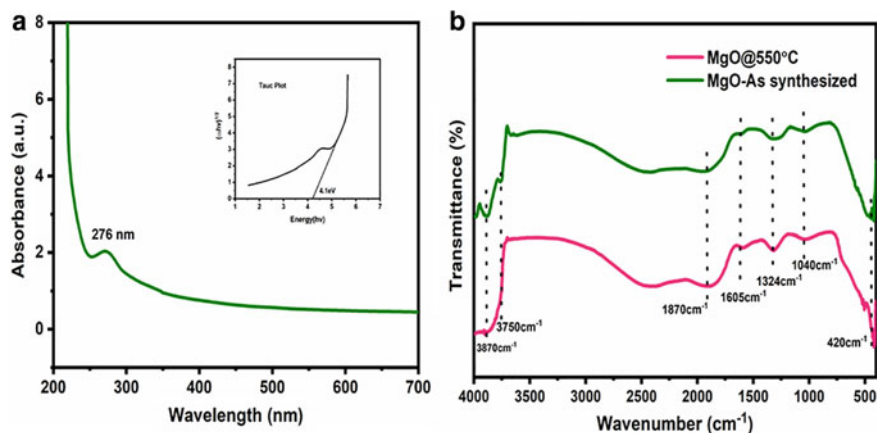


**Fig. 2** **a** Absorption spectrum of MgO@550 °C nanoparticles (Inset: Tauc plot) and **b** FTIR spectra of synthesized samples

### 3.2 UV–Visible Spectroscopy

The optical characteristics of the synthesized MgO nanoparticles annealed at 550 °C were examined by UV–Visible spectroscopy. The annealed MgO nanoparticles showed an absorbance band at 276 nm as depicted in Fig. 2a. The typical Tauc plot (function of absorption vs. energy) was employed to calculate the bandgap of the produced MgO nanoparticles as shown in inset of Fig. 2a and is written as [6, 21]

$$(\alpha h\nu) = A(h\nu - E_g)^n, \quad (2)$$

where “ $h\nu$ ” denotes the photon energy, “ $E_g$ ” is bandgap energy, “ $\alpha$ ” denotes absorption coefficient, and “ $A$ ” is a constant. The value of 1/2 is used for “ $n$ ” for direct transitions. The bandgap is estimated to be 4.1 eV using the above relation which is lower than the bandgap energy of MgO in bulk state (7.65 eV). This can be associated with the quantum size effect [22].

### 3.3 Fourier Transform Infrared Analysis (FTIR)

The data about the functional groups that exist on the surface of the samples are extracted by FTIR analysis. FTIR spectra of prepared samples are presented in Fig. 2b in the range of 4000–400  $\text{cm}^{-1}$ , revealed the presence of different chemical entities present on the surface. The stretching vibrations of the water molecules’ hydroxyl groups (–OH), which are present due to physical adsorption on the surface of samples, were responsible for the bands in the region of 3600–3880  $\text{cm}^{-1}$  [23–25]. Bands at 1605  $\text{cm}^{-1}$ , 1324  $\text{cm}^{-1}$  were ascribed to the bending vibrations of

water molecules (H–O–H). The aromatic stretching vibrations of various bioactive compounds are associated with  $1040\text{ cm}^{-1}$  band [20]. The metal–oxygen band vibrations were assigned to the region below  $1000\text{ cm}^{-1}$ . The band at  $420\text{ cm}^{-1}$  confirmed the MgO formation [26, 27].

### 3.4 Photocatalytic Studies

The photocatalytic performances of tea extract-mediated MgO@550 °C nanoparticles are evaluated by degrading BG and CV dyes in visible light exposure. The absorption spectra of both dyes, BG (624 nm) and CV (590 nm), are recorded with respect to the light exposure time [5]. The characteristic absorption band of each dye was rapidly reduced in the absorption spectra of BG and CV, as displayed in Figs. 3a, b respectively, in the presence of the photocatalyst as light contact duration increased to 120 min. There was a rapid reduction in the absorption band within the first 10 min of the light exposure, and afterward, there is a slow decrease in absorption band which was seen. However, it was observed that, in the absence of the photocatalyst, there was no noticeable change in the absorption spectra of the dyes. Relation (3) is used to calculate the degradation efficiency of prepared photocatalysts [28, 29]:

$$\text{Photodegradation efficiency (\%)} = \frac{C_o - C}{C_o} \% \quad (3)$$

Here,  $C$  represents the dye concentration at a particular time and  $C_o$  represents the original dye concentration. The degradation efficiencies of annealed MgO nanoparticles for BG and CV dyes were found to be 86% and 94%, respectively, after 120 min. The variations in degradation efficacy maybe because of the various molecular structures of the dyes [30]. Only 9.6% of CV and 7.8% of BG degradation were witnessed in the absence of the photocatalyst after 120 min of light exposure time. A red shift in the maximum absorption band was observed for both dyes with increasing light exposure time indicating the degradation of dye molecules into other substances.

The sample's remarkable degradation efficiency may be ascribed to its reduced crystallite size, that increases the photocatalyst's surface area-to-volume ratio and, as a result, the number of reactive sites increases [31]. The high surface area-to-volume ratio could therefore ease the reaction and/or interaction between the dye molecules and the photocatalyst, enhancing the degradation efficiency. Further, the kinetics of the photodegradation of the sample were studied via the pseudo-first-order kinetic model (plot  $\ln(C_o/C)$  vs. time “ $t$ ”) as shown in Fig. 3c [32]. Green extract-mediated synthesized MgO nanoparticles' potential for reuse as a photocatalyst in the removal of BG and CV dyes has also been investigated. Before being used for each cycle, the NPs were properly cleaned three times in a centrifuge using ethanol and DIW. The photodegradation studies were carried out in the identical circumstances, and the outcomes revealed a slight decrease (9%) in the degradation efficiencies even

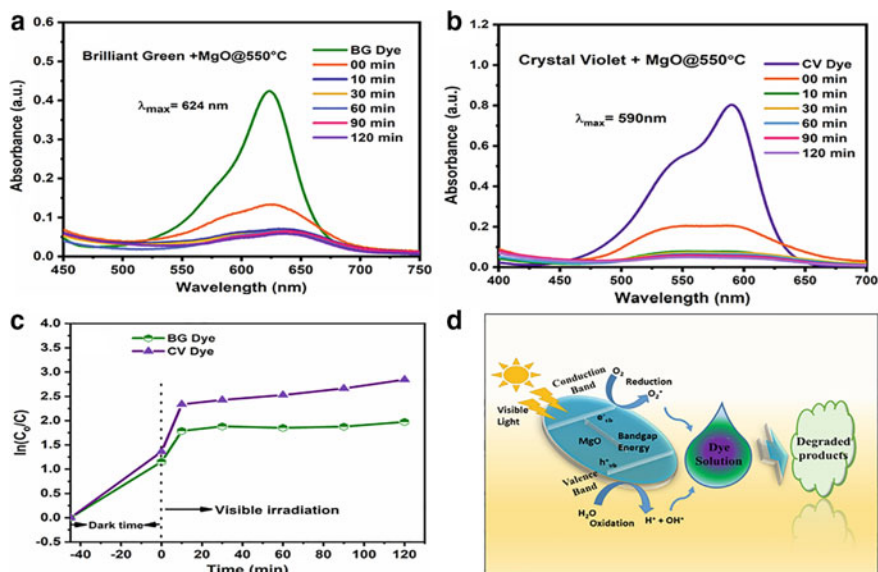
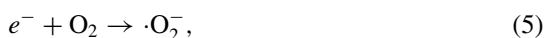
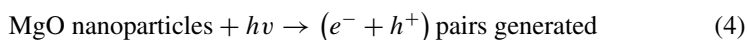


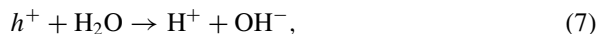
**Fig. 3** **a** Time-dependent UV–visible absorption curves of brilliant green dye with MgO@550 °C photocatalyst. **b** Time-dependent UV–visible absorption curves of crystal violet dye with MgO@550 °C photocatalyst. **c** Degradation kinetics. **d** Schematic representation of photocatalytic activity

after the third cycle. The results demonstrated photostability and reusability of the annealed MgO nanoparticles.

### Probable Mechanism of Photodegradation

The possible mechanism of photocatalytic degradation was reported previously [5, 33, 34]. The probable cause of photodegradation of organic dyes is considered to be the photo-induced electron ( $e^-$ )–hole ( $h^+$ ) pair generated reactive oxygen species (ROS): superoxide ( $O_2^{\cdot-}$ ) and hydroxyl ( $OH^{\cdot}$ ) radicals. When visible light irradiates the solution containing dye molecules and the photocatalyst, the photo-generated ( $e^- - h^+$ ) undergoes reduction and oxidation processes on the surface of the photocatalyst to generate ROS which further reacts with the dye molecules and breaks them into other degraded products ( $H_2O$ ,  $CO_2$ , etc.) [30]. The graphic illustration of the photocatalytic mechanism is presented in Fig. 3d and could be summarized with the following Eqs. (4)–(9) [5]:





As illustrated, the ROS generated by photo-excited electron–hole pairs were the prominent species for degrading the dye molecules adsorbed on the surface of MgO nanoparticles into other smaller molecules in the initial stage [29, 35].

## 4 Conclusions

The *Camellia sinensis* (tea) extract-mediated green MgO nanoparticles are proven to be economical, environmentally benign, and less likely to expose the users to harmful compounds or their by-products. Facile co-precipitation method was used to obtain green MgO nanoparticles using tea extract and further used in photocatalytic removal of organic dyes (brilliant green and crystal violet dyes). MgO nanoparticles annealed at 550 °C demonstrated notable photocatalytic properties in degrading brilliant green (BG: 86%) and crystal violet (CV: 94%) dyes under visible irradiation in 120 min. The prepared MgO nanoparticles showed very good reusability even after three reaction cycles. Because of its higher photocatalytic efficacy in the removal of organic dyes, MgO is found to be an exciting candidate for environmental remediation.

**Acknowledgements** The authors are very thankful for characterization facilities (FTIR and XRD) offered by UGC-DAE CSR (Kolkata and Indore), respectively.

**Author Contributions** Pinky Yadav: conception and outline of study, analysis, writing the initial draft. Muskan Batra and Nancy Yadav: acquisition of data, Ayana Bhaduri: Conception & supervision, final revision, and edition.

**Declaration of Interest Statement** The authors declare that they have no known conflict of interests.

## References

1. Kumar SA, Jarvin M, Inbanathan SSR, Umar A, Lalla NP, Dzade NY, Algadi H, Rahman QI, Baskoutas S (2022) Facile green synthesis of magnesium oxide nanoparticles using tea (*Camellia sinensis*) extract for efficient photocatalytic degradation of methylene blue dye. *Environ Technol Innov* 28:102746. <https://doi.org/10.1016/j.eti.2022.102746>
2. Taourati R, Khaddor M, Laghzal A, El Kasmi A (2020) Facile one-step synthesis of highly efficient single oxide nanoparticles for photocatalytic application. *Sci Afr* 8. <https://doi.org/10.1016/j.sciaf.2020.e00305>



3. Bhattacharya D, Ghoshal D, Mondal D, Paul BK, Bose N, Das S, Basu M (2019) Visible light driven degradation of brilliant green dye using titanium based ternary metal oxide photocatalyst. Res Phys 12:1850–1858. <https://doi.org/10.1016/j.rinp.2019.01.065>
4. Anandan S, Kumar Ponnusamy V, Ashokkumar M (2020) A review on hybrid techniques for the degradation of organic pollutants in aqueous environment. Ultrason Sonochem 67:105130. <https://doi.org/10.1016/j.ultsonch.2020.105130>
5. Yadav P, Saini R, Bhaduri A (2022) Facile synthesis of MgO nanoparticles for effective degradation of organic dyes. Environ Sci Pollut Res. <https://doi.org/10.1007/s11356-022-21925-0>
6. Bhaviya Raj R, Umadevi M, Parimaladevi R (2020) Enhanced photocatalytic degradation of textile dyeing wastewater under UV and visible light using ZnO/MgO nanocomposites as a novel photocatalyst. Part Sci Technol 38:812–820. <https://doi.org/10.1080/02726351.2019.1616863>
7. Yadav P, Bhaduri A (2023) Chemically synthesized manganese oxide nanorods for effectual organic dye removal and energy storage application. Mater Chem Phys 299:127495. <https://doi.org/10.1016/j.matchemphys.2023.127495>
8. Yadav P, Bhaduri A (2020) Synthesis and structural characterization of ZnO-graphene nanocomposite by chemical co-precipitation method. Int J Innov Res Phys 1:19–24. <https://doi.org/10.15864/ijirp.1204>
9. Mhlabi MM, Ngila CJ, Mamba BB (2015) Recent developments in environmental photocatalytic degradation of organic pollutants: the case of titanium dioxide nanoparticles—a review. J Nanomater 2015. <https://doi.org/10.1155/2015/790173>
10. Jayakumar G, Albert Irudayaraj A, Dhayal Raj A (2017) Photocatalytic degradation of methylene blue by Nickel oxide nanoparticles. Mater Today Proc 4:11690–11695. <https://doi.org/10.1016/j.matpr.2017.09.083>
11. Stankic S, Suman S, Haque F, Vidic J (2016) Pure and multi metal oxide nanoparticles: synthesis, antibacterial and cytotoxic properties. J Nanobiotechnol 14:1–20. <https://doi.org/10.1186/s12951-016-0225-6>
12. Bai Z, Zheng Z, Zhang Z (2015) One-pot synthesis of highly efficient MgO for the removal of Congo red in aqueous solution. J Mater Chem C 3:10715–10722. <https://doi.org/10.1039/b000000x>
13. Wahab R, Ansari SG, Dar MA, Kim YS, Shin HS (2007) Synthesis of magnesium oxide nanoparticles by sol–gel process. Mater Sci Forum 558–559:983–986. <https://doi.org/10.4028/www.scientific.net/msf.558-559.983>
14. Deepa B, Rajendran V (2018) Investigation of organic solvents assisted nano magnesium oxide nanoparticles and their structural, morphological, optical and antimicrobial performance. Mater Res Exp 5. <https://doi.org/10.1088/2053-1591/aaa0b5>
15. Sutapa IW, Wahid Wahab A, Taba P, Nafie NL (2018) Dislocation, crystallite size distribution and lattice strain of magnesium oxide nanoparticles. J Phys Conf Ser 979:12021. <https://doi.org/10.1088/1742-6596/979/1/012021>
16. Essien ER, Atasié VN, Okefor AO, Nwude DO (2020) Biogenic synthesis of magnesium oxide nanoparticles using *Manihot esculenta* (Crantz) leaf extract. Int Nano Lett 10:43–48. <https://doi.org/10.1007/s40089-019-00290-w>
17. Ammulu MA, Vinay Viswanath K, Giduturi AK, Vemuri PK, Mangamuri U, Poda S (2021) Phytoassisted synthesis of magnesium oxide nanoparticles from *Pterocarpus marsupium* rox.b heartwood extract and its biomedical applications. J Genet Eng Biotechnol 19. <https://doi.org/10.1186/s43141-021-00119-0>
18. Suresh J, Yuvakkumar R, Sundrarajan M, Hong SI (2014) Green synthesis of magnesium oxide nanoparticles. Adv Mater Res 952:141–144. <https://doi.org/10.4028/www.scientific.net/AMR.952.141>
19. Khan A, Shabir D, Ahmad P, Khandaker MU, Faruque MRI, Din IU (2021) Biosynthesis and antibacterial activity of MgO-NPs produced from *Camellia-sinensis* leaves extract. Mater Res Express 8. <https://doi.org/10.1088/2053-1591/abd421>

20. Venkatachalam A, Jesuraj JP, Sivaperuman K (2021) *Moringa oleifera* leaf extract-mediated green synthesis of nanostructured alkaline earth oxide (MgO) and its physicochemical properties. J. Chem. 2021. <https://doi.org/10.1155/2021/4301504>
21. Yadav P, Bhaduri A (2021) Synthesis of ZnO-graphene nanocomposite by chemical coprecipitation method and its structural characterizations. AIP Conf Proc 2369:020057. <https://doi.org/10.1063/5.0061115>
22. Bindhu MR, Umadevi M, Kavin Micheal M, Arasu MV, Abdullah Al-Dhabi N (2016) Structural, morphological and optical properties of MgO nanoparticles for antibacterial applications. Mater Lett 166:19–22. <https://doi.org/10.1016/j.matlet.2015.12.020>
23. Yousefi S, Ghasemi B, Tajally M, Asghari A (2017) Optical properties of MgO and Mg(OH)<sub>2</sub> nanostructures synthesized by a chemical precipitation method using impure brine. J Alloys Compd 711:521–529. <https://doi.org/10.1016/j.jallcom.2017.04.036>
24. Fatiqin A, Amrulloh H, Simanjuntak W (2021) Green synthesis of MgO nanoparticles using *Moringa oleifera* leaf aqueous extract for antibacterial activity. Bull Chem Soc Ethiop 35:161–170. <https://doi.org/10.4314/bcse.v35i1.14>
25. Umaralikhhan L, Jamal Mohamed Jaffar M (2018) Green synthesis of MgO nanoparticles and its antibacterial activity. Iran J Sci Technol Trans A Sci 42:477–485. <https://doi.org/10.1007/s40995-016-0041-8>
26. Balakrishnan G, Velavan R, Mujasam Batoor K, Raslan EH (2020) Microstructure, optical and photocatalytic properties of MgO nanoparticles. Results Phys 16:103013. <https://doi.org/10.1016/j.rinp.2020.103013>
27. Salman KD, Abbas HH, Aljawad HA (2021) Synthesis and characterization of MgO nanoparticle via microwave and sol–gel methods. J Phys Conf Ser 1973. <https://doi.org/10.1088/1742-6596/1973/1/012104>
28. Diana P, Saravanakumar S, Prasad KH, Sivaganesh D, Chidhambaram N, Isaac RSR, Alshahrani T, Shkir M, AlFaify S, Ali KSS (2021) Enhanced photocatalytic decomposition efficacy of novel MgO NPs: impact of annealing temperatures. J Inorg Organomet Polym Mater 31:3027–3036. <https://doi.org/10.1007/s10904-021-01896-4>
29. Zheng Y, Cao L, Xing G, Bai Z, Huang J, Zhang Z (2019) Microscale flower-like magnesium oxide for highly efficient photocatalytic degradation of organic dyes in aqueous solution. RSC Adv 9:7338–7348. <https://doi.org/10.1039/C8RA10385B>
30. Munawar T, Mukhtar F, Yasmeen S, Naveed-ur-Rehman M, Nadeem MS, Riaz M, Mansoor M, Iqbal F (2021) Sunlight-induced photocatalytic degradation of various dyes and bacterial inactivation using CuO–MgO–ZnO nanocomposite. Environ Sci Pollut Res 28:42243–42260. <https://doi.org/10.1007/s11356-021-13572-8>
31. Mageshwari K, Mali SS, Sathyamoorthy R, Patil PS (2013) Template-free synthesis of MgO nanoparticles for effective photocatalytic applications. Powder Technol 249:456–462. <https://doi.org/10.1016/j.powtec.2013.09.016>
32. Mahmoud HR, Ibrahim SM, El-Molla SA (2016) Textile dye removal from aqueous solutions using cheap MgO nanomaterials: adsorption kinetics, isotherm studies and thermodynamics. Adv Powder Technol 27:223–231. <https://doi.org/10.1016/j.appt.2015.12.006>
33. Reddy Yadav LS, Lingaraju K, Manjunath K, Raghu GK, Sudheer Kumar KH, Nagaraju G (2017) Synergistic effect of MgO nanoparticles from electrochemical sensing, photocatalytic-dye degradation and antibacterial activity. Mater Res Express 4. <https://doi.org/10.1088/2053-1591/aa5b49>
34. Rochkind M, Pasternak S, Paz Y (2015) Using dyes for evaluating photocatalytic properties: a critical review. Molecules 20:88–110. <https://doi.org/10.3390/molecules20010088>
35. Liu S, Wei X, Lin S, Guo M (2021) Preparation of aerogel Mg(OH)<sub>2</sub> nanosheets by a combined sol–gel-hydrothermal process and its calcined MgO towards enhanced degradation of paraoxon pollutants. J Sol–Gel Sci Technol 99:122–131. <https://doi.org/10.1007/s10971-021-05561-7>

# IV Characteristics and Subthreshold Slope Analysis of Si and SiGe-Based Dual-Gate MOSFET



Ashutosh Pandey and Kousik Midya

**Abstract** With the aggressive scaling of MOSFET, different short channel effects have become more prominent which has affected the performance of scaled devices. To address the short channel effects, novel device structures and material with higher carrier mobility have been proposed to replace conventional Si MOSFET. In this study, a detailed comparative study of performance of dual-gate MOSFET with Si and SiGe substrates has been compared. SiGe-based device has shown better potential for low-power devices due to its lower threshold voltage. Although, it has been observed that Si-based device can provide higher subthreshold slope.

**Keywords** DG-MOSFET · Visual-TCAD · Simulation

## 1 Introduction

Continuous shrinking in dimension of MOSFET towards nanoscale region has made short channel effects more and more prominent. Conventional MOSFET seems to be failed to address the issues as channel length is moving towards less than 50 nm. The major problems were related to increased leakage current and delay due to parasitic capacitances. Researchers have reported different gate engineering techniques to overcome the problems. Devices with different gate structures like gate-all-around (GAA), tri-gate (TG), and dual-gate (DG) MOSFETs have been proposed to overcome the short channel effects [1]. Dual-gate MOSFET is a promising candidate due to smaller dimension, reduced leakage current, not so complex structure, and high current gain compared to its counterparts. Dual-gate MOSFET consists of two separate channels, which are controllable separately by two gates [2]. This provides better control on channels using gate voltage.

---

A. Pandey · K. Midya (✉)

Department of Electronics and Communication Engineering, Ajay Kumar Garg Engineering College, Ghaziabad, Uttar Pradesh 201009, India

e-mail: [kmidya@gmail.com](mailto:kmidya@gmail.com)

From application perspective, subthreshold slope and analogue/RF performance are the key factors for a MOSFET, and DG-MOSFET shows its superiority in both cases compared to a conventional MOSFET [3].

Substrate material also plays an important role in performance of the device. Short channel effects like degradation in subthreshold slope swing, higher leakage current, drain induced barrier lowering, etc., are being more and more prominent specially for Si-based scaled devices. Lower carrier mobility and lower saturation velocity are mainly responsible for the substandard performance of Si-based devices. Therefore, it became necessary to find alternative materials to enhance performance of the scaled MOSFETs. III–V materials seems to be most promising as they can provide higher drive current due to greater carrier mobility [4]. Although, unavailability of native oxide for III–V materials restricts their application in many cases. Unlike other III–V compound semiconductor SiGe substrate doesn't suffer from lack of native oxide [4]. Therefore, SiGe has been emerged as most promising replacement of Si for the scaled devices.

This work aims at systematic study of DG-MOSFET with Si and SiGe substrate. Comparative study of IV characteristics and subthreshold slope swing is the key factors of this work.

## 2 Device Structure

Cross-sectional schematic diagram of n-channel DG-MOSFET is shown in the following Fig. 1. For all devices, gate length of 20 nm has been used for simulation. Silicon-dioxide of thickness 20 nm has been used as dielectric material for both devices.  $1 \times 10^{15}/\text{cm}^3$  substrate doping has been used.  $1 \times 10^{20}/\text{cm}^3$  donor doping concentration has been used for source and drain region. Polysilicon is considered as gate electrode. In this study, DG-MOSFETs with p-Si and p-SiGe substrates are studied. For SiGe substrate, mole fraction of Si of 0.7 has been considered.

Device specifications are shown in Table 1.

**Fig. 1** Schematic diagram of the DG-MOSFET

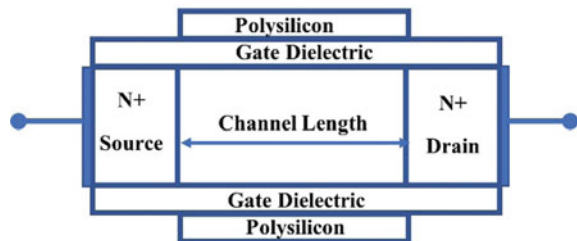


**Table 1** Device specification of Si and SiGe-based DG-MOSFETs

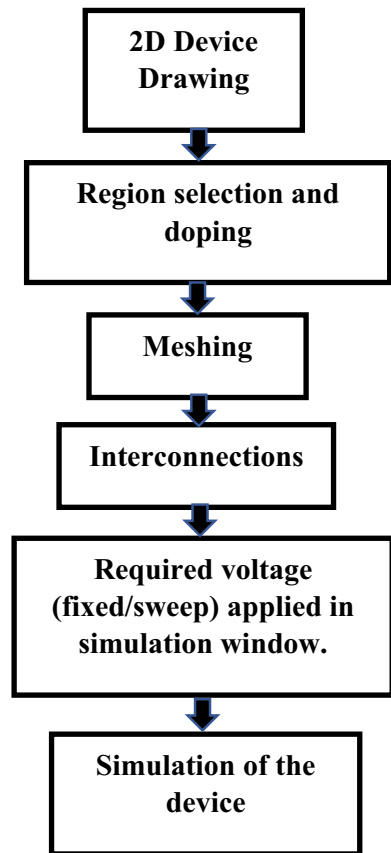
S. No.	Substrate	Channel length (nm)	Mole fraction (x)	Substrate doping Conc. (cm <sup>-3</sup> )	Gate material	Oxide thickness (nm)	Gate electrode
1	p-Si	20	0	1 × 10 <sup>15</sup>	SiO <sub>2</sub>	20	Poly-Si
2	p-Si <sub>x</sub> Ge <sub>1-x</sub>	20	0.7	1 × 10 <sup>15</sup>	SiO <sub>2</sub>	20	Poly-Si

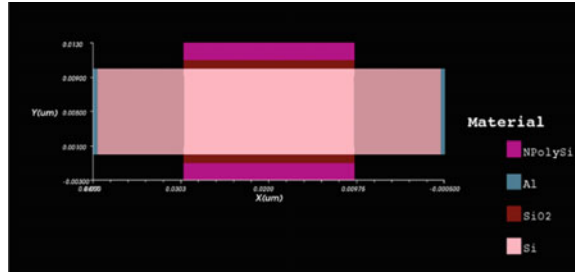
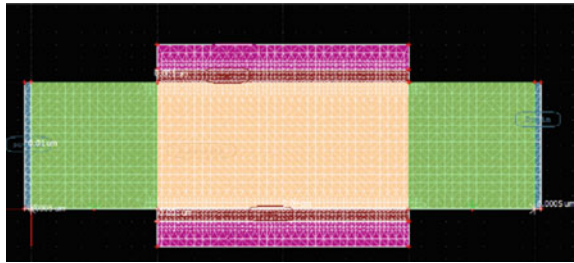
### 3 Simulation

Devices have been simulated in Visual-TCAD version 1.8.0–1. The flow chart of the simulation process steps is shown in Fig. 2.

Device drawing has been followed by meshing and refining of the same to obtain appropriate result. Gate/drain voltage sweep was performed in simulation window keeping other at constant value. Figure 3 shows the 2D device drawing of the device

**Fig. 2** Simulation process steps



**Fig. 3** 2D device structure**Fig. 4** Meshing of the device

with Si substrate (in TCAD). Device structure after meshing and refining is shown in Fig. 4.

## 4 Results and Discussion

### 4.1 Input Characteristics

Input characteristics of DG-MOSFETs with Si and SiGe substrate have been measured. For this measurement, drain-to-source voltage ( $V_{DS}$ ) was kept constant at 0.75 V. Gate voltage was varied from 0 to 2 V with step voltage of 0.05 V. Figure 5 shows the input characteristics of both the devices with SI and SiGe substrate and with gate length of 20 nm.

The result shows lower threshold voltage for SiGe substrate. Higher carrier mobility results in lower threshold voltage.

### 4.2 Output Characteristics

Output characteristics have been measured with constant gate voltage of 0.75 V, and drain voltage was swept from 0 to 1 V. Figure 6 shows the output characteristics. Little improvement in saturation current has been observed for SiGe-based device.

**Fig. 5** Input characteristics ( $I_D - V_{GS}$ ) for the devices with **a** Si and **b** SiGe substrate

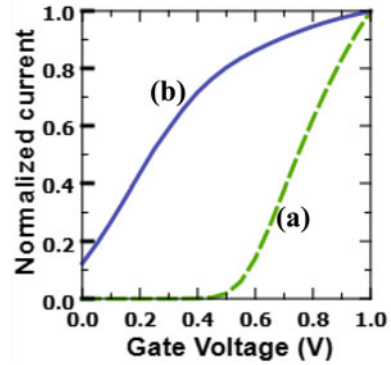
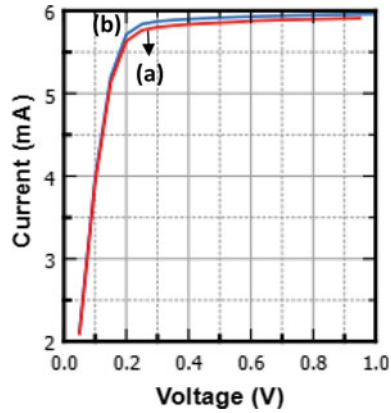


**Fig. 6** Output characteristics ( $I_D - V_{DS}$ ) of DG-MOSFET with **a** Si and **b** SiGe substrate



It is well reported that difference in  $I_{D,SAT}$  for Si and SiGe-based devices increases with the gate voltage [5].

### 4.3 Subthreshold Slope Analysis

In subthreshold region, drain current exponentially decreases with the  $V_{DS}$ . Subthreshold slope in inverse of subthreshold swing which is expressed as

$$S = \log\left(\frac{kT}{q}\right)\left(1 + \frac{C_d}{C_{OX}}\right)$$

where

- $C_d$  Depletion layer capacitance
- $C_{OX}$  Gate oxide capacitance.

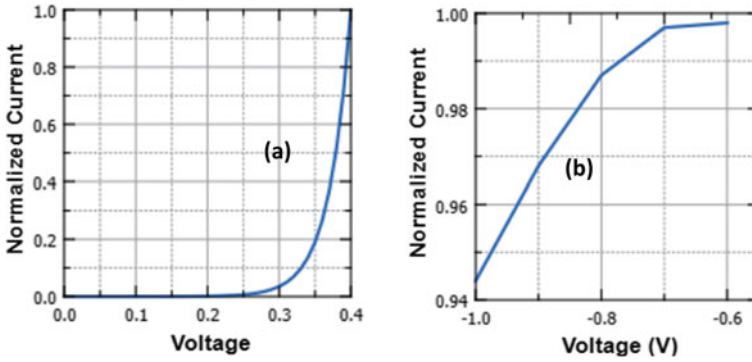
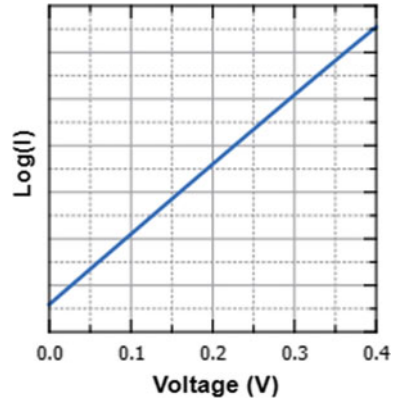


Fig. 7  $I_D - V_{DS}$  graph in subthreshold region for a Si and b SiGe substrate

Fig. 8 Subthreshold swing for Si substrate



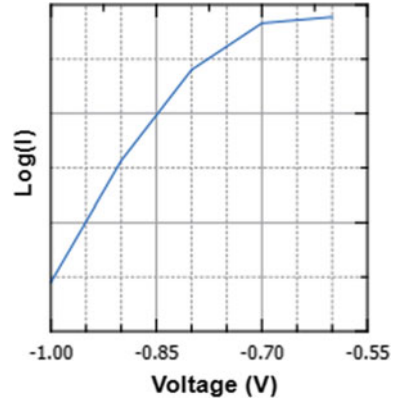
The log of drain current shows a linear relationship with the drain-source voltage. Subthreshold slope is important to estimate how fast drain current goes towards zero in subthreshold region. Additionally, in some modern analogue applications, subthreshold region is only used to obtain higher gain [6].

Figure 7 shows the output characteristics graph only in subthreshold region. The graph indicates higher slope in subthreshold region which is obtained for Si substrate. To get better understanding,  $\text{Log}(I_D) - V_{DS}$  graph is shown in Figs. 8 and 9.

For Si substrate,  $\text{Log}(I_D)$  varies with  $V_{DS}$  following linear relationship. However, for SiGe substrate, non-linear relationship has been observed.



**Fig. 9** Subthreshold swing for SiGe-based DG-MOSFET



## 5 Conclusion

Input and output characteristics of DG-MOSFETs with Si and SiGe substrates have been studied in detail. Significant decrease in threshold voltage has been observed in SiGe-based device, which is attributed to its higher carrier mobility. Much difference has not been observed in saturation current for both the devices. Si-based device shows higher subthreshold slope compared to SiGe-based device.

## References

1. Ramesh R (2017) Influence of gate and channel engineering on multigate MOSFETs—a review. *Microelectron J* 66:136–154
2. Zimmermann D (1970) Dual-gate MOSFET static characteristics generated for mixing applications
3. Mendiratta N, Tripathi SL (2020) A review on performance comparison of advanced MOSFET structures below 45 nm technology node. *J Semicond* 41(6):061401
4. Adhikari MS, Singh Y (2017) High performance multi-channel MOSFET on InGaAs for RF amplifiers. *Superlattices Microstruct* 102:79–87
5. Paul BC, Raychowdhury A, Roy K (2005) Device optimization for digital subthreshold logic operation. *IEEE Trans Electron Devices* 52(2):237–247
6. Quinones EJ, John S, Ray SK, Banerjee SK (2000) Design, fabrication, and analysis of SiGeC heterojunction PMOSFETs. *IEEE Trans Electron Dev* 47(9):1715–1725

# Structural and Sensing Properties of Sb<sub>2</sub>O<sub>3</sub>-Doped Tin Oxide Thick Film Gas Sensor



Poonam Yadav, Satish Kumar Yadav, Ankit Kumar Vishwakarma, Sesh Mani Yadav, and Lallan Yadava

**Abstract** Two types of sensing paste undoped tin oxide (SnO<sub>2</sub>) and 5 wt% antimony oxide (Sb<sub>2</sub>O<sub>3</sub>) doped SnO<sub>2</sub> have been prepared and are screen-printed on designed alumina substrate which are named as sensor S1 (undoped SnO<sub>2</sub>) and S2 (5 wt% Sb<sub>2</sub>O<sub>3</sub>-SnO<sub>2</sub>). From XRD measurements, crystallite sizes were determined, and it is found to be 29.51 nm for sample S1 and 27.09 nm for S2. Sensing behavior of the fabricated sensors was investigated for acetone and propanol gas with varying concentration (0–5000 ppm) at different fixed temperature 150, 200, and 250 °C in the testing chamber in which provisions are made for gas inlet/outlet and electrical connections. The responses of the fabricated sensors (S1 and S2) were measured, and it is found that sensor S2 exhibited the highest response ~ 63.15 for acetone gas over propanol gas ~ 60.46% at 5000 ppm at fixed temperature 250 °C. The observed recovery time of sensor S2 is found to be 39 s and 61 s for acetone and propanol gas, respectively.

**Keywords** XRD · Crystallite size · Acetone gas · Propanol gas · Sensing response · Recovery time

---

P. Yadav · S. K. Yadav · S. M. Yadav · L. Yadava (✉)  
Thin-Film Laboratory, Department of Physics, Deen Dayal Upadhyaya Gorakhpur University,  
Gorakhpur, Uttar Pradesh 273009, India  
e-mail: [nisaly06@rediffmail.com](mailto:nisaly06@rediffmail.com)

A. K. Vishwakarma  
Department of Physics, Dr. Shakuntala Mishra National Rehabilitation University, Lucknow,  
Uttar Pradesh 226017, India

## 1 Introduction

Among the semiconductor, metal oxides-based gas sensors tin oxide ( $\text{SnO}_2$ ) are frequently used by researcher due to their unique physical and chemical properties and its potential applications for the detection of various toxic and flammable gases such as  $\text{H}_2$ ,  $\text{CH}_4$ ,  $\text{CO}$ ,  $\text{H}_2\text{S}$ ,  $\text{CO}_2$ , LPG, and organic vapors [1–3].  $\text{SnO}_2$  is an n-type semiconductor having a wide band gap 3.6 eV at 300 k, and due to its mechanical and chemical stability, it can be used in different aspects such as gas sensors, solar cells, and optoelectronics devices [4]. Undoped  $\text{SnO}_2$  thin/thick film sensor shows less response to the target gas due to low electrical conductivity since carrier density and mobility are low. To improve the response of the sensor toward a specific target gas, many elements metal/metal oxides were used as a dopant source since it improves the structural, electrical, and optical characteristics of the undoped  $\text{SnO}_2$  films. Earlier workers have doped transition metal ions such as Al, Co, Fe, Zn, and Sb [5, 6]. Kim et al. [7] reported transparent conducting Sb-doped  $\text{SnO}_2$  thin films grown by pulsed-laser deposition and studied the structural, electrical, and optical properties of these films as a function of doping amount, substrate temperature, and oxygen partial pressure during deposition. Kim et al. [8] reported the structural, electrical, and optical properties of the  $\text{Sb}_2\text{O}_3$ -doped  $\text{SnO}_2$  films deposited on glass substrate by using pulsed-laser deposition method. They observed that electrical resistivity decreases as a function of  $\text{Sb}_2\text{O}_3$ -doping amount until 6 wt%, and then it reaches a minimum value of  $\rho \sim 3 \times 10^{-3} \Omega \text{ cm}$  and above 6 wt% of  $\text{Sb}_2\text{O}_3$  resistivity increases again. Ahmad et al. [9] presented enhancement of infrared shielding property of  $\text{SnO}_2$  using Sb as a dopant and observed that with Sb doping  $\text{SnO}_2$  retains its tetragonal structure; however, crystallite size reduces and it is the lowest for antimony doped tin oxide (ATO-4). Feng et al. [10] studied the sensing performance of highly doped Sb/ $\text{SnO}_2$  and reported that antimony (Sb) doped  $\text{SnO}_2$ , Sb ions, produces a new shallow band level and oxygen vacancies acting as donor in  $\text{SnO}_2$ . Sb doping inhibits  $\text{SnO}_2$  grain growth; result is decrease in crystallinity slightly. Gupta et al. [11] presented structural/microstructural, optical, and electrical investigations of Sb– $\text{SnO}_2$  thin films deposited by spray pyrolysis and studied that there is small decrease in the lattice parameters of the tetragonal unit cell with added Sb content. Saadeddin et al. [12] presented synthesis and characterization of single and Co-doped  $\text{SnO}_2$  thin films for optoelectronic applications and found that both types of thin films have a dense morphology with a smooth surface and they are polycrystalline. Drude model was applied for ATO films in order to deduce the carrier concentration, the optical mobility as well as resistivity. Jariwala et al. [13] reported preparation and characterization of antimony doped tin oxide thin films synthesized by Co-evaporation of Sn and Sb using plasma-assisted thermal evaporation and observed that  $\text{SnO}_2$ : Sb films have identified the critical role of Sb dopant for achievement of best quality TCO, which can be replaced for ITO films for various optoelectronics device applications. Haddad et al. [14] studied the influence of fluorine doping on the microstructure, optical, and electrical properties of  $\text{SnO}_2$  nanoparticles and found that the crystallinity and optical properties of the  $\text{SnO}_2$  nanomaterials depend strongly on fluorine doping rate.

Lavanya et al. [15] presented the development of a selective hydrogen leak sensor based on chemically doped SnO<sub>2</sub> for automotive applications and observed that the Co-doped SnO<sub>2</sub>-based sensor exhibited high sensitivity and good selectivity toward hydrogen compared to undoped SnO<sub>2</sub> and Mn-doped SnO<sub>2</sub> ones. In the present study, we investigated the role and effects of dopant Sb<sub>2</sub>O<sub>3</sub> in SnO<sub>2</sub>. The response of the fabricated thick film gas sensors S1 and S2 for detection of acetone and propanol gas (0–5000 ppm) at different fixed temperature is presented. The last section concludes the findings.

## 2 Materials and Methods

### 2.1 Characterization

The structural properties of the samples were examined by X-ray diffraction using D-8 advanced unit equipped with Cu-k $\alpha_1$  radiation having wavelength 1.5406 Å as a source [16]. XRD patterns for undoped SnO<sub>2</sub> and 5 wt% Sb<sub>2</sub>O<sub>3</sub>-doped SnO<sub>2</sub> were recorded in the  $2\theta$  range from 26 to 66.

### 2.2 Sensing Measurement Set-Up

The experimental setup which was used to determine the response of sensors (S1, S2) consists of a locally made chamber along with dual DC power supply (DL-3203) and a digital multimeter (Aplab 107-N) as shown in Fig. 1. Sensors were exposed to hydrocarbon vapors (acetone and propanol) in the air ambient at varying concentration (0–5000 ppm) at different fixed temperatures 150, 200, and 250 °C. Response is recorded by measuring the electrical resistance of sensor in air and presence of target gas [17].

## 3 Results and Discussions

### 3.1 X-Ray Diffraction (XRD)

The XRD pattern of undoped and Sb<sub>2</sub>O<sub>3</sub>-doped SnO<sub>2</sub> film is shown in Fig. 2. The diffracted pattern peaks appear at the angle  $2\theta \sim 26.7^\circ, 34.2^\circ, 38.1^\circ, 52.2^\circ, 54.9^\circ, 58.3^\circ,$  and  $64.7^\circ$  belonging to the planes (110), (101), (200), (211), (220), (002), and (112), respectively. Corresponding planes respective to their peaks confirm the tetragonal structure of the samples. Using Debye-Scherrer formula crystallite size is calculated [18]:  $d = k \cdot \lambda / \beta \cdot \cos \theta$ , where  $\lambda$  is wavelength of X-ray source,  $k$  is

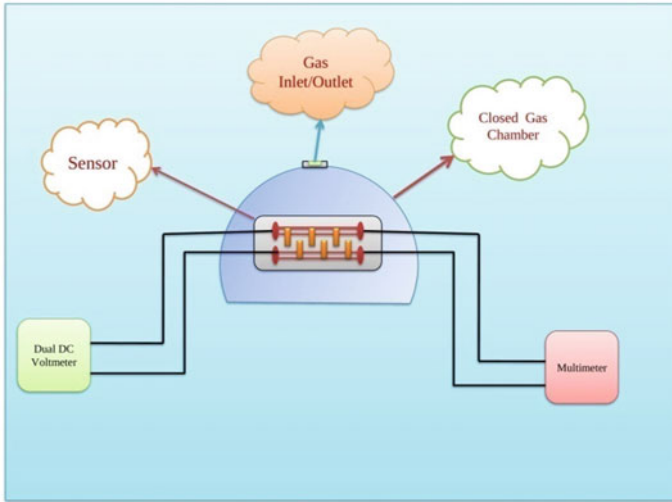
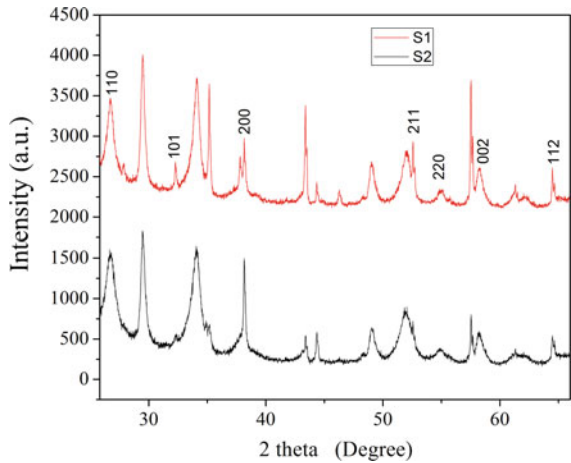


**Fig. 1** Sensing measurement setup

shape factor usually as a value 0.94;  $\theta$  is diffraction angle and  $\beta$  gives full width half maxima (FWHM). The XRD measurement reflects the average crystallite size which was found to be  $\sim 29.51$  nm and  $\sim 27.09$  nm for undoped  $\text{SnO}_2$  and 5 wt%  $\text{Sb}_2\text{O}_3$ -doped  $\text{SnO}_2$  samples, respectively, indicating decrease in average crystallite size with  $\text{Sb}_2\text{O}_3$  content. It is observed that  $\text{Sb}_2\text{O}_3$ - $\text{SnO}_2$  structure lowers the crystallinity of  $\text{SnO}_2$ . Thus, added  $\text{Sb}_2\text{O}_3$  content acts as a crystal growth inhibitor.

**Fig. 2** X-ray diffraction pattern of sensors S1 and S2



### 3.2 Gas Sensing Behavior and Mechanism

The response of gas sensor is determined using formula

$$S = \left[ \frac{R_a - R_g}{R_a} \right] \times 100, \quad (1)$$

where  $S$  = response,  $R_a$  = resistance in air ambient, and  $R_g$  = resistance in presence of gas [19, 20]. The response of fabricated sensors is measured for acetone and propanol gas with varying concentration (0–5000 ppm) in air ambient at the different fixed temperatures ranges (150–250 °C). The response for sensors S1 and S2 with varying concentration of acetone at fixed temperatures 150, 200, and 250 °C is shown in Fig. 3a–c. It is observed from figure that as the concentration increases, response increases, and it shows its maximum value at 250 °C. The response curve for other target gas propanol is shown in Fig. 3d–f. The values of response for sensors S1 and S2 for target gas (0–5000 ppm) at fixed temperature 250 °C are listed in Table 1. We observed that sensor S2 exhibits maximum response (~ 63.15) toward acetone gas (5000 ppm) at fixed temperature 250 °C. The maximum response for propanol gas at (5000 ppm) at fixed temperature 250 °C is found to be ~ 60.46. Figure 3g shows a comparative response of sensor S2 for exposed gases acetone and propanol at 250 °C temperature.

The sensing mechanism is explained on the basis of adsorption of the oxygen species when sensor is exposed in air and the interaction with analyte. Initially, pre-adsorption oxygen on the surface would trap electron due to strong electron negativity of oxygen and producing adsorbed oxygen anions ( $O_{2(ads)}$ ,  $O_{2(ads)}^-$ ,  $2O_{(ads)}^-$ ). In the presence of reducing gases on the surface of sensor, it will result in a reaction between adsorbed charged oxygen ions and the reducing gas that releases captured electrons back to the conduction band of the sensor's material, thus resulting in a decrease of the potential barrier and the carrier's concentration is increased which caused the sensor resistance to be reduced. The reaction is as follows: [21, 22]

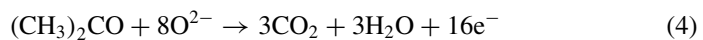
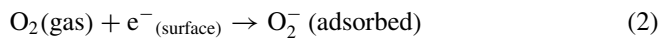


**Fig. 3** **a** Response versus acetone gas concentration for sensors S1 and S2 at 150 °C temperature. **b** Response versus acetone gas concentration for sensors S1 and S2 at 200 °C temperature. **c** Response versus acetone gas concentration for sensors S1 and S2 at 250 °C temperature. **d** Response versus propanol gas concentration for sensors S1 and S2 at 150 °C temperature. **e** Response versus propanol gas concentration for sensors S1 and S2 at 200 °C temperature. **f** Response versus propanol gas concentration for sensors S1 and S2 at 250 °C temperature. **g** Comparative response of acetone and propanol gas for sensor S2 at 250 °C fixed temperatures

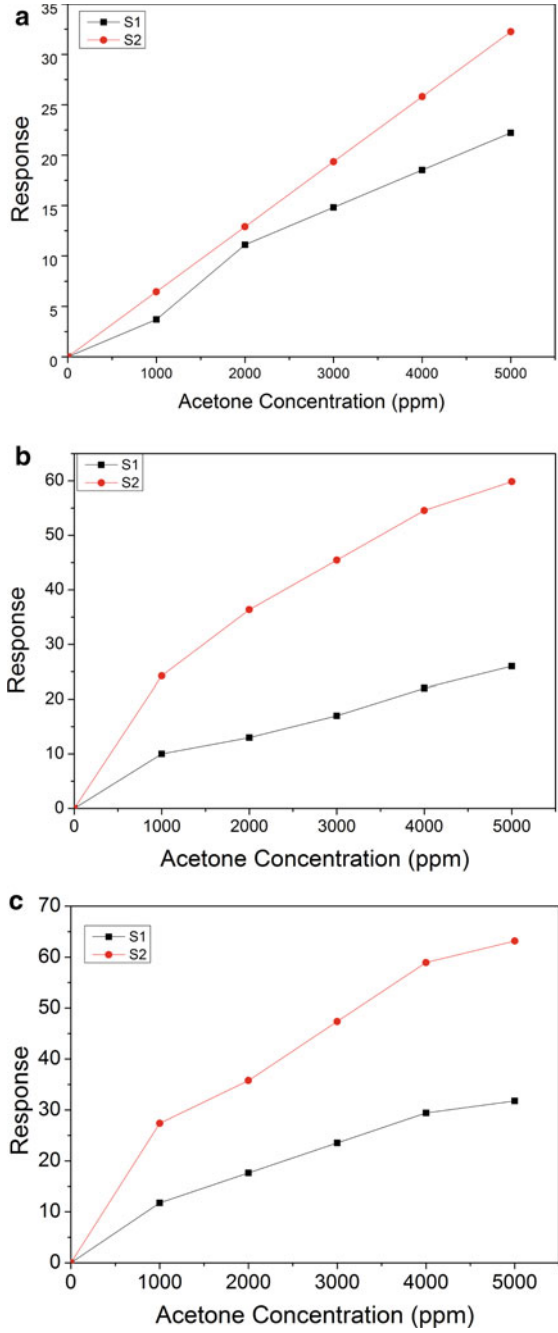


Fig. 3 (continued)

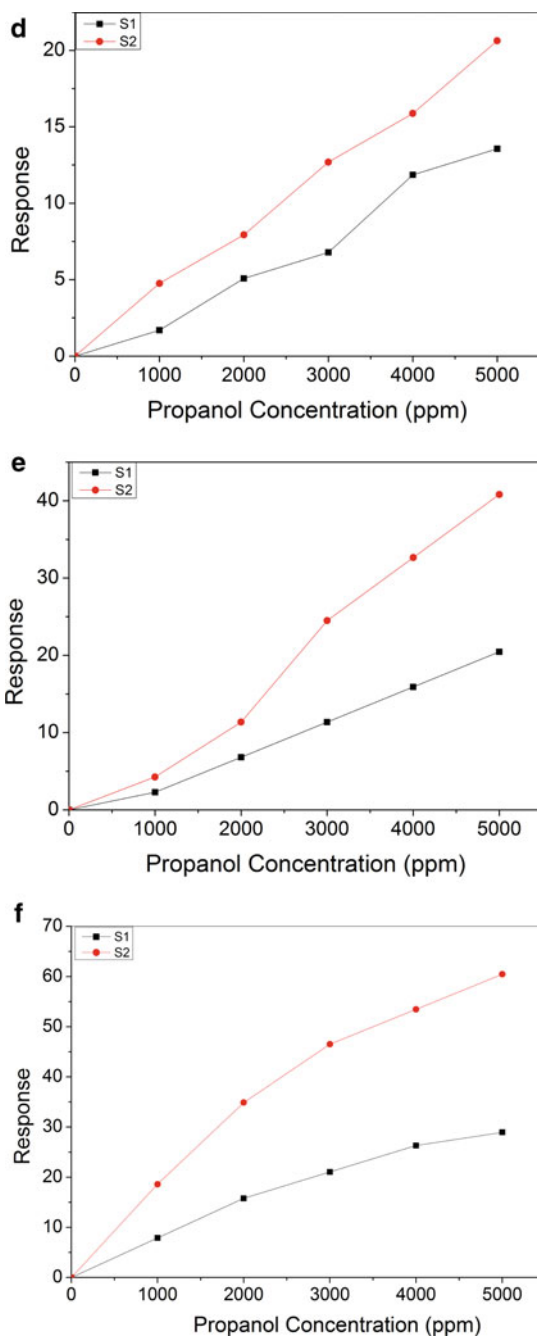
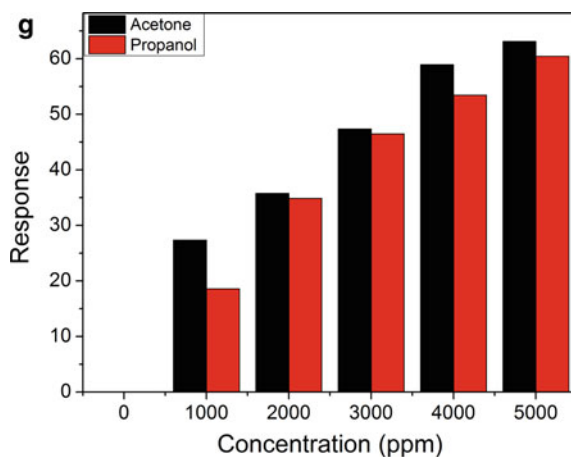




Fig. 3 (continued)



**Table 1** Sensing response value for sensors S1 and S2 for acetone and propanol gas for 5000 ppm at temperature 250 °C

Target gas	S1	S2
Acetone	31.76	63.15
Propanol	28.95	60.46

## 4 Conclusion

The structural and sensing behavior of undoped SnO<sub>2</sub> (S1) and 5 wt% Sb<sub>2</sub>O<sub>3</sub>-doped SnO<sub>2</sub> (S2) thick film gas sensor is examined. XRD measurement reveals that crystallite size is found to be 29.51 and 27.09 nm for sensors S1 and S2. The average crystallite size decreases with the Sb<sub>2</sub>O<sub>3</sub>-doping contents. The response of sensors (S1 and S2) is observed for acetone and propanol gas with varying concentration (0–5000 ppm) at different fixed temperatures (150, 200, and 250 °C). We concluded that the sensor S2 has exhibited maximum response (~ 63.15) for acetone gas for 5000 ppm at temperature 250 °C which is 1.04 times more than propanol gas. Thus, the present paper demonstrates that Sb<sub>2</sub>O<sub>3</sub> (5 wt%) doped SnO<sub>2</sub> sensor is a suitable detector for acetone gas.

## References

1. Mude BM, Mude KM, Raulkar KB, Zade RN, Yenorkar SM, Yawale SP (2017) Study of CO<sub>2</sub> gas detection by multilayer SnO<sub>2</sub>–ZnO–PPy sensor. *Int Res J Sci Eng Spec Issue A1*:143–148
2. Degler D, de Carvalho HWP, Kvashnina K, Grunwaldt J-D, Weimar U, Barsan N (2016) Structure and chemistry of surface-doped Pt: SnO<sub>2</sub> gas sensing material. *Roy Soc Chem Adv* 6:28149–28155
3. Yawale SP, Yawale SS, Lamdhade GT (2007) Tin oxide and zinc oxide based doped humidity. *Sens Actuators A* 135:388–393

4. Soussi L, Garmim T, Karzazi O, Rmili A, El Bachiri A, Louardi A, Erguig H (2020) Effect of (Co, Fe, Ni) doping on structural, optical and electrical properties of sprayed SnO<sub>2</sub> thin film. *Surf Interfaces* 19:100467
5. Wang J, Li D, Xu C, Yuan X, Yang P (2020) Numerical study on photoelectric characteristics of Mo-doped SnO<sub>2</sub>. *Superlattices Microstruct* 138:106387
6. Liu Z, Yang P (2017) Optoelectronic performances on different structures of Al-doped ZnO. *J Am Ceram Soc*. <https://doi.org/10.1111/jace.15818>,1-12
7. Kim H, Pique A (2004) Transparent conducting Sb-doped SnO<sub>2</sub> thin films grown by pulsed-laser deposition. *Appl Phys Lett* 84:218
8. Kim GW, Park KY, Anwar MS, Seo YJ, Sung CH, Koo BH (2012) Preparation and properties of Sb<sub>2</sub>O<sub>3</sub>-doped SnO<sub>2</sub> thin films deposited by using PLD. *J Korean Phys Soc* 60:1548–1551
9. Ahmad T, Ansari MZ (2022) Enhancement of infrared shielding property of SnO<sub>2</sub> using Sb as a dopant. *Mater Res Express* 9:105902
10. Feng Z, Gaiardo A, Valt M, Fabbri B, Casotti D, Krik S, Vanzetti L, Ciana MD, Fioravanti S, Caramori S, Rota A, Guidi V (2022) Investigation on sensing performance of highly doped Sb/SnO<sub>2</sub>. *Sensors* 22:1233
11. Gupta S, Yadav BC, Dwivedi PK, Das B (2013) Structural/microstructural, optical and electrical investigations of Sb–SnO<sub>2</sub> thin films deposited by spray pyrolysis. *Mater Res Bull* 48(9):3315–3322
12. Saadeddin I, Pecquenard B, Manaud JP, Decourt R, Labrugere C, Buffeteau T, Campet G (2007) Synthesis and characterization of single and Co-doped SnO<sub>2</sub> thin films for optoelectronic applications. *Appl Surf Sci* 253:5240–5249
13. Jariwala C, Dhivya M, Rane R, Chauhan N, Rayjada PA, Raole PM, John PI (2013) Preparation and characterization of antimony doped tin oxide thin films synthesized by co-evaporation of Sn and Sb using plasma assisted thermal evaporation. *J Nano Electron Phys* 5:02029
14. Haddad N, Ben Ayadi Z, Mahdhi H, Djessas K (2017) Influence of fluorine doping on the microstructure, optical and electrical properties of SnO<sub>2</sub> nanoparticles. *J Mater Sci Mater Electron* 28:15457–15465
15. Lavanya N, Sekar C, Fazio E, Neri F, Leonardi SG, Neri G (2017) Development of a selective hydrogen leak sensor based on chemically doped SnO<sub>2</sub> for automotive applications. *Int J Hydrogen Energy* 42:10645–10655
16. Vishwakarma AK, Yadava L (2018) Fabrication and characterization of CdS doped ZnO nano thick films. *Vacuum* 155:214–218
17. Sharma AK, Vishwakarma AK, Yadava L (2021) Sensing and structural characteristics of TiO<sub>2</sub> thick film for LPG sensor. *Mater Today Proc* 38:2123–2126
18. Vishwakarma AK, Majid SS, Yadava L (2019) XANES analysis and structural properties of CdS-doped TiO<sub>2</sub>. *Vacuum* 165:239–245
19. Yadava L, Verma R, Dwivedi R (2010) Sensing properties of CdS-doped tin oxide thick film gas sensor. *Sens Actuators B* 144:37–42
20. Vishwakarma AK, Yadava L (2018) Structural and sensing characteristics of CdS-TiO<sub>2</sub> film as LPG sensor at room temperature. *Asian Reson* 7:46–49
21. Vishwakarma AK, Yadav N, Yadava L (2019) Detection of toluene using CdS-TiO<sub>2</sub> thin film gas sensor. *Sens Lett* 17:1–3
22. Shankar P, Rayappan JBB (2015) Gas sensing mechanism of metal oxides: the role of ambient atmosphere, type of semiconductor and gases—a review. *Sci Lett J* 4:126

# Synthesis and Characterization of Highly Luminescent and Stable Cesium Lead Halide Perovskite Nanocrystals for Optoelectronic Applications



Sultan Ahmad, Mohd. Bilal Khan, Mohammad Salman Khan, Hasan Abbas, Ankur Mishra, Reeba Marry Thomas, Asim Khan, and Zishan Husain Khan

**Abstract** High-quality CsPbI<sub>2</sub>Br perovskite nanocrystals (PNCs) have been successfully synthesized using a direct probe sonication method in the presence of organic capping molecules, without the use of polar solvents. This method is simple, scalable, and achieved in a single step. From the transmission electron microscopy (TEM), it is found that the morphology of the CsPbI<sub>2</sub>Br perovskite nanocrystals (PNCs) is cubic with average crystal size range 10–15 nm. Further, presence of Cs, Pb, I, and Br in CsPbI<sub>2</sub>Br PNCs has been confirmed by energy dispersive X-ray spectroscopy (EDAX). X-ray diffraction (XRD) study also reveals cubic nature of CsPbI<sub>2</sub>Br (PNCs). Additionally, UV–Vis spectroscopic study of CsPbI<sub>2</sub>Br (PNCs) shows optical absorption in the visible range, with an optical bandgap of 1.91 eV. A broad emission peak of CsPbI<sub>2</sub>Br PNCs is observed around 645 nm. This method provides a promising route for single step, facile and cost effective synthesis of stable and highly luminescent CsPbI<sub>2</sub>Br PNCs in ambient atmosphere.

**Keywords** Perovskite · Perovskite nanocrystals · Perovskite solar cells · Nanocrystals

## 1 Introduction

Hybrid lead halide perovskites have gained peculiar attention in the research community due to their exceptional optoelectronic properties, low cost, and ability to be processed using solution-based techniques in the field of solar cells, photodetectors, light emitting diodes, and lasers [1, 2] After achieving significant progress in bulk perovskite materials, researchers have extended their investigations to the

---

S. Ahmad · Mohd. B. Khan · M. S. Khan · H. Abbas · A. Mishra · R. M. Thomas · A. Khan · Z. H. Khan (✉)

Department of Applied Sciences and Humanities, Faculty of Engineering and Technology, Jamia Millia Islamia, New Delhi, India  
e-mail: [Zishanhk@jmi.ac.in](mailto:Zishanhk@jmi.ac.in)

nanoscale level in the field of metal halide perovskites [1–3]. Perovskite nanocrystals (PNCs) have attracted a lot of attention due to their distinctive properties such as tunable bandgaps, narrow emission, and strong light-absorption coefficients that result from the combination of excellent optoelectronic properties of bulk perovskite materials, and the quantum confinement effects seen in nanoscale materials [4]. The researchers first focused on developing nanocrystals (NCs) of organic/inorganic hybrid perovskites and later moved on to synthesizing NCs of purely inorganic cesium-based perovskites [5, 6]. At present, there are only a few reports on the synthesis of  $\text{CsPbX}_3$  ( $X = \text{Br, I, Cl}$ ) PNCs. High-temperature hot injection is mostly used method for synthesizing  $\text{CsPbX}_3$  PNCs [7]. The hot-injection method, while is effectively in producing  $\text{CsPbX}_3$  PNCs with high PLQYs, is often considered a tedious process that usually requires an inert atmosphere. Sun et al. reported a method for synthesis of  $\text{CsPbX}_3$  PNCs at room temperature [8]. This method, however, needs a pre-synthesized cesium precursor solution at higher temperatures in an inert atmosphere. Although room temperature syntheses are generally simpler, they tend to produce nanocrystalline morphology with relatively lower PLQYs [8].

In this work, we present a single-step probe sonication method which does not require polar solvents for the synthesis of  $\text{CsPbI}_2\text{Br}$  PNCs. This method involves mixing the appropriate precursor powders such as  $\text{Cs}_2\text{CO}_3$ ,  $\text{PbI}_2$ , and  $\text{PbBr}_2$ , along with capping ligands such as oleylamine and oleic acid in a nonpolar solvent (mineral oil) in ambient atmospheric conditions. Through this approach, the use of sonication triggers the creation of a complex between cesium and oleate, which is soluble in nonpolar solvents. This complex reacts with  $\text{PbI}_2$  and  $\text{PbBr}_2$  to produce colloidal  $\text{CsPbI}_2\text{Br}$  PNCs in the presence of oleylamine and oleic acid.

## 2 Materials and Methods

### 2.1 Materials

All the chemicals used in the synthesis process, namely  $\text{Cs}_2\text{CO}_3$  (99% purity cesium carbonate),  $\text{PbI}_2$  (99% purity lead(II) iodide),  $\text{PbBr}_2$  (99% purity lead(II) bromide), mineral oil (light), oleic acid (90%, technical grade), hexane ( $\geq 97.0\%$  purity HPLC grade, GC), and oleylamine (70%, technical grade), were procured from Thermo Fisher Scientific and used without any further purification.

### 2.2 Synthesis of $\text{CsPbI}_2\text{Br}$ Perovskite Nanocrystals (PNCs)

$\text{CsPbI}_2\text{Br}$  PNCs were synthesized using a one-step probe sonication method. For the synthesis of  $\text{CsPbI}_2\text{Br}$  PNCs, 0.1 mmol of  $\text{Cs}_2\text{CO}_3$ , 0.2 mmol of  $\text{PbI}_2$  and 0.1 mmol

of  $\text{PbBr}_2$  precursor powders were mixed with 10 ml of mineral oil, 0.5 ml of oleylamine, and 0.5 ml of oleic acid using probe sonication at a 30-W power for 10 min. After applying the probe sonication, the reaction colour turned into an “Orange Red” colour from a colourless mixture which is indicating the formation of perovskite nanocrystals. The resulting nanocrystal dispersions were purified by centrifugation at 9000 rpm for 10 min to eliminate the impurities, followed by redispersion of the nanocrystal precipitates in 5 ml of hexane using mild sonication. Further, centrifugation at 2000 rpm was used to eliminate any large nanocrystals, resulting in highly luminescent and stable  $\text{CsPbI}_2\text{Br}$  PNCs.

### 2.3 Characterization

To study the properties of the as-synthesized  $\text{CsPbI}_2\text{Br}$  PNCs, various characterization techniques were employed. The morphology of the  $\text{CsPbI}_2\text{Br}$  PNCs was examined using TEM (Technai, F30 S-Twin). The X-ray diffraction pattern of the  $\text{CsPbI}_2\text{Br}$  PNCs thin film was obtained at room temperature using X-ray diffractometer (Rigaku Smart-Lab). Optical absorption and photoluminescence studies of  $\text{CsPbI}_2\text{Br}$  PNCs were conducted using UV–visible spectroscopy (Perkin Elmer-Lambda 850+) and photoluminescence spectrophotometry (Shimadzu-RF5301PC), respectively.

## 3 Results and Discussions

The morphology of as-synthesized  $\text{CsPbI}_2\text{Br}$  perovskite nanocrystals (PNCs) is studied using transmission electron microscopy (TEM). It is revealed that as-synthesized  $\text{CsPbI}_2\text{Br}$  PNCs show well defined cubic shapes as presented in Fig. 1. The average crystal size of  $\text{CsPbI}_2\text{Br}$  PNCs is calculated from ImageJ software in the range of 10–15 nm. Further, Cs, Pb, I, and Br are presented in the  $\text{CsPbI}_2\text{Br}$  PNCs which has been confirmed by energy-dispersive X-ray spectroscopy (EDX) mapping as shown in Fig. 2.

The X-ray diffraction pattern of as-synthesized perovskite  $\text{CsPbI}_2\text{Br}$  PNCs film is shown in Fig. 3. The XRD pattern of  $\text{CsPbI}_2\text{Br}$  PNCs films presents the peaks located at different  $2\theta$  values such as  $14.95^\circ$  (100),  $20.9^\circ$  (110),  $25.55^\circ$  (111),  $29.41^\circ$  (200),  $32.54^\circ$  (210), and  $34.90^\circ$  (211) which is in agreement with the literature [9]. The lattice parameter corresponding to  $2\theta$  value  $14.75^\circ$ ,  $20.9^\circ$ , and  $25.65^\circ$  is calculated as  $a = 5.95 \text{ \AA}$ ,  $b = 6.03 \text{ \AA}$  and  $c = 6.01 \text{ \AA}$ , respectively. The calculated value of lattice parameters is approximately equal to that of cubic crystals, which further confirms the formation of  $\alpha$ -cubic crystal.

Figure 4 shows UV–Vis absorption spectra of  $\text{CsPbI}_2\text{Br}$  PNCs which agrees with that of reported results [9].  $\text{CsPbI}_2\text{Br}$  perovskite NCs cover the entire visible range from 450 to 700 nm. The optical band gap of the  $\text{CsPbI}_2\text{Br}$  PNCs is calculated from the Tauc plot, which is about to 1.91 eV [10].

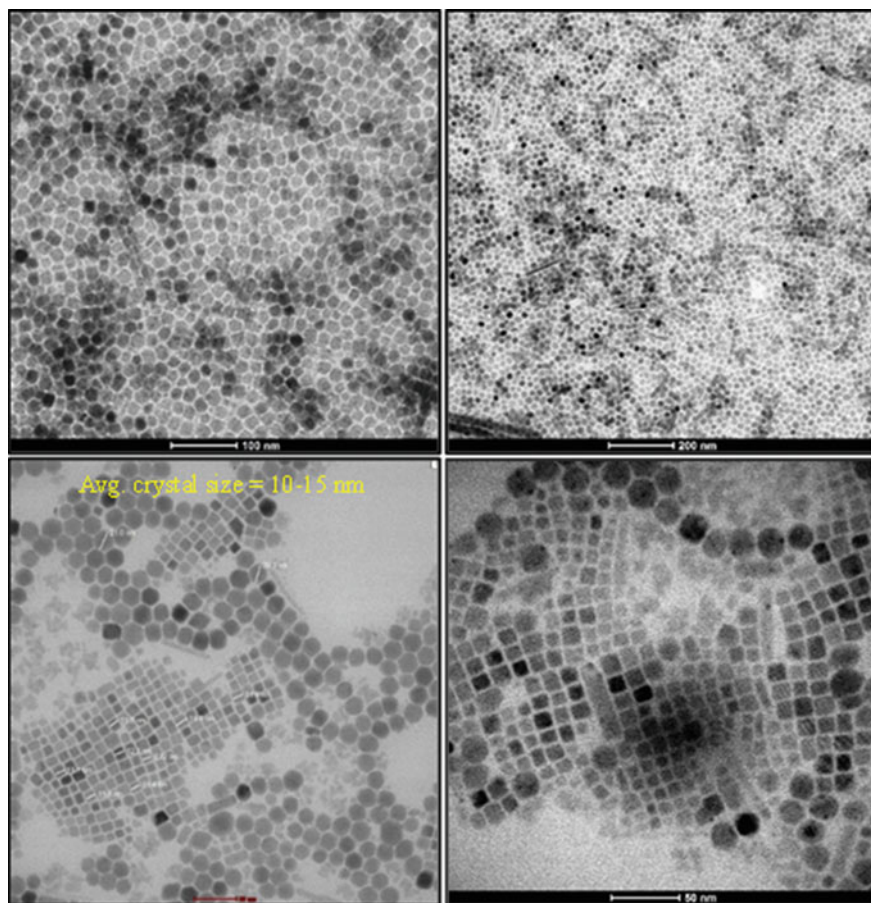


**Fig. 1** TEM images of CsPbI<sub>2</sub>Br perovskite nanocrystals (PNCs)

PL emission spectra of CsPbI<sub>2</sub>Br PNCs are presented in Fig. 5. A broad emission peak centred around 640 nm is observed when CsPbI<sub>2</sub>Br PNCs are excited by 460 nm. The emission peak at 640 nm (1.93 eV) is attributed to CsPbI<sub>2</sub>Br PNCs, which is in the red region of the visible spectrum suggesting the radiative recombination of electrons and holes in the bandgap region [9, 10]. Further, it is found that PLQYs of the CsPbI<sub>2</sub>Br PNCs are calculated to be 80%. The photoluminescence study of CsPbI<sub>2</sub>Br nanocrystals suggests that they have potential applications in the upcoming flexible perovskite solar cells technology.

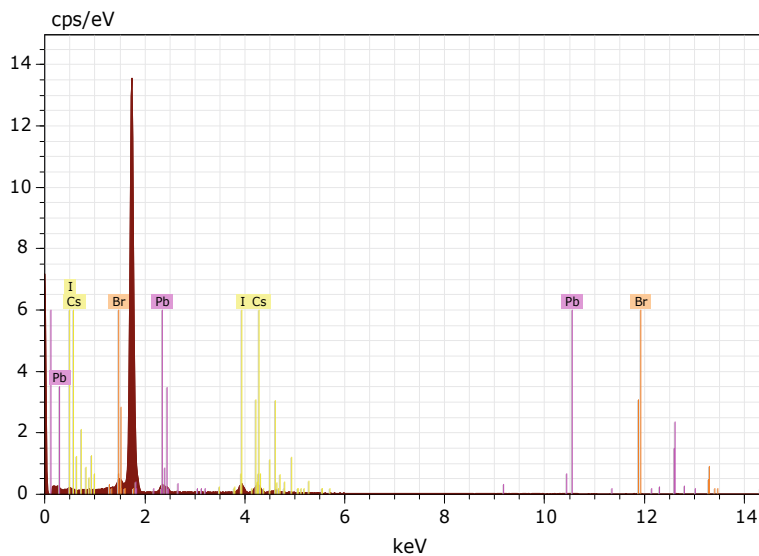


Fig. 2 EDAX spectra of CsPbI<sub>2</sub>Br perovskite nanocrystals (PNCs) film on Si substrate

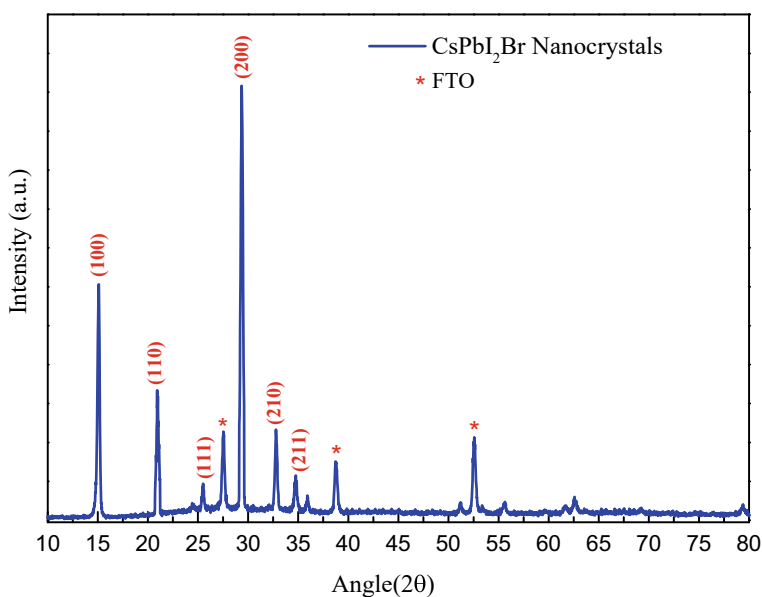
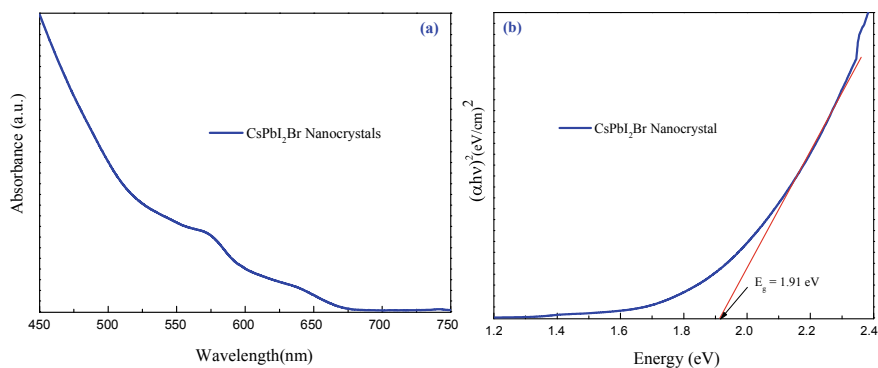
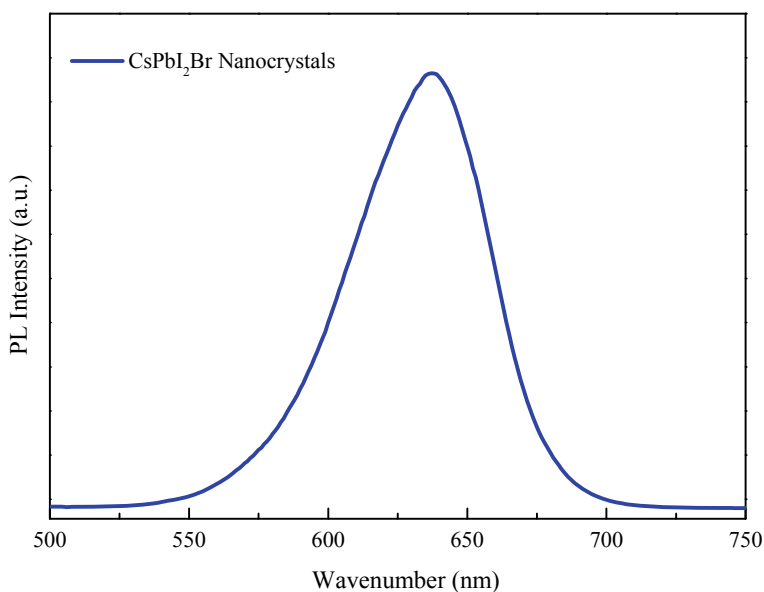


Fig. 3 XRD spectra of CsPbI<sub>2</sub>Br nanocrystals film on FTO substrate



**Fig. 4** **a** Uv–Vis absorption spectra, **b** Tau's plot of CsPbI<sub>2</sub>Br nanocrystals



**Fig. 5** Photoluminescence (PL) spectra of CsPbI<sub>2</sub>Br nanocrystals

## 4 Conclusion

On the basis of above results, it is concluded that the highly luminescent and stable CsPbI<sub>2</sub>Br perovskite nanocrystals (PNCs) have been successfully synthesized using a novel approach. These perovskite nanocrystals showed PLQYs of 80%. The morphology of these perovskite nanocrystals was found to be cubic, which



was further confirmed using XRD data. The optical band gap of these perovskite nanocrystals was 1.91 eV on the basis of UV–Vis absorption spectra. The PL spectra show broad emission peaks centred around 640 nm and which suggests radiative recombination of electron and holes in band gap region.

**Acknowledgements** One of the Author, Mohd. Bilal Khan expresses gratitude towards CSIR, Govt. of India for their support in the form of a Research Associateship (File No. 09/0466(11082)/2021-EMR-I).

**Conflict of Interest** The authors declare that they have no conflict of interest.

## References

1. Ahmad S, Abbas H, Khan MB, Nagal V, Hafiz AK, Khan ZH (2021) ZnO for stable and efficient perovskite bulk heterojunction solar cell fabricated under ambient atmosphere. *Sol Energy* 216:164–170
2. Schmidt LC, Pertegás A, González-Carrero S, Malinkiewicz O, Agouram S, Minguez Espalargas G et al (2014) Nontemplate synthesis of  $\text{CH}_3\text{NH}_3\text{PbBr}_3$  perovskite nanoparticles. *J Am Chem Soc* 136(3):850–853
3. Gallardo JJ, Blanco E, Sanchez-Coronilla A, Pinero JC, Navas J (2020) Tuning the structural, optical and photoluminescence properties of hybrid perovskite quantum dots by A-site doping. *Appl Mater Today* 18:100488
4. De Roo J, Ibáñez M, Geiregat P, Nedelcu G, Walravens W, Maes J et al (2016) Highly dynamic ligand binding and light absorption coefficient of cesium lead bromide perovskite nanocrystals. *ACS Nano* 10(2):2071–2081
5. Gao L, Zeng K, Guo J, Ge C, Du J, Zhao Y et al (2016) Passivated single-crystalline  $\text{CH}_3\text{NH}_3\text{PbI}_3$  nanowire photodetector with high detectivity and polarization sensitivity. *Nano Lett* 16(12):7446–7454
6. Shamsi J, Urban AS, Imran M, De Trizio L, Manna L (2019) Metal halide perovskite nanocrystals: synthesis, post-synthesis modifications, and their optical properties. *Chem Rev* 119(5):3296–3348
7. Bekenstein Y, Koscher BA, Eaton SW, Yang P, Alivisatos AP (2015) Highly luminescent colloidal nanoplates of perovskite cesium lead halide and their oriented assemblies. *J Am Chem Soc* 137(51):16008–16011
8. Sun S, Yuan D, Xu Y, Wang A, Deng Z (2016) Ligand-mediated synthesis of shape-controlled cesium lead halide perovskite nanocrystals via reprecipitation process at room temperature. *ACS Nano* 10(3):3648–3657
9. Zeng Z, Zhang J, Gan X, Sun H, Shang M, Hou D et al (2018) In situ grain boundary functionalization for stable and efficient inorganic  $\text{CsPbI}_2\text{Br}$  perovskite solar cells. *Adv Energy Mater* 8(25):1801050
10. Atourki L, Bernabé M, Makha M, Bouabid K, Regragui M, Ihlal A et al (2021) Effect of doping on the phase stability and photophysical properties of  $\text{CsPbI}_2\text{Br}$  perovskite thin films. *RSC Adv* 11(3):1440–1449

# Facile Synthesis of Lead-Free Mixed Halide Double Perovskite $\text{Cs}_2\text{AgBiX}_6$ ( $\text{X} = \text{Br, I}$ ) Nanocrystals (NCs) for Photovoltaics Applications



Mohammad Salman Khan, Mohd. Bilal Khan, Sultan Ahmad, Hasan Abbas, Asim Khan, Ankur Mishra, Reeba Marry Thomas, and Zishan Husain Khan

**Abstract** Cesium-based lead-free perovskites are promising alternatives to the organic–inorganic lead perovskites due to lead toxicity and moisture/oxygen sensitivity of the latter. Perovskites can be synthesized in the form of single perovskite structures having the general formula  $(\text{ABX}_3)$  as well as double perovskite structures with the formula  $(\text{A}_2\text{B}^{\text{I}}\text{B}^{\text{III}}\text{X}_6)$ . Double perovskites structures have several advantages over single perovskite structures in terms of phase stability. Ag and Bi-based Cs halide double perovskites ( $\text{Cs}_2\text{AgBiX}_6$ ) are significantly promising among different double perovskite structures. The theoretical predictions have shown that the  $\text{Cs}_2\text{AgBiI}_6$  has the most suitable optoelectronic characteristics among their bromide and chloride counterparts. Experimentally, the synthesis of  $\text{Cs}_2\text{AgBiI}_6$  is challenging due to the formation of thermodynamically more stable  $\text{Cs}_2\text{Bi}_2\text{I}_9$ . On the other hand,  $\text{Cs}_2\text{AgBiBr}_6$  is a stable composition, but it is undesirable in solar cell applications due to its larger bandgap. In the present work, we report the facile synthesis and characterization of stable mixed halide  $\text{Cs}_2\text{AgBiX}_6$  ( $\text{X} = \text{Br, I}$ ) nanocrystals which show better stability than  $\text{Cs}_2\text{AgBiI}_6$  and have smaller band gap in comparison with that of  $\text{Cs}_2\text{AgBiBr}_6$ .

**Keywords** Double perovskite · Mixed-halide · Lead-free · Nanocrystals (NCs) · Phase stability · Photovoltaics

---

M. S. Khan · Mohd. B. Khan · S. Ahmad · H. Abbas · A. Khan · A. Mishra · R. M. Thomas · Z. H. Khan (✉)

Organic Electronics and Nanotechnology Research Laboratory, Department of Applied Sciences and Humanities, Faculty of Engineering and Technology, Jamia Millia Islamia, New Delhi 110025, India  
e-mail: [Zishanhk70@gmail.com](mailto:Zishanhk70@gmail.com)

## 1 Introduction

Lead (Pb) halide perovskites, with the generic chemical formula  $ABX_3$ , have received a lot of attention from both the scientific and industrial communities. Here, A is a  $CH_3NH_3^+$  ( $MA^+$ ),  $CH(NH_2)_2^+$  ( $FA^+$ ), or  $Cs^+$  cation, B is a  $Pb^{2+}$  cation, and X is a  $Cl^-$ ,  $Br^-$ , or  $I^-$  anion [1, 2]. The remarkable 3D perovskite structure that includes a  $ns^2$  electronic structure at the outermost orbital and higher-quality charge carrier characteristics such as better carrier mobility and relaxed carrier without traps, accounts for the excellent optical features of the lead-based perovskite NCs. However, Pb toxicity is frequently seen as a drawback, which motivates researchers to identify alternative substitutes. Recently, lead-free perovskite NCs have been reported by using non-hazardous metal ions in place of  $Pb^{2+}$  in the perovskite structures [3]. The 3D double perovskites  $AB^I B^{III} X_6$  (A: Cs,  $CH_3NH_3$ ;  $B^I$ : Ag, Au;  $B^{III}$ : Bi, In; X: Cl, Br, I) have been shown to be synthesized by substitution of one monovalent  $B^+$  and one trivalent  $B^{3+}$  cation for the  $Pb^{2+}$  cation. Lead-free double perovskites exhibit attractive optical and electrical characteristics, such as  $Cs_2AgBiBr_6$  [4]. The key factor limiting  $Cs_2AgBiBr_6$  photovoltaic performance is its large band gap. On the other hand,  $Cs_2AgBiI_6$  shows suitable bandgap but lacks stability [4]. It is highly desirable to develop effective approaches to synthesize the stable lead-free double perovskite compositions having suitable bandgap for solar cell applications. In this direction, several efforts have been made to modify the structure and to improve the photovoltaic characteristics. For instance, the bandgap of  $Cs_2AgBiBr_6$  has been successfully reduced from 2.12 to 1.86 eV via Sb impurity doping which has been attributed to the upshifting of valence band maximum resulting in the narrowing of bandgap due to higher energy levels of Sb 5 s states when compared with those of 6 s states [5, 6]. Synthesis of mixed halide compositions is another strategy which can be used to obtain stable Pb-free double perovskite compositions by suitably optimizing the ratio of halide ions in the compositions [5–7]. Traditionally, mixed halide compositions are synthesized using ion exchange method which is a complex multistep method not suitable for bulk synthesis [6, 7]. Herein, we report the facile one step synthesis and characterization of mixed halide (I/Br) double perovskite ( $Cs_2AgBiX_6$ : X = Br, I) nanocrystals.

## 2 Materials and Methods

### 2.1 Materials

All the chemicals used in the synthesis process, namely  $Cs_2CO_3$  (99% purity cesium carbonate), AgBr (99% purity silver(I) bromide),  $BiI_3$  (99% purity bismuth(III) iodide), mineral oil (light), oleic acid (90%, technical grade), oleylamine (70%, technical grade), and hexane ( $\geq 97.0\%$  purity HPLC grade, GC), were procured

from Thermo-Fisher Scientific and handled without going through extra purifying procedures.

## 2.2 *Facile Synthesis of Mixed Halide Double Perovskite Nanocrystals (DPNCs)*

The production of double perovskite nanocrystals (DPNCs) was made possible by the use of a facile synthesis approach. For the synthesis of  $\text{Cs}_2\text{AgBiX}_6$  ( $X = \text{Br}, \text{I}$ ), mixed halide DPNCs 0.1 mmol of  $\text{Cs}_2\text{CO}_3$ , 0.1 mmol of  $\text{AgBr}$ , and 0.4/0.5 mmol (for two different compositions) of  $\text{BiI}_3$  were mixed with 500  $\mu\text{L}$  of oleic acid, 500  $\mu\text{L}$  of oleyl amine and 10 ml of mineral oil and subjected to using probe sonication at the power of 60-W for 12 min until the initially colorless solution turned into red colored. At this stage the reaction flask was rapidly cooled down in an ice bath. The as-synthesized crude solution was centrifuged at 8000 rpm for 10 min to eliminate the impurities, followed by redispersion of the precipitates in 5 ml of hexane using mild sonication. Further centrifugation at 2000 rpm was used to eliminate any large crystals resulting and to achieve supernatant having well dispersed double perovskite nanocrystals.

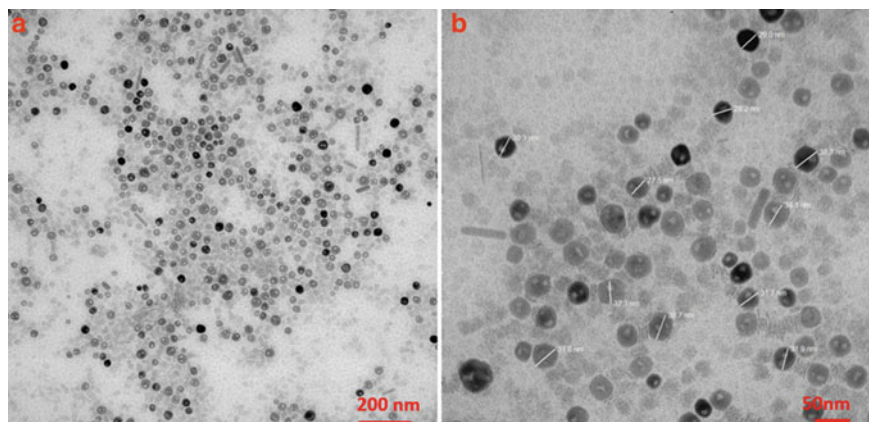
## 2.3 *Characterization*

To study the structural and optical properties of the as-synthesized double perovskite nanocrystals (DPNCs), various characterization techniques were employed. The morphology of the DPNCs was analyzed using TEM (Technai, F30 S-Twin). The x-ray diffraction pattern of the DNCs thin film was obtained at room temperature using x-ray diffractometer (Rigaku Smart-Lab). Optical absorption and photoluminescence studies of DPNCs were conducted using UV-visible spectroscopy (Perkin Elmer-Lambda 365<sup>+</sup>) and photoluminescence spectrophotometry (Shimadzu-RF-5301PC), respectively.

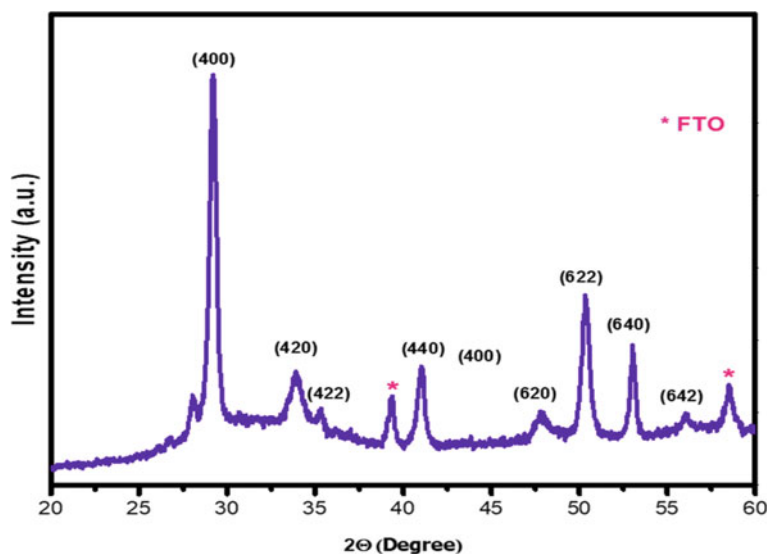
## 3 **Results and Discussion**

Figure 1a depicts a typical low magnification TEM image of pure double perovskite nanocrystals (DPNCs). It shows a narrow size distribution within the range of 15–30 nm. The well-dispersed DPNCs without any indication of aggregation are clearly apparent in the high magnification TEM image (Fig. 1b).

X-ray diffraction pattern of as-synthesized mixed halide double perovskite nanocrystal sample are shown in Fig. 2. In this double perovskite structure  $\text{AgBr}(\text{I})_6$ ,



**Fig. 1** TEM micrograph of purified DPNCs **a** Low-magnification **b** High-magnification TEM micrograph shows cubic shapes of NCs



**Fig. 2** XRD pattern of  $\text{Cs}_2\text{AgBiX}_6$  ( $X = \text{Br, I}$ ) mixed halide double perovskite nanocrystals

$\text{BiBr}(\text{I})_6$  octahedrons are alternatively connected by sharing bridged  $\text{Br}^-$  ( $\text{I}^-$ ) ions. The XRD pattern of  $\text{Cs}_2\text{AgBiX}_6$  ( $X = \text{Br, I}$ ) depicts the peaks located at  $2\theta$  values of  $29.24^\circ$ ,  $33.92^\circ$ ,  $35.26^\circ$ ,  $40.94^\circ$ ,  $47.82^\circ$ ,  $50.38^\circ$ ,  $53.06^\circ$ , and  $58.52^\circ$ , which can be indexed to (400), (420), (422), (440), (620), (622), (640), and (642) planes, respectively [7]. All the members of the compositional family  $\text{Cs}_2\text{AgBiX}_6$  show XRD peak positions very close to each other. However, these peak positions shift toward lower 2-theta values when one moves from  $\text{Cl}^-$  containing compositions to  $\text{I}^-$  containing

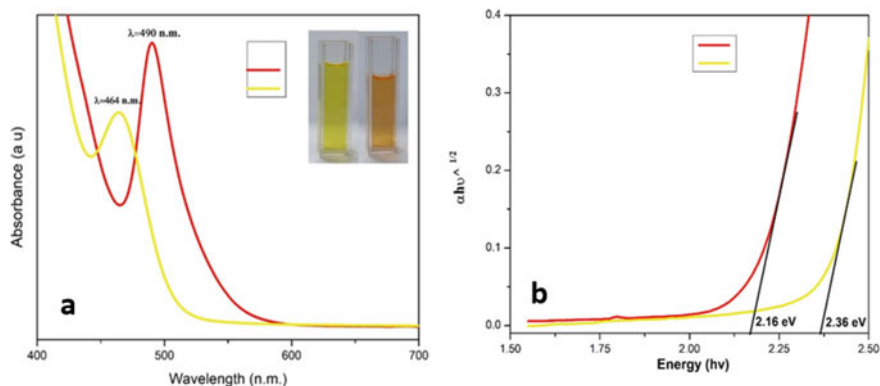


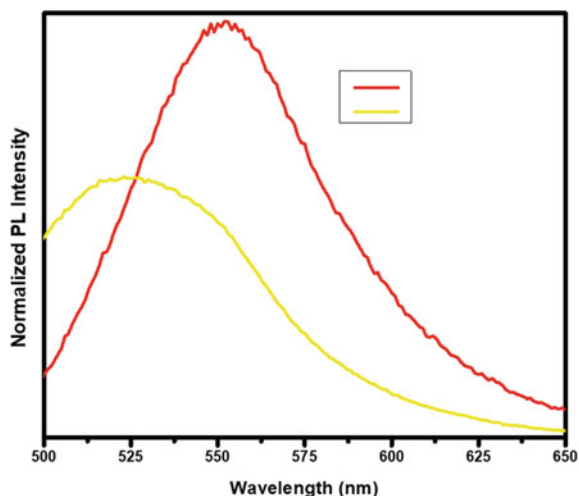
**Fig. 3** **a** UV-vis. absorption spectra. **b** Tau's plot (indirect bandgap) of DPNCs

compositions due to increase in the size of halogen ions [8]. For instance, diffraction peak corresponding to (400) plane of  $\text{Cs}_2\text{AgBiBr}_6$  occurs at  $31.14^\circ$ , while for  $\text{Cs}_2\text{AgBiI}_6$  it occurs at  $29.15^\circ$  [7]. In the present structure XRD peak for (400) plane appears at  $29.24^\circ$ , which is a clear indication of the successful synthesis of mixed halide  $\text{Cs}_2\text{AgBiX}_6$  nanocrystals containing  $\text{I}^-$  and  $\text{Br}^-$  ions.

Figure 3a shows the UV-vis absorption spectra of as-synthesized  $\text{Cs}_2\text{AgBiX}_6$  nanocrystals having different  $\text{I}^-$  content. With the increase in the amount of iodine ions, the UV-vis absorption spectra of double perovskite nanocrystal structure bathochromically shifts from 464 to 490 nm (Fig. 3a) and the optical bandgap is reduced from 2.36 to 2.16 eV. The decrease in optical bandgap on the increase in iodine ions may be due to smaller gap between the bonding and antibonding states of  $\text{Pb}^{2+}-\text{I}^-$  hybridized orbitals in comparison with that of  $\text{Pb}^{2+}-\text{Br}^-$  hybridized orbitals [7, 8].

PL spectra have been used to evaluate the effect of increase in the iodine content on the luminescent properties of lead-free mixed halide double perovskite nanocrystals (Fig. 4) which shows that the lead-free mixed halide DPNCs  $\text{Cs}_2\text{AgBiX}_6$  ( $\text{X} = \text{Br}, \text{I}$ ) has relatively broad emission in comparison with the reference material  $\text{Cs}_2\text{AgBiX}_6$  NCs. With increase in iodine contents, the PL emission is red shift from 523 to 552 nm. This result is consistent with the results of the UV-visible spectra and can be seen as the result of bandgap narrowing on increase of the iodine content [8].

**Fig. 4** Normalized photoluminescence (PL) spectra of DPNCs



## 4 Conclusion

We demonstrated the facile synthesis of lead-free mixed halide DPNCs with enhanced chemical and colloidal stability. The optical bandgap of these DPNCs was found to decrease when compared with that reference  $\text{Cs}_2\text{AgBiX}_6$  NCs, which may be due to the introduction of iodine ions in the lattice as confirmed by UV-vis absorption spectra. PL emission spectra showed red-shifted broad emission. We believe that the protocols used in this work may further be extended to other double perovskite compositions to achieve higher chemical stability toward the development of high performing lead hazard-free perovskite solar cells.

**Acknowledgements** One of the authors (Mohd. Bilal Khan) expresses gratitude toward CSIR, Govt. of India for their support in the form of a Research Associateship (File No. 09/0466(11082)/2021-EMR-I).

**Conflict of Interest** The authors declare that they have no conflict of interest.

## References

1. Ahmad S, Abbas H, Khan MB, Nagal V, Hafiz AK, Khan ZH (2021) ZnO for stable and efficient perovskite bulk heterojunction solar cell fabricated under ambient atmosphere. *Sol Energy* 216:164–170
2. Abbas H, Ahmad S, Parvaz M, Khan MB, Khan MS, Khan A, Alshahrie A, Khan ZH (2022) Surface optimization of metal halide perovskite solar cells using ZnS nanorods. *J Mater Sci Mater Electr* 33(27):21576–21587

3. Abbas H, Khan MS, Ahmad S, Parvaz M, Khan MB, Khan A, Alshahrie A, Khan ZH (2022) Reduction of extrinsic defects in ZnSe: perovskite composites based solar devices. *J Nanopart Res* 24(12):270
4. Dave K, Fang MH, Bao Z, Fu HT, Liu RS (2020) recent developments in lead-free double Perovskites: structure, doping, and applications. *Chem Asian J* 15(2):242–252
5. Lei L-Z, Shi Z-F, Li Y, Ma Z-Z, Zhang F, Xu T-T, Tian Y-T, Wu D, Li X-J, Du G-T (2018) High-efficiency and air-stable photodetectors based on lead-free double perovskite Cs<sub>2</sub>AgBiBr<sub>6</sub> thin films. *J Mater Chem C* 6(30):7982–7988
6. Ji F, Klarbring J, Wang F, Ning W, Wang L, Yin C, Figueroa JSM et al (2020) Lead-free halide double Perovskite Cs<sub>2</sub>AgBiBr<sub>6</sub> with decreased band gap. *Angew Chem* 132(35):15303–15306
7. Wu H et al (2021) Mixed-halide double Perovskite Cs<sub>2</sub>AgBiX<sub>6</sub> (X= Br, I) with tunable optical properties via anion exchange. *Chemsuschem* 14(20):4507–4515
8. Zhang Y et al (2019) Surface science and colloidal stability of double-perovskite Cs<sub>2</sub>AgBiBr<sub>6</sub> nanocrystals and their superlattices. *Chem Mater* 31(19):7962–7969



# Integrating Energy Devices for Wearable Electronics



Sultan Ahmed, Ahsan Ahmed, M. Parvaz, Sultan Ahmad, M. A. Gondal,  
and Mukesh Pratap Singh

**Abstract** Due to fossil fuel usage and population growth, sustainable energy options are in high demand. The storage of these resources plays an important role for future generation electronics. Globally, the technologies helpful in converting solar energy and its storage are attracting enormous attention. Two devices, a solar cell/ photovoltaic cell and an electrochemical capacitor or supercapacitor, can be used to store solar energy. Photosupercapacitor (PSCs) are promising because they combine a solar energy converter with a supercapacitor (SC) in a single device. Research into PSCs is booming because of their potential use in portable and wearable electronics. They show great promise as a replacement for conventional energy sources and as generators for the future. Due to their low production cost, a wide range of applications, and multi-axial adaptability, flexible/fiber and planar photosupercapacitor are attracting a lot of attention. This article discusses in depth the various varieties of photosupercapacitor, including their design configuration, working mechanism, and fabrication. In conclusion, the difficulties arising in integration of the individual devices, preserving excellent cyclic stability, and increasing the specific capacitance, and future applications are discussed.

---

S. Ahmed (✉) · S. Ahmad · M. P. Singh

Department of Applied Sciences and Humanities, Faculty of Engineering and Technology, Jamia Millia Islamia, Delhi 110025, India

e-mail: [usmanisultan@gmail.com](mailto:usmanisultan@gmail.com); [usmanisultan@jmi.ac.in](mailto:usmanisultan@jmi.ac.in); [sultan.ahmed@kfupm.edu.sa](mailto:sultan.ahmed@kfupm.edu.sa)

A. Ahmed

Department of Information Technology, College of Computer and Information Sciences, Majmaah University, Al-Majmaah 11952, Saudi Arabia

M. Parvaz

Department of Applied Sciences and Humanities, G N Group of Institutes, Greater Noida, Uttar Pradesh 201310, India

S. Ahmed · M. A. Gondal

Physics Department, IRC-Hydrogen and Energy Storage, King Fahd University of Petroleum and Minerals, P.O. Box 5047, Dhahran 31261, Saudi Arabia

M. A. Gondal

K. A. CARE Energy Research and Innovation Center, King Fahd University of Petroleum and Minerals, Dhahran 31261, Saudi Arabia

**Keywords** Supercapacitor · Solar cell · Photosupercapacitor · Wearable electronics

## 1 Introduction

Electronics of the twenty-first century rely heavily on access to reliable sources of energy. Historically, fossil fuels provided the world's vitality. However, the continued use of fossil fuels has resulted in several problems, including resource depletion. In addition to this, it poses a threat to the natural environment. Therefore, preventing energy crises has been an ongoing concern. Recent years have seen a sharp rise in the need for carbon-free, economically viable energy sources that can be reliably produced from renewable materials [1]. Because of the abundance of sunlight, the modern world is concentrating its efforts on solar energy. Solar energy technology is now within the financial reach of every sector of society. As a result, researchers are putting in a lot of time and effort into finding better ways to store and use solar energy in a variety of applications [2]. The amount of solar radiation available on Earth to be harnessed for energy production is vast. Indirect methods include using ocean currents (waves and tides) and thermal convection (wind farms) to collect solar energy. Biological photosynthetic activities only use a tiny percentage of the abundant sun energy (~ 0.02%). Therefore, it is greatly desired that technologies be developed that can capture solar energy, convert it to a usable form of energy, and store it on a huge scale.

PSC stands for "photosupercapacitor," and it refers to a device that combines a solar cell, which is used for energy harvesting, and a supercapacitor, which is used for energy storage. The use of portable electronic gadgets and devices, as well as the changing global energy landscape, have led to the integration of these two technologies into a single device. PSCs have a shared electrode and need an appropriate storage source like batteries, capacitors, or a storage capacitor to function [3]. In its most basic form, a supercapacitor (SC) is a type of energy storage device that is notable for its high-power density as well as its ability to be rapidly charged and discharged. Therefore, it can be utilized for a wide range of industrial and home applications that deal with greater currents because of energy spikes or shutdowns.

Solar power-driven energy storage systems have attracted increasing interest in recent years as a means of improving the performance and efficiency of electrochemical capacitors. Photovoltaic devices, such as solar cells collect the sun's rays and convert them to electricity through a process called photovoltaic conversion [4]. The separation of light-harvesting and energy storage devices requires space and several interfaces, lowering electrochemical capacitor storage efficiency. Consequently, PSCs, which combine a light-harvesting system with energy storage, have been the subject of extensive study and development as a means of addressing this problem [4]. Due to their use of renewable energy sources, they are seen as viable technology for the next generation's energy storage system. PSCs play a crucial part in the efficient use of energy sources like solar energy, which helps to reduce reliance

on non-renewable energy sources. As a result of their adaptability to solar variations, portability, and pliability, these gadgets can meet the requirement for electronics of the future. As a result, PSCs are viewed as a useful tool in the growing field of energy storage systems.

## 2 Photosupercapacitor Components

### Solar Cells

Bell produced a crystalline solar cell that converts solar energy into electricity with an efficiency of 4.5%. Six decades of outstanding growth have resulted in a 24% increase in efficiency. The conversion efficiency of semiconductor layered materials-based second-generation thin film solar cells was 26.3% [5]. Even though the initial generations of solar cells work well, the third generation, which includes quantum dot sensitized solar cells (QDSSCs), dye-sensitized solar cells (DSSCs), and the new perovskite solar cells (PeSCs) has many advantages, such as being transparent, easy to make, light, and able to work well in low-light conditions while still having a high efficiency of more than 30% [6]. Figure 1 depicts the evolution of solar cells over time.

### Supercapacitors

Supercapacitor (SC) is an electrochemical device that consists of negative and positive separated by an appropriate electrolyte [2]. In 1879, Helmholtz invented the

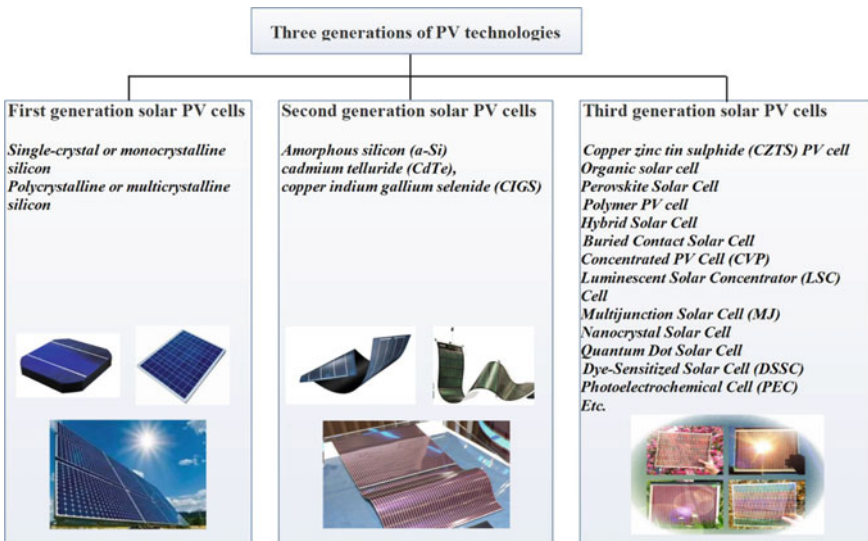


Fig. 1 Three generations of solar photovoltaic (PV) cells [8]. Copyright 2018, MDPI

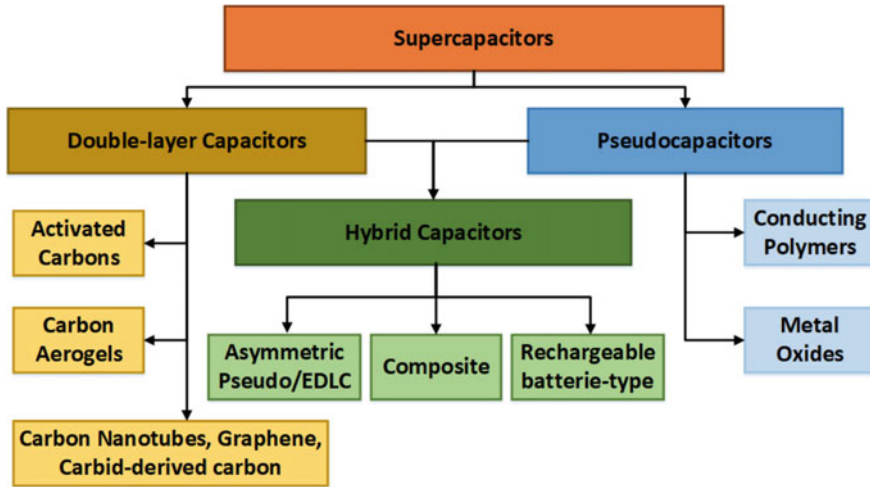
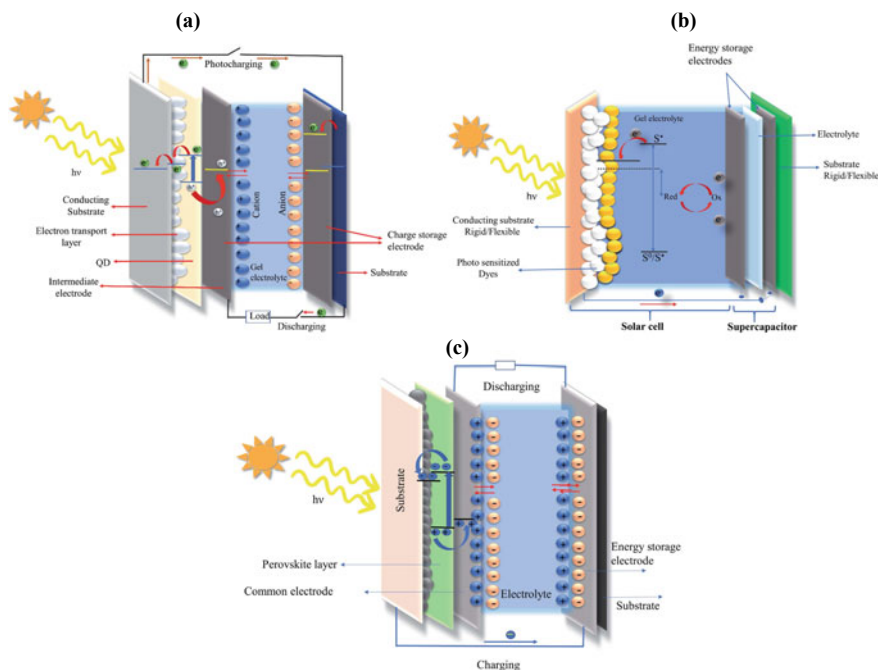


Fig. 2 Classification of supercapacitors [9]. Copyright 2023, Elsevier

very first electrochemical capacitor which was later in 1957 got patented by Becker. Despite showing excellent electrical properties, the capacitor showed inferior capacitance. Therefore, in 1975, B.E. Conway fabricated  $\text{RuO}_2$ -based capacitors and observed high efficiency and appreciable specific capacitance. Currently, depending on the charge storage mechanism and used electrode materials, SCs are classified broadly into three types: electrostatic double layer capacitors (EDLCs), pseudo or redox capacitors, and hybrid capacitors [7]. The configuration has been shown in Fig. 2.

### 3 Conclusions

The hybrid technology of PSC (using both storage system and energy harvesting in a single device) may soon be employed in space and military applications. It may be used as a power backup for electronic appliances. PSC can also be employed in hybrid electric vehicle (HEVs) and public transport. In this article, we have focused on the progress of PSC and its photo-electrochemical performance (Fig. 3).



**Fig. 3** Schematic illustration of **a** QDSC, **b** DSSC, and **c** PeSC based PSCs [3]. Copyright 2021, RSC

## References

1. Gani A (2021) Fossil fuel energy and environmental performance in an extended STIRPAT model. *J Clean Product* 297:126526
2. Ahmad S, Abbas H, Khan MB, Nagal V, Hafiz AK, Khan ZH (2021) ZnO for stable and efficient perovskite bulk heterojunction solar cell fabricated under ambient atmosphere. *Sol Energy* 216:164–170
3. Namsheer K, Rout CS (2021) Photo-powered integrated supercapacitors: a review on recent developments, challenges and future perspectives. *J Mater Chem A* 9(13):8248–8278
4. Manopriya S, Hareesh K (2021) The prospects and challenges of solar electrochemical capacitors. *J Energy Storage* 35:102294
5. Levi DH, Green MA, Hishikawa Y, Dunlop ED, Hohl-Ebinger J, Ho-Baillie AWY (2017) Solar cell efficiency tables (version 51). *Prog Photovolt* 26:70757
6. Suhail M, Abbas H, Khan MB, Khan ZH (2022) Chalcogenide perovskites for photovoltaic applications: a review. *J Nanopart Res* 24(7):142
7. Ahmed S, Ahmed A, Basha DB, Hussain S, Uddin I, Gondal MA (2023) Critical review on recent developments in conducting polymer nanocomposites for supercapacitors. *Synth Metals* 295:117326
8. Zhang T, Wang M, Yang H (2018) A review of the energy performance and life-cycle assessment of building-integrated photovoltaic (BIPV) systems. *Energies* 11(11):3157
9. Basha DB, Ahmed S, Ahmed A, Gondal MA (2023) Recent advances on nitrogen doped porous carbon micro-supercapacitors: new directions for wearable electronics. *J Energy Storage* 60:106581

# Enhanced Performance of Nanostructured WSe<sub>2</sub> as an Electrode Material for Supercapacitor



Asim Khan, Waseem Ashraf, Manika Khanuja, and Zishan Husain Khan

**Abstract** Since last few years, there has been a considerable rise in research focused on the engineering applications of 1D and 2D inorganic oxide-layered materials, with particular emphasis on transition metal dichalcogenides. However, despite WSe<sub>2</sub> being an important layered material with potential uses in energy storage and other areas, its investigation has been restricted due to issues concerning its synthesis and other related factors. Recently, researchers have discovered that the 2D form of WSe<sub>2</sub> can be successfully used in photodetectors, field effect transistors, and other novel optoelectronic devices. Our study aims to explore the potential of WSe<sub>2</sub> further by developing a cost-effective hydrothermal method for synthesizing WSe<sub>2</sub> nanostructures with enhanced performance. By employing a range of characterization techniques, including UV–vis spectroscopy, PL spectroscopy, FESEM, Raman spectroscopy, and X-ray diffraction, we were able to gain insights into the properties and structure of the synthesized material. Furthermore, we assessed the material’s applicability as an electrode material for supercapacitors by performing cyclic voltammetry to calculate its capacitance. Our work contributes to the expanding field of materials science and engineering, with a focus on energy storage, by providing new perspectives on the synthesis, characterization, and potential applications of WSe<sub>2</sub> nanostructures.

**Keywords** Energy storage · WSe<sub>2</sub> · Supercapacitors · TMDs · Hydrothermal method · FESEM · Cyclic voltammetry

---

A. Khan · Z. H. Khan (✉)

Department of Applied Sciences and Humanities, Jamia Millia Islamia, New Delhi, India  
e-mail: [zishanhk70@gmail.com](mailto:zishanhk70@gmail.com)

W. Ashraf · M. Khanuja

Centre for Nanoscience and Nanotechnology, Jamia Millia Islamia, New Delhi, India

## 1 Introduction

Lithium-ion batteries (LIBs) and supercapacitors (SCs) are currently addressing the commercial needs of handheld devices and electric cars. Supercapacitors, in other words ultracapacitors or electrochemical capacitors, have become a subject of significant scientific interest as advanced energy storage devices due to their unique properties such as ultrahigh power density, long operating lifetime, fast charging and discharging, safe operation, and low maintenance cost [1–5]. Supercapacitors are classified into two types based on the energy storage mechanism: electric double-layer capacitors (EDLCs) and pseudocapacitors. EDLCs store energy by physically adsorbing ions at the electrode/electrolyte interface, while pseudocapacitors store energy by transferring charges between the electrochemically active electrode surface and the electrolyte ions. Graphene and other 2D nanomaterials, such as transition metal dichalcogenides (TMDs), transition metal oxides (TMOs), phosphorene, and hexagonal boron nitride (hBN) have been gaining attention due to their exceptional physical and chemical properties as electrode materials [6–9]. TMDs and other transition metal chalcogenides (TMCs) have gained interest due to their high electrical conductivity, multiple oxidation states, high surface area, and theoretical specific power. Researchers have studied TMD nanomaterials, such as  $\text{TiS}_2$ ,  $\text{MoS}_2$ , and  $\text{WS}_2$ , for various applications, including energy storage and dye degradation due to their sheet-like morphology. Recently, layered tungsten diselenide ( $\text{WSe}_2$ ) has drawn attention due to its efficient electro/photocatalytic activity and acid stability. In this study, we explored the capacitive behavior of  $\text{WSe}_2$  nanosheets as an electrode material for supercapacitors [10–12].

## 2 Materials, Methods, and Instrumentation

The hydrothermal/solvothermal method is a low-cost synthesis method, by which a large quantity of products can be synthesized. Using this method, the preferred quantities of the  $\text{WSe}_2$  precursors, i.e., selenium (Se) powder, sodium borohydride ( $\text{NaBH}_4$ ), sodium tungstate dihydrate ( $\text{Na}_2\text{WO}_4 \cdot 2\text{H}_2\text{O}$ ) were mixed in dimethyl formamide (DMF) according to their atomic weight percentage. Then the mixture was kept into the Teflon-lined stainless steel autoclave in oven at 240 °C for 48 h. The temperature of the autoclave was brought down to room temperature by natural cooling process and blackish material was taken out from the autoclave which was then washed several times with DI water and ethyl alcohol ( $\text{C}_2\text{H}_5\text{OH}$ ) using vacuum filtration process and then dried at 60 °C under vacuum for 24 h. The final powder was then ground for 30 min using mortar pestle. Finally, the powder of the blackish material containing  $\text{WSe}_2$  nanosheets were obtained.

To confirm the formation of  $\text{WSe}_2$  nanosheets, X-ray diffractogram (XRD) of as produced nanosheets have been recorded using XRD (Smart Lab Guidance Rigaku) instrument. FESEM (Zeiss, Sigma) was used to study the morphology of the powder

sample. A single beam UV–vis spectroscopy (Perkin Elmer Lambda 365) was used for the purpose of bandgap.

### 3 Results and Discussion

#### 3.1 Structure and Morphology

The powder X-ray diffraction (XRD) pattern in Fig. 1a indicates that the as-synthesized WSe<sub>2</sub> nanoparticles are crystalline in nature. The main planar 2D peak is centered at  $2\theta$  (hkl) value of  $14.28^\circ$  (002). XRD patterns show that the diffraction peaks appear better resolved indicating better crystallinity. The peaks observed have also assigned to the hexagonal WSe<sub>2</sub> with a P63/mmc space group (ICDD No. 38-1388). Additionally, the XRD pattern also show a strong diffusive background and weak peaks, indicating that the WSe<sub>2</sub> layers are packed in a highly disordered manner with uneven stacking.

SEM image clearly shows the nanosheets of WSe<sub>2</sub>. Figure 1b shows the SEM image of the obtained nanosheets, which exhibit a clear sheet structure in the form of flower-like morphology. This suggests that the WSe<sub>2</sub> nanosheets synthesized in this

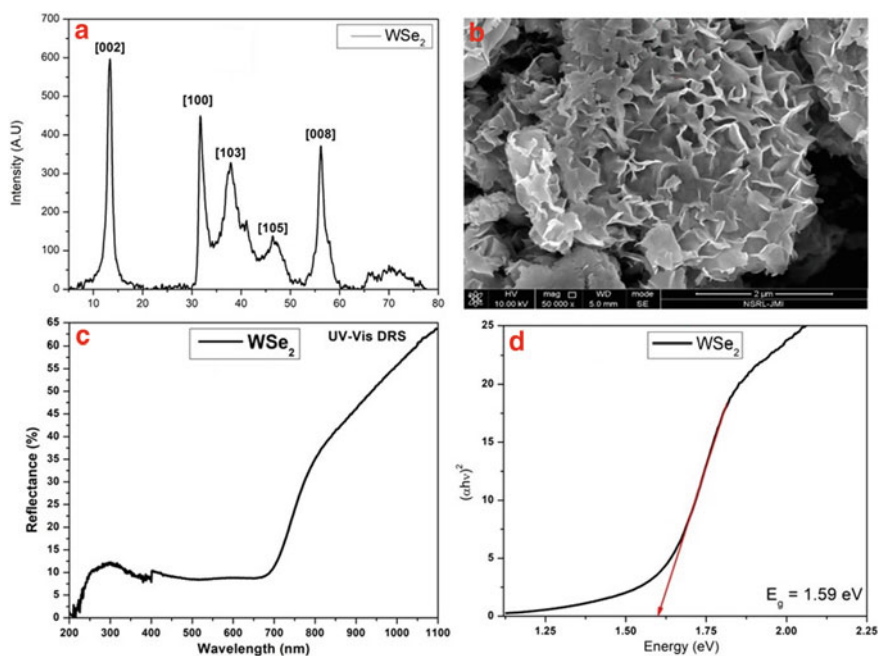


Fig. 1 a XRD, b SEM, c UV–vis DRS, and d Bandgap



study have a high surface area, which could potentially be useful for various applications. Furthermore, the electro transparency observed in the nanosheets are found to be high, indicating extremely low stacking in the sample which is in close alignment with XRD. This is a desirable characteristic for materials in electronic applications as it must facilitate the efficient electron transport. Overall, the morphology analysis of the synthesized WSe<sub>2</sub> nanosheets using SEM provides valuable insight into their structure and surface morphology.

The optical characterization of the sample has been performed using diffuse reflectance spectroscopy (DRS) Fig. 1c. The WSe<sub>2</sub> powder was used for DRS, the spectroscopic informations were obtained by analyzing the DRS data. Based on the UV–vis DRS spectra of WSe<sub>2</sub> Fig. 1c, the optical energy bandgap has been determined using Kubelka–Munk function,  $F(R)$ .

$$F(R) = (1 - R)^2/2R$$

where  $R$  is the diffuse reflectance recorded for the sample.

Extrapolating the Kubelka–Munk function plot to zero provides the values of the direct bandgap to be 1.59 eV for WSe<sub>2</sub> as shown in Fig. 1d. This bandgap suggests higher optical activity in visible and IR region of electromagnetic spectrum.

### 3.2 Electrochemical Analysis

The electrochemical property and ORR (oxygen reduction reaction) activity of WSe<sub>2</sub> nanostructures have been studied in an electrolyte solution (1 M Na<sub>2</sub>SO<sub>4</sub>), Fig. 2a shows the cyclic voltammetry (CV) curves of the sample measured at a range of potential scan rate from 20 to 100 mVs<sup>-1</sup>. The CV curves reveal that the WSe<sub>2</sub> exhibits higher current densities at higher scan rates. This indicates better electrochemical activity at higher scan rates when compared with lower scan rates. The corresponding

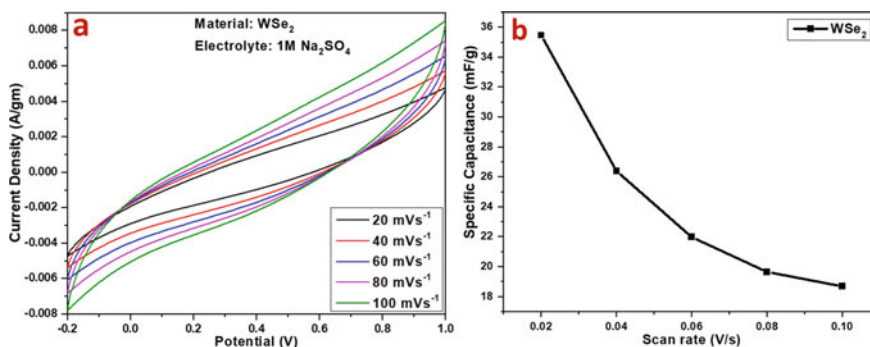


Fig. 2 a CV curves and b Capacitance versus scan rate

specific capacitance is shown in Fig. 2b, which shows higher capacitance at lower scan rates [13].

## 4 Conclusion

WSe<sub>2</sub> nanosheets were successfully synthesized using low-cost hydrothermal method for the application as an electrode material for supercapacitor applications. The higher specific capacitance of ~ 36 mF/g was obtained at a scan rate of 20 mV. The as-synthesized nanomaterial showed physical and chemical properties better than their bulk counterparts that showed the results are interesting and may be utilized in various applications such as energy storage, photocatalysis, gas and chemical sensing applications, and many others.

## References

1. Sajjad M, Cheng F, Lu W (2021) Research progress in transition metal chalcogenide-based anodes for K-ion hybrid capacitor applications: a mini-review. *RSC Adv* 11(41):25450–25460
2. Novoselov KS, Geim AK, Morozov SV, Jiang D, Zhang Y, Dubonos SV, Grigorieva IV, Firsov AA (2004) Electric field effect in atomically thin carbon films. *Science* 306(5696):666–669
3. Geim AK, Novoselov KS (2007) The rise of graphene. *Nat Mater* 6(3):183–191
4. Ashraf W, Khan A, Bansal S, Khanuja M (2022) Mechanical ball milling: a sustainable route to induce structural transformations in tungsten disulfide for its photocatalytic applications. *Phys E Low Dimens Syst Nanostruct* 140:115152
5. Chhowalla M, Shin HS, Eda G, Li LJ, Loh KP, Zhang H (2013) The chemistry of two-dimensional layered transition metal dichalcogenide nanosheets. *Nat Chem* 5(4):263–275
6. Xu M, Liang T, Shi M, Chen H (2013) Graphene-like two-dimensional materials. *Chem Rev* 113(5):3766–3798
7. Wang L, Sasaki T (2014) Titanium oxide nanosheets: graphene analogues with versatile functionalities. *Chem Rev* 114(19):9455–9486
8. Gupta A, Sakthivel T, Seal S (2015) Recent development in 2D materials beyond graphene. *Prog Mater Sci* 73:44–126
9. Tang Q, Zhou Z (2013) Graphene-analogous low-dimensional materials. *Prog Mater Sci* 58(8):1244–1315
10. Bhimanapati GR, Lin Z, Meunier V, Jung Y, Cha J, Das S, Xiao D et al (2015) Recent advances in two-dimensional materials beyond graphene. *ACS Nano* 9(12):11509–11539
11. Kannichankandy D, Pataniya PM, Sumesh CK, Solanki GK, Pathak VM (2021) WSe<sub>2</sub>-PANI nanohybrid structure as efficient electrocatalyst for photo-enhanced hydrogen evolution reaction. *J Alloys Comp* 876:160179
12. Ashraf W, Fatima T, Srivastava K, Khanuja M (2019) Superior photocatalytic activity of tungsten disulfide nanostructures: role of morphology and defects. *Appl Nanosci* 9:1515–1529
13. Singh D, Singh A, Ojha SK, Ojha AK (2023) Facile synthesis of layered 2H-WSe<sub>2</sub> nanosheets for asymmetric supercapacitor device application. *Synth Metals* 293:117263